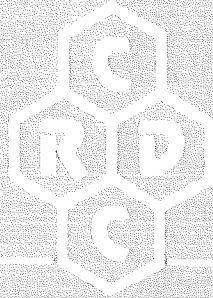


AD **A159697**



CHEMICAL
RESEARCH &
DEVELOPMENT
CENTER

CRDC-SP-84009

PROCEEDINGS OF THE
1983 SCIENTIFIC CONFERENCE
ON
OBSCURATION AND AEROSOL RESEARCH

Edited by JAN FARMER
RONALD H. KOHL

RONALD H. KOHL & ASSOCIATES
Tullahoma, TN 37388

PROPERTY OF U.S. AIR FORCE
AEDC TECHNICAL LIBRARY
ARNOLD AFB, TN 37389

JULY 1984

US Army Armament, Munitions & Chemical Command
Aberdeen Proving Ground, Maryland 21010

UNCLASSIFIED

SECURITY CLASSIFICATION OF THIS PAGE (When Data Entered)

REPORT DOCUMENTATION PAGE		READ INSTRUCTIONS BEFORE COMPLETING FORM
1. REPORT NUMBER CRDC-SP-84009	2. GOVT ACCESSION NO.	3. RECIPIENT'S CATALOG NUMBER
4. TITLE (and Subtitle) PROCEEDINGS OF THE 1983 SCIENTIFIC CONFERENCE ON OBSCURATION AND AEROSOL RESEARCH		5. TYPE OF REPORT & PERIOD COVERED Special Publication 1983 Scientific Conference
		6. PERFORMING ORG. REPORT NUMBER
7. AUTHOR(s) Edited by Jan Farmer and Ronald H. Kohl		8. CONTRACT OR GRANT NUMBER(s) DAAG29-81-D-0100, D.O.0512
9. PERFORMING ORGANIZATION NAME AND ADDRESS Ronald H. Kohl & Associates Route 2, Box 283B Tullahoma, TN 37388		10. PROGRAM ELEMENT, PROJECT, TASK AREA & WORK UNIT NUMBERS 1L161102A71A
11. CONTROLLING OFFICE NAME AND ADDRESS Commander, Chemical Research & Development Center ATTN: DRSMC-CLJ-IR (A) Aberdeen Proving Ground, Maryland 21010-5423		12. REPORT DATE July 1984
		13. NUMBER OF PAGES 407
14. MONITORING AGENCY NAME & ADDRESS (if different from Controlling Office) Commander, Chemical Research & Development Center ATTN: DRSMC-CLB-PS (A) Aberdeen Proving Ground, Maryland 21010-5423		15. SECURITY CLASS. (of this report) UNCLASSIFIED
		15a. DECLASSIFICATION/DOWNGRADING SCHEDULE NA
16. DISTRIBUTION STATEMENT (of this Report) Approved for public release; distribution unlimited.		
17. DISTRIBUTION STATEMENT (of the abstract entered in Block 20, if different from Report)		
18. SUPPLEMENTARY NOTES Prior to 1 July 1983, the Chemical Research and Development Center (CRDC) was known as the Chemical Systems Laboratory (CSL).		
19. KEY WORDS (Continue on reverse side if necessary and identify by block number)		
Obscurants	Absorption	Light
Obscuration	Extinction	Electromagnetic Scattering
Aerosol	Scattering	Sizing
Aerosols	Transmission	Millimeter Wave Radiation
Aerosol Properties	Smoke	Submillimeter Wave Radiation (continued)
20. ABSTRACT (Continue on reverse side if necessary and identify by block number) Forty-two papers on current or recent research are included under the headings of Physical and Chemical Properties of Aerosols, Aerosol Characterization Methods and Optical Properties of Aerosols.		

19. (continued)

Infrared	Optical Properties
Visible Radiation	Anomalous Diffraction
Electromagnetic Waves	Attenuated Total Reflection
Spherical Particles	Reflection Spectroscopy
Mie Scattering	ATR
Rayleigh Scattering	Far-Infrared
Raman Scattering	Refractive Index
Concentration Sampling	Index of Refraction
Particle Dynamics	Inversion
Plumes	Inversion Techniques
Diffusive Mixing	Gypsum
Aerosol Growth	Natural Minerals
Nucleation	Minerals
Smoke Generation	Metal
Aerosol Generation	Beamsplitters
Photoionization	Metallic Particles
Conductivity	Powdered Minerals
Chemical Characterization	Complex Refractive Index
Phosphorus Smoke	Effective Media
Fluorescence	High Energy Laser
Aerosol Clusters	Particles
Spheres	Aerosol Particles
Cylinders	Thermophoresis
Rough Particles	Magnetic Sphere
Irregular Particles	SERS
Nonspherical Particles	Surface Enhanced Raman Scattering
Particle Clusters	Dielectric Particles
Particle Aggregates	Conducting Particles
Particle Chains	Cylindrical Particles
Infrared Emission	Fibers
Cooperative Scattering	Conducting Fibers
Dependent Scattering	Aerosol Screens
Multiple Scattering	Gas-Aerosol Reactions
Radiative Transfer	Transport Phenomena
Coagulation	Aerosol Measurement
Condensation	Spheroids
Liquid Drop	Laser Pulses
Drop Growth	Target Signatures
Fog Oil Smoke	Optical Pulses
Diesel Oil Smoke	Pulse Propagation
Particle Mechanics	Clouds
Plume Mechanics	Laser
Atmospheric Optics	Radiation Transport
Atmospheric Dispersion	Analysis
Cloud Dynamics	Fourier Analysis
Scavenging	Polariton
Aerosol Collectors	
Aerosol Elimination	
Aerosol Characterization	
Particle Sizing	
Hygroscopic Smokes	
Particle Size Distribution	
Particle Orientation Distribution	
Optical Constants	

PREFACE

The 1983 Chemical Systems Laboratory Scientific Conference on Obscuration and Aerosol Research was held 20-24 June, 1983, at the Edgewood Area of Aberdeen Proving Ground, Maryland. The Conference is held annually, the last full week in June, under the direction of Dr. Edward W. Stuebing, Research Area Coordinator, Aerosol Science, from whom it receives its unique and productive character.

The Conference is an informal forum for scientific exchange and stimulation amongst investigators in the wide variety of disciplines required for a total description of an obscuring aerosol. The participants develop some familiarity with the Army aerosol/obscuration science research program and also become personally acquainted with the other investigators and their research interests and capabilities. Each attendee is invited to talk on any aspect of a topic of interest and may make last minute changes or alterations in his talk as the flow of ideas in the Conference develops.

While all participants in the Conference are invited to submit written papers for the Proceedings of the Conference, each investigator who is funded by the Army Smoke Research Program is requested to provide one or more written papers which document specifically the progress made in his funded effort in the previous year and which indicate future directions. Also, the papers for the Proceedings are collected in the fall to allow time for the fresh ideas which arise at the Conference to be incorporated. Therefore, while the papers in these proceedings tend to closely correspond to what was presented at the Conference, there is not an exact correspondence.

The reader will find the items relating to the Conference itself, the list of attendees, the agenda, and the contents of the Conference sessions in the appendixes following the Proceedings papers and the indexes pertaining to them.

The use of trade names in these proceedings does not constitute an official endorsement or approval of the use of such commercial hardware or software. These proceedings may not be cited for purposes of advertisement.

Reproduction of this document in whole or in part is prohibited except with permission of the Commander, Chemical Research and Development Center, ATTN: DRSMC-CLJ-IR (A), Aberdeen Proving Ground, Maryland 21010. However, the Defense Technical Information Center is authorized to reproduce the document for United States Government purposes.

This report has been approved for public release.

BLANK

CONTENTS*

	Page
I. PHYSICAL AND CHEMICAL PROPERTIES OF AEROSOLS	9
A. <u>Particle Formation, Evolution and Composition</u>	
CHEMICAL CHARACTERIZATION OF SELECTED MILITARY OBSCURANTS R. S. Brazell, R. W. Holmberg and J. H. Moneyhun	11
AN INVESTIGATION OF A CRYOGENIC MATRIX ISOLATION APPROACH FOR CHARACTERIZING PHOSPHORUS ACID AEROSOL A. Snelson	23
THE PHOTOIONIZATION OF CLUSTERS AND THE ONSET OF METALLIC CONDUCTIVITY A. W. Castleman, Jr.	25
AEROSOL GENERATION: STUDIES OF NUCLEATION AND GROWTH PROCESSES J. R. Brock	35
B. <u>Plume Mechanics</u>	
DIFFUSIVE MIXING PROCESSES J. Latham	41
C. <u>Particle Dynamics: Orientation Effects, Concentration Sampling, and Size/Shape Analysis</u>	
THE ORIENTATION DISTRIBUTION OF NONSPHERICAL AEROSOL PARTICLES IN THE ATMOSPHERE; NEW DEVELOPMENTS Isaiah Gallily and E. M. Krushkal	49
MEASUREMENT OF THE KINETICS OF SOLUTION DROPLETS IN A CONTINUOUSLY MIXED CHAMBER G. O. Rubel and J. W. Gentry	59
TIME EVOLUTION OF PARTICLE SIZE DISTRIBUTION DURING AEROSOL COAGULATION K. W. Lee, H. Chen and J. A. Gieseke	71
D. <u>Aerosol Elimination</u>	
AEROSOL ELIMINATION WITH CHARGED SCAVENGERS Daryl L. Roberts	83
PROGRESS IN THE CLEARING OR MODIFYING OF AEROSOL CLOUDS BY SCAVENGING TECHNIQUES J. Podzimek and J. J. Martin	99
II. AEROSOL CHARACTERIZATION METHODS	113
A. <u>Particle Shape Descriptions and the Value of Effective Size Parameters</u>	
WHAT IS THE PHYSICAL MEANING OF A "SIZE" OF A NONSPHERICAL AEROSOL PARTICLE? FALLACIES AND POSSIBLE SOLUTIONS Isaiah Gallily	115

*See also page 375 for the indexes of the authors and the organizations of the authors.

II. AEROSOL CHARACTERIZATION METHODS (continued)	
B. <u>Optical Inversion Methods for Size Distribution (Including Optical Particle Size Analyzers)</u>	
A NEW METHOD OF MULTI-SPECTRAL INVERSION BASED ON THE ANOMALOUS DIFFRACTION MODEL	
James D. Klett	121
A CONSTRAINED EIGENFUNCTION EXPANSION METHOD AND A NONLINEAR REGRESSION PROCEDURE FOR THE INVERSION OF MIE SCATTERING DATA	
B. P. Curry and E. L. Kiech	125
QUANTITATIVE DETERMINATION OF THE EFFECTS OF CONSTRAINTS ON SOLUTIONS TO INVERSION PROBLEMS	
C. D. Capps and G. M. Hess	139
C. <u>Optical Constants of Liquids and Powders</u>	
ATR METHOD FOR DETERMINING OPTICAL CONSTANTS OF POWDERS	
V. P. Tomaselli and K. D. Möller	141
OPTICAL PROPERTIES OF COMPRESSED POWDERS	
Marvin R. Querry	147
OPTICAL PROPERTIES OF MINERALS AT MILLIMETER AND SUBMILLIMETER WAVELENGTHS	
M. A. Ordal, L. L. Long, R. J. Bell and R. W. Alexander, Jr.	159
OPTICAL PROPERTIES OF METALS IN THE SUBMILLIMETER AND MILLIMETER WAVELENGTHS	
R. E. Paul, M. A. Ordal, L. L. Long, R. W. Alexander, Jr., and R. J. Bell	161
CAPACITIVE GRID BEAMSPLITTERS FOR FAR-INFRARED AND MILLIMETER WAVE INTERFEROMETERS	
K. D. Möller and V. P. Tomaselli	171
III. OPTICAL PROPERTIES OF AEROSOLS	183
A. <u>Infrared Emission from Aerosols</u>	
IR EMISSIVE CLOUD STUDY	
P. Ase, R. Remaly and A. Snelson	185
B. <u>Nonlinear Phenomena at High Energy</u>	
INTERACTION OF A 5 kW LASER BEAM WITH PARTICULATE AEROSOLS	
H. L. LaMuth, P. P. Balog and K. W. Lee	187
HIGH ENERGY LASER INTERACTION WITH MATTER	
M. Lax	191
C. <u>Interaction of Radiation and Spherical (Including Layered) Particles</u>	
LASER ENHANCED THERMOPHORETIC DEPOSITION	
T. F. Morse and J. W. Cipolla, Jr.	193
ELECTROMAGNETIC SCATTERING BY MAGNETIC SPHERE	
Milton Kerker	207
FLUORESCENCE BY MOLECULES EMBEDDED IN SMALL PARTICLES	
Milton Kerker	209
SURFACE ENHANCED RAMAN SCATTERING (THEORY)	
Milton Kerker	211
SURFACE ENHANCED RAMAN SCATTERING (EXPERIMENTS)	
Milton Kerker	213
SCATTERING CROSS SECTIONS FOR LARGE FINITELY CONDUCTING SPHERES WITH ROUGH SURFACES--FULL WAVE SOLUTIONS	
Ezekiel Bahar and Swapan Chakrabarti	215

III. OPTICAL PROPERTIES OF AEROSOLS (continued)

D. Interaction of Radiation and Nonspherical Particles (Including Aggregates)
with or without Cooperative Effects

EXTINCTION BY DUMBBELLS AND CHAINS OF SPHERES R. T. Wang	223
ANGULAR SCATTERING AND POLARIZATION BY RANDOMLY ORIENTED DUMBBELLS AND CHAINS OF SPHERES R. T. Wang and B. Å. S. Gustafson	237
FOURIER ANALYSIS OF LIGHT SCATTERED FROM NONSPHERICAL PARTICLES C. D. Capps, R. L. Adams, A. R. Tokuda and G. M. Hess	249
TRIANGULAR SURFACE PATCH MODEL FOR TEMPERATURE RISE CALCULATIONS FOR THIN SHELL PARTICLES--TRIANGULAR SURFACE PATCH MODELS D. T. Auckland, C. C. Cha and R. H. Andreo	257
STRUCTURE OF POLARITON MODES H. Weil and T. B. A. Senior	273
PERTURBATION THEORY FOR SCATTERING FROM DIELECTRIC SHORT CYLINDERS R. D. Haracz, L. D. Cohen and A. Cohen	281
NEW THEORETICAL APPROACH TO SCATTERING FROM THIN FIBERS Melvin Lax and Gælen Daum	293
EXTINCTION OF ELECTROMAGNETIC RADIATION BY FINE CONDUCTING FIBERS D. H. Holze, C. D. Capps and G. M. Hess	309
ELECTROMAGNETIC THEORY OF SCATTERING AND ABSORPTION FROM FINITE ELONGATED OBJECTS Jeanne C. Pedersen, Norman E. Pedersen and Peter C. Waterman	315
THEORETICAL INVESTIGATION OF FIBERS D. L. Dye, D. H. Holze and G. M. Hess	329

E. Propagation/Multiple Scattering in Aerosol Media and Radiative Transfer

DOUBLE SCATTERING BY RANDOMLY ORIENTED LONG CYLINDERS Ariel Cohen, Leonard Cohen, Richard Haracz and Smadar Egert	337
MULTIPLE-SCATTERING-INDUCED FALSE TARGETS A. Zardecki, S. A. W. Gerstl and J. F. Embury	343
COMPUTATION OF RADIATIVE TRANSFER Peter C. Waterman, Jeanne C. Pedersen and Norman E. Pedersen	355
MULTIPLE SCATTERING OF OPTICAL PULSES IN SCALE MODEL CLOUDS Richard A. Elliott	367

INDEXES FOR PAPERS IN THESE PROCEEDINGS.	375
--	-----

A. Index of Authors.	377
B. Index of Authors' Organizations	379

APPENDIXES	381
----------------------	-----

A. Photographs of Conference Attendees	383
B. List of Conference Attendees.	389
C. Conference Agenda	399
D. Contents of the Conference Sessions	401

BLANK

I. PHYSICAL AND CHEMICAL PROPERTIES OF AEROSOLS

	PAGE
A. PARTICLE FORMATION, EVOLUTION AND COMPOSITION	11
B. PLUME MECHANICS	41
C. PARTICLE DYNAMICS: ORIENTATION EFFECTS, CONCENTRATION SAMPLING, AND SIZE/SHAPE ANALYSIS	49
D. AEROSOL ELIMINATION	83

BLANK

CHEMICAL CHARACTERIZATION OF SELECTED MILITARY OBSCURANTS

R. S. Brazell, R. W. Holmberg, and J. H. Moneyhun
Oak Ridge National Laboratory
Oak Ridge, Tennessee 37831

ABSTRACT

Various smokes and obscurants have been analyzed and defined chemically in support of inhalation toxicology studies designed to evaluate the risk associated with passive or accidental troop exposure. The chemical characterization is to identify constituents useful for monitoring the exposure environment to assure a compositionally uniform aerosol for the exposure studies and to assist in evaluating the toxicological hazards. The characterization also allows for comparisons of the smokes produced under controlled laboratory conditions and those produced under more variable field conditions to assess the relevancy of the inhalation studies. Smokes which have been examined include those produced from diesel oil, fog oil, red phosphorus containing butyl rubber, and white phosphorus contained in a felt matrix. The results on the diesel oil will be submitted for publication as follows:

R. A. Jenkins, R. W. Holmberg, J. S. Wike, and J. H. Moneyhun, "The Chemical and Physical Characterization of Diesel Fuel Smoke in Inhalation Exposure and Toxicology Studies," Final Report, USAMBRDL (1983).

Reports on the chemical characterization of red phosphorus which contain comparative data on white phosphorus will be submitted as follows:

R. S. Brazell, R. W. Holmberg, and J. H. Moneyhun, "Application of HPLC/Flow Injection Analysis for the Determination of Polyphosphoric Acids in Phosphorous Smokes," J. of Chromatogr. (1983).

R. S. Brazell, R. W. Holmberg, J. H. Moneyhun, and D. D. Pair, "Physical and Chemical Characterization of Red Phosphorous Butyl Rubber Smoke," USAMBRDL (1983).

A brief discussion of the major findings on all the smokes is included in this report. Specific compositional changes which relate to the generation environment will also be described for some aerosols.

RED AND WHITE PHOSPHOROUS SMOKES

Red phosphorous butyl rubber (RPBR) smoke has been produced at steady concentrations with an extrusion combustion generator developed at ORNL (1). In this system the RPBR is extruded through a small orifice at a constant rate. The emerging filament is burned, and the resulting smoke is delivered to an exposure chamber. The concentration of the aerosol is controlled by the extrusion rate and air flow. The humidity is controlled by adding dry air or steam to the feed stream air. Samples for analysis are collected directly from the exposure chamber.

The combustion of phosphorus in air produces phosphorous pentoxide (P_4O_{10}) which immediately hydrates with the moisture present in air to form a dense white cloud composed of a complex

mixture of phosphoric acids. Despite the appreciable organic content of the RPBR formulation (5% butyl rubber) which is also burned, the concentration of organic compounds in the gas phase and particulate phase has been found to be very low. The particulate phase contains less than 0.04% of organic materials.

Chemically the aerosol may be regarded as an aqueous solution of phosphoric acids. Individual phosphoric acids have been resolved by thin layer chromatography, nuclear magnetic resonance, and by high performance anion exchange chromatography using a specific post column detector. The latter method of determination provided the greatest amount of resolution, fastest analysis time, and the highest specificity. Since it also provided quantitative data, it was the method routinely used to characterize the aerosol.

A typical chromatogram showing individual separated phosphoric acids is shown in Figure 1. The sample was collected at an aerosol concentration of 1.8 mg/L, 58% relative humidity, 20°C chamber temperature, and 252 m/min air velocity (250 L/min air flow) across the burn site. The first peak corresponds to orthophosphoric acid and the remaining peaks to pyrophosphate, tripolyphosphate, etc., up to the P₁₃ polymer. All of these peaks are straight chain linear phosphates. The large "envelope" is believed to be an unresolved mixture of longer straight chain (> P₁₄), branched, and cyclic polyphosphates. Analysis of the samples on a column which provided greater resolution allowed determinations up to the P₁₈ polymer, but since the concentration of these higher species was very low they were not routinely determined. None of the lower valent oxy acids of phosphorus were detected. Tetrameta- and trimetaphosphate were found to contribute less than 1% of the total amount of phosphate each. They eluted at 42.5 and 53 min, respectively, in the chromatogram shown.

The composition of the aerosol as a function of various generator conditions was investigated and the results for the acids are shown in Table I. There were only slight variations in the contributions of each species with no major compositional differences as the concentration was varied. As the chamber humidity was varied from 20 to 100%, however, some differences were noted (e.g., the concentration of the higher polymers increased with humidity and the level of orthophosphate decreased). These changes probably occur because of the increased rate of depolymerization due to the increased acidity of the aerosol at low humidities. As the air velocity was increased across the burn site only slight changes occurred.

A study was also conducted to partially simulate the aging process of the phosphorous smoke cloud in the field. This involved sealing the exposure chamber to prevent loss of the aerosol once a steady state concentration had been established. Samples were then withdrawn periodically and over a two hour period it was determined that the unresolved "envelope" almost completely disappeared while the concentration of orthophosphates and the lower polymeric forms increased. Again these transitions

probably occur because of the rapid hydrolytic depolymerization of the polymers in the acid aerosol. Exact compositional changes are outlined in Table I and a profile of an aged and unaged aerosol sample is shown in Figure 2.

Smoke from RPBR and WP-F was also produced under free-burning conditions which are expected to more closely simulate the smoldering, ground-burning conditions that occur in the field. These samples were analyzed to evaluate the similarities of the generator vs free-burn and RPBR vs WP-F smokes. The HPLC profiles for the two formulations were very similar with regard to the number of compounds detected and their concentration levels. P₁₁ was the highest polymeric phosphate found and no cyclic compounds were determined. Contributions for the individual phosphates are shown in Table I. The major difference between the generator and free burn aerosols was the absence of higher polymeric forms in the free burn. Some differences are expected, however, since the burn rate and temperature are not controlled in the latter.

Particle size distribution for the RPBR aerosol was determined using a Mercer type cascade impactor. In general, the mass median size was slightly affected by concentration and humidity (up to 80%) and considerably affected by aerosol age. All determinations gave mass median diameters of less than 1 μm except with the aged aerosol where mass median diameters up to 1.5 μm were observed after 20 min in the closed chamber. Statically burned RPBR and WP-F produced smokes having diameters slightly greater than 1 μm . Overall, the aerosols were within the respirable range.

DIESEL AND FOG OIL SMOKES

Smoke from diesel and fog oil have been produced under laboratory conditions by injecting the fuel onto a Vycor heater at 600°C (2). The vaporized fuel is swept into a stream of air by nitrogen carrier gas and as the fuel contacts the cooler air it condenses to form a smoke cloud. The resulting smoke is delivered to the exposure chambers from which samples for analysis are collected.

Diesel fuel is a complex mixture of aromatic and aliphatic hydrocarbons which corresponds to the crude petroleum fraction distilling from 160° to 370°C. The exposure atmosphere contains a liquid particle phase and lower boiling components in the gas phase. Both phases have been sampled and characterized. High performance liquid chromatography (HPLC) and high resolution gas chromatography (HRGC) provided the greatest resolution for individual constituents and were used for the analyses.

The amount of fuel in the vapor phase was estimated by measuring the change in the apparent concentration of a non-volatile tracer in the particulate phase of the aerosol. This approach has been previously described (3). As the aerosol concentration was varied from 0.96 mg/L to 6.88 mg/L the vapor phase concentration varied from 0.31 mg/L to 1.08 mg/L with an average value of 22% remaining in the vapor phase (range 11-30%). An independent direct method of analysis which involved trapping the

vapor phase constituents was used to examine the aerosol concentration between 0.26 and 1.0 mg/L. These results gave an average value of 12% of the fuel in the vapor phase. Overall, the data showed that the vapor concentration increased with increasing particle concentration. An HRGC profile comparing the fuel, particulate phase and vapor phase is shown in Figure 3.

The particulate phase was separated by HPLC into fractions and each of these analyzed by HRGC. The first fraction contained straight and branched chain hydrocarbons from n-C₁₁H₂₄ to n-C₂₀H₄₂. The remaining fractions contained one, two, and three ringed aromatic compounds, respectively. The concentrations of the more volatile hydrocarbons and alkyl substituted benzenes were lower in the particulate phase than in the actual fuel. All other constituents were present at approximately the same level as found in the neat fuel. Figure 4 shows a typical HPLC profile and GC analysis of two fractions of the particulate phase. Specific compounds were identified by GC/Mass Spectrometry.

The particle size distribution was determined by cascade impactor samples, and mass median diameters ranging from 0.5 to 1 µm were found.

Fog oil is a higher distilling fraction of crude petroleum than diesel oil. It is also a very complex mixture of compounds found to contain approximately 30% by weight aromatic and 70% by weight aliphatic hydrocarbons as determined by fourier transform nuclear magnetic resonance. Most individual constituents are unresolvable by GC without prior fractionation by HPLC. The HPLC profiles were very similar to those obtained for diesel. Figure 5 shows the results obtained for the HRGC analysis of the two-ringed aromatic fraction. Although many of the peaks were resolved, many of the constituents were unseparable as evidenced by the large "envelope".

REFERENCES

1. R. W. Holmberg and J. H. Moneyhun, "A System for the Continuous Generation of Phosphorous Aerosol from Red Phosphorous Butyl Rubber," Proc., Smoke/Obscurants Symposium VI, Adelphi, MD, April 27-29, 1982, pp. 767-775.
2. R. W. Holmberg, J. H. Moneyhun, and T. M. Gayle, "Chemical Characterization and Toxicologic Evaluation of Airborne Mixtures: Generating, Monitoring, and Controlling Petroleum Aerosols for Inhalation Chamber Studies," ORNL/TM-8903, Oak Ridge National Laboratory, Oak Ridge, TN (in press).
3. R. A. Jenkins, T. M. Gayle, J. S. Wike, and D. L. Manning, "Toxic Materials in the Atmosphere," ASTM STP 786, 1982, pp. 153-166.

ACKNOWLEDGEMENT

Research supported under Army Project Order No. 9600 by the U. S. Army Medical Research and Development Command, Fort Detrick, Frederick, MD 21701, performed at Oak Ridge National Laboratory under U. S. Department of Energy contract W-7405-eng-26 with the Union Carbide Corporation.

TABLE I. COMPOSITION OF THE PHOSPHORIC ACIDS IN PHOSPHOROUS SMOKES

Parameter Under Investigation	Generation Conditions			Composition (%)						
	Air Velocity (m/min)	% Relative Humidity	Aerosol Concentration (mg PO ₄ ⁻³ /l)	ortho-Phosphate	pyro-Phosphate	tripoly-Phosphate	tetrapoly-Phosphate	P ₅ -P ₁₃	Higher Polyphosphates	
Humidity	252	20	1.4	20.0	7.9	5.4	6.3	27.1	32.8	
		45		17.6	4.9	6.0	6.2	34.8	29.1	
		58		7.1	2.1	3.0	2.6	17.2	67.4	
		80		4.9	1.8	2.6	2.5	17.3	69.8	
		100		4.0	1.9	2.5	3.0	17.7	69.7	
Air Velocity	123	45	1.3	15.0	3.9	4.7	4.8	30.5	40.7	
	252			17.6	4.9	6.0	6.2	34.8	29.1	
	493			22.2	5.0	6.3	7.4	43.5	13.4	
Aerosol Concentration	252	51	0.8	17.6	7.7	5.7	5.7	26.3	36.9	
			2.0	12.4	4.1	4.1	4.5	26.9	48.0	
			4.6	16.8	7.7	5.8	6.2	30.3	33.2	
Aerosol Age	252	30	1.5	9.5	3.6	3.9	4.5	24.3	53.3	
				Unaged	16.6	7.0	3.4	3.0	12.1	57.9
				30 min	31.6	14.0	5.5	4.7	15.2	29.0
				60 min	49.0	22.1	7.2	5.4	13.9	2.4
Free Burning	252	38								
				RPBR	1.7	22.8	19.6	13.3	11.5	32.8
WP-F			2.1	23.8	26.6	16.3	11.3	22.0	--	

ORNL-DWG 83 - 17112

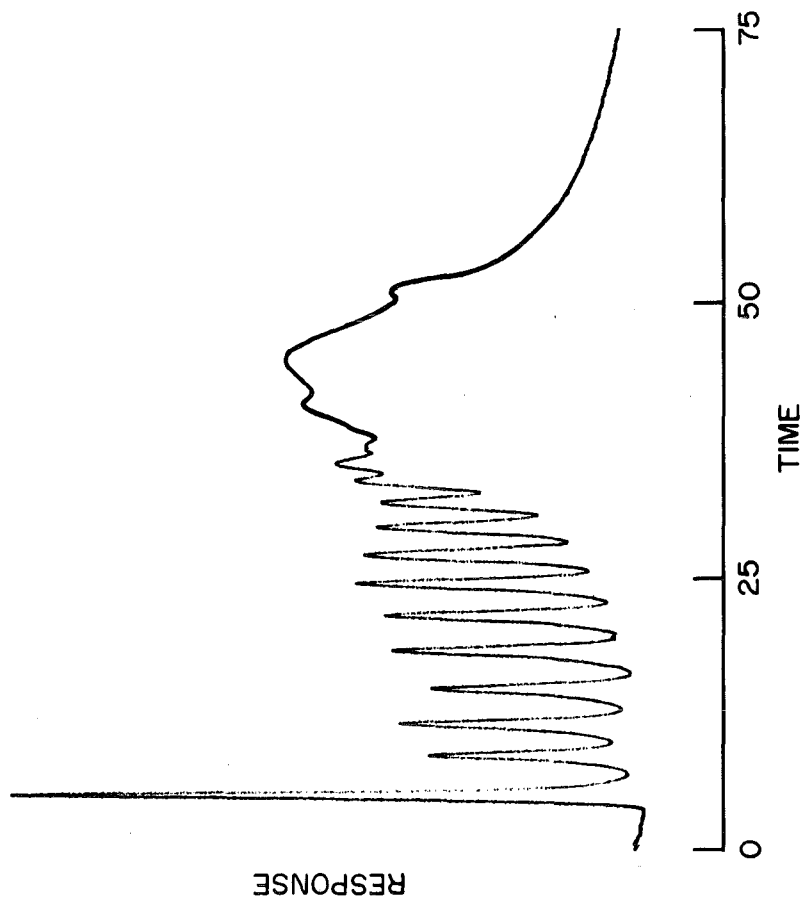


Figure 1. Phosphoric acids in generator produced RPBR aerosol.

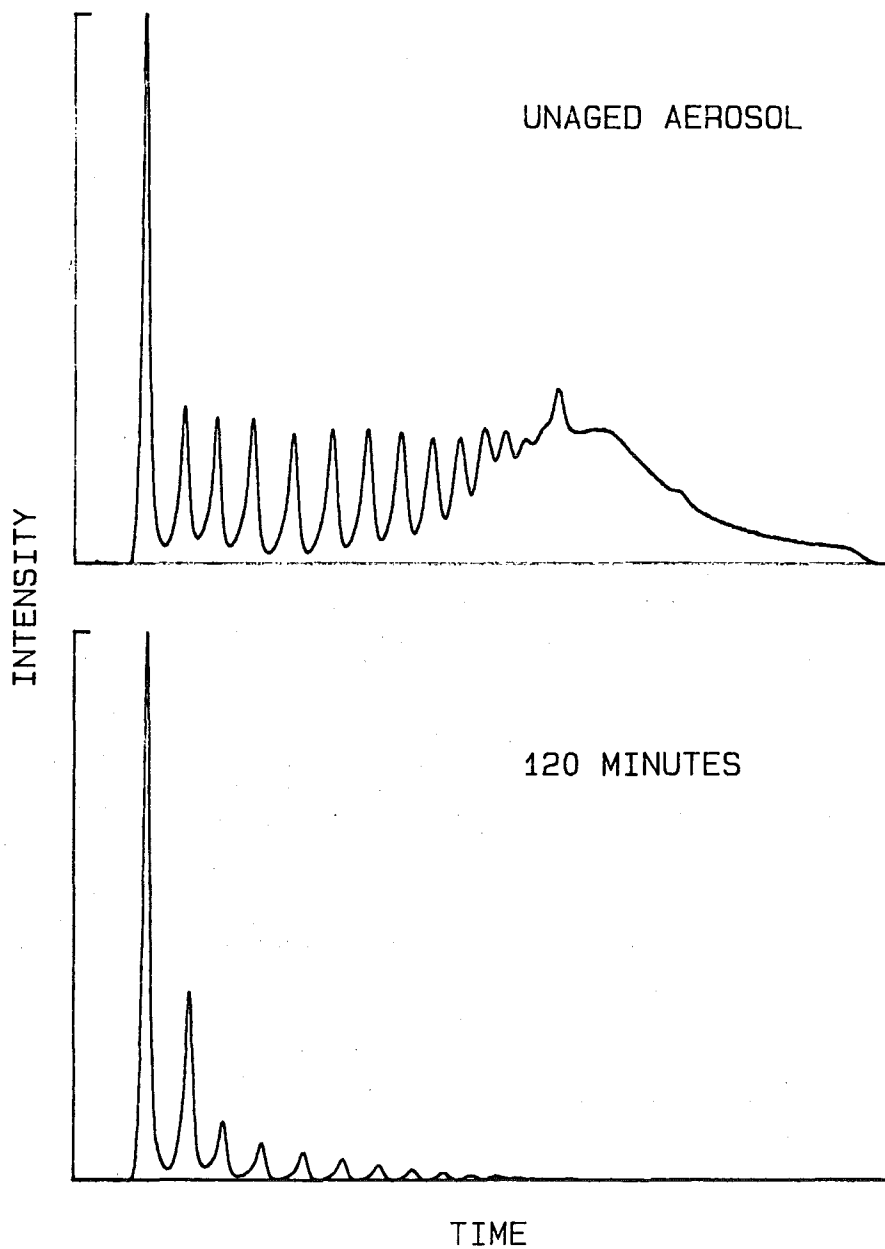


Figure 2. Aged (120 min) and unaged RPBR aerosol. HPLC profiles of phosphoric acids.

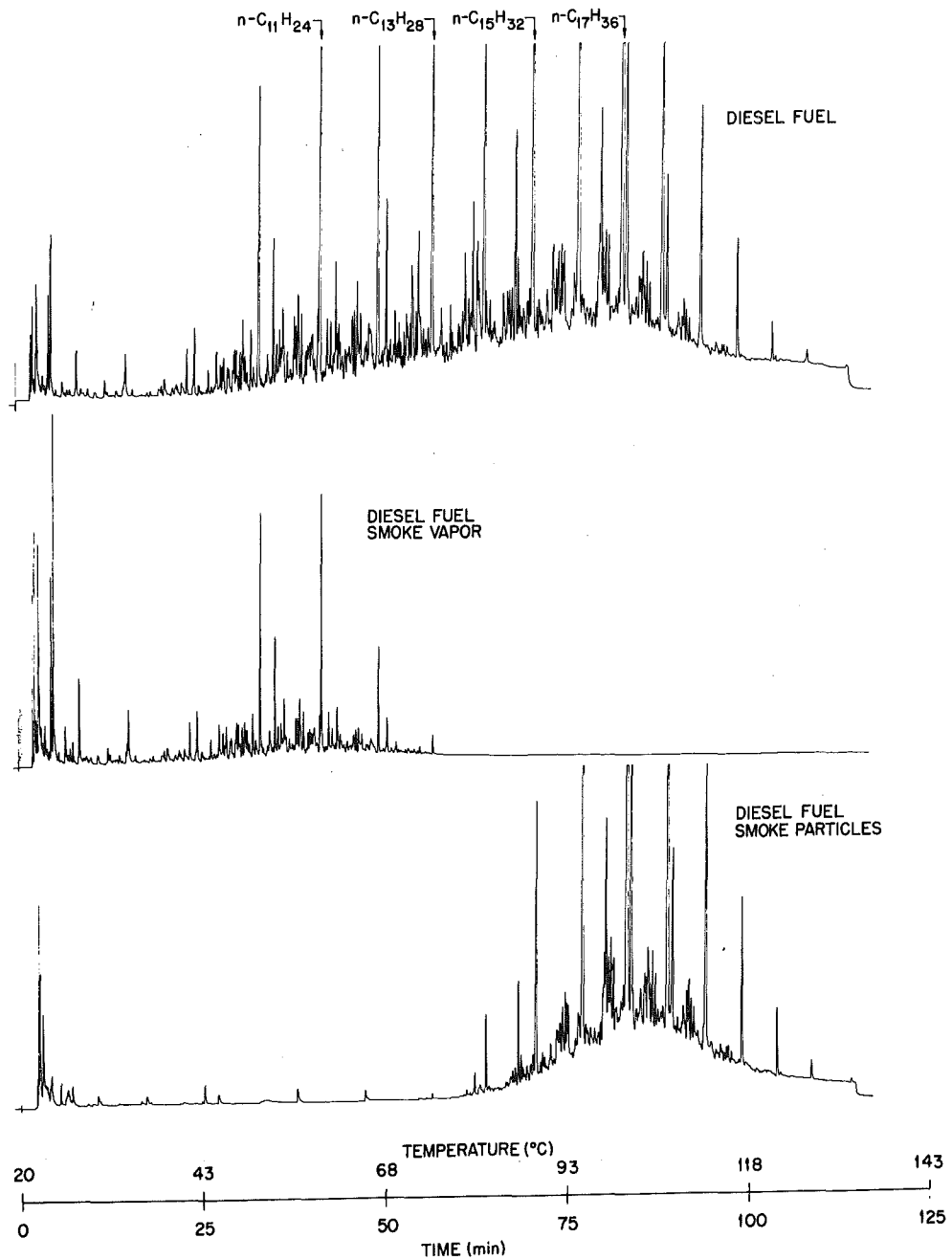


Figure 3. Comparisons of diesel fuel and vapor and particulate phases of diesel smoke. HRGC profiles obtained on 30 meter SE-52 fused silica capillary column.

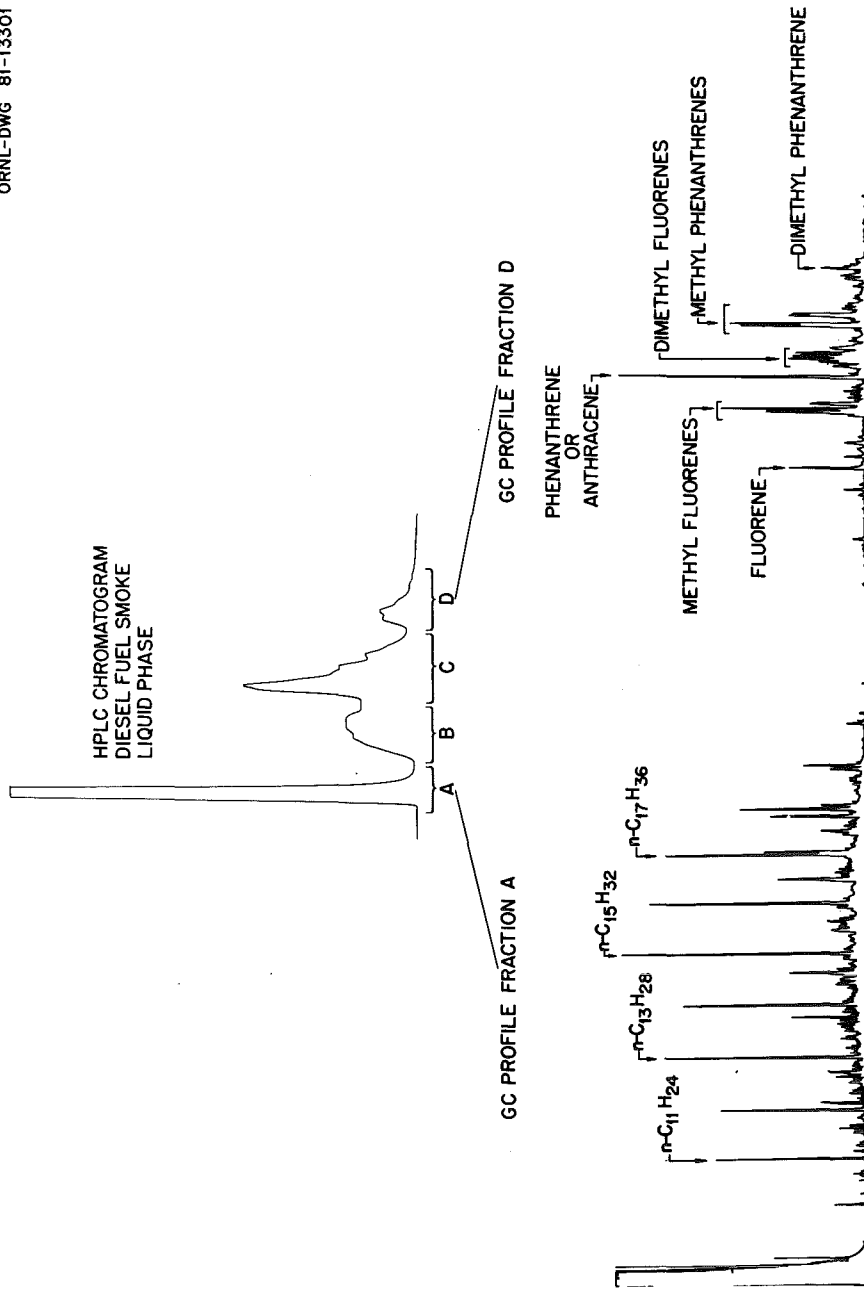


Figure 4. Profiles of diesel smoke particulate phase. HRGC of the aliphatic and three-ringed aromatic HPLC fractions on a 30 m SE-52 capillary column.

ORNL DWG 83-14017

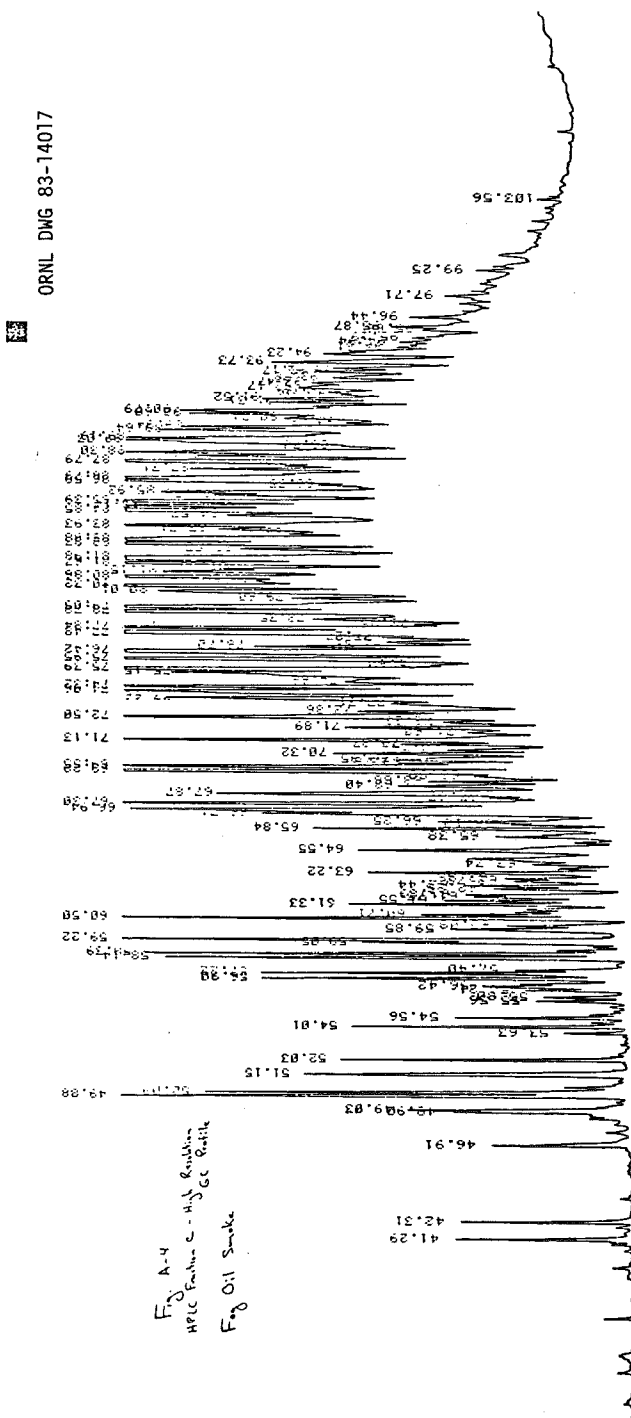


Figure 5. Two-ringed aromatic fraction of fog oil. HRGC on 30 m SE-52 capillary column.

BLANK

AN INVESTIGATION OF A CRYOGENIC MATRIX ISOLATION APPROACH
FOR CHARACTERIZING PHOSPHORUS ACID AEROSOL

A. Snelson
IIT Research Institute
Chicago, Illinois 60616

ABSTRACT

A matrix isolation cryostat has been adapted to sample gas streams containing aerosols for the latter's subsequent analysis by infrared spectroscopy. The aerosol sampling was made in basically one of two modes: 1) the aerosol and its carrier gas were both condensed at 10K on the IR transmitting surface; or 2) the aerosol alone was condensed on the IR transmitting surface maintained at a temperature insufficient to condense the carrier gas. IR spectra of the condensed air + aerosol or the aerosol alone were then obtained. By suitably varying the temperature of the IR transmitting surface, the air was distilled off leaving the aerosol behind. For aqueous aerosols containing non-volatile solutes, the water could be partially or completely removed by raising the temperature of the condensed material to approximately 200K followed by recooling to 10K for spectral analyses.

The new aerosol sampling and analytical approach has been applied to determine the composition of smokes resulting from burning red or white phosphorus in air. Reference spectra of aqueous aerosols of the following phosphorus acids were obtained: H_3PO_2 , D_3PO_2 , H_3PO_3 , H_3PO_4 , $H_4P_2O_7$, polyphosphoric acids and $(HPO_3)_n$. The cryogenic spectra of these aqueous acids showed improved spectral resolution compared to their ambient temperature solution counterparts. The dehydration procedure noted above resulted in spectra of much improved quality. For H_3PO_2 and D_3PO_2 , isotope frequency shift data were used to make a new vibrational assignment for these species.

Comparison of the cryogenic phosphorus acid reference spectra with those of the aerosol obtained from burning red and white phosphorus in air at $\approx 50\%$ relative humidity indicates the latter did not correspond to any one individual acid or to a simple mixture thereof. A few experiments were made in which phosphorus was burned in air at relative humidities from 0 to 25%, with residence times in the reactor before sampling of from 1.2 to 10 seconds. The spectral data so obtained indicated that the initial hydrolysis product had a strong absorption feature at $\approx 7.5 \mu$ which moved to longer wavelengths as the extent of hydrolysis increased. The origin of this band (not found in any of the reference phosphorus acid spectra) and its relation to the anomalous 8μ feature of phosphorus smokes are discussed.

The above study was supported by the Chemical Systems Laboratory, U.S. Army Research and Development Command under Contract No. DAAK11-81-K0007. The final report was submitted June 1983.

BLANK

THE PHOTOIONIZATION OF CLUSTERS AND THE ONSET OF METALLIC CONDUCTIVITY

A. W. Castleman, Jr.
Department of Chemistry
The Pennsylvania State University
University Park, PA 16802

INTRODUCTION

Currently work on the problem of nonmetallic-metallic transition and the onset of metallic conductivity is being very actively pursued in many laboratories (1). The findings from such studies have wide ranging applied as well as fundamental implications. Germane to the subject matter of this conference is the problem of determining the dependence of metallic conductivity on size, which has a direct bearing on the complex refractive index of conducting systems. Aerosols comprised of metal particles, or their partially oxidized compounds, are frequently made up of very small sized primary particles. These individual aggregated particles often have only limited points of contact through which conducting electrons can pass from one to the other. Another area of aerosol science to which studies described in this paper are relevant is that of the changing ionization potential of a system as a function of the degree of clustering. The ability of particles to acquire charge through interaction with atmospheric ions or to undergo charge transfer with other particles is directly related to this factor on which there is currently a paucity of experimental data. Work in our laboratory is being pursued to provide information of changing ionization potentials and hence information on work functions of both conducting aggregates and clusters comprised of single and mixed component dielectrics.

Other areas to which such results have important implications include surface science, especially regarding the physical basis for catalysis and the forces responsible for the absorption of substances on surfaces (2,3). Data on the work function of sub-micron systems is also relevant to the field of microelectronics and printed circuits. Finally, results in this field provide basic data crucial in furthering an understanding of the properties of condensed matter.

The purpose of this paper is to provide a very elementary overview of metallic-nonmetallic transitions including attention to systems comprised of various components or with differing densities. It summarizes for the aerosol community some recent progress in treating the work function changes of metallic systems as a function of their degree of aggregation and introduces workers in the field to some recent techniques for studying the work functions of isolated aggregates utilizing molecular beam techniques coupled with photoionization sources and mass spectrometric detection methods (4-6).

ELEMENTARY CONCEPTS ABOUT METALLIC CONDUCTIVITY

Recently, there have been several reviews addressed to the subject of metallic conductivity (2,7-9). These have been presented at various levels of sophistication with some introducing the non-specialist to current advances in the area while others have been addressed to the specialist working in the field. The band theory of solids is well developed (10), but the reader interested in elementary concepts is referred to DeKock and Gray (11). They discuss both lithium and beryllium as simple examples of the basic reasons why metals are conductive. By combining the atomic orbitals for a system such as lithium, it is easy to see how the 2s atomic levels become split into bonding, non-bonding, and anti-bonding molecular orbitals. In the case of a large array, the energy level spacings become very small and the band for the 2s has a very high degree of degeneracy for a large system (e.g., a mole of atoms). The 1s levels are well separated from the 2s levels, and the 2s levels are only half filled since each orbital permits double occupancy in accordance with the Pauli principle. Additionally, the close overlap between the split 2p levels and a 2s level provides additional energies accessible to the electrons in the system and in a large array of atoms the electrons are delocalized and are free to move upon an infinitesimally small excitation energy. DeKock and Gray also demonstrate why the overlap between the 3p and 3s orbitals enables a system such as beryllium to be a conductor even though the 3s levels are totally occupied. Only infinitesimal excitation is necessary to promote the electrons to the 3p levels which then enable the system to conduct.

Another concept which is useful in understanding the metallic conductivity concerns the Goldhammer-Herzfeld concept of neutral polarization of atoms (2). Here it is conceived that the neutral polarization effects enable the valence electrons to become free. On this basis, the Clausius-Mossotti equation can be viewed as an expression which will enable an assessment of which systems are metallic and which are non-metallic (2). Consider the equation

$$\frac{n^2-1}{n^2+2} = \frac{R}{V} = \frac{\epsilon-1}{\epsilon+2}, \quad (1)$$

where R is the molar refractivity, V molar volume, n optical refractive index and ϵ the high-frequency dielectric constant. For values of R/V less than or equal to 1, the systems are non-metallic while for R/V equal to or greater than 1, they are conducting. (See a recent review by Edwards and Sienko (2) who have plotted systems of both a metallic and non-metallic character and have demonstrated the validity of this early simple concept developed during the 1910's and 20's.) Clearly, for R/V to become equal to or exceed unit, ϵ must approach infinity.

Another factor which must be considered is that due to changes in density. Clearly, a system with infinite separation of the atoms cannot display metallic conductivity. Edwards and Sienko (2) have reasoned that three factors must be considered. First, the ionization potential of the atom; second, the electron affinity of the system; and third, Δ the degree of the electrons' wavefunction overlap in the system. For a system to conduct electrons one atom must first lose an electron, hence the importance of ionization potential (I_p); second, a neighboring one must take on the electron and therefore a dependence on electron affinity (E_a); and third, there must be some overlap possible in the wavefunctions. As the difference, D ,

$$D = I_p - E_a - \Delta \quad (2)$$

goes to zero, the system becomes fully conducting. In the case of clusters, one additional factor must be considered, namely that of the changing workfunction due to the size of the system which includes both the degree of aggregation related to the overlap and the image potential of an electron removed from the condensed (aggregated) phase. One way of looking at the problem is through the classical equations of electrodynamics. This problem has been treated by Wood (12) and involves three terms: first, the work function for the image potential at a flat plane; second, the correction due to a surface of curvature; and third, the coulomb effect in removing the electron from a non-grounded aggregate. This leads to the expression

$$W(R) = W_\infty + \frac{3}{8} \frac{e^2}{R_S} \quad (3)$$

where W represents the work function, R_S radius of the equivalent sphere and e elementary charge. In the case of small clusters and aerosols, all of these factors play a role but are not fully understood. Some experimental approaches to the problem are discussed in the next section.

EXPERIMENTAL

Details of the experimental apparatus employed in the present measurements are given elsewhere (6). Basically, it consists of two main sections; in the first chamber the molecules of interest are produced and in the second chamber they are detected. The species to be investigated are generated as follows: Sodium metal is vaporized in a high temperature oven and the resulting atoms and clusters are coexpanded with Ar through a 300 μm tubular nozzle.

Once formed, the clusters enter through a skimmer into a detection chamber where they are photoionized and mass analyzed. The ionization region and mass spectrometer are located about 30 cm downstream from the skimmer entrance. Upstream from this region is a large plate with a 1 cm diameter hole which serves to block the sodium in the beam and prevent it from condensing on the ion optics. A beam stop, which can be positioned from outside of the chamber, is located immediately upstream from this plate and is used to establish the beam constituents. The mass spectrometer can be raised or lowered in order to intersect the beam with either an electron-impact ionization source or the light entrance slit.

Photoionization of atoms and molecules in the beam is accomplished by use of a 500 Watt xenon arc lamp equipped with a 68 mm diameter, four element f/0.7 UV condensing lens. The desired wavelength is selected with a 0.25 meter, f/3.0 monochromator whose grating is blazed at 240 nm. The linear dispersion is 33Å/mm and runs are generally made with a slit width of 1 mm. After the light exits from the monochromator it enters the second chamber perpendicular to the molecular beam and is focused into the interaction region. The light intensity is measured as a function of wavelength with a thermopile detector (Model 360001, Scientect, Inc.). Although at low wavelengths xenon arc lamps have a lower relative output than mercury lamps, they possess the advantage of having a much smoother output spectrum below 400 nm. Once the ions are formed, they are extracted and focused with a series of ion optic plates into a quadrupole mass spectrometer and pulse counted. The counts are collected in a multichannel analyzer.

Sodium metal is vaporized in a two-chamber oven (6). The first chamber contains the metal and the second section serves to prevent large collections of sodium or impurities from clogging the nozzle. This is accomplished by heating the second part, which houses a copper mesh trap, to a temperature about 100 to 150°C hotter than the first one. In order to produce a colder beam, the sodium is coexpanded with a buffer gas; argon, typically at a pressure of 100 torr, is usually employed for this purpose. The first and second chambers and the nozzle are all heated separately. Typical operating temperatures are about 750, 850 and 900 K, respectively. A temperature of 750 K corresponds to a sodium pressure of 1 to 2 torr.

Surrounding the inner tubular nozzle is a jacket which has an entrance tube for reactant gases and an annular exit opening adjacent to the tube exit. The width of the opening is on the order of a few thousandths of an inch but gradually changes over a period of time because of corrosion by the caustic reactant gases used. The annular region serves as a second nozzle through which the reactant gas is introduced. Ideally it is desired that the sodium molecules and reactant gas be kept separate

until the actual expansion where mixing can occur without any danger of condensation of the product molecules on the nozzle or jacket surface. In reality a build-up of salt or oxide occurs which eventually clogs either the nozzle tube or jacket opening. This is partly alleviated by increasing the distance between the tube ID and the annular opening. Either a thicker walled tube can be used or, as was done here, a second tube can be placed around the nozzle tube producing an effective dead space.

The double expansion type source is particularly useful for making molecules which are otherwise difficult to produce in the gas phase. The molecules which have been formed and observed so far are Na_n ($n=1$ to 10), Na_nCl ($n=2, 3$) and Na_nO , K_nO ($n=2$ to 4). Na_nCl was made using either HCl or Cl_2 as the reactant gas in the jacket. Na_nO was made using N_2O or O_2 . Many other similar types of molecules can also be produced by use of the appropriate reactant gas.

EXPERIMENTAL FINDINGS

Using the aforementioned method, the photoionization of metallic systems as a function of their degree of clustering is readily obtained. An example comes from our recent work on sodium aggregates. Figure 1 shows typical photoionization spectra taken for Na_4 where the abrupt onset of ionization at the threshold wavelength is readily observed (4). A comparison of the results is given in Table I. The frequently discussed (13) alternation between odd and even systems, thought to be due to the pairing of electrons in the even numbered ones, is only evident in the newer higher resolution data up to the pentamer.

It is instructive to compare these values for the classical equation (Eq. 3) for the influence of particle shape (spherical chosen for comparison); see Figure 2. Two values for the size of the sodium atom are chosen for making the calculations to equate radius of an equivalent sphere with the number of atoms in the system. One of these is based on the covalent radius while the other is based on the nearest neighbor distance derived for a sodium lattice from x-ray data (14). It is evident that the classical expression is not in very good accord with the experimental findings.

Herrmann, et al. (15), have also compared their measurements with various calculations including the classical equation and several semi-quantitative molecular orbital results. They took the coefficient in the classical equation to be $1/2$ instead of $3/8$ in Equation (3) and chose an early and erroneous value for the sodium work function, 2.3 instead of 2.7 eV (16). Two other investigators have reported findings which are relevant to the problem concerning the size dependence of the work function of metallic systems. Smalley (1c,e) has observed the work function of Cu_9 to be less than 5.58 while that of Cu_{29} is greater than 4.98 eV. Using an appropriate covalent radius, as well as a

value based on the lattice parameter for copper, the classical predictions are 6.68-6.87 eV and 6.02-6.15 eV, respectively. In the case of iron clusters, Kaldor (1c) has shown the work function for Fe₃ through Fe₅ to be greater than Fe₂ and Fe₁₃ through Fe₁₇ to be greater than Fe₁₂. Both of these findings are in contradiction with the classical equation and other theoretical predictions (1c).

Herrmann, et al.(15), compared their results with several quantum mechanical calculations available at that time, finding rough agreement between experiment and theory but showing large discrepancies in terms of the even greater predicted variation in ionization potential for odd and even clusters than observed experimentally. However, as seen from the present work, the alternation between odd and even systems, often attributed as being due to the pairing of electrons in the even numbered cluster systems, is not within experimental error present beyond the pentamer. See the data given in Table I.

More recently, Flad, et al. (18), have calculated ionization energies for sodium clusters up to Na₈. The values, converted to eV, are given in Table I for two different structures pertaining to computed equilibrium geometries. Interestingly, considering the range expected for the two structures, the agreement between experiment and theory is quite good for all except Na₇.

Goddard and coworkers (2) have considered the ionization potentials and electron affinities for nickel clusters. In their results, based on an SCF method, the ionization potential of nickel should converge to the bulk value for clusters greater than 89, having reached the bulk value and then dipped below it at cluster size 43. The failure of the classical expression to account for predictions of this quantum mechanical model is evident from the fact that the predicted classical work function is 6.6 eV at Ni₄₃ while the quantum mechanical calculated value is 5.5 eV. Furthermore, Goddard's results suggest that the electron affinity does not converge to the bulk value at sizes even as large as Ni₈₉.

It should be evident to the reader that there is need for additional experimental and theoretical work on this important problem.

STUDIES OF COMPOUNDS COMPRISED OF METAL AGGREGATES: SUB-CHLORIDES AND SUB-OXIDES OF SODIUM

Recently we have turned attention to an investigation of the photoionization of sub-oxides and sub-chlorides of sodium for further comparison with theory (5,6). Table II gives the values derived for the appearance potential of each of the species investigated. Also included in the table are previous measurements by us for the dimer sub-oxide of sodium (6) and literature values for the potassium systems. The values for the metal sub-oxides are seen to fall dramatically, leveling off to an essentially constant value for the trimer and tetramer species. The

precipitous drop in the ionization potentials, as well as the leveling effect, was more abrupt than expected. The values do not differ greatly from the analogous metallic species, but in the case of sodium they do fall below the bare metal cluster as seen by comparison of Tables I and II for the tetramer.

Perhaps the most interesting observation is that the ionization potential of sodium containing metal clusters is somewhat reduced by oxidation compared to the bare metal tetramer. It has been reported that the work function of sodium is appreciably lowered by the presence of impurities (16). In fact, the work function for polycrystalline sodium was long believed (16) to be 2.3 eV but is now accepted to be 2.75 eV. The discrepancy between early and recent measurements has been traced to surface contamination. Surprisingly, our results for potassium fail to reveal a similar effect.

Clearly, continued work on higher order metallic sub-oxides of varying systems promises to provide further interesting data from which to gain insight into such problems as surface oxidation, the influence of oxygen on the metallic conductivity of thin films, and chemistry and physics of surfaces in general.

ACKNOWLEDGMENTS

Support of the Department of the Army under Grant DAAG29-82-K-0160 and the U.S. Department of Energy under grant DE-AC02-82-ER60055 is gratefully acknowledged. The author thanks Drs. Robert G. Keesee, Karen Peterson, Olof Echt, and Misters Phan Dao and Robert Farley for helpful discussions during the course of the work.

REFERENCES

1. See for instance (a) H. C. Gatos, Ed., Surface Science, North-Holland, Amsterdam, Vol. 106 (1981). (b) Journal De Physique, Tome 38, Colloque C-2, Supplement No. 7. (1977). (c) T. H. Maugh, II, Science, 219, 1413 (1983); also see other articles in this series. (d) W. H. Crumley, J. L. Gole, and D. A. Dixon, J. Chem. Phys. 76, 6439 (1982). (e) D. E. Powers, S. G. Hansen, M. E. Geusic, D. L. Michalopoulos, and R. E. Smalley, J. Chem. Phys., 78, Part 1, 2866 (1983). (f) E. L. Muetterties, T. N. Rhodin, E. Band, C. F. Brucker, and W. R. Pretzer, Chemical Reviews, 79, 91 (1979). (g) G. Delacretaz, J. D. Ganiere, R. Monot, and L. Wöste, Appl. Phys. B, 29, 55 (1982). (h) M. M. Kappes, R. W. Kunz, and E. Schumacher, Chem. Phys. Lett., 91, 413 (1982). (i) R. C. Baetzold and R. E. Mack, Inorg. Chem., 14, 686 (1975). (j) A. J. C. Varandas, and V. M. F. Morais, Molecular Physics, 47, 1241 (1983). (k) H.-O. Beckmann, Chem. Phys. Lett., 93, 240 (1982). (l) S. C. Richtsmeier, D. A. Dixon, and J. L. Gole, J. Phys. Chem., 86, 3942 (1982). (m) J. L. Gole, G. J. Green, S. A. Pace, and D. R. Preuss, J. Chem. Phys., 76, 2247 (1982). (n) D. Plavsic, J. Koutecký, G. Pacchioni, and V. Bonacic-Koutecký, J. Phys. Chem., 87, 1096 (1983). (o) C. H. Wu, J. Phys. Chem., 87, 1534 (1983). (p) J. B. Hopkins, P. R. R. Langridge-Smith, M. D. Morse, and R. E. Smalley, J. Chem. Phys., 78, 1627 (1983). (q) L. J. Rothberg, D. P. Gerrity, and V. Vaida, J. Chem. Phys., 74, 2218 (1981). (r) V. E. Bondybey, G. P. Schwartz, and J. H. English, J. Chem. Phys., 78, 11 (1983).
2. T. H. Upton and W. A. Goddard, III, in Chemistry and Physics of Solid Surfaces (R. Vanselow and W. England, Eds.), CRC Press, Inc., Vol. III, p. 127 (1983). See also C. F. Melius, T. H. Upton and W. A. Goddard III, Solid State Communications, 28, 501 (1978); T. H. Upton, W. A. Goddard III, and C. F. Melius, J. Vac. Sci. Technol., 16, 531 (1979).

3. R. P. Messmer, in The Nature of The Surface Chemical Bond (T. N. Rhodin and G. Ertl, Eds.), North-Holland, Chapter 2 (1979).
4. K. I. Peterson, P. D. Dao, R. W. Farley, and A. W. Castleman, Jr., "Photoionization of Sodium Clusters," *J. Chem. Phys.* (in press).
5. P. D. Dao, K. I. Peterson, and A. W. Castleman, Jr., "The Photoionization of Oxidized Metal Clusters," *J. Chem. Phys.* (in press).
6. K. I. Peterson, P. D. Dao, and A. W. Castleman, Jr., "Photoionization Studies of Na₂Cl and Na₂O and Reactions of Metal Clusters," *J. Chem. Phys.* 79, 777 (1983).
7. M. J. Sienko, *Acc. Chem. Res.*, 15, 87 (1982).
8. J. A. A. J. Perenboom and P. Wyder, *Physics Reports*, 78, 173 (1981).
9. I. D. Morokhov, V. I. Petinov, L. I. Trusov, and V. F. Petrunin, *Sov. Phys. Usp.* 24, 295 (1981).
10. C. Kittel, Introduction to Solid State Physics, 2nd Edition, Chapter 11, John Wiley and Sons, Inc., London (1960).
11. R. L. DeKock, and H. B. Gray, Chemical Structure and Bonding, The Benjamin/Cummings Publishing Company, pp. 444-450 (1980).
12. D. M. Wood, *Phys. Rev. Lett.*, 46, 749 (1981).
13. A. Herrmann, S. Leutwyler, E. Schumacher, and L. Wöste, *Helvetica Chimica Acta*, 61, 453 (1978).
14. G. C. Demitras, C. R. Russ, J. F. Salmon, J. H. Weber, G. S. Weiss, Inorganic Chemistry, Prentice-Hall, Inc., Chap. 2, p. 34 (1972).
15. A. Herrmann, E. Schumacher, and L. Wöste, *J. Chem. Phys.*, 68, 2327 (1978).
16. R. J. Whitefield and J. J. Brady, *Phys. Rev. Lett.*, 26, 380 (1971).
17. N. D. Lang and W. Kohn, *Phys. Rev. B*, 3, 1215 (1971).
18. J. Flad, H. Stoll, and H. Preuss, *J. Chem. Phys.*, 71, 3042 (1979).
19. (a) E. J. Robbins, R. E. Leckenby, and P. Willis, *Adv. Physics*, 16, 739 (1967). (b) P. J. Foster, R. E. Leckenby and E. J. Robbins, *J. Phys. B*, 2, 478 (1969). (c) E. J. Robbins, R. E. Leckenby and P. Willis in The Properties of Liquid Metals (P. D. Adams, H. A. Davies, S. G. Epstein, Eds.), Taylor & Francis, Ltd., London, p. 739 (1966).
20. C. E. Moore, Atomic Energy Levels, Vol. I, Circular of the National Bureau of Standards 467 (1949).
21. H. M. Rosenstock, K. Draxl, B. W. Steiner, and J. T. Herron, Eds., Journal of Physical and Chemical Reference Data, Vol. 6, Suppl. No. 1, pp. 378,379 (1977).

TABLE I. APPEARANCE POTENTIALS FOR ALKALI CLUSTERS, Na_x (eV)

x	Present Study	Prior Values		
		Ref. 13 (exp)	Ref. 19 (exp)	Ref. 18 (Theory)
1	5.13 ± 0.04	5.14^a	--	5.10
2	4.87 ± 0.04	4.934 ± 0.011	4.9 ± 0.1	5.01
3	3.93 ± 0.04	3.97 ± 0.05	3.9 ± 0.1	4.01^b 4.25^b
4	4.24 ± 0.04	4.27 ± 0.05	4.2 ± 0.1	3.98^b 4.14^b
5	3.95 ± 0.04	4.05 ± 0.05	$3.9 - 4.3$	4.03^b 4.07^b
6	3.97 ± 0.04	4.12 ± 0.05	$4.05 - 4.35$	3.87^b 4.08^b
7	4.06 ± 0.04	4.04 ± 0.05	$3.9 - 4.15$	3.95
8	≈ 3.9	4.1 ± 0.05	4.0 ± 0.1	3.95^b 4.05^b

^aRef. 20; ^bComputed for two different structures

TABLE II. APPEARANCE POTENTIALS (eV)

x	Present Measurements: M_xO	
	M = Na	M = K
1	$(6.5 \pm 0.7)^a$	---
2	5.06 ± 0.04	4.7 ± 0.4
3	3.90 ± 0.15	3.65 ± 0.04
4	3.95 ± 0.10	3.62 ± 0.04

^adata from ref. 21

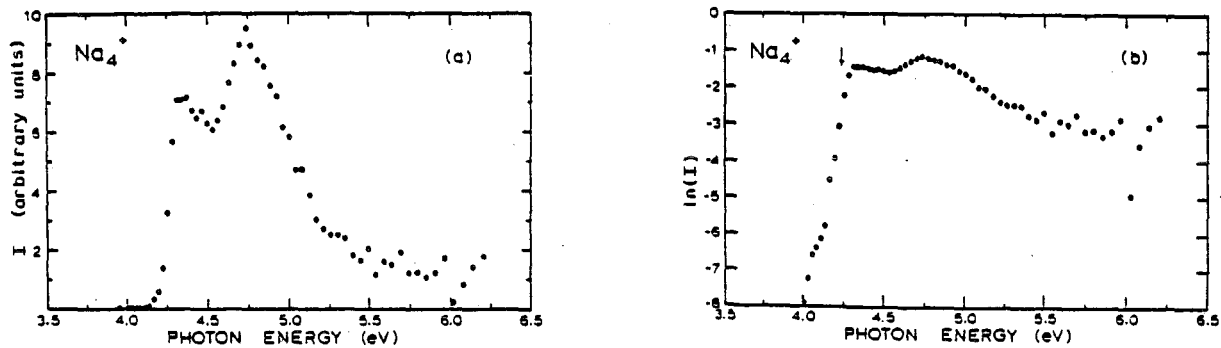


FIGURE 1: a) Plot of relative ion intensity versus photon energy for Na_4^+ ; b) Data displayed in a semilogarithmic plot.

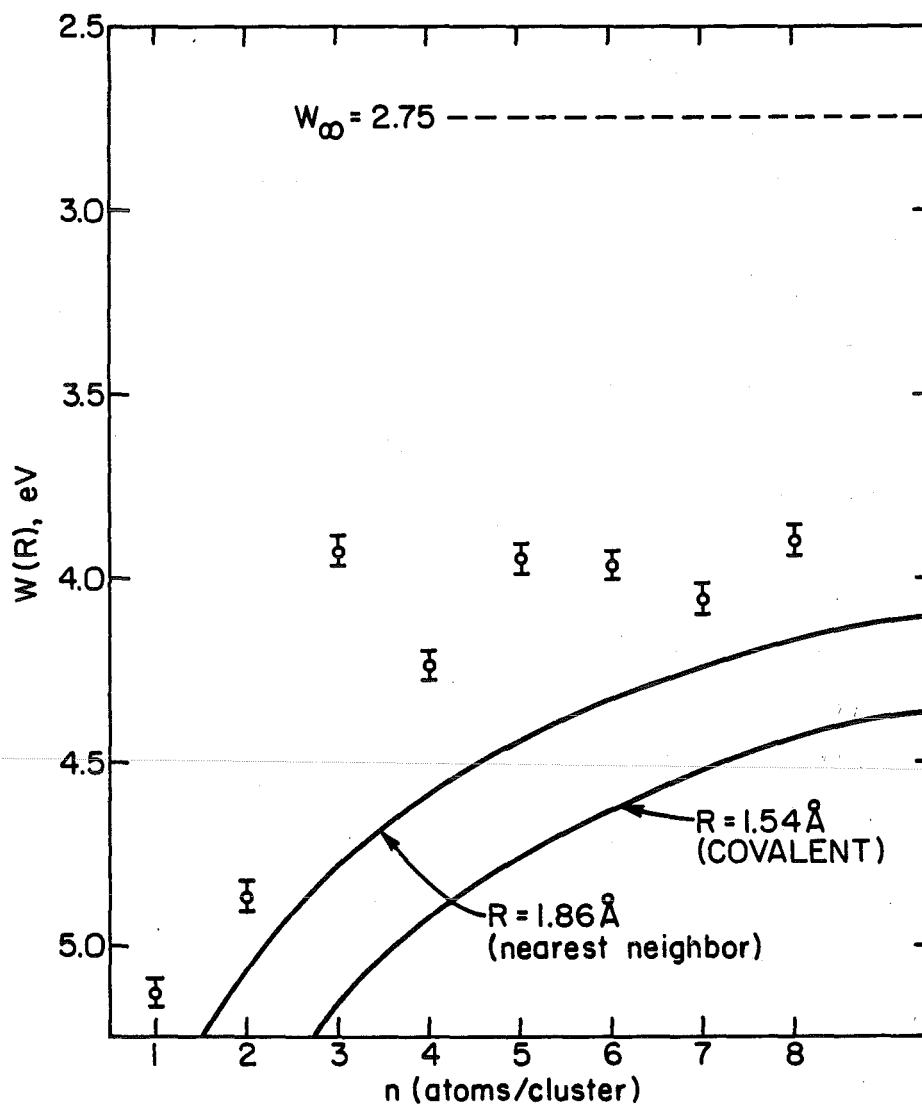


FIGURE 2: Plot of work function versus number of atoms in a cluster using Equation (4). The conversion between number and equivalent spherical size was made using $r = 1.86 \text{ \AA}$ for the nearest neighbor distance in sodium and $r = 1.54 \text{ \AA}$ (16) based on the covalent radius. Present experimental data are shown \bullet .

AEROSOL GENERATION: STUDIES OF NUCLEATION
AND GROWTH PROCESSES

J. R. Brock
Department of Chemical Engineering
University of Texas at Austin
Austin, Texas 78712

ABSTRACT

Experimental and theoretical research has been carried out on nucleation and growth processes in generation of oil condensation aerosols and ferromagnetic chain aerosols. Some of the recent results are summarized in this report. This work has been presented, published and submitted for publication as follows:

J. R. Brock, "New aspects of aerosol growth processes," Plenary Lecture, American Association for Aerosol Research, 2nd Annual Meeting, College Park, MD, April 1983.

J. R. Brock and P. Kuhn, "Nucleation and growth of multicomponent aerosols," Am. Assoc. for Aerosol Research, 2nd Annual Meeting, College Park, MD, April 1983.

J. R. Brock, "Simulation of aerosol dynamics," in R. E. Meyer, Ed. Theory of Disperse Multiphase Flow, Academic Press, NY, 1983.

J. R. Brock, "On growth processes of condensation aerosols," in Transactions of the 28th Conference of Army Mathematicians; ARP Report 83-1, 1983.

J. R. Brock, "New aspects of aerosol growth processes," Aerosol Science and Technology 2 139 (1983).

T. H. Tsang and J. R. Brock, "Simulation of condensation aerosol growth by condensation and evaporation," Aerosol Science and Technology 2 311-321 (1983).

J. R. Brock and J. L. Durham, "Aqueous aerosol as a reactant in the atmosphere," in J. Calvert, Ed. Acid Rain, Ann Arbor Press, 1983.

T. H. Tsang and J. R. Brock, "Approach to asymptotic limit distributions in Ostwald ripening," Submitted for publication.

J. R. Brock and P. Kuhn, "Growth of condensation aerosols in a laminar coaxial jet: experiment," Submitted for publication.

P. Pan and J. R. Brock, "Growth of condensation aerosols in a laminar coaxial jet: theory," Submitted for publication.

J. R. Brock and P. Kuhn, "Alteration of nucleation rates by unsaturated organic acids," Submitted for publication.

INTRODUCTION

The efficiency of an aerosol obscurant for electromagnetic radiation depends on many factors including particle size, shape, composition and concentration. For an obscurant propagating in the atmosphere, particle size, shape, composition, and concentration are determined by the processes of particle generation and growth as well as by advection, dispersion and other processes of atmospheric motion. While some qualitative features of these various processes are recognized, our knowledge is incomplete. Improvements in aerosol obscurant technology must depend in part on development of the basic knowledge of the various processes cited above.

The work outlined here is intended to add to the technological base of the U.S. Army's obscuration program and to contribute to fundamental knowledge of aerosol physics and chemistry. This part of our work focuses on the nucleation and growth processes involved in initial generation of an obscurant aerosol. Parts of our theoretical and experimental program are outlined below.

Theory

One aim of our investigations has been to develop accurate and efficient numerical methods for simulation of aerosol growth processes. Recent work on simulation of condensation/evaporation is summarized here. The condensation/evaporation problem for a single component aerosol is most easily expressed by the time evolution equations for aerosol and vapor in a spatially homogeneous system:

$$\frac{\partial n(x,t)}{\partial t} = - \frac{\partial}{\partial x} [\Psi(x,S) n(x,t)] \quad (1)$$

which is coupled to the monomer conservation equation. In terms of the supersaturation ratio, S :

$$\frac{dS}{dt} = - \int_{x^*}^{\infty} dx \Psi(x,S,t)n(x,t) - x^* \Psi(x^*,S) n(x^*,t) \quad (2)$$

where $n(x,t)dx$ is the number of particles with masses in the range x, dx , Ψ is the particle growth rate by condensation/evaporation and S is the vapor supersaturation. x^* represents the mass of the smallest stable particle.

In comparison with the coagulation term, the condensation/evaporation term in eq. (1) is deceptively simple in appearance. However, it is a first-order non-linear hyperbolic equation whose numerical solution is difficult, as evidenced by the numerous published attempts at numerical solution of other hyperbolic equations (simulation of advection, for example). The difficulty lies in the fact that most numerical schemes for hyperbolic equations give rise to numerical dispersion and numerical diffusion.

Many methods have been tried to reduce dispersion, such as by introduction of a dissipative term in the Galerkin finite element formulation or use of filtering schemes. These have not been found

to be suitable for condensation/evaporation simulation.

A robust numerical scheme for condensation/evaporation should be free of numerical dispersion while numerical diffusion is minimized. Eulerian numerical schemes create numerical dispersion whereas Lagrangian schemes do not suffer from this difficulty. Using Bonnerot and Jamet's approach, Varoglu and Finn derived a finite element method incorporating characteristics for the diffusion-convection equation. This scheme is free of numerical dispersion. Recently, Neumann derived an Eulerian-Lagrangian numerical scheme for the diffusion-convection equation which is also free from numerical dispersion and controls numerical diffusion.

In our work, we have modified and combined Varoglu and Finn's method with Neumann's method because of the requirements of the condensation/evaporation term. This new method has been successful and agrees with analytical solutions where they are available.

As one example, we have investigated the accuracy of this numerical scheme by comparison with the asymptotic solution due to Lifshitz and Slyozov (LS) for the "Ostwald ripening" (non-linear) problem in the continuum regime. Fig. 1 shows the approach to the LS asymptotic result and the good agreement for long time. We have also carried out these studies in the free molecule and transition regimes.

Numerical simulation work is also under way on the early stages of particle growth beginning with homogeneous nucleation. This work is incorporated in our experimental studies of oil condensation aerosol and ferromagnetic chain aerosol.

Experiment

Experimental investigations are continuing on the formation and growth of oil and phosphorous condensation aerosols and on the formation and growth of ferromagnetic chain aerosols.

Investigations of the formation of aerosol by nucleation of multicomponent oil vapor mixtures in a laminar coaxial jet have continued. The experimental system described in previous proceedings has been substantially improved to permit the acquisition of accurate particle size distribution data. With installation of automatic control of nozzle temperature, the effects of variation of nozzle temperature on particle size distribution have been investigated. An improved numerical inversion procedure has also been developed and tested to permit good estimates of particle size distributions from optical particle counter data obtained from the experiments.

Our published work should be consulted for complete presentation of the large body of experimental data developed from these studies. A few typical examples of that data will be given here. Fig. 2 shows the development of the particle size distribution for pure dibutyl phthalate as a function of axial distance from the nozzle exit. The size distribution is plotted in terms of the non-dimensional similarity variable $\rho = D_p/D_{p_i}$, where D_p is particle diameter and D_{p_i} is the diameter of the "interface

separating the regions of condensation and evaporation. The results may be understood qualitatively through the theory of particle growth by condensation/evaporation described in part by eqs. (1) and (2).

Work has continued on the interesting finding reported previously of large increases in apparent nucleation rates produced by addition to the oil aerosol material of small amounts of classes of unsaturated organic acids. We have now demonstrated the existence of a strong temperature effect as indicated in Fig. 3 showing rapid increase of total particle concentration and decrease of mean particle diameter as nozzle temperature is increased. Studies to clarify the mechanism of these effects are continuing.

Our work on generation of ferromagnetic chain particles is continuing. This includes development of detailed particle growth models and construction of an experimental system to permit quantitative tests of theoretical models. Results obtained so far in a less refined experimental system still show definite trends. In this system, iron aerosol is produced by homogeneous nucleation of iron vapor produced by heating pure iron sample in Ar and He atmospheres at various pressures. Aerosol samples are obtained by sampling on electron microscope grids and particle size and chain length distributions are determined from photographs of these samples using a JEOL JEM transmission microscope. The following qualitative results are confirmed by repeated experiments: (1) As the distance from the evaporation source increases so does the chain length (from $\sim 0.01 \mu\text{m}$ to $\sim 1 \mu\text{m}$); (2) As the inert gas pressure increases so does the primary particle size (from $\sim 60 \text{ \AA}$ to $\sim 80 \text{ \AA}$); (3) Chain concentration and length increase with time span pulse producing evaporation of the iron sample (explanation: vapor concentration is increased by increasing pulse length); (4) Primary particle size and chain length increase with increasing source temperature (explanation: obviously, iron vapor concentration (vapor pressure) is increased by raising source temperature); (5) Increase of applied external magnetic field strength increases primary particle size and chain length (the latter effect is unexpected and is still under investigation); (6) Decreasing the host gas temperature (down to liquid N_2 temperatures) increases the average primary particle diameter and broadens the chain length distribution. These various effects are being comprised in our ferromagnetic chain nucleation and growth model now under development.

ACKNOWLEDGMENT

This work was supported by the Chemical Systems Laboratory, U.S. Army, Aberdeen Proving Ground.

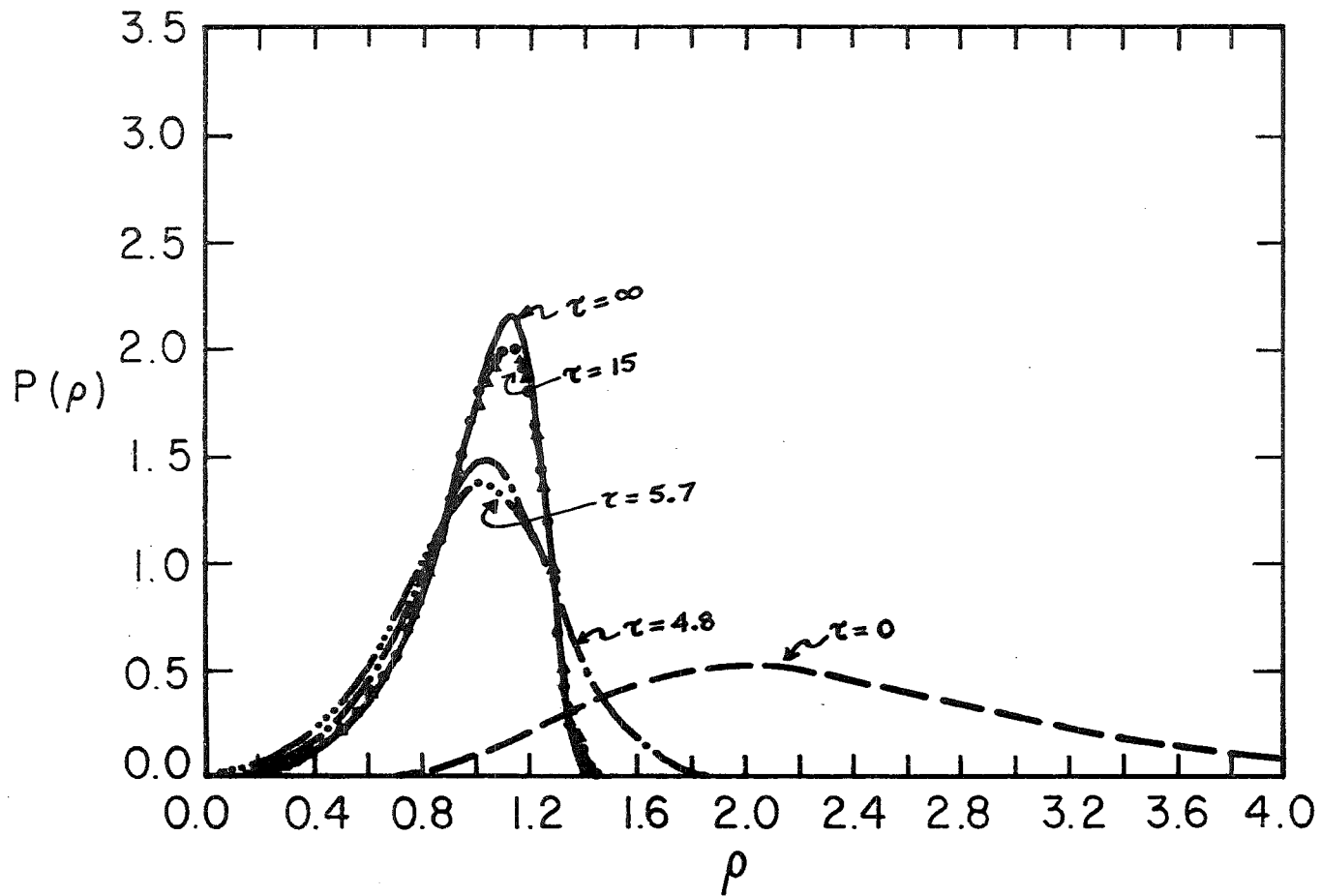


Figure 1. Approach to asymptotic limit distribution during "Ostwald ripening" of a continuum aerosol. $P(\rho)$ is the nondimensional particle size distribution function and τ is the nondimensional particle diameter. ρ is the nondimensional time. Initial distribution is very broad and asymptotic limit is approached very slowly. See text and references for discussion.

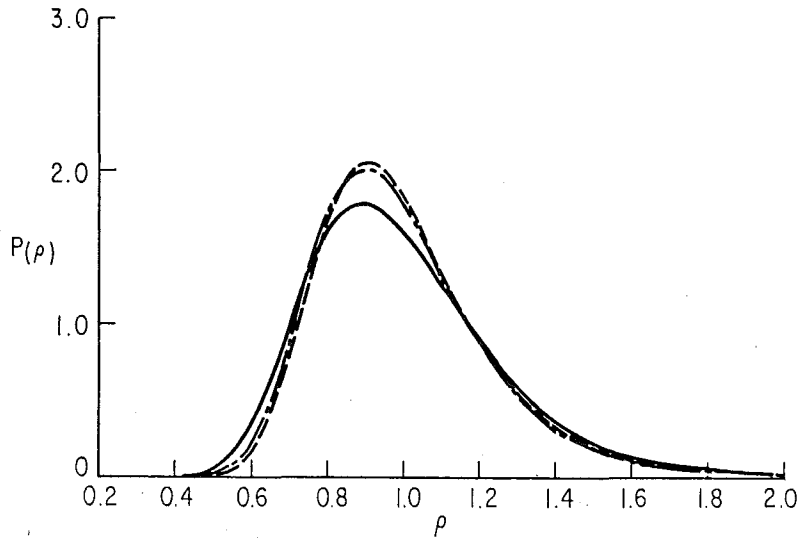


Figure 2. Development of particle size distribution for dibutyl phthalate aerosol as a function of axial distance from nozzle exit in experimental laminar coaxial jet system. $P(\rho)$ is nondimensional distribution and ρ is nondimensional particle diameter. See definitions in text.
 — 50 nozzle diameters; - - - 70 nozzle diameters; - - - 100 nozzle diameters

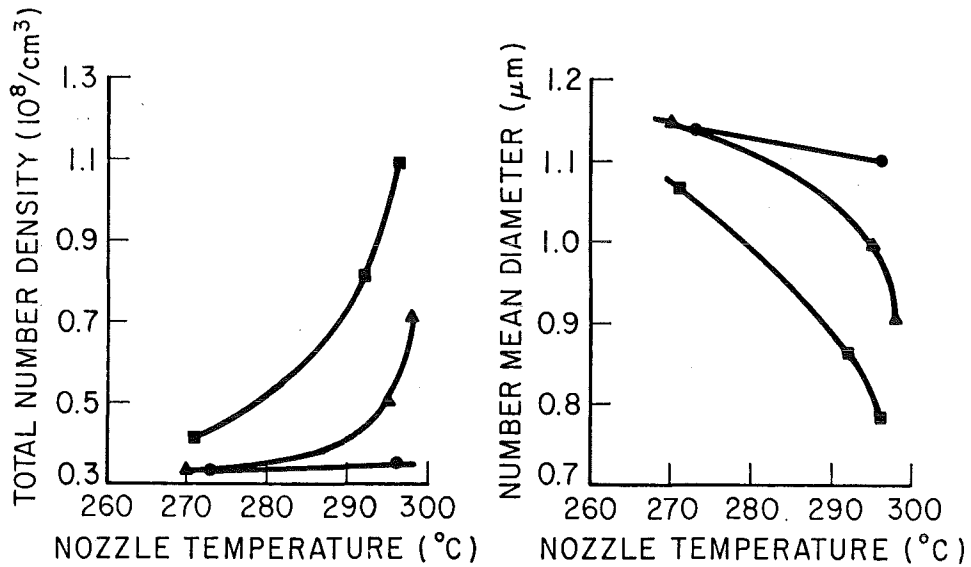


Figure 3. Effect of additive organic acid on dihexyl phthalate aerosol particle number concentration and number mean diameter as a function of nozzle temperature in experimental laminar coaxial jet system.

●—● 0% additive; ▲—▲ 1% additive; ■—■ 2% additive

DIFFUSIVE MIXING PROCESSES

J Latham

Physics Department, UMIST,
Manchester M60 1QD,
England

ABSTRACT

This paper outlines a diffusive model of the turbulent mixing of volumes of dry and cloudy air. It was developed for use in cloud physics where it is established that the entrainment of environmental air into a cloud, with subsequent mixing and associated phase-change, can have a profound effect upon its properties and behaviour. The model, and its successful testing against observation, is described in considerably greater detail in a paper by M B Baker and J Latham entitled "A diffusive model of the turbulent mixing of dry and cloudy air" which was published in the Quarterly Journal of the Royal Meteorological Society (1982, 108, 871-898).

We believe that it could readily be developed to treat other turbulent mixing processes such as those which involve chemical change.

THE DIFFUSIVE MIXING MODEL

We present a model of the turbulent mixing of a spherical blob of droplet-free air, of original diameter λ_B , temperature T_B , and supersaturation S , $S(\leq 0)$ and a cloud, represented by a spherical shell surrounding the blob of outer diameter λ_C ($> \lambda_B$), temperature T_C , supersaturation $S = 0$ and liquid water content L . The blob contains a distribution $n(m_B)$ of cloud condensation nuclei comprised of NaCl particles of mass m in equilibrium at the relative humidity $H = S + 1$. This distribution is identical to that assumed to be contained within the droplets in the surrounding cloud so that when turbulent mixing occurs at any level the total concentration of particles (droplets plus CCN) remains constant. The entire system is assumed to be moving upwards with a speed W .

The turbulent mixing of all properties transported is represented by diffusion with a single coefficient K determined on dimensional grounds from λ_B and ϵ , the rate of dissipation of turbulent energy within the cloud: $K = (\lambda_B^4 \epsilon)^{1/3}$. If we assume that the turbulent motions transport energy, liquid water, water vapour and dry air simultaneously, we have

$$\frac{\partial h}{\partial t}(\underline{R}, t) + W \frac{\partial h}{\partial z}(\underline{R}, t) - K \nabla^2 h(\underline{R}, t) = Q_h(\underline{R}, t) \quad (1)$$

$$\frac{\partial \rho_1}{\partial t}(\underline{R}, t) + W \frac{\partial \rho_1}{\partial z}(\underline{R}, t) - K \nabla^2 \rho_1(\underline{R}, t) = Q_1(\underline{R}, t) \quad (2)$$

$$\frac{\partial \rho_v}{\partial t}(\underline{R}, t) + W \frac{\partial \rho_v}{\partial z}(\underline{R}, t) - K \nabla^2 \rho_v(\underline{R}, t) = Q_v(\underline{R}, t) \quad (3)$$

$$\frac{\partial \rho_a}{\partial t}(\underline{R}, t) + \omega \frac{\partial \rho_a}{\partial z}(\underline{R}, t) - K \nabla^2 \rho_a(\underline{R}, t) = Q_a(\underline{R}, t) \quad (4)$$

$$\frac{\partial n}{\partial t}(r_i, \underline{R}, t) + \omega \frac{\partial n}{\partial z}(r_i, \underline{R}, t) - K \nabla^2 n(r_i, \underline{R}, t) = Q_n(r_i, \underline{R}, t) \quad (5)$$

ρ_a , ρ_l and ρ_v are the densities of dry air, liquid water and water vapour, respectively; $n(r_i, \underline{R}, t)$ is the number density of droplets with radii in the interval $(r_i, r_i + dr_i)$; and \underline{R} is the radial vector. The energy term

$$h = [C_a \rho_a + C_l (\rho_l + \rho_v)] T + \rho_v L_v, \quad (6)$$

where C_a and C_l are the specific heat of dry air and liquid water respectively and $L_v (= 2.26 \text{ KJ g}^{-1})$ is an average value of the latent heat of vapourization of water. Equation (6) defines the temperature T in terms of the parameters of the problem.

The source terms Q are:

$$Q_n(\underline{R}, t) = -[L_v Q_v(\underline{R}, t) + \rho_a(\underline{R}, t) g \omega(t)] \quad (7)$$

$$Q_v(\underline{R}, t) = -4\pi \rho_w \sum_i n(r_i, \underline{R}, t) r_i^2 \dot{r}_i(\underline{R}, t) \quad (8)$$

$$Q_l(\underline{R}, t) = -\dot{Q}_v(\underline{R}, t) \quad (9)$$

$$Q_n(r_i, \underline{R}, t) = \frac{n(r_i, \underline{R}, t)}{\rho_a(\underline{R}, t)} \cdot Q_a(\underline{R}, t) \quad (10)$$

$$Q_a(\underline{R}, t) = -\rho_a(\underline{R}, t) \cdot \frac{Q_T(\underline{R}, t)}{T(\underline{R}, t)} + \frac{g \omega(t)}{R_a T(\underline{R}, t)} \quad (11)$$

where ρ_a is the density of liquid water, g the acceleration due to gravity and R_a the gas constant per kilogramme of air.

$$Q_T(\underline{R}, t) = \frac{Q_h(\underline{R}, t)}{[C_a \rho_a(\underline{R}, t) + C_l (\rho_l(\underline{R}, t) + \rho_v(\underline{R}, t))]} \quad (12)$$

The droplet growth equation is

$$\dot{r}_i(\underline{R}, t) = \frac{D \rho_a(T) / \rho_w}{(r_i + a)} \left[S(\underline{R}, t) - \frac{A}{r_i} + \frac{B m_a}{r_i^3} \right] \quad (13)$$

where

$$\rho_a(\underline{R}, t) = 1.8 \times 10^9 \exp(-5400/T(\underline{R}, t)) \quad (14)$$

is the saturation vapour density (g m^{-3}), D is the coefficient of molecular diffusion ($\text{cm}^2 \text{s}^{-1}$), the supersaturation S is expressed as a percentage, r_i is measured in micrometres, m_a in grammes, and the constants A and B possess the values 0.115 and 1.4×10^{13} respectively. $a (= 5 \mu\text{m})$ is a characteristic length associated with the non-ideality in water condensation.

The rate of change of supersaturation

$$\dot{s}(\underline{R},t) = (100 + s(\underline{R},t)) \frac{Q_V(\underline{R},t)}{\rho_V(\underline{R},t)} - \frac{5.4 \times 10^3 Q_T(\underline{R},t)}{T^2(\underline{R},t)} - \frac{3.42 \times 10^{-2} W(t)}{T(\underline{R},t)} \quad (15)$$

The precision of the foregoing equations could be increased, but such refinements were deemed unnecessary in view of the very approximate relationship between this diffusion formulation and the mixing process within clouds. We note that the diffusivity representation is best applied to situations in which λ_B exceeds the characteristic spatial scale of the turbulent eddies. Although buoyancy gradients generated by evaporation will deform the volume under examination, we assume that spherical symmetry is preserved during the mixing process.

Figure (1) illustrates the predicted time variation of the fields of liquid water content, L , supersaturation, S , and temperature, T , resulting from the mixing of a blob of air of size $\lambda_B = 100\text{m}$ and relative humidity 80% with a cloud of size $\lambda_C = 200\text{m}$ and liquid water content $L = 0.5\text{g m}^{-3}$, $W = 0\text{m s}^{-1}$. In the first case illustrated (A,B,C) the cloud consists of droplets of radius $3\mu\text{m}$ and in the second (D,E,F), $r = 20\mu\text{m}$. Since the turbulent energy dissipation rate $\epsilon = 10^{-2}\text{m}^2\text{s}^{-3}$ the characteristic mixing times

$$\tau_{TC} = (\lambda_C^2/\epsilon)^{\frac{1}{2}} = 160\text{s} \quad (16)$$

$$\tau_{TB} = (\lambda_B^2/\epsilon)^{\frac{1}{2}} = 100\text{s} \quad (17)$$

We see, when $r = 3\mu\text{m}$, that evaporation of droplets carried by turbulence into the interior of the blob is a very rapid process - presumably because of the high surface/volume ratio of the droplets - so that the supersaturation rises from -20% to close on 0% in about 10s. The temperature difference (originally 2K) follows a similar pattern - since its changes are governed by evaporation when the latter is rapid - lagging just slightly behind the changes in S . Evaporation is confined more or less entirely to the region originally occupied by the blob. The liquid-water-content distribution takes considerably longer to level out because evaporation inhibits its increase in the early stages of mixing; but nevertheless the gradient has been substantially reduced after 20 seconds, a period much less than the turbulent mixing times τ_{TC} and τ_{TB} .

Figure (1) shows that when the cloud consists of larger drops ($r = 20\mu\text{m}$) the rate of increase of minimum supersaturation S towards zero is reduced - because evaporation is less effective - but is still essentially completed within 20 seconds. The temperature equalization curves again follow those of S , and there is a corresponding in-

crease in the rapidity with which the gradient in L levels out. In this case turbulence distributed the undersaturation significantly into the cloud. Mixing is largely completed after 20s.

Figure (2) shows the time-development of the initially monodisperse spectrum ($r = 20\mu\text{m}$; the droplet concentration $N = 15\text{cm}^{-3}$; $L = 0.5\text{g m}^{-3}$) at $R = \lambda_B/2$, the location of the original interface between the cloudy and undersaturated air ($H = 80\%$) $W = 0.0\text{m s}^{-1}$. It is seen that the combination of evaporation and turbulent mixing introduces many new categories into the droplet size distribution.

Figure (3) presents the calculated spatial fields of L and S, at various times, for two different values of ϵ , the turbulent energy dissipation rate; $W = 0\text{m s}^{-1}$. In this case, the original spectrum, illustrated (A) in Figure 5, has a liquid water content $L = 1.0\text{g m}^{-3}$. It contains ten size classes (radii between 3 and $12.5\mu\text{m}$) and is based on ones encountered in field studies on the summit of Great Dun Fell (Blyth, et al., 1980). In this case $\lambda_{TC} \sim 130\text{s}$ when $\epsilon = 10^{-2}\text{m}^2\text{s}^{-3}$ (A,B) and $\lambda_{TC} \sim 270\text{s}$ when $\epsilon = 10^{-3}\text{m}^2\text{s}^{-3}$ (C,D); the corresponding values of λ_{TB} are 74s and 160s. When the mixing is rapid (A,B) the supersaturation becomes uniformly distributed within 20s, and gradients in L are eliminated well before 50s. With slower mixing the equalisation of both L and S is slower but is completed in times less than τ_{TC} . In both cases undersaturations are created within the region occupied by the original cloud, a characteristic feature of the situations in which the cloud spectrum contains large drops - with correspondingly high values of evaporation time τ_T (Baker, et al., 1980).

In figure (4) we present, for the cases covered by figures (1) and (3), information on the rates at which the total amount of evaporation and the distribution of liquid water approach their final values. f (in curves A,B,C,D) is the ratio of the total evaporation that has occurred at time t (expressed in Figure (4) as the dimensionless time t/τ_c) to that which has occurred when the cloud and blob are fully mixed. In curves E,F,G,H

$$f = 1 - \frac{(L_c - L_o)_t}{(L_c - L_o)_{t=0}} = 1 - \Delta L/L \quad (18)$$

where $\Delta L = (L_c - L_o)_t$ is the difference, at time t , between the liquid water content in the centre of the original blob ($R = 0$) and at the edge of the cloud ($R = \lambda/2$); L is the original liquid water content in the cloud.

The curves displayed in Figure (4) show clearly that: evaporation is completed long before the gradients in L are eliminated; uniformity in L is achieved - generally

in times much less than τ_{TC} ; evaporation proceeds most effectively when droplets are small and mixing is fast. Further calculations (not illustrated) show that uniformity in S is achieved more quickly for increased values of L .

In Figure (5) we present various spectra resulting from the mixing with undersaturated air of a volume of cloud possessing an original liquid water content $L = 0.5g\ m^{-3}$ and the size distribution (A) mentioned earlier, $W = 0\ m\ s^{-1}$. For the particular dimensions chosen ($\lambda_c = 144m$, $\lambda_B = 60m$) the final - well-mixed - value of L , if the humidity of the entrained air is 70% and the temperatures are as indicated, is $0.32g\ m^{-3}$. Curve B presents the classical spectrum, with $L = 0.32g\ m^{-3}$, which was obtained by the application of the droplet growth equation to all droplets in the original spectrum. All droplets have evaporated, so the peak radius has shifted substantially (whereas the peak concentration is virtually unchanged) and the reduction in radius is greater for the smaller droplets. Curve C, $L = 0.32g\ m^{-3}$, is obtained from our diffusive model with $\epsilon = 10^{-3}m^2s^{-3}$. This spectrum is seen to have a peak radius only slightly below that of the original spectrum (A) but a substantially reduced peak concentration. Thus the spectrum C, predicted from our model, lies between the classical spectrum B and the extreme inhomogeneous spectrum but is very much closer to the latter - which is not shown since its similarity to B would cause confusion in presentation.

In Figure (6) we present three spectra resulting from the turbulent mixing of spectrum A - the same as in Figure (5) - with a blob of undersaturated air, $W = 0m\ s^{-1}$. The dimensions and temperatures, given in the legend, are the same for all three calculations. In B and C the relative humidity $H = 70\%$ and the final water content $L = 0.32g\ m^{-3}$. In B, $\epsilon = 10^{-3}m^2s^{-3}$ and in C, $\epsilon = 10^{-2}m^2s^{-3}$. Curves B and C are very similar, but B is more 'inhomogeneous' - smaller reduction in peak radius - consistent with the associated slower mixing in this case. Curve D ($L = 0.18g\ m^{-3}$) was obtained with $H = 40\%$ and $\epsilon = 10^{-3}m^2s^{-3}$. This spectrum, although very different from one predicted by the classical description of mixing/evaporation (see, for example, Figure (4) Curve B), is substantially different from the equivalent 'extreme inhomogeneous' or 'dilution only' spectrum (again not shown) in which the shape of curve A would be preserved, and the mean radius would be the same as in A. This large departure from the extreme inhomogeneous spectrum may be attributed to the greater role of evaporation (relative to dilution) in producing the final spectrum (D).

Acknowledgements

Dr M B Baker of the University of Washington, Seattle, USA, played the primary role in the development of the diffusive mixing model described herein.

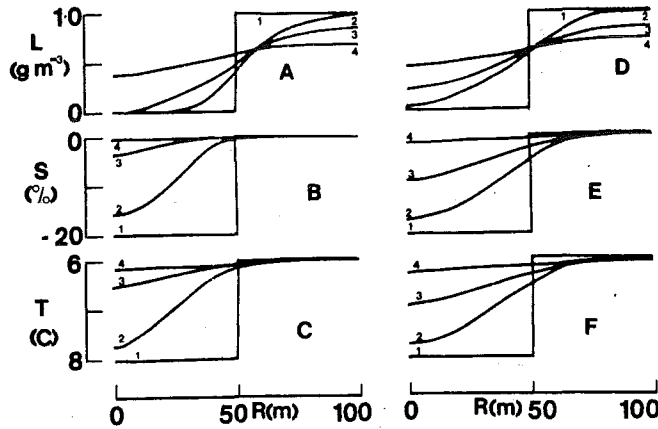


FIGURE 1. Calculated radial distributions of liquid water content, L , supersaturation S and temperature T at various times t during the turbulent mixing of a water cloud with a spherical blob of undersaturated air centrally embedded within it at $t=0$. Single category spectra. $\lambda_B = 100\text{m}$; $\lambda_C = 200\text{m}$; $\epsilon = 10^{-2}\text{m}^2\text{s}^{-3}$; $m_s = 10^{-16}\text{g}$; $L = 1.0\text{g m}^{-3}$ $H = 80\%$; $T_B = 281\text{K}$; $T_C = 279\text{K}$. A,B,C, $r = 3\mu\text{m}$; D,E,F, $r = 20\mu\text{m}$. 1, $t = 0$; 2, $t = 5\text{s}$; 3, $t = 10\text{s}$; 4, $t = 20\text{s}$.

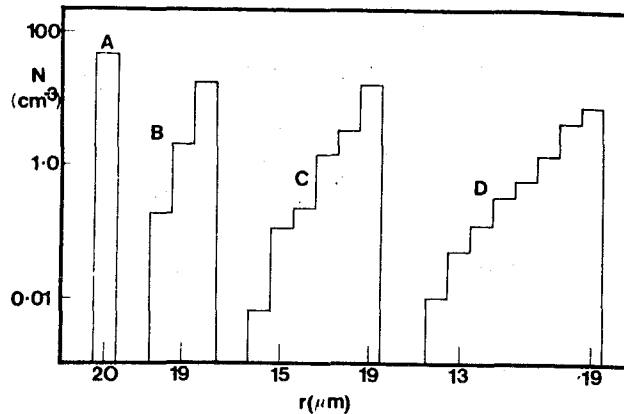


FIGURE 2. Calculated drop-size spectra at $R = \lambda_B/2$ at various times t during the turbulent mixing of a water cloud with a spherical blob of undersaturated air centrally embedded within it at $t=0$. Single category spectrum. $r = 20\mu\text{m}$; $\lambda_B = 100\text{m}$; $\lambda_C = 200\text{m}$; $\epsilon = 10^{-2}\text{m}^2\text{s}^{-3}$; $m_s = 10^{-16}\text{g}$; $L = 0.5\text{g m}^{-3}$; $H = 80\%$; $T_B = 281\text{K}$; $T_C = 279\text{K}$ A, $t = 0$; B, $t = 5.1\text{s}$; C, $t = 10.2\text{s}$; D, $t = 124\text{s}$.

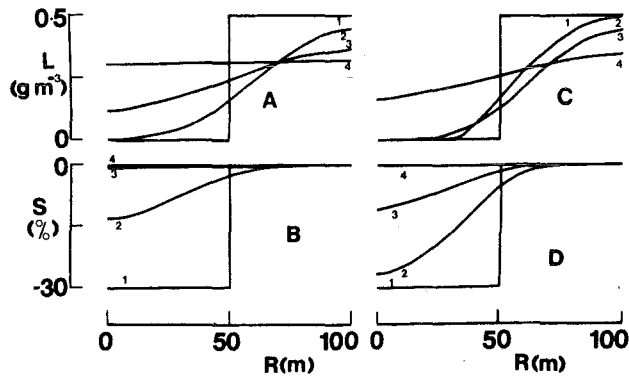


FIGURE 3. Calculated radial distributions of liquid water content, L , and supersaturation S at various times t during the turbulent mixing of a water cloud with a spherical blob of undersaturated air centrally embedded within it at $t=0$. Ten category spectrum. $\lambda_B = 60\text{m}$; $\lambda_C = 144\text{m}$; $m_B = 10^{-16}\text{g}$; $L = 0.5\text{g m}^{-3}$; $H = 70\%$; $T_B = 281\text{K}$; $T_C = 279\text{K}$. A,B, $\epsilon = 10^{-2}\text{m}^2\text{s}^{-3}$; C,D, $\epsilon = 10^{-3}\text{m}^2\text{s}^{-3}$. 1, $t = 0$; 2, $t = 8\text{s}$; 3, $t = 20\text{s}$; 4, $t = 50\text{s}$.

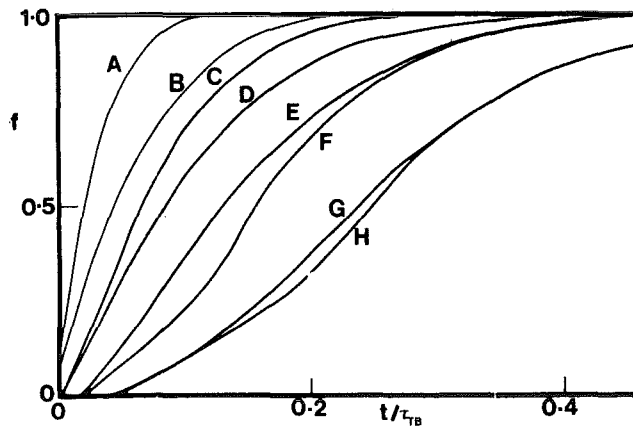


FIGURE 4. Calculated variation with dimensionless time t/τ_{TB} of the parameter f (defined in the text) which governs the rate at which the evaporative process and the redistribution of liquid water occurs during the turbulent mixing of a water cloud with a spherical blob of undersaturated air centrally embedded within it at $t/\tau_{TB}=0$; $m_B = 10^{-16}\text{g}$; $T_B = 278\text{K}$; $T_C = 279\text{K}$; $L = 1.0\text{g m}^{-3}$. Curves A,D,E,F are for a single category spectrum, $r = 3\mu\text{m}$ (A,F), $r = 20\mu\text{m}$ (D,E). Curves B,C,G,H are for the 10-category spectrum (Fig.2). Curves A,B,C,D are for evaporation; curves E,F,G,H for liquid water. Curves A,D,E,F: $\lambda_B = 100\text{m}$; $\lambda_C = 200\text{m}$; $\epsilon = 10^{-2}\text{m}^2\text{s}^{-3}$; $H = 80\%$. Curves B,G $\lambda_B = 60\text{m}$; $\lambda_C = 144\text{m}$; $\epsilon = 10^{-2}\text{m}^2\text{s}^{-3}$; $H = 70\%$. Curves C,H $\lambda_B = 60\text{m}$; $\lambda_C = 144\text{m}$; $\epsilon = 10^{-3}\text{m}^2\text{s}^{-3}$; $H = 70\%$.

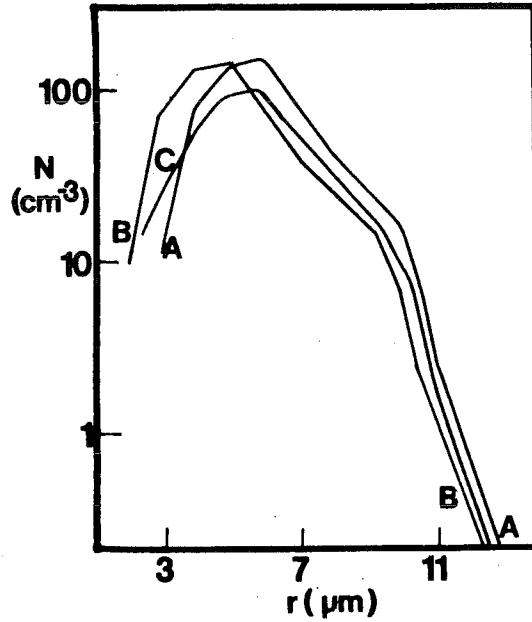


FIGURE 5. Droplet size distribution (C) at $t = 72s$ calculated by application of the diffusive model to the mixing of a spherical blob of undersaturated air with a water cloud possessing the size distribution (A) at time $t=0$. Spectrum (B) is calculated on the classical model of mixing. The liquid water content in A is $0.5g\ m^{-3}$ and in B and C, $0.32g\ m^{-3}$. $\lambda_B = 60m$; $\lambda_C = 144m$; $\epsilon = 10^{-3}m^2s^{-3}$; $H = 70\%$; $T_B = 281K$; $T_C = 279K$; $m_s = 10^{-16}g$.

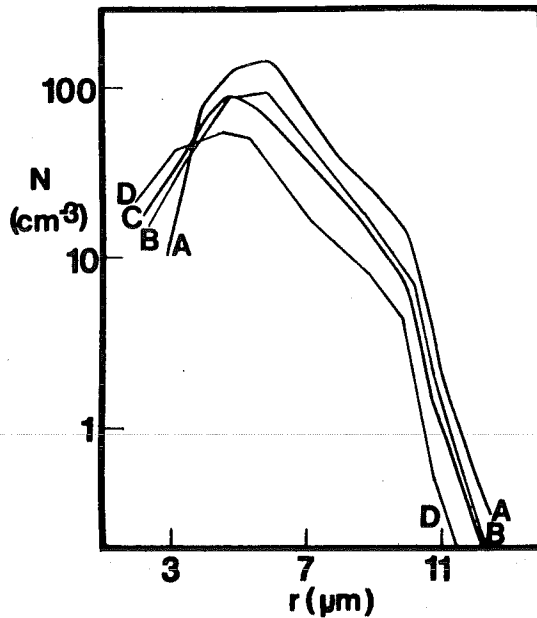


FIGURE 6. Droplet size distributions (B), (C) and (D) calculated by application of the diffusive model to the mixing of a spherical blob of undersaturated air with a water cloud possessing the size distribution (A) at time $t=0$. $\lambda_B = 60m$; $\lambda_C = 144m$; $T_B = 281K$; $T_C = 279K$; $m_s = 10^{-16}g$; $L = 0.5g\ m^{-3}$. B, $\epsilon = 10^{-3}m^2s^{-3}$, $H = 70\%$; C, $\epsilon = 10^{-2}m^2s^{-3}$, $H = 70\%$; D, $\epsilon = 10^{-3}m^2s^{-3}$, $H = 40\%$

THE ORIENTATION DISTRIBUTION OF NONSPHERICAL AEROSOL
PARTICLES IN THE ATMOSPHERE; NEW DEVELOPMENTS

Isaiah Gallily and E.M. Krushkal

Department of Atmospheric Sciences,
The Hebrew University of Jerusalem, Jerusalem, Israel 91904

PUBLICATIONS

E.M. Krushkal and Isaiah Gallily, "On the Orientation Distribution Function of Nonspherical Aerosol Particles in a General Shear Flow. Part I. The Laminar Case.", accepted for publication in the *J. Colloid and Interface Science* (1983).

INTRODUCTION

The orientation distribution of nonspherical particles in space is a significant factor which determines system properties with a directional dependence. Thus, the mean settling velocity of a cloud of orientable particles (1), the ensemble-orientationally averaged particles' diffusion tensor (2-4) and the optical-orientation interaction in a dispersion of morphologically (and optically) unisotropic particles (5-7) constitute but a few examples for the role of that distribution in system behavior. Also, the orientation of nonspherical particles (or long molecules) in a liquid medium is of great importance in rheology (8-11).

In essence, orientable particles within a flowing medium are affected by:

- i. The directing action of velocity gradients and external torques, and
- ii. The stochastic, randomizing influence of the rotational Brownian motion of the particles and the micro-turbulence of the fluid when existing.

For nonspherical *aerosol* particles in the free atmosphere, the orientation will very likely depend on the turbulence of the latter.

AIM OF STUDY

The undertaken study was planned to be conducted in the following three stages:

- i. Calculation of the orientation distribution function F of *straight fiber-like* and *planar platelet-like* aerosol particles imbedded in a general (realistic) gradient flow which can be assumed as one "realization" of the turbulent field;
- ii. Calculation of the orientation in the turbulent atmosphere;
- iii. Experimental verification of the theoretical results.

It is the first stage which is reported here.

FORMULATION OF THE PROBLEM

We considered a system of small spheroidal particles immersed in a general shear laminar flow which is given in their vicinity by

$$\mathbf{u}(\mathbf{x}, t) = \mathbf{W}(t) \cdot \mathbf{x} \quad [1]$$

where \mathbf{u} is the velocity, \mathbf{W} the gradient, and \mathbf{x} and t are the location vector and time, respectively.

For a medium free of external torques, and in the absence of a concentration source, the orientation density function of the particles F is described in orientation space by the Fokker-Planck equation

$$\partial F / \partial t + \nabla \cdot (\mathbf{F}\boldsymbol{\omega} - \mathbf{D} \cdot \nabla F) = 0 \quad [2]$$

in which $\boldsymbol{\omega}$ is the rotational velocity of the particles and \mathbf{D} is their *rotational* diffusion tensor.

THE ROTATIONAL VELOCITY COMPONENTS

The rotational velocity $\boldsymbol{\omega}$ of ellipsoidal particles in a *creeping* flow was calculated by Jeffery (12) in general but given by him only for a simple Gouette flow; likewise, it was later obtained by Hinch and Leal (13) and Takserman-Krozer and Ziabicki (14) for restricted situations. So, to get the necessary *general* expressions, we adopted the external (x_k) and body (x'_k) systems of coordinates shown in Fig. 1 and used the known kinematic relations between the (body) components of $\boldsymbol{\omega}$ and the temporal change of the Euler angles φ, θ, ψ as well as the equations of Jeffery (12)

$$\omega_i = (1/2) [V'_{kj} + S'_{kj} (a_j^2 - a_k^2) / (a_j^2 + a_k^2)] \quad [3]$$

where $i, j, k \rightarrow 1, 2, 3$, the vorticity component V'_{kj} is given by $V'_{kj} = W'_{Rj} - W'_{jR}$, the strain component S'_{kj} is $S'_{kj} = W'_{Rj} + W'_{jR}$, $W'_{kj} = \partial u'_k / \partial x'_j$, and a_1, a_2, a_3 are the semi-axes of the ellipsoidal particle with a_1 along x'_1 .

By the similarity transformation from x_k to x'_k , and for rotational ellipsoids ($a_2 = a_3$) which can simulate long cylinders or flat disks when their aspect ratio is appropriately adjusted, we finally got that

$$\dot{\varphi} = (V_{32}/2) + c_{10}^2 \theta (E_{31} c \varphi - E_{21} s \varphi) + \lambda [(1/2) S_{32} c_2 \varphi - Q_1 s_2 \varphi] \quad [4]$$

and

$$\dot{\theta} = G_{2131} c^2 \theta - G_{2213} s^2 \theta + (\lambda/2) [Q_2 + Q_1 c_2 \varphi + (1/2) S_{32} s_2 \varphi] \quad [5]$$

where, for the sake of brevity, we denoted

$$E_{ik} = (1/2) (V_{ik} + \lambda S_{ik}), \quad G_{ijkl} = E_{ij} c \varphi + E_{kl} s \varphi, \quad Q = (1/2) (W_{22} - W_{33}),$$

$$Q_2 = (1/2) (W_{22} + W_{33} - 2W_{11}), \quad V_{ik} = W_{ik} - W_{ki}, \quad S_{ik} = W_{ik} + W_{ki}, \quad W_{ik} = \partial u_i / \partial x_k, \quad c_m \theta = \cos m \theta,$$

$$\cos^m \theta, \quad s_m \theta = \sin m \theta, \quad s^m \theta = \sin^m \theta, \quad \text{and similarly for } \varphi; \lambda, \text{ the geometric factor, is defined by}$$

$$\lambda = (R^2 - 1) / (R^2 + 1), \quad R \text{ being the aspect ratio of the particles.}$$

The special cases of the previously studied simple shear and extensional flows are easily derived from the above expressions.

THE SOLUTION OF THE FOKKER-PLANCK EQUATION

Introducing the dimensionless parameters $\tilde{W}_{ik} = W_{ik} / W_0$ and $\tilde{t} = \tau W_0$, we could write the Fokker-Planck equation ([2], [4], [5]) as

$$\partial F / \partial \tilde{t} + (1/\sin \theta) \frac{\partial}{\partial \theta} (F \dot{\theta} \sin \theta) + \frac{\partial}{\partial \varphi} (F \dot{\varphi}) = \Delta F / \alpha \quad [6]$$

where α , the rotational Peclet number is $\alpha = W/D$ and D is the mid-diameter rotational diffusion coefficient; the sign \sim is henceforth omitted for simplicity.

The normalization condition is expressed by

$$\int_0^{2\pi} \int_0^\pi F \sin \theta \, d\theta \, d\varphi = 1. \quad [7]$$

According to the theory of Fourier series, the solution of [6] can be obtained in the form of

$$F = \sum_{n=0}^{\infty} \sum_{m=0}^n (1 - \frac{1}{2} \delta_{m0}) [A_{on}^m(t) c_m \varphi + A_{1n}^m(t) s_m \varphi] P_n^m(c\theta) \quad [8]$$

as long as F has a Laplacian in θ and φ . Furthermore, such a function can be *uniformly* approximated at any t by a *finite* series of orthogonal spherical harmonics.

Now, by inserting [8] into [6] and taking account of the symmetry properties of F which are deduced from physical considerations, we got the system of the simultaneous equations for $A_{kn}^m(t)$

$$dA_{kn}^m/dt = [n(n+1)/\alpha] A_{kn}^m - \sum_{j=n-2}^{n+2} \sum_{p=n-2}^{m+2} \sum_{l=1}^2 (1 + \delta_{m0}) [D_{l,jn}^{p,m} A_{kj}^p + (-1)^k C_{l,jn}^{p,m} A_{1-k,j}^p] \quad [9]$$

for which the expressions for $D_{l,jn}^{p,m}$ and $C_{l,jn}^{p,m}$ are given in Table 1 where V_{ik} , S_{ik} and Q_1, Q_2 are defined as beforehand and the indices j and n are even. The coefficients $d_{jn}^{p,m}$ of Table 1 are brought out in Table 2 according to the position indicated in the last column of the latter. In Table 2, $e_1 = 1/[2(2n-1)(2n+1)]$, $e_2 = 1/[2(2n-1)(2n+3)]$ and $e_3 = 1/[2(2n+1)(2n+3)]$; all other $d_{n'n'}^{m'm'}$ coefficients, including those of negative indices and those related to index combinations not appearing in the table, are zero as well as the corresponding $D_{l,jn}^{p,m}$ and $C_{l,jn}^{p,m}$ coefficients. The value $A_{00}^0 = 1/2\pi$ is obtained from the normalization condition [7] and $A_{1n}^0 = 0$ since $\sin m\varphi = 0$ for $m=0$.

It turns out that, if we take the stationary gradient field

$$W = \begin{pmatrix} W_{11} & 0 & 0 \\ 0 & W_{22} & W_{23} \\ 0 & W_{32} & W_{33} \end{pmatrix} \quad [10]$$

which includes Couette $(0, 0, qx_2)$ and extensional flows as special cases, and for small enough λ values, then, for $n \leq N = 2$, we obtain a correspondence with the solution of Peterlin (8) in the first order of λ ($w_0 = q$) and with the solution of Takserman-Krozer and Ziabicki (14), as it should be.

NUMERICAL CALCULATIONS

The particles whose orientation distribution was calculated were long prolate ellipsoids of aspect ratio $5 \leq R \leq 10^3$ and thin oblate spheroids of aspect ratio $0.01 \leq R \leq 0.1$. The characteristic dimension of these particles was taken to be $(a)_r \sim 10^{-5} - 10^{-3}$ cm; so, their rotational (mid-diameter) diffusion coefficient was $D \sim 1 \text{ sec}^{-1}$, as calculated from continuum theory (15). The typical flow velocities were assumed to be 1-10 m. sec^{-1} and the typical gradients 1 - 10 sec^{-1} , all of which correspond to Peclet numbers of $\alpha \sim 1 - 10$. Various models of flow were considered including those of a point source and a laminar jet and of a time-varying nature. The initial orientation adopted was a random one.

The system of the o. d. e. [9] was treated by a high-accuracy d.e. solver, based on the extrapolation method of Burlish and Stoer (16), and all summation operations were performed with double precision. For stationary flows and sufficiently large t , when $\partial F/\partial t \approx 0$, the solution coincided with that achieved by us through the Gauss elimination method. A fast convergence of the solution for F was achieved; thus, the calculations were carried out for $\alpha = 1$ with $n \leq N = 4, 6$, and for $\alpha = 10$ with $N = 10 - 14$, which was quite satisfactory.

EXAMPLES

As typical examples, we present here the cases of *point source* and *laminar jet* flows.

Point Source Flow

Here $u = q_0 r / 4\pi r^3$, where r is the radius vector, and

$$W_{ik} = (\delta_{ik} / r^3) - (3x_i x_k / r^5) \quad [11]$$

with $W_0 = q_0 / 4\pi r_0^3$, r_0 being a typical length and q_0 a constant; W_{ik} is considered to be a constant in the immediate neighborhood of the (small) particles.

The orientation distribution function is given in Fig. 2 as $F(\theta, \varphi)$ vs. θ for $\varphi = 0, \pi/4, \alpha = 1, R = 50 (\lambda \approx 1)$, $R = 0.02 (\lambda \approx -1)$, a platelet) and for the (arbitrary) space point $x_1 = 1, x_2 = x_3 = 0.4$. Also, in Fig. 3 we bring out curves of maximal values of F, F_m , as a function of time for $0.02 \leq R \leq 50, 1 \leq \alpha \leq 10$, and the same space point as that of Fig. 2; the position of the first maxima noted too. The preferred orientation, which is manifested by a deviation from curve A (Fig. 2), is seen to be more pronounced for platelets (curves 1, 2) than for cylinders (curves 7, 8) at $\alpha = 10$; but this difference is diminished with the decrease of α . A perspective, schematical view of particles' orientation is presented in Fig. 4 which arises from the spherical symmetry of the field.

A Circular Laminar Jet

The fluid velocities within such a jet are given by Schlichting as $u_x = (2 \gamma^2 \nu / x_1) f(\xi)$ and $u_r = (\gamma \nu \xi / x_1) [1 - (\xi^2/4)] f(\xi)$ where $\xi = \gamma r / x_1, f(\xi) = [1 + (\xi^2/4)]^{-2}$, ν is the kinematic viscosity, and γ is determined by the jet's momentum $J, J = (16/3) \pi \rho \gamma^2 \nu^2$ (ρ being the fluid's density). For this flow, the gradient components, which are taken to be constant in the vicinity of the (small) particles too, are $W_{11} = -\eta [1 - (3\xi^2/4)], W_{1r} = -\eta \xi, W_{r1} = W_{11} \xi / \gamma$ and $W_{rr} = \eta [1 - (3\xi^2/2) + (\xi^4/16)]/2 + (u_r/r)$ where r and x_i are non-dimensionalized by r_0 again; $\eta = 2\gamma^2 \nu / [x_1^2 (1 + \xi^2/4)^3]$.

The dependence of F on θ at $\varphi = 0, \pi/4$ is given in Fig. 5 for $\alpha = 1, \gamma = 1$, various particle aspect ratios R , the (arbitrary) space point $x_1 = 1, \xi = 0.5, x_2 = x_3$, and $W_0 = \alpha D = 2 \gamma^2 \nu / r_0^2$. A perspective, schematical illustration of the orientation is shown in Fig. 6 which stems from the axial symmetry of the jet.

CONCLUSIONS

° The stage of the research presented here provides one with a working method to calculate the orientation distribution of long cylinders and platelets in a general laminar flow for various (realis-

tic) particles' aspect ratios and flow conditions characterized by intermediate values of α .

◦ The solution for F comprises those of previous studies as special cases.

◦ The character of F shows regularities distinguished by perceptible maxima which indicate preferred orientation.

◦ Significant differences exist between the orientation of cylinders and platelets for flow fields whose gradient decreases with distance.

The next stage of the study is currently in progress.

ACKNOWLEDGEMENTS

This study was performed under contract DAJA 45-83-C-004 with the European Research Office, U.S. Army, whose kind help is hereby gratefully acknowledged.

REFERENCES

1. Brenner, H., and Happel, J., "Low Reynolds Number Hydrodynamics", Prentice-Hall, N.J., Chaps. 5-8 (1965).
2. Brenner, H., and Condiff, D.M., *J. Colloid Interface Sci.*, 41, 228 (1972).
3. Eisner, A.D., and Gallily, I., *ibid.*, 81, 214 (1982).
4. Eisner, A.D., and Gallily, I., *ibid.*, 88, 185 (1982).
5. Heller, W., Wada, E., and Papazian, L.A., *J. Polymer Sci.*, 47, 481 (1967).
6. Okano, K., and Wada, E., *J. Chem. Phys.*, 34, 405 (1961).
7. Spurny, K.R., *et al.*, in "Fundamentals of Aerosol Science" (D.T. Shaw, ed.), John Wiley, N.Y., Chap. 5 (1978).
8. Peterlin, A., *Z. Phys.*, 111, 232 (1938).
9. Brenner, H., and Condiff, D.M., *J. Colloid Interface Sci.*, 47, 199 (1974).
10. Stewart, W.E., and Sorensen, J.P., *Trans. Soc. Rheol.*, 16, 1 (1972).
11. Rallison, J.M., *J. Fluid Mech.*, 84, 237 (1978).
12. Jeffery, G.B., *Proc. Roy. Soc. A*, 102, 161 (1923).
13. Hinch, E.J., and Leal, L.G., *J. Fluid Mech.*, 92, 591 (1979).
14. Takserman-Krozer, R., and Ziabicki, A., *J. Polymer Sci.*, A1, 491 (1963).
15. Gans, R., *Ann. Phys.*, 86, 628 (1928).
16. Burlish, R., and Stoer, *J. Num. Math.*, 8, 1 (1966).

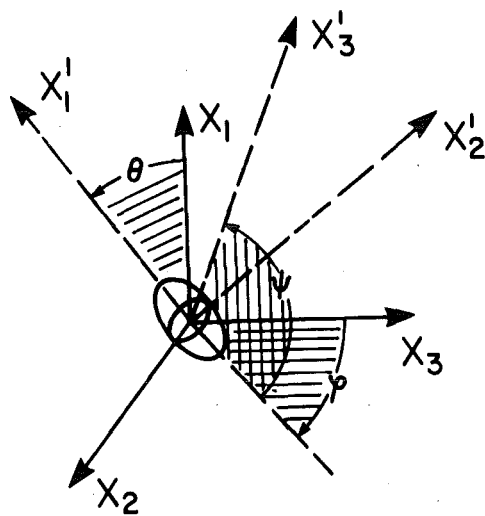


Fig. 1. The Euler angles and the two systems of coordinates.

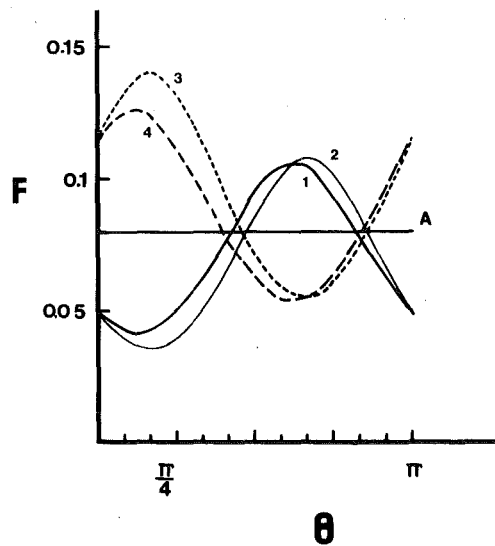


Fig. 2 The orientation distribution function F vs. θ for the point source field; $\alpha = 1$, $R = 0.02$ (platelets) and $R = 50$ (long cylinders); $t \geq 2$.

— $R = 50$, 1 - $\varphi = 0$, 2 - $\varphi = \pi/4$
 - - - $R = 0.02$, 3 - $\varphi = 0$, 4 - $\varphi = \pi/4$
 A - $t = 0$

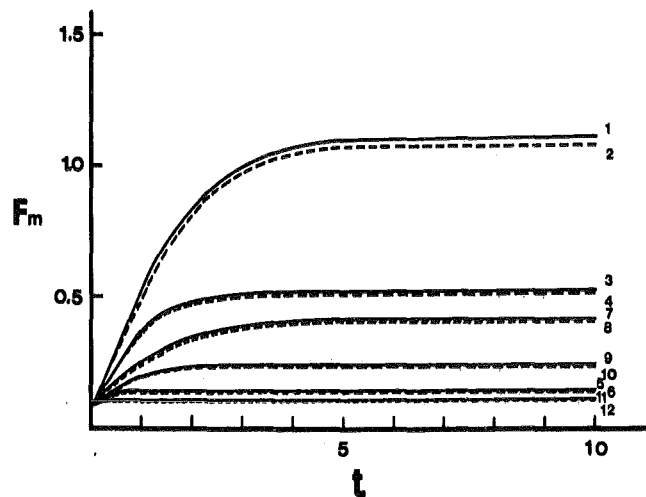


Fig. 3. The maximum values of F vs. t for: $\alpha = 1, 5, 10$; $R = 0.02, 0.1, 10, 50$, and their positions.

1 - $\alpha = 10, R = 0.02$; 2 - $\alpha = 10, R = 0.1$; 3 - $\alpha = 5, R = 0.02$; 4 - $\alpha = 5, R = 0.1$;
 5 - $\alpha = 1, R = 0.02$; 6 - $\alpha = 1, R = 0.1$; ($\theta_m = \pi/6, \varphi_m = \pi/4, t \geq 1$).

7 - $\alpha = 10, R = 50$; 8 - $\alpha = 10, R = 10$; ($\theta_m = 3\pi/4, \varphi_m = \pi/4, t \geq 2$).

9 - $\alpha = 5, R = 50$; 10 - $\alpha = 5, R = 10$; 11 - $\alpha = 1, R = 50$; 12 - $\alpha = 1, R = 10$

($\theta_m = 2\pi/3, \varphi_m = \pi/4, t \geq 1$).

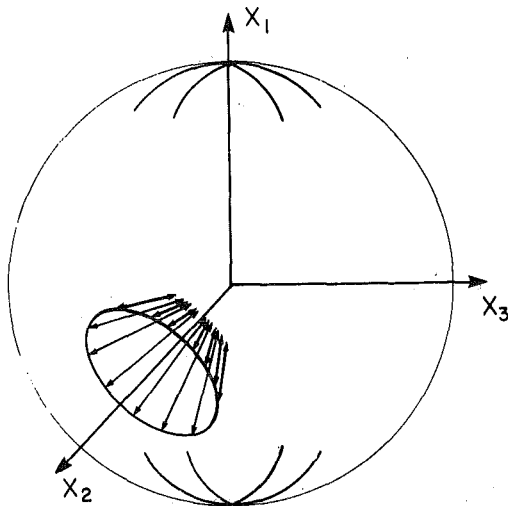


Fig. 4. A perspective view of particle orientation in a point source field (schematic).

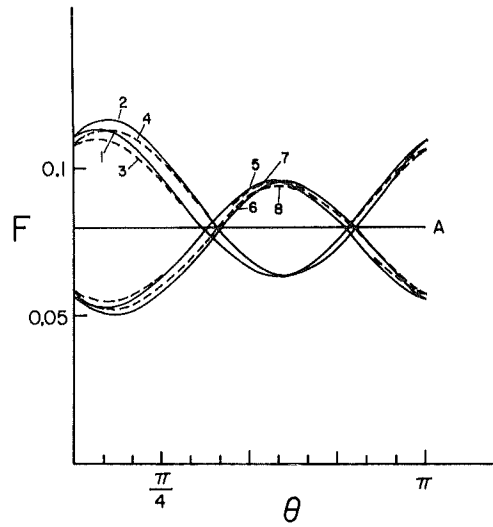


Fig. 5. The orientation distribution function F vs. θ in a laminar jet flow; $t \geq 2$.

- 1 - $R = 0.01, \varphi = 0$; 2 - $R = 0.01, \varphi = \pi/4$; 3 - $R = 0.2, \varphi = 0$;
 4 - $R = 0.2, \varphi = \pi/4$; 5 - $R = 100, \varphi = 0$; 6 - $R = 100, \varphi = \pi/4$;
 7 - $R = 5, \varphi = 0$; 8 - $R = 5, \varphi = \pi/4$.

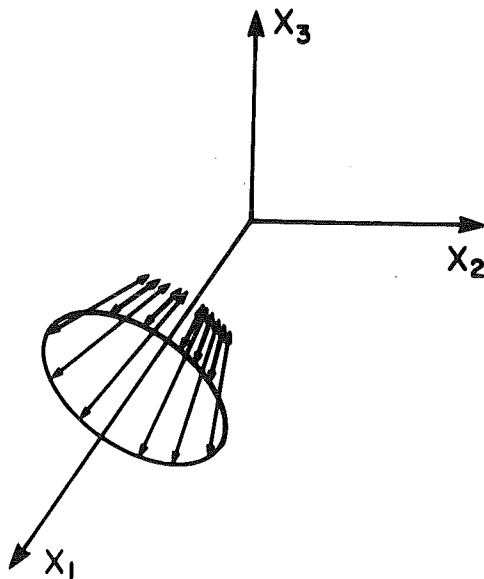


Fig. 6. A perspective view of particle orientation in a laminar jet field.

Table 1. The coefficients $D_{l,jn}^{pm}$ and $C_{l,jn}^{pm}$.

l	p	m	$D_{l,jn}^{pm}$	$C_{l,jn}^{pm}$	location of d_{jn}^{pm} in Table 2
1	$m \pm 1$	1,2,3...	$\delta_{nj}(\rho-m)V_{12}/4$ $+ \lambda d_{jn}^{pm} S_{12}$	$\delta_{nj} V_{13}/4$ $+ (\rho-m)\lambda d_{jn}^{pm} S_{13}$	I
2	$m \pm 2$	0,2,4...	$\lambda d_{jn}^{pm} [2a_1(1-\delta_{m0})$ $+ a_2 \delta_{m0} \delta_{\rho 0}]$	$m \delta_{jn} \delta_{\rho m} V_{32}/2$ $+ (\rho-m)\lambda d_{jn}^{pm} S_{32}/2$	if $p=m=0$ III else II

Table 2. The coefficients $d_{nn'}^{mm'}$.

n'	I		II		III	
	m'	$d_{nn'}^{mm'}$	m'	$d_{nn'}^{mm'}$	m'	$d_{nn'}^{mm'}$
$n-2$	$m-1$	$-e_1(n-2) \prod_{i=0}^2 (n+m-i)$	$m-2$	$\frac{e_1}{2}(n-2) \prod_{i=0}^3 (n+m-i)$	0	$-e_1 \prod_{i=0}^2 (n-i)$
n	$m-1$	$3e_1(2m-1)/2$	$m-2$	$\frac{3e_2}{2} \prod_{i=1}^2 (n-m+i)$ $\times (n+m-i+1)$	0	$e_2 n(n+1)$
$n+2$	$m-1$	$-e_3(n+3) \prod_{i=1}^3 (n-m+i)$	$m-2$	$-\frac{e_3}{2}(n+3) \prod_{i=1}^4 (n-m+i)$	0	$e_3 \prod_{i=1}^3 (n+i)$
$n-2$	$m+1$	$e_1(n-2)(n+m)$	$m+2$	$e_1(n-2)/2$		
n	$m+1$	$3e_2(2m+1)/2$	$m+2$	$3e_2/2$		
$n+2$	$m+1$	$e_3(n+3)(n-m+1)$	$m+2$	$-e_3(n+3)/2$		

MEASUREMENT OF THE KINETICS OF SOLUTION DROPLETS IN A
CONTINUOUSLY MIXED CHAMBER

G. O. RUBEL
USAMCCOM, Chemical Research and Development Center
Aberdeen Proving Ground, Maryland 21010

and

J. W. Gentry
University of Maryland
Department of Chemical Engineering
College Park, Maryland 20783

ABSTRACT

An experimental system is designed for the measurement of the evaporation and growth kinetics of individual solution droplets. Electrostatically charged droplets, nominally tens of micrometers in diameter, are suspended in a hyperboloidal electrodynamic chamber by balancing the droplet weight against a uniform electrostatic field. By controlling the mixing dynamics in the chamber with specific flow configurations, a continuously mixed chamber is achieved. Consequently the instantaneous chamber relative humidity is predicted from an exponential law with a characteristic relaxation time which is given by the ratio of the chamber volume and the gas volumetric flow rate. The evaporation and growth kinetics of phosphoric acid droplets are measured for relative humidity changes between 30 and 80%. Comparison between experimental and theoretical instantaneous droplet masses reveals less than a 5% deviation.

The present system is employed to analyze the effect of adsorbed hexadecanol surfactant molecules on the evaporation and growth kinetics of phosphoric acid droplets. It is found a critical coverage exists which will transform the droplet kinetics from a continuum to a slip flow controlled process.

Concomitantly, the condensation coefficient is reduced from unity to 4.0×10^{-5} as droplet kinetics occur in the presence of a complete monolayer of hexadecanol.

1. INTRODUCTION

Previous methods to measure the kinetics of solution droplets can be divided into two main categories: single particle and many particle kinetic studies. Single particle studies involve the suspension of droplets using mechanical [1], aerodynamic [2], photophoretic [3] and electrodynamic forces [4].

The use of mechanical structures, such as microscope slides, to support droplets for visual observation has the disadvantage of perturbing the droplet surface and thus interfering with the mass transfer. Both aerodynamic and photophoretic suspensions

introduce secondary processes which complicate the droplet kinetics: ventilation effect for aerodynamic suspension and nonadiabatic effects for photophoretic suspension. Employment of electrodynamic suspension to measure the evaporation kinetics of solution droplets has been demonstrated by Rubel [5] to be an accurate and nonintrusive technique.

Rubel measured the evaporation rates of binary oil droplets, composed of di-n-butylphthalate and dioctylphthalate, in the presence of an oil vapor free environment. By controlling the characteristic time of mixing of the electrodynamic balance chamber to be much less than the characteristic time of droplet evaporation, the chamber oil vapor concentration is maintained at a negligible value. Consequently, it was demonstrated the binary oil solution acts thermodynamically ideal over a wide range of solution concentrations.

However, due to the relatively high vapor pressure of water, within the dynamic range of mixing rates attainable in the electrodynamic chamber, the characteristic time of water-based solution droplets is comparable to the characteristic time of mixing. Thus to quantitatively analyze the droplet kinetics, knowledge of the time dependent water vapor concentration is required. To this end by specifically controlling the mixing dynamics internal to the suspension chamber, a continuously mixed chamber is established. Consequently, the instantaneous chamber relative humidity is predicted from an exponential law with a characteristic relaxation time which is given by the ratio of the chamber volume and the gas volumetric flow rate. Thus from knowledge of the initial conditions and the droplet physio-chemical properties, the time-dependent droplet mass is predicted from continuum mass transfer theory. The evaporation and growth kinetics of phosphoric acid droplets are measured for relative humidity changes between 30 and 80%. Comparison between theory and experiment reveals less than a 5% deviation.

The present system is used to analyze the effect of adsorbed surfactants (hexadecanol) on the evaporation rates of phosphoric acid droplets. It is found a critical coverage exists which will transform the droplet kinetics from continuum to a free molecule controlled process. Concomitantly, the evaporation/condensation coefficient is reduced from unity to 4.0×10^{-5} which is in close agreement with the value of 3.5×10^{-5} reported by Derjaguin [6].

The present single particle kinetic study system is superior to many particle kinetic study techniques which employ light scattering data to deduce particle size

[7] in that detailed knowledge of the particle optical properties is not required. Furthermore, due to the hydrodynamic complexities associated with a continuous aerosol stream, the single particle electrodynamic/mixed chamber system represents a more characterizable system and therefore permits more accurate quantitative analysis.

2. EXPERIMENTAL SYSTEM

Earlier Rubel [8] designed an experimental technique which employed electrodynamic balance to measure the thermodynamic mass and diameter increase of hygroscopic droplets with increasing relative humidity.

For a well-mixed chamber the instantaneous rate of change of some extensive property of the gas internal to the chamber is proportional to the difference between the instantaneous value and the value of the property in the external source. The time-dependent value of the property is modeled by an exponential law with a characteristic relaxation time which is given by the ratio of the chamber volume and the gas volumetric flow rate. To guarantee complete mixing in the hyperboloidal chamber, toroidal baffles are positioned at the top and bottom of the hyperboloidal chamber. By drawing an equivalent volume of gas through the upper baffle, a uniform well-mixed chamber is achieved.

Figure 1 shows the schematic of the experimental system for the measurement of the growth and evaporation kinetics of solution droplets. Two separate humidification flows are employed, one stabilized at a high relative humidity and the other at a low relative humidity. Each humidification line controls the level of humidity by varying the proportions of the total inlet flow that pass through a dessicator and a water bubbler. Both humidification lines pass the same quantity of air per unit time. To measure the evaporation kinetics of solution droplets, the electrodynamically stabilized droplet is brought to equilibrium with the gas flow emanating from the high humidity line. Previous to this conditioning, the wet bulb temperature of the high humidity line is measured using a condensation/light scattering hygrometer. Once the droplet is stabilized, the diameter of the droplet is measured with a 35mm objective in conjunction with an image splitter. From knowledge of the initial relative humidity, the density of the solution droplet is determined and thus the initial mass of the droplet is known. This assumes of course that the solution properties are well characterized which is the case for orthophosphoric acid and water solutions.

With the high humidity flow conditioning the chamber, the wet bulb temperature of the low humidity line is monitored. To initiate evaporation, a two-way valve is used

to enter the suspension chamber. Since the flow line Reynolds number is generally less than 1000 and thus laminar hydrodynamics exist, the low humidity flow drives the high humidity gas through the flow line without mixing. Thus the time-dependent relative humidity internal to the chamber is driven by the mixing of a constant external source of humidity.

As the chamber relative humidity decreases, the droplet begins to evaporate. As shown by Frickel, et al. [9], the suspended droplet moves in a closed orbit unless the weight of the droplet is balanced against a uniform electric field. At this point the droplet is stationary and the balancing voltage is proportional to the mass of the droplet. Thus, as the relative humidity decreases and the droplet evaporates, the status of the droplet is optically observed. By adjusting the weight balancing direct current voltage so that the droplet remains stationary during the evaporation phase, the time-dependent mass is recorded. To study the kinetics of growth, the complete procedure is reversed. This merely required the repositioning of the two-way valve so that now high relative humidity gas represents the external source.

To study the effect of adsorbed surfactant molecules on the evaporation rates of phosphoric acid solution droplet, the experimental system is designed so the humidified air can be partially saturated with surfactant gas. The partial saturation is achieved by passing the humidified air through a glass tube which contains a specific quantity of surfactant material, in the present case hexadecanol. To augment the surfactant pressurization of the humidified air, the tube temperature is elevated by applying heating tape directly to the glass tube. By regulating the inlet flow rate and the tube temperature, a controlled degree of hexadecanol gas saturation is achieved. To achieve a dramatic reduction in the droplet kinetics, a critical coverage of adsorbed surfactant molecules is required. To achieve the critical coverage, a minimum degree of gas saturation is required. Thus tube temperature was elevated until observed kinetics were substantially reduced to hexadecanol monolayers.

3. RESULTS

Figure 2 shows the evaporation rates of phosphoric acid droplets measured in the electrodynamic chamber using both a well-mixed flow and a poorly-mixed flow. The initial droplet diameter is 94 micrometers and the initial and final relative humidities are 77 and 28% respectively. Except for the early stages of evaporation, i.e., less than three seconds, the evaporation rate of the solution droplet is more rapid in the well-mixed chamber. This is understandable from the viewpoint that, for the poorly-

mixed chamber, the external source of gas arrives at the droplet surface having experienced less mixing therefore driving the evaporation process more vigorously. However, the chamber is not well mixed and the parcels of gas previously protected by the geometry of the chamber begin to gradually mix with the external source. This subsequently reduces the evaporation rate, the effective rate of mixing is lower than that of the well-mixed chamber, and the total time required for droplet evaporation is substantially increased.

Figure 3 reveals the growth kinetics of a phosphoric acid droplet, initial diameter 76 micrometers, as measured in the well-mixed electrodynamic chamber. The initial relative humidity is 13% and the final relative humidity is 59%. As in the case of droplet evaporation, the kinetics are rapid initially and then slow as the equilibrium properties of the solution droplet are achieved.

The dramatic reduction in the evaporation rate of phosphoric acid droplets, due to the presence of adsorbed surfactant hexadecanol molecules, is shown in Figure 4. In comparison, for the same initial and final relative humidities, the kinetics of an acid droplet without a critical coverage of hexadecanol are shown. In the presence of the hexadecanol monolayer, the evaporation kinetics are no longer diffusion controlled but belong to the slip flow regime.

4. QUANTITATIVE ANALYSIS

Chamber Relative Humidity

Since the chamber volume is well mixed, the instantaneous chamber relative humidity $S(t)$ is given by

$$S(t) = S_e + (S(0) - S_e) e^{-\beta t} \quad (1)$$

where $S(0)$ is the initial chamber relative humidity and $\beta = V/V_C$.

Droplet Mass Transfer

The quasistationary isothermal molar flux toward a solution droplet composed of a nonvolatile solute and a water solvent was derived by Fuchs [10] using flux matching boundary conditions. Recognizing the mass transport within one mean free path of the droplet is controlled by kinetic processes, Fuchs derived the steady state concentration field surrounding a droplet subject to the boundary condition that the kinetic and diffusive flux be equivalent. The resulting water molar flux is

$$\frac{dn}{dt} = \frac{4\pi P^o r^2}{RT} \left(\frac{S_\infty - S_r}{\frac{4}{\infty V} + \frac{r^2}{D(r + \lambda)}} \right) \quad (2)$$

(a) Mass Transfer in the Absence of Monolayers

For water solutions free of surface active compounds, the condensation coefficient is approximately unity. In the present study, droplet radii are greater than 20 micrometers and

$$\frac{r^2}{D(r + \lambda)} \gg \frac{4}{\infty V}$$

Thus to an excellent approximation, equation 2 becomes

$$\frac{dn}{dt} = \frac{4\pi DP^o}{RT} r(S_\infty - S_r) \quad (3)$$

This molar flux is the expression derived by Maxwell [12] using continuum arguments.

The droplet saturation ratio is given by

$$S_r = a(p) \quad (4)$$

where $a(p)$ is the water activity of the solution characterized by the solute weight percent p . For the specific solution of orthophosphoric acid and water, the water activity can be modeled by a cubic polynomial in p as well as the solution density. Use is made of the auxiliary relations

$$m = M_w n + p(0)m(0)$$

and

$$r = (3m/4\pi\rho)^{1/3} \quad (5)$$

where m is the instantaneous mass of the droplet, $m(0)$ is the initial droplet mass and $p(0)$ is the initial weight percent acid.

Substituting eq. 1-5 into eq. 3 results in a first order nonlinear differential equation for the water mole number. Using a fourth order Runge Kutta numerical scheme, the water mole number is calculated as a function of time. The time-dependent droplet mass is calculated from eq. 5. For the kinetic data shown in Figures 3 and 4, the gas volumetric flow rate is 10.20 cm³/sec; and with a chamber volume of 60 cm³,

the chamber relative humidity relaxation time, β^{-1} , is 5.88 seconds. Comparison between experiment and theory reveals less than a 5% deviation for condensational and evaporational kinetics as measured in the well-mixed electrodynamic chamber. For distinction, the kinetics of evaporation of phosphoric acid droplets for the same conditions except for a relaxation time of 2.94 seconds are calculated. Thus a reduction by a factor of two in the relaxation time results in significant differences between theory and experiment.

(b) Mass Transfer in the Presence of Monolayers

Considerable research has been conducted on the evaporation rates of water with adsorbed monolayers [14]. Recently Derjaguin [1] analyzed the passivation of condensational growth of drops of water and salt solutions and reported the existence of a critical coverage of hexadecanol which resulted in a dramatic reduction in the water condensation coefficient. As a part of this study, the evaporation rates of phosphoric acid droplets with adsorbed monolayers of hexadecanol are measured. Figure 4 shows the evaporation of a phosphoric acid droplet for initial and final relative humidities of 60 and 30% respectively. The partial pressure of hexadecanol is maintained so the adsorbed coverage exceeds the critical coverage for the water/acid solution. Consequently, the droplet evaporation is greatly reduced.

To determine the water condensation coefficient in the presence of adsorbed hexadecanol monolayers, equation 3 is utilized to compare theoretical and experimental decay rates. Figure 5 reveals the excellent agreement between theory and experiment when the condensation coefficient of water assumes the value of 4.0×10^{-5} . This value of the coefficient is close to the value 3.5×10^{-5} reported by Derjaguin [6] for the condensation coefficient of water in the presence of hexadecanol. However, since the calculated evaporation rate for $\alpha = 3.5 \times 10^{-5}$ results in a deviation between theory and experiment exceeding measurement errors, it is suggested the dissociated acid solution tends to ionize the hydrocarbon molecules thereby resulting in a less compact monolayer and a higher water condensation coefficient.

5. CONCLUSION

An extremely accurate and rapid experimental system has been developed for the measurement of the evaporation and growth kinetics of solution droplets in a well-mixed chamber. By employing electrodynamic balance and specific hydrodynamic conditions, the kinetics of growth and evaporation can be measured with less than a 5% error. The system has been employed to study the kinetics of phosphoric acid droplets

with and without adsorbed monolayers. Results indicate the water condensation coefficient in the presence of hexadecanol surfactants is reduced from unity to 4.0×10^{-5} , greater than the value reported for pure water by Derjaguin. The possibility of surfactant ionization is postulated and further research into the effect of solution pH on the water condensation coefficient is suggested.

6. REFERENCES

1. G. O. Rubel, Measurement of the Condensational Growth of Single Hygroscopic Acid Aerosol Droplets, J. Aerosol Science, vol. 12, pp 551-292, 1981.
2. R. H. Frickel, R. E. Shaffer and J. B. Stamatoff, Chambers for the Electrodynamic Containment of Charged Aerosol Particles, ARCSL-TR-77041, USARRADCOM, A.P.G., MD, 1978.
3. N. A. Fuchs, Evaporation and Droplet Growth in Gaseous Media, Pergamon Press, Oxford, 1959.
4. H. S. Carslaw and J. C. Jeager, Conduction of Heat in Solids, Clarendon Press, Oxford, 1959.
5. J. C. Maxwell, Collected Scientific Papers, vol.11, Cambridge Univ. Press, 1890.
6. N. H. Fletcher, The Physics of Rainclouds, Cambridge Univ. Press, London, 1966.
7. V. La Mer, Retardation of Evaporation by Monolayers, Pergamon Press, Oxford, 1962.

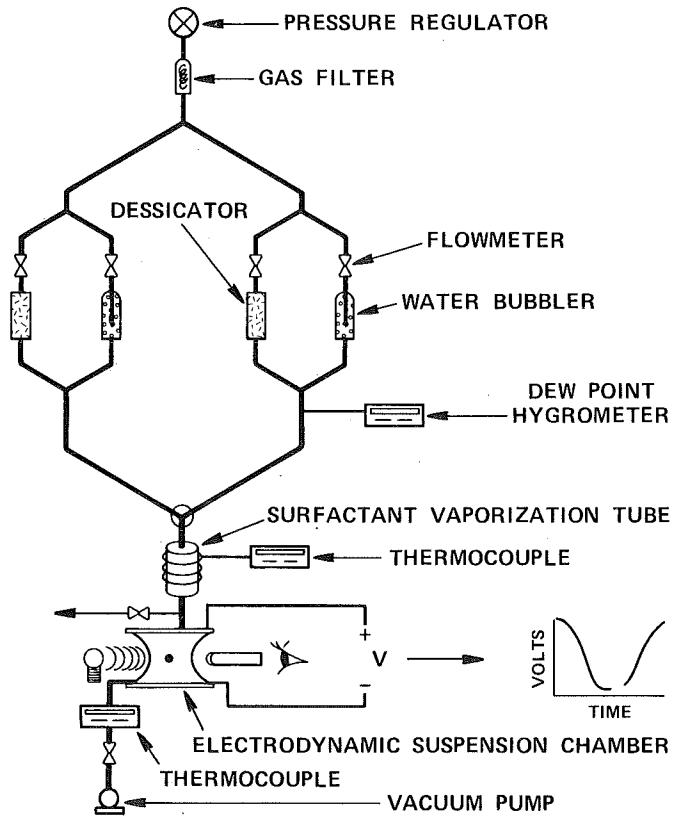


Figure 1. Schematic of aerosol growth/evaporation measurement system.

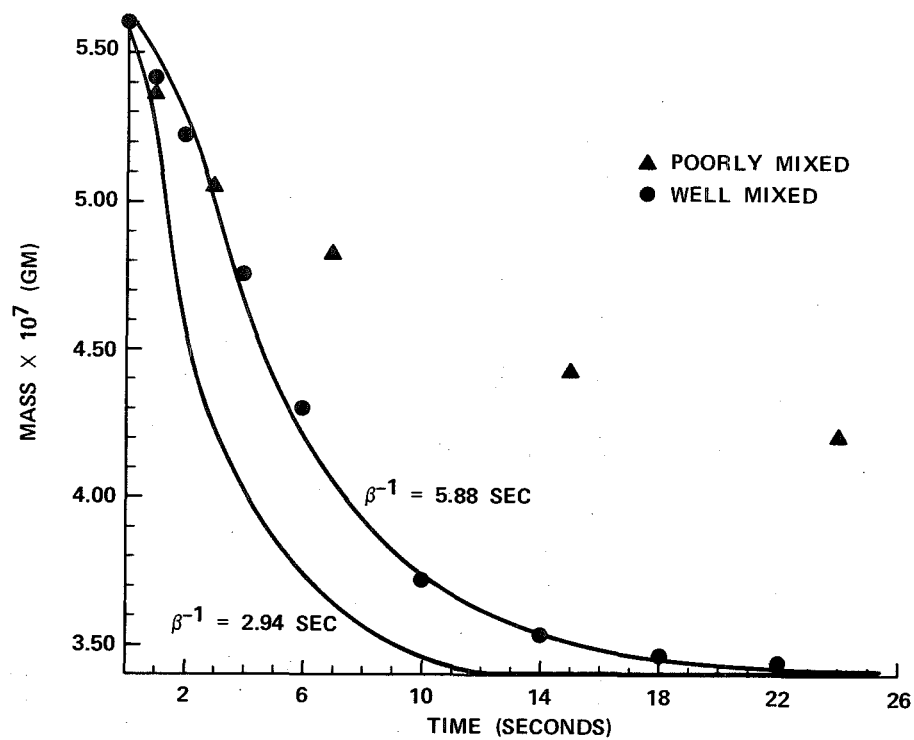


Figure 2. Comparison of the evaporation rate of phosphoric acid droplets in the poorly-mixed chamber ($\Delta\Delta\Delta$) and the well-mixed chamber (ooo). Also shown is the close agreement between theory (—) and experiment (ooo) when the chamber relaxation time is given by the ratio of the chamber volume and the volumetric flow rate.

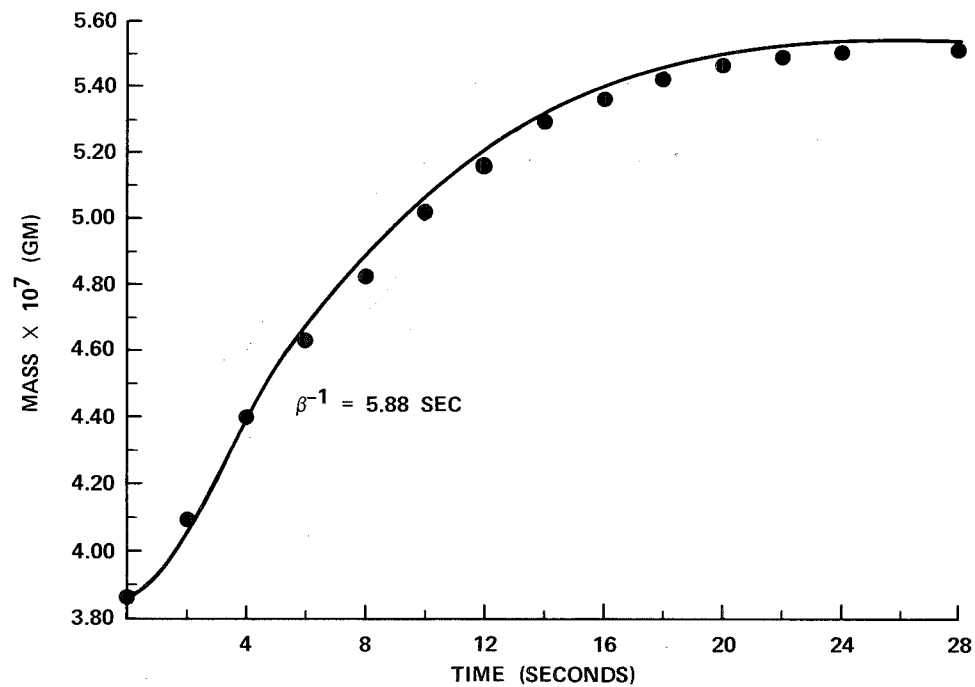


Figure 3. Comparison of the measured growth rate of phosphoric acid droplets (ooo) and the theoretical values (—) for a chamber relaxation time of 5.88 sec. The initial and final relative humidities are 13 and 59% respectively.

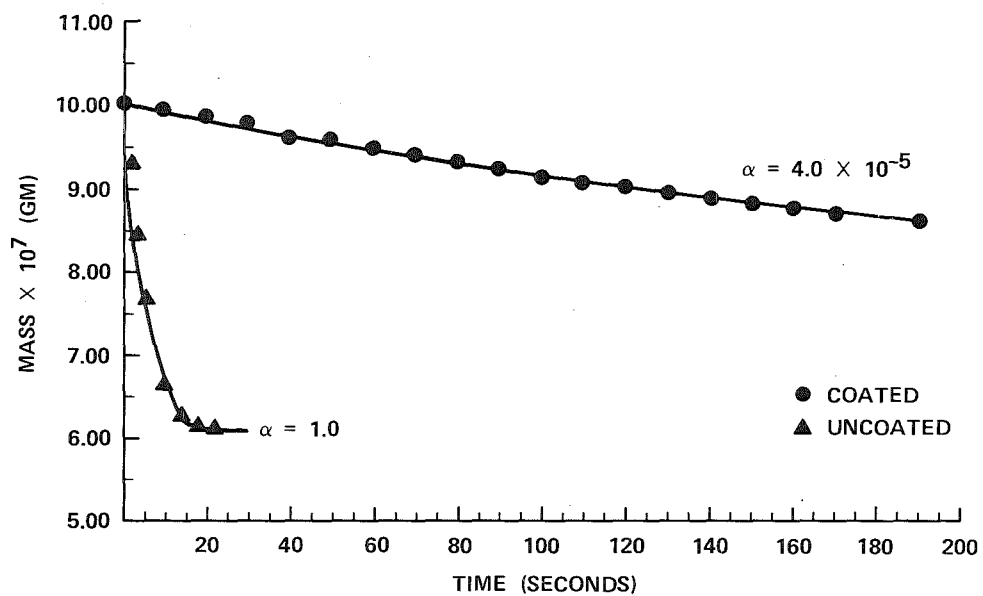


Figure 4. Measurement of the evaporation rate of phosphoric acid droplets with and without a critical coverage of adsorbed hexadecanol surfactant molecules. In the presence of the hydrocarbon monolayer, the water condensation coefficient is reduced from unity to 4.0×10^{-5} .

TIME EVOLUTION OF PARTICLE SIZE DISTRIBUTION DURING AEROSOL COAGULATION

K. W. Lee, H. Chen, and J. A. Gieseke
BATTELLE
Columbus Laboratories
505 King Avenue
Columbus, Ohio 43201

ABSTRACT

Coagulation of aerosol particles in the free-molecule regime has been studied theoretically by converting the governing partial integro-differential equation into a set of two ordinary differential equations. The approach assumes that the size distribution of an aerosol attains or can at least be represented by a time-dependent lognormal distribution function during the coagulation process. The calculations have been performed and the results found to be in good agreement with results for previous theories. In addition, an asymptotic size distribution function is found as an alternative solution for the self-preserving particle size distribution function for Brownian coagulation of an aerosol in the free-molecule regime. A substantial portion of this work has been accepted for publication as follows: Lee, K. W., Chen, H., and Gieseke, J. A., "The Lognormally Preserving Size Distribution for Brownian Coagulation in the Free-Molecule Regime", submitted to Aerosol Sci. & Tech. (1984).

INTRODUCTION

Many important physical properties of suspended aerosol particles such as light scattering, electrostatic charges, and toxicity as well as their behavior involving physical processes such as diffusion, condensation, and thermophoresis depend strongly upon their size distribution. Applications such as atmospheric science, combustion technology, inhalation toxicology, and nuclear safety analyses often deal with particles whose sizes are smaller than the mean free path of the gas molecules. An important aerosol behavior mechanism affecting the size distribution of such small particles is Brownian coagulation. In many basic and applied fields, the time-dependent size distribution due to the particle coagulation is therefore of fundamental importance and interest.

Previous work on Brownian coagulation of aerosol particles in the free-molecule regime includes Hidy and Brock (1970), Lai, et al. (1972), Tolfo (1977), and Brockmann, et al. (1982). In particular, Lai, et al., proposed a size distribution that is attained by coagulating aerosols. Their solution and the work of Friedlander and Wang (1966) for the continuum regime are referred to as the self-preserving size distribution theory and have been used extensively by many investigators for both theoretical and experimental aerosol studies. That theory is based on an assumption regarding the form of the size distribution and the results have proven to be convenient for representing the size distribution of an aerosol that has already been coagulating for a long time.

Recently Lee (1983) took another approach based on the use of an integration method of moments and suitable approximations to provide an analytical solution that resolves the size distribution of a coagulating aerosol in the continuum regime over the entire period of time. Time-dependent size distributions of particles undergoing Brownian coagulation were assumed to preserve a lognormal

function. As a result of this approach it was possible to examine quantitatively many important and interesting characteristics of the Brownian coagulation process such as the effects of time and the initial spread of the particle size distribution on the number decay, on the increase of the mean particle size, and on the change in the standard deviation.

The purpose of the present work is to extend that theory to include the coagulation of aerosol particles in the free-molecule regime. A simple means is provided for calculating the time-dependent size distribution of a coagulating aerosol. Further, an explicit analytic form of the asymptotic size distribution that applies to the free-molecule regime is proposed.

TIME EVOLUTION OF SIZE DISTRIBUTION

The size distribution of an aerosol in the free-molecule regime undergoing Brownian coagulation is governed by the following equation by Muller (1928):

$$\frac{\partial n(v,t)}{\partial t} = \frac{1}{2} \int_0^v \beta(v-\bar{v},\bar{v})n(v-\bar{v},t)n(\bar{v},t)d\bar{v} - n(v,t) \int_0^\infty \beta(v,\bar{v})n(\bar{v},t)d\bar{v} \quad (1)$$

coupled with the kernel (Hidy and Brock, 1970)

$$\beta(v,\bar{v}) = K(v^{1/3} + \bar{v}^{1/3})^2 \left(\frac{1}{v} + \frac{1}{\bar{v}} \right)^{1/2}, \quad (2)$$

where $n(v,t)$ is the particle size density function, t is the time, $\beta(\bar{v},v)$ is the collision kernel for two particles of volume v and \bar{v} , K is the collision coefficient $\left[= \left(\frac{3}{4\pi} \right)^{1/6} \left(\frac{6kT}{\rho} \right)^{1/2} \right]$, k is the Boltzmann constant, T is the absolute temperature, and ρ is the particle density.

The essential and critical assumption to be made in the present study is that time-dependent size distribution of an aerosol undergoing Brownian coagulation can be represented by a lognormal function. The lognormal size distribution function is written as:

$$n(v,t) = \frac{N}{3\sqrt{2\pi} \ln\sigma} \exp \left[\frac{-[\ln^2\{v/v_g\}]}{18 \ln^2\sigma} \right] \frac{1}{v} \quad (3)$$

where $v_g(t) [= 4\pi r_g^3/3]$ is the geometric number mean particle volume, $r_g(t)$ is the geometric number mean particle radius, $\sigma(t)$ is the geometric standard deviation based on particle size, and $N(t)$ is the number of particles. It should be noted that, although the assumption just employed restricts the solution to the form of a lognormal function, the three size parameters of the distribution N , σ , and v_g are allowed to vary with time. This type of treatment was successfully applied to the aerosol coagulation problem for the continuum regime (Lee, 1983) and for the low Knudsen number regime (Cohen and Vaughan, 1971; Reed, et al., 1980). Many experimental results and numerical calculations

often indicate that particle size distributions during coagulation indeed fit a lognormal function. Even if a distribution is found not to be truly lognormal, it is customary to represent calculated or measured size distributions with equivalent geometric size parameters such as N , σ , and r_g that are computed from the discretized size spectrum.

The k^{th} moment of a lognormal size distribution is written as:

$$M_k = \frac{1}{3\sqrt{2\pi} \ln\sigma} \int_0^{\infty} v^k \exp\left[\frac{-\ln^2(v/v_g)}{18 \ln^2\sigma}\right] \frac{dv}{v} \quad (4)$$

where k is a real number. Among M_k 's, $M_0 (=N)$ represents the total number of particles and M_1 the total volume of particles. After combining Equation (1) with Equation (4), the following is obtained:

$$\frac{dM_k}{dt} = \frac{1}{2} \int_0^{\infty} \int_0^{\infty} [(v+\bar{v})^k - v^k - \bar{v}^k] \beta(v, \bar{v}) n(v, t) n(\bar{v}, t) dv d\bar{v} \quad (5)$$

It is noted that the collision kernel $\beta(v, \bar{v})$ appearing in Equation (2) is in a form that appears to be rather difficult to expand into a series with a manageable number of terms while covering a wide range of the particle size that has to be dealt with in a coagulation problem. In order to overcome this difficulty, we approximate $\left(\frac{1}{v} + \frac{1}{\bar{v}}\right)^{1/2}$ with $b \left[\left(\frac{1}{v}\right)^{1/2} + \left(\frac{1}{\bar{v}}\right)^{1/2}\right]$ where b is to be calculated by:

$$b = \frac{\int_0^{\infty} \int_0^{\infty} v^k \beta(v, \bar{v}) n(v) n(\bar{v}) dv d\bar{v}}{\int_0^{\infty} \int_0^{\infty} \left[\left(\frac{1}{v}\right)^{1/2} + \left(\frac{1}{\bar{v}}\right)^{1/2}\right] v^k \beta(v, \bar{v}) n(\bar{v}) \cdot n(v) dv d\bar{v}} \quad (6)$$

Calculations with Equation (6) indicate that the values for b depend upon the initial geometric standard deviation σ_0 and on the moment to be integrated. As shown in Table I, the value for b at $t = 0$ ranges from $1/\sqrt{2}$ for $\sigma_0 = 1.0$ and $k = 0$ to 0.7550 for $\sigma_0 = 3.0$ and $k = 2$. As $t \rightarrow \infty$, however, b would approach 0.7415 regardless of σ_0 for the reason to be discussed later. For simplicity, b will be assumed constant by taking the average of the listed initial and final values for $k = 0$ and 2, respectively. This type of simplification is regarded as being suitable, considering that the assumption regarding the form of the size distribution is more critical. Both this assumption and the above simplification will be checked out later in this work.

Substituting Equation (2) into Equation (5) and writing the results for $k = 0$ and 2, we have

$$\frac{dM_0}{dt} = -bK[M_{2/3}M_{-1/2} + 2M_{1/3}M_{-1/6} + M_{1/6}M_0] \quad (7)$$

$$\frac{dM_2}{dt} = 2bK[M_{5/3}M_{1/2} + 2M_{4/3}M_{5/6} + M_{7/6}M_1] \quad (8)$$

for $k = 1$, Equation (5) becomes

$$M_1 = \text{constant}, \quad (9)$$

which is a trivial solution indicating that the total volume of particles is conserved.

The properties of a lognormal function are such that the following equation is true for any k^{th} moment.

$$M_k = M_0 v_g^k \exp\left(\frac{9}{2} k^2 \ln^2 \sigma\right) \quad (10)$$

If Equation (10) is written for $k = 0, 1$ and 2 and subsequently solved for v_g and σ in terms of M_0, M_1 , and M_2 , we have

$$\ln^2 \sigma = \frac{1}{9} \ln\left(\frac{M_0 M_2}{M_1^2}\right) \quad (11)$$

$$v_g = M_0^{-3/2} M_1^2 M_2^{-1/2} \quad (12)$$

Substituting Equation (10) for the moments appearing in Equations (7) and (8) and substituting Equations (11) and (12) thereafter, we have

$$\begin{aligned} \frac{dM_0}{dt} = & -bK \left[M_0^{151/72} M_1^{-13/36} M_2^{19/72} + 2M_0^{131/72} M_1^{7/36} M_2^{-1/72} + \right. \\ & \left. M_0^{127/72} M_1^{11/36} M_2^{-5/72} \right] \end{aligned} \quad (13)$$

$$\begin{aligned} \frac{dM_2}{dt} = & 2bK \left[M_0^{19/72} M_1^{-97/36} M_2^{31/72} + 2M_0^{-1/72} M_1^{-77/36} M_2^{11/72} + \right. \\ & \left. M_0^{-5/72} M_1^{-73/36} M_2^{7/72} \right] \end{aligned} \quad (14)$$

It should be noted that the integro-differential equation given by Equation (1) has just been converted into a set of two first order ordinary differential equations. Since there are now two unknown variables, M_0 and M_2 , and there are also two equations, the solution can readily be obtained using any standard numerical package for solving first order equations. Here M_1 is a constant which is known from the initial condition as already discussed with Equation (9). After

M_0 and M_2 are solved from Equations (13) and (14), v_g and σ can be computed using Equations (11) and (12). Subsequently, the size distribution for any time can be constructed with Equation (3). Compared with a direct integration method in which the particle size distribution of interest must be divided into many finite size intervals and then changes in the number of particles in each size interval due to the particle collision must be programmed, the present approach provides a simpler and more straightforward means. The present method considers particles over the entire size range from zero to infinity as mathematically reflected by a lognormal distribution function. Therefore, a continual shift of the particle size distribution toward the large particle size range which is inherent in an aerosol coagulation does not pose the problem of "loss of particles" that occurs frequently in a direct numerical integration method.

Figures 1 through 3 show the results calculated for the total particle number, the geometric standard deviation, and the mean particle volume, respectively. A standard Adams-Moulton integration package was utilized in the calculation. The obtained values for N and v_g were nondimensionalized against the corresponding initial values N_0 and V_{g0} and plotted against a dimensionless time, $Kv_{go}^{1/6} N_0 t$. The average values listed in Table I were used for b which appears in Equations (13) and (14).

Many interesting points emerge from the calculations with respect to the time-dependent characteristics of the size distribution of an aerosol as it undergoes Brownian coagulation. In Figure 1 particles of an aerosol with a wider size distribution are shown to coagulate at a higher rate, as expected. Regardless of their initial geometric standard deviation however, all size distributions are seen to eventually reach the one with an identical geometric standard deviation as depicted in Figure 2. Thus, the size distribution of an initially monodispersed aerosol becomes broader as time elapses, while that of a highly dispersed aerosol becomes narrower distributed. The time required for an aerosol to attain such an asymptotic value, σ_∞ , is shown to depend upon the initial size spread varied from σ_0 . As will be derived analytically later, this asymptotic value is found to be 1.355. Figure 3 shows that the mean particle volume of the size distribution increases comparatively rapidly for the case with an initially large-size spread. In general, it can be stated that the spread of the initial size distribution plays an important role on the subsequent time evolution of the distribution. However, as a sufficiently long period of time elapses, the coagulation rates become identical regardless of the original spread of the distribution owing to the fact that an aerosol attains a fixed geometric standard deviation.

In order to validate the present calculation method, Figure 4 has been prepared in which the number decay for an aerosol with an initial σ of 1.4 as calculated by Brockmann, et al., is utilized. Also included is the result of a direct numerical integration method based on Gelbard (1979) as

reported by Brockmann, et al. It is seen in the comparison that the result of the present approach is in excellent agreement with previous studies. It should be noted however that the agreement on the total number concentration as shown in Figure 4 does not necessarily mean the particle size distribution indeed maintains a lognormal function as assumed in this study. For a more rigorous validation, it might be necessary to compare present results with accurate numerical calculations for complete size distribution. Nonetheless, the successful firsthand comparison shown in Figure 4 indicates that the assumptions and the simplifications employed in the present study are not only attractive for analyses but suitable physically.

ASYMPTOTIC BEHAVIOR OF SIZE DISTRIBUTION

As already discussed and shown in Figure 2, the size distribution of a coagulating aerosol approaches a lognormal function with a fixed geometric standard deviation independent of the initial size spread of a distribution. The equation representing the size distribution in this asymptotic behavior regime was explored by Lee, et al. (1984). They quantified the asymptotic geometric standard deviation observed in Figure 2 as

$$\ln^2 \sigma_{\infty} = \frac{2}{15} \ln 2 \quad \text{or} \quad \sigma_{\infty} = 1.355 \quad (15)$$

where the subscript ∞ represents a variable for $t \rightarrow \infty$.

The size distribution function for the asymptotic distribution is obtained from Equations (3) and (15) to yield:

$$\frac{n(v)v}{N_{\infty}} = \frac{1}{\sqrt{\frac{12}{5}} \pi \ln 2} \exp \left[\frac{-\ln^2(v/v_{g\infty})}{\frac{12}{5} \ln 2} \right] \quad (16)$$

The distribution is seen to be in a particularly simple form to accommodate a number of data in one scale if the dimensionless terms $n_{\infty}v/N_{\infty}$ and $v/v_{g\infty}$ are utilized. In terms of the particle size that is more frequently used in experimental measurements, Equation (16) becomes

$$\frac{n(r)r}{N_{\infty}} = \frac{1}{\sqrt{\frac{15}{4}} \pi \ln 2} \exp \left[\frac{-\ln^2(r/r_{g\infty})}{\frac{15}{4} \ln 2} \right] \quad (17)$$

The asymptotic size distribution just obtained is shown in Figure 5 where it is seen that the asymptotic distribution given by Equation (17) is somewhat similar to that obtained previously by Lee (1983, 1984) for the continuum regime. Despite the fact that the form of coagulation kernel for the continuum regime differs considerably from that shown in Equation (2), it is interesting to see that the two size distributions are not far different. This is not too surprising however if one notes that an asymptotic size distribution does not depend upon the properties of the particle or

of the gas medium such as the particle density, the gas viscosity, and the gas temperature.

CONCLUSIONS

A theoretical analysis of Brownian coagulation for aerosol particles in the free-molecule regime has been made using the lognormal size distribution assumption. With the approach presented, it was possible to calculate the particle number decay and the change in the size distribution of a coagulating aerosol as a function of time. The assumption and the simplification employed in the present study have been found to be reasonable when the results were compared with other available studies.

The calculated results show that the initial geometric standard deviation has a pronounced effect on the subsequent time evolution of the size distribution. Further, the results indicate that there is an asymptotic size distribution that is attained after a certain period of time. The required time to attain such an asymptotic distribution depends upon the initial geometric standard deviation of the size distribution.

A lognormal form of the size distribution behavior in the asymptotic behavior regime was derived. The obtained size spread of the distribution is found to be slightly larger than that for the continuum regime as derived by the lognormally preserving size distribution theory.

As evident from the solution technique employed, the present results do not offer exact solutions. Nonetheless, due to its particular simplicity both in concept and procedure and due to its comprehensive results, it was possible to study many important characteristics of Brownian coagulation from the approach taken in this study. Therefore the technique and results shown in the paper may become a useful means for designing experimental programs or for interpreting measured data.

REFERENCES

- (1) Brockmann, J. E., McMurry, P. H., and Liu, B.Y.H., *Aerosol Sci. & Technol.*, 1, 163-178 (1982).
- (2) Cohen, E. R., and Vaughan, E. U., *J. Colloid Interface Sci.*, 35, 612 (1971).
- (3) Friedlander, S. K., and Wang, C. S., *J. Colloid Interface Sci.*, 22, 126 (1966).
- (4) Gelbard, F., *The General Dynamic Equation for Aerosols*, Ph.D. Thesis, California Institute of Technology (1979).
- (5) Hidy, G. M., and Brock, J. R., *The Dynamics of Aerocolloidal Systems*, Pergamon, Elmsford, New York (1970).
- (6) Lee, K. W., *J. Colloid Interface Sci.*, 92 (2), 315-326 (1983).
- (7) Lee, K. W., *J. Colloid Interface Sci.*, "Characteristics of Lognormally Preserving Size Distribution During Brownian Coagulation", in preparation (1984).

- (8) Lee, K. W., Chen, H., and Gieseke, J. A., "The Lognormally Preserving Size Distribution for Brownian Coagulation in the Free-Molecule Regime", accepted for publication in Aerosol Sci. & Technol. (1984).
- (9) Lai, F. S., Friedlander, S. K., Pich, H., and Hidy, G. M., J. Colloid Interface Sci., 39 (2), 395-405 (1972).
- (10) Muller, H., Kolloidbeihfte, 27, 223 (1928).
- (11) Reed, L. D., Lee, K. W., and Gieseke, J. A., Nucl. Sci. Eng., 75, 167 (1980).
- (12) Tolfo, F., J. Aerosol Sci., 8, 9-19 (1977).

TABLE I. VALUES OF b OBTAINED BY EQUATION (6)

σ_0	$k = 0$			$k = 2$		
	$t = 0$	$t = \infty$	Avg	$t = 0$	$t = \infty$	Avg
1.0	0.7071	0.7415	0.7243	0.7071	0.7415	0.7243
1.355	0.7415	0.7415	0.7415	0.7415	0.7415	0.7415
1.5	0.7663	0.7415	0.7539	0.7637	0.7415	0.7526
2.0	0.8360	0.7415	0.7887	0.7689	0.7415	0.7552
2.5	0.8636	0.7415	0.8025	0.7596	0.7415	0.7506
3.0	0.8755	0.7415	0.8085	0.7550	0.7415	0.7482

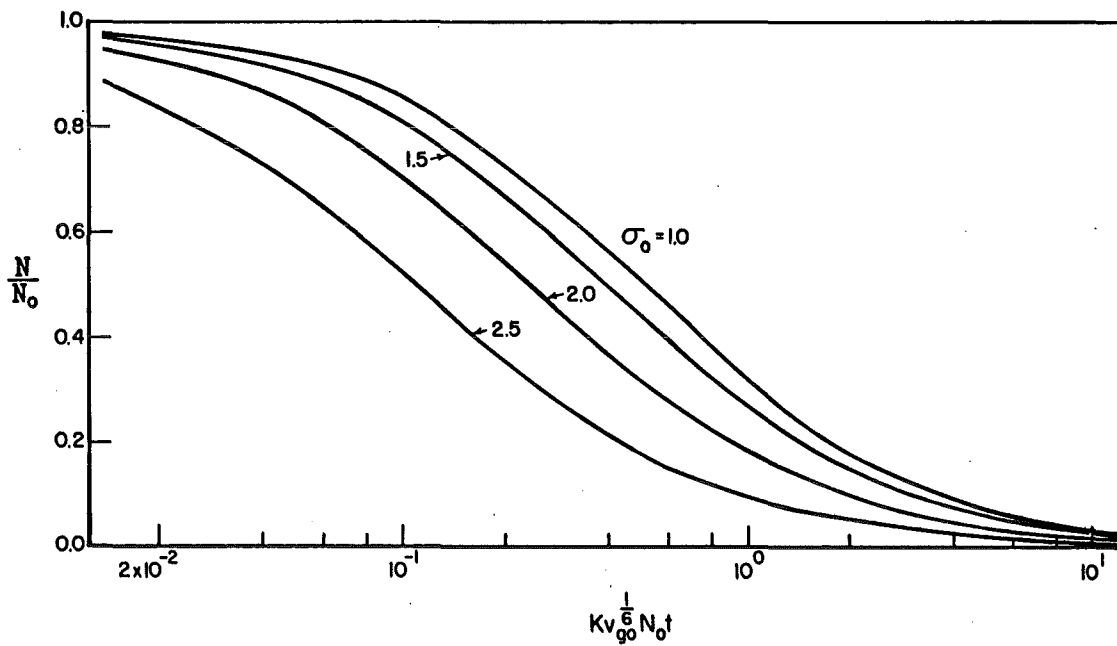


FIGURE 1. N/N_0 AS A FUNCTION OF DIMENSIONLESS TIME

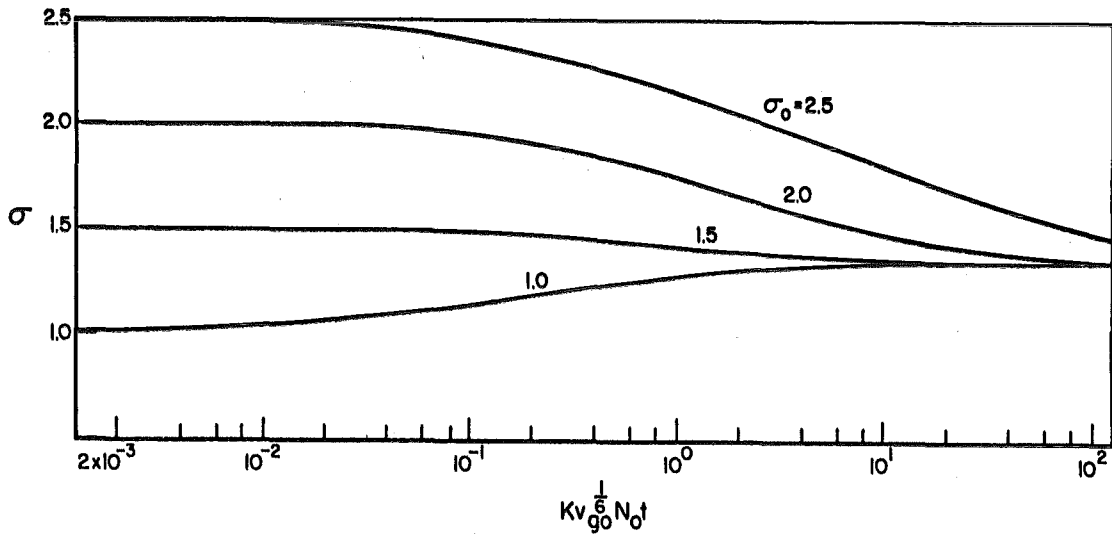


FIGURE 2. σ AS A FUNCTION OF DIMENSIONLESS TIME

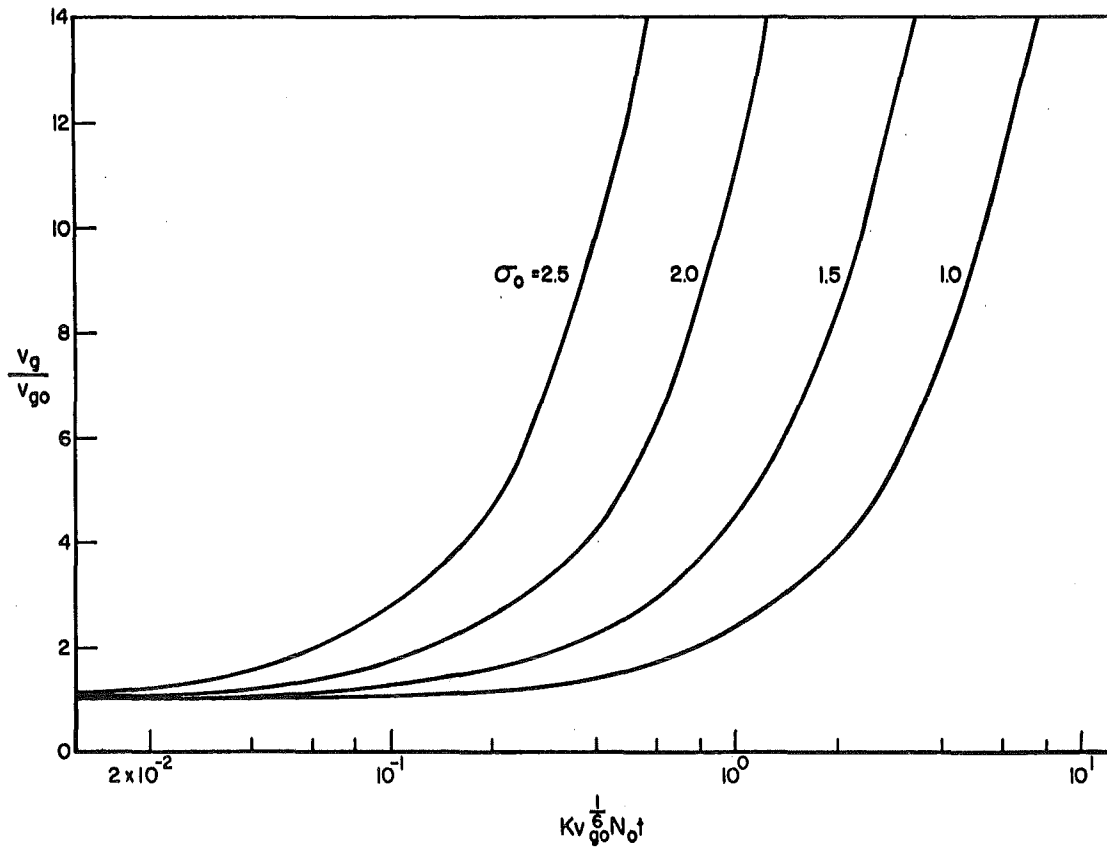


FIGURE 3. v_g/v_{go} AS A FUNCTION OF DIMENSIONLESS TIME

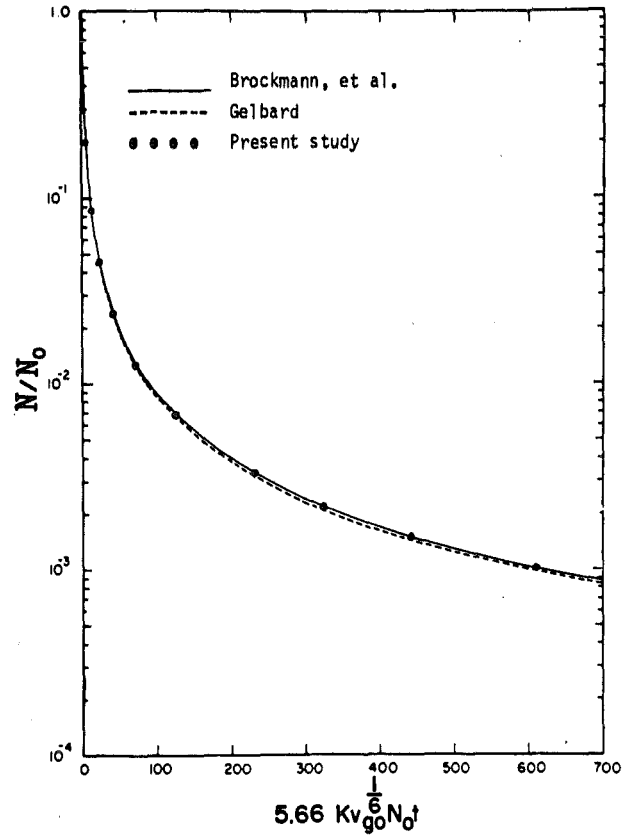


FIGURE 4. COMPARISON OF PREDICTED DECAY IN TOTAL NUMBER WITH THOSE GIVEN BY BROCKMANN, ET AL., AND BY GELBARD ($\sigma_0 = 1.4$)

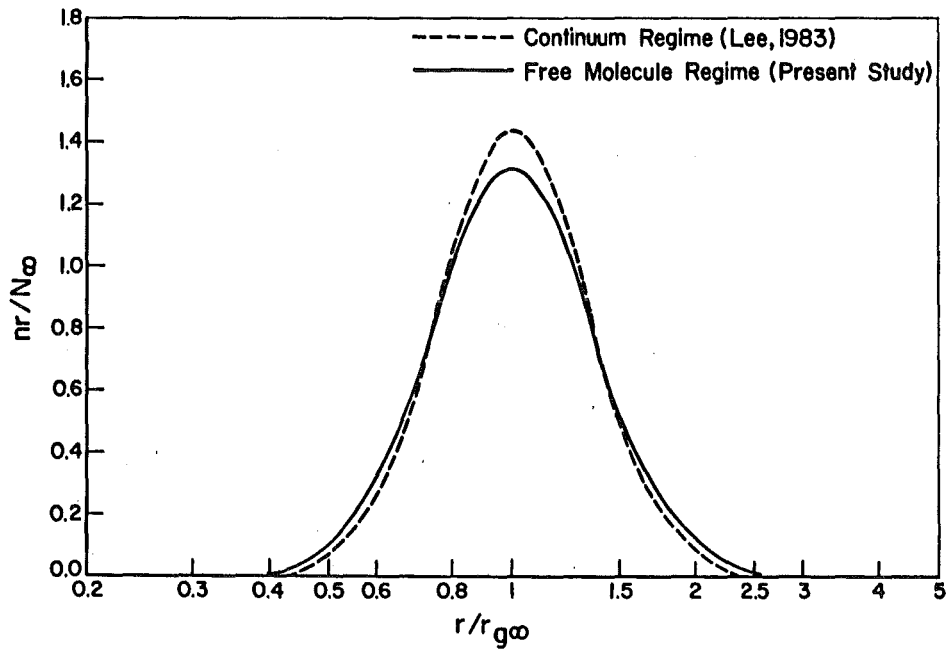


FIGURE 5. THE ASYMPTOTIC SIZE DISTRIBUTION OBTAINED BY THE THEORY OF LOGNORMALLY PRESERVING SIZE DISTRIBUTION

BLANK

AEROSOL ELIMINATION WITH CHARGED SCAVENGERS

Daryl L. Roberts
SRI International
Menlo Park, CA 94025

ABSTRACT

A computer model has been developed to predict the behavior of a cloud of particles that is released intentionally to dissipate another cloud of particles. The intentionally released particles are considered to be charged spheres, and the particles to be dissipated are considered to be dielectric rods. The spheres settle much faster than the rods allowing the possibility of sphere/rod collisions (coagulation) and thereby the eventual dissipation of the cloud of rod-like particles.

The computer code allows rod/sphere coagulation by the mechanisms of Brownian motion and interception. The interception mechanism arises because of the difference in settling velocity between the rods and spheres (differential sedimentation). One other mechanism (inertial impaction) was considered but shown to be negligible. Electrical forces caused by the charge on the spheres are accounted for in the Brownian motion and interception mechanisms. Rod/sphere coagulation may lead to formation of a web of rods and spheres. When this web forms, the computer code allows rod/rod collisions as well as rod/sphere collisions.

In addition to coagulation, the code predicts the settling velocity of the rod/sphere agglomerates and the web structure (if it forms), and it allows the cloud of spheres to expand by electrostatic repulsion. Existing literature expressions were used to represent the various parts of the model. In all cases, however, the literature analyses applied only to simple situations; much of the model is therefore approximate. Further research is anticipated to improve the model and make comparisons with experimental data.

1. INTRODUCTION

The present study is directed toward the intentional deployment of a smoke cloud to clear away some other cloud of smoke that itself is having a negative effect on whatever military objective may be at hand. Overall, this process may be called dissipation of aerosols. The physics of this process is much like particle/particle coagulation, a topic well studied by aerosol scientists (e.g., Fuchs, 1964). Five factors, however, make this problem one that is on the frontier of aerosol science and one that is not yet amenable to a full understanding: (1) the intentionally released cloud consists of charged particles which introduce electrical forces that are not adequately understood; (2) the flow field near a rod/sphere agglomerate is unknown; (3) the settling velocity of a rod/sphere agglomerate is unknown; (4) cloud dispersion phenomena are poorly understood; and (5) the behavior of nonspherical particles is poorly understood.

Nevertheless, it is possible to approximate the dissipation process. In the present study, we have used various literature analyses that represent portions of the dissipation process. In general, we have assumed that the rods and spheres act independently even when they are attached to one another. The results, therefore, must be regarded as semiquantitative.*

* This work was undertaken under contract DAAK-11-83-K-0001 for the Munitions Division of the Chemical Research and Development Center.

2. MATHEMATICS AND PHYSICS OF DISSIPATION MODEL

The basic concept of the model is that a cloud of charged particles (collectors) is released above a cloud of particles to be dissipated (collectees). The collector cloud falls by gravity through the collectee cloud. During this fall, collectees attach themselves to collectors by various mechanisms such as Brownian motion, interception, and inertial impaction. When the collectors have fallen to the ground, therefore, a certain number of collectees have been removed from the collectee cloud. The purpose of the model is to determine how fast and to what extent (efficiency) the collector cloud dissipates the collectee cloud and how the dissipation time and efficiency depend on the physical parameters of the system (e.g., collector size, collector charge, mass of collectors deployed). For the immediate interests of the Army, the theory developed here considers the collectors to be spherical particles and the collectees to be rod-like particles.

2.1 Basic Collision Events

In the following paragraphs, we describe three basic processes by which rods can be dissipated by the cloud of charged spheres.

2.1.1 Single Rod with Single Sphere. We consider only motion induced by Brownian forces, electrostatic forces, and gravitational forces. For the present application, the rod-like particles are considered to have a settling velocity much lower than that of the spheres. Gravity, therefore, produces a relative velocity that is simply the settling velocity of the spherical particles. Collision of particles with different settling velocities is sometimes called differential sedimentation.

To deduce the rate of collision between the spheres and rods, therefore, we must consider the situation of a sphere falling rod at a velocity U past a stationary rod. As the rod approaches the sphere, the rod may collide with and stick to the sphere by Brownian diffusion (with or without electrical attraction). Additionally, a rod may be on a fluid streamline that brings the rod to touch the sphere surface (interception), or a rod may depart from the streamline under its own inertia and impact the surface of the sphere (inertial impaction). In part of the dissipation model, therefore, we consider the capture of a single rod by a single sphere with the mechanisms of Brownian motion, interception, and inertial impaction, accounting for electrical forces as needed within these mechanisms.

2.1.2 Single Rod with Rod/Sphere Agglomerate. When a rod attaches to a sphere, the captured rod falls with the sphere and itself becomes a site to which other rods may attach. Hence we must consider the capture mechanisms of Brownian motion, interception, and inertial impaction (including electrical forces within these mechanisms) for a single rod falling past another rod at some velocity U . A rod has a greater drag per unit mass than a sphere, and the fall velocity of a sphere/rod agglomerate is lower than that of the sphere alone. This problem is quite complex because of the unknown flow field around a rod/sphere agglomerate.

2.1.3 Single Rod with Web Structure. As rods attach themselves to spheres, the rods may eventually bridge the distance between the spheres. This bridging can cause formation of a web or net of interconnected rods and spheres. This web will capture rod-like particles as it falls. Hence we need to analyze the capture efficiency of single rods by a falling web structure.

This problem can be likened to filtration in that the rods can be thought of as flowing through a fibrous mat. However, we must realize that the web structure will be irregular and that one characteristic of filters, known as the void fraction, will not be known. In addition, the electric charges that were present originally on the spheres will be distributed in some unknown way. In fact, the electric charge may have bled off through the tips of rods during the web formation stage (e.g., the field formed at the tip of the rod may cause a corona discharge into the surrounding air). Consequently, we expect this capture process to be far more complex than normal filtration.

2.2 Cloud Dispersion

The cloud of collector particles may be dispersed by wind or by the influence of the method of deployment. For example, deployment may be out of a nozzle, and the fate of the cloud will be influenced by this nozzle. In the present model, we ignore these fluid mechanics questions simply because they represent significant research problems in themselves. However, a cloud of charged particles in a stationary fluid will expand because of electrostatic repulsion, and we account for this process.

2.3 Settling

The settling of a single collector sphere, of a rod/sphere agglomerate, and of a web or net of spheres and rods must be accounted for in the dissipation model. Prediction of this settling velocity would be simple if the only particles of interest were single spheres with no neighboring spheres. The fall speed of a rod/sphere agglomerate and of a web structure, however, is difficult to predict. In addition, the drag on the individual spheres in a group of spheres is, in general, different from the drag on a single isolated sphere (Fuchs, 1964, p. 46).

2.4 Mathematics of Physical Phenomena

Below we give the equations used in the dissipation computer code for the capture efficiencies of the three basic collision mechanisms, for the cloud dispersion rate, and for the settling velocity.

2.4.1 Collision of Single Rods with Single Spheres. Diffusion of rods is discussed in some detail by de la Torre and Bloomfield (1981). The translational diffusion coefficient of a rod is given by

$$D_{t,r} = \frac{[\ln(L_r/d_r) + \gamma]kT}{3\pi\mu L_r} \quad (1)$$

where L_r is the length of the rod, d_r is the rod diameter, k is the Boltzman constant, T is the absolute temperature, and μ is the fluid viscosity. The coefficient γ is an empirical one with a suggested value of 0.38 (de la Torre and Bloomfield, 1981). In the computer code, we have assumed that the spheres are large enough that their diffusion coefficient is negligible. Therefore, the number of rod collisions with a single sphere per unit time is given by

$$F = 4\pi D_{r,t} N_r (r_s + r_{eff}) \quad (2)$$

where N_r is the number of rods per unit gas volume, r_s is the radius of the sphere, and r_{eff} is an effective rod radius, accounting for its random orientation with respect to the sphere (see Lee and Shaw, 1983).

When the particles exert additional forces on one another, the collision rate (Equation 2) is modified. In this instance we have

$$F = \frac{4\pi D_{r,t} N_r (r_s + r_{eff})}{W} \quad (3)$$

where

$$W = (r_s + r_{eff}) \int_{r_s+r_{eff}}^{\infty} x^{-2} \exp\left(\frac{\phi(x)}{kT}\right) dx \quad (4)$$

where $\phi(x)$ is the potential energy of the force of interaction between the two particles; that is,

$$\phi(x) = \int_x^{\infty} F(r) dr \quad (5)$$

where $F(r)$ is the (radially symmetric) force exerted on one particle by the other.

In the present application we wish to account for the force exerted by a charged sphere on an uncharged, polarizable rod. Consideration of basic physics shows that a polarized rod tends to line up in the direction of an applied field. If we assume that the rods can be treated like prolate spheroids and that for practical purposes the rods are always aligned toward the center of the sphere, we find that

$$F = \frac{4\pi D_r t N_r r_s (1 + L_r/d_s)}{W} \quad (6)$$

with

$$W = \left(1 + \frac{L_r}{d_s}\right) \int_0^{\left(1 + \frac{L_r}{d_s}\right)^{-1}} \exp(-CU^4) dU \quad (7)$$

and

$$C = \frac{Q^2 v_r}{2r_s^4 kT} \left[\frac{1}{\epsilon_r - 1} + N_{x'} \right]^{-1} \quad (8)$$

where the shape factor $N_{x'}$ is given by

$$N_{x'} = \frac{1}{\delta^2 - 1} \left\{ \frac{\delta}{(\delta^2 - 1)^{1/2}} \ln [\delta + (\delta^2 - 1)^{1/2}] - 1 \right\} \quad (9)$$

In Equation (9), δ is the major/minor axis ratio of the prolate spheroid. In the computer code, we approximate δ by

$$\delta = \frac{L_r}{d_r} \quad (10)$$

We now turn attention to rod/sphere collisions caused by interception and impaction. Interception of spherical particles by spherical particles under the influence of electrical forces has been studied by Kraemer and Johnstone (1955). These investigators used the unperturbed flow fields from previous fluid mechanics research, wrote equations for electrical

forces of various kinds, and solved the equations numerically. Their Figure 4 is the relevant one for our application (also Figure 48k of Fuchs, 1964). This figure presents the collection efficiency versus a collection parameter that depends on particle charge for various values of the interception parameter. The collection parameter, K_T , is given by

$$K_T = \frac{(\epsilon_1 - 1) r_1^2 Q^2}{(\epsilon_1 + 2) 3\pi r_2^5 \mu U_0} \quad (11)$$

where ϵ_1 is the dielectric constant of the uncharged sphere, r_1 and r_2 are the radii of the uncharged (collectee) particle and of the charged (collector) particle, respectively, and Q is the charge on the collector particle.

To apply this analysis to our application, we have chosen to use the volume equivalent radius of the rods for the quantity r_1 in Equation (11). The volume equivalent radius of a rod is

$$R_{eq} = \left(\frac{3d^2 L_r}{16r} \right)^{1/3} \quad (12)$$

We have chosen to neglect the mechanism of impaction in our dissipation model, a safe assumption for the present application. The Stokes number is subcritical for most conditions of interest (see Friedlander, 1977, p. 103).

To summarize our treatment of the collision of single rods with single spheres, we use Equations (6) through (10) to account for Brownian diffusion in the presence of an electrically induced dipole attractive force, and Equations (11) and (12) with a digitized form of Kraemer and Johnstone's Figure 4 for interception in the presence of the electrical force. Impaction is neglected.

2.4.2 Collection of Rods by Rod/Sphere Agglomerates. We have treated rod collection by a rod/sphere agglomerate the same as rod collection by a sphere. This process is probably the least well understood collection scenario in the overall dissipation model. We identify this capture process as one needing further research.

2.4.3 Collection of Rods After Web Formation. If a web forms, it will continue to fall and capture more rods by a filtration-like process. Analyses of filtration use expressions for particle capture by single fibers (e.g., Tsiang and Tien, 1981; Emi, et al., 1982) or by single spheres (e.g., Lee and Gieseke, 1979). These analyses use the flow fields developed by Kuwabara (1959) in describing filtration of spheres by fibrous or packed bed filters. If a web forms in the dissipation process, it will be an array of fibers (rods) and spheres. Therefore, as a first approximation, it is reasonable to consider the rods and spheres as acting separately to compute the overall collection efficiency of the web as it falls.

The other issue we must face is how to deal with electrical forces during the web filtration process. There have been some analyses of electrical forces in filtration (e.g., Banks, et al., 1983). In our problem, however, we do not know the distribution of charge in the web. Even if we assumed conservation of charge during the web formation process and an even distribution of charge throughout the web, the geometry of a web does not lend itself to an analysis of the electric field in and around the web. Consequently, we have chosen to ignore electrical forces in the web filtration process.

With these approximations, we have used literature analyses for the collection mechanisms of Brownian diffusion and interception. For fibers, we use Equation (33) of Lee and Liu (1982). For spheres we have used Equation (25) of Lee and Gieseke (1979) for the Brownian diffusion mechanism and Equation (25) of Lee and Gieseke (1980) for the interception mechanism.

2.4.4 Cloud Dispersion. A cloud of charged particles expands by repulsive forces such that the time rate of change of the concentration of particles is

$$-\frac{dN_p}{dt} = \frac{4\pi N_p^2 Q^2}{f} \quad (13)$$

where N_p is the number concentration of charged particles and f is the drag on one particle (e.g., $f = 3\pi\mu d_s$ for a sphere). The total number of charged particles is given by

$$N_T = V_c N_p \quad (14)$$

where V_c is the volume occupied by the charged cloud. Since N_T is constant, we can show that

$$\frac{dV_c}{dt} = \frac{4\pi Q^2}{f} N_T \quad (15)$$

Equation (15) could be integrated if the drag were constant. However, because rods are continually added to the spheres in the present application, the drag changes with time. Therefore, in the computer code, Equation (15) is solved numerically as an ordinary differential equation.

We made two approximations in applying Equation (15) in the actual computer code. First, because of gravitational forces, we expect that the primary direction of expansion of the cloud will be horizontal. Hence we assume that the cloud takes the form of a disk with a thickness H_0 and an area A_c . With this approximation, Equation (15) becomes

$$\frac{dA_c}{dt} = \frac{4\pi Q^2 N_T}{f H_0} \quad (16)$$

The second approximation is that the cloud expands only for 10 seconds or only to the walls of a chamber (if dimensions are known). This 10-second approximation is somewhat arbitrary, but we

intuitively realize that forces other than the electrical dispersion forces will change the cloud dispersion at some point. Hence it is unreasonable to allow the endless expansion predicted by Equation (15).

2.4.5 Settling. To predict the fall velocity of the spheres or spheres with rods attached, we use the results developed separately for spheres and rods. This approach is a crude approximation; prediction of the drag on sphere/rod agglomerates is a subject needing basic research.

The fall velocity of a single isolated sphere is given by Stokes' law

$$m_s g = 3\pi\mu d_s U_s \quad (17)$$

where m_s is the mass of the sphere, g is the gravitational constant, and U_s is the settling velocity, and where we have equated the gravitational forces to the fluid drag forces. For a single rod, the force balance is (Fuchs, 1964, Eq. 12.13)

$$m_r g = \frac{4\pi\mu L_r U_s}{2.002 - \ln Re_r} \quad (18)$$

where the Reynolds number for the rod is

$$Re_r = \frac{\rho U_s d_r}{\mu} \quad (19)$$

Equation (18) is valid for $Re_r < 0.5$, a condition easily met in the present application. If we assume that the rods and spheres act independently in a rod/sphere agglomerate, then a force balance yields

$$(m_s + n_r m_r)g = \left(3\pi\mu d_s + \frac{n_r 4\pi\mu L_r}{2.002 - \ln Re_r} \right) U_s \quad (20)$$

where n_r is the number of rods attached to one sphere. Because Re_r depends on U_s , Equation (20) is an implicit equation for U_s that is solved numerically within the computer code.

3. SAMPLE CALCULATIONS

Several calculations were made with the code to indicate the reasonableness of the predictions and the variables to which the results are most sensitive. None of the sample calculations represents any known actual deployment situation. In this sense, the code results have not been compared with any experimental data.

Input data required by the code are shown in Table 1.

TABLE 1. INPUT DATA REQUIRED TO RUN PROGRAM "COLLECT"*

Quantity	Variable Name	Code Units
Collector parameters		
Collector particle diameter	COLLD	meters
Density of collector material	COLLRHO	kg/m ³
Mass of deployed collectors	COLLMASS	kg
Number of charges per sphere	COLLQ	dimensionless
Rod parameters		
Rod length	ELROD	meters
Rod diameter	DROD	meters
Rod material density	RHOROD	kg/m ³
Dielectric constant of rod	EPSROD	dimensionless
Number of concentration of rods	CONCROD	number/m ³

* User is also asked if the computer run is meant to represent outdoor deployment or a chamber deployment.

We chose a set of standard input parameters (standard conditions Table 2) and made a variety of calculations, changing only one parameter at a time from standard conditions. We made calculations under identical conditions representing an outdoor deployment and a chamber deployment. The physical difference in these deployments is that the chamber cross sectional area limits the expansion of the collector cloud. In addition, we expect intuitively that the cloud deployed in the chamber will not spread as far vertically as the outdoor cloud. This factor is accounted for approximately in the code, but we emphasize that the cloud dispersion mechanics is in need of basic investigation.

In the following discussion, we give graphical results showing the total fall time and rod collection efficiency for a variety of conditions. Efficiency is the total number of rods collected divided by the total number of rods initially inside the volume swept by the collector

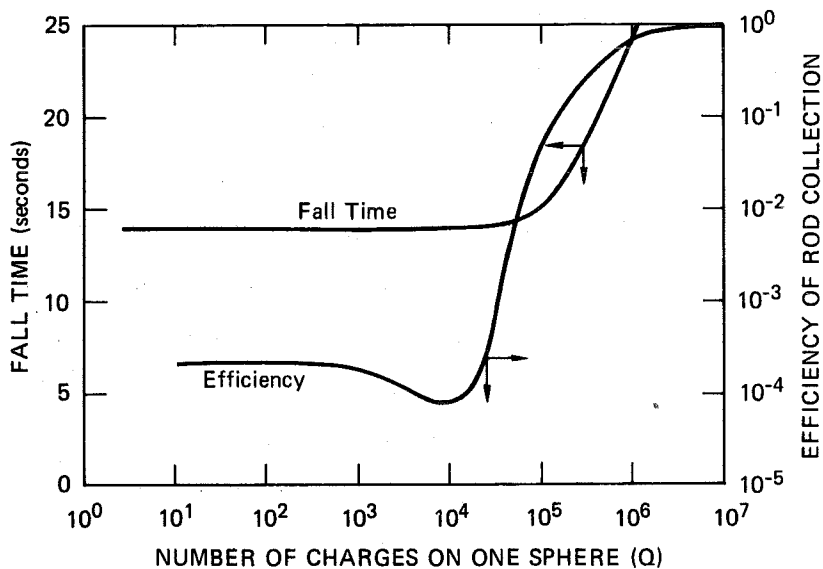
TABLE 2. STANDARD CONDITIONS FOR SAMPLE DISSIPATION CALCULATION

Quantity	Value
Collector parameters	
COLLD	$75 \cdot 10^{-6} \text{ m}$
COLLRHO	$1,100 \text{ kg/m}^3$
COLLMASS	1 kg
COLLQ	10^6
Rod parameters	
ELROD	$100 \cdot 10^{-6} \text{ m}$
DROD	$0.5 \cdot 10^{-6} \text{ m}$
RHOROD	2500 kg/m^3
EPSROD	10^9
CONCROD	$10^9/\text{m}^3$
Miscellaneous	
If chamber experiment, chamber = 2.4 m high, 6 m ² area; if outdoor experiment, deployment height = 10 m	

cloud. As simple as this definition may seem, the subtlety is that the volume swept by the collector cloud depends on the rate of dispersion of the collector cloud; hence this volume is not a constant from run to run. Consequently, it is possible for more rods to be collected in a given run but for the efficiency to go down.

The number of charges on the collecting sphere is expected to be a key parameter, and we present the results of calculations made for a range of charge values. Calculations shown in Figure 1 are for standard conditions in a chamber for $10 < \text{COLLQ} < 10^6$; those in Figure 2 are for an outdoor experiment under the same conditions. One major point of interest is that there is essentially no influence of particle charge until the number of charges exceeds 10^4 per spherical particle. This feature is expected because the induced dipole force is negligible in most applications. Only by purposely charging the spheres does this force become effective. We do not expect that 10^4 charges will be the critical point for all conditions, but it behooves experimentalists to discover where this point lies for any particular system.

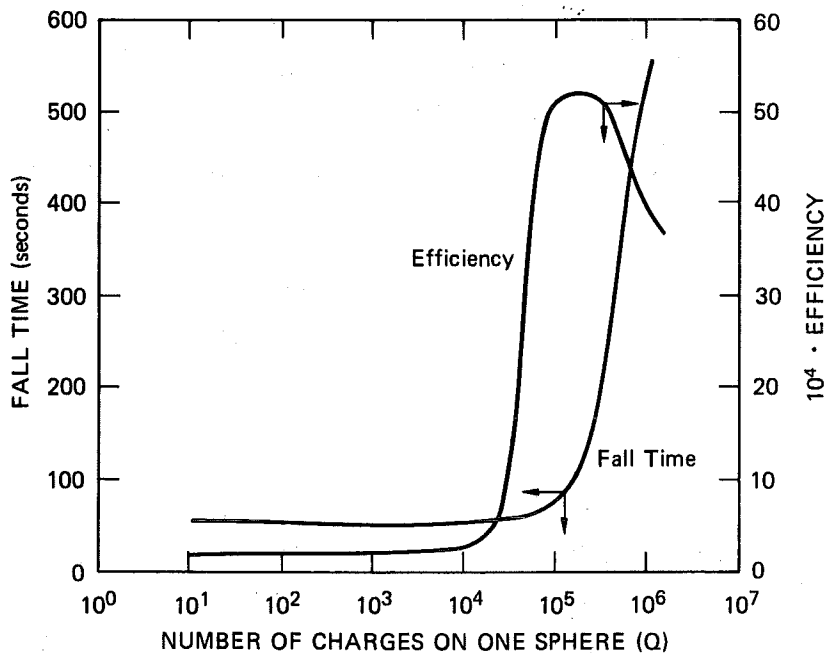
Another point, characteristic of all sample calculations (including many not shown here), is that the cloud expands much farther in the outdoor experiment. To represent the chamber experiments, the expansion is restricted to the cross-sectional area of the chamber itself. Table 3 lists the area of the cloud predicted to be covered for the chamber and outdoor conditions (recall that the maximum area in the chamber is 6 m² and that growth of the outdoor area is stopped after 10 seconds). We see that significant expansion is predicted in the outdoor experiment for $\text{COLLQ} > 10^5$. This expansion is the cause of the seemingly low efficiency for the outdoor conditions. The walls of the chamber terminate this expansion, and the rods are collected with a good efficiency for $\text{COLLQ} > 10^5$. These results may not predict expansion accurately, but they point out that outdoor results may differ substantially from chamber results.



JA-5492-6

FIGURE 1 EFFECT OF SPHERICAL COLLECTOR CHARGE, CHAMBER CONDITIONS

Charge is insignificant for $Q < 10^3$; some cloud expansion begins at $Q \cong 2000$. Electrostatic attraction causes good capture efficiency for $Q \gtrsim 5 \cdot 10^5$. The fall time increases as rods attach themselves to the falling spheres.



JA-5492-7

FIGURE 2 EFFECT OF SPHERICAL COLLECTOR CHARGE, OUTDOOR CONDITIONS

Fall time is increased with respect to chamber experiment because of higher deployment height. Cloud expands dramatically for $Q \gtrsim 5 \cdot 10^5$ and a drop in overall efficiency results.

TABLE 3. MAXIMUM AREA OF COVERAGE FOR COLLECTOR CLOUD
VERSUS NUMBER OF CHARGES PER COLLECTOR

Number of Charges per Collector Sphere	A_{\max} (square meters)	
	Chamber	Outdoor
10	1.0	1.0
100	1.01	1.0
1000	1.86	1.01
10^4	6.0	1.94
10^5	6.0	88.0
10^6	6.0	4390

4. CONCLUSIONS AND RECOMMENDATIONS

We have developed a computer code that models the dissipation of a cloud of rod-like particles by an intentionally released cloud of charged spherical particles. The code incorporates a variety of physical phenomena including rod/sphere and rod/rod coagulation, charged cloud dispersion, and settling. For all these phenomena, existing literature analyses are quite simplified; consequently, the overall model is approximate.

In some sample calculations, we found a major difference between predicted dissipation efficiency for indoor (confined) and outdoor (unconfined) conditions. For the outdoor conditions, electrostatic repulsion is predicted to cause a rapid expansion of the charged spheres. This expansion leads to low overall capture efficiency because the cloud is spread over too large an area. Under indoor (confined) conditions, the cloud of spheres can expand only as far as the walls of the chamber. We are uncertain of the accuracy of the expression for cloud expansion that is used in the computer code. Some comparison with experiment is needed.

The initial sample calculations showed that the charge on the spheres was not effective until the number of charges exceeded 10^4 per particle.

We view the model developed in this study as a first approximation to a complex process. The model incorporates many approximations based on existing literature analyses of simpler situations. The results must be regarded as semiquantitative. Further research is needed to refine the model and compare predictions with experimental data.

REFERENCES

- Banks, D. O., M. S. Hall, and G. J. Kurowski, "Numerical Determination of Electrically Enhanced Fiber Collection Efficiency," J. Aerosol Sci., 14, 87-97 (1983).
- Barot, D. T., C. Tien, and C. S. Wang, "Accumulation of Solid Particles on Single Fibers Exposed to Aerosol Flows," AIChE J., 26, 289-92 (1980).
- de la Torre, J. G., and V. A. Bloomfield, "Hydrodynamic Properties of Complex, Rigid, Biological Macromolecules: Theory and Applications," Quart. Rev. Biophys., 14, 81-139 (1981).
- Emi, H., C. Kanaoka, and Y. Kuwabara, "The Diffusion Collection Efficiency of Fibers for Aerosol Over a Wide Range of Reynolds Numbers," J. Aerosol Sci., 13, 403-13 (1982).
- Friedlander, S. K., Smoke, Dust and Haze (John Wiley and Sons, New York, 1977).
- Fuchs, N. A., The Mechanics of Aerosols (Pergamon Press, New York, 1964).
- Kraemer, H. F., and H. F. Johnstone, "Collection of Aerosol Particles in Presence of Electrostatic Fields," Ind. Eng. Chem., 47, 2426-34 (1955).
- Kuwabara, S., J. Phys. Soc. Japan, 14, 527 (1959).
- Lee, K. W., and J. A. Gieseke, "Collection of Aerosol Particles by Packed Beds," Env. Sci. Tech., 13, 466-70 (1979).
- Lee, K. W., and J. A. Gieseke, "Note on the Approximation of Interceptional Collection Efficiencies," J. Aerosol Sci., 11, 335-41 (1980).
- Lee, K. W., and B.Y.H. Liu, "Experimental Study of Aerosol Filtration by Fibrous Filters," Aerosol Sci. Tech., 1, 35-46 (1982)
- Lee, P. S., and D. T. Shaw, "Dynamics of Fibrous Type Particles: Brownian Coagulation and Charge Effect," to appear in Aerosol Science and Technology (1983).
- Tsiang, R. C., and C. Tien, "Trajectory Analyses of Particle Deposition in Model Filters Composed of Parallel Fibers," Can. J. Chem. Eng., 59, 595-601 (1981).

NOMENCLATURE

A_c	area covered by collector cloud
C	dimensionless form of potential energy for induced dipole force; Equation (8)
d_r	diameter of rod
d_s	diameter of sphere
$D_{t,r}$	translational diffusion coefficient of a rod
f	fluid drag on a particle
F	number of collisions per unit time between two particles
$F(r)$	the force exerted by one particle on another; a function of the separation distance r
g	gravitational constant (9.8 m/s/s)
H_0	the initial thickness of the collector cloud
k	the Boltzman constant
K_T	collection parameter determining the efficiency of capture of a charged sphere for an uncharged, polarizable particle
L_r	length of a rod
m_r	the mass of a rod
m_s	the mass of a sphere
n_r	the number of rods attached to one sphere
N_p	the number concentration of charged particles
N_r	the number concentration of rods in collectee cloud
N_T	the total number of charged particles in a cloud
$N_{x'}$	the depolarization factor for the x' direction in a prolate spheroid
Q	the charge on a particle; 1.6×10^{-19} coulomb times the number of elementary charges
r_{eff}	the orientation-averaged effective radius of a rod
r_s	the radius of a sphere
r_1	radius of uncharged sphere being collected by charged sphere
r_2	radius of charged sphere collecting an uncharged sphere
R_{eq}	volume equivalent radius of a rod; Equation (12)
Re_r	the Reynolds number based on the rod diameter; Equation (19)
t	time
T	absolute temperature
U_0	the free stream velocity far from an object
U_s	the settling velocity
V_c	the volume occupied by the cloud of charged collector particles
V_r	the volume of a rod
W	effect of additional forces on Brownian coagulation; Equation (4)

Greek Symbols

ϵ_1	the dielectric constant of an uncharged sphere being collected by a charged sphere
ϵ_r	the dielectric constant of the rod
γ	an empirical coefficient for prediction of rod diffusion coefficients; Equation (1)
μ	fluid viscosity
$\phi(x)$	potential energy of a force acting between two bodies at a distance x from one another

BLANK

PROGRESS IN THE CLEARING OR MODIFYING OF
AEROSOL CLOUDS BY SCAVENGING TECHNIQUES

J. Podzimek and J.J. Martin

Mechanical and Aerospace Engineering and
Graduate Center for Cloud Physics Research
University of Missouri-Rolla
Rolla, MO 65401

ABSTRACT

The paper describes the progress which has been made during the past year in the investigation of the clearing of a smoke cloud by scavenging techniques. More detailed discussion is presented on the mode of falling planar scavengers, on the flow field around disk type models and on the smoke particle deposition. A comparison of the calculated particle deposition rate and measured total number of particulates on the obverse and reverse disk side shows the importance of the deposition on the backside. The number of particulates with $0.2 < d < 2.5 \mu\text{m}$ deposited on an oscillating disk is usually higher than that on a stationary model.

INTRODUCTION

Many authors discussed the importance of aerosol scavenging by natural and man-made scavengers (e.g., Pruppacher and Klett, 1978, or Program and Abstracts of the 4th International Conference on Precipitation Scavenging, Dry Deposition, and Resuspension, 1982). The problem has many facets such as the description of a scavenger motion, aerosol particle deposition under the influence of body forces of different nature, interaction of several scavengers falling close to each other and the dynamic effect of the whole scavenging zone. This contribution focuses on a disk (oblate ellipsoid) type scavenger for its relation to the smoke aerosol scavenging which has been discussed in several of our previous studies (Podzimek, 1981; Podzimek and Martin, 1982).

MOTION OF A FREE FALLING DISK

Several of the old measurements with disks have been discussed in the works by Willmarth, et al. (1964), Podzimek (1965, 1967), Stringham, et al. (1969), Schemenauer (1969), Sasyo (1971), Jayaweera (1972), Podzimek (1980), and Podzimek (1982). There seems to be fairly good agreement between different authors concerning the mode of motion of a falling disk. Until the disk starts to oscillate noticeably ($Re_c \cong 100$), the agreement between the settling rate, V_z , and the drag coefficient, C_{DZ} , of a disk falling in liquids and in the air is good if the plotting is referred to the appropriate parameter of similarity (Reynolds, Re_c , and Best number, Be_c). In this sense, the introduction of the "equivalent" disk for featuring the fall of planar bodies with more complex shapes is justified (Jayaweera, 1972). The attempts to characterize the disk's oscillatory motion by a parameter of similarity (e.g., Willmarth's stability number, I ; Strouhal number) or to formulate analytically the disk motion in a viscous fluid are still in the rudimentary stage (Sasyo, 1971; Steward and List, 1980; Podzimek, 1981 and 1982).

Only a few measurements with falling planar scavengers were made in addition to those described

earlier (Podzimek, 1981). They were aimed at completing the relationship between the amplitude, δ , and the frequency, f_c , of a falling planar scavenger (collector) and the corresponding Reynolds number, Re_c , and Willmarth's stability number, I . For instance, the motion of a paper disk falling in the air is featured by a moderate change of the amplitude, δ , and frequency, f_c , with Re_c , until $Re_c \cong 1,500$. Beyond this value, a dramatic change of δ with Re_c was observed (Fig. 1). However, a reverse relationship was found for oscillatory frequency, f_c . These relationships were perfectly true also for the stability number (related to scavenger's moment of inertia), I (Fig. 2). The two curves in Fig. 2 for each of the dependencies of f_c and δ and I were obtained from two independent sets of measurements.

The conclusion from the previous and current experiments with scavengers falling in quiescent air and at a side wind are the following: the fall of symmetrical planar scavengers can be described by an "equivalent" disk model for $20 < Re_c < 200$, and the drag coefficient C_D is calculated in the standard way. In this domain a simple relationship exists between Re_c and Best's number Be_c ($Be_c = C_D Re_c^2$). Slight side wind has a marked effect on the scavenger's behavior when the scavenger starts perceivably to oscillate ($Re_c > 90$). During a well established oscillatory motion, the amplitude, wavelength and frequency of the collector's motion are functions of the Reynolds number and Willmarth's stability number. The frequency of oscillating paper disks can reach several units or tens of Hz and is greater with increasing Re_c . From the time lapse camera and the stroboscopic pictures the characteristic amplitudes, frequencies and accelerations of the falling paper (and other material) disk models were determined and used for the simulation of the aerosol deposition on a disk placed in a small aerodynamic wind tunnel (Podzimek, 1981).

PARTICLE DEPOSITION ON THE STATIONARY AND OSCILLATING DISK-UNCHARGED MODELS

The wind tunnel experiments have been preferred to the settling chamber filled with smoke for higher reproducibility of the measurements (due to the much longer exposure time of the disk). The current experiment set-up is depicted in Fig. 3. A small aerodynamic wind tunnel (7) with the diameter of the test section of 13.0 cm was operated at velocities ranging from 0.25 m/s up to several m/s. The entrance of the wind tunnel was connected with an aerosol generator (2 to 5) and a Kr-85 aerosol neutralizer (6). The outlet of the tunnel was extended into a fume hood. Air velocity was monitored and evaluated from the pressure measurements with the pressure transducer. The velocity profile in the test section was determined by a hot wire anemometer before the series with aerosol deposition had started. During each experiment the aerosol concentration and size distribution was monitored by Laser Cavity Active Scattering Aerosol Spectrometer (9 and 10)--Model ASAS-300A, Particle Measuring Systems, Inc., Boulder--which measures in four different ranges (each containing 15 size groups) the particle diameters from 0.157 μm to 3.00 μm . Independently, the particle size

distribution was evaluated from the scanning electron microscopical pictures. In addition, a special device (12) was used for simulating the motion of free oscillating models, which were suspended on a needle in the tunnel's test section (15), and a generator of high electrostatic charges (13).

Vast majority of the experiments has been performed with TiCl_4 aerosol (reaction with water vapor yielded probably TiO_2 spherical particles). Several experiments were run with red phosphorus or sodium chloride aerosol. The mean size distribution of TiCl_4 aerosol is plotted in the diagram (Fig. 4), from which one assumes that the median of the particle diameters evaluated in our experiments is around $0.6 \mu\text{m}$. Using two electrical furnaces (4 and 5 in Fig. 3) operated at the mean temperature around 700°C one obtained very reproducible particle sizes.

The models of disks with diameters ranging from 0.45 cm to 1.0 cm and thicknesses between 0.05 to 0.1 cm were made of glass, plexiglass and brass. Their exposure time (to the smoke aerosol) was usually 2 minutes; however, several time exposures as long as 5 minutes and 10 minutes were made, especially for low air velocities. The model oscillatory frequency and maximal angle deflection amounted to several Hz and 10° . The size and position of the deposited aerosol on models have been evaluated in an optical microscope at a magnification of $1000\times$. Special studies of particle distribution--mainly close to the rim--have been done with an electron microscope.

Deposited TiCl_4 smoke particles on stationary models showed a typical pattern for the disk's front and back side (Fig. 5). The deposition of particulates with $d = 0.5 \mu\text{m}$ has its maximum close to the rim and declining concentrations toward the center of the obverse side of the disk. On the reverse side the particle deposition is more uniform with higher particle density close to the rim and with a secondary maximum between $0.4 < r/R < 0.6$. Particulates with $D > 1.0 \mu\text{m}$ are found at higher concentration all over the obverse side of the disk and also on the reverse side although in a smaller concentration. The evaluation of 11 pairs of curves representing the deposition of the smoke aerosol (with $d \approx 0.5 \mu\text{m}$) on the obverse and reverse side of a disk leads to the conclusion that the ratio $(\Sigma n_{\text{obv}})/(\Sigma n_{\text{rev}})$ is 0.986 with a standard deviation of 0.135 . The ratio is insensitive to the increase of Re from 80 to 320 .

Aerosol deposition on the models slightly oscillating around an axis going along the disk's diameter was marked by lower deposition on the front side (Fig. 6). For 5 pairs of aerosol deposition curves, pertaining to the obverse and reverse side, the ratio $\Sigma n_{\text{obv}}/\Sigma n_{\text{rev}}$ is 0.846 with a standard deviation of 0.065 for particulates with $d \approx 0.5 \mu\text{m}$ and $80 < Re_c < 320$. During these experiments the chosen frequencies from 10 Hz to 60 Hz correspond to the highest oscillation rates observed on paper disks (at higher Re) falling in the air (Podzimek, 1982). The pattern of deposited particles on the reverse side was usually more uniform than that on the front side. A noticeable effect of the increased frequency from 10 to 60 Hz was observed. The mean ratio of $(\Sigma n_{\text{ob}})/(\Sigma n_{\text{rev}})$ was 0.913 for

10 Hz and 0.745 for 60 Hz.

The most interesting seems to be the finding of the higher particle deposition rate on the reverse side of an oscillating disk. However, this does not seem to affect dramatically the total scavenging efficiency of an oscillating model in comparison to a stationary one. The scavenging efficiency was calculated according to the formula

$$E = \frac{N_{\text{dep}}}{N_{\text{tot}}} = \frac{\sum \frac{A}{A_s} (n_{oi} + n_{ri})}{\sum n_i \pi (R + r_i)^2 v}$$

where A, A_s are the disks and the evaluated stripe (170 μm wide) areas, n_{oi}, n_{ri} , are the numbers of deposited particles counted (in different size classes) on the obverse and reverse side of the disk; n_i and r_i are the concentrations and radii (size classes) of the particles in the airflow of velocity v , and R is the disk's radius. The mean scavenging efficiency calculated from all measurements with quiescent models for both sides of a glass disk was 0.700% (Fig. 7) and that for all oscillating models was 1.092% for 10 Hz and 1.42% for 60 Hz (Fig. 8).

ELECTRIC CHARGE EFFECT

The electric charge effect on the smoke particle deposition on disks was studied in the wind tunnel with aerosol particles not "neutralized" and with particles in charge equilibrium after the generated smoke passed through a diluting system (addition of filtered air) with a Kr-85 neutralizer (6 in Fig. 3). The metallic disks, or disks made of dielectric material coated by gold (15), were charged (13) to voltages between 0 and 10 kV. Electrical charging of the models has been done in two different ways: model was permanently connected with the generator during the experiment and the model was charged only for 3 seconds at the beginning of the experiment. The electrostatic field homogeneity was supported by inserting a grounded thin brass sheet along the plexiglass tunnel walls in the test section.

The models which were charged had been made of conductive material (brass), of dielectric material (plexiglass and glass) and of glass coated by a thin gold layer. The deposition of smoke particles on dielectric models was featured by a higher particle deposition on the opposite site to the point where the electrostatic charge was applied. Mean scavenging (collection) efficiency for glass disks scavenging smoke particles with diameters smaller than 1.40 μm was 2.690 for 1 kV potential difference, 5.450 for 2 kV and 9.535 for 5 kV (calculated from approximately 4 individual measurements). For metallic disks there was an indication of lower collection efficiencies; and for dielectric materials coated by gold, an unusually high collection efficiency (several times more than 20%) was found. Future investigation might explain these anomalous depositions as well as the large spread of

data apparent from the plotting in Figs. 7, 8 and 9. Very detailed evaluation of particles deposited along the rim of a disk charged with 5 kV led to the conclusion that, by neglecting the number of particles deposited at the rim, one can underestimate the total collision efficiency by 50%.

COMPARISON OF SCAVENGING EFFICIENCIES WITH A SIMPLE MODEL

A simple model of aerosol scavenging by planar collectors (ice crystal) has been developed by Martin, et al. (1980). This work was based on the previous studies by Grover, et al. (1977), and Pitter (1977) and included the creeping flow equations of a viscous air around an ice crystal, approximated by an oblate ellipsoid, and the equations of the aerosol particle motion. The latter are derived from a simple relationship between particle acceleration and the forces acting on the particle

$$m_p \frac{dv}{dt} = m_p g \frac{(\rho_p - \rho_a)}{\rho_p} - \frac{6\pi\mu_a r_p}{(1 + \alpha Kn)} (v_p - u) + F_{th} + F_{Df} \quad (1)$$

In eq. (1), m_p , v_p , ρ_p , r_p are the mass, velocity, density and radius of an aerosol particle, g is the gravitational acceleration, ρ_a , μ_a , u are the density, dynamic viscosity and velocity of the air, $\alpha = 1.26 + 0.44 \exp(-1.1 Kn^{-1})$ is a correction term to the Stokes resistance law for small particulates dependent on the Knudsen number ($Kn = \lambda/r_p$; λ = mean free path of air molecules). Only four of the forces acting on an aerosol particle were originally considered: the gravitation force (with the buoyancy force correction), drag force, thermophoretic force (Pruppacher and Klett, 1978),

$$F_{th} = - \frac{12\pi\mu_a r_p (k_a + 2.5 \frac{k_p K}{p_n}) k_a \nabla T}{5(1 + 3 Kn)(k_p + 2 k_a + 5 k_p Kn)p} \quad (2)$$

and diffusiphoretic force (Pruppacher and Klett, 1978),

$$F_{dif} = - 6\pi r_p \mu_a \frac{0.74 D_{va} M_a \nabla \rho_v}{(1 + \alpha Kn) M_w \rho_a} \quad (3)$$

In eqs. (2) and (3), k_a , k_p mean the thermal conductivities of air and particle; M_a , m_p are molecular weights of air; and particle, D_{va} is the diffusivity of water vapor in air and ∇T and $\nabla \rho_a$ are gradients of the temperature and density of water vapor.

In addition to the outer forces affecting the smoke particle deposition on a thin oblate spheroid, the electrostatic force, F_e , was assumed. Assuming that only a surface charge on the collector, $Q_c = q_c R_c^2$, and the charge on the particle Q_p is effective, one can write in oblate spheroidal coordinates (Martin, et al., 1980)

$$F_e = \frac{Q_p Q_c \operatorname{sech} \xi \sin^{-1} [(1 - A_c)^{1/2}]}{R_c^2 \operatorname{sech} \xi_o [1 - A_c^2]^{1/2} \left[\frac{\pi}{2} - \sin^{-1} A_c \right] [\sinh^2 \xi + \cos^2 \rho]^{1/2}}$$

q_c is a numerical factor (e.g., 1.5); A_c is the axis ratio of a spheroid with the main semi-axis R_c ($A_c = b/R_c = 0.05$). Q_p is the charge of a smoke particle which can equal to one, two, three...of elementary charges.

The approximation of a disk by an oblate ellipsoid can certainly lead to some particle trajectory distortion, especially close to the rim. One might expect that the collision efficiency of a disk, defined as

$$E = \frac{\pi Y_c^2}{\pi(R_c + r_p)^2}, \quad (4)$$

or the corresponding collision kernel,

$$K = E\pi(R_c + r_p)^2 (v_{\infty,R} - v_{\infty,r}) \quad (5)$$

(Y_c is the distance measured perpendicular to the disk's axis far from the collector with the radius R_c ; $v_{\infty,R}$, $v_{\infty,r}$ are the velocities of the collector and particle far from the disk), will differ from that for an oblate ellipsoid of the thickness b . The discussion of the features of such a model and of the limitations of its application has been made by Martin, et al. (1980).

From the comparison of the calculated and measured scavenging efficiencies (Fig. 7, 8 and 9), one concludes that there is a reasonable agreement of both techniques. However, the comparison could be done actually for a model $Re_c = 50$ and experiments with Re_c between 70 and 80. Also, the numerical model does not show clearly the deposition on the reverse side of the disk, whereas the measurement does. These arguments lead to the conclusion that the total number of deposited smoke particles ($0.2 < d_p < 2.8 \mu\text{m}$) on the front side of a disk at $Re \approx 80$ is a little lower than that predicted from the numerical model. Further, the swinging of the disks will cause an increase in particle deposition on its reverse side. However, this increase is not very significant and lies usually within the normal fluctuation of the measured numbers of deposited particles.

The electric charge effect is very significant and can increase the collection efficiency of one order of magnitude if compared to the uncharged disk. However, it should be emphasized that this dramatic increase in scavenging efficiency of charged models was only observed if the collector (scavenger) was permanently connected with the charge generator. Initial charge on the collector is usually neutralized during several tens of seconds if the collector is disconnected from the generator and if a dense smoke flow is maintained around the collector.

CONCLUSION

The experimental and theoretical study of smoke particle deposition on the obverse and reverse

side of a thin disk at Re around 80 showed that:

1) One cannot neglect the deposition on the reverse side of the collector because the numbers of deposited particles on both sides are comparable (for $d_p < 1.4 \mu m$).

2) The number of deposited particles is relatively insensitive to the increase in Re from 80 to 320 for particle diameters $d_p < 0.7 \mu m$.

3) The influence of the model oscillation (corresponding to the observed highest frequencies with paper models--up to 60 Hz) does not lead to a significant increase of the particle deposition; higher deposition rates were observed on the backside of swinging models if the angular amplitude did not surpass $\pm 10^\circ$.

4) The diffusiophoretic forces influence insignificantly small particle deposition ($d_p < 0.2 \mu m$) and the thermophoretic forces play a greater role only for $Re_c < 10$.

5) The electrostatic charge effect is very important ($E > 10.0\%$); however, maintaining sufficiently high charge on the collector is difficult.

6) There is reasonably good agreement between this work and the experimental studies by Sood and Jackson (1969) and Knutson, et al. (1976). In mean, the measured collection efficiencies (around 1% for both sides) are smaller than the values calculated numerically for the same Re_c . The potential explanation of this discrepancy can be found in the imperfect modeling of particle deposition at the rim, in the different size of a disk in the numerical model (Martin, et al., 1980), and in the wind tunnel experiments. Another potential explanation is the not well-known smoke particle density--which might be a function of its size--and the difficult small particle counting, especially close to the rim at a microscope magnification 1000x.

Several of the above mentioned problems, such as the particle deposition at the disk's rim or the deposition under the influence of electrostatic forces, are currently studied.

ACKNOWLEDGEMENT

The authors are indebted to their student research assistants V. Wojnar, A. Keshavarz, and G. Stowell for their enthusiastic work. Mrs. V. Maples ably helped in preparing the manuscript for print. The present study was supported by the U.S. Army, Grant DAAK 11-81-C-0075.

REFERENCES

- Grover, S.N., H.R. Pruppacher, and A.E. Hamielec, 1977: A numerical determination of the efficiency with which spherical aerosol particles collide with spherical water drops due to inertial impaction and phoretic and electric forces, *J. Atmos. Sci.*, 34, 1655-1669.
- Jayaweera, K.O.O., 1972: An equivalent disk for calculating the terminal velocities of plate-like crystals, *J. Atmos. Sci.*, 29, 596-598.

- Knutson, E.O., S.K. Sood, and J.D. Stockham, 1976: Aerosol collection by snow and ice crystals, Atmos. Envir. 10, 395-402.
- Martin, J.J., K.P. Wang, and H.R. Pruppacher, 1980: A theoretical determination of the efficiency with which aerosol particles are collected by simple ice crystal plates, J. Atmos. Sci., 37, 1628-1638.
- Pitter, R.L., 1977: Scavenging efficiency of electrostatically charged thin ice plates and spherical aerosol particles, J. Atmos. Sci., 34, 1797-1800.
- Podzimek, J., 1965: Movement of ice particles in the atmosphere, Proc. Int. Conf. on Cloud Physics, Tokyo-Sapporo, May, p. 224.
- Podzimek, J., 1967: The growth of an ice crystal in a mixed cloud (in Czech), part I and I, Doctor of Science Thesis, Charles University, Praha, p. 320.
- Podzimek, J., 1981: Clearing of military smoke cloud with scavenging technique, Fin. Rep. DAAG 29-79-C-0073, U.S. Army Res. Office, UMR-Rolla, June, p. 121.
- Podzimek, J., 1982: Study of the motion of bodies simulating the fall of ice crystals, Preprint Vol. Conf. on Cloud Physics, Nov., Chicago, AMS, Boston, 103-106.
- Podzimek, J., and J.J. Martin, 1982: Deposition of submicron particulates on model scavengers, Program and Abstracts of the 4th Int. Conf. on Precip. Scavenging, Dry Deposition and Resuspension, Nov. 28-Dec. 3, 1982, Santa Monica, CA, UCLA, p. 90.
- Podzimek, J., P.C. Yue, D.E. Reed, and M.S. Schenewerk, 1980: Fog dispersion with artificial scavengers, 3rd WMO Scient. Conf. on Weather Modif., Clermont-Ferrand, July, 341-347.
- Program and Abstracts of the 4th Int. Conference on Precipitation Scavenging, Dry Deposition and Resuspension, Nov. 28-Dec. 3, 1982, Santa Monica, CA, UCLA, 132.
- Pruppacher, H.R., and J.D. Klett, 1978: Microphysics of Clouds, D. Reidel Publ., p. 714.
- Sasyo, Y., 1971: Study of the formation of precipitation by the aggregation of snow particles and the accretion of cloud droplets on snowflakes, Papers in Met. and Geophys., 22, 69-142.
- Schemenauer, R.S., 1969: Measurements of the drag coefficients and characteristic motions of snow crystals: Graupel and Small Hail Models, M.S. Thesis, Univ. of Toronto, November.

- Sood, S.K., and M.P. Jackson, 1969: Scavenging of atmospheric particulate matter by falling hydrometeors, Preprint Int. Conf. on Condens. and Ice Nuclei, Sept. NCSAV, Praha, 299-303.
- Stewart, R.E., and R. List, 1980: The aerodynamics of freely falling disks and implications for understanding the free fall motions of atmospheric particles, Proc. 8th Int. Conf. on Cloud Physics, Clermont-Ferrand, July, 299-302.
- Stringham, G.E., D.B. Simons, and H.P. Guy, 1969: The behavior of large particles falling in quiescent liquids, Geolog. Survey Profess. Paper, 562-C, U.S. Gov. Print Office, Washington, D.C.
- Willmarth, W.W., N.E. Hawk, and R.L. Harvey, 1964: Steady and unsteady motions and wakes of freely falling disks, Physics Fluids, 7, 197-208.

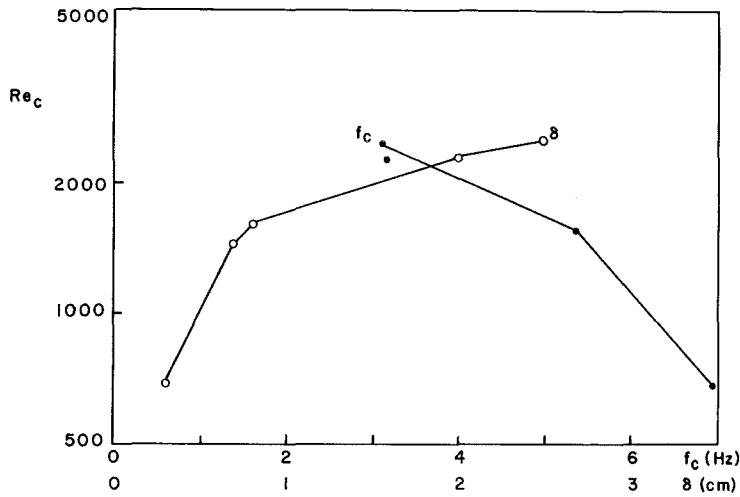


FIGURE 1. DISK'S FREQUENCY, f_c , AND AMPLITUDE, δ , IN DEPENDENCE ON THE REYNOLDS NUMBER. Paper disk ($\rho = 0.97 \text{ gcm}^{-3}$, paper thickness 0.017 cm) was settling in quiescent air.

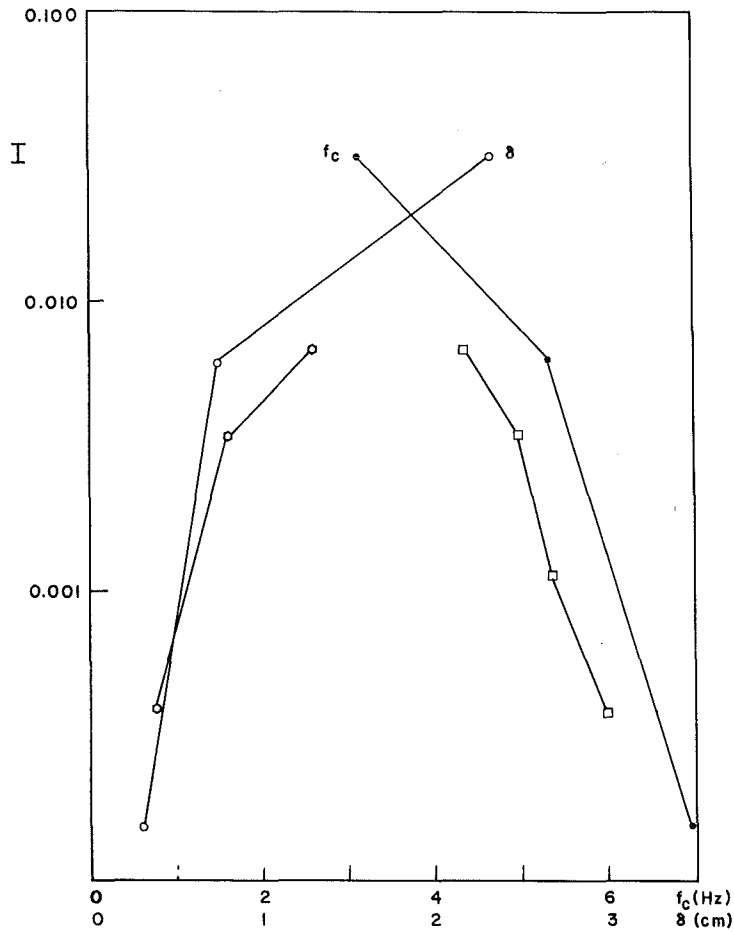


FIGURE 2. DISK'S FREQUENCY, f_c , AND AMPLITUDE, δ , IN DEPENDENCE ON WILLMARTH'S STABILITY NUMBER, I . Paper disk ($\rho = 0.97 \text{ gcm}^{-3}$, paper thickness 0.017 cm) was settling in quiescent air.

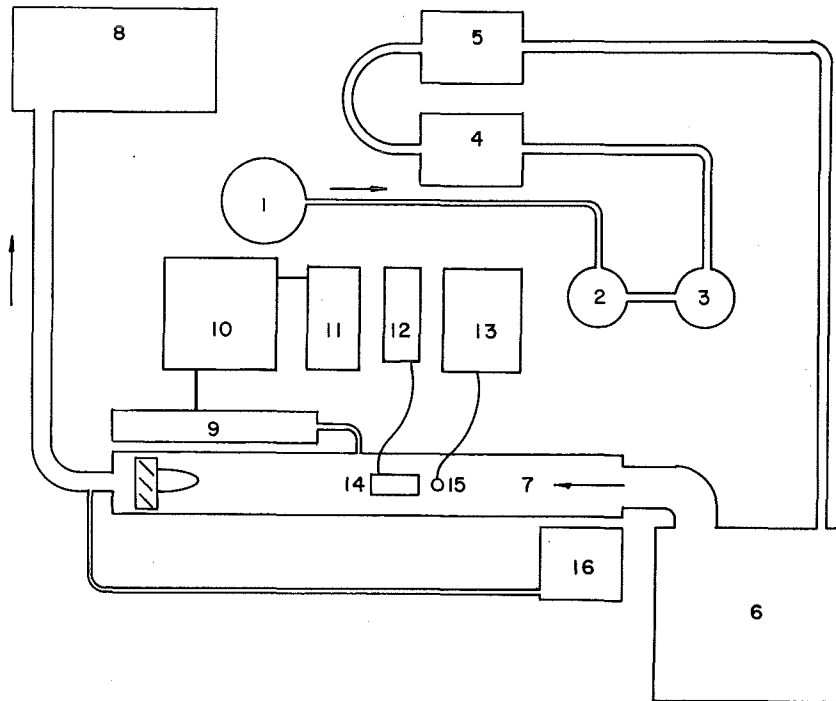


FIGURE 3. WIND TUNNEL EXPERIMENTS WITH SMOKE PARTICLE DEPOSITION ON SCAVENGERS. 1 - nitrogen gas container; 2 - bubbling flask (humidifier); 3 - TiCl_4 smoke particle generator; 4 and 5 - electrical furnaces; 6 - aerosol dilution with clean air and Kr-85 neutralizer; 7 - plexiglass wind tunnel with flow straighteners and propeller; 8 - fume hood; 9 to 11 - Laser Cavity Aerosol Spectrometer ASAS-300A; Laser probe (9), recording unit (10), printer (11); 12 - power unit for vibrating device (14); 13 - electrostatic generator for model charging (15); 16 - pressure transducer for air flow control.

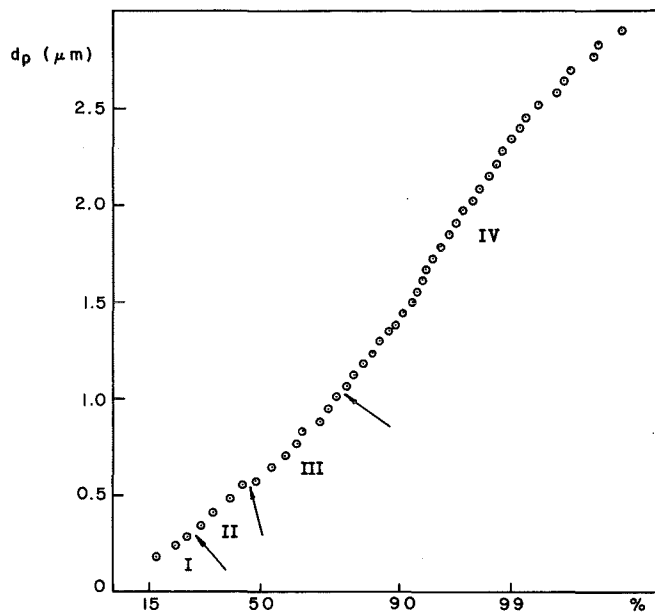


FIGURE 4. TiCl_4 SMOKE AEROSOL CUMULATIVE SIZE DISTRIBUTION. Particles from different size ranges of ASAS-300A are marked by arrows.

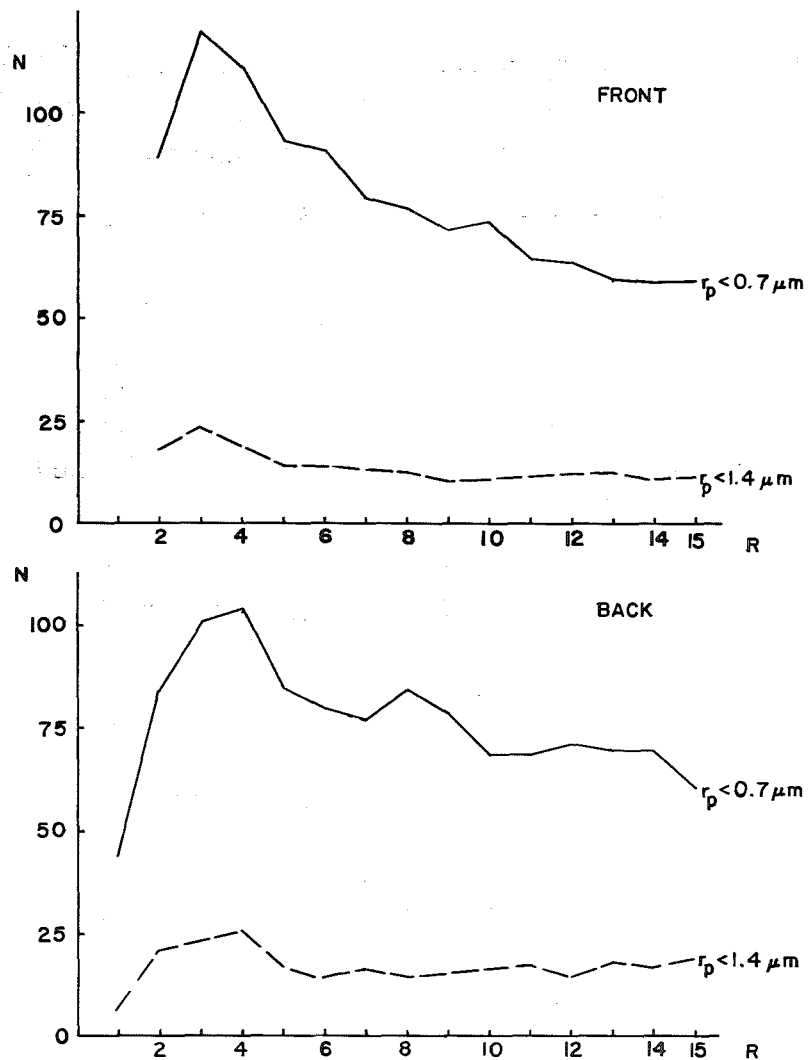


FIGURE 5. NUMBER OF SMOKE PARTICLES DEPOSITED ON A STATIONARY GLASS DISK ($Re_c=320$). Number of particles deposited on the disk's front and back surface (in relative units) in dependence on the distance from the rim ($R=1$). Disk's center is $R=15$.

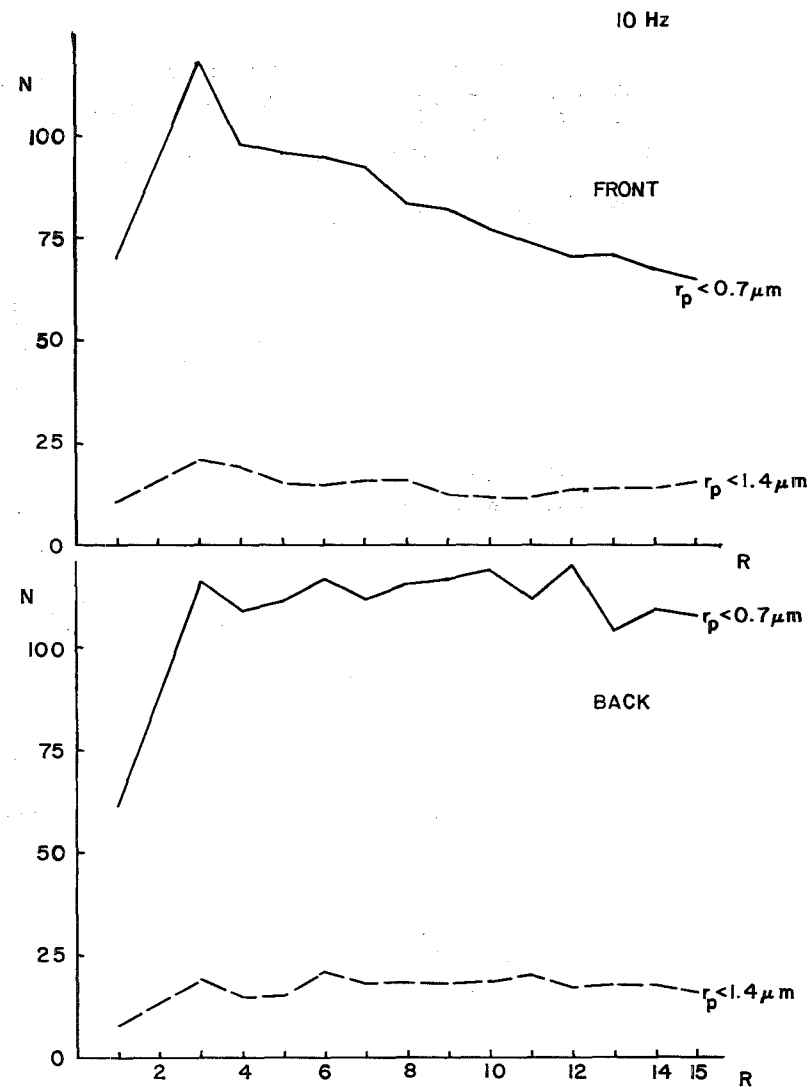


FIGURE 6. NUMBER OF SMOKE PARTICLES DEPOSITED ON AN OSCILLATING GLASS DISK ($Re_c=320$). Number of particles deposited on the disk's front and back surface (in relative units) in dependence on the distance from the rim. Disk's radius is 2.25 mm.

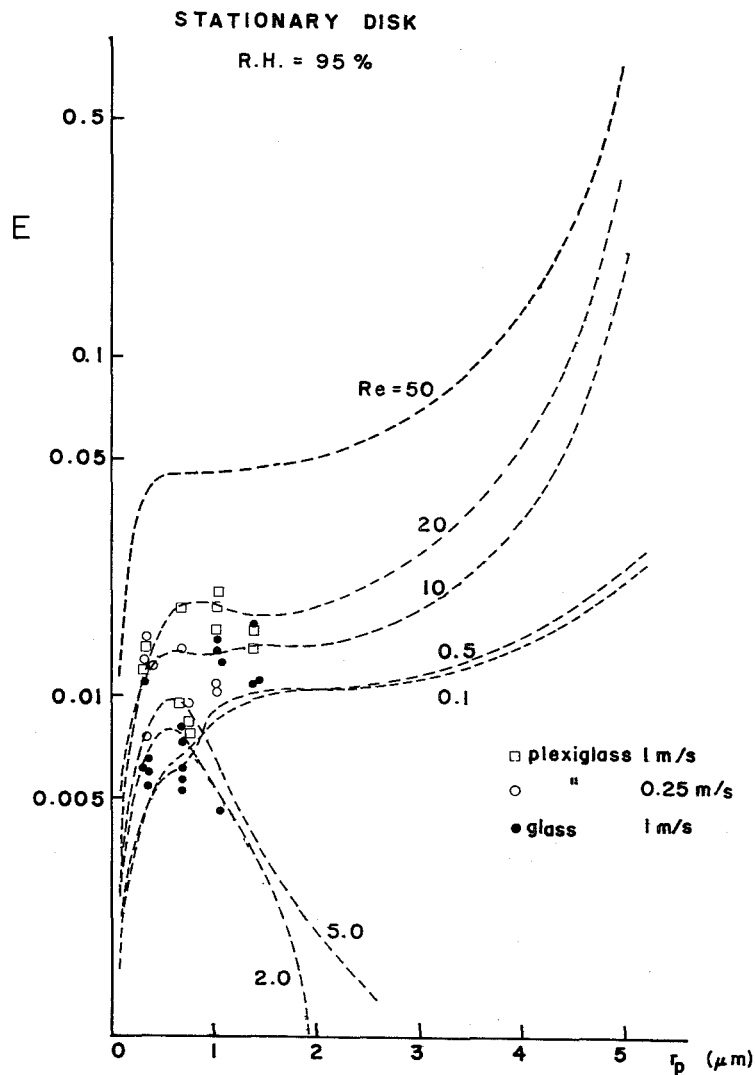


FIGURE 7. CALCULATED COLLISION EFFICIENCY CURVES FOR AN OBLATE SPHEROID (Re_c from 0.1 to 50, smoke particle radii, r_p , from 0.1 to 5.0 μm). Comparison with collection efficiencies of a stationary disk measured in the wind tunnel.

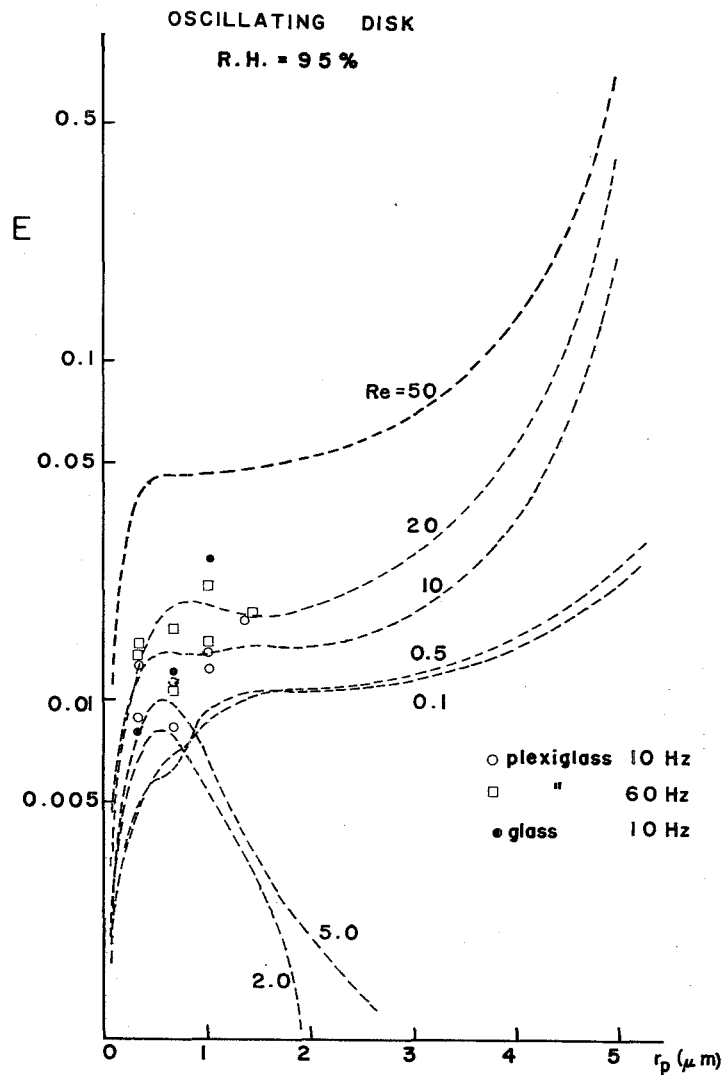


FIGURE 8. CALCULATED COLLISION EFFICIENCY CURVES FOR AN OBLATE SPHEROID (Re_c from 0.1 to 50, smoke particle radii, r_p , from 0.1 to 5.0 μm). Comparison with collection efficiencies of an oscillating disk (10 Hz, 60 Hz, $\alpha = \pm 10^\circ$) in the wind tunnel.

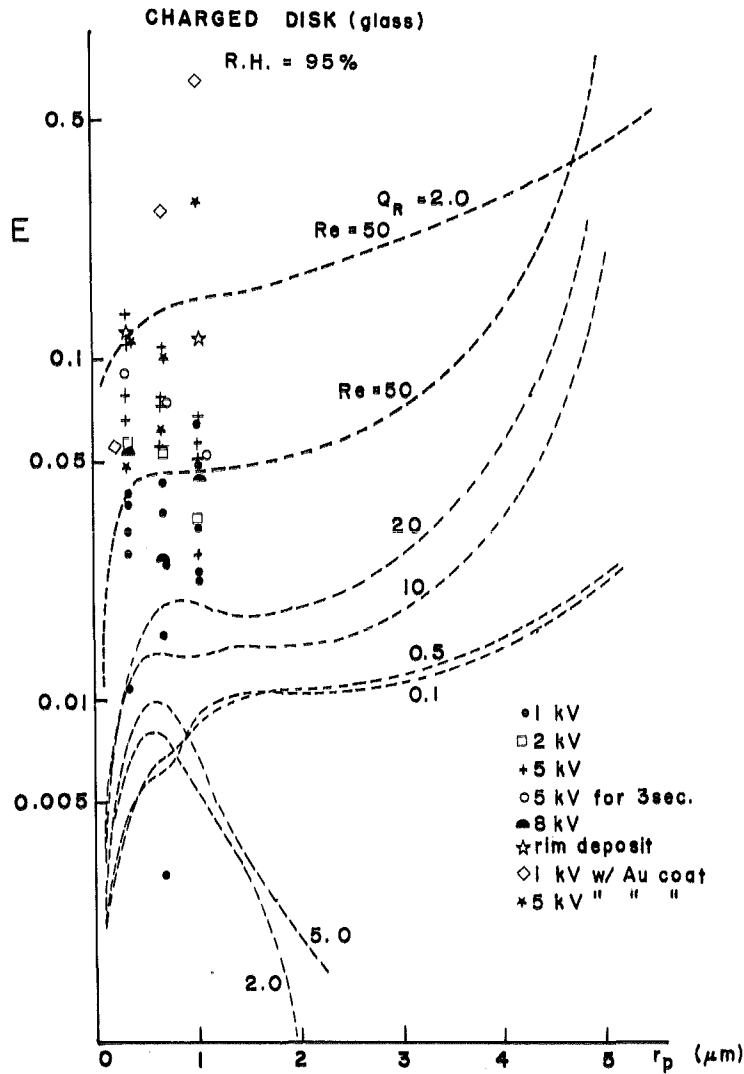


FIGURE 9. CALCULATED COLLISION EFFICIENCY CURVES FOR AN OBLATE SPHEROID ($A_C=0.05$; Re_C from 0.1 to 50; smoke particle radii, r_p , from 0.1 to 5.0 μm). Comparison with collection efficiencies of charged disk collectors (1 kV to 8 kV). A calculated curve for $Re_C=50$ and collector charge $Q_C=2.0$ esu cm^{-2} is plotted in the diagram.

II. AEROSOL CHARACTERIZATION METHODS
(Other than Aerodynamic Methods - See IC)

	PAGE
A. PARTICLE SHAPE DESCRIPTIONS AND THE VALUE OF EFFECTIVE SIZE PARAMETERS	115
B. OPTICAL INVERSION METHODS FOR SIZE DISTRIBUTION (INCLUDING OPTICAL PARTICLE SIZE ANALYZERS)	121
C. OPTICAL CONSTANTS OF LIQUIDS AND POWDERS	141

BLANK

WHAT IS THE PHYSICAL MEANING OF A "SIZE" OF A NONSPHERICAL
AEROSOL PARTICLE? FALLACIES AND POSSIBLE SOLUTIONS

Isaiah Gallily

Department of Atmospheric Sciences
The Hebrew University of Jerusalem
Jerusalem, Israel 91904

THE PHILOSOPHY BEHIND AEROSOL SIZE DETERMINATION

Size *per se* is a pure geometric concept; in aerosol science it is used as an applicable measure to characterize certain behavior properties of the particles. Thus, if we specify, though incompletely, the important aerosol phenomena as: transport mechanics, light scattering, particle/molecules mass-heat transfer, and particle/gas chemical reactions, then what one always aims at is the knowledge of as small as possible a set of size-numbers which describes the above processes.

THE SPECIFICITY OF NONSPHERICAL PARTICLES

To bring out this specificity, let us point out the known situation concerning *spherical* particles in which a single geometric parameter, viz., the diameter, is assigned to each one of them and is sufficient in most cases to characterize a *group* of phenomena such as: aerosol sedimentation, inertial impaction, diffusion, etc. The situation with *nonspherical* particles (Fig. 1) is far from being that simple since:

1. The physical meaning of a particle size as a useful parameter for *all* of the above phenomena is not clear in many cases even for regular particles;
2. The intuitive modelling of an irregular particle by a regular one is not solidly based and is highly dependent on the *level of accuracy* desired;

3. The number of size parameters tends to be infinitely high (Fig. 2).

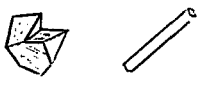
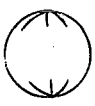
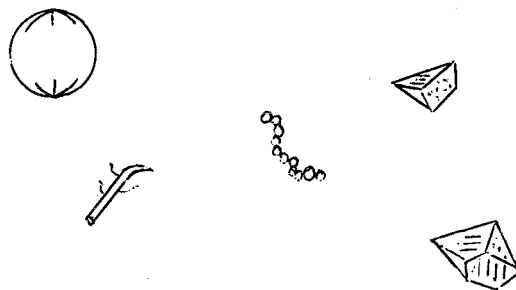
Shape	Nonspherical, Regular/Irregular 	Spherical 
Characterizing Size	?	Diameter

Fig. 1. Shape and characterizing size of one particle.



ETC.

Fig. 2. Size distribution within a particle ensemble.

COMMON SIZE MEASURES OF NONSPHERICAL PARTICLES

Let us concentrate essentially on the two most common size-measures employed and discuss the limitations and shortcomings of their use.

Geometric

1. Projected Area Diameter, D_p

This is defined as the diameter of a circle whose area is equal to the area of the particle projected on a certain plane. Obviously, D_p is *not* an inherent characteristic of the particle since it depends on the inclination of the latter to the above plane.

If the inclination is randomly distributed and the (irregular) particle is convex, then, by Cauchy's theorem (1), the surface area of the particle is equal to four times its orientationally-averaged projected area. In other cases, the inclination is surely not random, as found by Gallily (2), and is probably determined also by the interaction between the particle and the collecting surface. D_p has only a statistical meaning.

ii. Volumetrically Equivalent Diameter, D_e

This is defined as the diameter of a sphere which is volumetrically equivalent to the considered particle. D_e is now an inherent property of the latter; it precludes, however, the existence of cavities within the particle itself which may be significant when gaseous chemical reactions occur.

One can formally define here *shape factors* α_i by the relationships

$$S = \alpha_{s,i} D_i^2 \quad [1]$$

and

$$V = \alpha_{v,i} D_i^3 \quad [2]$$

where $i \rightarrow p, e$.

The important question is how D_p and D_e relate to aerosol sedimentation, impaction, diffusion and so on. In this respect the study of Stein, *et al.* (3), shows that, if a relation exists, it is by no means a simple one.

Operational

1. Aerodynamic, D_a , or Stokes, D_s , Diameters

These are respectively defined as the diameters of a sphere with a unit density, or the actual density of the particle ρ_p , which has the same time-averaged sedimentation velocity $\bar{u}_{\omega, \tau}$ along the direction of the actuating external force as that of the particle. The diameters are given by

$$D_a = (18 \mu \bar{u}_{\omega, \tau} / g)^{1/2} \quad [3]$$

and

$$D_s = (18 \mu \bar{u}_{\omega, \tau} / \rho_p g)^{1/2} \quad [4]$$

where μ is the dynamic viscosity of the medium.

The rationale on which the above size-measures are based hinges on the assumption that the sedimentation of *nonspherical* particles is described by an equation similar to that of the *spherical* ones, viz.

$$u_{\infty} = (\rho_p D_s^2) g / 18 \quad [5]$$

and the (tacit) assumption that the inertial impaction of the former is dependent only on the obstacle's Reynolds number, the interception number of the particle and Stokes number Stk defined by the equation

$$Stk = (\rho_p D_s^2) u_o / 18 \mu W \quad [6]$$

in which D_s appears. u_o and W are the initial upstream velocity of the particle and a typical length of the collector, respectively.

It turns out that the above assumed similarities between nonspherical and spherical particles do not exactly hold.

INADEQUACY OF THE AERODYNAMIC DIAMETER CONCEPT

Sedimentation

It has been shown that the sedimentation of nonspherical orientable particles in still air can be visualized as a series of discrete *random flights* in which the settling particle changes its spatial orientation on account of its ever-existing Brownian rotation (4). Consequently, the (vertical) trajectory it traverses in a certain time, and hence its average (vertical) velocity and its aerodynamic diameter D_a (or its Stokes diameter, D_s) turn to be a stochastic quantity with an inherent *spread* of values. Also, essentially the same phenomenon can be considered as a Taylor dispersion (5, 6).

The sedimentation of elongated particles in a laminar flow, and their Stokes diameter (or the aerodynamic diameter), were calculated and experimentally found to be dependent on the velocity gradient (7). Thus, it can be stated that the operational size-measures named the aerodynamic diameter (or Stokes diameter) of especially highly non-isometric fiber-like and (probably) flake-like aerosol particles is a property which is:

- i. Essentially stochastic, non-constant;

and

- ii. Dependent on field-gradients and so, in principle, on the type of apparatus or sampling instrument used.

The studies of Spurny, *et al.*, concerning sampling of asbestos fibers (8) as well as the studies of

Cohen *et al.* (9) clearly support the above second deduction.

Inertial Impaction

The inertial impaction of elongated particles on various obstacles was shown to be determined by both particles' translation and rotation (10, 9). It has been found that the collision efficiency of these particles cannot be solely described by the Stokes number, Stk (Eq. [5]); the rotational aspect of the motion, which causes sometimes an enhanced interception with the collecting surface, as well as the initial orientation of the particles do play an important role in the phenomenon. Thus, the aerodynamic (or the Stokes diameter) which is manifested in the $(\rho_p D_s^2)$ group of [5] is an *insufficient* size-parameter to characterize inertial impaction too.

POSSIBLE SOLUTIONS

The problem related to a *useful* size-measure for nonspherical (and especially highly non-isometric) aerosol particles seems far from being solvable. Geometrically, the shape of most types of these particles is irregular which makes their description by a small set of characterizing numbers impossible as yet. Also, behaviorally, the motion of the particles is generally very complicated which renders the relation between the latter and the shape features quite complex. However, some ways of approach may be conceived. One of these ways may be broken down into:

1. Recognizing the physics of the phenomenon of interest;
2. Solving the problem theoretically with the assumption that every needed particle parameter can be supplied at request;
3. Finding the size-parameters which are important;
4. Determining these parameters by experiments.

For regular particles such as straight cylinders or thin platelets, as an example, the time-averaged sedimentation velocity is a very weak function of their length (4, 11). So, the aerodynamic diameter in this case will essentially depend on particle's diameter that is here the size to be measured. The impaction properties of the above particles, however, are affected also by their length which cannot be ignored.

For irregular particles, one line of solution relates to their "successful" modelling by simple geometric forms but this brings one to questions of the desired accuracy of behavior prediction. In the case of the particle ensemble mentioned above, it may be possible by "intelligent intuition" based on many studies to obtain the lower and upper model-shape limits for the description of the phenomenon.

CONCLUSIONS

•The *useful* size-measures necessary to characterize the behavior of nonspherical aerosol particles still constitute a difficult problem.

•It may be necessary to assign different such measures to different phenomena of interest.

•The case of irregular particles stands apart since one needs here to model the particles by simpler forms which is related to the question of the desired accuracy of quantitative description.

REFERENCES

1. Cauchy, A., *Acad. Sci. Paris*, 13, 1060 (1841); see in "Aerosol Technology in Hazard Evaluation", T.T. Mercer, Academic Press, N.Y., 1973, p. 68.
2. Gallily, I., *J. Colloid Interface Sci.*, 37, 403 (1971).
3. Stein, F., Esmen, N.A., and Corn, M., *Atmos. Environ.*, 3, 443 (1969).
4. Gallily, I., and Cohen, A.H., *J. Colloid Interface Sci.*, 56, 443 (1976).
5. Brenner, H., *ibid.*, 71, 189 (1979).
6. Goren, S.L., *ibid.*, 71, 209 (1979).
7. Gallily, I., and Eisner, A.D., *ibid.*, 68, 320 (1979).
8. Spurny, K.R., Gentry, J.W., and Stoeber, W., in "Fundamentals of Aerosol Science" (D.T. Shaw, ed.), John Wiley, N.Y., 1978, Chaps. 5-7.
9. Cohen, A.H., Schiby, D., Gallily, I., Holsaender, W., Mause, P., Schless, D. and Stoeber, W., GAF 8th Conference, Proceedings, W. Germany, 1980, pp. 299-309.
10. Gallily, I., and Cohen, A.H., *J. Colloid Interface Sci.*, 68, 338 (1979); *ibid.*, 71, 628 (1979).
11. Stoeber, W., in "Assessment of Airborne Particles" (T.T. Mercer, P.E. Morrow and W. Stoeber, eds.), Thomas, Springfield, Illinois, 1972, pp. 273-287.

A NEW METHOD OF MULTI-SPECTRAL INVERSION
BASED ON THE ANOMALOUS DIFFRACTION MODEL

James D. Klett
Senior Research Associate
National Research Council
Atmospheric Sciences Laboratory
White Sands Missile Range
White Sands, NM 88002

ABSTRACT

An analytical solution to the problem of inverting multispectral extinction measurements including absorption effects has been constructed, via Laplace transform theory, under the assumption that the particulate extinction efficiency is given by the anomalous diffraction model of van de Hulst. A solution representation in terms of a finite series of associated Laguerre polynomials is carried out to provide a framework for coping with the problem of limited extinction information.

A purely formal and theoretical description of the model has been submitted for publication in Pure and Applied Geophysics under the title: "Anomalous diffraction model for inversion of multispectral extinction data including absorption". Another paper containing further elaboration and development of the model as well as illustrative numerical examples has been submitted to Applied Optics under the title: "Optical inversion model based on the anomalous diffraction approximation".

MODEL & SOLUTION

The anomalous diffraction extinction efficiency for spherical particles of radius r and complex index of refraction $m=n-in'$ may be expressed as:

$$Q = 2 + 4\text{Re}\{K(\tilde{w})\}, \quad (1)$$

with

$$K(\tilde{w}) = \frac{\exp(-\tilde{w})}{\tilde{w}} + \frac{\exp(-\tilde{w})-1}{\tilde{w}^2}, \quad (2)$$

$$\tilde{w} = \rho(i+\tan\beta) = \tilde{k}r, \quad (3)$$

and where $\text{Re}\{K(\tilde{w})\}$ denotes the real part of $K(\tilde{w})$, k is the wavenumber, $\rho=2(n-1)kr$ is the phase parameter, and $\tan\beta = n'/(n-1)$.¹ The corresponding extinction coefficient for a distribution of particles $f(r)$ is

$$\tau(k) = \pi \int_0^{\infty} r^2 Q(\rho) f(r) dr. \quad (4)$$

To solve Eqs.(1)-(4) for $f(r)$ one may begin by defining a complex extinction coefficient as follows:

$$T(\tilde{k}) = 4\pi \int_0^{\infty} r^2 f(r) K(\tilde{k}r) dr. \quad (5)$$

This function is related to $\tau(k)$ by

$$\tau(k) = \text{Re}\{T(\tilde{k})\} - T(0), \quad (6)$$

where $T(0) = M_2$, the second moment of $f(r)$. Now introduce a new dependent variable $F(r)$ such that

$$f(r) = \frac{1}{4\pi} \frac{d(F(r)/r)}{dr}. \quad (7)$$

Then Eq.(5) and its inverse in terms of $F(r)$ form a Laplace transform pair:

$$T(\tilde{k}) = \int_0^{\infty} F(r) \exp(-\tilde{k}r) dr, \quad (8)$$

and

$$F(r) = \frac{1}{2\pi i} \int_C T(\tilde{k}) \exp(\tilde{k}r) d\tilde{k}, \quad (9)$$

where the contour path C lies to the right of any singularities in $T(\tilde{k})$.

REPRESENTATION FOR FINITE DATA

In order to implement the above solution when only limited extinction information is available, we may expand $T(\tilde{k})$ in a series of generalized Laguerre polynomials of orders n and l as follows:²

$$F(r) = r \exp(-br) \sum_{n=0}^{\infty} \frac{n! A_n L_n^1(br)}{(n+1)!}, \quad (10)$$

with

$$L_n^1(x) = \sum_{m=0}^n \frac{(-1)^m (n+1)! x^m}{(n-m)! (m+1)! m!}. \quad (11)$$

From Eq.(8) the corresponding expansion for $T(\tilde{k})$ is

$$T(\tilde{k}) = \sum_{n=0}^{\infty} \frac{\tilde{k}^n A_n}{(\tilde{k}+b)^{n+2}}. \quad (12)$$

Eq.(10) is a complete representation, and therefore so is Eq.(12) by Parseval's theorem.^{3,4} Also, $T(\tilde{k})$ as given by Eq.(12) has the same asymptotic behavior as Eq.(5) for large k , which is the reason for expanding in terms of L_n^1 .

One may now proceed to determine the A_n in Eq.(12) using Eq.(6) and truncating the series according to the number of extinction measurements available. This produces a set of linear equations in A_n of the form

$$\sum_{j=1}^J C_{ij} A_j = \tau(k_i), \quad (13)$$

for measurements at wavenumbers k_i , $i=1,2,\dots,I \geq J$. Since the inversion problem is mathematically ill-conditioned, the required matrix inversion of Eq.(13) must be stabilized in some fashion. A suitable procedure is the method of constrained linear inversion where the constraint is one of an a priori form for the coefficient vector \vec{A} ($\rightarrow(A_i)$). Then the solution may be expressed as

$$\vec{A} = (C^T C + \gamma I)^{-1} (C^T \vec{\tau} + \gamma \vec{A}_0), \quad (14)$$

where I is the identity matrix, C^T is the transpose of C , and $\gamma > 0$ is a stability parameter.^{5,6} Encouraging results with this approach have been achieved for the case that both the initial coefficient vector \vec{A}_0 and the expansion parameter b (see Eq.(10)) are chosen to provide the best Gamma distribution fit to the extinction data. Further related strategies and model development are in progress.

REFERENCES

1. van de Hulst, H. C., Light Scattering by Small Particles (Wiley, New York, 1957), 470pp.
2. Piessens, R., and Branders, M., Proc.IEEE, 118, 1517-1522 (1971).
3. Luke, Y. L., The Special Functions and Their Approximations, v.2 (Academic Press, New York, 1969).
4. Morse, P. M., and Feshbach, H., Methods of Theoretical Physics, v.I (McGraw-Hill, New York, 1953), 997pp.
5. Phillips, D. L., J. Assoc. Comput. Mach. 9, 84-97 (1962).
6. Twomey, S., J. Assoc. Comput. Mach. 10, 97-101 (1963).

BLANK

A CONSTRAINED EIGENFUNCTION EXPANSION METHOD AND A NONLINEAR
REGRESSION PROCEDURE FOR THE INVERSION OF MIE SCATTERING DATA

B. P. Curry and E. L. Kiech
Calspan Field Services, Inc.
Arnold Air Force Station, TN 37389

ABSTRACT

This paper concerns the inversion of the particle size distribution function from synthetic Mie scattering data. This work and related material have been presented in the following publications: AEDC-TR-83-32, AEDC-TR-83-52, and AIAA Thermophysics Conference, Montreal, Canada, June 1-3, 1983. Sponsored by Chemical Research and Development Center, U.S. Army.

1.0 Introduction

For several years Calspan/AEDC personnel have been developing in situ particle diagnostics methods based on the properties of the Mie scattering theory as it applies to a polydisperse distribution of uniform dielectric spheres. Examples of this work are reported in Refs. 1 - 7. Some particle size information can be obtained directly from ratios of scattered light measurements - e.g., polarization ratios (Refs. 3 - 5, 8), ratios of scattering measurements at two different angles (Refs. 1 - 3, 9), ratios of scattering or transmission measurements at two different wavelengths (Ref. 10) and ratios of differential-to-extinction cross sections (Ref. 1 - 3, 11) or differential-to-back scattering cross sections. These different measurements all yield weighted averages of particle size - i. e., unspecified moments of the particle size distribution function (PSDF). Without some additional knowledge of the PSDF, however, it is difficult to infer from such measurements precisely what moment of the PSDF is being determined. Further, gross errors in the interpretation of these scattering measurements may be made if an average diameter inference is interpreted, for example, as a mass median diameter when the actual measurement may be more appropriately interpreted as that diameter which corresponds to the mean optical surface area (which can sometimes exceed the mean geometrical surface area) of a distribution of particles.

Obviously, the most satisfactory way to avoid misinterpreting particle diagnostics based on light scattering measurements is to determine the PSDF itself. Any desired moment of the PSDF may then be obtained by simple quadrature. We have investigated the characteristics of four different methods by which to obtain the PSDF by inversion of the Fredholm integral equation which describes the scattering of light by a distribution of spherical particles whose complex refractive index is known. This paper presents the two most successful methods we have developed to date.

2.0 Light Scattering Theoretical Background

Light scattering measurements may be interpreted in terms of scattering cross sections which are

determined by the physical and optical properties of the scatterers. If an incident light beam whose power is $\Phi_0(\lambda)$ is scattered by a distribution of particles whose complex, refractive index is $n(\lambda)$ and whose number density is n , the power scattered into a given solid angle $\Delta\Omega_i$ is stated as

$$\Phi(\theta_i, \alpha_i, \lambda) = \Phi_0(\lambda) n \lambda_i \int_{\Delta\Omega_i} \int_0^\infty \frac{d\sigma}{d\Omega}(\theta, \alpha, n(\lambda), x) f(D) dD d\Omega \quad (1)$$

where $f(D)$ is the normalized PSDF, $x = \frac{\pi D}{\lambda}$ is the size parameter for a particle of diameter D illuminated by an incident light beam whose wavelength is λ , and θ and α are, respectively, the scattering angle and azimuthal angle in a particle-centered, spherical polar coordinate scattering geometry. The azimuth α is defined as the angle between the incident electric field axis (if the source is polarized) and the scattering plane. The scattering length λ_i is the projection of the focal volume onto the incident beam axis, and it is entirely determined by the collection optics at each detector location.

As long as the focal volume is much larger than a single particle, the incident beam may be regarded as if it were a plane wave and the scattering cross section may be stated in terms of Mie scattering functions. Specifically, for a polarized light source and polarization-resolving detectors, the component of scattered light whose electric field vector is perpendicular to the scattering plane is associated with the differential scattering cross section

$$\frac{d\sigma_\perp}{d\Omega}(\theta, \alpha, n(\lambda), x) = \left(\frac{\lambda}{2\pi}\right)^2 i_1(x, \theta, n(\lambda)) \sin^2\alpha, \quad (2)$$

and the parallel scattering component is associated with the differential scattering cross section

$$\frac{d\sigma_\parallel}{d\Omega}(\theta, \alpha, n(\lambda), x) = \left(\frac{\lambda}{2\pi}\right)^2 i_2(x, \theta, n(\lambda)) \cos^2\alpha. \quad (3)$$

The Mie scattering intensity functions $i_1(x, \theta, n(\lambda))$ and $i_2(x, \theta, n(\lambda))$ can be calculated using readily available Mie scattering computer programs, such as Ref. 12.

Equations (1 - 3) show that particle size information can be extracted from the dependence of the scattered light intensity on the three independent variables: wavelength, scattering angle, and polarization state. We shall henceforth designate any experimental combination of these variables as the set of independent variables $\{Y_i\}$, $i = 1, 2, 3 \dots N$, where N is the total number of independent measurements. Equation (1) also shows that the scattered light intensity is proportional to the unknown particle number density n . In order to eliminate the number density from the particle size inversion procedure, we prefer to normalize the measurements by an appropriate reference quantity such as the 90° scattering cross section or the extinction cross section (averaged over wavelengths). After having determined the PSDF, one can compute the cross section for extinction or for whatever absolute intensity measurement may be available and then determine the particle number density separately from the PSDF.

The advantage of this procedure over that of retaining the number density as an additional regression parameter is the ability to tolerate large uncertainties in the absolute magnitude of the scattering data, provided the relative scattering measurements conform to the accuracy required by the PSDF inversion procedure.

Letting the set of appropriately normalized scattering measurements be denoted as $G(Y_i)$, $i = 1, 2, \dots, N$, we can state the integral equation from which the PSDF is determined in the familiar form

$$G(Y_i) + E(Y_i) = \frac{1}{N_0} \int_0^{\infty} K(x, Y_i) F(x) dx, \text{ where } N_0 = \int_0^{\infty} K_0(x) f(x) dx \quad (4)$$

In this equation, the kernels $K(x, Y_i)$ are just the differential cross sections defined in Eqs. (2 and 3) integrated over the appropriate detector-subtended angles. The denominator, N_0 in Eq. (4), plays the role of a normalization constant if the kernel $K_0(x)$ is chosen so as to have minimal dependence on x . Equation (4) is an example of what has been called the "ill-posed problem" because of the presence of residual errors $E(Y_i)$. These are an inextricable combination of experimental and computationally induced errors. Were it not for the presence of residual errors and for the finite aspect of the measurements, one could solve Eq. (4) by standard methods based on the properties of integral transforms (Ref. 13). Unfortunately, however, the presence of residual errors introduces unreal, oscillatory (sometimes negative) solution values when one attempts to solve Eq. (4) without regard for the effect of the residual errors. Consequently, most successful solution procedures of which we are aware are based on various schemes to minimize some kind of weighted sum of the squares of the residual errors (e.g., Refs. 6, 7, 14 - 17).

2.1 Solution of the Integral Scattering Equation

In order to solve Eq. (1), which is a Fredholm integral equation of the first kind if N_0 is temporarily regarded as a constant, let us consider parametric forms of the PSDF

$$f_1(x) = f_1(x, C_1, C_2, \dots, (N)) \quad (5)$$

and

$$f_2(x) = f_2(x, C_1, C_2, \dots, C_r, P_1, P_2 \dots P_s) \quad (6)$$

where N is the total number of measurements and $r + s \leq N$.

In Eqs. (5) and (6) the constants C_1, C_2 , etc., are to be regarded as members of a set of linear expansion coefficients for the expansion of the PSDF in basis functions. Our first procedure considers the basis functions to be known functions of x having no additional parameters. The linear expansion coefficients are determined by a formal variational procedure in which the sum of the squared residual errors is

minimized subject to a specified constraint. This solution procedure was designated a "constrained eigenfunction expansion" in Ref. 1 because the basis functions are eigenfunctions of the Mie scattering kernels.

Our second solution procedure involves a linear expansion of the PSDF in basis functions which depend in a nonlinear fashion on x and on the parameters P_1, P_2, \dots, P_s . The composite set of parameters $C_1, C_2, \dots, C_r + P_1, P_2, \dots, P_s$ is regarded as the set of regression parameters for a multivariate, nonlinear regression procedure which seeks to minimize the sum of the squared residual errors. We have used as basis functions lognormal distributions, cubic splines, Gaussians, and other functions whose height and width are taken to be parameters of the regression.

In the next two sections we discuss the most significant characteristics of both these PSDF inversion procedures. Since the constrained eigenfunction expansion solution was derived in considerable detail in Ref. 7, we review, in Section 2.2 only the most significant results of that derivation. The nonlinear regression technique is, however, discussed in considerable detail in Section 2.3.

2.2 Constrained Eigenfunction Expansion

By a well-known theorem, one can show that the optimum complete basis set for a linear expansion of the PSDF consists of eigenfunctions of the symmetric kernel operator $M_{(x', x)} = \sum_{i=1}^N K(x', Y_i) K(x, Y_i)$. These eigenfunctions can be computed from eigenvectors of the kernel covariance matrix (in the input domain), which is defined as

$$N(Y_i, Y_j) \equiv \int_0^{\infty} K(x, Y_i) K(x, Y_j) dx \quad (7)$$

by use of the normalized transformation

$$\phi_i(x) = \lambda_i^{-1/2} \sum_{k=1}^N U_i(Y_k) K(x, Y_k) \quad (8)$$

where U_i and λ_i are, respectively, the "ith" eigenvector and the "ith" eigenvalue of the kernel covariance matrix N . The direct solution of Eq. (7) which minimizes the residual errors without introducing any solution constraints was published by Capps, et al. (Ref. 14). Recently, we generalized this solution to incorporate variational constraints and inverse weighting of the kernels by the estimated imprecision values (square root of the estimated variances) for each input channel (Ref. 7). Our derivation shows that the solution expansion coefficients which incorporate a trial function constraint can be written as

$$c_i = \left(\frac{Y}{\lambda_i} c_i^T + c_i^0 \right) / \left(1 + \frac{Y}{\lambda_i} \right) \quad (9)$$

*Parentthesis
out of place*

where the coefficients $C_i^T = \int_0^\infty f_i^T(x) \phi_i(x) dx$ are the expansion coefficients for the trial function $f^T(x)$, γ is a lagrange multiplier (smoothing parameter), and the coefficients C_i^0 are the imprecision weighted direct solution coefficients

$$C_i^0 = \lambda_i^{-1/2} \sum_{k=1}^N U_i(Y_k) \frac{G(Y_k)}{\Delta G(Y_k)} \quad (10)$$

In these equations $\Delta G(Y_k)$ designates the estimated imprecision of the "kth" scattering measurement and the eigenfunctions, eigenvectors, and eigenvalues are calculated as previously indicated but are based on the imprecision weighted kernels $K^W(x, Y_i) = K(x, Y_i) / \Delta G(Y_i)$. In addition, the normalization function $N_0 = \int_0^\infty K_0(x) f(x) dx$ has, for the moment, been absorbed into the kernels as a normalization constant restricting the choice of the normalization kernel $K_0(x)$ to being slowly a varying function of x . This restriction will later be removed. The PSDF is expanded in terms of these coefficients as

$$f(x) = \sum_i C_i \phi_i(x) \quad (11)$$

and the residual errors are calculated from

$$E(Y_i) = \sum_j C_j \lambda_j^{1/2} U_j(Y_i) - G(Y_i) / \Delta G(Y_i) \quad (12)$$

If one denotes the error-free PSDF by $f^0(x)$, then the solution error norm is bounded by

$$\int_0^\infty |f(x) - f^0(x)|^2 dx \leq \sum_{i=1}^N \lambda_i^{-1} \sum_{k=1}^N |E(Y_k) / \Delta G(Y_k)|^2 \quad (13)$$

showing that the only solution components which contribute valid information to the recovered PSDF are those which satisfy

$$\lambda_i \gg \sum_{k=1}^N \left| \frac{E(Y_k)}{\Delta G(Y_k)} \right|^2 \quad (14)$$

as was first shown by Twomey (Ref. 17). Invalid solution components must be suppressed, else the recovered PSDF will exhibit unphysical behavior. Suppression can be accomplished by deleting from the PSDF expansion those components which violate the above inequality (as was done in Ref. 14), by use of the constrained expansion coefficients presented here and in Ref. 7, or by a combination of the two methods.

If one knew the actual errors in each measurement channel, the residual errors resulting from both smoothing and experimental errors could be computed from

$$\frac{E(Y_i)}{\Delta G(Y_i)} = \sum_{j=1}^N \frac{U_j(Y_i)}{(1 + \frac{\gamma}{\lambda_j})} \left[\frac{\gamma}{\lambda_j^{1/2}} (C_j^T - C_j^0) + \sum_{k=1}^N U_j(Y_k) \frac{\delta G(Y_k)}{\Delta G(Y_k)} \right] \quad (15)$$

where $\delta G(Y_k)$ denotes the (unknown) actual error in the "Kth" measurement. This equation shows that, as γ increases, the effect of actual experimental error is damped at the expense of the introduction of error due to smoothing. In actuality, since one doesn't know the actual experimental errors, the residual errors must be regarded as being entirely the result of the smoothing process. If one can reliably estimate the optimum value of the smoothing parameter, the computed residual error will approximately equal the experimental error.

Our solution procedure determines the optimum smoothing level by seeking a minimum in a parameter which is denoted the "Residual Relative Variance" (RRV) in Ref. 7. This parameter is a weighted average of the residual errors. Its minima are found to correspond to the values of γ at which near equality is found between one or more pairs of the coefficients C_i and $\frac{\gamma}{\lambda_i} C_i^T$. In practice, our solution technique employs a doubly iterative calculation sequence in which, at any stage of iteration, the smoothing parameter is increased until either a true minimum of the RRV is found (with respect to γ) or else the slope of the RRV is found to be negative and flat within a specified tolerance. The solution is then checked to see whether it differs from the previous iterate within a specified tolerance. If the difference exceeds the tolerance, the current solution is taken to be the trial function for the next iteration cycle. The entire iteration sequence is begun by the specification of the initial trial function, and the sensitivity of the results to the choice of initial trial function is controlled by the specification of the "flat slope" criterion and the iteration convergence criterion.

Once the PSDF has been determined, solution error bounds can be calculated based on the assumption that the input errors are Gaussian. If the solution is based on the use of imprecision weighted kernels, the PSDF variance is rigorously expressed as

$$|\Delta f(x)|^2 = \sum_{i=1}^N \lambda_i^{-1} \frac{|\phi_i(x)|^2}{1 + \frac{\gamma}{\lambda_i}} \quad (16)$$

If the solution is based on unweighted kernels, the PSDF variance can be calculated, approximately, from

$$|\Delta f(x)|^2 = \sum_{i=1}^N \lambda_i^{-1} |\phi_i'(x)|^2 \frac{\sum_{k=1}^N |U_i'(Y_k) \Delta G(Y_k)|^2}{1 + \frac{\gamma}{\lambda_i} \sum_{k=1}^N |U_i'(Y_k) \Delta G(Y_k)|^2} \quad (17)$$

where the prime denotes eigenfunctions, eigenvectors, or eigenvalues of the unweighted scattering kernels.

The equations presented in this section and in Ref. 7 reduce identically to those of Ref. 14 when $\gamma \rightarrow 0$ and $\Delta G(Y_j) \rightarrow 1$. If the imprecision of each measurement is proportional to the magnitude of each

measurement, weighting by input imprecision values is equivalent to weighting by the kernel norms as was done in Ref. 14. In such a case, Eqs. (16) and (17) are also equivalent.

The preceding equations were all derived under the assumption that the normalization kernel $k_0(x)$ varied sufficiently slowly to permit the normalization function $N_0 = \int_0^{\infty} k_0(x) dx$ to be treated as a constant. This restriction is easily removed if the normalizing kernel is representable as a member of or a linear combination of members of the set of kernels which correspond to the input channels. Thus, if

$$k_0(x) = \sum_{i=1}^N a_i k(x, Y_i) \quad (18)$$

where the a_i are arbitrary expansion coefficients, the normalization function can be evaluated, approximately, as

$$N_0 = \sum_{i=1}^N a_i \Delta G(Y_i) \sum_{j=1}^N C_j^T \lambda_j^{1/2} U_j(Y_i) \quad (19)$$

since the trial coefficients are the PSDF expansion coefficients for the previous iteration cycle. When this form of the normalization function is used, the PSDF expansion coefficients must be modified in Eq. (9) by replacing each direct solution coefficient C_i by the product $N_0 C_i^0$. Similarly, the smoothed expansion coefficients C_j in Eq. (12) must be replaced by the ratio C_j/N_0 in order to calculate the residual errors correctly. We refer to the use of N_0 as a functional dependent on the properties of the PSDF in the solution procedure as "active normalization"; whereas "passive normalization" indicates the consideration of N_0 as a constant which can be absorbed into the definition of the kernels. The solution procedure is sometimes less rapidly convergent when active normalization is employed, but it is more stable in the presence of experimental errors than when passive normalization is used. Further, the residual error corresponding to convergence of the iteration sequence has been found to be a fairly good estimate of the experimental error in the inputs when deconvolutions of simulated scattering data containing known levels of Gaussian-distributed noise have been performed.

2.3 Nonlinear Regression

Our second inversion procedure seeks to determine the PSDF by a nonlinear regression involving numerical application of the principle of least squares.

Assuming that $f(x)$ can be adequately expressed as a function of the parameters (P_i) and that the errors, $E(Y_i)$, in Eq. (1) are normally distributed, the principle of least squares states that the best approximation to $f(x)$ is that function $f(x, \{P_i\})$ in which the choice of the set of regression parameters $\{P_i\}$ minimizes the sum of the squares of the residuals between the calculated and measured scattering

inputs $G(Y_i)$, weighted by the inverse of each input's associated standard deviation. The selection of the fitting function, $f(x, P_i)$, is a fundamental part of the regression procedure and is based on several considerations. If $f(x)$ is known to be of a certain type (such as a lognormal) then the fitting function should be of the same type. Usually, however, nothing is known before hand about the characteristics of $f(x)$. In this case a wide range of fitting functions can be selected and the regression technique should specify the best set of parameters given the functional form of the fitting function and the measured inputs $G(Y_i)$. Since each independent parameter lends the fit an additional degree of freedom, the maximum number of parameters should be used for the most flexible fitting function subject to limits which will now be stated.

Three major factors limit the number of usable, independent regression parameters: 1) the number of independent parameters must be no more than the number of independent inputs $G(Y_i)$; 2) as the fitting function becomes more flexible, more of the noise in the inputs will be incorrectly interpreted as good data. A judgement must be made (based on the signal-to-noise ratio of the data) regarding how much flexibility the fitting function can have and still remain acceptably free of the influence of noise; 3) computer limits restrict one's flexibility in finding a minimum in the surface representing the residual errors as a function of the regression parameters. As more parameters are added, the time required to find a minimum in the residual error hypersurface increases rapidly, and the hypersurface tends to develop secondary minima sometimes causing the nonlinear regression algorithm to converge to a local minimum instead of the absolute minimum of the residual error hypersurface.

Prior to the development of the current procedure, several standard nonlinear regression algorithms were used to determine $f(x, \{P_i\})$ for various case studies of synthetic data. During these studies, it became apparent that the heavy coupling among the parameters of $f(x, \{P_i\})$ made convergence very difficult for the standard iterative procedures. Consequently, a new nonlinear regression procedure was developed which was expected to be more stable when dealing with highly-coupled parameters. The procedure starts with initial values for the parameters of $f(x, \{P_i\})$ yielding an initial value for Q , the sum of the squared residual errors. Each succeeding step of the iteration seeks the minimum of Q with respect to a multiplet of parameters of increasing order. For each multiplet, the minimum is sought repeatedly with respect to each member of the multiplet (with all other members held constant) until no further reduction in Q is found. The program then repeats this process with the next higher order multiplet until the order of the last convergent multiplet equals the number of parameters. The procedure used to minimize Q with respect to each parameter is quadratic minimization. Three Q 's are calculated corresponding to three initial values of a parameter. The vertex of the parabola through these three points is used as the next estimate of the minimum and replaces one of the three initial

points. The process continues until there is no further reduction in Q . Since this nonlinear regression technique seeks the minimum closest to the starting point, the regression must be started with several different sets of initial parameters to determine whether there are any other minima in the Q hypersurface within the region of interest.

3.0 Inversion of the PSDF from Noisy, Synthetic Mie Scattering Data

The inversion procedures discussed in the previous sections are now tested by inverting the particle distribution function from computer generated Mie scattering data to which Gaussian distributed random noise has been added. The situation considered here is that of scattering at small forward angles by very absorptive aerosols (carbon). On account of the dipolar surface plasmon resonance (which occurs for carbon spheres at about $0.22 \mu\text{m}$ wavelength) carbon is very strongly absorptive at all wavelengths from the ultraviolet to the infrared. Consequently, little is gained by using additional wavelengths for particle size inversion experiments. The work of Ref. 7 suggests that the optimal scattering configuration for carbon aerosol size inversion experiments is a multiangular configuration whose smallest angle is about 5° (polarization information is lost at smaller angles) and whose wavelength is as small as the smallest particles of interest. Figure 1 shows the result of regression of the PSDF from ten sets of scattering inputs containing 5% noise level for a bimodal PSDF. The noise-free inputs are stated in Table 1. Figure 2 shows the corresponding mass-normalized PSDF's. The same scattering data have been deconvolved using the constrained eigenfunction expansion method. The recovered number normalized PSDF (corresponding to the average of 10 sets of noisy input data at 5% noise level) and the associated 68% confidence limits are shown in Fig. 3. Figure 4 shows the corresponding mass-normalized PSDF. The constrained eigenfunction method yields good deconvolutions, in this situation, because the scattering kernels are very sensitive to submicron particles as was shown in Ref. 7. Other calculations in different scattering geometries have convinced us that success can be assured, using the constrained eigenfunction expansion method, only when the scattering inputs are optimally chosen for the size range spanned by the PSDF. The optimization procedures are discussed in Refs. 7 and 14. In contrast, the choice of inputs is much less critical for the nonlinear regression method.

4.0 Concluding Remarks

This paper has presented the characteristics of two particle size inversion methods: 1) a constrained eigenfunction expansion deconvolution technique; and 2) a nonlinear regression technique. Both these methods are described in detail in Refs. 7 and 18.

Inversion of noisy, computer-synthesized scattering data permits the constrained eigenfunction expansion deconvolution technique and the nonlinear regression technique to be compared on an equal footing. The results of that comparison using various scattering geometries described here and in Refs.

7 and 18 are the following conclusions:

1) The nonlinear regression technique is more stable and less sensitive to choice of inputs than is the constrained eigenfunction expansion technique. In some scattering geometries, the nonlinear regression technique can recover a fairly accurate PSDF using kernels with insufficient information content for deconvolutions based on the constrained eigenfunction expansion technique.

2) The nonlinear regression technique is less versatile than the constrained eigenfunction expansion technique. Currently, only bimodal PSDF complexity can be treated using completely free parameters. A trimodal PSDF can be recovered by a multi-step approach in which the three modal diameters are frozen at the values suggested by a residual error contour analysis presented in Ref. 8 and developed further in Ref. 18. The widths and relative heights of these three modes are then treated as free parameters. This approach permits the regression to be reduced in scope from eight free parameters to five free parameters. The latter is the same as the number of free parameters required for regression of a bimode. In contrast, the use of twelve scattering inputs in the constrained eigenfunction expansion deconvolutions is equivalent to regression of a tetramodal PSDF. In general $3N-1$ free parameters are required by either procedure to recover a PSDF whose complexity is represented by N modes.

3) The nonlinear regression method currently runs on a large main frame computer. In contrast, the constrained eigenfunction expansion method can be run on minicomputers and microcomputers. This method can, therefore, easily be incorporated into a self-contained Mie scattering - based particle sizing instrument package, provided one is careful to choose an optimal scattering geometry for each particle diagnostics application. We are currently attempting to reduce the complexity of the nonlinear regression method to permit development of a similar self-contained instrument concept based on this inversion method.

REFERENCES

1. J. W. L. Lewis, B. P. Curry, and D. P. Weaver, "Determination of the Size Distribution Function for Particles in a Hypersonic Flow Field," AEDC-TR-77-101 (AD-A056923), July 1978.
2. J. W. L. Lewis, B. P. Curry, and D. P. Weaver, "Measurement of the Particle Size Distribution in a Pulsed Hypersonic Flow Facility," AIAA Journal Vol. 21, No. 2, Feb. 1983, pp. 247-252.
3. B. P. Curry, D. P. Weaver, and J. W. L. Lewis, "Development of Mie Scattering Techniques for In Situ Particle Diagnostics at AEDC," AEDC-TR-80-3 (AD-A092716), Nov. 1980.
4. B. P. Curry, J. W. L. Lewis, H. M. Powell, and J. H. Jones, "Light Scattering Measurement of Sizes and Number Densities of Submicron Aerosols Emitted by a Small Liquid Bipropellant Thrustor," Proceedings of JANNAF 12th Plume Technology Meeting, Vol. 1, CPIA Publication 332, Dec. 1980, pp. 47-56.

5. B. P. Curry, J. W. L. Lewis, J. H. Jones and H. M. Powell, "Time-and-Space-Dependence of Particulate Effluent in the Exhaust Plume of a Pulsed Liquid Bipropellant Engine," AEDC-TR-80-44 (AD-A106525), Oct. 1981.
6. B. P. Curry, L. C. Vorhees, and E. L. Kiech, "Development of Computer Codes to Invert the Particle Size Distribution Function of Homogeneous Spherical Aerosols from Mie Scattering Measurements," AEDC-TR-82-11, November 1982.
7. B. P. Curry and E. L. Kiech, "Two Particle Size Inversion Procedures for Interpretation of Mie Scattering Measurements," AEDC-TR-83-32.
8. M. Kerker, The Scattering of Light and Other Electromagnetic Radiation, Academic Press, New York, 1969.
9. J. R. Hodkinson, "Particle Sizing by Means of the Forward Scattering Lobe," Applied Optics, Vol. 5, No. 5, May 1966, pp. 839-844.
10. P. C. Ariessohn, S. A. Self, and R. H. Eustis, "Two-Wavelength Laser Transmissometry for Measurements of the Mean Size and Concentration of Coal Ash Droplets in Combustion Flows," Applied Optics, Vol. 19, No. 22, Nov. 15, 1980, pp. 3775-3781.
11. J. D. Spinhirne, J. A. Reagan, and B. M. Herman, "Vertical Distribution of Aerosol Extinction Cross Section and Inference of Aerosol Imaginary Index in the Troposphere by LIDAR Technique," J. Applied Meteorology, Vol. 19, 1980, pp. 426-438.
12. J. V. Dave, "Subroutines for Computing the Parameters of the Electromagnetic Radiation Scattered by a Sphere," Report 3203237, IBM Scientific Center, Palo Alto, Calif., May 1968.
13. K. S. Shifrin and A. Ya Porelman, "The Determination of the Spectrum of Particles in a Dispersed System from Data on its Transparency," Optics and Spectroscopy, Vol. 15, 1963, pp. 185-289.
14. C. D. Capps, R. L. Henning, and G. M. Hess, "Analytic Inversion of Remote Sensing Data," Applied Optics, Vol. 21, No. 19, 1 October 1982, pp. 3581-3587.
15. D. L. Phillips, "A Technique for the Numerical Solution of Certain Integral Equations of the First Kind," J. Assoc. for Computing Machinery, Vol. 9, 1962, pp. 84-97.
16. S. Twomey, "On the Numerical Solution of Fredholm Equations of the First Kind by the Inversion of the Linear System Produced by Quadrature," J. Assoc. for Computing Machinery, Vol. 10, 1963, pp. 97-101.
17. S. Twomey, "The Application of Numerical Filtering to the Solution of Integral Equations Encountered in Direct Sensing Measurement," Journal of the Franklin Institute, Vol. 279, No. 2, February 1965, pp. 95-189.
18. B. P. Curry, and E. L. Kiech, "Improved Methods to Invert the Particle Distribution Function from Mie Scattering Measurements," AEDC-TR-83-52.

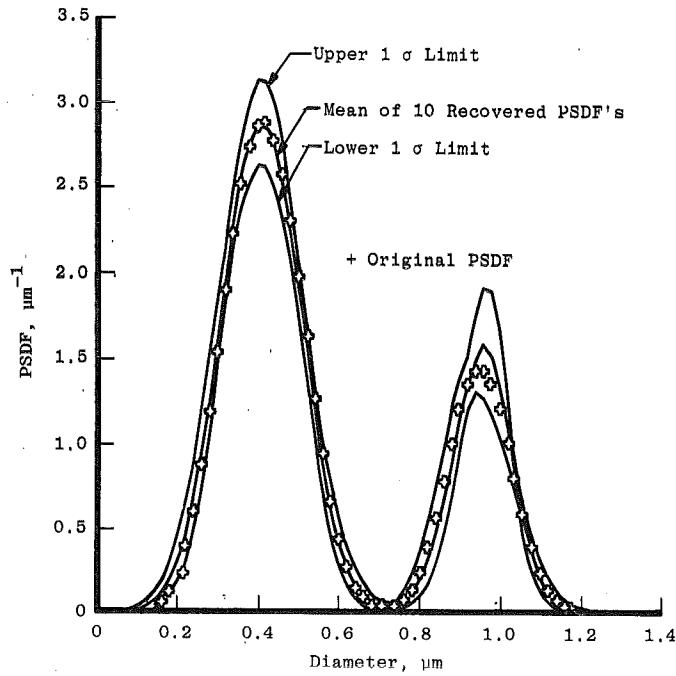


FIGURE 1. Number-Normalized Bimodal PSDF Regressed from the Scattering Inputs of Table 1 with 5% Gaussian Noise Level.

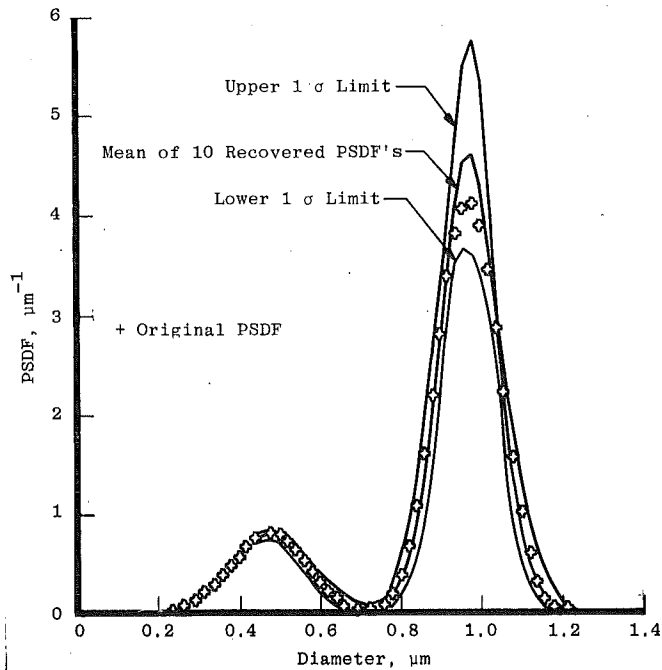


FIGURE 2. Mass-Normalized Bimodal PSDF Regressed from the Scattering Inputs of Table 1.

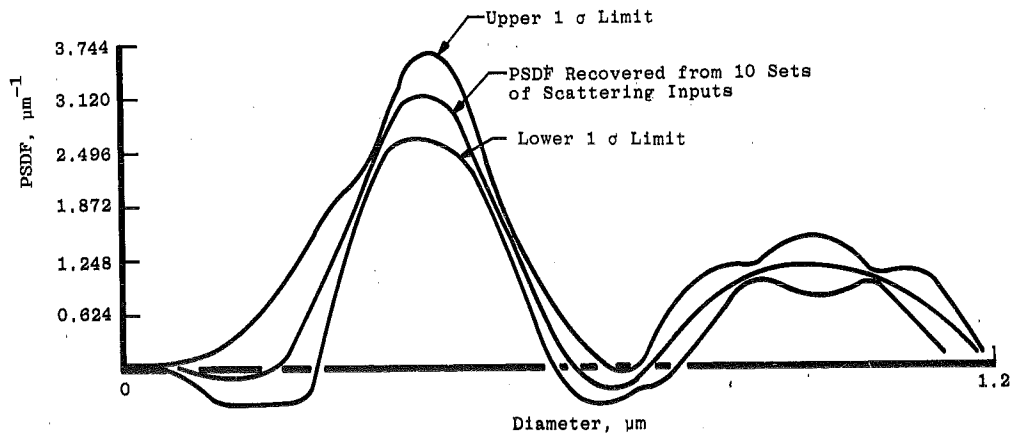


FIGURE 3. Number-Normalized Bimodal PSDF Deconvolved from the Scattering Inputs of Table 1.

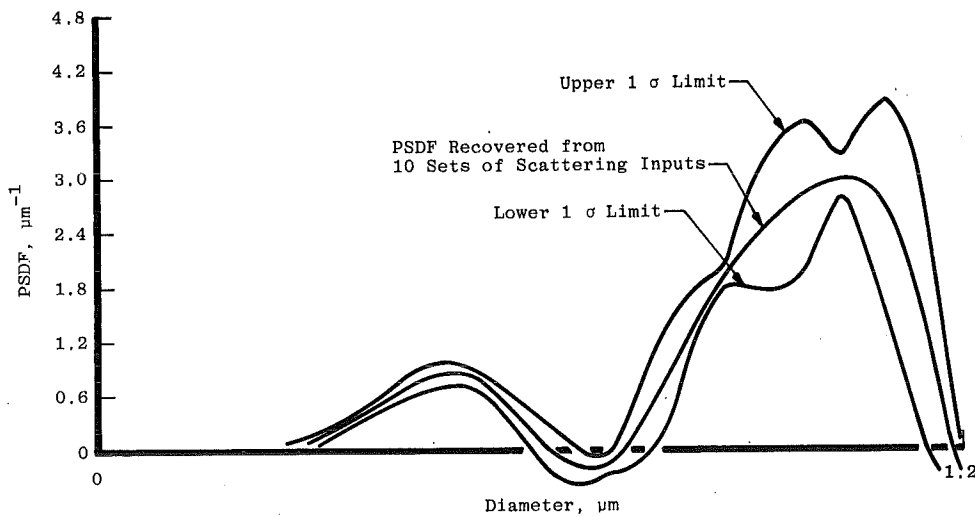


FIGURE 4. Mass-Normalized Bimodal PSDF Deconvolved from the Scattering Inputs of Table 5.

Angle, deg	Polarized Scattering Inputs*	
	Perpendicular	Parallel
5	3.19	2.96
10	1.64	1.17
15	0.713	0.520
20	0.625	0.335
25	0.305	0.128
30	0.271	0.141

*Normalized by the mean of all inputs.

TABLE 1. Error-Free Scattering Inputs for the PSDF in Figure 1.

BLANK

Quantitative Determination of the Effects
of Constraints on Solutions to Inversion Problems

C. D. Capps and G. M. Hess
Boeing Aerospace Company
P.O. Box 3999
Seattle, WA 98124

ABSTRACT

An analytic inversion technique has been developed for Fredholm type remote-sensing problems. A principal result of this work was that only that portion of the solution lying in the space spanned by the kernels could be determined from the data. Often, however, there exists additional knowledge about the solution that could be used. For example, if the solution is a particle size distribution then it must be non-negative. Some other inversion methods, such as constrained linear inversion and the method of Landweber, make use of a smoothing constraint. However, the effects of the data and the constraint are so entangled that it is not possible to separate their individual influences on the solution. The present work shows how it is possible by using the analytic method and the assumption that the solution can be adequately represented by a finite Fourier series to apply a constraint to obtain the portion of the solution in the space orthogonal to the space spanned by the kernels. As the two parts of the result are independent, the one determined by the data and the other by the constraint, their relative contributions can be studied.

A condensed version of these results appears in Inverse Optics, Anthony J. Devaney, Editor, Proc. SPIE 413, 138-142 (1983).

An extended and more nearly rigorous version has been submitted to Applied Optics.

BLANK

ATR METHOD FOR DETERMINING
OPTICAL CONSTANTS OF POWDERS

V. P. Tomaselli and K. D. Möller
Fairleigh Dickinson University
Physics Research Laboratory
Hackensack, NJ 07601

ABSTRACT

This report describes the evaluation and use of an apparatus designed to measure the infrared optical constants of powders. A helium-neon source (3.39 μ m) is used and the attenuated total reflection (ATR) method is employed. Data for a carbon black powder are reported. This work has been submitted for publication to Applied Optics.

DISCUSSION

We have constructed an apparatus (Figure 1) which has been used to measure the real and imaginary parts of the complex index of refraction of powders. A laser source (L_1) illuminates the interface between sample (S) and prism (P). The beam incident to the interface penetrates the sample and, for a lossy material, is attenuated. The reduced reflected light is sensed by detector D, amplified (A) and displayed on a strip chart recorder (R). A reference signal from the chopper (C) is used for phase sensitive detection. Alignment and orientation of prism are accomplished using an auxiliary visible laser (L_2) and mirror (M_2).

An error analysis was performed to evaluate the method and select the optimum instrument parameters. The choice of angle of incidence was made on this basis. Also, measurements on a test material, toluene, were made as a check of the instrument sensitivity and computation algorithm. We were able to obtain the real part (n) of the refractive index to less than 1% error compared to published results. The error in the absorption coefficient (k) was 44% but is expected for this apparatus for a sample of relatively low ($k \approx 0.01$) absorption. For the carbon black powders of interest here, $k \approx 0.2$, and the predicted error is expected to be of the order of a few per cent. The errors in this method are very sensitive to the magnitude of k as well as the angle of incidence.

Figure 2 shows the results of measurements of parallel and perpendicular reflectance for toluene at 3.39 μ m. The open circles are for data obtained using the apparatus described above. The solid lines are results calculated from (n,k) data given by Goplen, et al.⁽¹⁾ The agreement is quite good.

⁽¹⁾T. G. Goplen, D. C. Cameron, and R. N. Jones, Appl. Spectrosc. 34, 657 (1980)

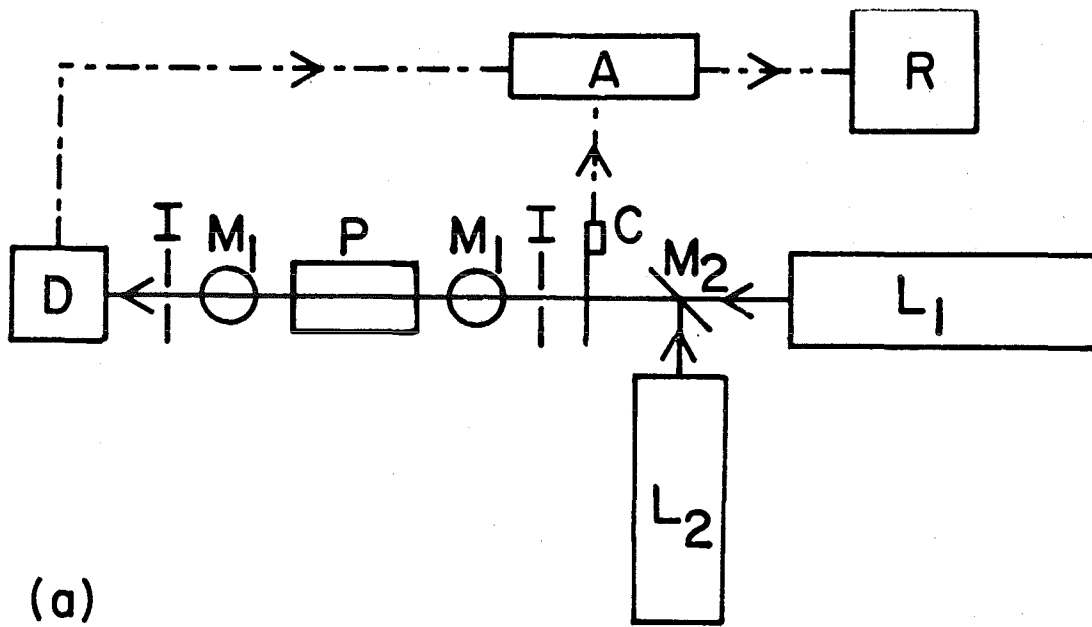
The powder of interest in this work is a carbon black (Mogul-L, Cabot Corp., Boston, MA). Suspensions of the carbon black powder in nujol oil were prepared having weight fractions of 0 to 0.50. ATR measurements were made on the various sample mixtures. Suspending the powder in a liquid of known or measurable optical properties provides a method of dealing with the surface effects caused by the discontinuities of the powder. Data is recorded for an effective medium which has properties that depend upon those of the constituents and their relative weight fraction in the mixture. The objective is to extract the optical constants of the powder from measurements made on the mixture(s).

Figures 3 and 4 show the dependence of n and k on weight fraction (f_w) for the carbon black powder. The error bars indicate deviations from the average of several measurements. For comparison at $f_w = 0.30$, $\Delta n/n = 1.3\%$ and $\Delta k/k = 9.7\%$. As expected, errors in absorption coefficient are usually larger than those for refraction index.

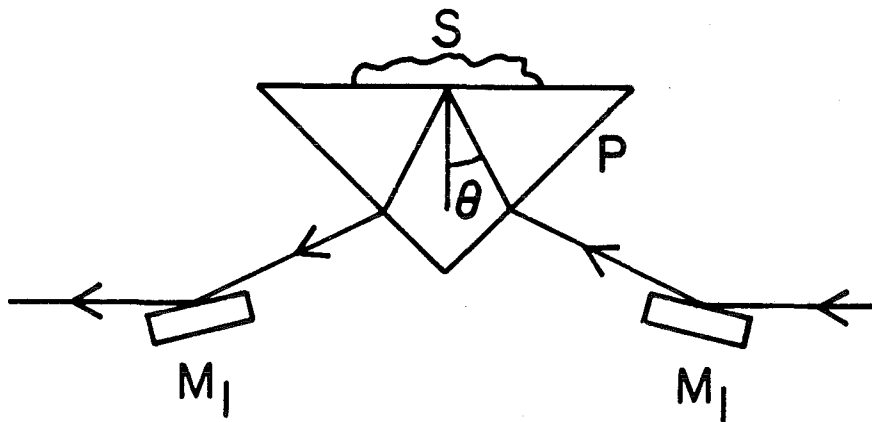
The n vs f_w data of Figure 3 can be fit to a linear curve (correlation coefficient = 0.997) and gives a pure powder extrapolated value ($f_w = 1.0$) of 1.64. This compares to a value of 1.57 (4% difference) found earlier using specular reflectance measurements on pressed powder pellets⁽²⁾. The k vs f_w data in Figure 4 behave similarly (correlation coefficient = 0.923) and yield $k = 0.50$ at $f_w = 1.0$. This is a 31% difference compared to the value ($k = 0.68$) reported in reference 2.

The linear behavior of $n(f_w)$ and $k(f_w)$ and corresponding extrapolation to pure powder values is not generally obtained. From effective medium theory, one can show that this fortuitous behavior is a result of the similarity of the bulk optical properties of the powder and host materials.

⁽²⁾V. P. Tomaselli, et al., Appl. Optics, 20, 3961 (1981)



(a)



(b)

Figure 1 - Schematic diagram of apparatus used to make ATR measurements. (a) Top view of components. Solid line is path of laser radiation, broken line is path of electrical signal. Components are: L_1 infrared laser ($3.391\mu\text{m}$ output), L_2 visible laser (used for positioning of prism when mirror M_2 is inserted in path), C-chopper, M_1 - plane mirror, P - prism, I - irises, D - detector, A - amplifier and R - recorder. (b) Side view of prism showing sample S and path of laser beam.

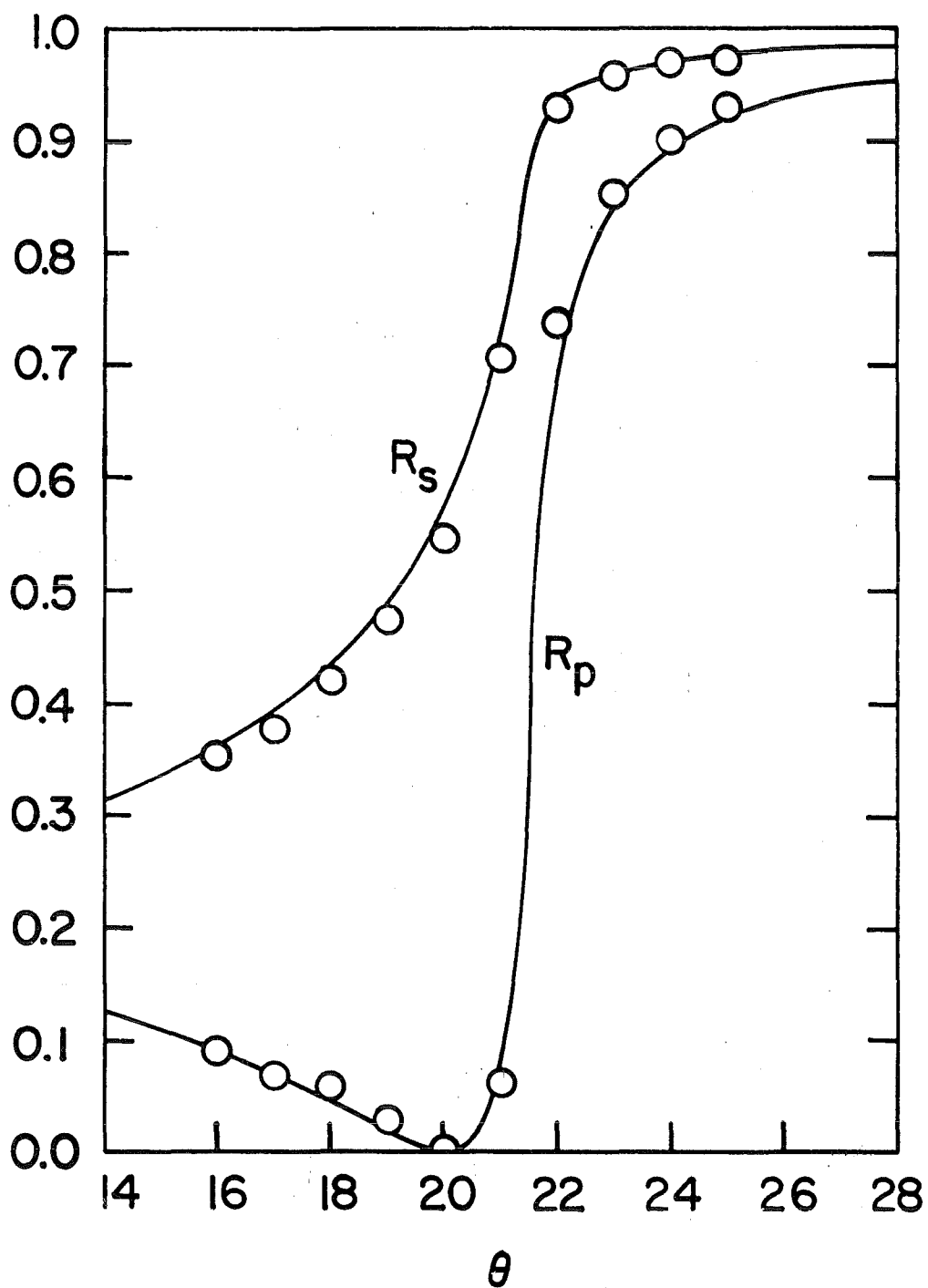


Figure 2 - Reflectance curves for toluene. Solid curves are calculated data. Open circles are measured data obtained with apparatus described in text.

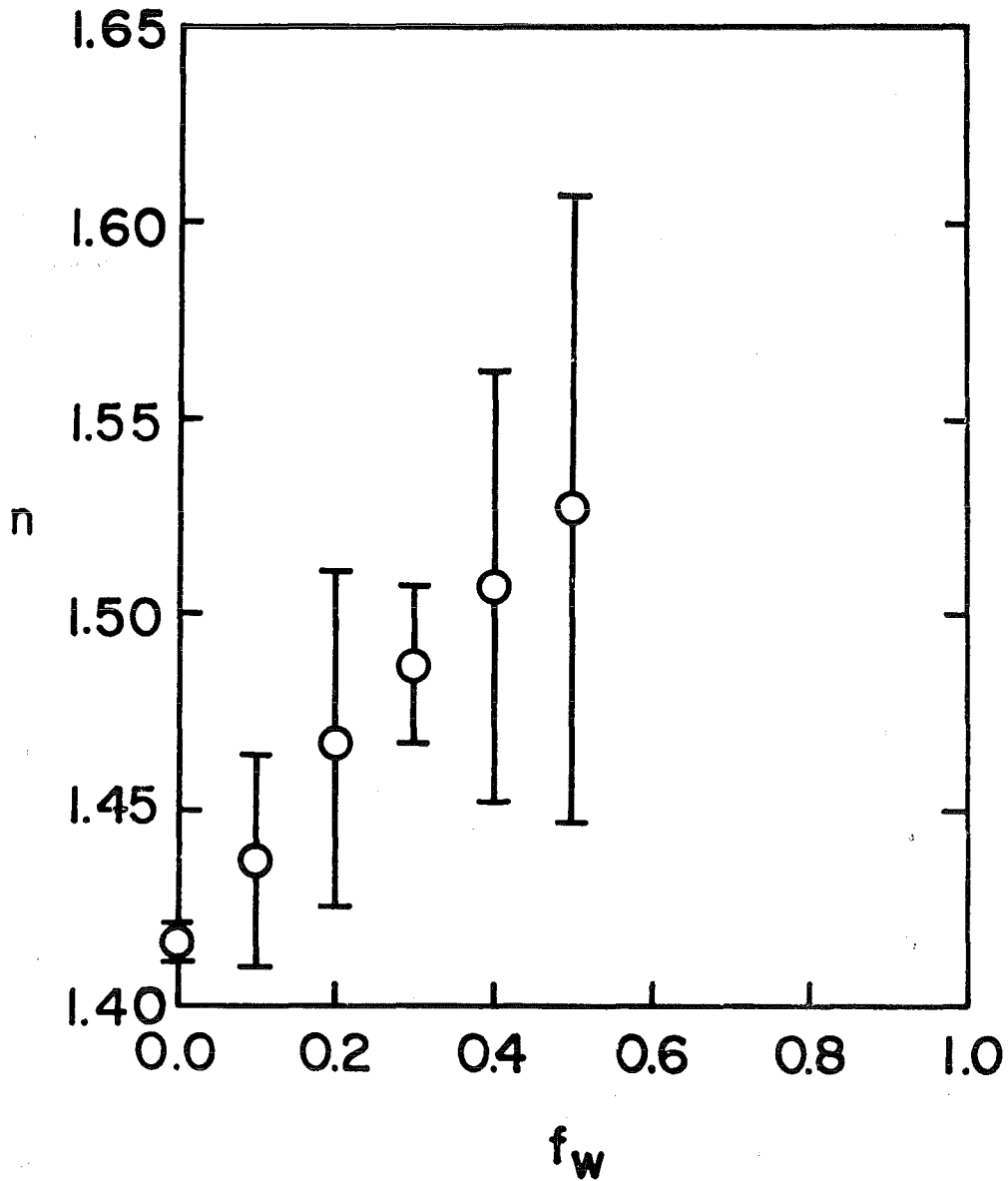


Figure 3 - Index of refraction of Mogul L carbon black suspensions as a function of weight fraction of powder in host material. Error bars represent deviations from the average value of several measurements.

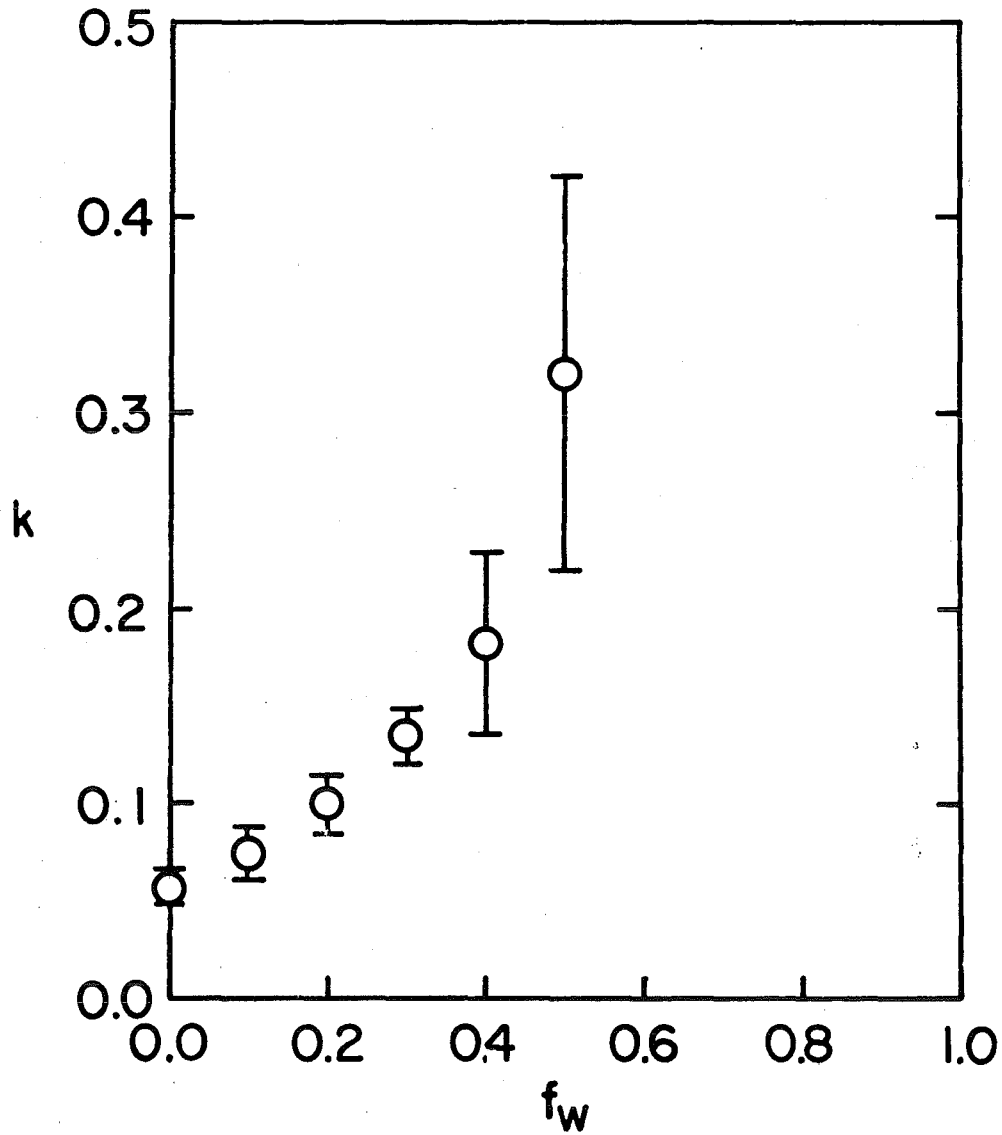


Figure 4 - Absorption coefficient of Mogul L carbon black suspension as a function of weight fraction of powder in host material. Error bars represent deviations from the average value of several measurements.

OPTICAL PROPERTIES OF COMPRESSED POWDERS

Marvin R. Querry
Department of Physics
University of Missouri-Kansas City
Kansas City, Mo. 64110

ABSTRACT

Specular reflectance spectra were obtained in the infrared and/or visible spectral region for compressed powders of selected natural minerals. Spectral values of the complex refractive indices were then obtained by applying Kramers-Kronig methods to the reflectance spectra.

INTRODUCTION

Many minerals occur in nature only as small particles, i.e. powders, which precludes preparation of bulk single crystal samples suitable for reflectance measurements. Clay minerals are examples of such materials. Also the clay minerals are relatively low on the hardness scale and if bulk crystalline specimens could be acquired they could not be polished to specular reflectance by use of conventional methods. In order to obtain reflectance spectra of such minerals we reduced them to powder by grinding and then compressed the powder into 13 mm diameter disc-shaped pellets by placing the powder between polished stainless steel rams and applying pressure with a hydraulic press. The die used for this purpose was rated at a maximum of 10 tons of force applied to the 13 mm surface. Most pellets, however, were pressed by applying an 8 ton force.

Two primary traits are desirable in the pellets. First, a specular surface, and second, because most natural minerals are either optically uniaxial or biaxial, a random orientation of the particles is desirable. Specular surfaces are necessary because rough surfaces reflect incident radiant flux specularly and diffusely. Application of the Fresnel equations to determine the complex refractive index $N = n + ik$ assumes zero diffuse reflectance. If diffuse reflectance is present, then, for dielectric materials, values of N computed from measurements of only the specular component will provide values of n (k) that are low (high) compared to the true value of n (k). The random orientation of the particles within the pellet assures that the reflectance spectrum and subsequent values of N are representative of all optical directions within crystalline particles.

Natural minerals that we have investigated by use of the pellet method are listed in Column 1 of Table 1. The hardness (Mohs Scale) and mass density ρ_m are listed in Columns 2 and 3, respectively. The mass density of the pellets ρ_p and the ratio ρ_p/ρ_m are listed in Columns 4 and 5, respectively. Accepted values for the range of refractive indices n_D at 589 nm wavelength are listed in Column 6 and n_p determined for the pellet in Column 7. Values of n_p in parentheses in Columns 7 and 8 have been corrected for mass density by use of the Lorentz-Lorenz formula. Values of n_p at 2.5 μ_m wavelength are

listed in Column 8. Values of k for these minerals are not available in the scientific literature thus similar comparisons for k could not be made.

Detailed descriptions of these and investigations of the optical properties of some crystalline minerals, aqueous solutions, diesel fuel, and water are provided in Reference 1.

GYPSUM

As an example, we provide a brief description of the investigation of the optical properties of gypsum "powder" in the infrared spectral region. Preliminary investigations of gypsum crystals were presented previously (2).

The specular reflectance spectra measured at 6.5 degrees angle of incidence for a gypsum pellet pressed with 8 tons force, the same pellet repressed with 14 tons force, and the ratio of the specular reflectance of the 8T (8 tons) pellet to that of the 14T (14 tons) pellet are shown in Fig. F1-1. The ratio reflectance spectrum led us to conclude that the 14T pellet possessed a smoother surface and thus greater specular reflectance throughout the spectral range, and that there were possibly slight spectral shifts in the infrared bands in the two pellets. The decrease in relative reflectance with increasing wave number indicated that the 14T pellet should yield superior values of N for gypsum "powder". Values of n and k computed by Kramers-Kronig methods applied to the specular reflectance spectrum of the 14T pellet are presented in Figs. F1-2 and F1-3, respectively.

According to the Fresnel equations the specular reflectance R at normal incidence for a smooth surface is given by

$$R = \frac{(n-1)^2 + k^2}{(n+1)^2 + k^2} \quad (1)$$

We see that measurements of R are sensitive to k^2 . If $k = 0.05$, then $k^2 = 0.0025$ and reflectance measurements with some degree of confidence in the fourth significant digit are required to determine k. Typical uncertainty in our reflectance measurements is $(\Delta R/R) = 0.025$, which, at best, provides some degree of confidence in the third significant digit.

In order to determine better values of k for gypsum powder we mixed varying minute quantities of gypsum powder with KBr and pressed the mixtures into 13 mm dia. pellets. Thirteen separate gypsum/KBr pellets were formed and transmittance spectra were obtained in the 300-4,000 cm^{-1} region. Transmittance spectra for three of the pellets are shown in Fig. F1-4. From the thirteen transmittance spectra four spectra were chosen which possessed the least scattering that is often a characteristic of KBr pellets. These four transmittance spectra were converted to absorbance spectra and the six possible subtractions

of one absorbance spectrum from another were made; this resulted in six difference spectra. Three absorbance spectra and the six difference spectra are shown in Figs. F1-5 & F1-6. The three difference spectra possessing the least evidence of scattering were then chosen for further analysis. Before we describe the analysis of the three difference spectra, let us first cast the procedures in this paragraph into mathematical form.

Let us assume that the fractional transmittance T through a gypsum/KBr pellet is given by

$$T = \frac{(1-R)^2 e^{-\alpha x}}{1-R^2 e^{-2\alpha x}}, \quad (2)$$

where R is the reflectance of the surfaces of the KBr pellet, α is an attenuation coefficient due to absorption by the gypsum and scattering by the gypsum and KBr particles, and x we temporarily assign to the effective thickness of the gypsum in the pellet. Let us further assume that n for the KBr is 1.4-1.5 so that $R \approx 0.04$ and $R^2 = 0.0016$. Furthermore, the largest that $e^{-2\alpha x}$ will be is 1 corresponding to $\alpha = 0$; thus we may write for our gypsum/KBr pellet

$$T = (1-R)^2 e^{-\alpha x}. \quad (3)$$

The absorbance A is given by $A = -\log(T)$, where log represents log of base 10; thus

$$A = -2 \log(1-R) + \alpha x c \quad (4)$$

$$= -2 \log(1-R) + c \alpha_a x + \alpha_s t c, \quad (5)$$

where we have recast αx into the form $\alpha x = \alpha_a x + \alpha_s t$ which represents absorption a and scattering s, and $c = 0.43429$. Again, x represents the effective thickness of the gypsum and t is the thickness of the gypsum/KBr pellet. A difference between two absorbance spectra is

$$A_2 - A_1 = -2 \log[(1-R_2)/(1-R_1)] + c \alpha_a (x_2 - x_1) + (c \alpha_s t)_2 - (c \alpha_s t)_1 \quad (6)$$

Assuming $R_1 = R_2$ and $(\alpha_s t)_1 = (\alpha_s t)_2$ we have

$$A_2 - A_1 = c \alpha_a (x_2 - x_1); \quad (7)$$

$$= c 4 \pi k \nu (x_2 - x_1). \quad (8)$$

Thus, if the gypsum/KBr pellets are adequately prepared, the difference spectra $A_2 - A_1$ are directly proportional to k. However, one cannot measure the effective thickness x of the gypsum in the pellets.

We now return to the further analysis of the three difference spectra. The primary difference between two difference spectra is in the factor $x_2 - x_1$ which cannot be measured. Two of the three

difference spectra were thus normalized to the third difference spectrum. The normalization factor was an average of ratios determined at the centers of the strong absorption bands of gypsum where k is relatively large. The average of the three normalized difference spectra was divided by $4\pi\nu$ throughout the 300-4,000 cm^{-1} region. This process produced the relative k spectrum shown in Fig. F1-7 and F1-8. Actually the relative k spectrum is a product $c\Delta x$ spectrum. The smoothed fractional standard deviation $\Delta k/k$ is shown in Fig. F1-9; $\Delta k/k$ was obtained as a byproduct of averaging the three normalized difference spectra. The ordinate scale for $\Delta k/k$ in Fig. F1-9 is from 0 to 1.0; note that $\Delta k/k$ is very large in regions where k is very small but is less than $\Delta k/k$ for KK analysis for small k .

It is impossible to determine the effective thickness x of the gypsum in the pellets. Thus we applied a calibration factor to the relative k spectrum shown in Figs. F1-7 and F1-8. The calibration factor was determined in the following manner. Values of k were available from Kramers-Kronig analysis of the reflectance spectrum of the gypsum pellets. At the centers of four of the strong infrared bands the ratios of k values from KK analysis to relative k values from transmittance were computed and averaged. The average of the four ratios was the calibration factor applied to the relative k spectrum throughout the 300-4,000 cm^{-1} region. The calibration factor corresponded to $1/c\Delta x$. Values of k determined in this manner are shown graphically as the dashed line in Fig. F1-10. The solid line in Fig. F1-10 is the k spectrum determined by KK analysis of the reflectance spectrum of the 8T gypsum pellet.

We noted from Fig. F1-10 that the infrared band at 3,550 cm^{-1} , which is a characteristic of the Y optical direction of gypsum, is stronger from the transmittance measurements of the gypsum/KBr pellet than from KK analysis of the reflectance spectrum of the 8T pellet. We attribute this to a more random orientation of the gypsum particles in the gypsum/KBr pellet than in the 8T gypsum pellet. Preferred (010) orientation of the gypsum particles in the 8T pellet was described previously (2). Also, we note from Fig. F1-10 that, in spectral regions where k is relatively small, k values from the transmittance measurements yield more accurate values of k . There is a general increase in base level k values for KK analysis from about 1,300 cm^{-1} to 4,000 cm^{-1} which would be expected when diffuse reflectance increases as frequency increases. The diffusely reflected radiant flux will be interpreted by the KK algorithms as absorption and k values will thus increase as diffuse reflectance increases. This is exactly the situation that we observe with the 8T gypsum pellet.

Next, we determined values of n that were consistent with the calibrated k spectrum from the transmittance measurements and with the reflectance of the 8T pellet. This was accomplished by using the Fresnel reflectance equation

$$R = \frac{(Z - \cos\theta)(Z^* + \cos\theta)}{Z + \cos\theta} \quad (9)$$

$$Z^2 = N^2 - \sin^2\theta. \quad (10)$$

Values of n were systematically adjusted by use of a least squares method in Eqns. (9) and (10) until the measured value of R was obtained. The n spectrum thus obtained is the dashed curve in Fig. F1-11. The solid-line curve in Fig. F1-11 is the n spectrum of the 8T pellet obtained by Kramers-Kronig methods. Differences in the two n spectra in Fig. F1-10 were attributed to differences in the orientation of gypsum particles in the gypsum/KBr pellet and the 8T gypsum pellet.

REFERENCES

1. M.R. Querry, "Optical properties of natural minerals and other materials in the 350-50,000 cm^{-1} spectral region," Final Technical Report, U.S. Army Research Office Contract DAAG-29-C-0131, August 1983, 383 pages.
2. M.R. Querry & R.L. Strecker, "Optical properties of gypsum," Proceedings of the 1982 CSL Scientific Conference on Obscuration and Aerosol Research, In Press.

ACKNOWLEDGEMENT

Supported in part by U.S. Army Research Office Contract DAAG-29-79-C-0131.

TABLE 1. Data for natural minerals pressed into pellets

Mineral		Hardness	ρ_m (g/cm ³)	ρ_p (g/cm ³)	n_D	n_p (589 nm)	n_p (2.5 μ m)
Colemanite	8T	4.5	2.40	2.06	1.586 - 1.614	1.301 (1.356)	1.311 (1.368)
Gypsum	8T	2.0	2.32	2.10	1.5205 - 1.5296		1.344 (1.381)
Illite	8T	2.0	2.70-2.78	2.46	1.555 - 1.610	1.195 (1.174)	1.331 (1.367)
Kaolin	8T	2.0-2.5	2.57-2.68	2.13	1.553 - 1.570	1.263 (1.326)	1.341 (1.426)
Kernite	8T	2.5	1.73	1.91	1.454 - 1.488	1.285 (1.256)	1.283 (1.254)
Limonite (Al.)	8T	5.0-5.5	4.09-4.48	0.694	2.150 - 2.415	1.225 (1.335)	1.40 (1.619)
Limonite (Ga.)	8T	5.0-5.5	4.09-4.48	0.561	2.150 - 2.415		
Montmorillonite	8T	1.0-2.0	1.98-2.06	1.10	1.475 - 1.534		
Pyrolusite	8T	1.0-2.0	4.75	0.732	1.303 - 1.623	1.176 (1.244)	1.418 (1.604)
Vermiculite (Cn.)	3T	1.5-2.0	2.26-2.35	0.848	1.525 - 1.581		
Vermiculite (Id.)	3T	1.5-2.0	2.26-2.35	0.869	1.525 - 1.561		
Wavellite	8T	3.5-4.0	2.31-2.46	0.851	1.520 - 1.561	1.259 (1.315)	1.235 (1.283)
Gypsum	14T	2.0	2.32	0.952	1.5205 - 1.5296		1.420 (1.444)
Pyrolusite	16T	1.0-2.0	4.75	0.724	1.303 - 1.623		1.882 (1.998)

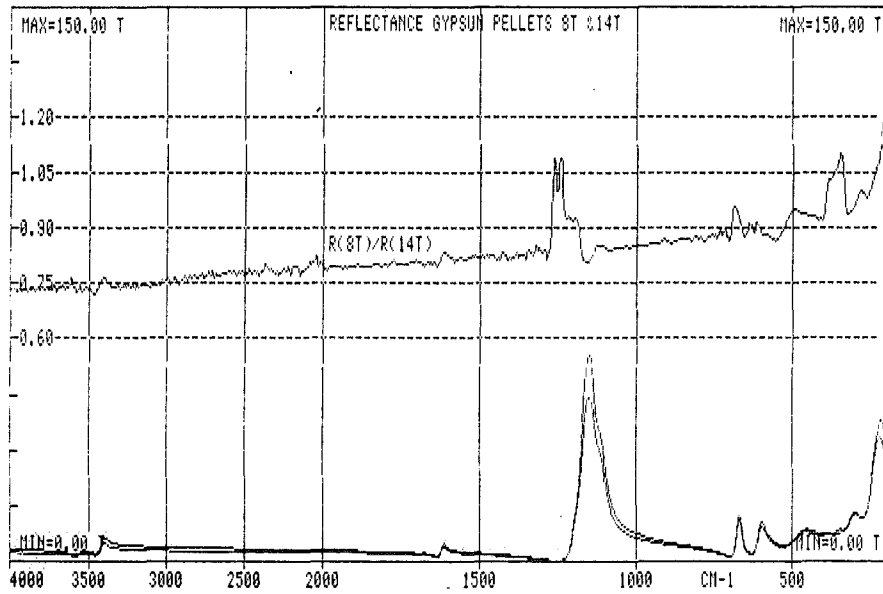


Figure F1-1. Reflectance spectra R(8T) and R(14T) of the 8T and 14T gypsum pellets, and ratio reflectance R(8T)/R(14T) in the 180-4,000 cm^{-1} wave-number region.

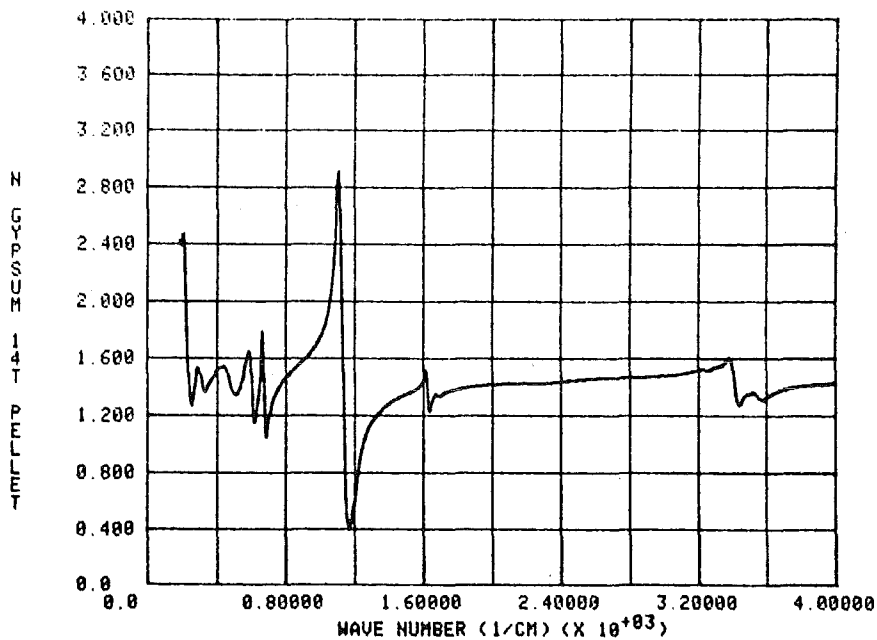


Figure F1-2. Index of refraction n of the 14T gypsum pellet in the 180-4,000 cm^{-1} wave-number region.

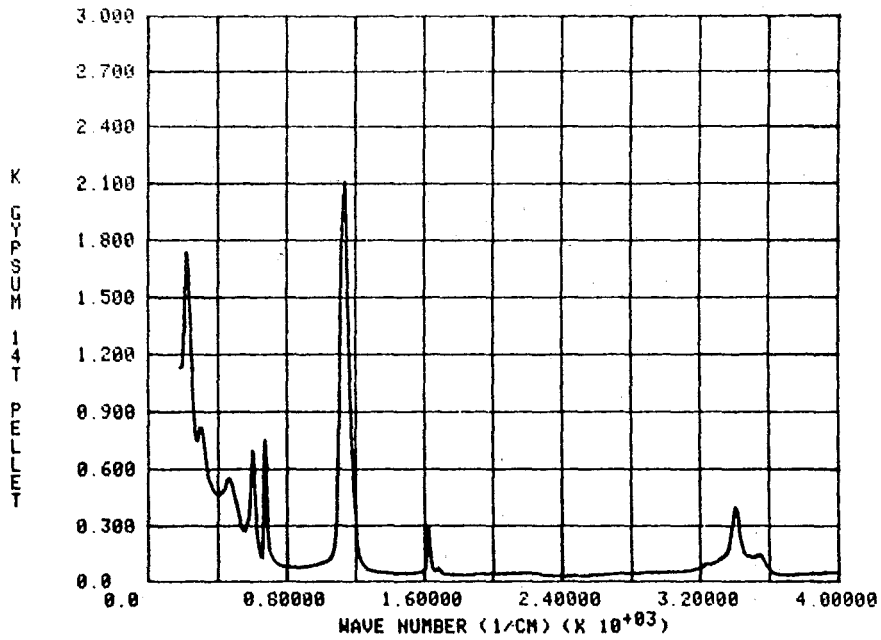


Figure F1-3. Extinction coefficient k of the 14T gypsum pellet in the $180\text{-}4,000 \text{ cm}^{-1}$ wave-number region.

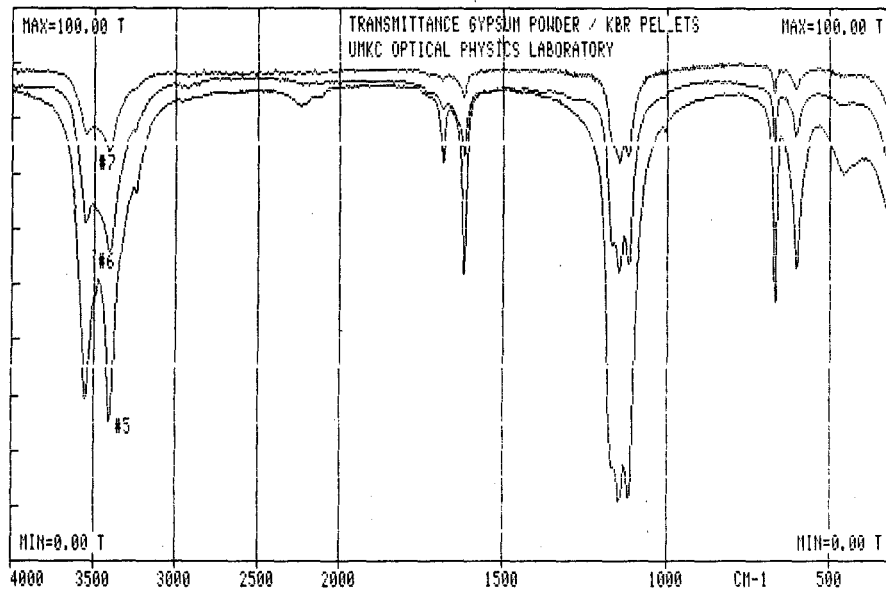


Figure F1-4. Transmittance spectra of three of the gypsum-powder/KBr pellets in the $300\text{-}4,000 \text{ cm}^{-1}$ wave-number region.

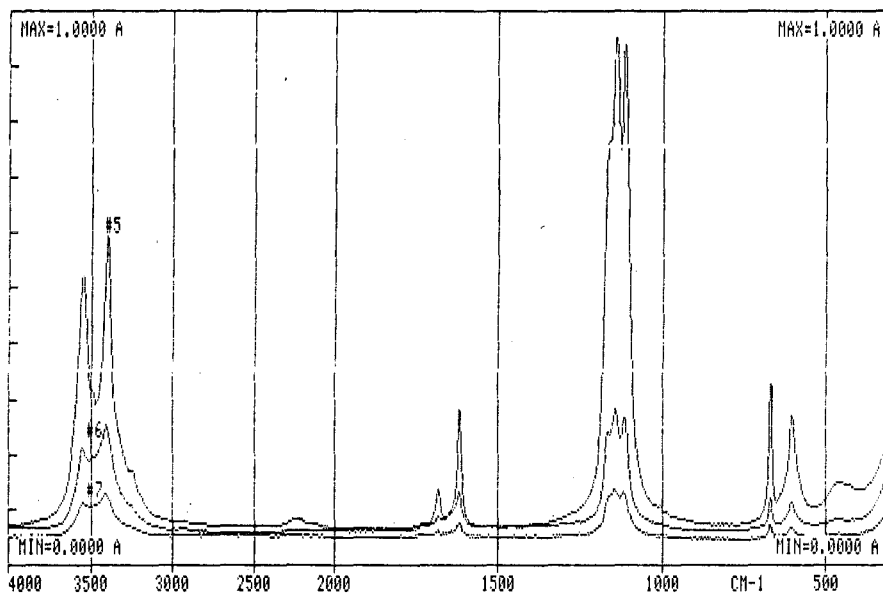


Figure F1-5. Absorbance spectra of three of the gypsum-powder/KBr pellets in the 300-4,000 cm^{-1} wave-number region.

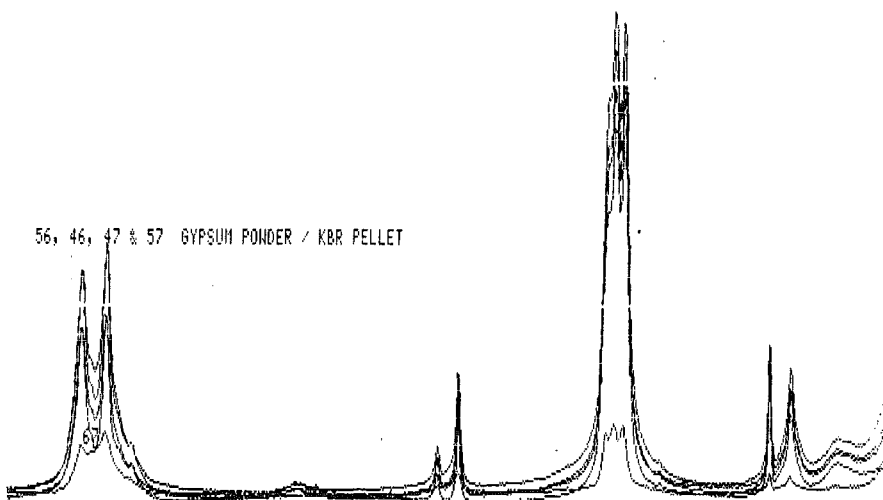


Figure F1-6. Five difference spectra obtained from four absorbance spectra for the gypsum-powder/KBr pellets in the 300-4,000 cm^{-1} wave-number region.

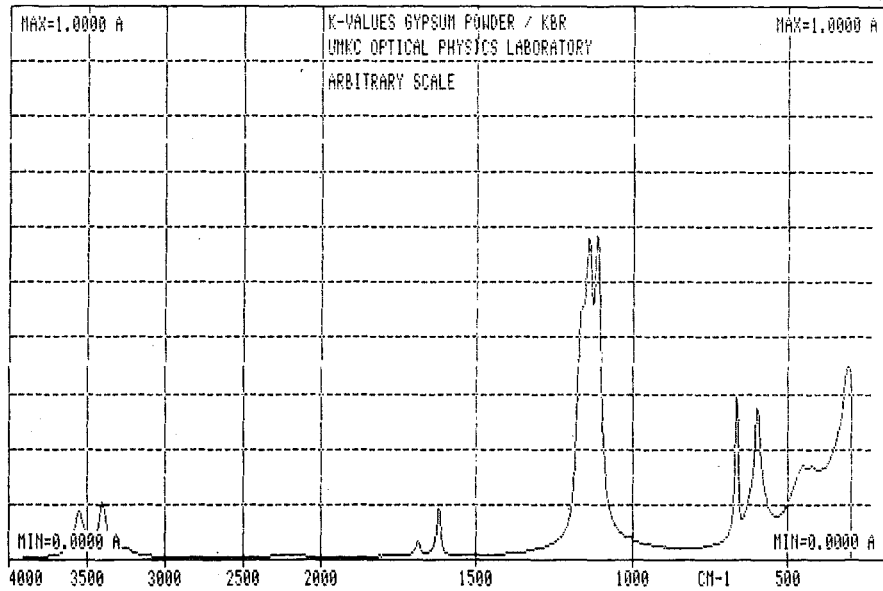


Figure F1-7. Relative k spectrum for gypsum from the average of three normalized difference spectra of the gypsum-powder/KBr pellets; 300-4,000 cm^{-1} wave-number region.

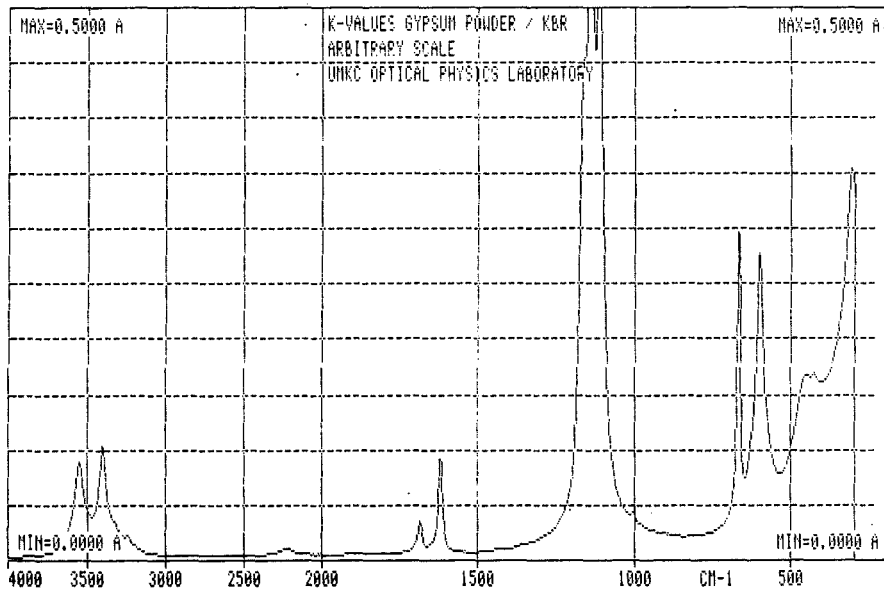


Figure F1-8. Relative k spectrum for gypsum from the average of three normalized difference spectra of the gypsum-powder/KBr pellets, expanded ordinate scale; 300-4,000 cm^{-1} wave-number region.

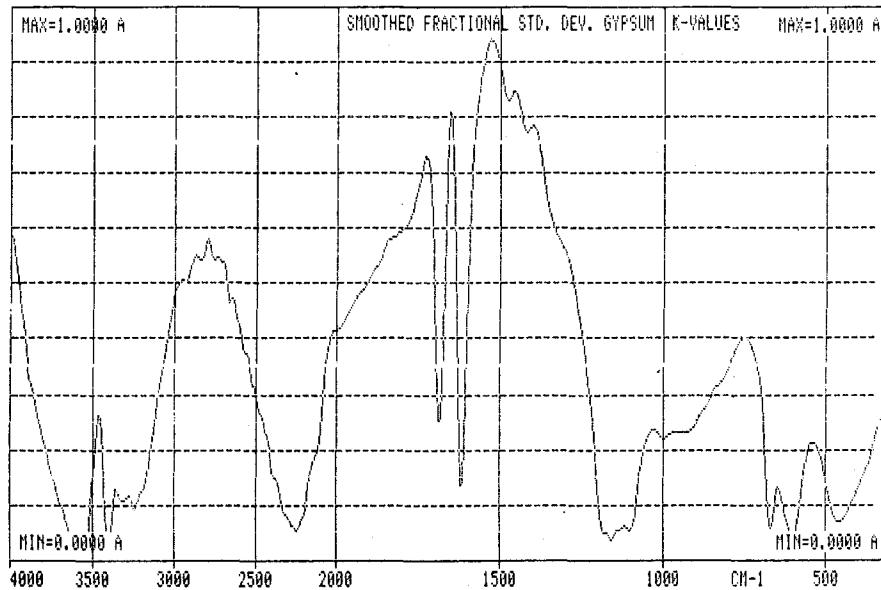


Figure F1-9. Smoothed fractional standard deviation Dk/k obtained from the three normalized difference spectra; 300-4,000 cm^{-1} wave-number region.

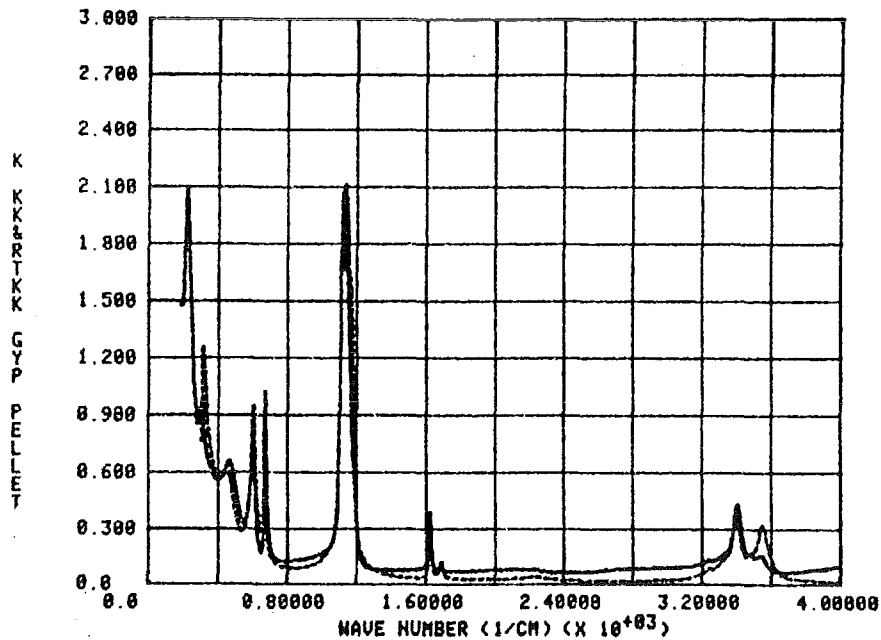


Figure F1-10. Comparison of k spectra for gypsum obtained from KK analysis (solid line) of the reflectance spectrum of the 8T pellet and from transmittance (dashed line) measurements of the gypsum-powder/KBr pellets, 300-4,000 cm^{-1} region.

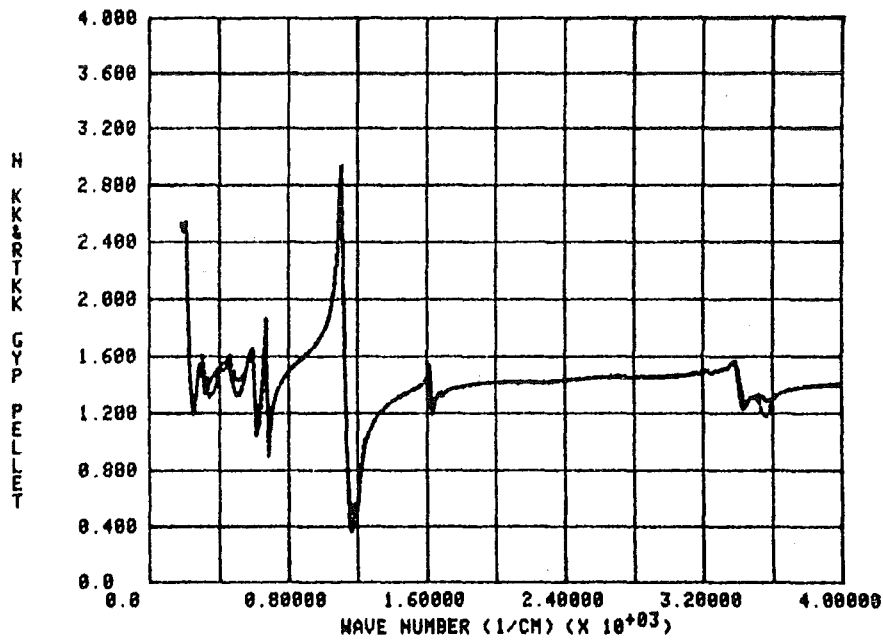


Figure F1-11. Comparison of n spectra for gypsum obtained from KK analysis (solid line) of the reflectance spectrum of the 8T pellet and from application of the Fresnel equation (dashed line) to the k spectrum from transmittance measurements and the reflectance spectrum of the pellet; 300-4,000 cm^{-1} region.

OPTICAL PROPERTIES OF MINERALS
AT MILLIMETER AND SUBMILLIMETER WAVELENGTHS*

M. A. Ordal, L. L. Long, R. J. Bell and R. W. Alexander, Jr.
Physics Department, University of Missouri-Rolla
Rolla, Missouri 65401

ABSTRACT

The optical constants of several naturally occurring minerals have been measured at submillimeter wavelengths and these measurements are currently being extended to longer wavelengths.

INTRODUCTION

The optical constants of naturally occurring minerals are often difficult to measure because single crystals are nonexistent. This is particularly true for clays. One must then resort to the use of powders. Last year we reported transmission measurements on hot-pressed polyethylene-powder sample pellets. Because of the large contribution of scattering to the attenuation, we have changed to reflection measurements of pure pressed powders (i.e., no binder). The reflection spectra are then Kramers-Kronig analyzed to yield the real and imaginary parts of the optical constants, n and k , respectively.

RESULTS

Pressed powder samples were made from fine powders of kaolinite, montmorillonite, muscovite, gypsum, and limonite. Reflectance measurements were made from 10 cm^{-1} to 400 cm^{-1} using a RIIC for infrared interferometer. The reflectance spectra were then Kramers-Kronig analyzed to obtain n and k . Figure 1 shows n and k obtained in this way for gypsum.

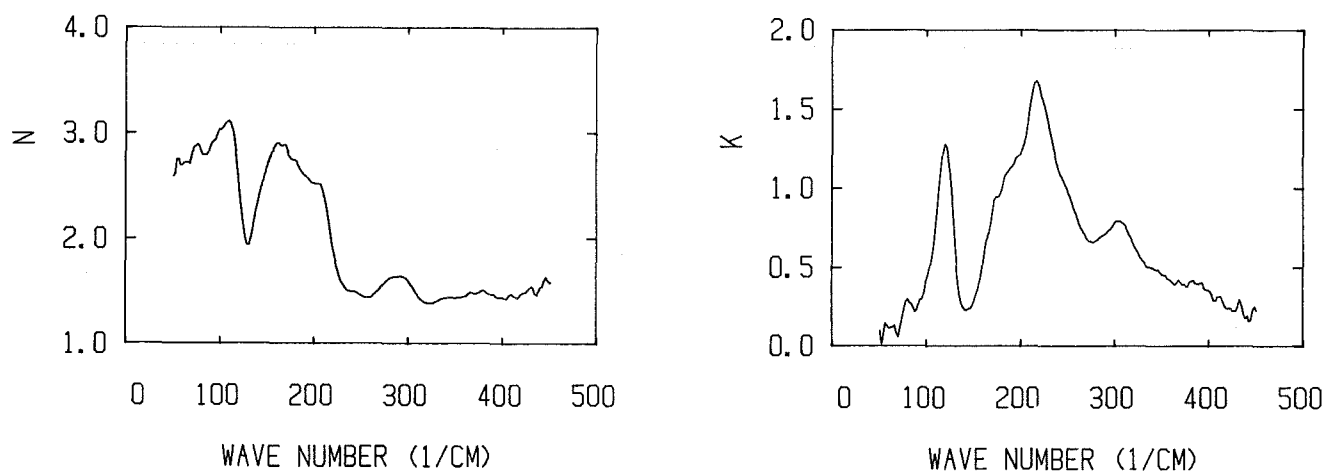


FIGURE 1. n AND k FOR GYPSUM. The real and imaginary parts of the refractive index for gypsum obtained from a Kramers-Kronig analysis of the reflectivity of a pressed powder sample.

*This work was supported by contract DAAK-11-82-C-0052 with the US Army Chemical Systems Laboratory.

DISCUSSION

Two problems are encountered in attempting to determine optical constants from pressed powder samples. First, most powders cannot be pressed to the density of the crystalline material; and second, most of the crystals are anisotropic. It is not well understood how the optical constants determined from pressed powder reflectance depend upon the sample density and how one should extrapolate the measured values to the crystalline density. Some effort made by Volz¹ and Querry² suggests that the reflectivity scales with volume density. When reflection measurements are made on pressed powders of an isotropic material, a complicated average over crystallite orientation is found.^{1,2}

Thus one is led to ask the question of how useful are the optical constants determined from pressed powders. First, such measurements clearly indicate the frequencies where absorption is strong. Second, the average over orientation must be done for a calculation of the transmission through an aerosol of particles; and perhaps the effective optical constants determined from powder reflectance are a good first approximation to this average. Third, the question of how well optical constants must be known in order that they do not significantly degrade the calculations made with approximate scattering theories is not settled. Thus it appears that the pressed powder method supplies useful optical constants, and, in any event, is the best technique developed to date. We intend to study a number of other naturally occurring minerals in the coming year.

FUTURE WORK

We are currently using an asymmetric interferometer to measure the optical constants in the 1 cm^{-1} to 50 cm^{-1} range. The asymmetric interferometer provides the real and the imaginary parts of the optical constants without need for a Kramers-Kronig analysis. We have found, however, that this instrument is extremely sensitive to sample flatness and surface roughness. Rough surfaces lead to higher values of k compared to those obtained from the usual reflectance measurement and Kramers-Kronig analysis. We have found that careful polishing improves our results. This will now allow us to extend our optical constants to 1 cm^{-1} .

REFERENCES

1. Frederick E. Volz, *Applied Optics* 22, 1842-55 (1983).
2. Marvin Querry, private communication.

OPTICAL PROPERTIES OF
METALS IN THE SUBMILLIMETER AND
MILLIMETER WAVELENGTHS*

R. E. Paul, M. A. Ordal, L. L. Long, R. W. Alexander, Jr., and R. J. Bell
Physics Department, University of Missouri-Rolla
Rolla, Missouri 65401

ABSTRACT

The optical parameters for metals at submillimeter and millimeter wavelengths have been surveyed from the open literature and analyzed using the Drude free electron model for Al, Cu, Au, Pb and W. Ni is added to the list in this presentation. The data for Fe in the literature are very scant. UMR measurements and approximations have been made for the optical parameters of Fe at the long wavelengths using a plane, parallel waveguide approach. The experiments and theory have the same functional dependence and shape (ϵ_{02} vs. λ in μm), but the coefficients are not in good agreement. More measurements are under way.

Fresnel's equations for metals in the submillimeter and millimeter wavelengths have been approximated to better than one percent. The magnitude of $\alpha \equiv (1-R)$ at the "principal angle" in the mm λ range is a universal constant 0.83.

I. INTRODUCTION

The optical properties of metals are needed to analyze the scattering and absorption of long wavelength radiation from metals formed in various shapes. To predict and measure these basic optical parameters, we first reviewed the literature and found that the Drude free electron model works well for at least five metals and has unknown promise for seven other metals including iron.¹ We found that long or short wavelengths are referenced to the scattering frequency of the metal, ω_p , with long wavelengths meaning $\omega^2 \ll \omega_p^2$ where $\omega \equiv 1/\lambda$.

Brändli and Sievers² developed a waveguide technique for measuring the important dielectric function (ϵ_{02} of $\epsilon_0 \equiv \epsilon_{01} + i\epsilon_{02}$) of metals in the submillimeter and millimeter wavelength regions. We tried other techniques but found theirs is the best so far.

For experimental determinations of the optical parameters of metals one wants as simple and accurate approximations as possible. To deal with the optical properties, we made approximations for Fresnel's equations in the submillimeter and millimeter wavelengths.

II. RESULTS

(A) From the literature:

We have searched the literature for optical properties in the infrared to mm λ of 12 metals (including Ni and Fe). We published: M. A. Ordal, L. L. Long, R. J. Bell, S. E. Bell, R. R. Bell, R. W. Alexander and C. A. Ward, *Applied Optics*, 22, 1099 (April, 1983).

*This work was supported by contract DAAK-11-82-C-0052 with the US Army Chemical Systems Laboratory.

- a. We learned that the Drude free electron model is very good for 5 of the 12 metals studied from the IR to mm λ .
- b. In the mm λ , ϵ_{02} of the metal governs most optical properties. $-\epsilon_{01}$ is 2 to 3 orders of magnitude smaller than ϵ_{02} .
- c. In the sub mm λ and mm λ , $-\epsilon_{01}$ is a constant $\approx \omega_p^2/\omega_\tau^2$ where ω_p is the plasma frequency, and ω_τ is the scattering frequency of the electrons. Also ϵ_{02} in the sub mm λ and mm λ ranges approximately equals $\omega_p^2/(\omega_\tau\omega)$.
- d. ϵ_{02} can often be well estimated in the mm λ using only the handbook dc resistivity, ρ_{dc} (in ohm-cm), of the metals. $\epsilon_{02} \approx 60/(\rho_{dc}\omega)$ in the submillimeter and millimeter λ . $-\epsilon_{01}$ can be estimated with less accuracy by ρ_{dc} and the lowest valence of the metal.¹
- e. More basic physics indicates a resonant-like form of $-\epsilon_{01}$ in that $-\epsilon_{01}$ and ϵ_{02} cross each other at $\omega = \omega_\tau$ and that the magnitude of $-\epsilon_{01}$ at $\omega = 0$ is twice that at $\omega = \omega_\tau$, i.e., $-\epsilon_{01}(\omega=0) = \omega_p^2/\omega_\tau^2$ and $-\epsilon_{01}(\omega=\omega_\tau) = (1/2)(\omega_p^2/\omega_\tau^2)$. Long wavelengths are for $\omega^2 \ll \omega_\tau^2$, i.e., ω_τ is the pivotal wavenumber for $\epsilon_{02} \geq -\epsilon_{01}$.
- f. As shown in Fig. 1, we have looked at the published data for nickel since Ni is very similar to iron and because the published data for Ni does not have the scatter that the Fe data has.¹ The fit¹ to the published Ni data results in $\omega_\tau = 4.70 \times 10^2 \text{ cm}^{-1}$ and $\omega_p = 3.88 \times 10^4 \text{ cm}^{-1}$ which produces the solid lines. To estimate ω_p and ω_τ from handbook data we used

$$\omega_p^2 = \frac{1}{(2\pi c)^2} \left[\frac{4\pi e^2}{m^* \epsilon_\infty} \left(\begin{array}{l} \text{lowest} \\ \text{valence} \\ \text{of metal} \end{array} \right) \left(6.02 \times 10^{23} \frac{\rho}{M} \right) \right] \quad (1)$$

and

$$\omega_\tau = \frac{\omega_p^2 \rho_{dc} (\text{ohm-cm})}{60} \quad (2)$$

where for Ni we estimate $m^* = 9.11 \times 10^{-28} \text{ gm}$, $\epsilon_\infty = 1$, lowest valence = 1, $\rho = 8.8 \text{ gm/cm}^3$, and $M = 58.71 \text{ gm/mole}$ with $c = 3 \times 10^{10} \text{ cm/sec}$, $e = 4.80 \times 10^{-10} \text{ esu}$, and $\rho_{dc} (\text{ohm-cm}) = 7.8 \times 10^{-6} \text{ ohm-cm}$. These valence and resistivity parameters yield $\omega_\tau \approx 260 \text{ cm}^{-1}$ and $\omega_p \approx 4.5 \times 10^4 \text{ cm}^{-1}$ for Ni. ϵ_{02} and $-\epsilon_{01}$ for these resistivity and valence based calculations are shown as dashed lines in the Fig. 1.

- g. Fitting the ϵ_{02} and $-\epsilon_{01}$ vs. ω data to find ω_p and ω_τ is very easy using simple Eqs. found by Mark Ordal and explained in the Ref. 1.

NICKEL

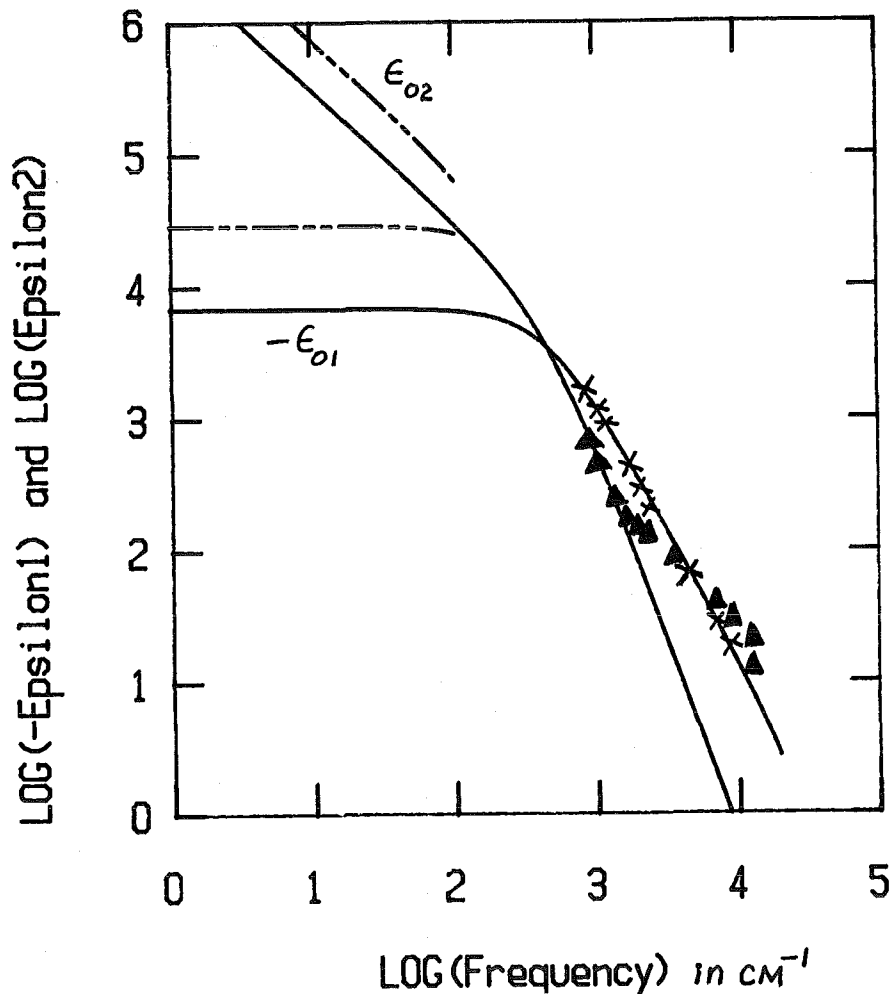


FIGURE 1. FOR NICKEL, PLOTS OF THE $\text{LOG}_{10} \epsilon_{02}$ AND $\text{LOG}_{10} (-\epsilon_{01})$ VERSUS $\text{LOG}_{10} \omega$ WITH THE WAVENUMBER $\omega \equiv 1/\lambda$. The data in Ref. 1 was used from an article (therein referenced) by Lynch, Rosei, and Weaver. The x are for $-\epsilon_{01}$ and the closed triangles go with ϵ_{02} . The solid curves apply for $\omega_p = 3.88 \times 10^4 \text{ cm}^{-1}$ and $\omega_T = 4.70 \times 10^2 \text{ cm}^{-1}$ (IR fit of data using Ref. 1 technique). The dashed lines are based on the values of $\omega_p \approx 4.5 \times 10^4 \text{ cm}^{-1}$ and $\omega_T = 2.60 \times 10^2 \text{ cm}^{-1}$ which are estimated from the dc resistivity and lowest valence of Ni ($\rho_{dc} = 7.8 \times 10^{-6} \text{ ohm-cm}$ and lowest valence = 1).

(B) Theories and approximations:

Theoretically for non-magnetic metals in the sub mm λ and mm λ with nonabsorbing overlayers (medium #1 in which $k_1 = 0$ and n_1 is not necessarily unity for $n_{c1} \equiv n_1 + ik_1$), we obtained simple approximations for the phase angles, δ , and absorptions, a , with $a \equiv 1-R$, for both polarizations to better than 1% where R is the reflectance of the metals.

- a. All four approximate equations depend mainly on $n_1/\sqrt{\epsilon_{02}}$ and $\cos \phi_1$ but only slightly on $-\epsilon_{01}$ where ϕ_1 is the angle of incidence.
- b. The magnitudes of \mathcal{A} in the mm λ for $\phi_1 \leq 89^\circ$ are of the order 10^{-2} to 10^{-4} .
- c. In the mm λ range there are simple and interesting connections between the \mathcal{A} 's and the phase angles, δ , involving only $n_1/\sqrt{\epsilon_{02}}$ and $\cos \phi_1$; the reflectivity is $r \equiv \sqrt{R} e^{i\delta}$.
- d. Fresnel equations for both polarizations for the submillimeter and millimeter wavelengths are:

$$1 - R_s \approx \left[\frac{2\sqrt{2} n_1 \cos \phi_1}{\sqrt{\epsilon_{02}} (1 - \epsilon_{01}/[2\epsilon_{02}])} \right] \xrightarrow[\omega \rightarrow 0]{\text{mm } \lambda} \left[\frac{2\sqrt{2} n_1 \cos \phi_1}{\sqrt{\epsilon_{02}}} \right] \quad (3)$$

with

$$\tan(\delta_s + \pi) \approx \left[\frac{\sqrt{2} n_1 \cos \phi_1}{\sqrt{\epsilon_{02}}} \right] \xrightarrow[\omega \rightarrow 0]{\text{mm } \lambda} \text{no change} \quad (4)$$

and

$$1 - R_p \approx \left[\frac{\left(\frac{2\sqrt{2} n_1}{\sqrt{\epsilon_{02}}} \right) \cos \phi_1}{\left(1 - \epsilon_{01}/[2\epsilon_{02}] \right) \cos^2 \phi_1 + \left(\frac{\sqrt{2} n_1}{\sqrt{\epsilon_{02}}} \right) \cos \phi_1 + \frac{n_1^2}{\epsilon_{02}}} \right] \xrightarrow[\omega \rightarrow 0]{\text{mm } \lambda} \left[\frac{\frac{2\sqrt{2} n_1 \cos \phi_1}{\sqrt{\epsilon_{02}}}}{\cos^2 \phi_1 + \frac{\sqrt{2} n_1 \cos \phi_1}{\sqrt{\epsilon_{02}}} + \frac{n_1^2}{\epsilon_{02}}} \right] \quad (5)$$

with

$$\tan \delta_p \approx \left[\frac{\frac{\sqrt{2} n_1 \cos \phi_1}{\sqrt{\epsilon_{02}}}}{\cos^2 \phi_1 - \frac{n_1^2}{\epsilon_{02}}} \right] \xrightarrow[\omega \rightarrow 0]{\text{mm } \lambda} \text{no change} \quad (6)$$

where $(\epsilon_{01}/\epsilon_{02})^2 \ll 1$ in the submm λ and $|\epsilon_{01}/\epsilon_{02}| \ll 1$ in the mm λ range. Also $(\epsilon_{11}/\epsilon_{02}) \ll -(\epsilon_{01}/\epsilon_{02})$ in both wavelength ranges. These assumptions result in the refraction angle into the metal being very near zero in all the equations above. $\epsilon_0 \equiv (\epsilon_{01} + i \epsilon_{02})$ is the dielectric function of the metal; ϕ_1 is the angle of incidence; and ρ_{dc} is the dc resistance in ohm-cm. The non-absorbing overlayer has an index of refraction $n_1 = \sqrt{\epsilon_{11}}$. The Drude free electron model has the electron scattering frequency, ω_τ , and plasma frequency, ω_p . The farther one goes into the mm λ range; the smaller is $(\omega/\omega_\tau) \approx -(\epsilon_{01}/\epsilon_{02}) \ll 1$ with $\omega = \omega_\tau$ at the cross-over of $-\epsilon_{01}$ and ϵ_{02} when they are plotted against λ or ω . ω_τ is usually of the order of a few hundred wavenumbers (see Table 13 in Ref. 1).

Examples are shown at $\omega = 10 \text{ cm}^{-1}$ for both Fe and Au in Fig. 2 where $A_s \equiv (1-R_s)$ and $A_p \equiv (1-R_p)$. We choose $\omega_T = 2.51 \times 10^3 \text{ cm}^{-1}$ and $\omega_p = 1.24 \times 10^5 \text{ cm}^{-1}$ for Fe and $\omega_T = 2.16 \times 10^2 \text{ cm}^{-1}$ and $\omega_p = 7.25 \times 10^4 \text{ cm}^{-1}$ for Au. $n_1 = 1$ for both plots.

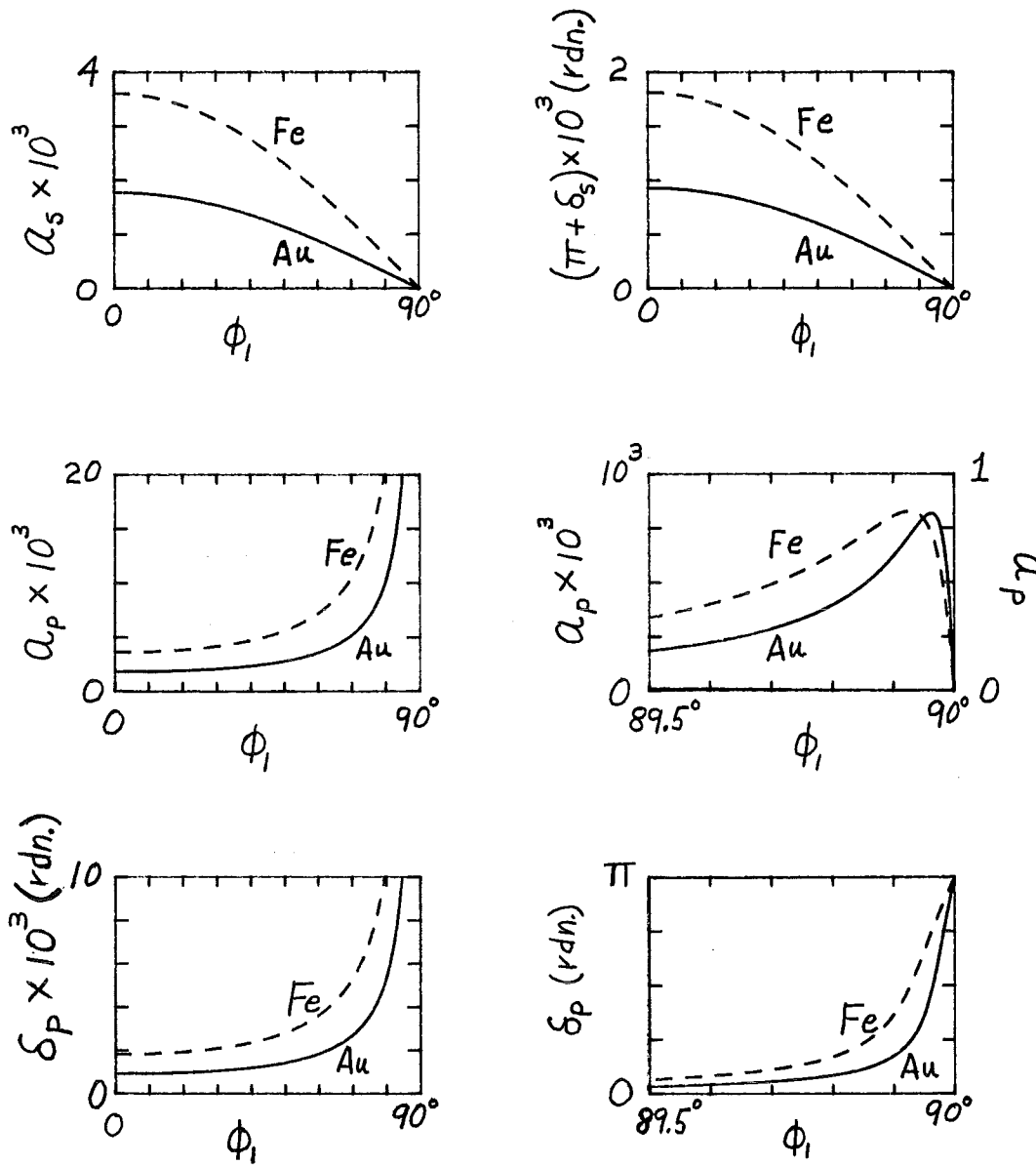


FIGURE 2. PLOTS OF $A_s \equiv (1-R_s)$, $A_p \equiv (1-R_p)$ AND THE PHASE ANGLES δ_s AND δ_p FOR Au AND Fe AT $\omega = 10 \text{ cm}^{-1}$. For Fe the ω_T and ω_p values used in these calculations are at the moment highly debatable.

e. The "principal angle", $\phi_{\text{principal}}$, is given by

$$\cos \phi_{\text{principal}} \approx \left\{ \left[n_1 / \sqrt{\epsilon_{02}} \right] / \left[1 + \epsilon_{01} / (4\epsilon_{02}) \right] \right\} \quad (7)$$

and the minimum reflectance is found in:

$$\begin{aligned} a_{\text{principal}} \equiv (1 - R_{\text{principal}}) &\approx \left(\frac{2\sqrt{2}}{2 + \sqrt{2}} \right) \left(1 + \frac{\epsilon_{01}/\epsilon_{02}}{2 + \sqrt{2}} \right)^{1/2} \\ \text{or} &\approx 0.828 \left[1 + 0.293 \left(\epsilon_{01}/\epsilon_{02} \right) \right]^{1/2} \\ \text{or} &\approx 0.828 \left[1 + 0.293 \left(\omega/\omega_T \right) \right]^{1/2}. \end{aligned} \quad (8)$$

Thus in the mm λ range $a_{\text{principal}} \approx 0.83$ is a universal constant, and $\phi_{\text{principal}}$ is extremely close to 90 degrees.

f. As is well known in the mm λ , n_0 and k_0 are nearly equal with somewhat higher precision:

$$k_0 - n_0 \approx \frac{-\epsilon_{01}}{\sqrt{2}\epsilon_{02}} \approx \left(\frac{\omega_p \sqrt{\omega}}{\sqrt{2}\omega_T^{3/2}} \right) \approx 0. \quad (9)$$

(C) Experiments:

Experiments on Fe were designed to measure ϵ_{02} . The technique is basically a plane-parallel mirror waveguide study.² Overdamping of the waves between close Fe metal layers (spaced by very thin plastic sheets) is the key feature to the technique. Also the metal surfaces studied are against a plastic and have not been exposed to air.

- ϵ_{02} is obtained directly from the measurements as is the real part of the surface impedance $R(\Omega)$.
- In the mm λ range if the Drude model is invoked the measurement of ϵ_{02} yields $\omega_p^2/(\omega_T\omega)$ or $(\omega_p^2/\omega_T)\lambda \times 10^{-4}$ for λ in μm (to high accuracy this completely describes the metals in the mm λ). The data, $R(\Omega)$ vs. ω , varies as [(a constant) $\sqrt{\omega}$] where ω is in cm^{-1} and $R(\Omega)$ is the surface impedance of the metal.²
- For the transmittance in the submm λ and mm λ ranges through a stack of parallel waveguides, one uses samples as shown in Fig. 3.

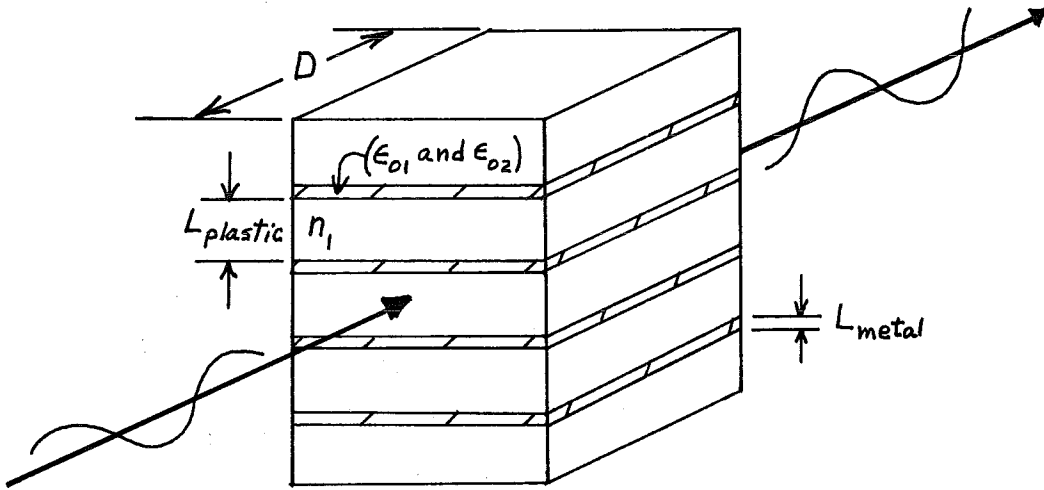


FIGURE 3. CRUDE DIAGRAM OF THE SAMPLE STACK USING PLANE-PARALLEL WAVEGUIDE PROCEDURES.

$$\alpha \equiv \left(\begin{array}{l} \text{absorption coefficient} \\ \text{of the entire stack} \\ \text{of plane, parallel} \\ \text{waveguides} \end{array} \right) \approx \left(\frac{\sqrt{2} n_1}{\sqrt{\epsilon_{02}} L} \right) \approx \left(\frac{\sqrt{2} n_1 \sqrt{\omega_r} \sqrt{\omega}}{L \omega_p \left(1 + \frac{\omega}{\omega_r}\right)^{1/2}} \right) \approx$$

$$\approx \left(\frac{n_1 \sqrt{\rho_{dc} (\text{ohm-cm})} \sqrt{\omega}}{\sqrt{30} L \sqrt{1 + \omega/\omega_r}} \right); \quad (10)$$

so

$$\alpha \xrightarrow[\omega \rightarrow 0]{\text{mm}\lambda} \left(\frac{\sqrt{2} n_1}{\sqrt{\epsilon_{02}} L} \right) \text{ or } \left(\frac{\sqrt{2} n_1 \sqrt{\omega_r} \sqrt{\omega}}{L \omega_p} \right) \text{ or } \left(\frac{n_1 \sqrt{\rho_{dc} (\text{ohm-cm})} \sqrt{\omega}}{\sqrt{30} L} \right) \quad (11)$$

where $(n_0 + i k_0)^2 \equiv (\epsilon_{01} + i \epsilon_{02})$ and

$$\epsilon_{02} = \left(\frac{\omega_p^2 / (\omega_r \omega)}{1 + (\omega / \omega_r)^2} \right) \xrightarrow[\omega \rightarrow 0]{\text{submm}\lambda \text{ and mm}\lambda} \left(\frac{\omega_p^2}{\omega_r \omega} \right) \equiv \left(\frac{\omega_p^2 \times 10^{-4} \lambda_{\mu\text{m}}}{\omega_r} \right) \quad (12)$$

and

$$-\epsilon_{01} \approx \left(\frac{\omega_p^2 / \omega_T^2}{1 + \left(\frac{\omega}{\omega_T} \right)^2} \right) \xrightarrow[\omega \rightarrow 0]{\text{sub mm}\lambda \text{ and mm}\lambda} \left(\frac{\omega_p^2}{\omega_T^2} \right) \quad (13)$$

d. ϵ_{02} for the mm λ range with $(-\epsilon_{01}/\epsilon_{02}) \ll 1$ is obtained from the experiments using:

$$\epsilon_{02_{\text{mm}\lambda}} \approx \left(\frac{\sqrt{2} n_1}{L \alpha} \right)^2 \left(\frac{\omega_p^2}{\omega_T \omega} \right) = \left(\frac{\omega_p^2 \times 10^{-4} \lambda_{\mu\text{m}}}{\omega_T} \right) \approx \left(\frac{60}{\omega \rho_{\text{dc}} (\text{ohm-cm})} \right) \quad (14)$$

where ω_p and ω_T are in wavenumbers and $\lambda_{\mu\text{m}}$, the vacuum wavelength, is in μm .

In Fig. 4 the experimental and estimated ϵ_{02} for Fe are shown with resultant data in the figure caption. It is not too surprising¹ that the experimental and dc resistivity estimates of the slope differ by a factor of three from experiment. We have

$$\frac{\omega_p^2}{\omega_T} \approx 1.7 \times 10^7 \text{ cm}^{-1} = 1.7 \times 10^3 \mu\text{m}^{-1} \quad (15)$$

and

$$\frac{\omega_p^2}{\omega_T} \approx \frac{60}{\rho_{\text{dc}} (\text{ohm-cm})} \approx 6.0 \times 10^6 \text{ cm}^{-1} = 6.0 \times 10^2 \mu\text{m}^{-1} \quad (16)$$

Annealing, mechanical straining, thin film effects, etc., might account for the differences. Much longer wavelength data has been taken, but signal-to-noise ratios must be improved before publishing.

Our new experiments under way with single frequency solid state sources in the mm λ range are vastly improving these results.

Iron

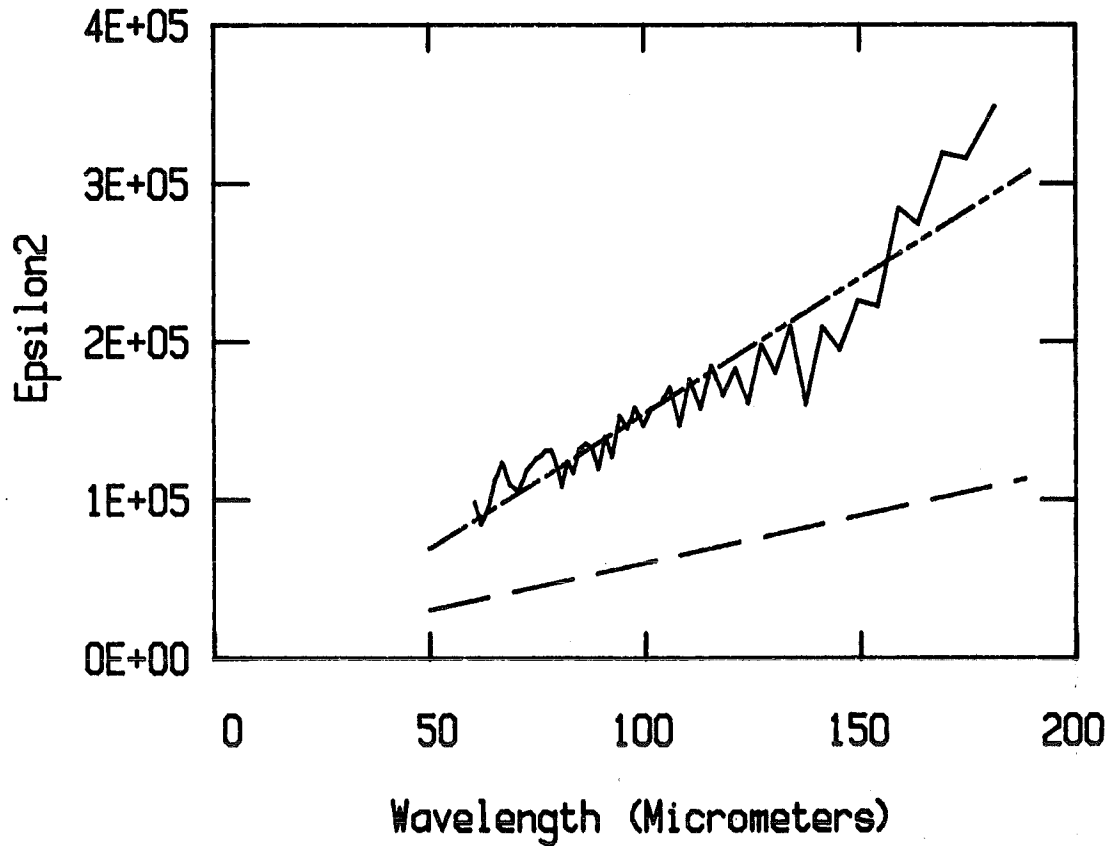


FIGURE 4. FOR Fe, LINEAR PLOTS OF ϵ_{02} VS λ IN μm . The jagged lines are the experimental data using Fourier transform spectroscopy techniques. The dash line with two short dashes is the result of a least square fit of the data. The simple dashed line is from resistivity based estimates of ϵ_{02} . The slope of the experimental data is $1.7 \times 10^3 \mu\text{m}^{-1}$ and $6.0 \times 10^2 \mu\text{m}^{-1}$ for the estimates. These crude estimates are being improved in current experiments.

III. FUTURE WORK

We're trying low-carbon steel shim stock as the sample. We're looking at thicker Fe plated on teflon film stacked samples. We're finishing the drying system for the asymmetric Fourier transform spectrometer; we have recently obtained InSb LHe mm λ detectors from the Naval Research Laboratories; we're buying isolators to use our two strong mm λ solid state sources for more precise mm λ measurements of ϵ_{02} ; and we're measuring the surface resistivities of the Fe films.

We're developing techniques to measure $-\epsilon_{01}$. We want to study Ni to help us with our understanding of iron.

REFERENCES

1. M. A. Ordal, L. L. Long, R. J. Bell, S. E. Bell, R. R. Bell, R. W. Alexander, Jr., and C. A. Ward, *Appl. Opt.* 22, 1099 (April, 1983).
2. G. Brändli and A. J. Sievers, *Phys. Rev. B* 5, 3550 (1972).

CAPACITIVE GRID BEAMSPLITTERS FOR FAR-INFRARED
AND MILLIMETER WAVE INTERFEROMETERS

K. D. Möller and V. P. Tomaselli
Fairleigh Dickinson University
Physics Research Laboratory
Hackensack, NJ 07601

ABSTRACT

This report describes the concept, fabrication and testing of a new type of beamsplitter designed to be used for far-infrared and submillimeter wave interferometers. The absence of interference fringes and an extended operating spectral range are the advantages of this new beamsplitter over the traditional clear types. A manuscript describing this work is in preparation and will shortly be sent to Applied Optics.

INTRODUCTION

Michelson interferometers are commonly used in Fourier transform spectrometers operating in the far-infrared spectral region. One of the main components in these instruments, and source of experimental difficulty, is the beamsplitter. Normally, mylar is used to make the beamsplitter. Its refractive index ($n=1.8$), however, is only half that required to produce a beamsplitter having optimum reflectance and transmittance properties. A second problem with mylar beamsplitters is the need to have the film thickness sufficiently large to produce the required reflectance at long wavelengths. A thick film, in turn, results in a fringe pattern due to constructive and destructive interference. Thus, while mylar has certain properties which make it useful as a beamsplitter material (transparency, mechanical stability, ease of handling), it also has serious shortcomings.

To overcome these problems and generate far-infrared spectra over an extended wavelength range, commercial instrument manufacturers use a series of beamsplitters. A positioning device that allows one of several beamsplitters to be inserted into the optical beam, without breaking the vacuum, is provided for. However, to obtain precise far-infrared spectra, for example - absorption band contours in liquids, it is desirable to obtain the spectrum using only one beamsplitter.

Two spectroscopic devices available to produce continuous far-infrared spectra over an extended spectral region are the lamellar grating and the Martin-Puplett⁽¹⁾ polarizing interferometer. Both are considerably more difficult to construct than the Michelson interferometer. Their advantages and disadvantages will be discussed below.

The lamellar grating interferometer operates as a wave front division device. The Michelson interferometer, by comparison, uses amplitude division. Inspired by the lamellar grating concept, we have produced capacitive grid beamsplitters: transparent mylar substrates (6 μ m thick) coated with copper evaporated through various masks. One pattern, which we will use for discussion only, mimics a diffraction grating. However, data will be reported for patterns produced as regular arrays of opaque dots.

A grating-like beamsplitter with a grating constant (a) which is larger than the wavelength (λ) will produce diffraction effects. If we compare a lamellar grating with a given (λ/a) ratio to a grating-type beamsplitter of same λ/a used in a normal Michelson interferometer, we see that the main disadvantage to the latter is the fact that the radiation passes through the beamsplitter twice. We would like to estimate the diffraction losses, in first order, resulting from the passage of light through the grating-like beamsplitter. Such a beamsplitter is, in effect, a grating superimposed on a transparent mylar film. For a double slit aperture with separation $a = 2d$ (d = slit opening), approximately half of the incident energy is diffracted out in first order. As will be discussed below, the zero order radiation, returning for a second pass through a diffraction grating beamsplitter, as in the normal Michelson configuration, will behave very similar to that produced by diffraction from a lamellar grating.

Michelson vs. Lamellar Interferometer

Consider a Michelson interferometer with an ideal beamsplitter B (Figure 1) and using monochromatic radiation. An ideal beamsplitter will be defined as a loss-less film which reflects half and transmits half of the incident radiation. After the first pass through the beamsplitter 50% of the incident beam reaches mirrors M_1 and M_2 respectively. Following reflection from the mirrors and a second pass through the beamsplitter, 50% reaches the detector and 50% is returned in the direction of the source. For some displacement x of mirror M_2 relative to its in-phase position, beams I and II interfere constructively; all radiant energy is directed toward the detector.

We now consider a lamellar grating, as shown schematically in Figure 2. Monochromatic radiation is incident at some angle to the grating normal so that 50% is reflected from the upper surfaces of the structure (III) and 50% is reflected from the lower, moving, and interpenetrating surfaces IV. For a given displacement (x) of one surface relative to the others, beams III' and IV' will undergo destructive interference for the zeroth order pattern shown. The energy is now distributed in the first order position (not shown). Conversely, when the zero order pattern is a maxima due to constructive interference of rays III' and IV', no energy is distributed in the first order positions. Thus the distribution of energy alternates between zeroth and first orders. The next higher orders can be neglected because of their low intensities.

The above discussion can be utilized in describing the capacitive grid beam-splitter used in the Michelson interferometer. For the first pass through the beam-splitter, radiation is diffracted into zero and first order positions. The first order pattern is lost, diffracted away from the optic axis of the system. For the second pass, the two reflected beams interfere in the directions of the detector and source as in the lamellar grating case. When the zeroth order radiation in the direction of the source is undergoing constructive interference, the corresponding zeroth order in the direction of the detector is undergoing destructive interference. The first order pattern in the detector direction has zero intensity, but the first order pattern in the source direction has a non-zero intensity. This will again result in losses.

If we consider that the two first order spectra contain the same intensity as does the zero order, we have, for the second pass, a loss of 50% of the incident energy. In addition, in the first pass through the beamsplitter, a loss of 50% of the incident light is realized. Thus, a total of 25% of the total incident intensity is utilized. A common feature of the lamellar grating and ideal Michelson interferometer is the use of 100% of the incident intensity for monochromatic radiation. By comparison, a real Michelson interferometer using a mylar beamsplitter has a reflectance of 0.15. The intensity of radiation in the direction of the detector is $[(0.15)(1-0.15)] = .128$ times the incident intensity. If this direction corresponds to constructive interference, the intensity is increased by a factor of 2 to $\sim 25\%$ of the incident light. The .15 reflectance value used in the above argument is the bulk material value. According to this estimate, the grating beamsplitter should perform as well as the clear mylar beamsplitter but not exhibit interference fringes.

Cut-Off Wavenumber

The similarity between the lamellar grating and diffraction grating beamsplitter can be exploited to analyze a restrictive condition on the cut-off wavenumber, $\bar{\nu}_c$. Consider a lamellar grating with periodicity a used in an interferometer configuration with an aperture diameter s and collection optic focal length F . Bell² has shown that the cut-off wavenumber, for which first order radiation enters the exit slit, is

$$\bar{\nu}_c = \frac{F}{as} \quad (1)$$

This condition places an upper limit on s to insure maximum efficiency. For wave numbers greater than $\bar{\nu}_c$, radiation from higher orders enters the exit aperture and, correspondingly, lowers the efficiency.

For the diffraction grating beamsplitter used in a Michelson interferometer, equation (1) may be adopted. If the grating constant a is modified to account for its projected periodicity in a plane perpendicular to the optic axis of the inter-

ferometer arm, the cut-off wavenumber condition becomes

$$\bar{\nu}_c = \frac{f}{\frac{a}{\sqrt{2}} s} \quad (2)$$

The numerator, f , must now be taken as the beamsplitter to exit slit distance. Equation (2) also contains the condition for spatial coherence. If the grating constant is too large, light wave from neighboring sections of a finite aperture would have an excessively large phase difference. As a result, a one-dimensional patterned beamsplitter, such as in the diffraction grating case, is not suitable for an instrument having the circular symmetry (about the optic axis) of a Michelson interferometer. Accordingly, we have considered patterned beamsplitters having two-dimensional arrays of square or circular opaque dots for the wavefront dividing, capacitive grid beamsplitters.

The capacitive grid beamsplitters were produced by vacuum evaporation of copper through a mask onto a $6\mu\text{m}$ thick mylar film substrate. Circular dot patterns were selected because commercially manufactured metal masks were readily available. Masks having various dot sizes and inter-dot distances were obtained. Thus it was possible to vary the area of the dots and the ratio of opaque to transparent areas of the beamsplitter.

The metal dots on the mylar substrate had a thickness of $4000\text{--}5000 \text{ \AA}$. Evaporation was done on both sides of the mylar film. Registration of the dot pattern could be easily accomplished by reversing the mask. Following vacuum deposition of the metal dots, the mylar substrate was stretched on a circular drumhead-type holder. All beamsplitters were investigated using a Michelson interferometer with focusing mirrors operated under vacuum. This instrument has been described previously³. The only filters used in the experiments were a 3mm thick quartz crystal and a black polyethylene sheet.

The various beamsplitters were compared using entrance and exit circular apertures chosen to have diameters of 12.5mm . This choice was made for practical considerations resulting from the spectrometer geometry. The beamsplitter - to - exit aperture distance, on axis, is 30cm ; periodicity constant of the beamsplitter, with 3.5mm diameter dots, was 5.5mm . With an aperture diameter of 12.5mm , the cut-off wavenumber as given by equation (2) is

$$\bar{\nu}_c = 300 / (12.5) (5.5 / \sqrt{2}) \approx 60\text{cm}^{-1}$$

If the aperture size (s) is increased, the cut-off wavenumber is reduced resulting in more cancellation in the wavelength range under consideration. Since a clear mylar beamsplitter does not have this restriction, it has, from this point of view, an advantage. However, for the longer wavelengths for which the patterned beamsplitter has been designed, this advantage vanishes.

Figures 3, 4, and 5 are the spectra obtained with a 50 μ m transparent mylar beamsplitter, 3.5mm diameter double-coated dot pattern beamsplitter, and a 175 μ m transparent mylar beamsplitter, respectively. The intensity scale is in relative units but is the same for all three cases. Weak absorption bands due to atmospheric water vapor in the 7cm long light pipe can be seen. The strong absorption bands in Figures 3 and 5 are interference fringes due to the mylar beamsplitter.

In most treatments of beamsplitters, the material is considered to be optically loss less. Naylor, et al.⁴, have accounted for the effect of absorption by mylar in beamsplitters. They calculate the reduction in modulating efficiency of a 100 μ m mylar beamsplitter as a function of wavenumber for several angles of incidence. The effect of absorption is clearly seen and is more significant for the higher wavenumbers. We have investigated a 225 μ m thick translucent beamsplitter and observed no appreciable transmission for wavenumbers above 80 cm^{-1} . By comparison clear mylar transmitted no radiation above 120 cm^{-1} for both 50 μ m and 175 μ m thickness. Also, a dotted beamsplitter prepared on a 6 μ m mylar substrate transmitted up to 200 cm^{-1} .

We have also investigated circular dot beamsplitters having a diameter of 1.0mm and 1.7mm and coated on one side only. We observed that these devices produced spectra whose intensity was 15 - 20% less than that of the spectra recorded using the 3.5mm dot double-coated beamsplitter. This 15 - 20% reduction was also confirmed using a 3.5mm dot single-coated beamsplitter. All of these beamsplitters were prepared on 6 μ m mylar substrates.

Conclusion

The capacitive grid beamsplitters described in this paper have the advantage of not producing interference fringes over a considerably large far-infrared spectral region. They yield approximately the same peak transmission as do the clear mylar beamsplitters. In addition, they are relatively easy to produce and eliminate the need to change beamsplitters if extended spectral region spectra are desired.

The discussion and estimates of the overall efficiency of clear and capacitive grid beamsplitters, presented above, have been confirmed. Using a single detector, the lamellar grating spectrometer is four times more efficient than the capacitive grid beamsplitter interferometer operated in the diffraction region. By comparison, the Martin-Puplett polarizing Michelson interferometer is half as efficient as the lamellar grating spectrometer but twice as efficient as our Michelson equipped with a circular dot capacitive grid beamsplitter.

REFERENCES

1. D. H. Martin and E. Pulett, *Infrared Phys.* 10, 105 (1969).
2. R. J. Bell, *Introductory Fourier Transform Spectroscopy* (Academic Press, New York, 1972), Chapter 15.
3. K. D. Möller and V. P. Tomaselli, *Proc. 1979 Chemical Systems Laboratory Scientific Conference on Obscuration and Aerosol Research*, R. H. Kohl, ed., Dec. 1980, p.359.
4. D. A. Naylor, R. T. Boreiko and T. A. Clark, *Applied Optics* 17, 1055 (1978).

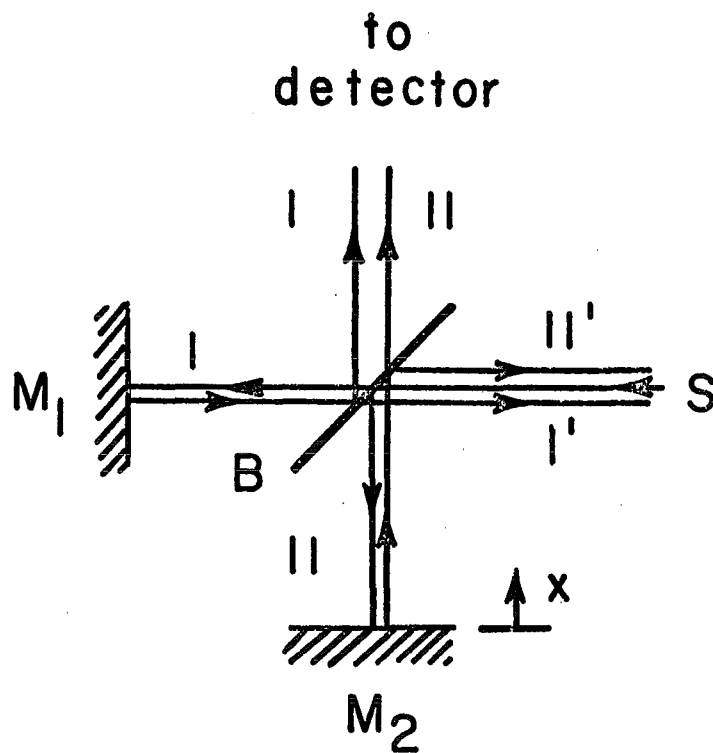


Figure 1 - Schematic diagram of Michelson interferometer. S is the source of radiation, B is beamsplitter, M_1 and M_2 are plane mirrors. Light paths I, II, I' and II' are shown displaced for pictorial reasons.

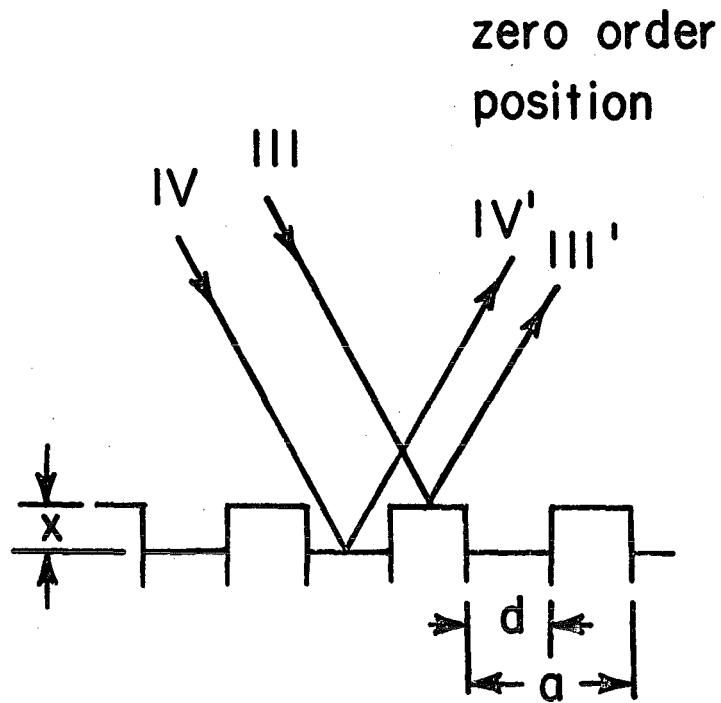


Figure 2 - Schematic diagram of lamellar grating, side view. Here a is the grating constant, d the step width and x the relative displacement of the interpenetrating surfaces.

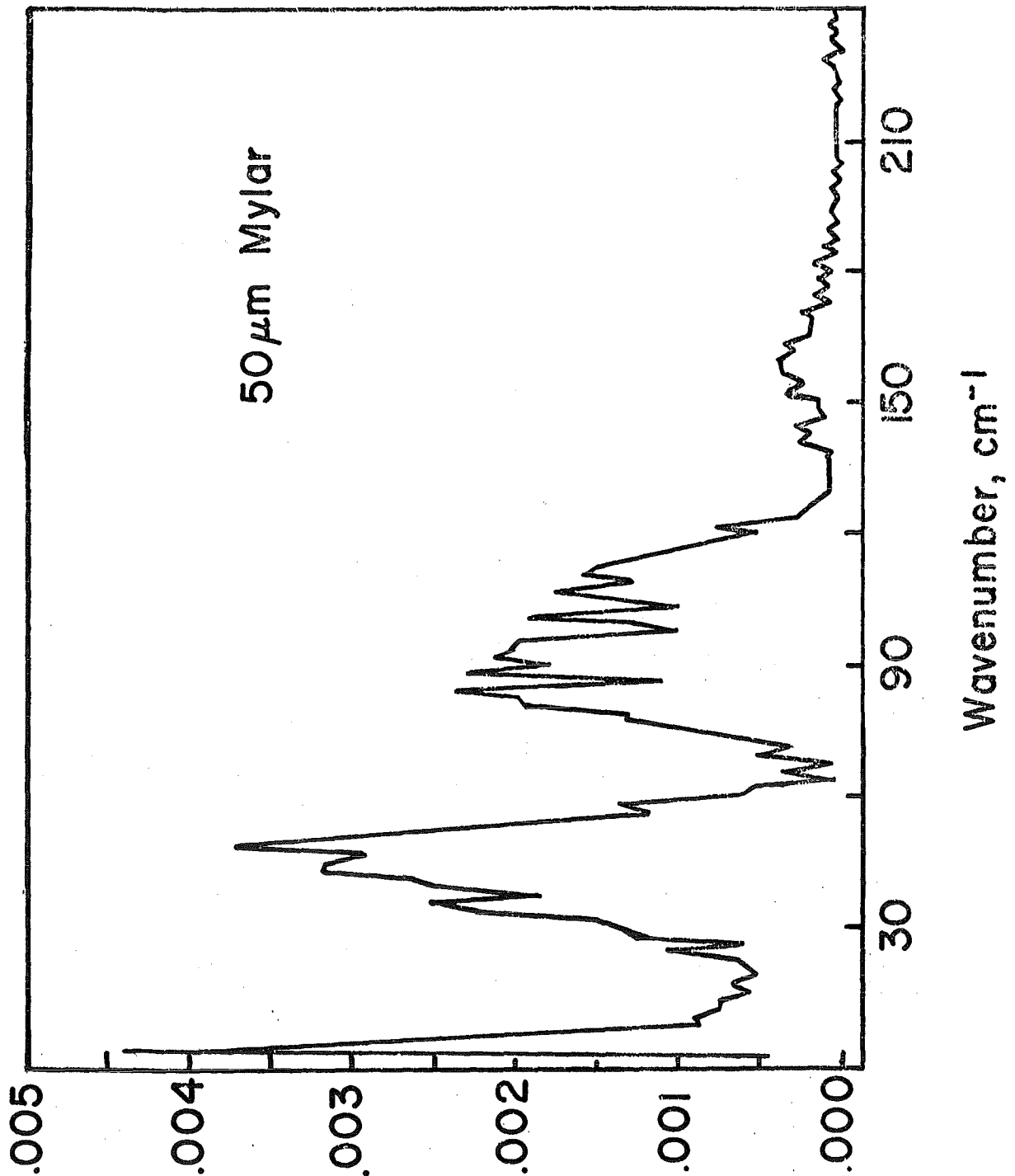


Figure 3 - Transmittance (arbitrary units) spectra obtained using a 50 μ m thick clear Mylar beamsplitter.

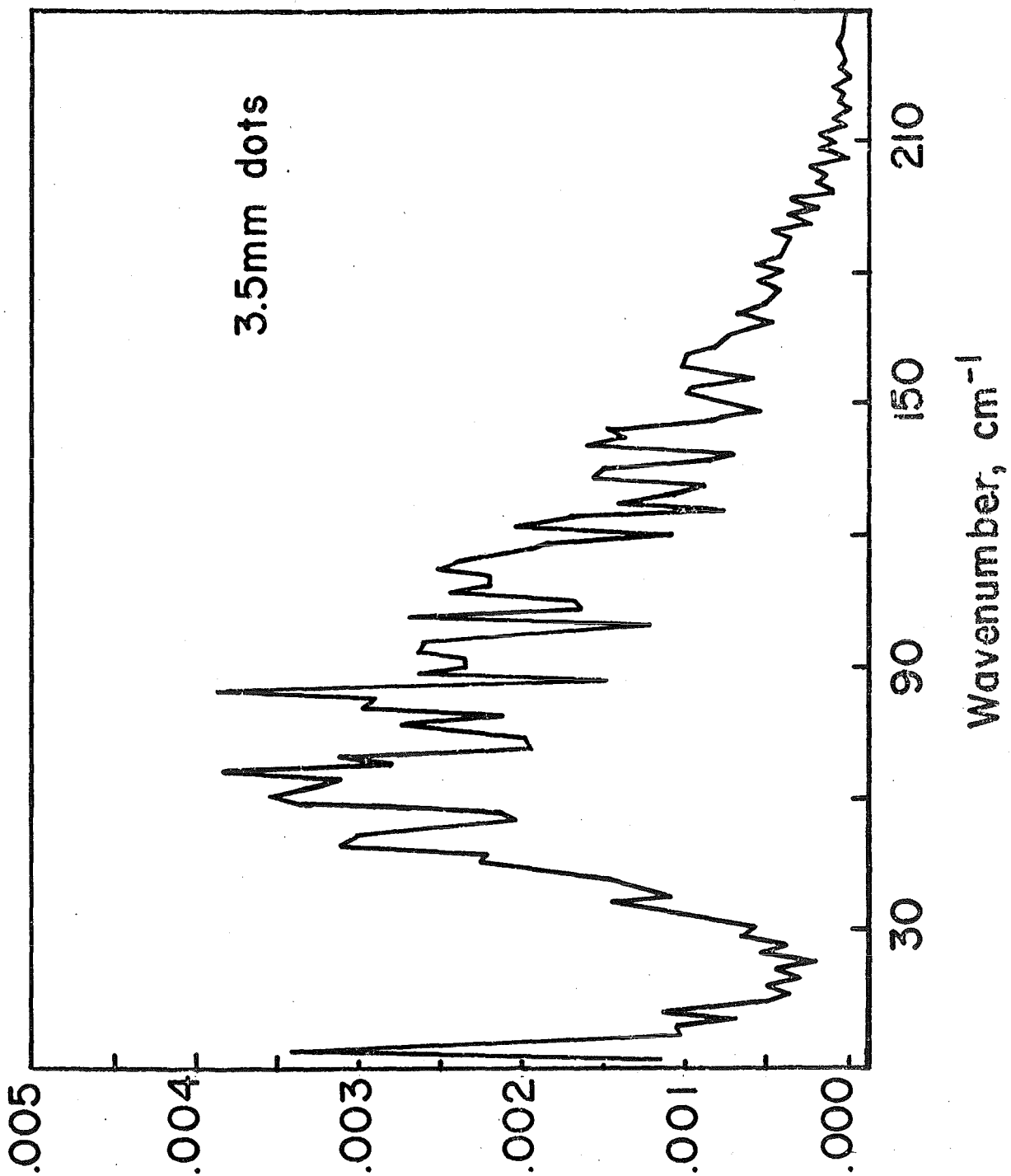


Figure 4 - Transmittance spectra (arbitrary units) obtained using a 3.5mm diameter, double-coated dot patterned beamsplitter.

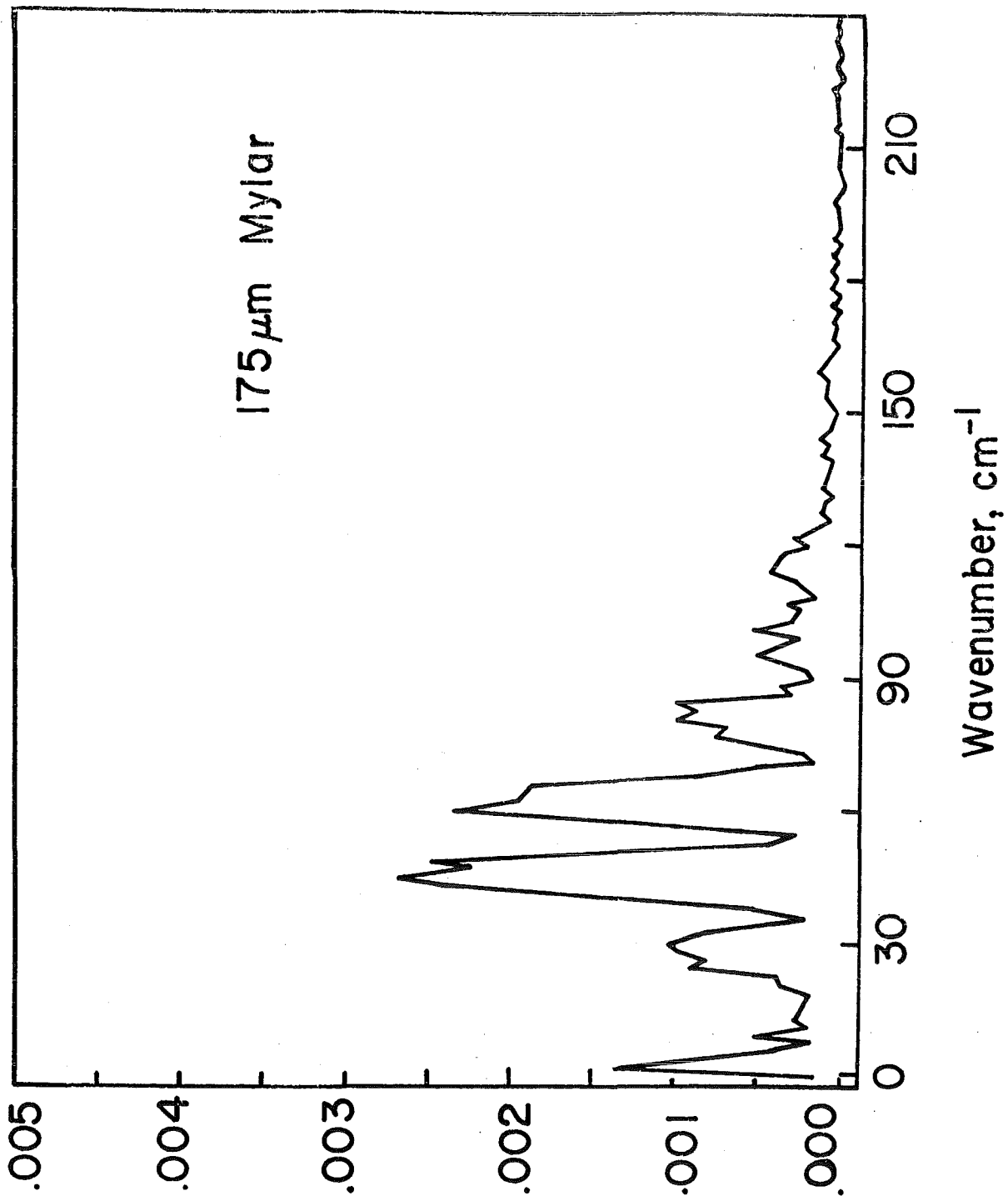


Figure 5 - Transmittance spectra (arbitrary units) obtained using a 175 μm thick, clear Mylar beamsplitter.

BLANK

III. OPTICAL PROPERTIES OF AEROSOLS

	PAGE
A. INFRARED EMISSION FROM AEROSOLS	185
B. NONLINEAR PHENOMENA AT HIGH ENERGY	187
C. INTERACTION OF RADIATION AND SPHERICAL (INCLUDING LAYERED) PARTICLES.	193
D. INTERACTION OF RADIATION AND NONSPHERICAL PARTICLES (INCLUDING AGGREGATES) WITH OR WITHOUT COOPERATIVE EFFECTS	223
E. PROPAGATION/MULTIPLE SCATTERING IN AEROSOL MEDIA AND RADIATIVE TRANSFER	337

BLANK

IR EMISSIVE CLOUD STUDY

P. Ase, R. Remaly and A. Snelson
IIT Research Institute
Chicago, Illinois 60616

ABSTRACT

An experimental program has been conducted to investigate pyrophoric materials and their explosive dissemination for the production of warm clouds with desirable IR emitting qualities. The following pyrophoric materials, pure, in solution and adsorbed on carbon were screened in the laboratory for this application: trimethyl aluminum, triethyl aluminum, trioctyl aluminum, diethyl aluminum, diethyl aluminum hydride, diethyl aluminum chloride, dibutyl aluminum ethoxide and diethyl zinc.

A system consisting of 10, 20 and 30% diethyl aluminum chloride adsorbed on carbon particulates was selected from both laboratory and preliminary field testing as offering good potential to achieve the program goals. Methods for explosively disseminating approximately 850 g of this material were developed. Six of these devices were tested at White Sands Missile Range. The reduced data from these tests are not yet available.

The above study was supported by the Chemical Systems Laboratory, Aberdeen Proving Ground, through the U.S. Army Missile Command, Redstone Arsenal, under Contract No. DLA 900-80-C-2853. The final report was submitted June 1983.

Further studies on these and other systems are currently under way.

BLANK

INTERACTION OF A 5 kW LASER BEAM
WITH PARTICULATE AEROSOLS

H. L. LaMuth, P. P. Balog, and K. W. Lee
Battelle, Columbus Laboratories
Columbus, Ohio 43201

ABSTRACT

Screening smokes and finely milled dielectric materials were uniformly dispersed within a newly designed and fabricated aerosol test chamber and subsequently exposed to CW CO₂ laser radiation at power levels up to 5 kW. Total optical extinction, and its corresponding absorption and 90 degree scattering components, were measured as a function of material concentrations and size distributions and of the laser fluence levels. Test data indicate that for the materials selected the absorbing materials provided significantly higher extinction than the scattering materials even at very high laser fluence levels.

INTRODUCTION

Battelle, Columbus Laboratories was under contract to Chemical Systems Laboratory, Research Division, to determine the ability of a variety of aerosols to be used as laser obscurants.* A number of candidate materials were identified and apparatus was fabricated to measure the extinction properties of these materials for CO₂ laser radiation. The selection process and preparation of the materials, the measurement and monitoring apparatus, and the test plan were discussed in an unclassified paper presented at Smoke/Obscurants Symposium VII held 26-28 April 1983 at Harry Diamond Laboratories in Adelphi, Maryland. That paper will appear in the unclassified proceedings of the Symposium. Test data and the detailed results will appear in the final report for the overall program. Therefore, only limited results are presented below.

BACKGROUND

A number of factors may be considered in selecting materials that could be used as obscurants to CO₂ laser radiation. These are material cost and availability, toxicity, effective extinction coefficient, efficiency, and ease with which a material can be disseminated and its persistence after dissemination. Each of these factors was considered in selecting candidate materials. In order to maximize persistence and efficiency, two particle size distributions were prepared, one with a mass mean diameter (MMD) of 1-2 μm and the other with an MMD of 3-4 μm . The majority of particles in these two distributions have physical diameters of a micrometer or less, which leads to extremely slow settling rates (less than 3.5×10^{-3} cm/sec) and very similar extinction for the two distributions for a given material. The test materials are shown on Figure 1. After preliminary grinding, the materials were each jet milled to achieve the proper size distributions.

*This work was sponsored by the Chemical Systems Laboratory, Research Division, under Contract Number DAAH01-81-D-A277, Mod. P00054, with Janon Embury COTR.

Additionally, quantification of both extinction and efficiency would be complicated by the potential for a laser beam to destroy the aerosol by vaporizing or burning it. Thus, materials that behaved as closely as possible to pure scatterers were selected for testing.

Two of the materials were used as references in order to quantify the portions of the total extinction associated with scattering and absorption. One reference was very fine soot (carbon black), which is nearly a perfect absorber. The other was NaCl, which has the lowest absorption properties of the candidates at $\sim 10.6 \mu\text{m}$. Also, because NaCl is relatively inexpensive, it was used extensively as a base material for testing and qualifying our experimental techniques. A third material, EA5763, is the material used in the IR grenades being developed by CSL for PM Smoke; EA5763 was used as a general effectiveness reference since extensive extinction data exist on it.

While particle shape greatly affects the extinction coefficient of aerosols, there was no attempt in this program to accommodate the differences among materials or to validate existing theories with the results. In general, while the crystal structures of the tested materials were different, jet milling further randomly shaped the particles. Thus, statistically, the aerosol shape factors should average out, and only the optical properties should determine the individual extinction coefficients.

INSTRUMENTATION

In order to measure the extinction properties of the aerosols, a number of different diagnostic techniques were necessary. One of the most critical elements of the experiment was to disseminate the aerosol in a way to achieve a known steady-state concentration. To this end a one-cubic-meter cylindrical chamber was fabricated. The chamber was made of Plexiglas, was 1.2 meters in diameter by 0.9 meter high, and was sealed at the top and bottom. Sampling ports, dissemination ports, and hermetically-sealed probes were installed for the various sensors. Also, two-inch NaCl windows were placed around the chamber perimeter to allow the scattered laser radiation to be measured. A three-inch laser input port and an eight-inch laser output port were also covered by NaCl windows. The system was completely sealed to prevent the aerosol from leaking from the test environment. A slow-speed, large-blade fan was used inside the chamber to achieve nonturbulent mixing.

The diagnostic instrumentation performed the following functions. Absolute and relative airborne aerosol concentrations were measured so that steady-state conditions could be achieved and monitored. Particle size distributions were measured to ensure that the airborne aerosol distribution did not differ from the prepared distribution. A single two-inch calorimeter was used to measure beam extinction and transmission. A cooled Mercury-Cadmium-Telluride radiometer was used to measure laser scattering at 90 degrees to the laser beam, while a large surface calorimeter was used to measure the integrated forward scattering of laser radiation. A photoacoustic spectrometer was used to measure laser radiation absorption by the aerosols. Absorption was compared to that for soot; scattering was compared to that for NaCl.

RESULTS

The initial phase of the program provided sufficient data to allow identification of the test materials with the largest extinction coefficients. The data were inadequate, however, for the identification of the test material with the highest extinction due to scattering because of (1) the added contributions of forward scattering, (2) too few test concentrations, and (3) the complex interrelationships between concentration and path length for quantifying the photoacoustic and 90-degree scattering detector output voltages.

Figure 1 shows how concentration affects the extinction, αC , where α is the areal extinction coefficient and C is the concentration. The mass mean diameters of the mass distributions for each material are also shown in the figure. Photoacoustic data show that those materials exhibiting the larger values (above 0.4 m^{-1}) for αC are also the only ones to exhibit measurable absorption (with the exception of NaCl at a concentration of 0.5 gm/m^3 , which is as yet an uncorroborated result). The 90-degree scattering data do not yield definite trends, though certain materials appear to be superior scatterers, i.e., 3-4 μm KCl, the road dust, and one uncorroborated point for EA5763 at a concentration of 0.7 gm/m^3 . The data also show that above certain fluence levels the physical characteristics of the materials are altered with melting and vaporization most likely occurring. Thus, the optical extinction exhibits nonlinear effects with regard to fluence levels.

The laser was also focused inside the test chamber for several materials. Above certain energy densities, these materials became incandescent. At the highest obtainable flux levels ($\sim 10^5 \text{ w/cm}^2$), no plasma formation was observed.

CONCLUSIONS

Absorbing materials tested in this program exhibited much higher extinction coefficients than the scattering (IR window) materials. Also, nonlinear effects were observed for certain materials as a function of power levels. That is, at higher laser powers, the extinction became greater than expected for the absorbing materials. This behavior was generally anticipated, which is why IR window materials were initially identified as candidate materials for CO₂ laser screening applications. It remains to be tested, however, whether the materials exhibiting the high absorption can also be good candidate screening materials in the presence of very high laser fluence levels. High fluence levels could lead to vaporization or other alterations in an aerosol's characteristics, thereby rendering it unfit as a screening material.

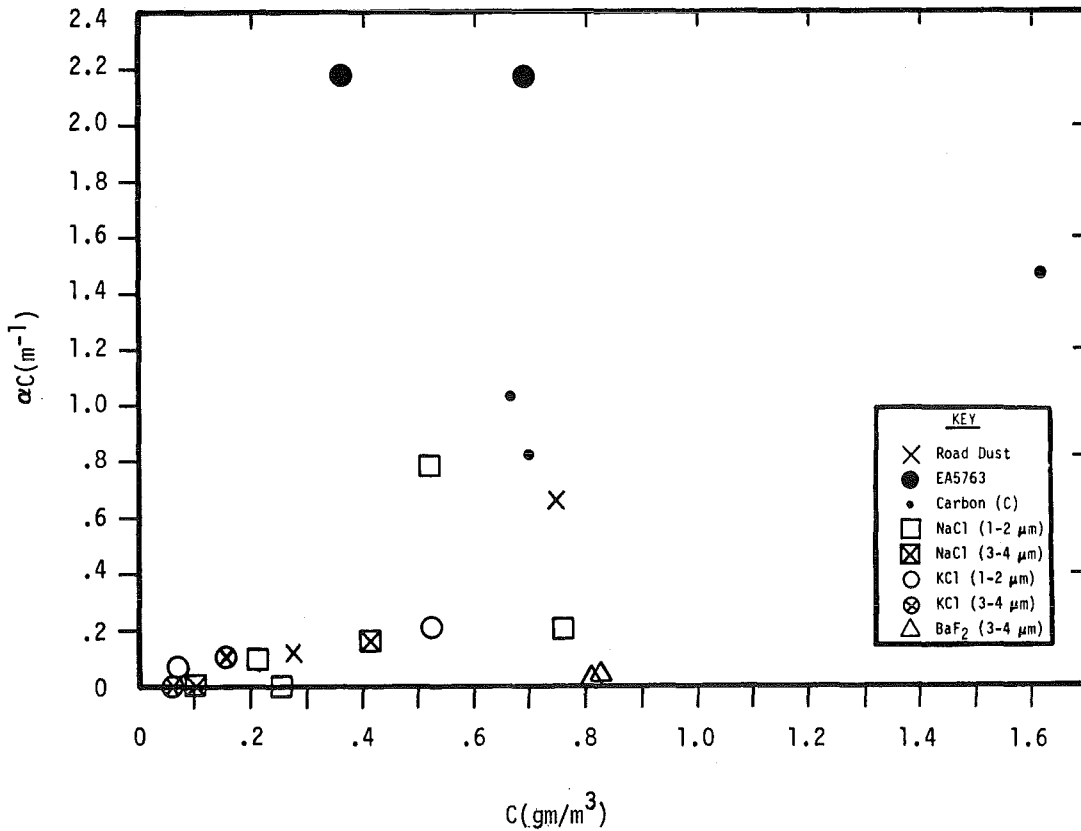


FIGURE 1. EXTINCTION AS A FUNCTION OF CONCENTRATION

HIGH ENERGY LASER INTERACTION WITH MATTER

M. Lax

Physics Department, City College of the City University of New York, New York, 10031

INTRODUCTION

We are concerned at this session with the propagation of a powerful laser beam through the atmosphere, and with the ability of aerosols, or smokes to attenuate this beam. I am the "new boy on the block," which means I don't know any of the answers. I am speaking at Ed Stuebing's request, so that I can act as a focus for any information you may have on the subject.

Most of the work in laser propagation and scattering has been done at power levels at which a *linear analysis* is possible. I shall exclude from this talk, any discussion of the linear problem, (on Thursday, however, I shall review briefly my own work on *linear* scattering of electromagnetic waves from a thin *dielectric, conducting fiber*.)

Since I know little about the subject, I have read the Proceedings of the Seminar on HEL Technology held in September 1981. I have also visited Lawrence Livermore Laboratory and talked to J. A. Fleck, Jr., J. R. Morris, and M. J. Feit about their work on "Time Dependent Propagation of High Energy Laser Beams Through The Atmosphere". I have also acquired a copy of their "FOURD" code, and have structured this code to improve its readability. However, even this reduced code is more than 8000 lines long. This code will obviously be easier to execute than to digest! At the typically quoted rate of 15 lines of debugged code per day, more than two years work was involved in writing it. Reports about it are dated from June 2, 1975 to December 15, 1978. I have written some much shorter code concerned with "Channeling of Intense Laser Beams" [J. Appl. Phys. 52, 109-125 (1981)]. Both of these codes, deal, in some approximation, with the hydrodynamics of the atmosphere as heated by the laser beam. However, *neither* code is *strictly* relevant to dealing with *discrete* particulates or aerosols.

At the opposite extreme is the final report "Aerosol Propagation Effects" by C. E. Caledonia and J. D. Teare of Physical Sciences Inc., which considers in detail the interaction of a laser beam with a single water droplet. In particular, the heating and vaporization of the droplet are considered under the assumption that the heating is uniform. Non-uniform heating of the droplet is considered within the geometrical optics approximation of the laser field. However, no solution is obtained for the case of non-uniform temperature distributions.

For the effect of the droplet on light propagation, Caledonia and Teare consider not only the heated droplet, but also the increase in temperature and water vapor in the region surrounding a droplet. They estimate the phase shift crudely using geometrical optics. They also average over a distribution of droplet sizes. Such linear average procedures can not be justified in a nonlinear problem.

At this conference a review has been given of work by James Wallace, David Smith and Fred Gebhardt (the latter using code due to H. Breaux) in which thermal blooming and an average treatment of the effect of aerosols is included in pulse propagation.

In summary, the "hole" in the literature on aerosols seems to be a *proper combined treatment of vaporization, heat conduction and convection* in the presence of non-uniform heating. In addition, one needs, probably, a wave-optics description of scattering and absorption by a droplet taking account of the modified index of refraction both inside, and in the vicinity of the droplet. If the problem were linear, and the droplets well separated, one could use the *cross section multiplied by a droplet concentration* to obtain a mean free path. However, we now have a non-uniform heating area localized in the vicinity of each droplet. The proper combination of hydrodynamics and beam propagation has not been attempted.

If we are concerned with *particulates*, melting will occur before *evaporation*. Moreover, a change in temperature, as well as a change into the molten state will have appreciable effects on the reflectivity and absorption of laser light. At sufficiently high powers one can have LSD (Laser Supported Detonation). For planar targets the *detonation* problem has been considered by A. Edwards, N. Ferriter, J. A. Fleck, Jr., and A. M. Winslow [UCRL-51689, "A Theoretical Description of the Interaction of a Pulsed Laser and a Target in an Air Environment"]. In this work, *non-uniform* heating is considered in detail, but for *planar* rather than spherical geometries. Also the above calculations were applied specifically to aluminum.

There is a question that can be raised about the above work, and proposed work. Is there a power level P_0 above which, we need not calculate the answer because vaporization, or melting (or plasma formation) is so important that any beam is highly attenuated? Conversely, will the region $P < P_0$ be treatable as a linear problem? In other words, will the interesting region be easy, and the difficult region not interesting? Murphy's law suggests the opposite will prevail!

LASER ENHANCED THERMOPHORETIC DEPOSITION

T.F. Morse, Brown University, Providence, R.I., U.S.A.
J.W. Cipolla, Jr., Northeastern University, Boston, Mass., U.S.A.

ABSTRACT

This paper concerns the influence of laser radiation on absorbing aerosol particles. The emphasis has been on physical situations pertinent to the processing of optical fiber preforms by the MCVD (Modified Chemical Vapor Deposition Process). This paper is to be published in Proceedings of the Third International Symposium on Lasers and Applications, Kanpur, India. Portions of this work are also to appear in the Journal of Heat Transfer and will be submitted to the Physics of Fluids.

When laser radiation interacts with an absorbing aerosol, volumetric heating induces temperature gradients in the gas supporting the aerosol. As a consequence of the fact that the aerosol particles are immersed in a gas with a temperature gradient, thermophoretic forces act upon the aerosol to move the absorbing particles from the path of the beam. Since thermophoresis is the dominant mechanism by which particles are deposited in the manufacture of optical fibers, our purpose is to investigate, both theoretically and experimentally, methods by which laser heating of a gas or aerosol will increase the rate of particulate deposition in such processes. We comment upon some preliminary experiments in which the phenomenon of laser induced thermophoretic motion has been clearly demonstrated. In addition, we will review a series of model problems that are pertinent to the actual geometries in which gradient index optical fibers are formed and shall indicate how laser radiation can markedly affect the efficiency with which aerosol particles can be deposited on a surface.

1. INTRODUCTION

It is by now an accepted fact that there is in progress an information revolution occasioned by the transmission of digital data over optical fibers. Their common place use will be facilitated as consequence of their greater bandwidth and their significantly lower cost/unit of information. It is estimated that by the year 1990, silicon based optical fibers will constitute a multi-billion dollar a year enterprise, replacing conventional copper cables.¹⁻³ The breakthrough in the transmission properties of the silicon-germanium fibers came over a decade ago when it was realized that previous high absorption losses were associated with trace impurities⁴, and that these could be eliminated by a Modified Chemical Vapor Deposition (MCVD) process in which oxygen is bubbled through silicon tetrachloride and germanium tetrachloride. The vapor pressure of impurities is higher than that of the silicon and germanium compounds, and this provides a mechanism by which these impurities can be removed. Consider oxygen along with the tetrachlorides of silicon and germanium flowing into a quartz tube on a glass lathe. The tube is then heated to 1500 K with a slowly moving burner; and within the tube, a chemical reaction produces the oxides of silicon and germanium as submicron sized aerosol particles that are thermophoretically deposited on the wall in front of the burner.⁵⁻⁷ See figure 1. By varying the ratio of the germanium tetrachloride to silicon tetrachloride in the reactants that provide the various layers that are deposited, it is possible to vary the index of refraction (germanium dioxide has a higher index of refraction than silicon dioxide) in successive layers to achieve a parabolic shape of the index of refraction as a function of radius. (The parabolic shape is desired due to the fact that rays that cross the axis and rays that are skew will have minimum dispersion between them for such a profile. This may be shown from a small perturbation solution of the Maxwell equations for wave transport in a graded index fiber).

After each layer is deposited, it is fused to the tube to form a vitreous, pore free layer, each layer with a different index of refraction, as a consequence of the different ratios of silicon dioxide/germanium dioxide. When the deposition process is completed, the tube is collapsed to form a solid rod from which the gradient index optical fiber is drawn. A rod will typically be of the order of 150 cm in length and 2 cm in diameter from which the order of ten kilometers of optical fiber will be drawn.

The motion of the aerosol particles in the deposition process is determined by the longitudinal component of the background gas velocity in the tube and the thermophoretic velocity of the aerosol which is proportional to the temperature gradient. In that which follows, we will attempt to indicate how this thermophoretic motion, responsible for aerosol deposition on the wall, may be increased with laser radiation.

2. THERMOPHORESIS

We have cited thermophoresis as the dominant mechanism by which particles are deposited on the tube wall, and it is perhaps appropriate to include a qualitative description of this phenomenon. When a particle is immersed in a background gas in which a temperature gradient is present, then, for the case in which this particle is of the order of the mean free path of the gas, it will be subjected to a thermophoretic

force in the direction of the lower temperature.⁸⁻¹⁰ This may be qualitatively understood by the following: molecules that originate one mean free path away on the high temperature side of the particle will exchange more energy and momentum with it than with molecules that impinge from the cooler side. For this reason, the net exchange of energy and momentum will be such that the particle is driven toward the low temperature gas. When the thermophoretic force and the drag associated with the ensuing particle motion are equated, the particle achieves a steady drift velocity of the form

$$V_T = -\frac{K\nu\nabla T}{T} \quad (1)$$

The kinematic viscosity is given by ν , and K is the thermophoretic coefficient which is dependent upon the mean free path and the thermal conductivities of the gas and the particle.¹¹ For our purposes here it shall be taken to be of order one and constant. The coupling of the aerosol concentration to the temperature gradients in the gas is of particular interest when the aerosol is responsible for the non-uniform temperature through absorption of the external radiation.

For particles that have a complex index of refraction and whose diameters are small compared with the wavelength with which they interact, the absorption coefficient will be given by the Rayleigh limit.¹²⁻¹⁴

$$\kappa = C\pi^2 \frac{d^3}{\lambda} I_m \left(\frac{n^2-1}{n^2+2} \right) \quad (2)$$

For silicon dioxide aerosol particles, the dominant component of the aerosols we study, with a complex index of refraction given by $n = 1.9 - 0.3i$,¹⁵ and interacting with $10.6\mu\text{m}$ radiation, a particle concentration of 10^{11} particles/ cm^3 will produce an absorption coefficient of the order of $.1 \text{ cm}^{-1}$. In our sample calculations, this will be the base value used for attenuation of laser radiation by aerosol particles.¹⁶ Since the absorption coefficient is proportional to local aerosol particle concentration, it will depend, in general, upon space and time.

3. LASER INTERACTION WITH AN ABSORBING AEROSOL

We have demonstrated experimentally that an aerosol may interact with laser radiation in such a manner as to induce not only convective motion but thermophoresis as well. When aerosol particles absorb laser radiation, they become heated, and on a time scale that is determined by thermal diffusivity and aerosol size, "instantaneously" (tens of microseconds) heat the surrounding gas. An intensity distribution in the laser beam becomes mirrored in the resulting gas temperature inducing thermophoretic forces that move the particles away from the laser beam and, in particular, from the region of maximum intensity.¹⁷⁻¹⁸ In order to observe this phenomenon, it is necessary that the more pronounced convective motions associated with buoyant heating not obscure the thermophoretic effects. That is, the convective motion must be at ninety degrees to the direction of thermophoretic motion in order that the smaller thermophoretic motion not be masked.

In figure 2a and 2b we see examples of such a qualitative experiment. A dense aerosol of titanium dioxide is enclosed in a tube 18 mm wide and 60 cm long, and the tube is held in the vertical position. Approximately ten Watts of laser radiation impinge on the top of the tube which is covered with an i.r. transmitting window. In figure 2a we see that the tube is completely obscured by the dense aerosol contained within it. In figure 2b we see the results of an interaction of approximately 10 Watts of carbon dioxide laser radiation with the aerosol. Initially, a buoyant motion upward is induced by the "instantaneous" laser heating which serves as a volumetric heating source. As natural convection moves the aerosol upward, absorption of the Gaussian laser beam induces a radial temperature gradient in the aerosol. Consequently, each particle experiences a self-induced temperature gradient and an outward force that, after a time the order of a second or two, clears the central region of all aerosol particles. This is a self-limiting process in that the particles responsible for the absorptive heating in the center of the laser beam induce a temperature gradient that moves them away from the beam. This is the mechanism that allows the beam to pass through the aerosol with essentially no attenuation. Such a thermophoretic "hole" is clearly indicated in figure 2b. It extends the full 60 cm of the tube with no change in radius as a function of height. This observation has led us to consider the one-dimensional calculations that will be done in the following.

4. THE FUNDAMENTAL EQUATIONS

The equations that describe the interaction of the laser radiation with either an absorbing aerosol or an absorbing gas are the energy equation, the equation of particle continuity, and the momentum equation. Although only specialized cases will be examined, we present these equations in a general form. The

energy equation, with a neglect of viscous dissipation and axial conduction (when compared with radial conduction), may be written as

$$\rho \underline{U} \cdot \nabla c_p T = k \nabla^2 T - \nabla \cdot \underline{q}_R \quad (3)$$

The divergence of the radiative heat flux vector \underline{q}_R is a term associated with laser heating. Since we are considering only aerosol-radiation interaction in the Rayleigh limit, and since re-radiation is neglected in these calculations, we may restrict our subsequent analysis to absorption. In this limit, the solution of the equation of radiative transfer may be expressed as follows.

$$\nabla \cdot \underline{q}_R = -\kappa I(r') \exp\left(-\int_0^x \kappa dz\right) \quad (4)$$

The absorption coefficient, κ , is, in general, dependent upon space and time; $I(r')$ is the radial distribution of laser intensity at wavelength λ .

The aerosol particles, typically much less than a micron in diameter, are not influenced by gravitational settling on the time scales of interest. Further, since there is a thermophoretic force on the particles associated with the temperature gradient, the particle path lines will not follow the fluid streamlines. We may write the steady state aerosol continuity equation as follows.

$$\underline{U} \cdot \nabla c = \nabla \cdot (D \nabla c - c \underline{V}_T) \quad (5)$$

where c is the particle concentration in gms/cm^3 , D is the coefficient associated with Brownian motion, and \underline{V}_T , the thermophoretic velocity, has been described above.

The steady state momentum equation describing the motion of the aerosol and background gas may be written in standard notation (assuming incompressible gas flow).

$$\rho \underline{U} \cdot \nabla \underline{U} + \rho \underline{g} + \nabla p = \mu \nabla^2 \underline{U} \quad (6)$$

where \underline{U} is the fluid velocity, p the pressure, \underline{g} the gravitational constant, and μ the dynamic viscosity. In that which follows, we will consider either the absence of macroscopic velocity, which corresponds to our qualitative experiment described above, or limit our analysis to the simple case of Poiseuille flow. In another work, we have used the Boussinesq approximation on the momentum equation to obtain a lowest order analysis of the effects of coupled buoyancy and thermophoretic motion.¹⁷

5. ONE-DIMENSIONAL ANALYSIS OF THERMOPHORETIC HOLE

We have shown in figure 2b a photograph of a thermophoretic hole induced in a dense, vertical, confined aerosol with approximately 10 Watts of $10.6\mu\text{m}$ CO_2 laser radiation. The stability of this hole was such that it was possible to move the mirrors guiding the laser into the vertical tube, and the aerosol particles would "avoid" the beam so that it was possible to "move" the hole. In this section, we wish briefly to analyze the equations that present a description of this phenomenon. The hole in figure 2b allows the laser beam to pass through the aerosol unattenuated. There is no measureable variation in this void over the vertical length of the 60 cm tube, so there appears at least some justification in making, as a lowest order analysis, an assumption of one dimensionality. This permits us to analyze the general equations to seek a balance between radial heat conduction, diffusion, and the thermophoretic force acting on the particulate distribution. In that which follows, we simplify our geometry to consider an aerosol confined between two parallel plates irradiated by constant laser intensity. The boundary conditions will be such that the walls will be at a constant temperature; and, with a given total amount of aerosol between the plates, we will examine the aerosol distribution as a function of laser intensity. Our energy equation for this simple one-dimensional case may be written as follows.

$$k \frac{d^2 T}{dx^2} + \kappa I = 0 \quad (7)$$

where for boundary conditions $T(+L/2) = T(-L/2) = T_w$. The equation for particle continuity may be written as

$$D \frac{dc}{dx} + cK \frac{dT}{dx} = 0 \quad (8)$$

The volumetric heat addition to the gas, for this simple case, is given by κI , where I is assumed to be uniform over the cross section of the enclosure. The absorption coefficient, κ , is proportional to the local particle concentration, c . The total laser power per unit width is given by $P = I/L$. The continuity equation simply states that in a one-dimensional system we must demand that the aerosol flux vanish. In this example, it is necessary to retain the contribution associated with the diffusion coefficient, and the continuity equation has a particularly simple solution.

$$c T^\gamma = \text{const} = c_w T_w^\gamma \quad (9)$$

where

$$\gamma = K \frac{\nu}{D} = KSc \quad (10)$$

and Sc is the Schmidt number. We now introduce dimensionless variables, $\psi = T/T_w$, $\phi = c/c_w$, $\kappa = \kappa_i \phi$, $x' = x/L$. The subscripted "i" terms are constant. This leads to a simple combined energy and continuity equation given as follows.

$$\frac{d^2\psi}{dx^2} + \left(\frac{L\kappa_i P}{kT_w}\right) \phi = 0 \quad (11)$$

and

$$\phi \psi^\gamma = \phi_w \quad (12)$$

with $\psi(+1/2) = \psi(-1/2) = 1$. For problems of interest, the Schmidt number will be of the order of several thousand. If we examine equation (12) in the limit of large Schmidt number, we observe immediately the effects of laser radiation. If ψ , the dimensionless temperature, is ever so slightly larger than 1.0, the value at the wall, then, it being raised to a very large power, γ , which is essentially the Schmidt number, will cause ϕ to be extremely small. Thus, any laser heating, in the steady state solution, will cause the particle density to be zero at that point. This is, essentially, the physical explanation for the observed presence of the thermophoretic hole, and the reason why laser radiation can be employed to increase particle deposition efficiency. Proceeding further with our simplified analysis, we note that particle conservation demands that

$$\int_{-1/2}^{1/2} \phi \, dx = 1 \quad (13)$$

and using the solution of the particle continuity equation

$$\phi_w = \left(\int_{-1/2}^{1/2} \psi^{-\gamma} \, dx\right)^{-1} \quad (14)$$

This allows us to write the energy equation solely in terms of the normalized temperature as follows.

$$\frac{d^2\psi}{dx^2} + L\kappa_i \frac{P}{kT_w} \psi^{-\gamma} \phi_w = 0 \quad (15)$$

This equation is now an integral equation as indicated by equation 14. It is convenient to define a parameter $G = \frac{L\kappa_i P}{2kT_w}$, and, after some analysis, we may write the solution to the energy equation in the large γ limit as

$$\psi = \psi_o \left[\cos(2x \cos^{-1}(\psi_o^{-\gamma/2})) \right]^{2/\gamma} \quad (16)$$

where ψ_o may be obtained from enforcing the wall boundary condition. This condition leads to the following expression.

$$(\psi_o^{-\gamma} - 1)^{-1/2} \frac{G\gamma}{4} = \tan^{-1}[\psi_o^{-\gamma/2}]^{1/2} \quad (17)$$

We now examine these solutions for the product $G\gamma$ large. This will hold for any laser powers of interest as a consequence of the size of the Schmidt number. The solution for the normalized center line temperature is given as

$$\psi_o = \exp\left[\left(\frac{2}{\gamma}\right) \ln\left(\frac{G\gamma}{2\pi}\right)\right] \left[1 + \frac{2}{\gamma} \ln\left(\frac{G\gamma}{2\pi}\right) \right] \quad (18)$$

The asymptotic result holds for $1 \ll G\gamma \ll 2\pi \exp(\gamma/2)$. We now may use Eq. (18) to eliminate ψ_o in Eq. (16) and present the lowest order solution as

$$\psi = \left[(G\gamma/2\pi)(\cos\pi x + (4\pi x/G\gamma)\sin\pi x) \right]^{-\frac{2}{\gamma}} \quad (19)$$

Substituting (19) into (14) and (12) then gives the solution for the dimensionless particle concentration.

$$\phi = \frac{\pi^2}{G\gamma} (\cos\pi x + (4\pi x/G\gamma)\sin\pi x)^{-2} \quad (20)$$

At the wall, $x = 1/2$; this becomes $\phi_w = \frac{G\gamma}{4}$. The principal results of this simple calculation are plotted in figure 3 for various values of $G\gamma$. The values of this parameter are 0.1, 10, 100, 1000, 10,000, and 20,000, and correspond, respectively, to laser powers of 0.002, 0.2, 2, 20, and 40 Watts. This is for the model system we have chosen with an initial absorption coefficient of 0.1 cm^{-1} . The curve shown for $G\gamma = 0.1$ was obtained from the exact solution given by equations (16) and (17).

The principal conclusion that may be drawn from this simple analysis is that, in situations where convection does not mask thermophoresis, the particles will be ultimately driven from the beam region with great effectiveness. This corresponds to the physical situation shown in figure 2b. In addition, as a consequence of the removal of particles from the beam, the heating caused in the steady state case is minimal.

Thus, the thermophoretic removal of particles from the beam region produces a self-limiting feature of beam absorption. Again, it is to be noted that this is to be the case only when buoyancy does not induce convective motion that will mask the appearance of this effect.

Although not described in detail here, we also wish to call attention to the fact that the above simple solution is only for a steady state analysis, and that there may well be significant transient heating before the particles evacuate the beam region. Other analyses we have carried out confirm this speculation, and the heating, even for the absorption coefficient used here, can be quite severe, i.e., of the order of several thousand degrees. At this point, it is clearly necessary to consider re-radiation from the heated particulate matter, and this is presently being examined. Our conclusions from this section and from our qualitative experiments indicate the presence of a "thermophoretic hole" when steady state has been reached and that only modest amounts of laser power are necessary to achieve this steady state. Naturally, the rate at which this asymptotic condition is approached will be a strong function of laser power. We are now conducting experiments in our laboratory of a more quantitative nature with a Coherent Radiation Model 41C industrial laser, with 275 Watts CW, and it is expected that more interesting results will be forthcoming in the near future.

6. LASER ENHANCED DEPOSITION PROCESSES IN MCVD

We have qualitatively described above how optical fiber preforms are made in the Modified Chemical Vapor Deposition Process (MCVD). In this section, we wish to consider how laser radiation can modify the efficiency with which particles in this process are deposited. Again, we will specify the geometry of figure 1. Oxygen and gaseous silicon tetrachloride with dopant germanium tetrachloride pass through a quartz tube on a glass lathe. The burner heats the reactants to produce an aerosol of silicon and germanium dioxide that deposits in front of the burner. As the gas carrying the aerosol moves downstream, its temperature decays approximately exponentially; and the thermophoretic force, proportional to the temperature gradient as discussed above, becomes vanishingly small. Typical deposition efficiencies for such a process are of the order of 50%. In an attempt to increase this deposition, we consider the interaction of laser radiation along the axis with the absorbing particulate matter. It is this particle concentration dependent absorption coefficient that couples the energy equation to the concentration equation in a highly nonlinear manner, thus necessitating numerical solutions. For this simple geometry, equation 3, the energy equation, may be written as follows.

$$\rho c_p U \frac{\partial T}{\partial z'} = k \frac{1}{r'} \frac{\partial}{\partial r'} r' \frac{\partial T}{\partial r'} + \kappa I \quad (21)$$

If we make equation 21 dimensionless with respect to $z' = r_0 z \text{ Pe}$, where Pe is the Peclet number, $r' = r/r_0$, $\Theta = T/(T_{\text{min}} - T_{\text{max}})$, and $U = U_m (1 - r^2)$. Thus, the energy equation becomes, in the large Pe limit,

$$(1 - r^2) \frac{\partial \Theta}{\partial z} = \frac{\partial^2 \Theta}{\partial r^2} + \frac{1}{r} \frac{\partial \Theta}{\partial r} + Q \quad (22)$$

As before, the volumetric laser heating term must be obtained from the equation of radiative transfer, and

$$Q = \kappa I_0 \frac{\exp(-\beta r_0^2 - \int_0^z \kappa dz)}{k(T_{\text{max}} - T_{\text{min}})} \quad (23)$$

where κ is proportional to the concentration, c . Using the value of the thermophoretic velocity from equation 1 in the continuity equation, (5), with the neglect of Brownian diffusion (negligible as a consequence of the large Schmidt number), and with $c/c_0 = \phi$, we obtain the following expression.

$$(1 - r^2) \frac{\partial \phi}{\partial z} = Pr K \frac{1}{r} \frac{\partial}{\partial r} \left[\frac{r \phi}{\Theta} \frac{\partial \Theta}{\partial r} \right] \quad (24)$$

Thus, equations 22-24 represent a coupled set of non-linear partial differential equations that must be solved numerically. The numerical techniques are quite straightforward and have been discussed in some detail elsewhere.¹⁸ We consider two sets of boundary conditions for our tube flow: first, an extension of the classic Graetz problem, in which a fully developed velocity profile enters a tube section with a temperature T_{in} , with the walls held at a colder temperature, T_w . See references 19-21.

For a sample calculation, we consider some parameters that are relevant to the conditions under which optical fiber preforms are made. The average gas temperature at which properties are evaluated is taken to be 1100 K, the kinematic viscosity $\nu = 1.386 \cdot 10^{-4} \text{ m}^2/\text{s}$, the thermal conductivity for oxygen at this temperature is given as $k = .0732 \text{ W/m K}$, the thermal diffusivity $\alpha = 1.97 \cdot 10^{-4} \text{ m}^2/\text{s}$, and the Prandtl number is taken as 0.7. In figure 4 we see the solution of the coupled energy and particle continuity equations for the case in which the inlet temperature is taken as 1500 K, and the wall temperature is 500 K. The aerosol concentration is such that the absorption coefficient at the inlet is $\kappa_0 = .1 \text{ cm}^{-1}$. This is a typical value for the absorption of 10.6 μm radiation by a silicon dioxide aerosol. We have also chosen the thermophoretic coefficient, K , to be equal to 0.9, a value somewhat high, but this compensates to some

degree to our assumption of constant thermal properties.⁶ Since we have used the assumption of a Poiseuille velocity distribution in our tube, it is a simple matter to obtain particle deposition efficiency as a function of which is the last particle pathline to impact with the tube. This is shown in figure 5. For example, for a particle starting at an initial value of $r = 0.5$, the deposition efficiency is approximately 50%. This represents a typical value for such processes.

Our numerical analysis of the energy equation, for the case of zero radiation, may be done (for the case of constant gas properties) independently of the equation for particle concentration. The results of this solution are identical to those of the eigenvalue solution of Graetz and others.²⁰⁻²² However, when laser radiation interacts with the absorbing particulate matter, through the volumetric heating term, the energy equation is coupled in a highly non-linear manner to the equation of particle conservation as described above. We assume, at this point, that the momentum equation is represented by the fully developed Poiseuille parabolic velocity distribution. In reality, extremely complicated secondary flows will be present in the actual experiment, and these will be a subject of a future investigation. In figures 6-7, we see the result of increasing laser intensity, when compared with figure 4. A parameter β that gives the half width of the laser intensity is taken to be 1.43 cm^{-1} . The maximum temperature reached in this series of calculations is 1900 K which corresponds to an additional 400 K of heating as a consequence of the presence of the axial laser. It is clear that this degree of heating will increase deposition efficiency but that further heating would be desirable. These particle pathlines are shown in figure 7. Additional heating could be accomplished by the addition of a saturable absorber such as SiF_4 that can be created at the location of the torch by dissociation of freon and reaction with SiCl_4 .

We now may consider the effects of laser enhanced thermophoresis with a wall temperature distribution that approximates the experimental source of wall heating. We assume a quadratic increase in temperature from 0 to L_1 .

$$T = T_{in} + (T_{max} - T_{min}) \frac{z^2}{L_1} \quad (25)$$

where T_{in} is the inlet temperature at $z = 0$, and T_{max} is the maximum wall temperature. From L_1 to L_2 we assume a linear decrease in temperature as follows.

$$T = T_{max} - (T_{max} - T_{min}) \frac{(z - L_1)}{L_2} \quad (26)$$

We consider an inlet temperature of 1000 K, a maximum wall temperature of 2000 K, $L_1 = r_0 Pe$ (20 cm), and $L_2 = 0.1 r_0 Pe$ (2cm), with the mean flow velocity taken as 0.2 m/s. It is further assumed that the wall temperature is constant beyond L_2 and is equal to T_{min} . Figures 8-10 show the result of increasing axial laser radiation, and in figure 11 we see a comparison for the deposition efficiency as a function of length. The maximum temperatures reached as a consequence of laser heating are 1900 K for 20 W/cm^2 , 2300 K for 80 W/cm^2 , and 2750 K for 120 W/cm^2 . These latter temperatures are such that vaporization of the silicon dioxide aerosol particles will occur; however, it does indicate that significant additional heating can occur with lasers of not unrealistically high power.

7. CONCLUSIONS

We have indicated how the laser radiation interacting with an absorbing aerosol can significantly influence the distribution of aerosol particles by the process of thermophoresis. In a situation in which it is possible to create buoyant convection at 90 degrees to the thermophoretic motion associated with laser heating, a region void of particles becomes evident. This thermophoretic hole has been observed experimentally, and has been analyzed with some simple one-dimensional considerations. We have also considered a two-dimensional flow situation that models the thermophoretic deposition process used in the fabrication of preforms from which gradient index optical fibers are drawn and have indicated that the addition of axial laser radiation may significantly improve particulate deposition in such processes.

8. ACKNOWLEDGEMENTS

This work was sponsored by a grant from the National Science Foundation through the Heat Transfer Program, Division of Mechanical Engineering and Applied Mechanics. The numerical calculations presented in this work were carried out on the Brown University Division of Engineering VAX 11-780 computer. The acquisition of this computer was made possible by grants from the National Science Foundation, the General Electric Company, and the Digital Equipment Corporation. We are also grateful for the use of the LEMS VAX computer at Brown University to text edit the manuscript and for the assistance of Prof. D. Bulterman in this task.

9. REFERENCES

- (1) E.A. Lacy, *Fiber Optics* (Prentice-Hall, Englewood Cliffs, New Jersey, 1982).
- (2) Yasuharu Suematsu and Ken-Icha Iga, *Introduction to Optical Fiber Communications* (John Wiley & Sons, New York, 1982).
- (3) The Winter 1980 issue of *The Western Electric Engineer* is completely devoted to various aspects of optical fibers and is a good introductory reference.
- (4) F.P. Kapron, D.B. Keck, and R.D. Maurer, *Appl. Phys. Lett.*, vol. 17, pp. 423-425, 1970.
- (5) P.G. Simpkins, S. Greenberg-Kosinski, and J.B. MacChesney, *J. Appl. Phys.*, 50, p. 5767 (1979).
- (6) K.L. Walker, F.T. Geyling, and S.R. Nagel, *J. Am. Ceramic Soc.*, vol. 63, p. 552 (1980).
- (7) K.L. Walker, G.M. Homsy, and F.T. Geyling, *J. Colloid. Interface. Sci.*, 69, p. 138 (1979).
- (8) N.A. Fuchs, *The Mechanics of Aerosols* (The MACMILLAN Co., New York, 1964).
- (9) G.M. Hidy and J.R. Brock, *The Dynamics of Aerocolloidal Systems*, International Reviews in Aerosol Physics and Chemistry, vol. 1, Pergamon Press, N.Y., 1971.
- (10) James R. Brock, *J. Colloid. Sci.*, 17, p. 768-780 (1962).
- (11) L. Talbot, R.K. Cheng, W.W. Schefer, and D.R. Willis, *J. Fluid Mech.*, vol 101, 1981, p. 737.
- (12) Gustav Mie, *Ann. d. Physik*, vierte Folge, Band 25, 1908, p. 377.
- (13) H.C. van de Hulst, *Light Scattering by Small Particles* (John Wiley and Sons, New York, 1957).
- (14) M.Kerker, *The Scattering of Light and Other Electromagnetic Radiation* (Academic Press, New York, 1956).
- (15) I. Simon and H.O. McMahon, *J. Am. Ceramic Soc.*, 36, p. 160, (1953).
- (16) T.F. Morse and J.W. Cipolla, Jr., *J. Colloid. and Interface. Sci.*, to be published.
- (17) C.Y. Wang, T.F. Morse, and J.W. Cipolla, Jr., *J. Heat Transfer*, "Laser Induced Natural Convection and Thermophoresis", to be published.
- (18) J. Cipolla, Jr., T. F. Morse, and C.Y. Wang, "Laser Induced Thermophoresis and Particulate Deposition Efficiency", Presented at A.S.M.E. Heat Transfer Meeting, Seattle, Wash., July, 1983.
- (19) L. Graetz, *Ann. d. Physik*, vol 25, 1885, pp. 337-357.
- (20) J.R. Sellars, M. Tribus, and J.S. Klein, *Trans. A.S.M.E.*, vol. 78, 1956, p. 441.
- (21) R.K. Shah and A.L. London, *Advances in Heat Transfer*, Supplement 1, 1978.

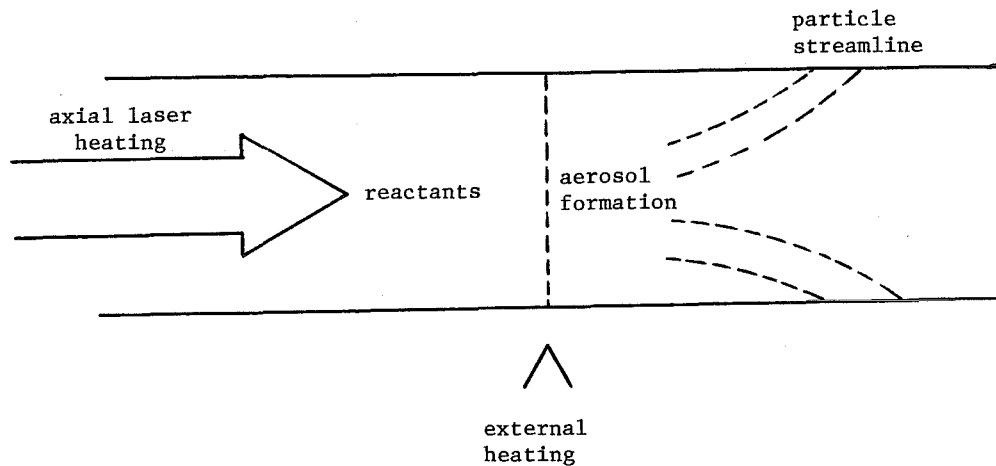


Fig. 1. Configuration

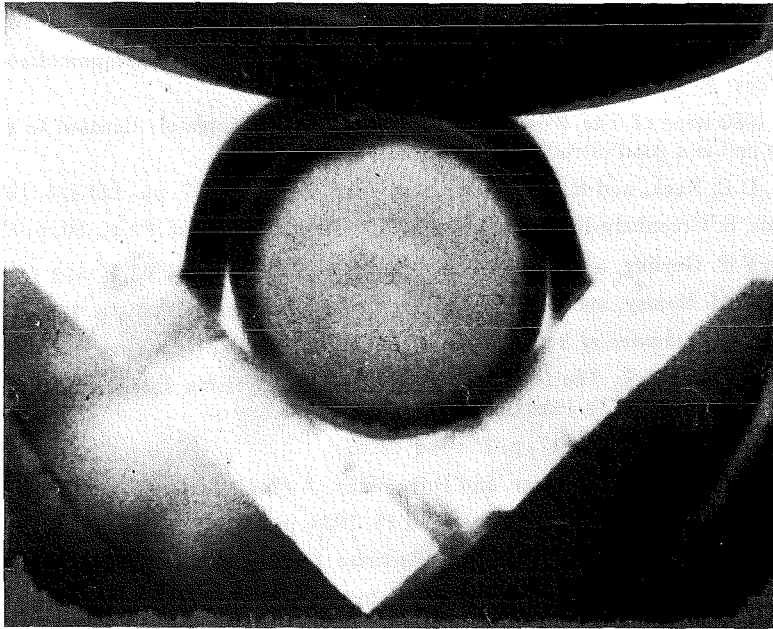


Fig. 2A. End of aerosol filled vertical tube, laser off

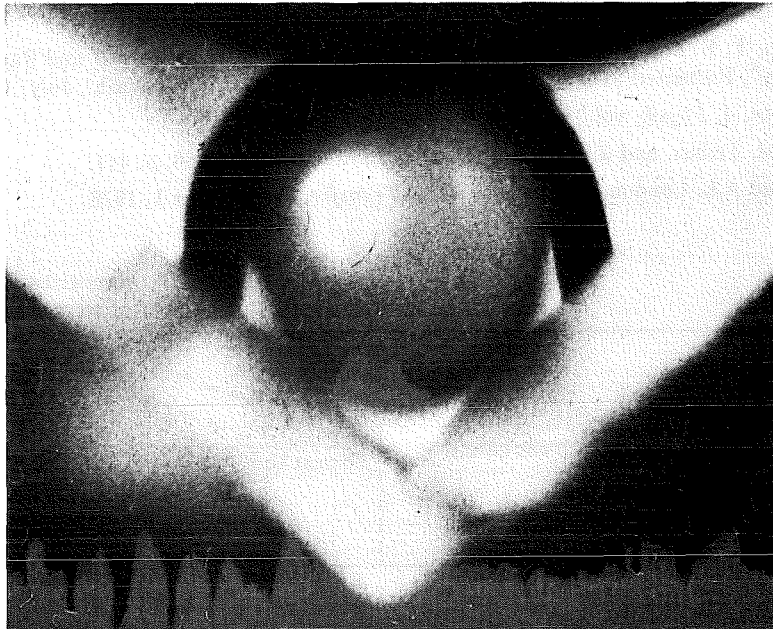


Fig. 2B. End view of aerosol filled vertical tube, laser on. "Laser induced thermophoretic hole"

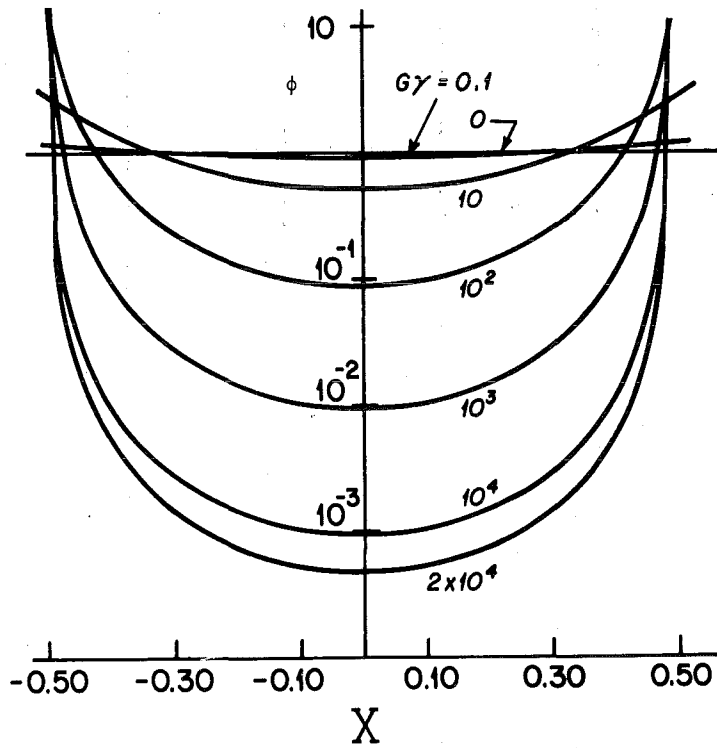


Fig. 3

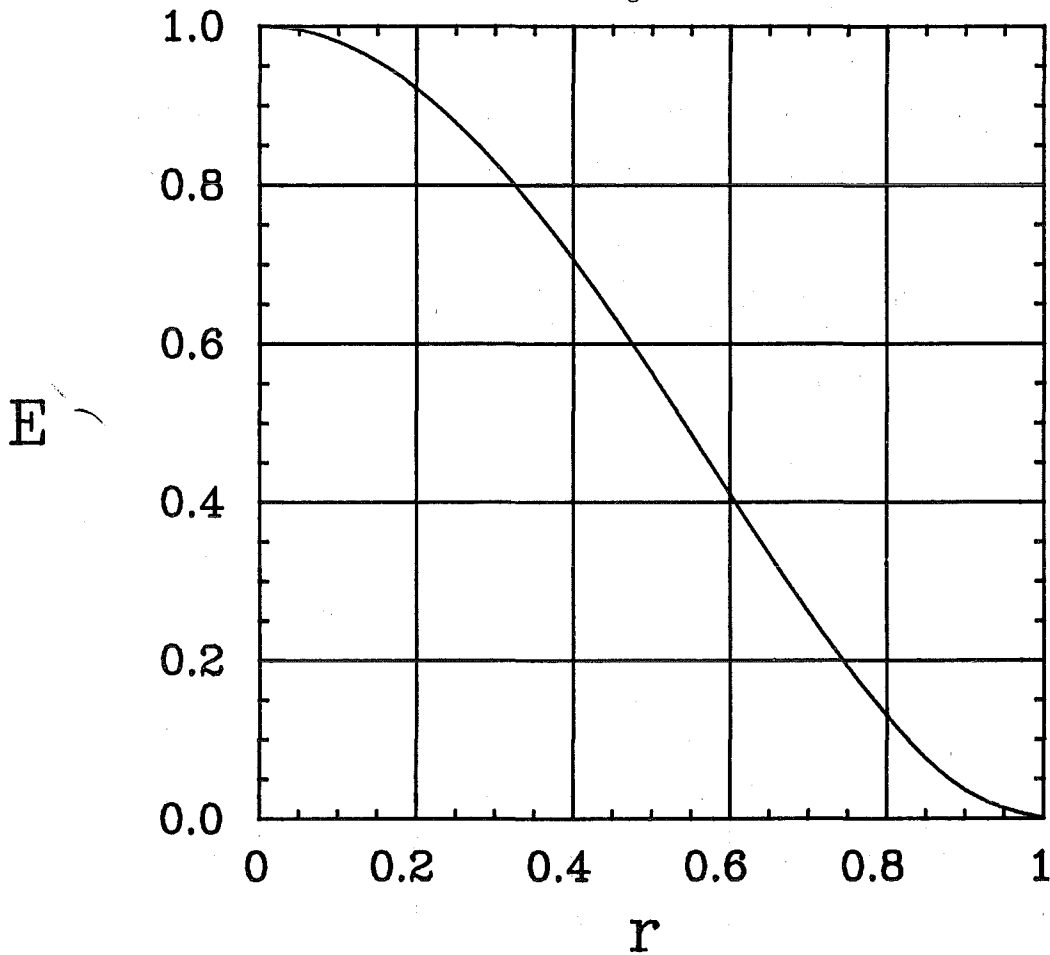


Fig. 4. $E = 1 - 2r^2 + r^4$

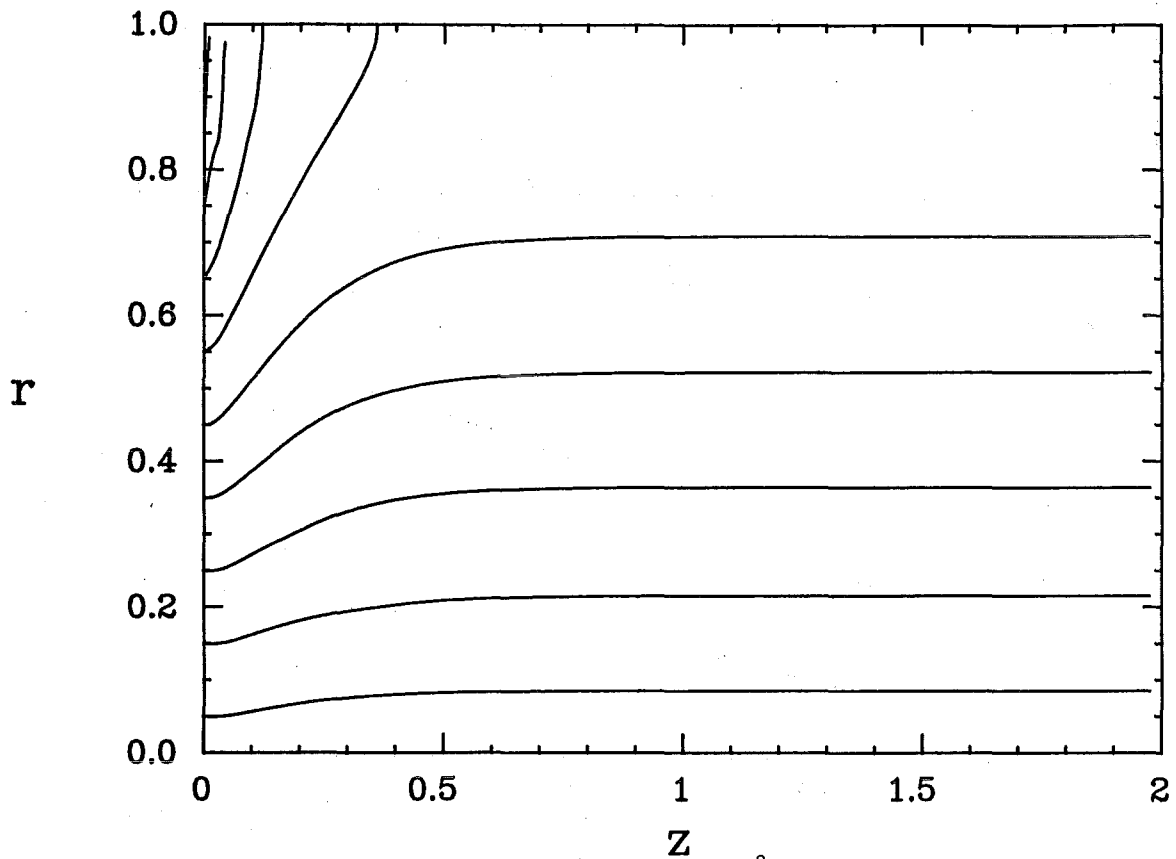


Fig. 5. $I_0 = 0 \text{ W/cm}^2$

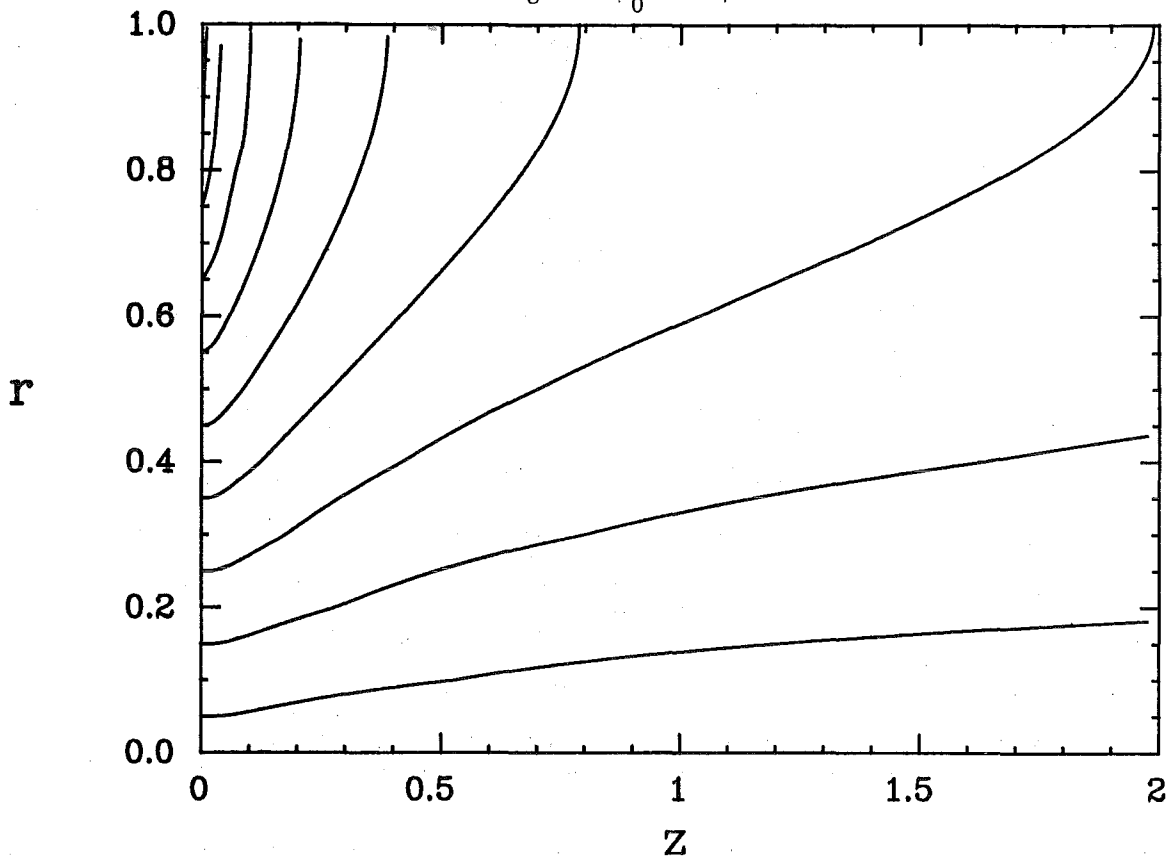


Fig. 6. $I_0 = 60 \text{ W/cm}^2$

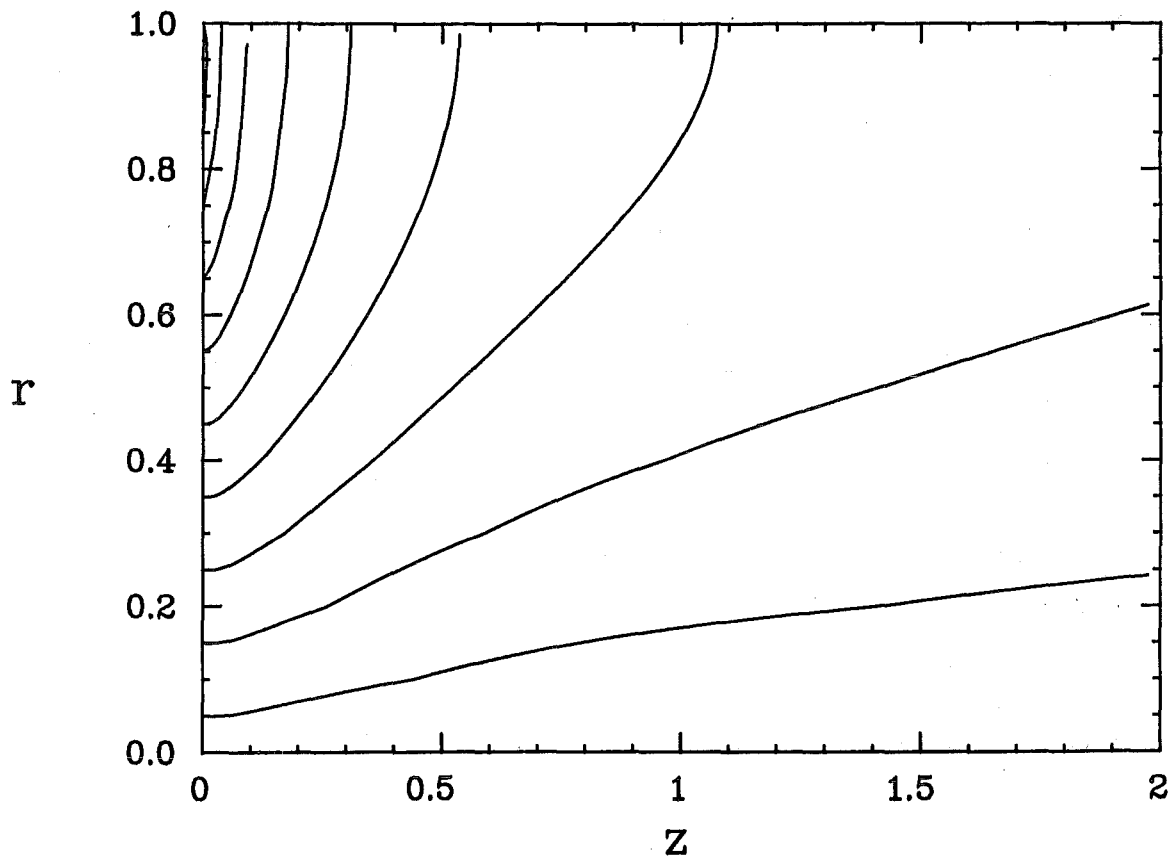


Fig. 7. $I_0 = 120 \text{ W/cm}^2$

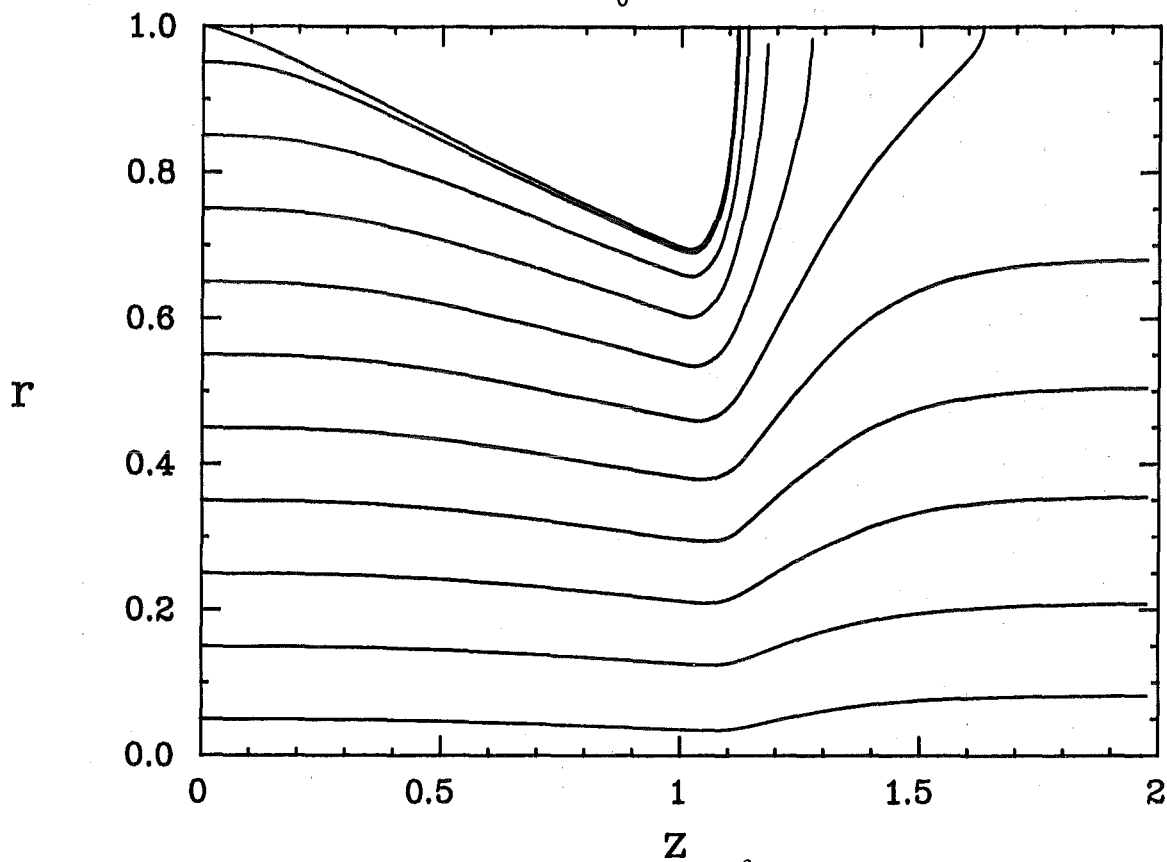


Fig. 8. $I_0 = 0 \text{ W/cm}^2$

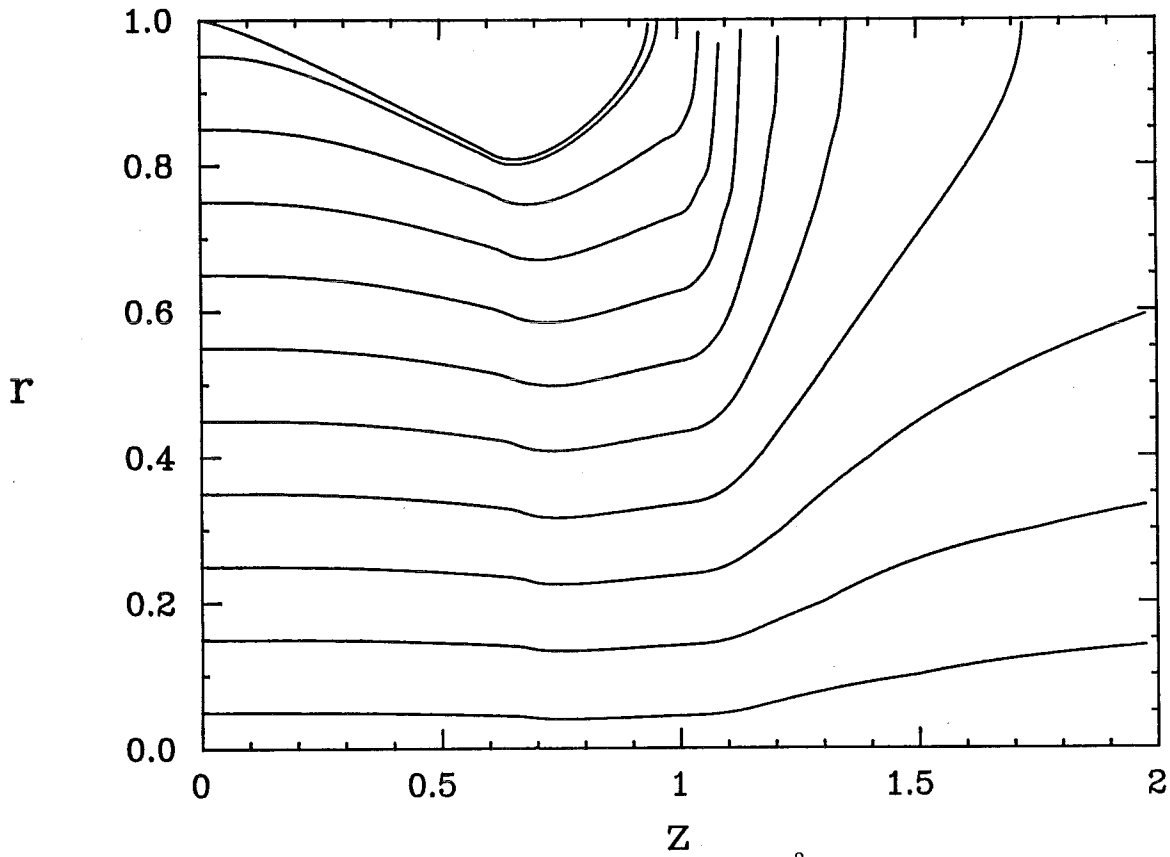


Fig. 9. $I_0 = 60 \text{ W/cm}^2$

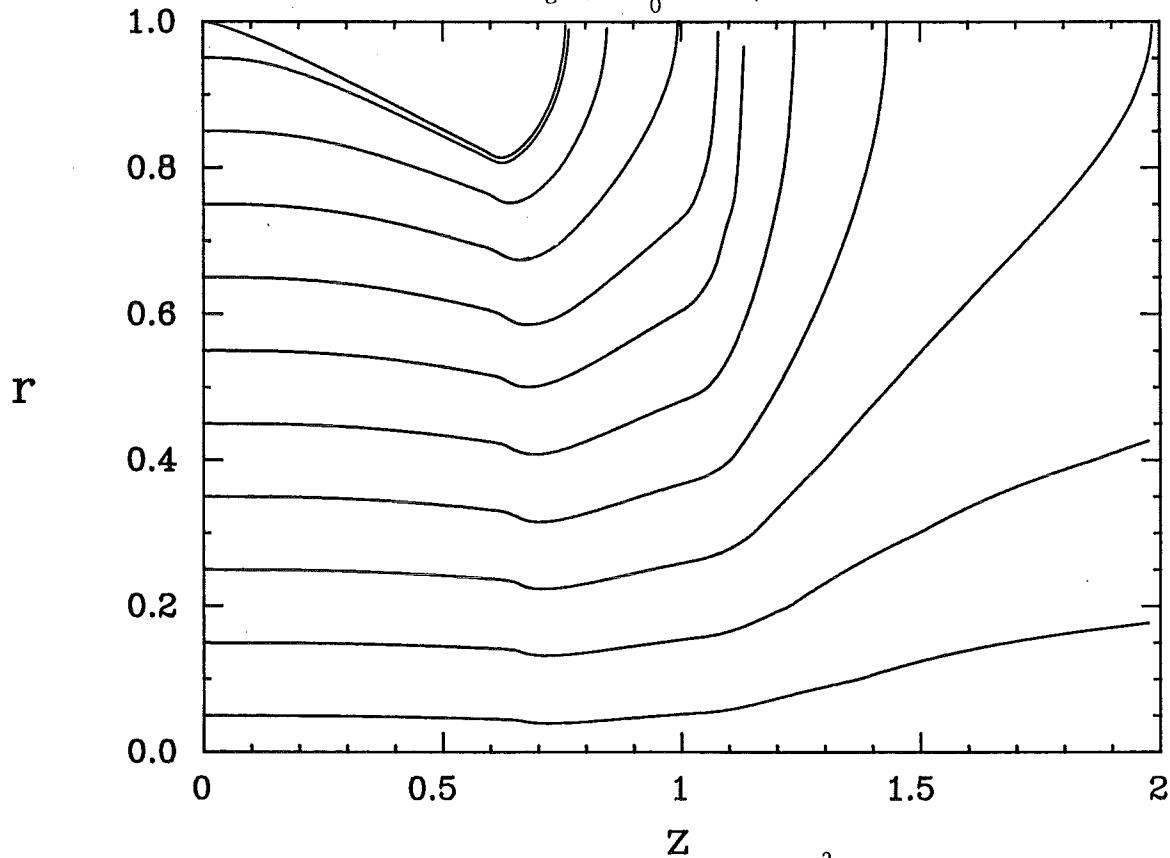


Fig. 10. $I_0 = 120 \text{ W/cm}^2$

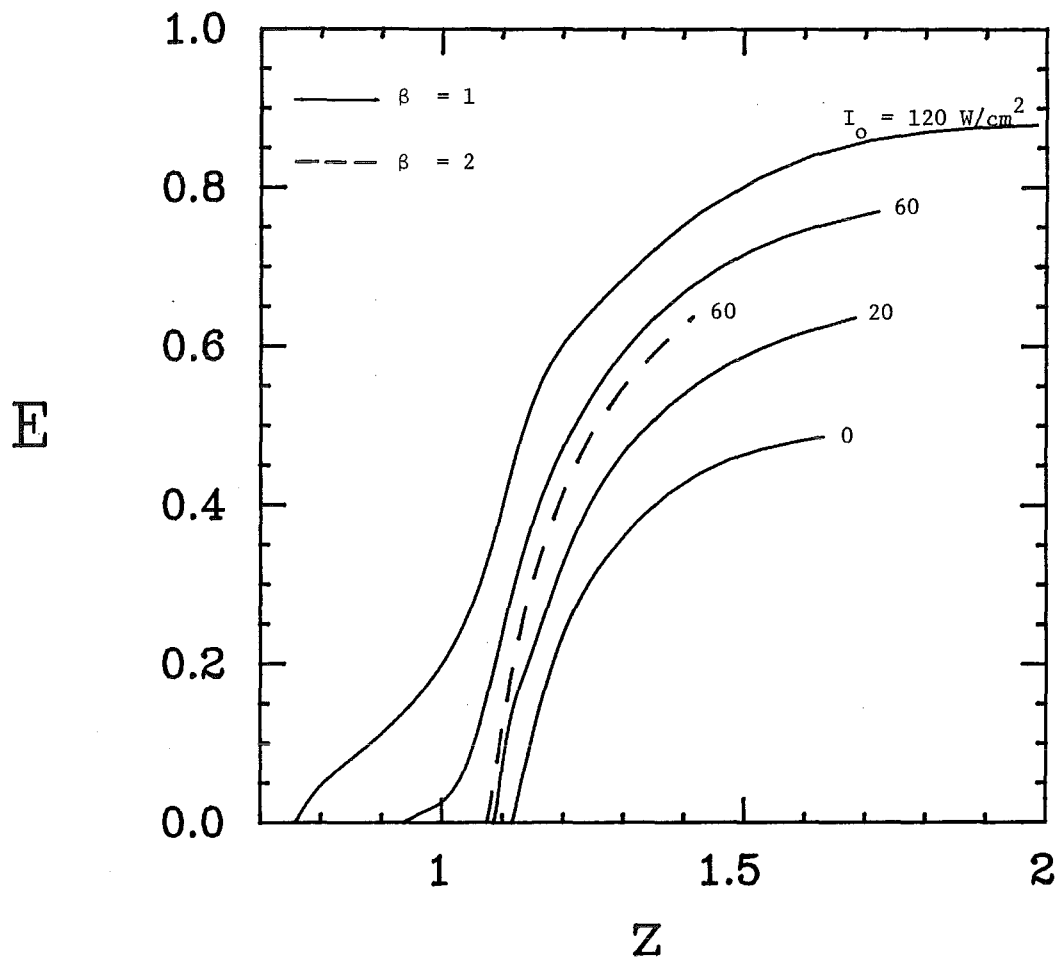


Fig. 11

BLANK

ELECTROMAGNETIC SCATTERING BY MAGNETIC SPHERE

Milton Kerker
Clarkson College of Technology
Potsdam, New York 13676

ABSTRACT

This work has been published as follows:

M. Kerker, D.-S. Wang and C.L. Giles, Electromagnetic scattering by magnetic spheres, J. Opt. Soc. Am. 73, 765-768 (1983).

We have encountered a number of unusual scattering effects for spheres composed of magnetic materials. Magnetic properties are not encountered at optical frequencies but may occur for far infrared and millimeter waves.

When $\epsilon = \mu$, it follows that the corresponding electric and magnetic expansion coefficients in the expressions for the scattering cross sections are equal ($a_n = b_n$) so that the backscatter (radar) cross section is zero. This is a general result, valid for spheres of any size; indeed it is also true for any axially-symmetric body illuminated along the axis of symmetry. It also follows with the linearly polarized incident radiation that the scattered radiation will be similarly polarized at all scattering angles.

In the small particle limit there will be a contribution from the magnetic dipole term in addition to that from the electric dipole. This interference between the electric and magnetic dipoles means that the usual angular and polarization patterns associated with Rayleigh scattering no longer hold. Indeed this interference between the electric and magnetic dipoles can result in complete polarization at various angles and in preferential backscatter. The special case of $m = 1$, i.e., $\epsilon = \mu^{-1}$ leads to particular simplification of the relations governing complete polarization and preferential backscatter.

BLANK

FLUORESCENCE BY MOLECULES EMBEDDED IN SMALL PARTICLES

Milton Kerker
Clarkson College of Technology
Potsdam, New York 13676

ABSTRACT

This work has been published as follows:

M. Kerker, M.A. Van Dilla, A. Brunsting, J.P. Kratochvil, P. Hsu, D.-S. Wang, J.W. Gray, and R.G. Langlois, Is the central dogma of flow cytometry true: That fluorescence intensity is proportional to cellular dye content? *Cytometry*, 3, 71-78 (1982).

The central dogma of flow cytometry is that the fluorescence from cells stained with fluorescent dyes is proportional to cellular dye content. Yet, when small particles containing fluorescent molecules are suspended in a medium of different index of refraction, there are intrinsic optical phenomena primarily due to the index mismatch which affect the angular distribution of both the intensity and polarization of the emitted fluorescence. The question which arises in flow cytometry is whether equal fluorescent intensities necessarily imply equal amounts of dye and also whether unequal intensities necessarily imply unequal amounts of dye.

The intensity and polarization of the illuminating radiation at the site of a fluorescent molecule determines its rate of excitation. The illumination intensity and polarization at sites inside small particles may differ from that in a uniform bulk medium because the radiation which reaches a particular site in a particle may have been strongly affected by reflection, refraction, absorption and scattering enroute to that site. Similarly, longer wavelength fluorescence undergoes comparable processes enroute from the emitting molecule through the particle to the detector. Accordingly, to be considered are: effects of particle morphology, particle orientation, and dye molecule distribution and orientation upon transport of the radiation at the exciting wavelength to the molecule; also transport of the radiation at the emitting wavelength from the molecule. Fluorescence polarization generated by photo selection as described above will be reduced if the excited molecules can rotate before emitting their fluorescence. Each of these factors may affect the measured fluorescence intensities in flow cytometers.

Theoretical calculations of fluorescent emission from uniform microspheres of radius comparable to or less than the wavelength of the exciting light have raised questions about the central dogma. These calculations, as well as a number of

associated experiments, indicated that fluorescence emitted from uniform solid polymer microspheres of equal dye content was a strong function of microsphere radius for values of radius between 0.08 and 0.40 μm and exciting light of wavelength about 500 nm. Fluorescence emission also depends on the angle at which the fluorescence is viewed and upon the polarization of the exciting radiation. We have been motivated to test the central dogma simply and realistically. Fluorescent emission intensities from four sizes of uniform fluorescent microspheres ranging in diameter from 0.93 μm to 4.18 μm were measured in a photometer with microspheres in suspension in a cuvette and in 2 different flow cytometers with orthogonal geometry in two different laboratories. These experimental results were compared with the results of theoretical calculations to determine the extent to which particle size influences flow cytometric measurements when particle size approaches cellular dimensions. Measurements and calculations were carried out cooperatively at three laboratories: Clarkson College of Technology (CCT), Potsdam, NY; Coulter Electronics Incorporated (CEI), Hialeah, FL; and Lawrence Livermore National Laboratory (LLNL), Livermore, CA.

Our experiments show that fluorescence emission is not isotropic and is a function of particle size which is in general agreement with theory. However, for commonly used flow systems with either orthogonal geometry or epiillumination, the results show that dependence of fluorescence emission on microsphere radius is small and should be even smaller for biological cells because they usually have an index of refraction much closer to that of the suspending medium (water) than do polymer microspheres.

SURFACE ENHANCED RAMAN SCATTERING (THEORY)

Milton Kerker
Clarkson College of Technology
Potsdam, New York 13676

ABSTRACT

This work has been published as follows:

1. M. Kerker and C.G. Blatchford, Elastic scattering, absorption, and surface-enhanced Raman scattering by concentric spheres comprised of a metallic and a dielectric region, *Physical Review* **B26**, 4052-4063 (1982).
2. H. Chew, D.-S. Wang and M. Kerker, Effect of surface coverage in surface-enhanced Raman scattering, Accepted for publication in *Physical Review*.

These papers extend earlier theoretical studies of our electrodynamic model of surface-enhanced Raman scattering (SERS) by molecules at the surface of small metal spheres.

In the first paper we first explore elastic scattering by inhomogeneous spheres comprised of two concentric spherical regions. This may be abnormally low if the dielectric constant of the external medium is intermediate between those of the two regions such as occurs when one of the regions is a metal with a real negative dielectric constant. The metal acts as an antireflecting coating. On the other hand, at another appropriate wavelength, there may be very large enhancement of the scattering due to the excitation of a dipolar surface plasmon. For a sphere in which the metallic region is silver, the incident radiation can be tuned over a range of optical wavelengths to give a variation of 10^6 in scattering cross section. This is illustrated in Fig. 1 where the scattering efficiency is plotted against wavelength (and also energy in electron volts) for a 10-nm radius sphere in air with an 8-nm radius core having a dielectric constant $\epsilon_1 = 2.25$ and a 2 nm thick coating for silver. This raises the interesting possibility of a smoke which is highly turbid at some optical wavelengths and quite clear at others.

Such objects may also exhibit very large SERS at the dipolar surface plasmon resonance with excitation profiles sharply dependent upon the relative thickness of the spherical shell. This is illustrated in Fig. 2 where the enhancement is plotted against excitation wavelength for a 10 nm radius silver sphere (solid line) and for spheres with 0.9, 0.8 and 0.5 nm radius cores having dielectric constants $\epsilon_1 = 2.25$. The manner in which the excitation profile varies with coating thickness resembles the variation in an earlier study of excitation profiles of spheroids with axial ratio.

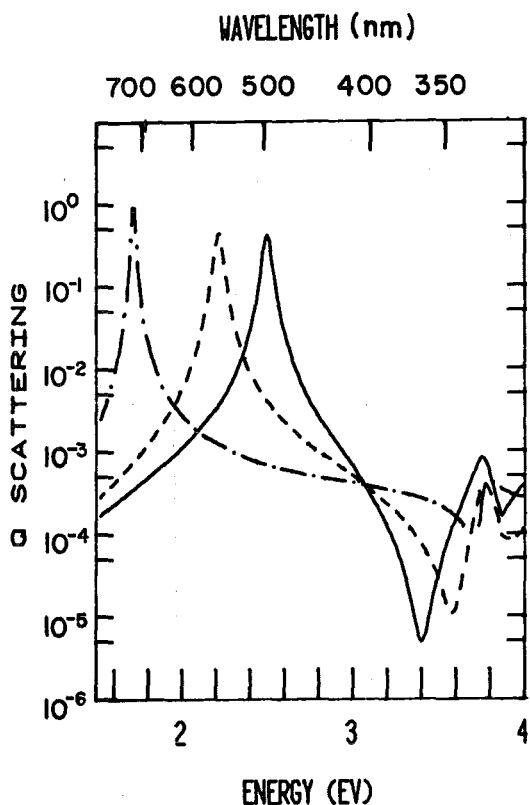


Fig. 1. Scattering efficiency vs. wavelength for an 8 nm radius core ($\epsilon_1=2.25$) and a 2 nm thick Ag coating in air (solid line). Other curves are for embedment of particle in more refractive media.

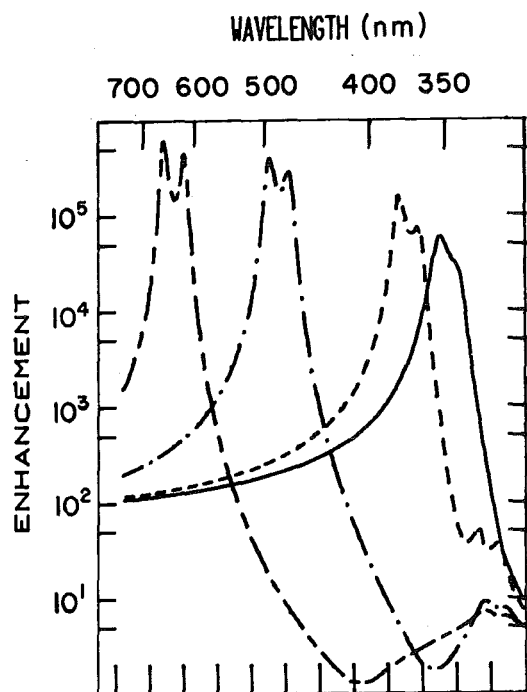


Fig. 2. Enhancement of Raman scattering with wavelength of 10 nm sphere. Solid line is for silver; other are for cores with $\epsilon_1=2.25$ and core radii (from right to left of 0.50, 0.80 and 0.90 nm).

In the second paper we consider the effect of submonolayer coverage on SERS. As a number of experimental studies show, for pyridine on silver, the peak intensity of some enhanced Raman lines increases to a maximum value at 0.2 to 0.4 of a monolayer and then decreases. We approach this problem by considering the effect of the mutual interaction of two Raman scattering molecules in the vicinity of a spherical particle in the context of our electrodynamic model of SERS. Our numerical results for 10, 50 and 100 nm radius silver particles in water show about 15% decrease of the Raman signal as the dipoles approach each other. These results indicate that the dipole-dipole interaction is not negligible but this effect alone is not large enough to change the enhancement factor qualitatively. Of course this two-body treatment oversimplifies the many-body interactions that occur in real systems. One must look to an extension of the model to the many-body problem before the effect of submonolayer coverage on SERS can be ascribed to such an electromagnetic interaction.

SURFACE ENHANCED RAMAN SCATTERING (EXPERIMENTS)

Milton Kerker
Clarkson College of Technology
Potsdam, New York 13676

ABSTRACT

This work has been published as follows:

1. O. Siiman, L.A. Bumm, R. Callaghan, C.G. Blatchford and M. Kerker, Surface-enhanced Raman scattering by citrate on colloidal silver, *J. Phys. Chem.* 87, 1014-1023 (1983).
2. C.G. Blatchford, O. Siiman and M. Kerker, Potential dependence of surface-enhanced Raman scattering (SERS) from citrate on colloidal silver, *J. Phys. Chem.* 87, 2503-2508 (1983).
3. O. Siiman, A. Lepp and M. Kerker, Combined surface-enhanced and resonance Raman scattering from the aspartic acid derivative of methyl orange on colloidal silver, *J. Phys. Chem.* (1983).

We have utilized Carey-Lea silver hydrosols stabilized by citrate in each of these studies of SERS. The preparative technique has been altered to give sols which are stable to coagulation. A quantitative analysis for adsorbed citrate by a radioactive exchange technique has permitted accurate determination of absolute enhancements. Experimental results for sols of different sizes and degree of aggregation are presented in (1). There was good agreement between the measured maximum enhancements of 2×10^5 to 4×10^5 and the electrodynamic calculations for the particle size histograms obtained by electron microscopy. However, a discrepancy between the sharp maxima in the measured absorption spectra of these sols as well as in the calculated SERS excitation profiles near 400 nm and the broad maxima in the measured SERS excitation profiles near 500 nm remains unresolved.

Theoretical analysis indicates that the electrochemical potential may affect the absorption spectrum and the SERS by depletion of conduction band electrons from the surface layer. Such depletion of electrons alters the dielectric constant of the surface layer and hence the optical properties of the silver particles. Experiments in (2) were designed to look for this effect. Although alteration of the electrochemical potential in a colloidal silver hydrosol did produce measured changes in both the absorption spectrum and SERS, it could not be attributed unambiguously to an electro-optical effect since there may have been aggregation-disaggregation effects which would have led to similar observations.

In (3) we have studied the resonance Raman spectrum of a chromophore in solution, the enhanced resonance Raman spectrum of this species adsorbed on colloidal silver and the enhanced normal Raman spectrum of this same species adsorbed on the same colloidal silver surface at frequencies where the species does not exhibit resonance Raman scattering. This has been made possible by selecting dabsyl (N-4-dimethylaminoazobenzene-4-sulfonyl) aspartate whose absorption spectrum overlaps with the SERS excitation spectrum for colloidal silver. This chromophore was placed on the surface of silver particles of a Carey-Lea sol by exchange with citrate. The enhanced resonance Raman and normal Raman spectra were distinctly different. The measured RR enhancements were 10^3 which, when combined with the estimated resonance effect, gave a total enhancement of 10^8 . However, the 10^3 enhancement was distinctly less than our initial expectation.

SCATTERING CROSS SECTIONS FOR LARGE FINITELY CONDUCTING SPHERES
WITH ROUGH SURFACES-FULL WAVE SOLUTIONS

Ezekiel Bahar
and
Swapan Chakrabarti
Electrical Engineering Department
University of Nebraska-Lincoln
Lincoln, NE 68588-0511

ABSTRACT

The scattering cross sections for large finitely conducting spheres with very rough surfaces are determined for optical frequencies using the full wave approach. For the roughness scales considered, the scattering cross sections differ significantly from those of smooth conducting spheres. Several illustrative examples are presented and the results are compared with earlier solutions to the problem.

1. Introduction

The purpose of this investigation is to determine the like and cross polarized scattering cross sections for electrically large finitely conducting spheres with very rough surfaces. Perturbation theory has been used to determine electromagnetic scattering by spheres with random rough surfaces provided that the parameter $\beta = 4k_0^2 \langle h_s^2 \rangle$ is much smaller than unity (where k_0 is the wavenumber and $\langle h_s^2 \rangle$ is the mean square height of the rough surface of the sphere, Barrick 1970). However, for large conducting spheres with $\beta \ll 1$, the total scattering cross sections are not significantly different from the physical optics cross section for smooth (unperturbed) conducting spheres.

In this paper the full wave approach is used to determine the scattering cross sections for large spheres with roughness scales that significantly modify the total cross sections. The full wave approach accounts for specular point scattering and Bragg scattering in a self consistent manner and the total scattering cross sections are expressed as weighted sums of two cross sections (Bahar and Barrick 1983). In Section 2 the problem is formulated and the principal elements of the full wave solution are presented. Illustrative examples at optical frequencies are presented in Section 3 and the results are compared with earlier solutions based on the perturbation approach (Barrick 1970) and a recent reformulated current method (Abdelazeez 1983).

2. Formulation of the Problem

The purpose of this investigation is to determine the like and cross polarized scattering cross sections at optical frequencies for large conducting spheres with very rough surfaces. The position vector \bar{r}_s to a point on the rough surface of the sphere is (see Fig. 1)

$$\bar{r}_s = h_0 \bar{a}_r + h_s \bar{a}_r \quad (2.1)$$

in which \bar{a}_r is the radius vector in the spherical coordinate system, h_0 , the radius of the unperturbed sphere, is large compared to the wavelength λ_0 of the electromagnetic wave, and h_s is the random surface

height measured along the radius vector \bar{a}_r . For a homogeneous isotropic rough surface height h_s , the spectral density function (Rice 1951, Barrick 1970, Ishimaru 1978) is the Fourier transform of the surface height autocorrelation function $\langle h(x,z), h'(x',z') \rangle$

$$W(v_x, v_z) = \frac{1}{\pi} \int \langle h_s h'_s \rangle \exp(iv_x x_d + iv_z z_d) dx_d dz_d \quad (2.2)$$

in which the symbol $\langle \cdot \rangle$ denotes statistical average and $\langle h_s h'_s \rangle$ is a function of distance measured along the surface of the sphere. It is assumed that the correlation distance ℓ_c for the rough surface height h_s is very small compared to the circumference of the sphere. The unit vectors \bar{n}^i and \bar{n}^f are in the directions of the incident and scattered waves and the vector \bar{v} is given by

$$\bar{v} = k_o (\bar{n}^f - \bar{n}^i) \quad (2.3)$$

where k_o is the electromagnetic wavenumber ($k_o = 2\pi/\lambda_o$).

$$\bar{n}^i = -\bar{a}_{y_o} \quad (2.4)$$

$$\bar{n}^f = \sin \theta_o^f \bar{a}_{x_o} + \cos \theta_o^f \bar{a}_{y_o} \quad (2.5)$$

in which \bar{a}_{x_o} , \bar{a}_{y_o} and \bar{a}_{z_o} are unit vectors in the reference coordinate system (see Fig. 1). Associated with a point on the surface of the unperturbed sphere is a local coordinate system x, y, z whose unit vectors are

$$\bar{n}_1 = (\bar{n} \times \bar{a}_{z_o}) / |\bar{n} \times \bar{a}_{z_o}|, \quad \bar{n}_2 = \bar{n} = \bar{a}_r, \quad \bar{n}_3 = \bar{n}_1 \times \bar{n} \quad (2.6)$$

Thus \bar{n}_2 is in the direction normal to the surface of the sphere and \bar{n}_1 and \bar{n}_3 are tangent to the surface of the sphere. When the distance r_d measured along the surface of the sphere is commensurate with the correlation distance ℓ_c

$$r_d = [(x-x')^2 + (z-z')^2]^{1/2} = (x_d^2 + z_d^2)^{1/2} \quad (2.7)$$

Thus for points on the surface of the sphere at a distance $r_d = \ell_c$, the surface height autocorrelation function is $\langle h_s h'_s \rangle = \langle h_s^2 \rangle / e$ (where $\langle h_s^2 \rangle$ is the mean square height and e is the Neperian number). The surface h_s consists of the spectral components

$$k_d < k = (v_x^2 + v_z^2)^{1/2} < k_c \quad (2.8)$$

where $k_d = 2\pi/d$ is the smallest wavenumber characterizing the rough surface of the sphere ($d = 2h_o$) and k_c is the spectral cutoff wavenumber (Brown 1978). Perturbation theory has been used to determine electromagnetic scattering by rough surfaces (Rice 1951, Burrows 1967, Valenzuela 1968, Barrick 1970, Brown 1978). To apply perturbation theory, it is necessary to assume that $\beta = 4k_o^2 \langle h_s^2 \rangle \ll 1$. For large conducting spheres, the scattered fields are primarily due to specular point scattering. Thus, if the mean square height $\langle h_s^2 \rangle$ of the rough surface is restricted by the perturbation condition $\beta \ll 1$, the

total scattering cross sections for spheres with rough surfaces is not significantly different from those of unperturbed conducting spheres.

Since the full wave approach (Bahar 1981, 1982, Bahar and Barrick 1983) accounts for specular point scattering and Bragg scattering in a self consistent manner, the perturbation restriction need not be imposed on the mean square height $\langle h_s^2 \rangle$ of the rough surface. In this work we consider spheres with large roughness scales whose scattering cross sections differ significantly from the cross sections of unperturbed spheres. Thus using the full wave approach the total normalized scattering cross sections per unit area $\langle \sigma^{PQ} \rangle$ is expressed as a weighted sum of two cross sections

$$\langle \sigma^{PQ} \rangle = \langle \sigma^{PQ} \rangle_\ell + \langle \sigma^{PQ} \rangle_s \quad (2.9)$$

in which $\langle \sigma^{PQ} \rangle_\ell$ is the cross section associated with the large scale unperturbed surface and $\langle \sigma^{PQ} \rangle_s$ is the cross section associated with the small scale surface h_s that is superimposed on the large scale surface. The first superscript P corresponds to the polarization of the scattered wave while the second superscript Q corresponds to the polarization of the incident wave. The scattering cross section $\langle \sigma^{PQ} \rangle_\ell$ is given by (Bahar 1981)

$$\langle \sigma^{PQ} \rangle_\ell = |\chi^s(v)|^2 \langle \sigma_\infty^{PQ} \rangle \quad (2.10)$$

in which χ^s is the characteristic function for the surface h_s

$$\chi^s(v) = \langle \exp iv h_s \rangle \quad (2.11)$$

and v is the magnitude of the vector \vec{v} (2.3). Thus the weighting function $|\chi^s|^2$ is less than unity. It approaches unity for $\langle h_s^2 \rangle \rightarrow 0$. For Gaussian rough surfaces h_s ,

$$|\chi^s|^2 = e^{-4k_o^2 \langle h_s^2 \rangle \cos^2(\theta_o^f/2)} = e^{-v_y^2 \langle h_s^2 \rangle} \quad (2.12)$$

Since in this work the unperturbed surface is assumed to be the surface of a large conducting sphere ($d \gg \lambda_o$), the cross section $\langle \sigma_\infty^{PQ} \rangle$ is given by the physical optics expression (Barrick 1970)

$$\langle \sigma_\infty^{PQ} \rangle = \delta_{PQ} |R_p|^2 \quad (2.13)$$

in which R_p is the Fresnel reflection coefficient for vertically (P=V) or horizontally (P=H) polarized waves and δ_{PQ} is the Kronecker delta. For Gaussian rough surfaces h_s , the term $\langle \sigma^{PQ} \rangle_s$ can be expressed as

$$\langle \sigma^{PQ} \rangle_s = \sum_{m=1}^{\infty} \langle \sigma^{PQ} \rangle_{sm} \quad (2.14)$$

where

$$\langle \sigma^{PQ} \rangle_{sm} = 4\pi k_o^2 \left[\frac{|D^{PQ}|^2 P_2(\vec{n}^f, \vec{n}^i | \vec{n})}{\vec{n} \cdot \vec{a}_y} \right] \cdot \exp(-v_y^2 \langle h_s^2 \rangle) \left(-\frac{v_y}{2}\right)^{2m} \frac{W_m(v_x, v_z)}{m!} p(h_x, h_z) dh_x dh_z \quad (2.15)$$

In (2.15) v_x, v_y and v_z are the components of \bar{v} (2.3) in the local coordinate system (2.6)

$$\bar{v} = v_x \bar{n}_1 + v_y \bar{n}_2 + v_z \bar{n}_3 \quad (2.16)$$

The shadow function $P_2(\bar{n}^f, \bar{n}^i | \bar{n})$ is the probability that a point on the rough surface is both illuminated by the source and visible to the observer given the slopes $\bar{n}(h_x, h_z)$ at the point (Smith 1967, Sanar 1969). The function $p(\bar{n}) = p(h_x, h_z)$ is the two-dimensional probability density of the slopes h_x and h_z . The expression D^{PQ} depends on the polarization of the incident and scattered waves, the unit vectors \bar{n}^i, \bar{n}^f and \bar{n} , and the relative complex permittivity ϵ_r of the conducting sphere. The function $W_m(v_x, v_z)/2^{2m}$ is the two-dimensional Fourier transform of $\langle h_s h'_s \rangle^m$. It can be expressed as follows

$$\begin{aligned} \frac{W_m(v_x, v_z)}{2^{2m}} &= \frac{1}{(2\pi)^2} \int \langle h_s h'_s \rangle \exp(iv_x x_d + iv_z z_d) dx_d dz_d \\ &= \frac{1}{2^{2m}} \int W_{m-1}(x'_x, v'_z) W_1(v_x - v_{x'}, v_z - v_{z'}) dv_{x'} dv_{z'} \\ &= \frac{1}{2^{2m}} W_{m-1}(v_x, v_z) \otimes W_1(v_x, v_z) \end{aligned} \quad (2.17)$$

In (2.17) the symbol \otimes denotes the two-dimensional convolution of W_{m-1} with W_1 .

It should be noted that for $\beta \rightarrow 0$ the scattering cross section (2.9) reduces to the scattering cross sections for large conducting spheres; for $\beta \ll 1$, it reduces to the perturbation solution (Burrows 1967) since in this case $|\chi^S| \approx 1$ and (2.14) reduces to the leading term $m = 1$ (Bragg scatter). In a recent analysis of wave scattering from a large sphere with rough surface (using a reformulated current method), Abdelazeez (1983) obtains a solution which corresponds to the first term in (2.9). Barrick (1970), who considered backscatter by spheres with small scale roughness, presents a solution that accounts for $\langle \sigma_\infty^{PQ} \rangle_\ell$ and the first term in (2.14). The weighting function $|\chi^S|^2$ that multiplies $\langle \sigma_\infty^{PQ} \rangle$ accounts for the degradation of the specular point scattering cross section due to the superimposed rough surface h_s . The second term in (2.9), $\langle \sigma_\infty^{PQ} \rangle_s$, accounts for diffuse scatter due to the rough surface h_s . The leading term in $\langle \sigma_\infty^{PQ} \rangle_s$ ($m=1$) corresponds to Bragg scatter (Rice 1951, Valenzuela 1968, Barrick 1970, Brown 1978). In the next section illustrative examples of spheres with very rough surfaces are considered. The significance of the different terms of the solution (2.9) are considered in detail and the results are compared to earlier solutions. On replacing $\langle \sigma_\infty^{PQ} \rangle$ (2.15) by the expression for large scatterers of arbitrary shape (such as ellipsoids), one can obtain the effects of surface roughness on large scatterers of any desired shape.

3. Illustrative Examples

Assuming a homogeneous isotropic random rough surface h_s , the surface height spectral density function (2.2) (Rice 1951) considered for the illustrative examples is

$$W(v_x, v_z) = W(k) = \begin{cases} \frac{2}{\pi} B/k^4 & k_d < k < k_c \\ 0 & k > k_c \text{ and } k < k_d \end{cases} \quad (3.1)$$

in which

$$k^2 = v_x^2 + v_z^2 \quad (\text{cm})^{-2} \quad (3.2)$$

The smallest wavenumber characterizing the rough surface h_s is

$$k_d = \frac{2\pi}{d} \quad (3.3)$$

where

$$d = 20 \lambda_o$$

is the diameter of the sphere and λ_o is the wavelength of the electromagnetic wave

$$\lambda_o = 0.555 \times 10^{-4} \text{ cm} \quad (k_o = \frac{2\pi}{\lambda_o} = 1.132 \times 10^5 \text{ cm}^{-1}). \quad (3.4)$$

The spectral cutoff number is (Brown 1978)

$$k_c = 4.5 \times 10^5 \text{ cm}^{-1} \quad (3.5)$$

The mean square height of the rough surface h_s is

$$\langle h_s^2 \rangle = \int_0^{k_c} \int_{k_d}^k \frac{W(k)}{4} k_d k_d \phi = \frac{B}{2} \left[\frac{1}{k_d^2} - \frac{1}{k_c^2} \right] \quad (3.6)$$

Thus the value of B (3.1) in terms of the parameter $\beta = 4k_o^2 \langle h_s^2 \rangle$ is

$$B = \frac{\beta k_c^2 k_d^2}{2k_o^2 (k_c^2 - k_d^2)} \quad (3.7)$$

For $\beta = 1.0$

$$(3.8)$$

the corresponding value of the mean square height is

$$\langle h_s^2 \rangle = 0.195 \times 10^{-10} \text{ cm}^2 \quad (3.9)$$

thus

$$B = 0.125 \times 10^{-2} \quad (3.10)$$

At optical frequencies the relative dielectric coefficient of aluminum is (Ehrenreich 1965)

$$\epsilon_r = -40 - i12 \quad (3.11)$$

The permeability of the sphere is assumed to be that of free space $\mu_o = 1$. For the unperturbed sphere, the probability density function of the slopes (2.15) is given by

$$p(h_x, h_z) dh_x dh_z = p(\gamma, \delta) d\gamma d\delta = \frac{\sin \gamma d\gamma d\delta}{2\pi} \quad (3.12)$$

where γ and δ are the latitude and azimuth angles in the spherical coordinate system.

In Fig. 2 the vertically polarized scattering cross section $\langle \sigma^{VV} \rangle$ (2.9) is plotted as a function of the scatter angle θ_o^f (see Fig. 1). The parameter $\beta = 4k_o^2 \langle h_s^2 \rangle = 1.0$. In addition to the plot of $\langle \sigma^{VV} \rangle$ (2.9) (the total cross section), plots are also given for the individual terms in (2.9); $\langle \sigma^{VV} \rangle_\ell = |R_V \chi^s|^2$, $\langle \sigma^{VV} \rangle_{s1}$ and $\langle \sigma^{VV} \rangle_{s2}$. The terms $\langle \sigma^{VV} \rangle_{sm}$ for $m \geq 3$ are negligible. The value of $\langle \sigma_\infty^{VV} \rangle = |R_V|^2$ (corresponding to the physical optics cross section for the unperturbed sphere) is also given for the purpose of comparison. Note that the total scattering cross section $\langle \sigma^{VV} \rangle$ for the rough sphere is significantly smaller than that of the unperturbed sphere $\langle \sigma_\infty^{VV} \rangle$. Furthermore, for $\beta = 1.0$ the contribution of the term $\langle \sigma^{VV} \rangle_s$ (2.9) is not negligible and $\langle \sigma^{VV} \rangle$ cannot be approximated by the first term $\langle \sigma^{VV} \rangle_\ell = |R_V \chi^s|^2$. The corresponding results ($\beta = 1.0$) for the horizontally polarized scattering cross sections $\langle \sigma^{HH} \rangle$ are presented in Fig. 3. These results are similar to the results for the vertically polarized waves except near the quasi-Brewster angle.

The cross-polarized section $\langle \sigma^{HV} \rangle = \langle \sigma^{VH} \rangle$ is presented in Fig. 4 for $\beta = 1.0$. In view of (2.13) there is no physical optics contribution to the cross-polarized cross section. Note also that for backscatter, $\theta_o^f = 0$, $\langle \sigma^{HV} \rangle$ becomes vanishingly small. For $\beta < 0.1$, the terms $\langle \sigma \rangle_{sm}$ for $m \geq 2$ are negligible. Furthermore since $e^{-\beta} \approx 0.9$ for $\beta = 0.1$, the perturbation solution (Barrick 1970) is approximately equal to the full wave solution. For very small values of β the full wave solutions equal those of the reformulated current method (Abdelazeez 1983) since the second term in (2.9), $\langle \sigma^{PQ} \rangle_s$ becomes very small compared to $\langle \sigma^{PQ} \rangle_\ell$. However, when the scale of the roughness is very small ($\beta < 0.1$), the scattering cross sections of rough spheres are not significantly different from that of unperturbed spheres. As β (the roughness of the surface) increases, the weighting function $|\chi^s|^2$ decreases and the contribution of the term $\langle \sigma^{PQ} \rangle_s$ increases. Furthermore, an increasing number of terms $\langle \sigma^{PQ} \rangle_{sm}$ ($m=1,2,3,\dots$) need to be evaluated as β increases.

4. Concluding Remarks

The full wave approach has been used to determine the scattering cross sections for electrically large conducting spheres ($d \gg \lambda_o$) with very rough surfaces. The total scattering cross sections are significantly modified by the rough surface when the parameter $\beta = 4k_o^2 \langle h_s^2 \rangle > 1$. In these cases the perturbation solutions are not valid. For $\beta \ll 1$ the full wave solutions reduce to the perturbation solution (Barrick 1970); however, for $\beta \ll 1$, the modification of the total scattering cross section is not very significant. The full wave solutions are compared with the perturbation solutions (Barrick 1970) and a recent solution based on the reformulated current method (Abdelazeez 1983). The full wave solutions presented here can also be used to determine the effects of surface roughness on the scattering cross sections for large conductors of different shapes such as ellipsoids.

Acknowledgments

This investigation was sponsored by the U. S. Army Research Office, Contract No. DAAG-29-82-K-0123.

The manuscript was typed by Mrs. E. Everett.

5. References

1. Abdelazeez, M. K. (1983), "Wave Scattering from a Large Sphere with Rough Surface," IEEE Transactions on Antennas and Propagation, Vol. AP-31, No. 2, pp. 375-377.
2. Bahar, E. (1981), "Scattering Cross Sections for Composite Random Surfaces--Full Wave Analysis," Radio Science, 16(6), pp. 1327-1335.
3. Bahar, E. (1982), "Scattering Cross Sections for Composite Surfaces with Large Mean Square Slopes--Full Wave Solution," International Journal of Remote Sensing, Vol. 3, No. 3, pp. 327-337.
4. Bahar, E., D. E. Barrick (1982), "Scattering Cross Sections for Composite Surfaces that Cannot be Treated as Perturbed Physical Optics Problems," Radio Science, Vol. 18, No. 2, pp. 129-137.
5. Barrick, D. E. (1970), Rough Surfaces, in Radar Cross Section Handbook, Chapter 9, Plenum Press, New York.
6. Brown, G. S. (1978), "Backscattering from Gaussian-Distributed Perfectly Conducting Rough Surfaces," IEEE Transactions on Antennas and Propagation, AP-26(3), pp. 472-482.
7. Burrows, M. L. (1967), "On the Composite Model for Rough Surface Scattering," IEEE Transactions on Antennas and Propagation, Vol. AP-21, pp. 241-243.
8. Ehrenreich, H. (1965), "The Optical Properties of Metals," IEEE Spectrum 2(3), pp. 162-170.
9. Ishimaru, A. (1978), "Wave Propagation and Scattering in Random Media in Multiple Scattering, Turbulence, Rough Surfaces and Remote Sensing," Vol. 2, Academic Press, New York.
10. Rice, S. O. (1951), "Reflection of Electromagnetic Waves from a Slightly Rough Surface," Communication of Pure and Applied Math, Vol. 4, pp. 351-378.
11. Sancer, M. K. (1969), "Shadow-Corrected Electromagnetic Scattering from a Randomly Rough Surface," IEEE Transactions on Antennas and Propagation, AP-17(5), pp. 577-585.
12. Smith, B. G. (1967), "Geometrical Shadowing of a Randomly Rough Surface," IEEE Transactions on Antennas and Propagation, AP-15(5), pp. 668-671.
13. Valenzuela, G. R. (1968), "Scattering of Electromagnetic Waves from a Tilted Slightly Rough Surface," Radio Science, Vol. 3, No. 11, pp. 1051-1066.

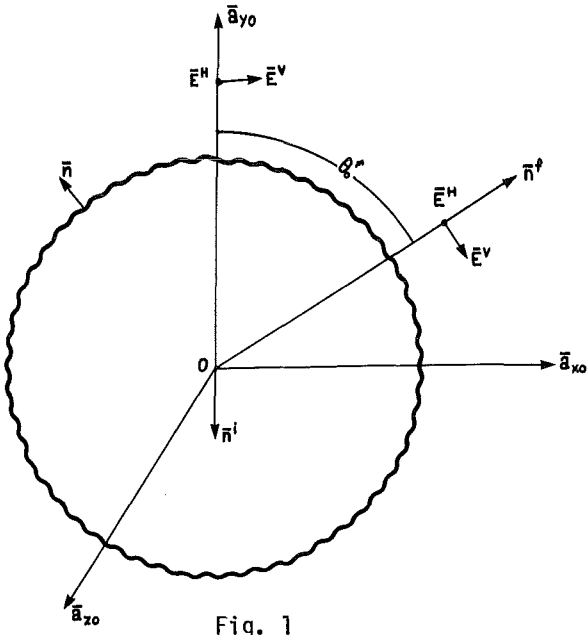


Fig. 1

Scattering of electromagnetic waves from a rough conducting sphere.

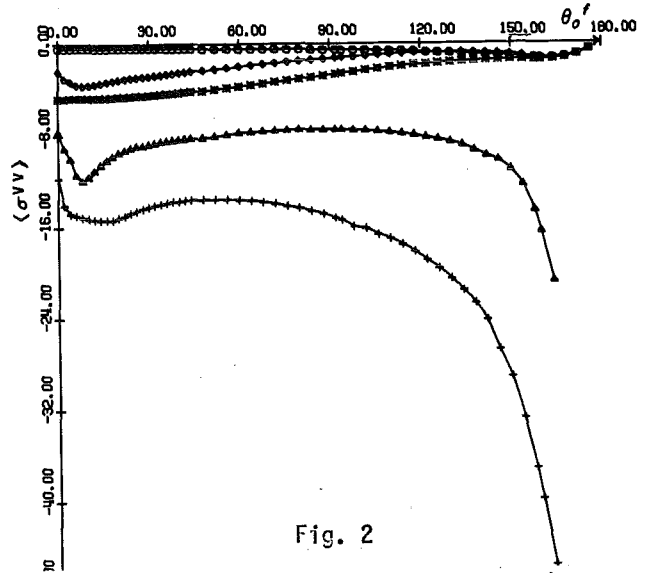


Fig. 2

Vertically polarized scattering cross section. $\beta = 1.0$ (\diamond) total cross section $\langle \sigma^{VV} \rangle$, (\circ) $\langle \sigma_{\infty}^{VV} \rangle = |R^{VV}|^2$, (X) $\langle \sigma^{VV} \rangle_{\ell} = |R^{VV} \chi^s|^2$, (Δ) $\langle \sigma^{VV} \rangle_{s1}$, (+) $\langle \sigma^{VV} \rangle_{s2}$.

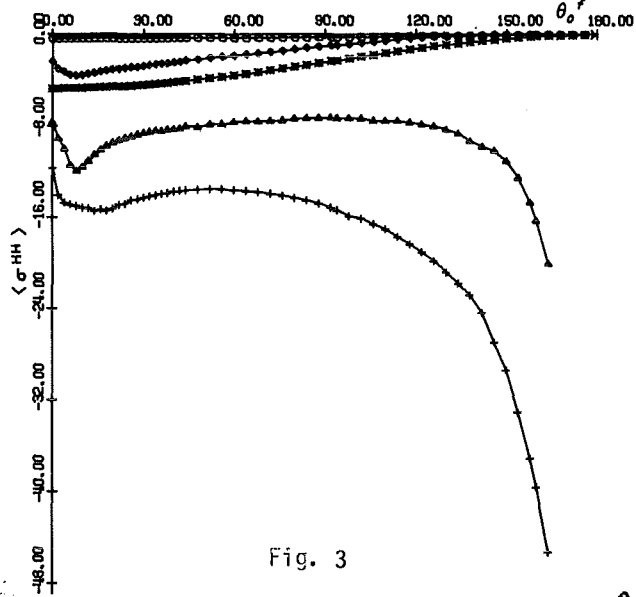


Fig. 3

Horizontally polarized cross section $\beta = 1.0$ (\diamond) total cross section $\langle \sigma^{HH} \rangle$, (\circ) $\langle \sigma_{\infty}^{HH} \rangle = |R^{HH}|^2$, (X) $\langle \sigma^{HH} \rangle_{\ell} = |R^{HH} \chi^s|^2$, (Δ) $\langle \sigma^{HH} \rangle_{s1}$, (+) $\langle \sigma^{HH} \rangle_{s2}$.

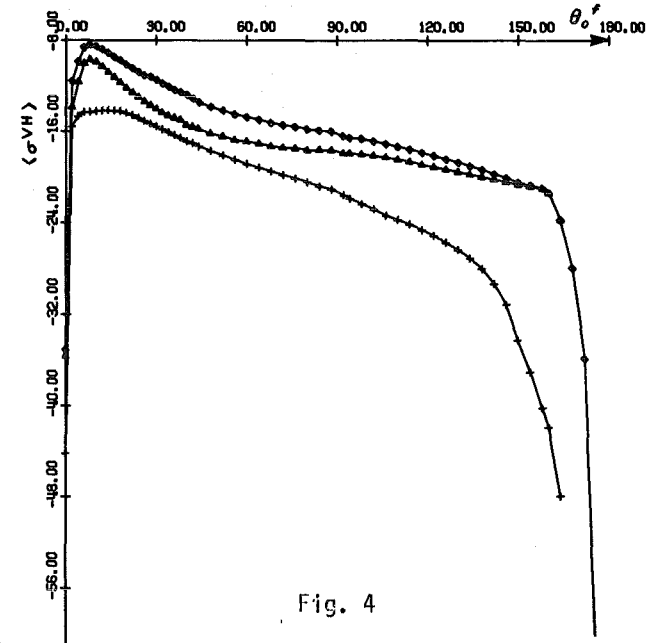


Fig. 4

Cross polarized cross section. $\beta = 1.0$ (\diamond) total cross section $\langle \sigma^{HV} \rangle = \langle \sigma^{VH} \rangle$, (Δ) $\langle \sigma^{HV} \rangle_{s1}$, (+) $\langle \sigma^{HV} \rangle_{s2}$.

EXTINCTION BY DUMBBELLS AND CHAINS OF SPHERES

R.T. WANG

Space Astronomy Laboratory, University of Florida
1810 N.W. 6th Street, Gainesville, Florida 32601

ABSTRACT

Extinction by preferentially oriented dumbbells and chains of spheres is measured by the microwave analog technique. Since all of the 12 measured arrays, each consisting of 2, 3, or 5 identical spheres, have axisymmetry, the extinction by random orientation of the array can be evaluated by taking the weighted average over 37 preferential orientations of each array (Wang and Schuerman, 1981). The resulting averaged extinction, $Q_{\text{ext},v} = \overline{C}_{\text{ext}}/\pi a_v^2$, is plotted versus $\rho = 4\pi a_v(m'-1)/\lambda$, where a_v is the radius of sphere equal in volume to the array. All individual P, Q plots, which show the detailed array-orientation dependence of the extinction, are also shown. This is an extension of our previous dependent scattering studies (Wang, 1980; Schuerman and Wang, 1981); the full results and discussion will be submitted to Applied Optics for publication.

INTRODUCTION

The analytical solution to the problem of cooperatively scattering spheres is still very difficult to obtain, and it is true even for the simplest case of two dependently scattering spheres (Bruning & Lo, 1971; see also the literature cited by Wang, et al., 1981). In the previous report (Schuerman and Wang, 1981) we presented a large body of extinction data for 2^n ($n=1, 2, 3$) neighboring spheres. Due to the slow data-accumulation speed, however, these contained only the array-orientation dependence of extinction when the array was rotated in a horizontal plane; thus the averaged extinction over random array orientations could not be derived. In addition, 4- and 8- sphere arrays lack axisymmetry thereby requiring an 8-fold increase in the number of needed particle orientations to arrive at the true random orientation data. In this paper we report a new set of extinction data accumulated in our relocated-to-Gainesville microwave facility using a computer-controlled orientation device (Schuerman, et al., 1981). 2, 3, or 5 identical plexiglass spheres were assembled in a thin cylindrical plastic film envelope to form a dumbbell or a linear chain, and the array was rotated in the beam to investigate the extinction at a fixed orientation or the averaged extinction over 37 such fixed orientations for each array. A small cylindrical spacer made of the same film material was also inserted between two neighboring spheres in an array to study the effect of separation distance on the net extinction.

SOME DETAILS OF EXPERIMENTAL PROCEDURE

The detailed procedure has been published elsewhere (Schuerman, et al., 1981; Wang and Greenberg, 1978; Lind, et al., 1965; Lind, 1966; Wang, 1968). Briefly stated, the experimental objective is to display the complex forward scattering amplitude $S(0)$ of an array as a function of its orientation in a cartesian coordinate P,Q. Such a display is called the P,Q plot. In the forward direction $\theta=0^\circ$, however, we have to discriminate the desired scattered wave against the very large, yet coherently-

arriving, beam. This is accomplished by a compensation technique which is available only in the microwave region at present. The beam signal in the absence of the target is cancelled at the output port of a hybrid junction into whose two input ports the beam wave and a properly amplitude-attenuated and phase-shifted reference wave (which is piped through a separate waveguide) are fed. As the target is brought into the beam, the off-balance wave from this output port is then linearly related to the desired $S(0)$. To display its two orthogonal components, this output off-balance wave is then 1000 c/s square-wave-modulated, split into 2 components and separately fed into 2 hybrid junctions to be mixed with 2 additional arms of unmodulated microwave reference waves. The phases of these 2 additional reference arms can be preadjusted so that the resulting 2 mixer outputs differ exactly 90° in phase from each other, the amplitudes being proportional to the 2 time-quadrature components of $S(0)$. While the particle is in the beam, it is rotated through its preselected orientations and the 2 orthogonal components of $S(0)$ at each orientation are recorded. Finally, by replacing the target by standard spheres of known $S(0)$ in quick succession, the tilt and the absolute magnitude of the P,Q coordinates can be calibrated.

In short, the P and Q components of a complex scattering amplitude $S(0)$ are proportional to the in-phase and the 90° -out-of-phase components of the $\theta=0$ scattered wave with respect to the phase of incident wave, respectively. Thus, if we denote the phase shift of the scattered wave by $\phi(0)$, it is equal to the tilt angle of the $S(0)$ vector from the P-axis. Furthermore, the well-known Optical Theorem then relates the extinction cross section (or total cross section) C_{ext} to $S(0)$:

$$C_{\text{ext}} = \frac{4\pi}{k^2} |S(0)| \sin \phi(0) = \frac{4\pi}{k^2} \text{Re} \{ \dot{S}(0) \} \quad (1)$$

All P,Q plots in this paper are calibrated in units of volume-equivalent extinction efficiency:

$Q_{\text{ext},v} = C_{\text{ext}}/\pi a_v^2$, so that

$$P = \frac{4}{x_v^2} |S(0)| \cos \phi(0), \quad Q = \frac{4}{x_v^2} |S(0)| \sin \phi(0) \quad (2)$$

where $x_v = ka_v =$ volume-equivalent size parameter

$a_v =$ radius of the sphere equal in volume to the scatterer.

The use of volume-equivalent size parameter in the normalization is due to our empirical findings that, at least in the size range investigated, the total volume of the scatterer seems to be one of the dominant factors in the extinction process (Wang and Schuerman, 1981; Schuerman, et al., 1981; Wang, 1982).

Similarly, we define the volume-equivalent phase-shift parameter ρ as $\rho_v = 4\pi a_v (m'-1)/\lambda = 2x_v (m'-1)$

where $m = m' - im'' =$ complex refractive index.

By reason of mathematical symmetry, all axisymmetric particles have a remarkable simplicity in their $\theta=0^\circ$ scattering patterns with respect to the orientation change (Wang and Schuerman, 1981),

resulting in a considerable reduction of the number of required measurements: One needs only to measure those $S(0)$'s as the particle axis is swept through 90° from the incident direction \vec{k} in 2 mutually orthogonal planes, the k-E plane and the k-H plane of the incident wave. The totality of the scattering quantities in other arbitrary particle orientations can be obtained by a simple linear composition of those contained in these 2 planes. Hence, all dumbbells and chains of spheres in this paper were prepared with axisymmetry.

Each sphere chain contains 2, 3 or 5 identical spheres. All spheres are made of plexiglass (polymethyl methacrylate) or lucite by Dupont's trade name. They are from 3 different commercial sources dating from 1967 to 1983. The refractive indexes were measured using 2 machined waveguide samples from each commercial source and by the classical standing-wave technique of Roberts and von Hippel (1946) in a waveguide-slotted line (see also Schuerman and Wang, 1981). These identical spheres were assembled by enveloping them in a thin plastic film (Xerox transparency sheet, ~ 0.15 mm thickness) to form a chain, and the chain was rotated in the incident beam to measure the orientation dependence of $S(0)$. The extent of error caused by the envelope is still unknown, but for the smallest-sized spheres the envelope was perforated to minimize this error source. The present indoor scattering range has 10.8 m for the transmitter antenna aperture to target center distance and 10.7 m for the target center to receiver aperture employing 50.8 cm diameter parabolic reflectors for both antennas. The result of wavefront examination indicates the measuring system may accommodate up to a ~ 20 cm length particle without serious errors due to curvature in the radiation pattern. Hence, the longest sphere chain has an overall length of 18.85 cm. The pertinent target parameters along with its coded ID numbers are listed in Table I for all 12 sets of chains investigated. 3- or 5- sphere chains have the center of gravity coincident with that of the sphere in the geometrical center and were found particularly simple to orient in the beam by means of our computer-controlled orientation mechanism. Dumbbells, however, were much more difficult to orient precisely by the same reason. Fortunately, the center-of-gravity movement during rotations was within the acceptable limit being partially compensated by stretchable guide strings employed in the target-tilt drive.

EXPERIMENTAL RESULTS AND ANALYSIS

The highly interesting and detailed phenomena of cooperative scattering by multiple spheres can be visualized by judicious analysis of experimental P,Q plots. Indeed, it may not be an exaggeration to say that a complete knowledge about the angular scattering follows the successful theoretical explanation of the subtle orientation effects on $S(0)$ as displayed in P,Q plots. Accurate P,Q plots are thus essential for the purpose, and we have long tried to isolate and minimize error sources. Among them we may mention the following major sources of error which persist and should be improved:

(1) Drift in the measured signal from the output port of null hybrid junction. This is primarily due to the difficulty in maintaining a constant 180° phase difference between the direct beam and the reference wave arriving at the input ports of hybrid, or in short, in maintaining a stable cancellation. These two waves traverse 2 different long paths before they enter the ports for mixing, and any factor which causes the fluctuation of the phases may be a source of drift. For example, the frequency-instability of the microwave source (incoherence), optical-path-length fluctuations due to temperature changes, ground/building vibrations and power-line surges are the possible disturbances. C_{ext} measurement errors may amount to $\sim 3\%$ for targets with $x_v \leq 3$ and $\sim 2\%$ for $3 \leq x_v \leq 6$ by the drift alone.

(2) Each array run is followed by two standard sphere runs for the absolute magnitude and the tilt of P,Q coordinates calibration. These standard spheres were selected out of 10 reliable ones in their mutual consistency and with the Mie theory results on $|S(0)|$ and $\phi(0)$ but are still subject to uncertainties of $\sim 2\%$ in $|S(0)|$ and $\sim 5^\circ$ in phase. Thus a similar extent of errors in measuring the $S(0)$ of an array may exist due to these calibration uncertainties.

(3) Array parameter uncertainties. The $S(0)$ of a given array may be affected by the thin plastic envelope or spacers by which it was assembled. This error is difficult to estimate, and all target parameters in Table I excluded the contribution by their envelopes or spacers.

(4) Finally, there exist the antenna-target multiple reflection errors associated with all $\theta=0$ measurements (Lind, 1966; Wang, 1968) which are particularly worse for particles with high backward-to-forward scattering ratios, r_{BF} 's. It is expected to give rise to the worst errors when the array is near some principal orientations whereby the cooperative scattering enhances the backscatter. In view of the small r_{BF} 's for all chain arrays when averaged over random orientations, this error source is estimated to contribute less than 1% in $S(0)$ measurement for all random sphere chains.

The cumulative error in C_{ext} measurement is estimated to be $\sim 10\%$ for arrays with $x_v \leq 3$ and $\sim 8\%$ for $3 \leq x_v \leq 6$ from the above considerations.

Individual P,Q plots for all 12 sets of arrays are shown in Figs. 1-12, where the averaged volume-equivalent extinction efficiency averaged over random orientations, $\overline{Q_{\text{ext},v}}$, is tabulated in each figure along with pertinent particle parameters. A more detailed account of target parameters is found in Table I. For each set, a single sphere identical to the component sphere of the chain was measured on its $S(0)$ and is shown as a vector marked SNGL SPHERE in each plot. A solid curve and a dotted curve in each P,Q plot, respectively, show the variation of $S(0)$ as the array axis is swept through 90° from the incident direction k toward the incident electric field direction (marked E) in the k -E plane and toward the incident magnetic field direction (marked H) in the k -H plane. A vector drawn from the coordinate origin to each orientation mark along the curve is the $S(0)$ vector at that orientation, and its absolute magnitude $|S(0)|$ can be obtained by comparing its length with that at the E orientation shown

in each figure (marked $|S(0)|_{\mathbb{E}}$). The projection of the $S(0)$ vector onto the calibrated Q axis gives the $Q_{\text{ext},v}$ at that array orientation.

A closer investigation of these P, Q plots reveals the following interesting features:

(1) All arrays except that shown in Figs. 1 & 10 have minimum extinctions when the axes are aligned toward the incident direction. Indeed, the total cross section of some arrays is comparable or even smaller than that of a single component sphere suggesting that the strongest cooperative scattering takes place at this k -orientation for any array. Furthermore, the extinction is also very sensitive to the mutual separation between neighboring spheres.

(2) The weakest cooperation between component spheres is observed at near E or H orientation where the array axis is perpendicular to the beam, i.e., the dependent scattering effect is at its minimum. In such orientations, the $S(0)$ vector of the array is not far from the $S(0)$ vector of a single sphere multiplied only in length by the total number of spheres in the array. This was already observed previously (Wang, 1980; Schuerman and Wang, 1981).

(3) Marked cooperative scattering phenomena were observed when the chain axis was less than $\sim 45^\circ$ from the incident direction. Further increase in this tilt angle χ away from the beam direction brings, in an ever decreasing speed, the $S(0)$ vector toward that at E or H orientations. At $\chi \sim 60^\circ$, the $S(0)$ vector is already close to the converging limit. This feature suggests that the dependent scattering effect is important only when a significant portion of one of the two interacting spheres is illuminated by the other's major angular scattering lobe.

(4) Forward scattering behavior of an array during the k - E plane sweep differs from that during the k - H plane sweep primarily when $\chi \geq 60^\circ$. Even when $\chi \geq 60^\circ$ the difference is comparable only to that by other axisymmetric particles such as cylinders or spheroids (Wang, 1982, paper II). Thus, even a preferentially-oriented sphere-chain is not a strong polarizer by its orientation dependence of extinction.

(5) 3 P, Q plots for contacting 2 spheres give us the opportunity to compare our earlier data (Schuerman and Wang, 1981) with these new data, i.e., to compare the dotted curves in Fig. 1, Fig. 3 and Fig. 10 of this paper with Fig. 8D, Fig. 8E and Fig. 8G of the above report. A pair of such corresponding figures refers to almost the same component-sphere parameters but differs in the way the dumbbell was assembled (with or without mounting envelope), with the measurement device (computer-controlled vs manual target orienting and signal recording), and in the definition of extinction efficiency. Considerable discrepancies were observed for the 2 smallest-sized dumbbells on the measured P, Q plots, especially near the orientation k . Nevertheless, the agreement between Fig. 10 and Fig. 8G, both referring to the largest-sized dumbbell, is fairly good. In view of the lack of a proper procedure for monitoring the cancellation stability and the failure to measure a single-sphere scattering in each run using the old technique, we give the new data higher accuracy.

The volume-equivalent extinction averaged over random chain orientations, $\overline{Q_{\text{ext},v}}$, is plotted against the volume-equivalent phase-shift parameter ρ_v and is displayed in Fig. 13. A number nearest to a data mark denotes the total number of spheres in the chain, and the suffix attached to each number indicates the measure of separation between neighboring spheres. For example, 2_0 and 5_0 mean the data refer to a contacting dumbbell and to a contacting 5-sphere chain, respectively, and 2_1 and 2_4 to a slightly separated dumbbell and to that separation gap increased approximately 4 times. Included in the same plot is a comparison Mie extinction curve for single spheres with the representative refractive index $m=1.61-i0.004$. From Fig. 13 we immediately notice the following marked extinction properties by random sphere chains which are more conspicuous than other axisymmetric particles (Wang and Schuerman, 1981): (1) Beyond the first major single-sphere resonance, $\rho_v \geq 4$, a chain is a more efficient obscurant than the equal-volume sphere. (2) For the size range investigated, the more the inter-sphere separation the more the extinction with the most rapid increase in extinction taking place when the inter-sphere gap is less than $\sim \frac{1}{4}$ diameter of the component sphere. (3) Although the total number of chains is quite limited, the plot indicates that random sphere-chains also exhibit resonance with respect to the variation in ρ_v whose first major peak together with the profile strongly depends on the aspect ratio as well as on the seemingly small inter-sphere separation gap.

SUMMARY

In summary, we find:

- (1) The most subtle details of dependent scattering by interacting spheres are best studied at $\theta=0^\circ$ and display the array-orientation effect on $S(0)$ in a P,Q plot form.
- (2) When the sphere-chain is perpendicular to the beam, the least interaction between spheres is observed. Hence, to a good approximation, the array's $S(0)$ vector is the vector sum of those of the component spheres.
- (3) Dependent scattering is important when an array axis is tilted less than $\sim 60^\circ$ from the beam direction where the most complicated interaction takes place. Also, the most rapid changes in the forward-scattering properties are observed when the neighboring spheres have a separation gap of less than about $\frac{1}{4}$ diameter of a component sphere, although the dependent scattering effect will persist for much larger separation distances.
- (4) The measurement system needs further improvement in phase stability so that one can hold the cancellation of the background long enough for the accurate display of a P,Q plot.

ACKNOWLEDGMENT

The author is indebted for helpful discussions with Drs. J.L. Weinberg and B.Å.S. Gustafson and for engineering assistance extended to him by other Space Astronomy Laboratory colleagues during this work. This work was jointly supported by the Army Research Office and the Air Force Office of Scientific Research.

REFERENCES*

- Bruning, J. H., and Lo, Y. T., IEEE Trans. Ant. Prop., AP-19, 378 (1971).
- Lind, A. C., Wang, R. T., and Greenberg, J. M., Appl. Opt. 4, 1555 (1965).
- Lind, A. C., Ph.D. Thesis, Rensselaer Polytechnic Institute, Troy, N.Y. (1966).
- Roberts, S., and von Hippel, A., J. Appl. Phys., 17, 610 (1946).
- Schuerman, D. W., and Wang, R. T., Experimental Results of Multiple Scattering, Final Rept., ARCSL-CR-81003, U.S. Army Chemical Systems Laboratory, Aberdeen, MD (Nov. 1981).
- Schuerman, D. W., Wang, R. T., Gustafson, B. Å. S., and Schaefer, R. W., Appl. Opt. 20, 4039 (1981).
- Wang, R. T., Ph.D. Thesis, Rensselaer Polytechnic Institute, Troy, N.Y. (1968).
- Wang, R. T., and Greenberg, J. M., Scattering by Spheroidal and Rough Particles, Final Rept., NASA NSG 7353 (Aug. 1978).
- Wang, R. T., in 'Light Scattering by Irregularly Shaped Particles', Schuerman, D. W., Ed. (Plenum, N.Y. 1980), p. 255.
- Wang, R.T., and Schuerman, D. W., in 'Proceedings, 1981 CSL Scientific Conference on Obscuration and Aerosol Research', R. Kohl, Ed., U.S. Army CSL, Aberdeen, MD.
- Wang, R. T., Greenberg, J. M., and Schuerman, D. W., Opt. Lett. 6, 543 (1981).
- Wang, R. T., in 'Proceedings, 1982 CSL Scientific Conference on Obscuration and Aerosol Research', R. Kohl, Ed., U.S. Army CSL, Aberdeen, MD.

TABLE I. MICROWAVE TARGET PARAMETERS

Target ID #	No. of Spheres in the Chain	Single Sphere Size Parameter	Complex Refractive Index	Surface-equivalent Size Parameter	Volume-equivalent Size Parameter	Volume-equivalent Phase-shift Parameter	Overall Length	Dimensionless* Separation Parameter
	n	x	$m=m'-im''$	x_s	x_v	ρ_v	L (cm)	ks
512000	2	2.176	1.629 -i0.0125	3.077	2.741	3.488	4.404	4.358
515000	5	"	"	4.865	3.720	4.680	11.02	"
532000	2	3.083	1.610 -i0.004	4.360	3.884	4.738	6.248	6.166
532001	2	"	"	"	"	"	7.19	8.03
532004	2	"	"	"	"	"	9.46	12.51
533000	3	"	"	5.340	4.446	5.424	9.373	6.166
533001	3	"	"	"	"	"	10.75	7.52
535000	5	"	"	6.894	5.272	6.432	15.62	6.166
535001	5	"	"	"	"	"	18.85	7.76
542000	2	4.346	1.63 -i0.01	6.147	5.476	6.900	8.809	8.693
542001	2	"	"	"	"	"	9.31	9.68
542002	2	"	"	"	"	"	10.03	11.11

* s =center to center separation distance between two neighboring spheres

FIGURES

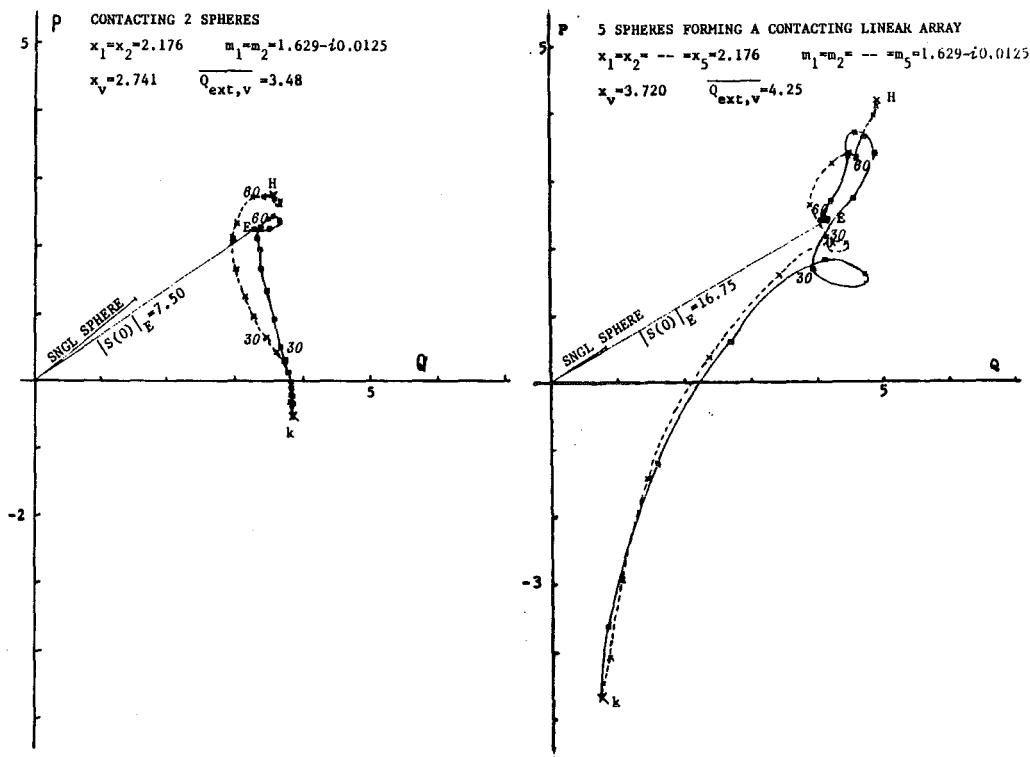


FIGURE 1. P,Q PLOT FOR TARGET #512000
 See also Sec. 2 and Table I.

FIGURE 2. P,Q PLOT FOR TARGET #515000
 See also Sec. 2 and Table I.

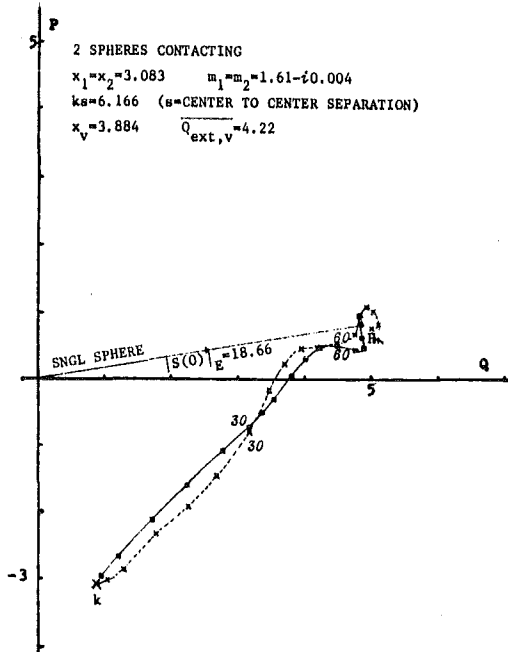


FIGURE 3. P,Q PLOT FOR TARGET #532000
See also Sec. 2 and Table I.

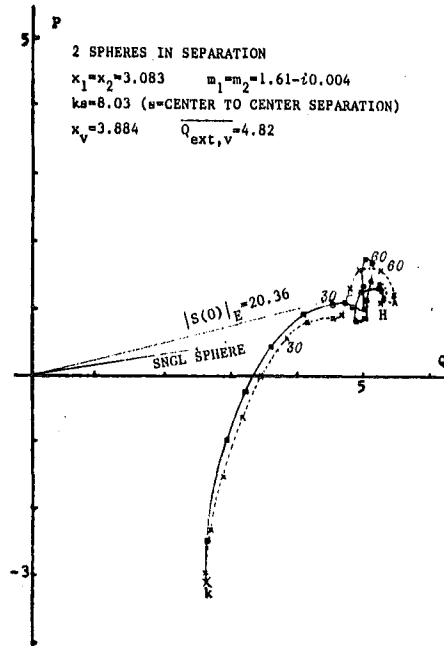


FIGURE 4. P,Q PLOT FOR TARGET #532001
See also Sec. 2 and Table I.

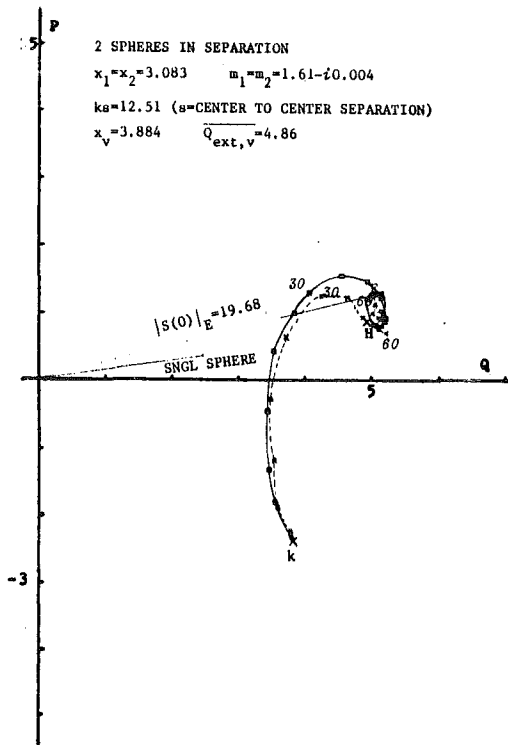


FIGURE 5. P,Q PLOT FOR TARGET #532004
See also Sec. 2 and Table I.

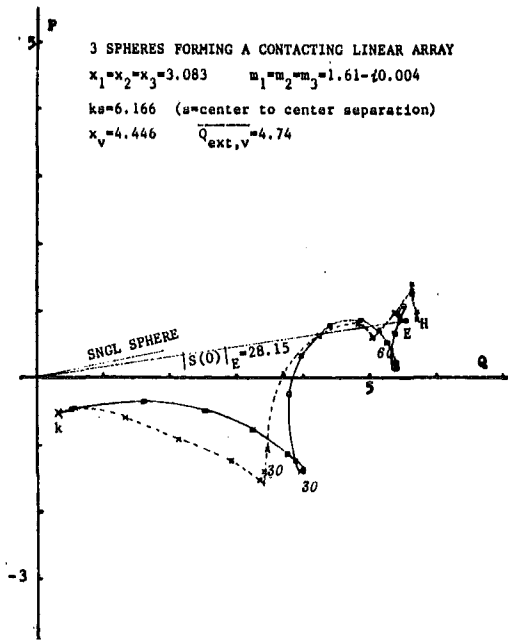


FIGURE 6. P,Q PLOT FOR TARGET #533000
 See also Sec. 2 and Table I.

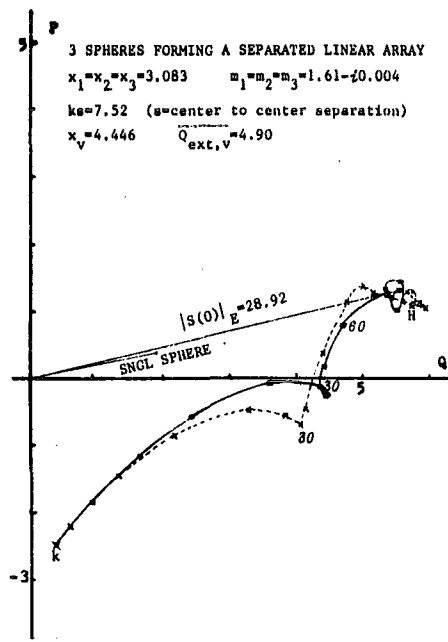


FIGURE 7. P,Q PLOT FOR TARGET #533001
 See also Sec. 2 and Table I.

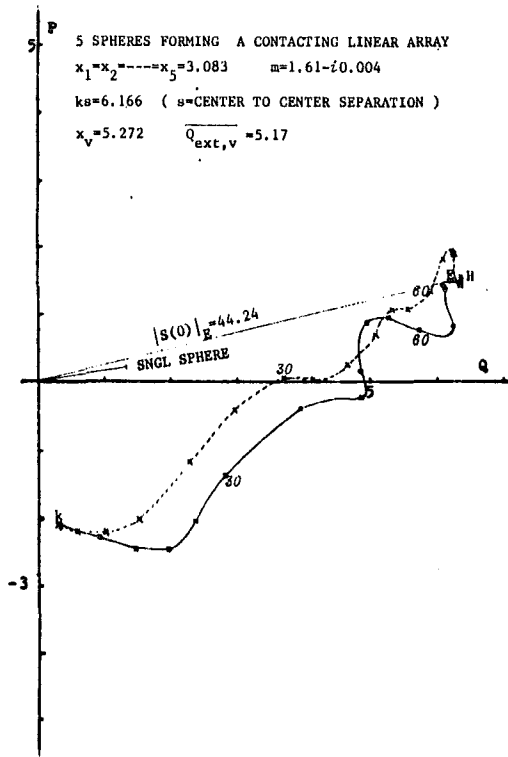


FIGURE 8. P,Q PLOT FOR TARGET #535000
 See also Sec. 2 and Table I.

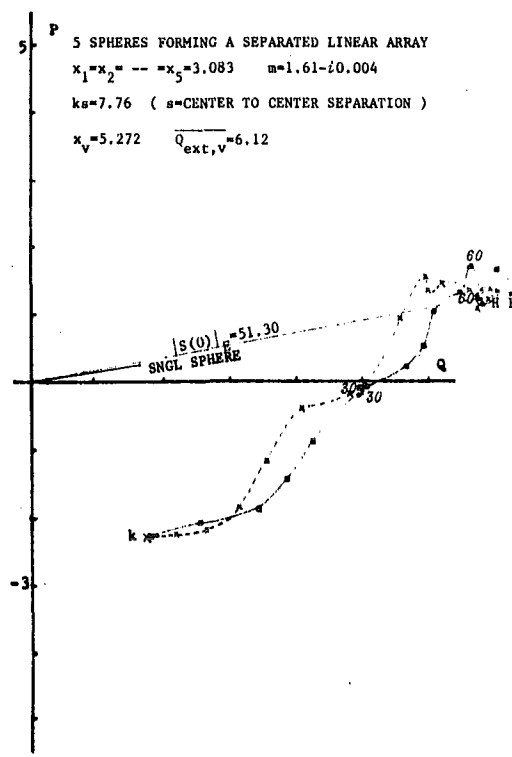


FIGURE 9. P,Q PLOT FOR TARGET #535001
 See also Sec. 2 and Table I.

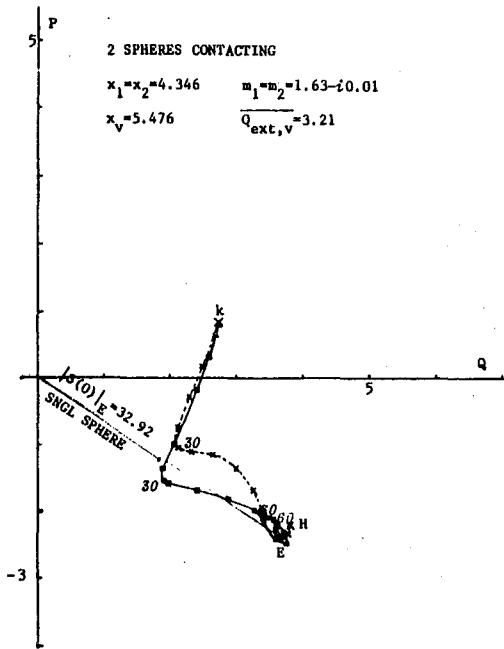


FIGURE 10. P,Q PLOT FOR TARGET #542000
See also Sec. 2 and Table I.

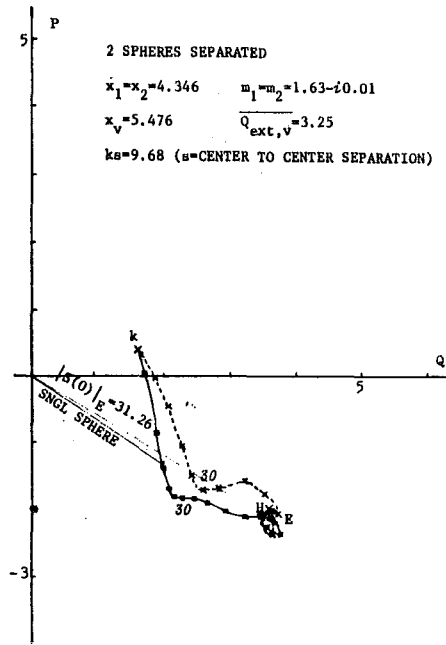


FIGURE 11. P,Q PLOT FOR TARGET #542001
See also Sec. 2 and Table I.

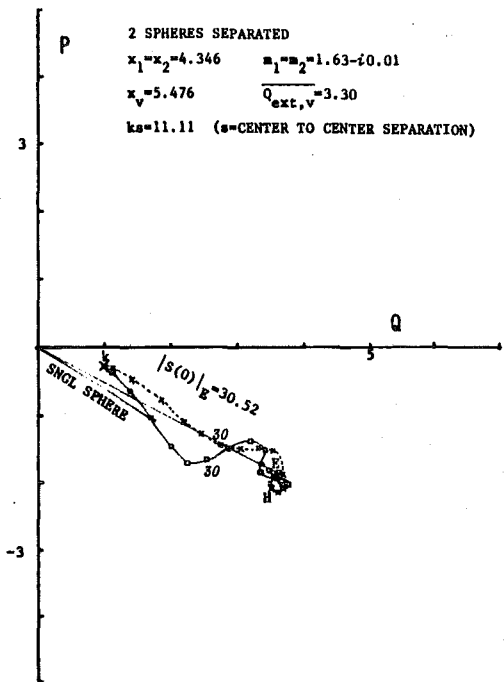


FIGURE 12. P,Q PLOT FOR TARGET #542004
See also Sec. 2 and Table I.

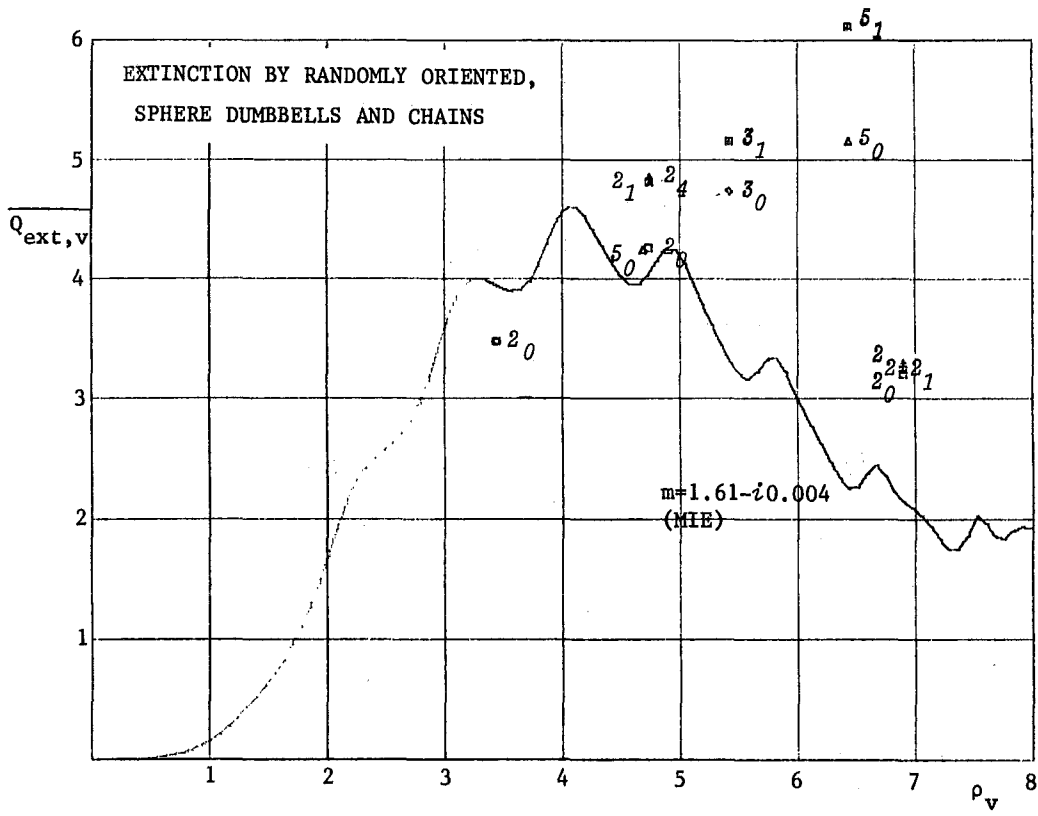


FIGURE 13. $\overline{Q_{ext,v}}$ VERSUS ρ_v PLOT FOR THE 12 SPHERE-CHAINS

The volume-equivalent extinction efficiency as averaged over random chain orientations is plotted against the volume-equivalent phase-shift parameter. The number next to each data mark denotes the total number of spheres in the chain, and the subscript attached to the number gives the measure of separation between neighboring spheres (0 means contacting; 1, slightly separated; and 4, further separated).

The continuous curve is the extinction curve from Mie theory for spheres.

BLANK

ANGULAR SCATTERING AND POLARIZATION BY RANDOMLY
ORIENTED DUMBBELLS AND CHAINS OF SPHERES

R. T. WANG AND B. Å. S. GUSTAFSON
Space Astronomy Laboratory, University of Florida
1810 N.W. 6th Street, Gainesville, Florida 32601

ABSTRACT

Phase functions and the degree of polarization of the scattered (microwave) radiation are measured for 12 sets of dumbbells and chains, each consisting of 2, 3 or 5 identical spheres in various inter-sphere separations. Due to the symmetry in array shape we can also measure the random-orientation average of these phase functions by taking the arithmetic mean observed for 35 orientations uniformly distributed over an octant of space. Surprisingly, it was observed that the angular scattering signatures of each component sphere were preserved at scattering angles $\theta \geq 90^\circ$ for these randomly-oriented chains. The full results and an extended analysis will be submitted to Applied Optics for publication.

INTRODUCTION

This paper deals exclusively with the microwave-scattering measurement results of angular distribution/degree of polarization for 12 dumbbells and chains of spheres in the angular range $0 \leq \theta \leq 170^\circ$. The $\theta=0$ data are derived from the extinction measurements (Wang, this volume). These measurement results, along with the Mie theory predictions for a component sphere in all individual arrays, are presented in Sec. 3 which follows the brief descriptions on experimental procedures of Sec. 2. The paper concludes with the summary in Sec. 4. All mathematical expressions related to the definitions of scattering quantities are referred to in our previous publication (Schuerman, et al., 1981). Except for some minor differences, we follow as closely as possible the format employed in the above paper for presenting our results.

BRIEF DESCRIPTION OF PERFORMING THE EXPERIMENT

Compared to the measurement of extinction, measurement of angular scattering is simplified since only one channel for recording the scattering, namely the intensity, is required. Yet, the 17-fold increase in the number of scattering angles, the 3 different combinations of transmitter/receiver antenna polarizations and the needed background-cancellation (nulling) procedure at each of the above sets of measurements make this experiment vastly more time-consuming than that for extinction. On the other hand, the smallness of the uncompensated background compared to the particle-scattered signal at most scattering angles makes the measurement less subject to errors from system instability.

The present facility employs a $\lambda=3.18$ cm microwave source and a 51 cm-diameter parabolic reflector as the transmitting antenna whose dipole-disk primary feed mounted on a waveguide rotary joint allows the continuous variation of the direction of polarization of the transmitted wave. 10.8 meters away from the antenna aperture and 2 meters above ground level on the beam center is the target site to which a scatterer is introduced and varied in orientation via a computer-controlled mechanism. The mechanism

has only thin nylon strings near the target site to ensure negligible contribution to the true scattering. A smaller (41 cm-diameter), but otherwise similar, receiving antenna is mounted on a movable cart which in turn is hinged to a rotatable drum on the floor level beneath the target site. The sweep of the movable cart thus allows the reception of the scattered wave over the angular range $0 \leq \theta \leq 170^\circ$ at a constant target-receiver distance of 5.2 meters. The opposite wall facing this receiver antenna is lined with microwave absorbers so as to prevent the secondary/stray scattered signal from entering the major reception cones of the antenna. A maximum target size of ~20 cm may be accommodated without serious errors by these antenna range considerations.

The microwave target parameters are listed in Table I, which is a duplicate of Table I of the preceding paper (Wang, this volume), except for slight differences in intersphere separation of the two largest-sized dumbbells. All particle arrays are axisymmetric (and are also mirror-symmetric) in shape so that by virtue of the mathematical symmetry one needs only to measure those at particle orientations uniformly distributed over an octant of space bounded by the bisectrix plane (van de Hulst, 1957) in order to assess the true random-orientation average of the received signal (Gustafson, 1980). This is an 8-fold increase in the data-acquisition speed compared to that for particles without symmetry (also see Schuerman, et al., 1981).

Mounted on the platform of the movable receiver antenna cart is a microwave hybrid junction (null junction) into whose two orthogonal input ports the signals from the antenna and from a reference waveguide circuitry (piped directly from the transmitter) are fed. In the absence of the scatterer, the mixer output from the output port of the hybrid is cancelled by adjusting the phase-shifter and the attenuator of the reference-wave circuitry. As the particle is brought into the site, the off-balance appearing in this output port is linearly proportional to the amplitude of the scattered wave. When 1000 Hz square-wave modulated and fed to a square-law detector and a 1000 Hz filter, the detected output D.C. signal is proportional to the square of the amplitude or intensity of the scattered wave. A high-gain lock-in amplifier/detector serves thereby for the noise-free performance of the detection/amplification.

In an actual run we measure 3 polarization components of the scattered intensity at each scattering angle θ . These components are: i_{11} where both the beam and the reception antennas are polarized vertical; i_{22} where both are horizontal; and i_{12} where the beam polarization is vertical with the reception polarization horizontal. At each of these polarization settings, the array is allowed to sweep through 44 preselected orientations with respect to the beam, of which 35 are used in computing the random-orientation average while the rest are special orientations for convenience in comparing with theoretical predictions. Immediately after attaining each of these 44 orientations, the mechanism is halted and the detected signal recorded onto a computer diskette before proceeding to the next orientation. The

random-orientation averages over the 35 orientations, denoted in this paper by I_{11} , I_{22} and I_{12} respectively, are also computed during the run along with their standard deviations.

Finally, the absolute-magnitude calibration of I_{11} and I_{22} (also i_{11} and i_{22}) is made by a standard sphere run in quick succession before and/or after the target run with that of I_{12} (and i_{12}) by a standard spheroid. For example, the I_{11} , I_{22} calibrations in this paper are made at $\theta=50^\circ$ by a sphere which possesses $x=5.001$, $m=1.629-i0.0125$, $i_{11}(50^\circ)_{\text{Mie}}=31.27$ and $i_{22}(50^\circ)_{\text{Mie}}=24.36$ with the I_{12} calibrations by a 2:1 prolate spheroid at $\theta=120^\circ$ with $x_v=5.807$, $m=1.61-i0.004$ and $I_{12}(120^\circ)_{\text{theoretical}}=3.0897$ (See Schuerman, et al., 1981). The scattering angles 50° and 120° were chosen because: (1) at these angles the intensities i_{11} , i_{22} and I_{12} of the calibration standards were known to peak; (2) the measurement error caused by background drift would be small; and (3) the choice of only one calibration angle per polarization would not only expedite the operation but also insure the accuracy/repeatability of target orienting during a lengthy measurement run. At the time of the present measurements, however, the system gain was not very stable due to power line fluctuations/surges and other disturbances. Hence, most of the data were taken with $\Delta\theta=20^\circ$ for I_{12} except for the 3 largest dumbbell sets (see Table I) where I_{11} 's were observed to have marked oscillations with respect to θ and hence all I_{11} data were measured with $\Delta\theta=5^\circ$. Therefore, all data at the intervening scattering angles such as at $\theta=5^\circ$, 15° , ... 165° , are the interpolated data via the use of the 3rd order Aitken-Lagrange interpolation technique (Todd, 1967).

EXPERIMENTAL RESULTS AND DISCUSSION

The measurement results for phase functions and degree of polarization versus scattering angle θ are displayed in Figs. 1A-5D, a total of 20 figures, in uniform format. Fig. 1A, 1B, 1C, and 1D are respectively for I_{11} , the perpendicular component, I_{22} , the parallel component, I_N and I_{12} , the total brightness and the cross-polarized component, and P, the degree of polarization; similar conventions apply for Figs. 2A-5D. Each group of figures contains the results for 2 or 3 arrays wherein all component spheres are identical in size/refractive index. Except for Figs. 1A-1D which show the contacting 2- and 5-sphere arrays of the smallest component sphere size, all figures are so grouped that all figures in a group refer to those arrays having the same total number of identical spheres differing only in the mutual separation between neighboring spheres. Each experimental dot in each figure represents the average over the 35 orientations uniformly distributed in an octant of space, and different arrays are identified by different symbols. Array parameters are found through Table I via the coded array ID number shown in the figure caption.

The first remarkable scattering property noted for all these arrays was the unusually high degree of polarization P near $\theta=140^\circ$. While in the previous investigation (Schuerman, et al., 1981) for random

spheroids, cylinders and disks P never exceeded $\pm 50\%$; the sphere-chains exhibited $\sim 75\%$ or more in the negative P at such backscattering angles. The only particles known by us to exhibit this property were spheres! This led us to infer that the scattering signature of component spheres might be preserved for backscatter angles. Accordingly, the Mie theory result for the component sphere is also plotted as a continuous curve in each figure. Some highly interesting features are noted by the examination of signatures displayed in these figures, comparison between figures for different arrays and comparison with Mie theory predictions for component spheres:

(1) All individual phase functions I_{11} , I_{22} and I_N have more marked oscillations with respect to θ variation as compared to those for other axisymmetric nonspheres (Schuerman, et al., 1981). At high scattering angles, $\theta \gtrsim 90^\circ$, these phase functions follow nicely the Mie theory predictions; and the larger the sphere size, the smaller the θ at which this trend starts to appear. For example, in the case of the largest component-sphere size $x=4.346$ (as shown in Figs. 5A-5D) the preservation of single-sphere scattering signature is evident at $\theta \gtrsim 60^\circ$. At the same time, it is also tempting to obtain the absolute magnitudes of I_{11} , I_{22} and I_N by simply multiplying the corresponding single-sphere magnitude by the total number of spheres in the chain, even though the magnitudes are also affected by the sphere-separations to some extent.

(2) On the other hand, the dependent scattering effect is conspicuous at the smaller scattering angles. In such cases the absolute magnitude of these phase functions is comparable or even smaller than that of a single sphere over $20^\circ \lesssim \theta \lesssim 80^\circ$; and the larger the sphere size the narrower this range, being $20^\circ \lesssim \theta \lesssim 35^\circ$ in the case shown in Figs. 5A-5D. The subtle cooperative scattering phenomenon also manifests itself as the existence of an unexplained bump/peak in the phase function whose angular position and width depend intricately on the array parameters as well as on the incident polarization (see Figs. 2A-2D, 3A-3C and 4A-4C).

(3) The cross-polarized component I_{12} is, in general, 1 to 3 orders of magnitude smaller than the corresponding I_{11} , I_{22} and I_N except near the $\theta=120^\circ$ peak where it may become comparable. Thus, for practical purposes I_{12} may be neglected in the computation of degree of polarization at other scattering angles. Being small and comparable in magnitude to the residual fluctuating background, the accuracy of I_{12} is questionable except near the peaks. All sphere-chains are observed to have an additional peak at $\theta \sim 0^\circ$ (Fig. 1C is the sole exception). In general, the larger the separation between neighboring spheres the smaller is the I_{12} magnitude at all scattering angles.

(4) By far the most striking scattering signature is seen through the θ dependence of the degree of polarization as shown in Figs. 1D, 2D, 3D, 4D and 5D. We have shown previously that polarization is the most sensitive measure to probe the target shape (Schuerman, et al., 1981). In the present sphere-chain case, the shape signature of polarization is so intensified that it preserves the strong

polarizability of individual spheres! Thus, by knowing the θ dependence of polarization for a component sphere in a chain, one could predict the angular positions θ at which the polarization by a chain peaks, its signs, profiles and even the absolute magnitude, to a fair degree of accuracy. For the 12 arrays investigated here, this preservation of polarization was generally observed beyond $\theta \gtrsim 45^\circ$, and the larger the intersphere separation the more marked the preservation. Also, for this particular size range the polarization averaged over all scattering angles is strongly negative with dominant peaks at $120^\circ \lesssim \theta \lesssim 155^\circ$. Hence, when illuminated by natural light, a monodisperse cloud of such chains will scatter strongly polarized light toward these angles in the scattering plane.

SUMMARY REMARKS

In summary, we find:

(1) The effect of dependent scattering by individual spheres in a randomly oriented chain is more important in the forward scattering angles ($\theta \lesssim 90^\circ$) than in the backward ($\theta \gtrsim 90^\circ$); and in the latter case it is a good approximation to treat the problem as independently scattering multiple spheres whereby the scattering signature of each component sphere is well preserved.

(2) Notice that the above remarkable feature (1) applies to random chains only. For a preferentially oriented chain, especially when the chain-axis is oriented in the beam direction, dependent scattering effects were observed at all scattering angles. Work is in progress to analyze the data from preferentially oriented chains.

(3) The degree of polarization is again found to be a powerful measure in probing the particle shape when the scatterer is randomly oriented.

ACKNOWLEDGMENT

The authors thank Drs. J. L. Weinberg and F. Giovane for valuable advice during this work. Special thanks are due to Mack Mann, R. C. Hahn and J. McKisson for the engineering help; and to Allen and Sherry Messer for the observation assistance. This work was jointly supported by the Army Research Office and the Air Force Office of Scientific Research.

REFERENCES

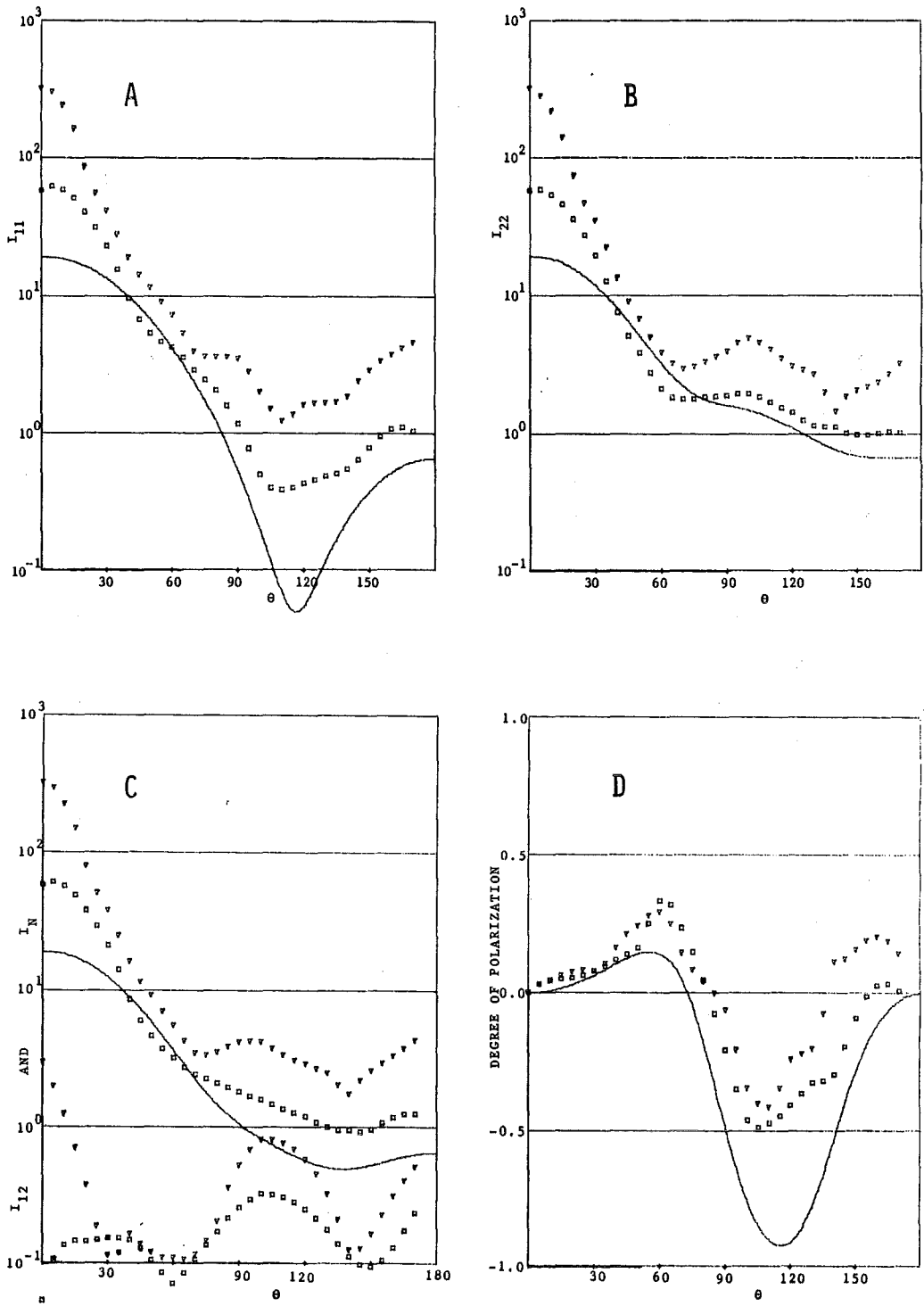
- Gustafson, B. Å. S., Reports from the Observatory of Lund, 17, p. 116 (1980).
Schuerman, D. W., Wang, R. T., Gustafson, B. Å. S., and Schaefer, R. W., Appl. Opt. 20, 4039 (1981).
Todd, J., in "Handbook of Physics," E. U. Condon and H. Odishaw, eds., McGraw-Hill, N.Y., p. 1-94 (1967).
Van de Hulst, H. C., Light Scattering by Small Particles, Wiley, N.Y. (1957).
Wang, R. T., this volume (1984).

TABLE I. MICROWAVE TARGET PARAMETERS

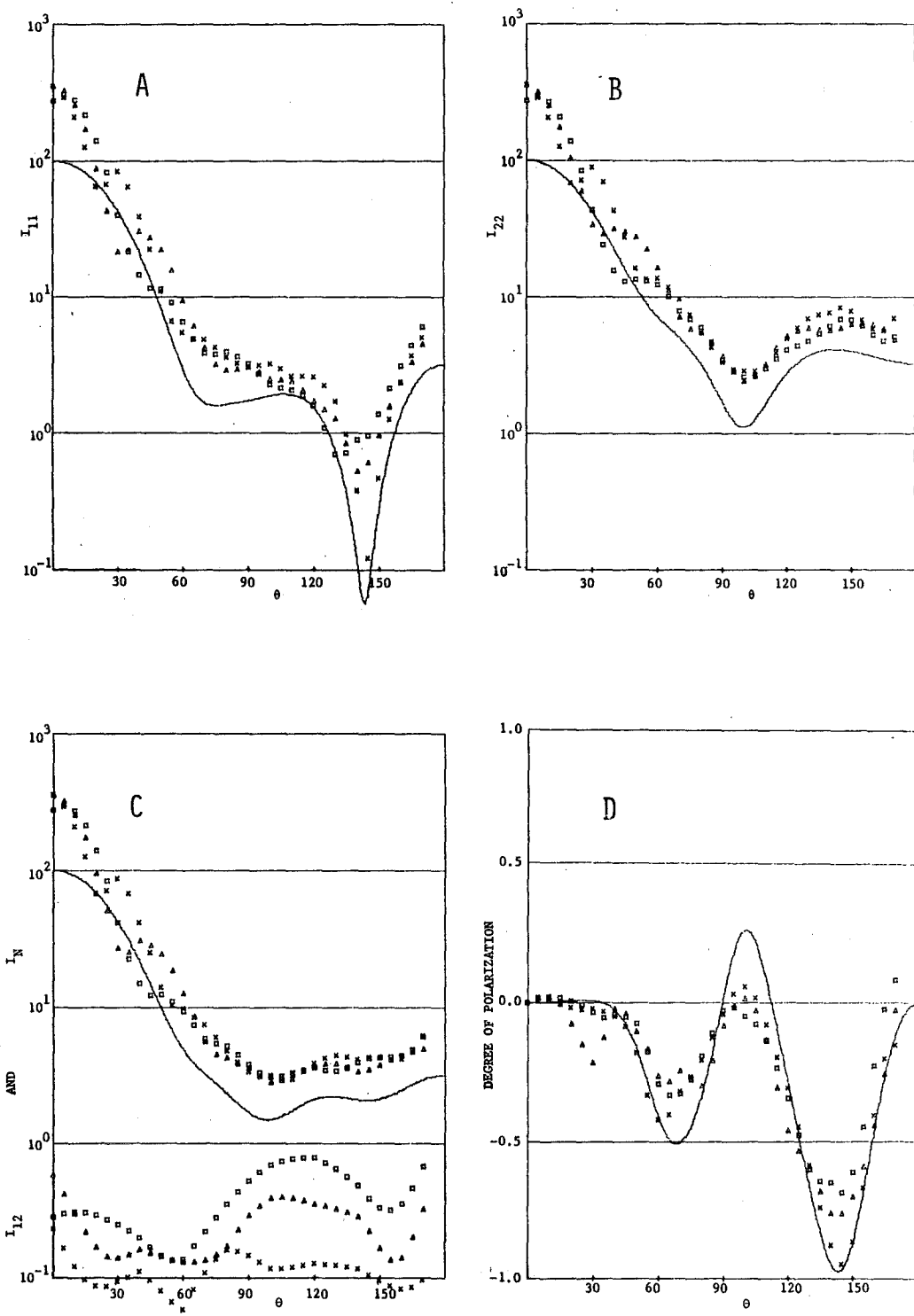
Target ID #	No. of Spheres in the Chain	Single Sphere Size Parameter	Complex Refractive Index	Surface-equivalent Size Parameter	Volume-equivalent Size Parameter	Volume-equivalent Phase-shift Parameter	Overall Length	Dimensionless* Separation Parameter
	n	x	$m=m'-im''$	x_s	x_v	ρ_v	L (cm)	ks
512000	2	2.176	1.629 -i0.0125	3.077	2.741	3.488	4.404	4.358
515000	5	"	"	4.865	3.720	4.680	11.02	"
532000	2	3.083	1.610 -i0.004	4.360	3.884	4.738	6.248	6.166
532001	2	"	"	"	"	"	7.19	8.03
532004	2	"	"	"	"	"	9.46	12.51
533000	3	"	"	5.340	4.446	5.424	9.373	6.166
533001	3	"	"	"	"	"	10.75	7.52
535000	5	"	"	6.894	5.272	6.432	15.62	6.166
535001	5	"	"	"	"	"	18.85	7.76
542000	2	4.346	1.63 -i0.01	6.147	5.476	6.900	8.809	8.693
542001	2	"	"	"	"	"	9.44	9.94
542002	2	"	"	"	"	"	9.86	10.76

* s=center to center separation distance between two neighboring spheres

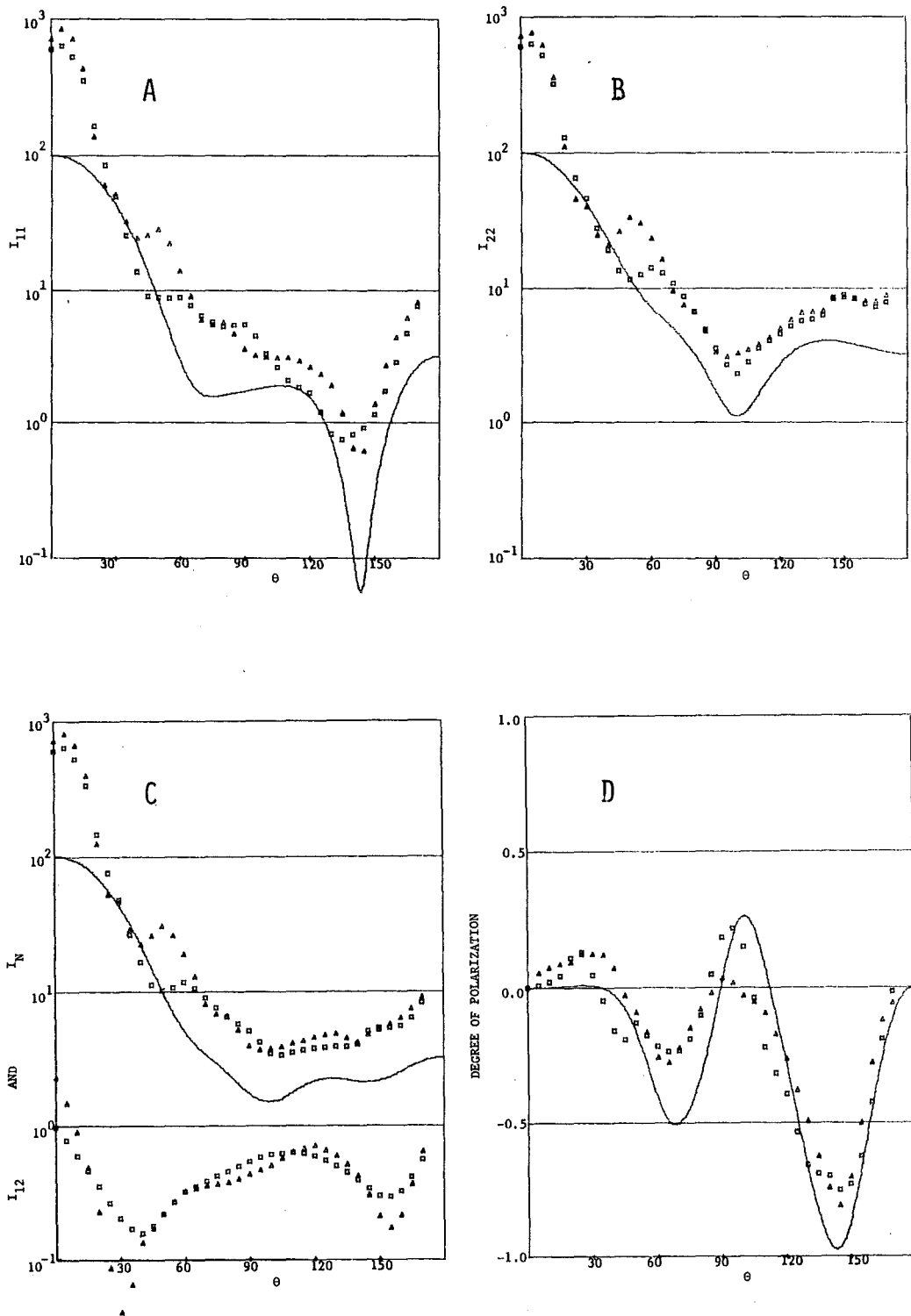
FIGURES



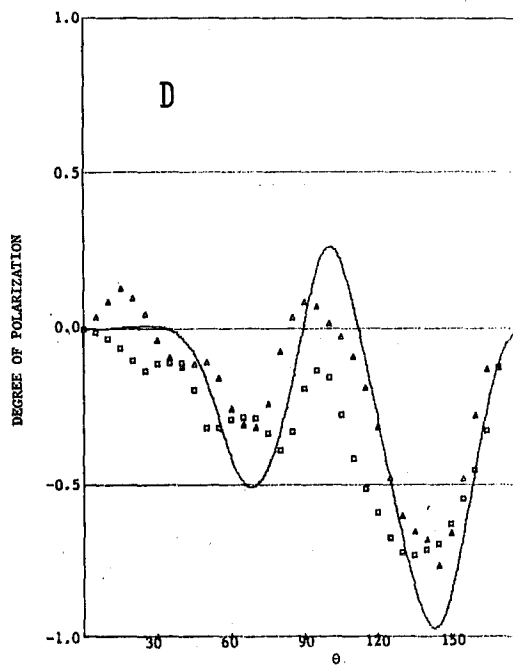
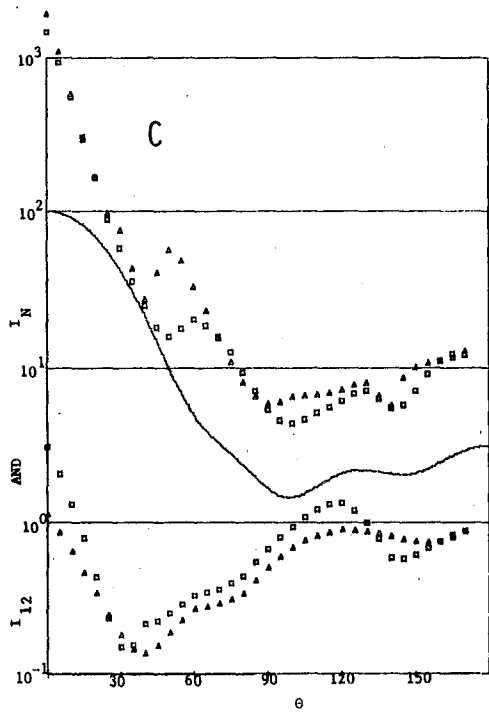
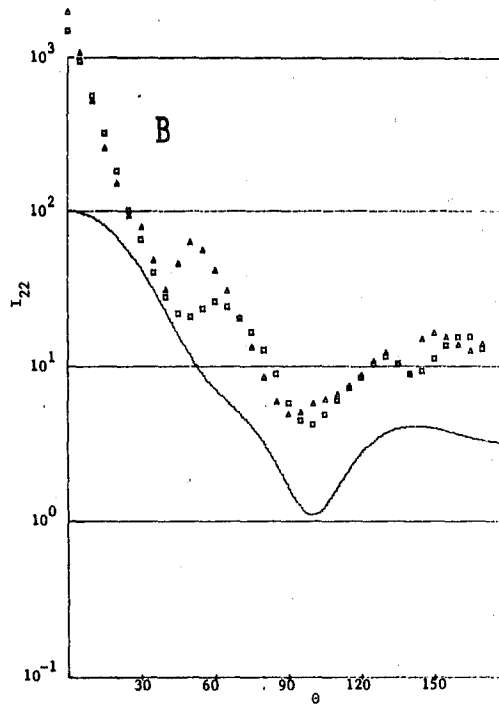
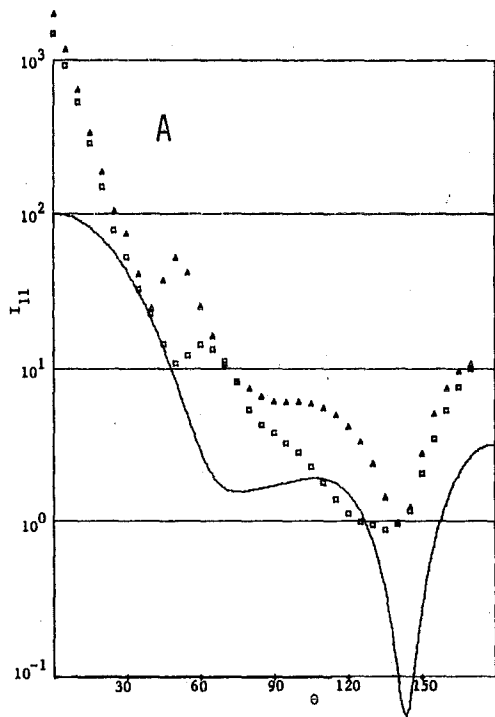
FIGURES 1A-1D ANGULAR DISTRIBUTION/POLARIZATION DATA FOR RANDOMLY ORIENTED SPHERE-CHAINS
 Target identification symbols: \square 512000 ; ∇ 515000. See also Sec. 3 and Table I.
 A continuous curve in each figure is the Mie theory prediction for a component sphere in the chain.



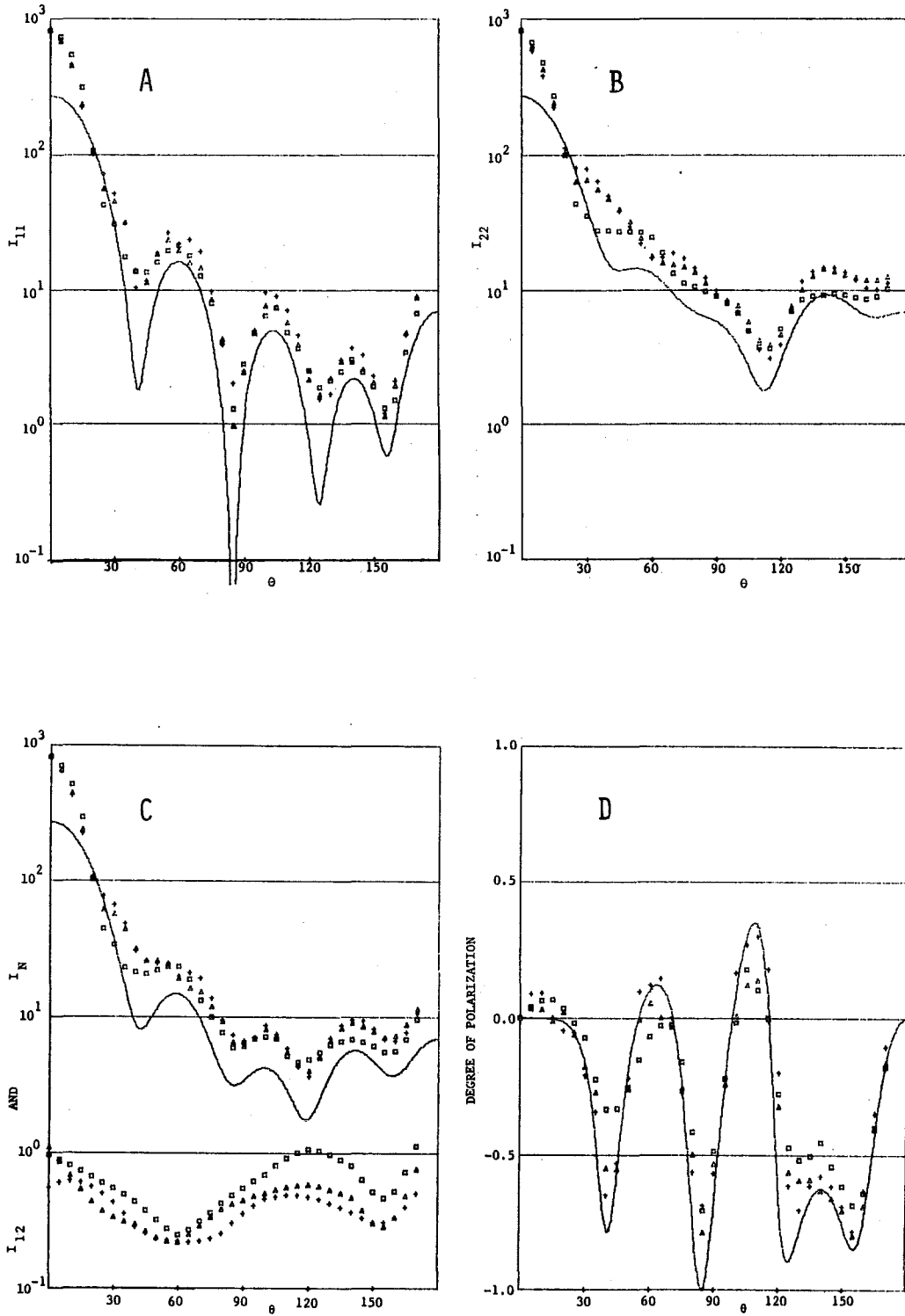
FIGURES 2A-2D. ANGULAR DISTRIBUTION/POLARIZATION DATA FOR RANDOMLY ORIENTED SPHERE-CHAINS
 Target identification symbols: \square 532000; \triangle 532001; \times 532004. See also Sec. 3 and Table I.
 A continuous curve in each figure shows the Mie theory prediction for a component sphere in the chain.



FIGURES 3A-3D. ANGULAR DISTRIBUTION/POLARIZATION DATA FOR RANDOMLY ORIENTED SPHERE-CHAINS
 Target identification symbols: \square 533000; \triangle 533001. See also Sec. 3 and Table I. A continuous
 curve in each figure shows the Mie theory prediction for a component sphere in the chain.



FIGURES 4A-4D. ANGULAR DISTRIBUTION/POLARIZATION DATA FOR RANDOMLY ORIENTED SPHERE-CHAINS
 Target identification symbols: \square 535000; \blacktriangle 535001. See also Sec. 3 and Table I. A continuous curve in each figure shows the Mie theory prediction for a component sphere in the chain.



FIGURES 5A-5D. ANGULAR DISTRIBUTION/POLARIZATION DATA FOR RANDOMLY ORIENTED SPHERE-CHAINS
 Target identification symbols: □ 542000; ▲ 542001; + 542002. See also Sec. 3 and Table I.
 A continuous curve in each figure shows the Mie theory prediction for a component sphere in the chain.

BLANK

Fourier Analysis of Light Scattered from Nonspherical Particles

C. D. Capps, R. L. Adams, A. R. Tokuda, G. M. Hess
Boeing Aerospace Company
P.O. Box 3999
Seattle, WA 98124

ABSTRACT

The scattering patterns, intensity versus angle, were photographically recorded for a set of individual spherical and nonspherical particles. These patterns were then digitized with a scanning microdensitometer, converted to curves of intensity versus angle, and the curves Fourier transformed. Features in the Fourier power spectra were compared with the microscopically determined size of the individual particles.

Introduction

The general problem of scattering of electromagnetic radiation from particles with a size on the order of the wavelength has been solved only for a few geometric shapes: spheres (Mie¹, 1908), infinite cylinders (Wait², 1955), and spheroids (Asano and Yamamoto³, 1975). Except for the case of small liquid droplets, practical aerosols are normally composed of irregularly-shaped particles for which solutions do not exist. This lack of a theory makes it difficult to predict or analyze the results of scattering experiments.

In order to assess the size information contained in the differential scattering pattern of irregular particles, we have experimentally obtained the patterns from individual particles of several different shapes and materials. These scattering patterns were analyzed using Fourier theory to obtain size information which was compared with the microscopically obtained size for each particle. The following sections describe the experimental procedure and the results and analysis.

Experimental Arrangement

The core of the measurement system was an electrodynamic balance for suspending single particles using electric fields. The theory of this device is given in a paper by Davis and Ray.⁴ Basically, the trap consisted of a cylindrically symmetric ring electrode with a hyperbolic inner face and two hyperbolic endcap electrodes. If the particle of interest acquired an electrostatic charge, a d.c. voltage between the endcaps cancelled the gravitational force and an a.c. voltage between the ring and endcaps stabilized the particle laterally and vertically. The voltage and frequency necessary to suspend a particle of a given charge to mass ratio are discussed in Reference 4.

In our arrangement a slit in the ring electrode allowed illumination of the particle and recording of the scattering pattern. A strip of Kodak TRI-X film was wrapped around the chamber in a circular arc centered on the particle to record this pattern. Due to mechanical obstacles the film captured the pattern only in a 168° arc, i.e., 6° from the direction of beam propagation to approximately 6° from the backscatter direction, in the plane of the beam and in a 6° arc perpendicular to this plane. Thus, a scattering pattern representing a band of elevation and azimuthal angles was recorded.

The focused beam of a 50 mw HeNe laser operating at a wavelength of 632.8 nm illuminated the individual particles. The laser was linearly polarized perpendicular to the scattering plane. As no polarization filter was used in front of the film, the recorded scattering pattern is the sum of both perpendicular and parallel polarization components of the scattered radiation.

The suspended particles also were observed with a long working distance microscope (60X magnification, 6 micron resolution) using backlighting with white light. The entire chamber was rotated so that the particle could be observed from the same direction as the incident laser beam. In general, the particles oriented themselves so that their longest dimension was vertical, i.e., perpendicular to the scattering plane. The asymmetric ones tended to maintain equilibrium positions about this axis. However, random air currents would cause them to rotate several degrees about the vertical axis. As it was not possible to simultaneously observe the particle and record a scattering pattern, there is uncertainty as to the precise rotational orientation of the particles for a given scattering pattern. Visual observation of the scattering pattern, however, showed that these rotational changes had periods of a few seconds. Exposure times of 1/50 to 1/100 of a second were used so that the data were not affected by the rotation of the particles.

Results

Four types of particles, described as follows, were used in this series of measurements.

Glass -	spheres 25 to 30 microns in diameter
Stainless steel -	fibers 8 microns in diameter and 200 to 300 microns long.
Carbon -	nearly spherical particles 30 to 50 microns in diameter.
Sodium chloride -	cubic crystals 20 to 30 microns on the edges.

Samples of all four substances were characterized using a scanning electron microscope for greater resolution than was possible optically.

As was pointed out in the introduction, no general solution exists for predicting scattering from the particles used in this study except for the spheres. The approach chosen was to treat the particles as totally absorbing, two-dimensional objects and to determine their size from the data using Fraunhofer diffraction theory. From Babinet's principle the off-axis scattering of such an object is the same as for a screen with a complementary aperture. Both square and circular apertures asymptotically satisfy the following relationship (see, for example, Born and Wolf⁵)

$$\text{size} = \frac{\text{wavelength}}{\text{angular spacing of intensity minima}} \quad (1)$$

This hypothesized relation suggests a Fourier analysis of the scattering pattern to test if

- 1) there is a dominant frequency which indicates a regular spacing of the minima and
- 2) the size, wavelength, and frequency satisfy Equation 1.

As the first step in the data analysis the photographically recorded scattering patterns were scanned on a scanning microdensitometer to obtain digitized values of the density versus position on the film strip. The scan line was taken along the intersection of the scattering plane, i.e., the plane perpendicular to the beam axis and the electric vector of this linearly polarized laser beam, and the film. For simplicity in analysis, the film had been bent into a circular arc centered on the particle with a radius of 62 mm for recording the scattering pattern. This gave a scale of 1.61×10^{-2} radians/mm on the film. Combining this with the published⁶ resolving power for TRI-X film of 100 cycles/mm gives an upper limit on resolution of 6.2×10^3 cycles/radian for the experiment. If Equation (1) is valid and the largest dimension in the scattering plane is 50 microns then the highest frequency expected is 80

cycles/radian, well below the limiting frequency of the film. In order to reduce data storage requirements and computer time for processing, a scanning step size of 96 microns and an aperture of 93 microns were chosen for the microdensitometer. This leads, according to the Nyquist criterion, to an upper limit on resolution of 324 cycles/radian for the digitized data.

The digitized density data were plotted and valid data sets chosen for analysis using the following criteria. In the near-forward scattering direction the starting point was chosen as near the edge of the film as cutting and processing defects allowed. The stopping point was when either the density dropped to the measured base density of the film strips or the end of the film was reached. Relative intensity values were then computed using a published⁶ characteristic curve for the film. These intensity curves were then normalized for convenience such that

$$\int_{\text{start}}^{\text{end}} I(\theta)d\theta = 1. \quad (2)$$

Figures 1, 3, 5, and 7 show the normalized intensity versus scattering angle plots for scattering from four different particles. A Fast Fourier Transform algorithm was then applied to each data set. The corresponding transforms are plotted in Figures 2, 4, 6, and 8, respectively, where the magnitude of the complex Fourier coefficient is plotted versus frequency.

Figure 2, which shows the transform for scattering from a 30 ± 6 micron glass sphere, shows a pronounced peak at a frequency of 40 cycles/radian, the peak at zero being the average value of the intensity function. Inserting this value in Equation (1) leads to a predicted size of 25 microns within the microscopic measurement uncertainty. The three other spectra fail to show a pronounced peak, although they exhibit structure, that could be used to test Equation (1). In conclusion then, the hypothesis advanced must be either rejected or modified on the basis of this data. One possibility is immediately suggested by a coincidence in the data. Due to the dynamic range of the film, only scattering data from $\sim 15^\circ$ to $\sim 80^\circ$ could be obtained for the sphere, Figure 1, while for the other three particles the data cover the range $\sim 10^\circ$ to $\sim 170^\circ$. It is possible, therefore, that only near-forward scattering data should be used to test Equation (1). In addition Figures 3, 5, and 7 show more pronounced and regular peaks at small scattering angles than they do in general. This approach is being investigated with further experiments and analysis. Although the spectra for the three nonspherical particles do not show a single pronounced peak, they do exhibit a regular harmonic structure that may be related to the size of the particle. This question is also under investigation.

In summary, the collected data do not support the hypothesis that periodicities in the complete angular scattering distribution are related to particle size by Equation (1). There is some evidence, though, that this relation may hold for near-forward scattering.

REFERENCES

- 1) G. Mie, *Ann. Physik.* 25, 377 (1908).
- 2) J. R. Wait, *Can. J. Phys.* 33, 189 (1955).
- 3) S. Asano and G. Yamamoto, *Appl. Opt.* 14, 29 (1975).
- 4) E. J. Davis and A. K. Ray, *J. Colloid and Interface Sc.* 75, 566 (1980).
- 5) Principles of Optics, M. Born and E. Wolf, Pergammon Press, Oxford, 1975.
- 6) Kodak Professional Black-and-White Film, Kodak Publication No. F-5, Eastman Kodak Company, Rochester, N.Y.

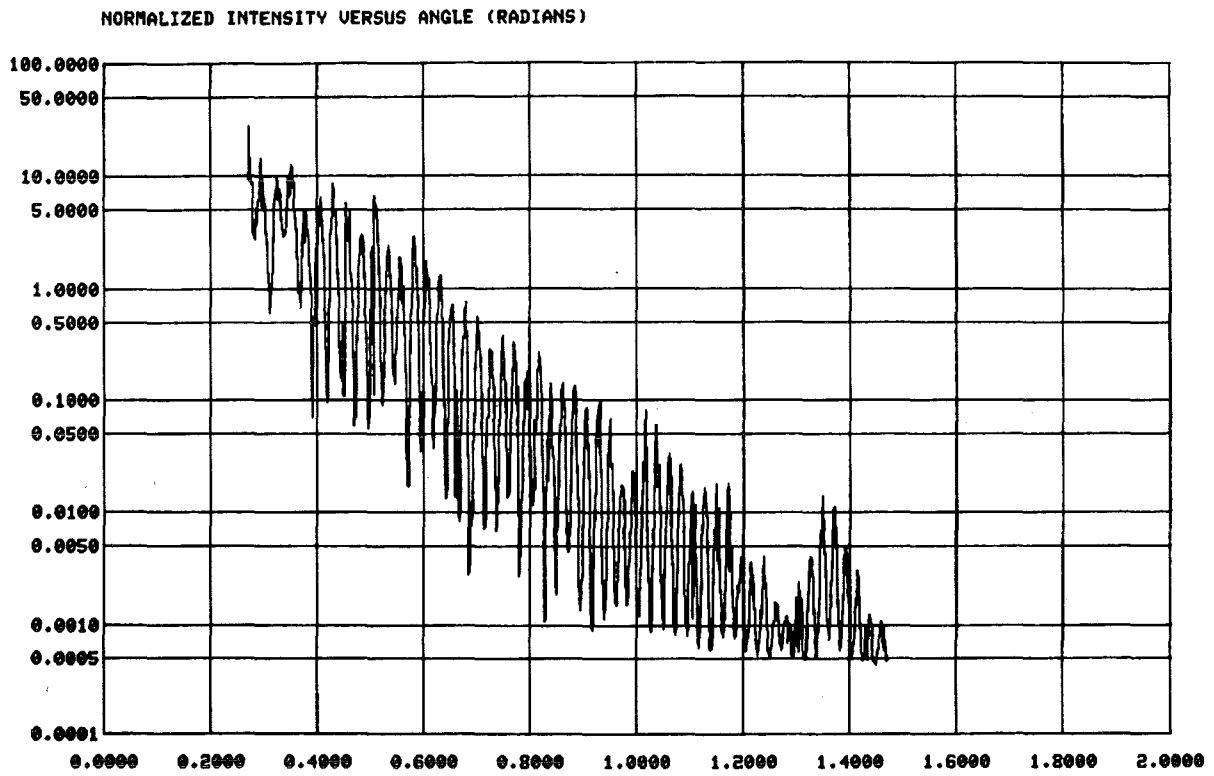


FIGURE 1. SCATTERING DISTRIBUTION FROM A SPHERE. The target was a 30 micron glass sphere.

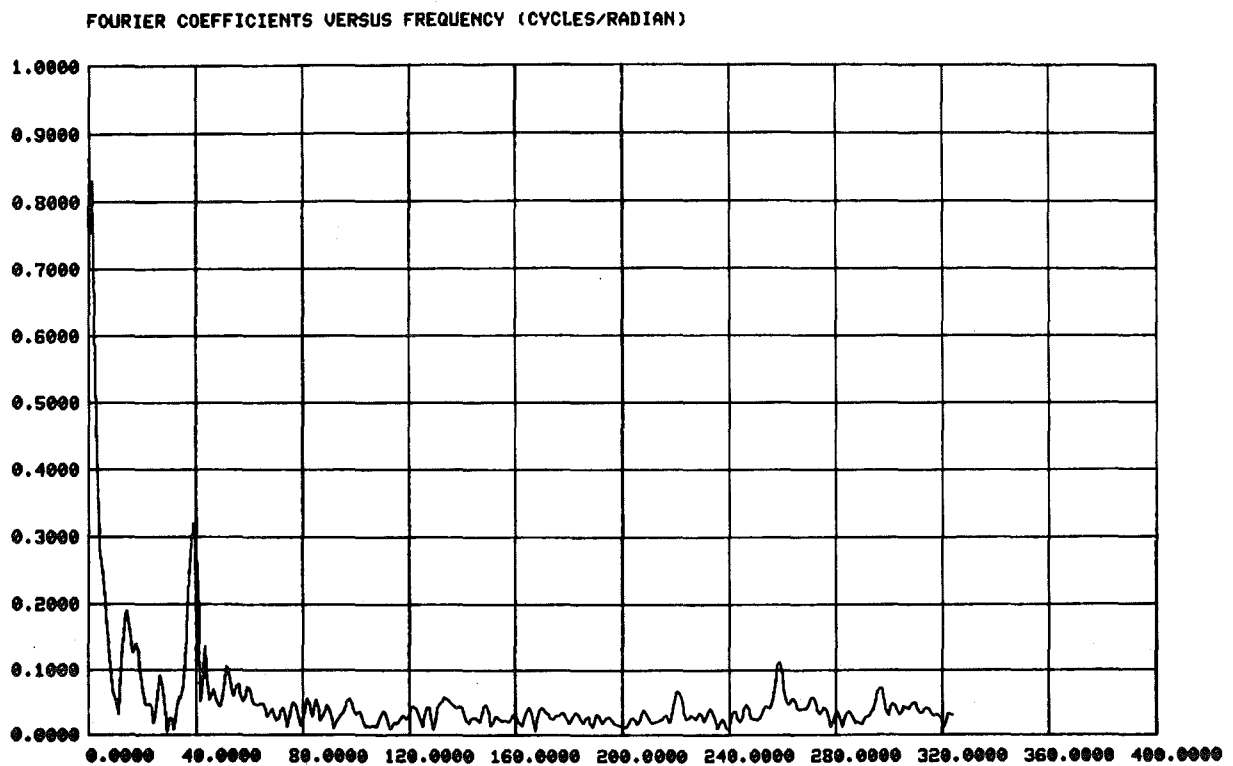


FIGURE 2. FOURIER SPECTRUM OF SPHERE'S SCATTERING PATTERN.

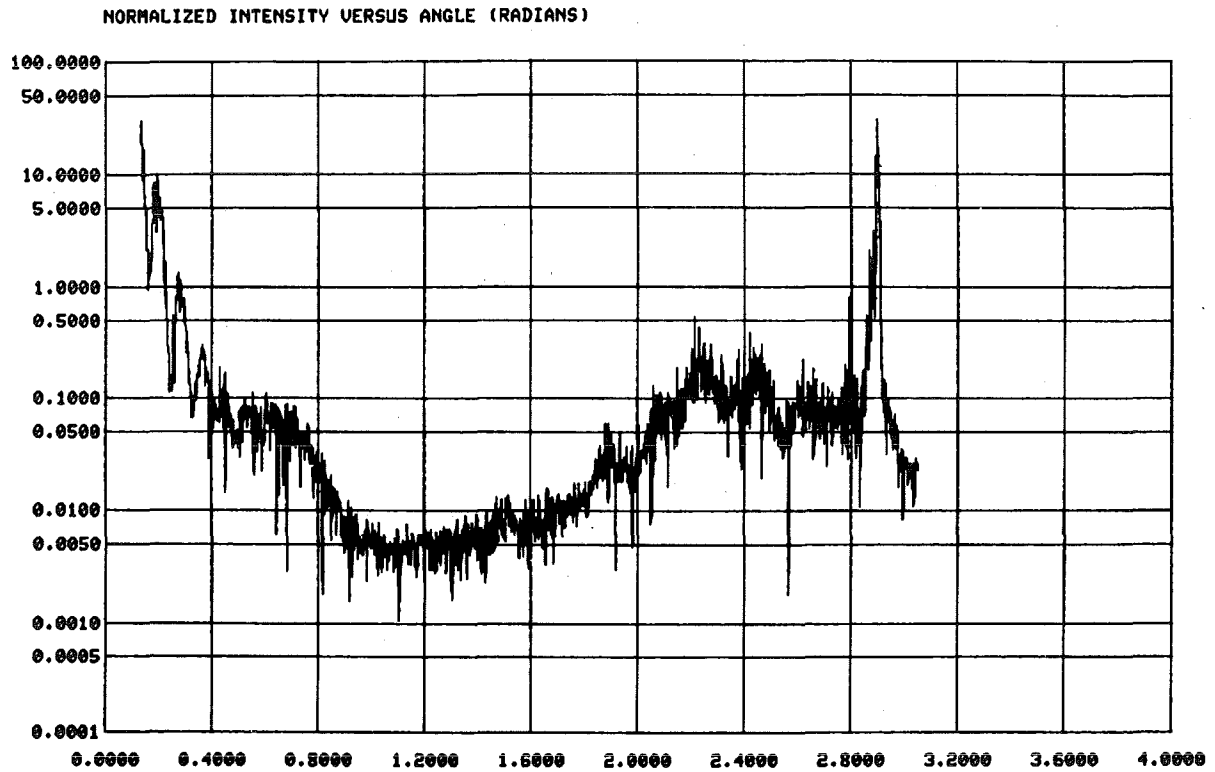


FIGURE 3. SCATTERING DISTRIBUTION FROM A FIBER. The target was a stainless steel fiber 8 microns in diameter and 200 microns long with the long axis perpendicular to the scattering plane.

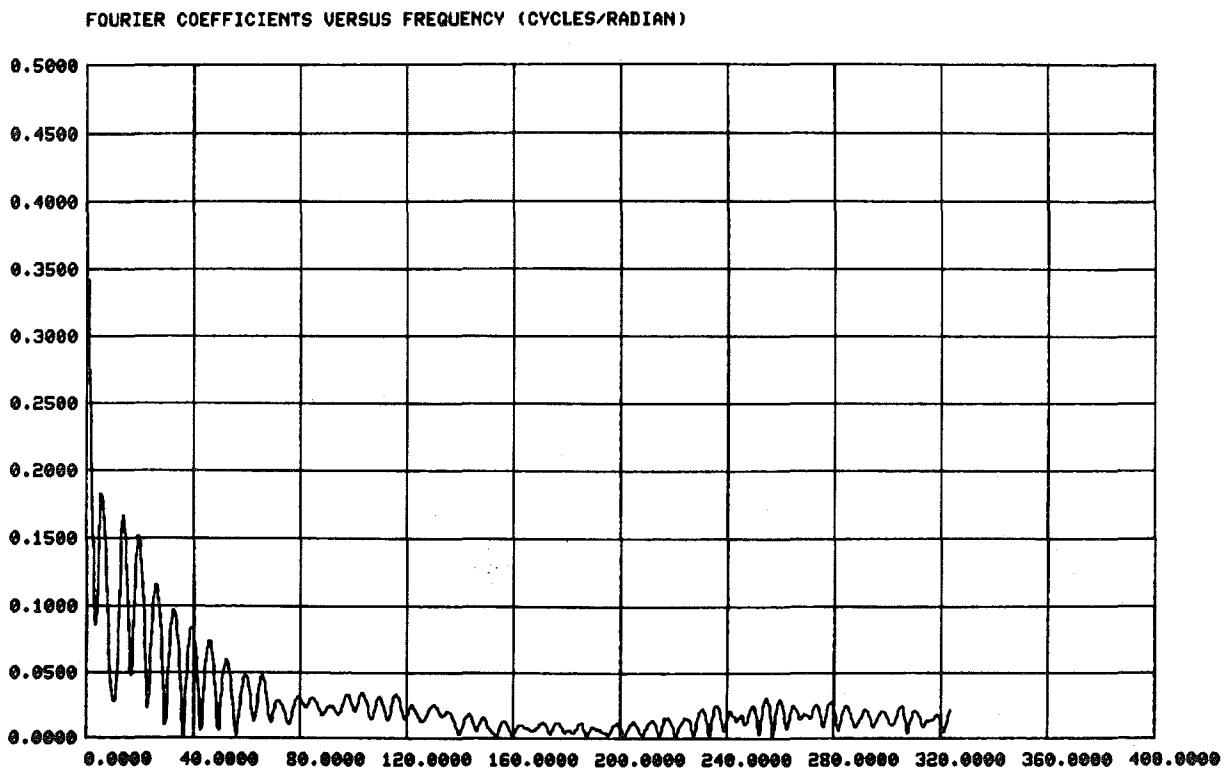


FIGURE 4. FOURIER SPECTRUM OF FIBER'S SCATTERING PATTERN.

NORMALIZED INTENSITY VERSUS ANGLE (RADIAN)

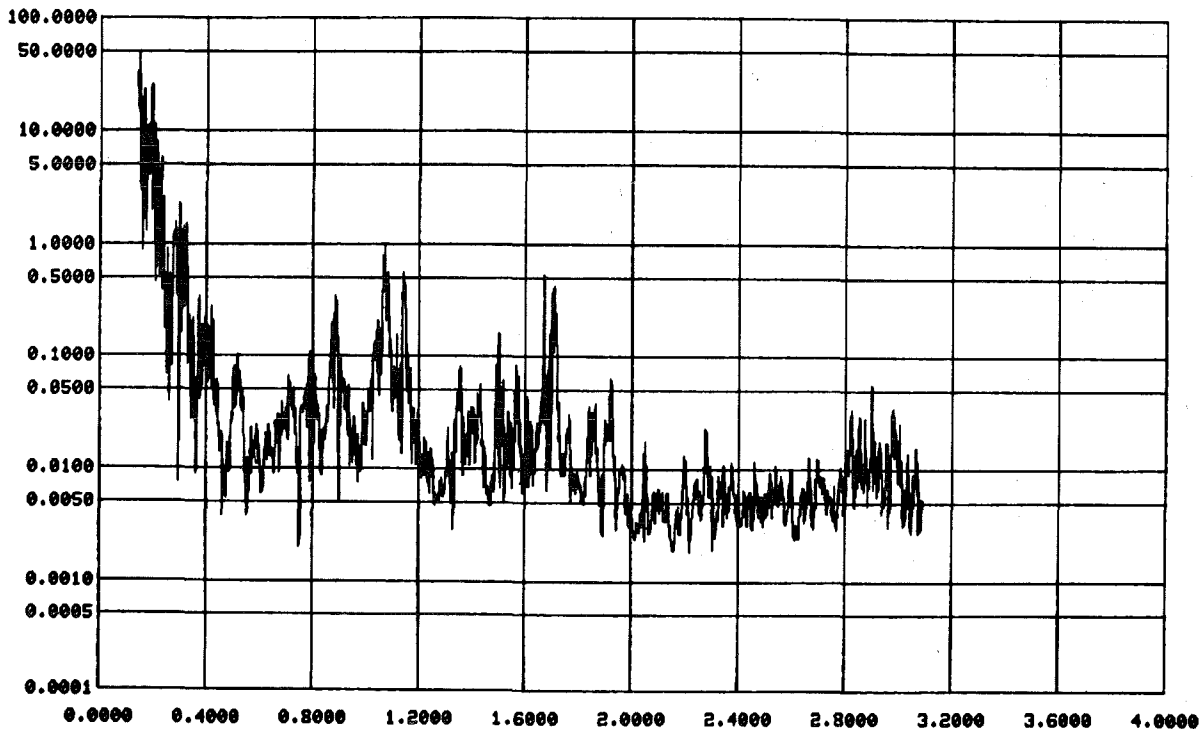


FIGURE 5. SCATTERING DISTRIBUTION FROM A NEAR-SPHERE. The target was a 30 micron carbon sphere with smooth, lumpy perturbations, this being ~ 3 microns from an average spherical surface.

FOURIER COEFFICIENTS VERSUS FREQUENCY (CYCLES/RADIAN)

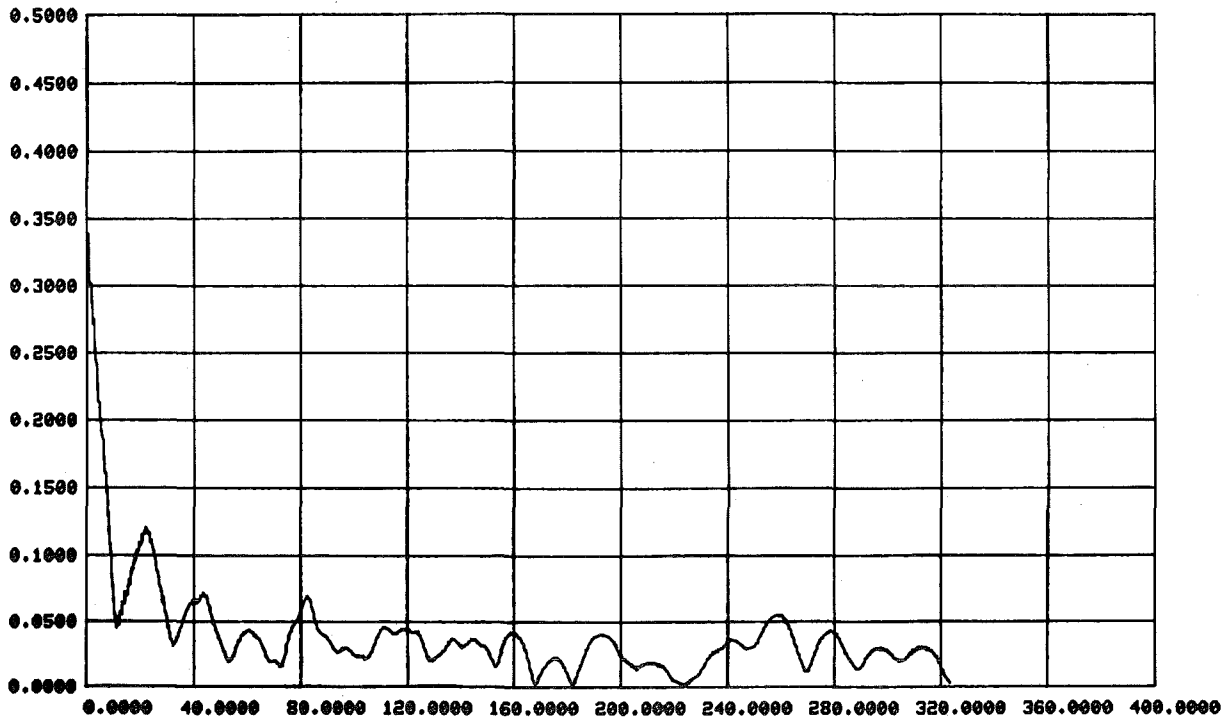


FIGURE 6. FOURIER SPECTRUM OF NEAR-SPHERE'S SCATTERING PATTERN.

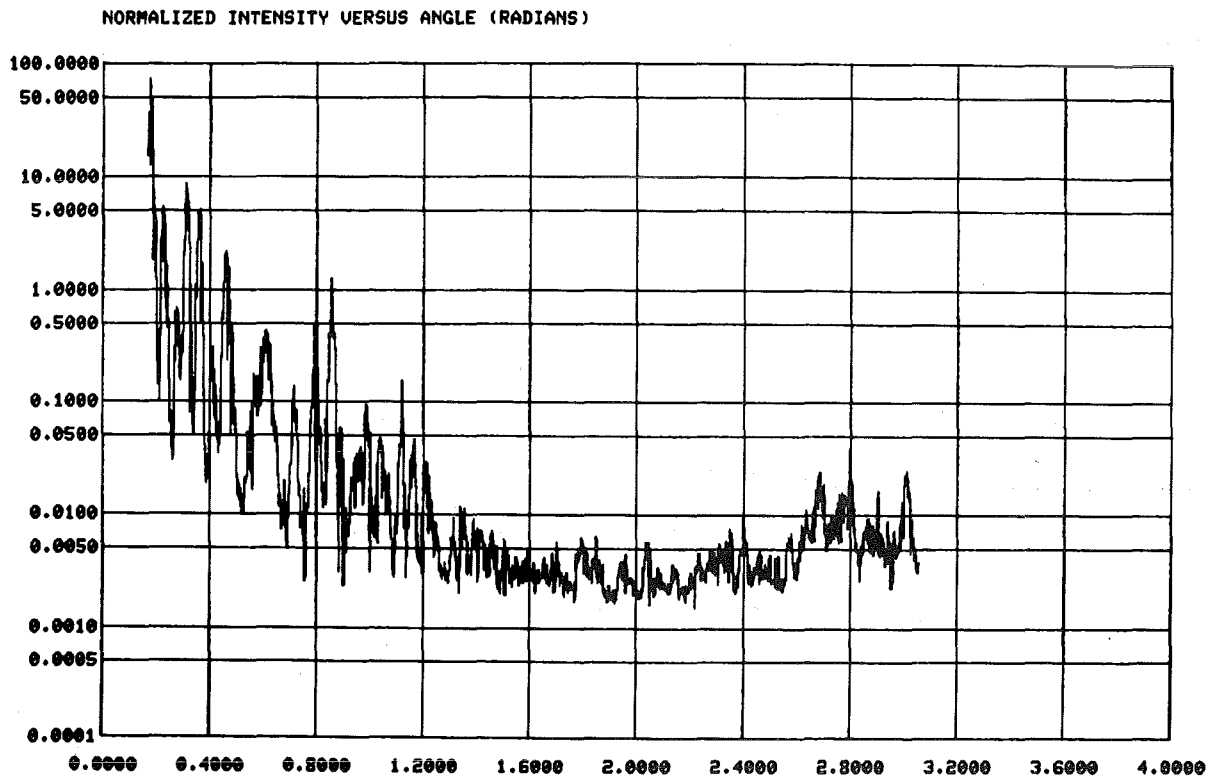


FIGURE 7. SCATTERING DISTRIBUTION FROM A CUBE. The target was a cubic sodium chloride crystal 30 microns on an edge.

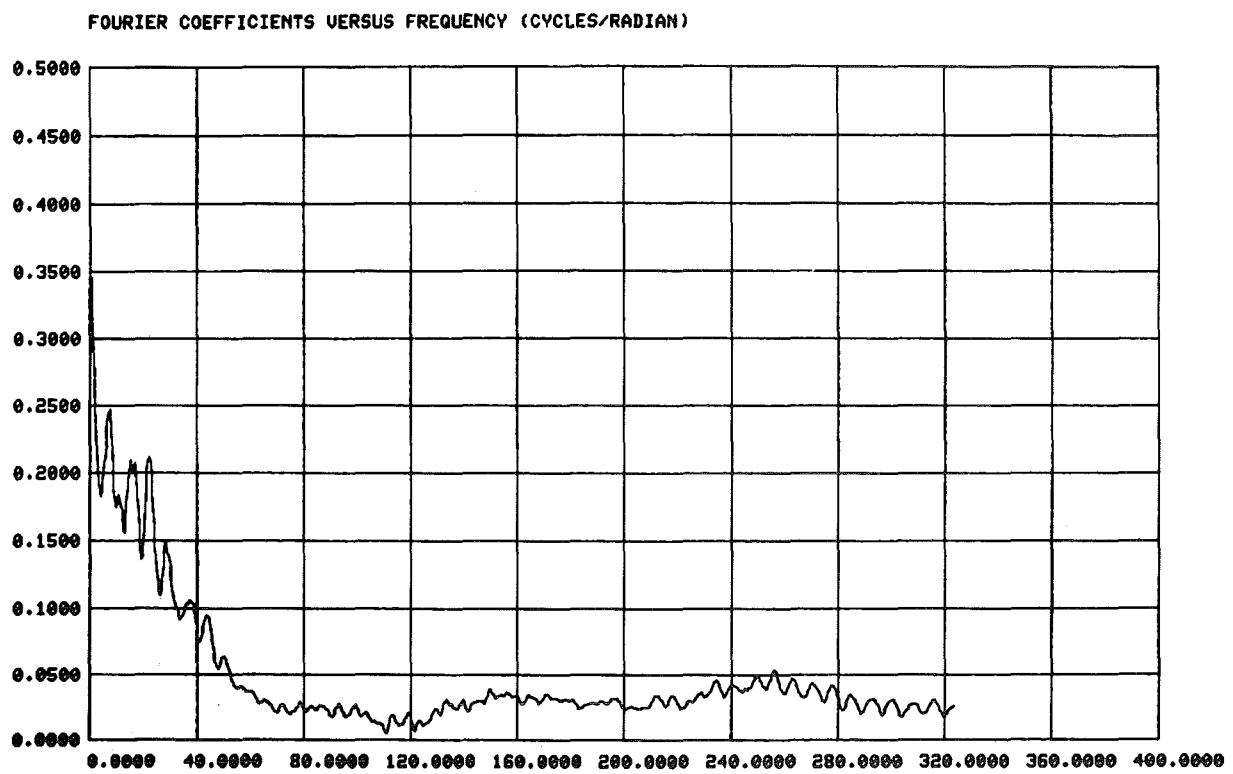


FIGURE 8. FOURIER SPECTRUM OF CUBE'S SCATTERING PATTERN.

BLANK

TRIANGULAR SURFACE PATCH MODEL FOR TEMPERATURE
RISE CALCULATIONS FOR THIN SHELL
PARTICLES - TRIANGULAR SURFACE PATCH MODELS

D.T. Auckland
C.C. Cha
R.H. Andreo
Syracuse Research Corporation
Merrill Lane
Syracuse, NY 13210

ABSTRACT

This paper presents a method for computing the temperature rise in arbitrarily shaped lossy thin shell scatterers which may be used for obscuration. The solution of an electric field integral equation is obtained by the method of moments using triangular surface patch basis functions. The response to transient excitations is obtained by a numerical inverse Fourier transform, and suitable assumptions are postulated concerning thin shells so that a simplified form of the heat equation can be used to calculate the total shell or plate wall temperature rise. The results that are given illustrate the penetrating fields inside an irregularly shaped two-dimensional shell and the temperature rise in a flat plate when it is excited by direct-current injection consisting of a double exponential pulse. The techniques presented here are directly applicable to thin shell or platelet aerosol obscuration whose overall size is not more than a wavelength or two.

INTRODUCTION

The interaction of electromagnetic radiation with the particles in an obscuration arises in numerous applications^(1,2,3). Natural and man-made aerosol obscuration (such as smoke, dust, and fog) scatter and absorb energy from radars, lidars, lasers, satellite communication links, and other sensors, thereby causing attenuation of the forward-propagating beam. In order to understand the effects of an aerosol or obscuration on the propagation of an electromagnetic wave, the interaction of electromagnetic radiation with a single particle must be known in detail. With the single-scattering approximation, the single-particle extinction cross section then determines the attenuation⁽⁴⁾, while in a multiple-scattering theory^(5,6) the attenuation depends on the single-particle properties as well as the interactions between particles^(7,8). Although the scattering and absorption by a single sphere or infinite circular cylinder has been extensively investigated using vector multipole expansions^(4,9), irregularly shaped particles require numerical solutions and have received much less attention^(10,11,12).

When an irregularly shaped particle has the physical form of a thin shell or plate, it is possible to obtain an efficient numerical solution for the electromagnetic field interaction problem. The technique outlined in this paper is based on an application of the method of moments⁽¹³⁾ to the solution of an electric field surface integral equation. Quantities of interest for obscuration design are the time average power thermally dissipated in the shell or platelet material for time harmonic excitation and total temperature rise of the material for transient excitation.

The original motivation for the formulation presented here came from efforts to determine the temperature rise in composite panels on an aircraft skin during a direct or nearby lightning strike^(14,15). It is proposed here that the same calculation is valid for thin shell or plate obscurants under appropriate simplifying assumptions. The temperature distribution and amount of power dissipated in an obscurant when the electromagnetic field operators and constitutive relationship are linear during electromagnetic field/particle interaction is a first step in addressing the nonlinear problems of plasma formation and atmospheric breakdown near the obscurant surface.

THIN SHELL FORMULATION

The problem of interest is depicted in Figure 1 where a homogeneous, isotropic thin shell particle characterized by permittivity ϵ , permeability μ , and conductivity σ is illuminated by an incident field $\underline{E}^o, \underline{H}^{o\dagger}$. This field is due to sources radiating in free space when the particle is absent. When the particle is present, induced polarization and conduction current, denoted by a total volume current density \underline{J} , flows in the shell walls giving rise to the field $\underline{E}^s(\underline{J}), \underline{H}^s(\underline{J})$ everywhere. Inside the shell wall volume, V , the integral equation that must be satisfied is

$$\underline{J} = [-i\omega(\epsilon - \epsilon_o) + \sigma] [\underline{E}^o + \underline{E}^s(\underline{J})] \quad (1)$$

where ϵ_o is the permittivity of free space which is everywhere outside V and ω is the angular frequency of the incident field.*

The operator \underline{E}^s may be written in terms of the magnetic vector potential, \underline{A} , as (16)

$$\underline{E}^s(\underline{J}) = +i\omega\mu_o \underline{A} - \frac{1}{i\omega\epsilon_o} \nabla (\nabla \cdot \underline{A}) \quad (2)$$

where

$$\underline{A} = \int_V \frac{\underline{J} e^{+ik|\underline{r} - \underline{r}'|}}{4\pi |\underline{r} - \underline{r}'|} dV' \quad (3)$$

[†] The time-harmonic electric field (suppressed $e^{-i\omega t}$ time dependence) is denoted by \underline{E} and the magnetic field by \underline{H} . These symbols are also used to indicate electric and magnetic field integro-differential operators. Quantities in parentheses will specifically identify sources of the field.

* This integral equation is for non-permeable materials. For permeable materials, a magnetic current density inside the volume is also involved in a more general formulation.

In the above, μ_0 is the permeability of free space, k is the wave number $\omega \sqrt{\mu_0 \epsilon_0}$, and \underline{r}' and \underline{r} locate source and field points, respectively.

Now if the shell wall thickness, d , is much less than the skin depth of the wall material, we make the following assumptions:

- ° \underline{J} is uniformly distributed across the shell wall dimension, s
- ° There is no component of \underline{J} in the \hat{s} direction

This leads to the development of an impedance sheet approximation to the shell wall⁽¹⁷⁾ which results in

$$\underline{E}_t^s(\hat{J}) - \frac{1}{(-i\omega(\epsilon - \epsilon_0) + \sigma)d} \hat{J} = -\underline{E}_t^o \quad \text{on } S \quad (4)$$

where

$$\hat{J} = \underline{J}d \quad (5)$$

and S is a surface inside V between the inner and outer shell wall surfaces. The subscript t denotes components tangential to S .

Equation 4 may be readily solved by applying the method of moments⁽¹³⁾. Here \hat{J} is expanded in terms of a suitable set of basis functions and Equation 4 is projected onto a space spanned by a suitable choice of testing functions by means of a symmetric product operator*. The resulting system of linear algebraic equations for the coefficients of the expansion which represents \hat{J} may be solved using readily available matrix methods. For two-dimensional shells, simple piecewise-linear one-dimensional basis functions are used. For three-dimensional shells and plates, triangular surface patch functions are used^(18,19). An example of a plate modeled by triangular surface patches is shown in Figure 3. The results of solving Equation 4 using triangular surface patch basis functions may be pictorially illustrated in an enlightening way as illustrated in Figure 4 where a plane wave excites a perfectly conducting cube. Here the arrows represent the vectorial direction and relative magnitude of $\text{Re}\{\hat{J}e^{-i\omega t}\}$, for $\omega t = 0$, everywhere on the cube surface.

* The symmetric product is defined by $\langle \underline{A}, \underline{B} \rangle = \int_S \underline{A} \cdot \underline{B} \, dS$.

The two-dimensional shell problem is much simpler numerically than three-dimensional shells or plates. Figures 5 and 6 give examples of interior field calculations performed for an irregularly shaped two-dimensional shell particle with and without a hole in the shell wall.

For particles which may be modelled as closed thin-walled shells, it may not always be possible to use the simple assumption concerning the distribution of \underline{J} across the shell wall. For example, if the thickness of the shell wall is not thin with regard to a skin depth in the wall material, then we must know the distribution of \underline{J} along \hat{s} , the direction normal to the surface S . The surface current density, $\hat{\underline{J}}$, in Figure 2 is actually related to \underline{J} by

$$\hat{\underline{J}} = \int \underline{J} ds \quad (6)$$

where the integration is performed over the entire thickness of the surface. A useful approximation to the distribution of \underline{J} can be obtained by the infinite slab model shown in Figure 7. Here, an infinite slab characterized by (μ, ϵ, σ) is situated between the $s = 0$ and $s = d$ planes. The region $s > d$ represents the exterior of the shell and the $s < 0$ region represents the interior region. The electric field, \underline{E} , and the electric current

$$\hat{\underline{J}} = \sigma \underline{E} \quad (7)$$

are assumed to be in the t direction and E_t is assumed to have the form

$$E_t = E_1 e^{(1-i)\frac{s}{\delta}} + E_2 e^{-(1-i)\frac{s}{\delta}} \quad (8)$$

where the skin depth, δ , is given by

$$\delta = \sqrt{\frac{2}{\omega \mu \sigma}} \quad (9)$$

Thus the t component of volume current density is

$$J_t = \sigma \left(E_1 e^{(1-i)\frac{s}{\delta}} + E_2 e^{-(1-i)\frac{s}{\delta}} \right) \quad (10)$$

Note that in writing Equation 8, we have assumed that $\sigma \gg \omega\epsilon$. The magnetic field associated with the E-field in Equation 8 is

$$H_s = \frac{-i}{\omega\mu} \frac{\partial E_t}{\partial s} = \frac{-(1+i)}{\omega\mu\delta} \left[E_1 e^{(1-i)\frac{s}{\delta}} - E_2 e^{-(1-i)\frac{s}{\delta}} \right] \quad (11)$$

Now, if the shell wall material is assumed to be a good conductor, very little E-field or H-field should exist in the shell interior region ($s < 0$). Also, in the low frequency region, electric current is responsible for most of the H-field. Since Equation 10 is an approximation of the volume polarization current which is charge-free, we can only require that the H-field for $s < 0$ is small. One approximation is to require that

$$H_s \Big|_{s=0} = 0 \quad (12)$$

This gives us

$$E_1 = E_2 = E \quad (13)$$

Therefore, we can approximate the distribution of \underline{J} by

$$J_t = \sigma E \left[e^{(1-i)\frac{s}{\delta}} + e^{-(1-i)\frac{s}{\delta}} \right] \quad (14)$$

where E is one-half of the magnitude of the E-field at $s = 0$. From Equation 6 we have

$$\int_0^d J_t(\omega) ds = \hat{J}_t(\omega) \quad (15)$$

Substituting Equation 14 into Equation 15, we obtain

$$E = \frac{(1-i)}{\delta\sigma} \cdot \frac{\hat{J}_t(\omega)}{\left[e^{(1-i)\frac{d}{\delta}} - e^{-(1-i)\frac{d}{\delta}} \right]} \quad (16)$$

The volume current density at the outer surface is, therefore,

$$\begin{aligned}
 [J_t(\omega)]_{z=d} &= \sigma E \left[e^{(1-i)\frac{d}{\delta}} + e^{-(1-i)\frac{d}{\delta}} \right] \\
 &= \frac{(1-i)}{\delta} \coth \left[(1-i)\frac{d}{\delta} \right] \hat{J}_t(\omega) \\
 &= \frac{(1-i)}{\delta} \hat{J}_t(\omega) \quad (\text{if } d \gg \delta)
 \end{aligned}
 \tag{17}$$

The above may be used in Equation 5 for a better approximation to \hat{J} for shell walls which enclose a volume (i.e., bubbles).

TEMPERATURE RISE COMPUTATION

The heat equation for the volume occupied by the panel is given by

$$\frac{\partial}{\partial t} (\xi m u) + \kappa \nabla^2 u + \nabla \kappa \cdot \nabla u = \rho |J|^2
 \tag{18}$$

where:

ξ = specific heat (cal/gm °C)

m = mass density (gm/cm³)

κ = thermal conductivity (cal/sec cm °C)

ρ = electrical resistivity (ohm cm)

t = time (sec)

u = temperature (°C)

J = time domain volume current density (inverse Fourier transform of $\hat{J}(\omega)$)

Equation 18 is a complicated nonlinear differential equation in general, especially when the temperature dependence of various parameters is considered. Instead of solving Equation 18 directly, an approximation of the temperature rise is obtained by solving

$$\xi_o m \frac{du}{dt} = \rho_o (1 + \alpha \Delta u) |J|^2
 \tag{19}$$

where the subscript "o" denotes "at room temperature (25°C)", α is the temperature coefficient of resistance, and $\Delta u = u - 25^\circ\text{C}$. Equation 19 is used based on the following considerations:

- ° The thermal conduction inside the panel as well as conduction and convection through the panel surface into the surroundings are neglected because the pulse duration of the source signal considered is very short (typically a few microseconds). Little temperature redistribution due to these factors is expected before the temperature reaches its peak value.
- ° The specific heat of most substances is essentially a constant between room temperature and 200°C, and a temperature rise beyond this range is not expected.
- ° A linear function of temperature $\rho = \rho_o(1 + \alpha\Delta u)$ is used for the resistivity.

The solution of Equation 19 is simply

$$\Delta u = \frac{1}{f(t)} \int_0^t f(\tau) P_o(\tau) d\tau \quad (20)$$

where

$$f(t) = e^{-\alpha \int_0^t P_o(\tau) d\tau} \quad (21)$$

and

$$P_o(t) = \frac{\rho_o}{\xi_m} |J(t)|^2 \quad (22)$$

The time-dependent volume current density, $\underline{J}(t)$, may be obtained by an inverse Fourier transform of $\underline{J}(\omega)$. Realistically, however, it is only possible to calculate $\underline{J}(\omega)$, using the triangular surface patch technique, at a finite number of frequencies. If a sufficient number of frequencies are chosen so that a piecewise-linear representation of $\underline{J}(\omega)$ is obtained, then the resulting band-limited approximation of $\underline{J}(\omega)$ may be transformed to the time domain numerically.

RESULTS FOR SQUARE PLATE

The surface current density, $\underline{J}(\omega)$, can be computed with sufficient accuracy in the frequency domain using a triangular patch model of the shell wall or platelet in a moment method solution of an electric field integral equation. The modification of this basic model for direct-injection excitation (as was needed for lightning) is derived in Reference 20. This problem specialization is illustrated in Figure 8. Figures 9 and 10 show an example of how 1 amp of current at a frequency of 100 kHz is distributed over a square plate when the top and bottom halves of the plate have different bulk conductivities, σ ($\mu = \mu_0$ and $\epsilon = \epsilon_0$). Applying the procedure outlined in the previous two sections to the square plate, when the injection current is assumed to be a double exponential, gives rise to the surface temperature rise distribution shown in Figure 11.

CONCLUSIONS

We have presented a method for computing the effects that an electromagnetic field has on an arbitrarily-shaped lossy thin shell obscurant. The triangular surface patch technique is general enough to accurately model a wide variety of irregular shapes into their resonance region. Though temperature rise results were presented for a thin flat plate excited by direct current injection (motivated by the lightning strike problem for which this work was funded), the same method is applicable for plane wave or pulse excitation, as would be the case for aerosol obscurants. The formulations presented here apply to the domain of linear interaction of the external electromagnetic field with the particle. However, it is emphasized that these calculations are an important first step in approaching the nonlinear phenomena of plasma formation and atmospheric breakdown caused by aerosol obscurants immersed in intense electromagnetic fields.

REFERENCES

1. S.K. Friedlander, Smoke, Dust, and Haze - Fundamentals of Aerosol Behavior, John Wiley and Sons, Inc., New York, 1977.
2. A useful set of references is the series of proceedings for 1979-1982 of the annual Chemical Systems Laboratory Scientific Conference on Obscuration and Aerosol Research, e.g., Proceedings of the 1982 Chemical Systems Laboratory Scientific Conference on Obscuration and Aerosol Research, Ronald H. Kohl and Associates, Tullahoma, TN, 1983.
3. G.C. Holst, "Infrared Transmission through Screening Smokes", Chemical Systems Laboratory Technical Report ARSCL-TR-80004 (AD AO 86773, available from DTIC), May 1980.
4. H.C. Van de Hulst, Light Scattering by Small Particles, John Wiley and Sons, Inc., New York, 1957.
5. R.H. Andreo, "Closure Hypotheses from the Method of Smoothing for Coherent Wave Propagation in Discrete Random Media", Optics Letters 8, 1983, pp. 82-84.

6. R.H. Andreo, "Discrete Methods and Schwinger Variation Principles for Random Scattering: The Coherent Field for Scattering from Particles", in Proceedings of the 1982 Chemical Systems Laboratory Scientific Conference on Obscuration and Aerosol Research, Ronald H. Kohl and Associates, Tullahoma, TN, 1983.
7. A. Ishimaru, Wave Propagation and Scattering in Random Media, Academic Press, New York, 1978.
8. P.L. Chow, W.E. Kohler, and G.C. Papanicolaou, eds., Multiple Scattering and Waves in Random Media, North-Holland, New York, 1981.
9. M.E. Kerker, The Scattering of Light and Other Electromagnetic Radiation, Academic Press, New York, 1969.
10. D.W. Schuerman, ed., Light Scattering by Irregularly Shaped Particles, Plenum Press, New York, 1980.
11. H. Masoudi and P.W. Barber, "Volume Integral Approach to Scattering by Irregularly Shaped Particles", in Proceedings of the 1982 Chemical Systems Laboratory Scientific Conference on Obscuration and Aerosol Research, Ronald H. Kohl and Associates, Tullahoma, TN, 1983.
12. H. Weil and C.M. Chu, "Scattering and Absorption by Thin Flat Aerosols", Applied Optics 19, 1980, 2066-2071.
13. R.F. Harrington, Field Computation by Moment Methods, The Macmillan Co., New York, 1968.
14. R.F. Wallenberg, D.T. Auckland, and J.A. Birken, "A Transfer Function Approach to Coupling to the Interior of a Composite/Metal Aircraft Based on a Triangular Patch Model", IEEE International Symposium on EMC, Santa Clara, California, September 1982.
15. D.T. Auckland, et al., "Interdiscipline Studies on the Structural/Electromagnetic Optimization of Advanced Composite Aircraft", Interim report prepared for the Naval Air Systems Command under Contract N00019-82-C-0088, Syracuse Research Corporation, Technical Report SRC TR 82-1596R2, December 1982.
16. R.F. Harrington, Time-Harmonic Electromagnetic Fields, McGraw-Hill Book Co., New York, 1961, Chapter 3.
17. R.F. Harrington and J.R. Mautz, "An Impedance Sheet Approximation for Thin Dielectric Shells", IEEE Transactions on Antennas and Propagation, July 1975, pp. 532-534.
18. S.M. Rao, "Electromagnetic Scattering and Radiation of Arbitrarily Shaped Surfaces by Triangular Patch Modelling", Ph.D. Dissertation, University of Mississippi, August 1980.
19. S.M. Rao, D.R. Wilton, and A.W. Glisson, "Electromagnetic Scattering by Surfaces of Arbitrary Shape", IEEE Transactions on Antennas and Propagation, Vol. AP-30, May 1982, pp. 409-418.
20. D.T. Auckland and C.C. Cha, "A Model for Direct-Strike Lightning Excitation of a Conducting Body", IEEE International Symposium on EMC, Santa Clara, CA, September 1982, pp. 418-425.

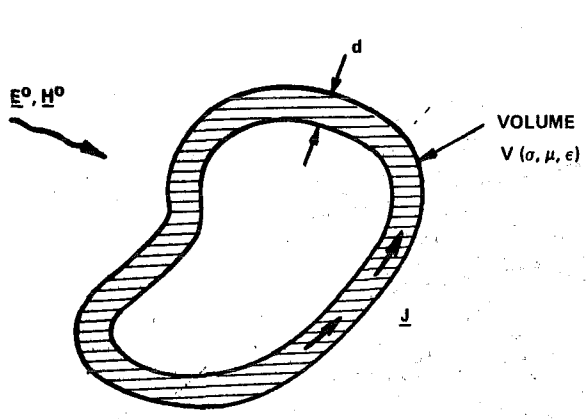


FIGURE 1. THIN SHELL IMMERSSED IN INCIDENT FIELD.

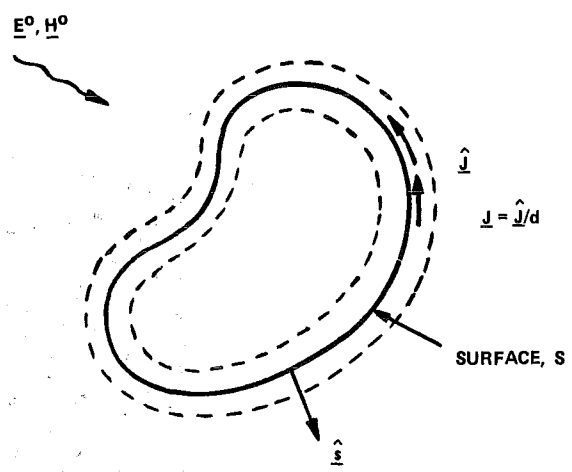


FIGURE 2. EQUIVALENT THIN SHELL SURFACE CURRENT SITUATION.

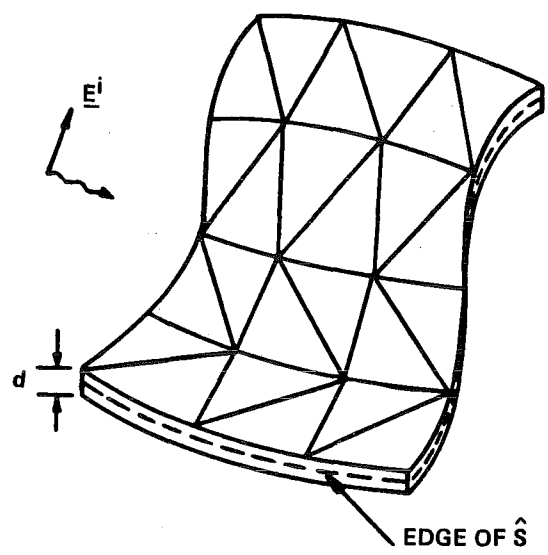


FIGURE 3. THIN IRREGULAR PLATE MODELED BY TRIANGULAR SURFACE PATCHES.

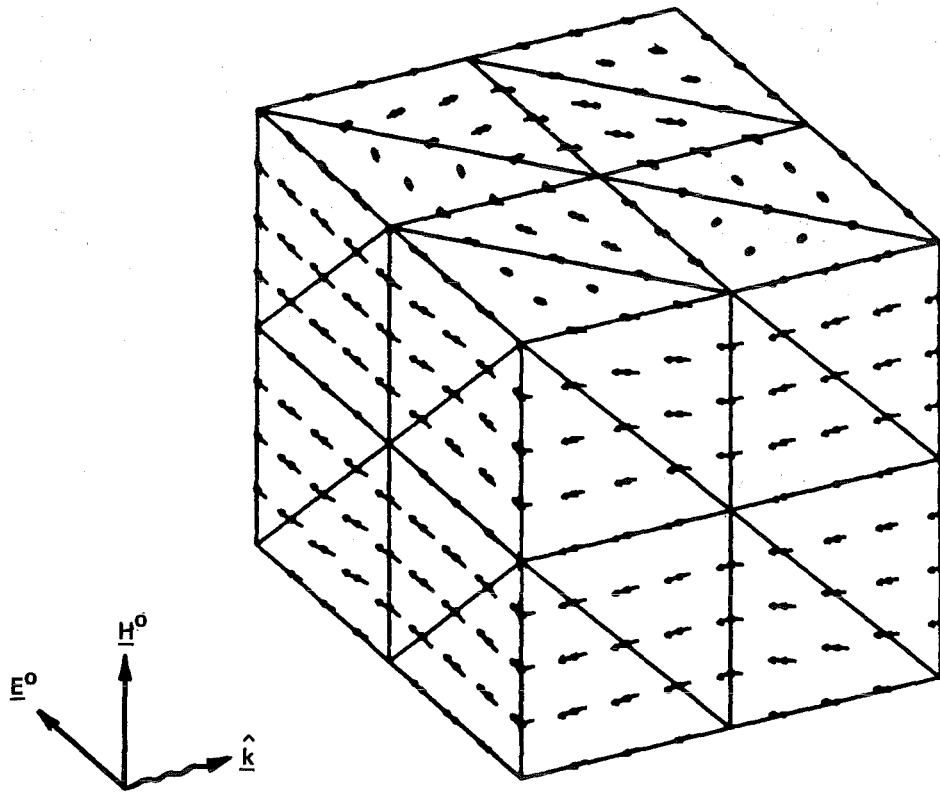


FIGURE 4. CURRENT DENSITY INDUCED BY PLANE WAVE INCIDENT ON 0.1λ CUBE.

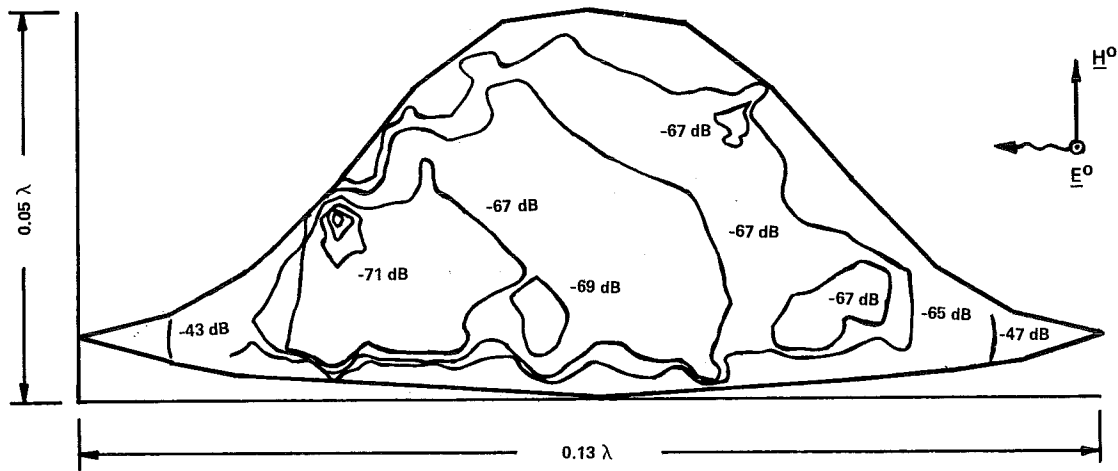


FIGURE 5. CONSTANT LEVELS OF $20 \log |E^{int}/E^o|$ INSIDE SHELL WITH THICKNESS $d = 1 \text{ mm}$, CONDUCTIVITY $\sigma = 10^4 \text{ mho/m}$, AND FREQUENCY OF 10 MHz.

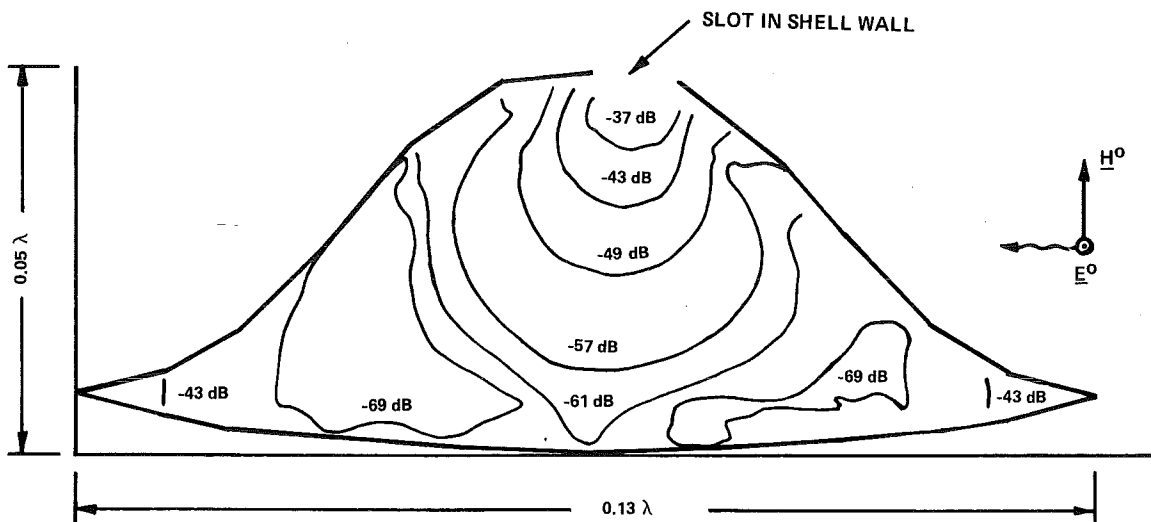


FIGURE 6. INTERIOR PENETRATING FIELDS OF SHELL IN FIGURE 5 WHEN SLOT IS CUT INTO SHELL WALL.

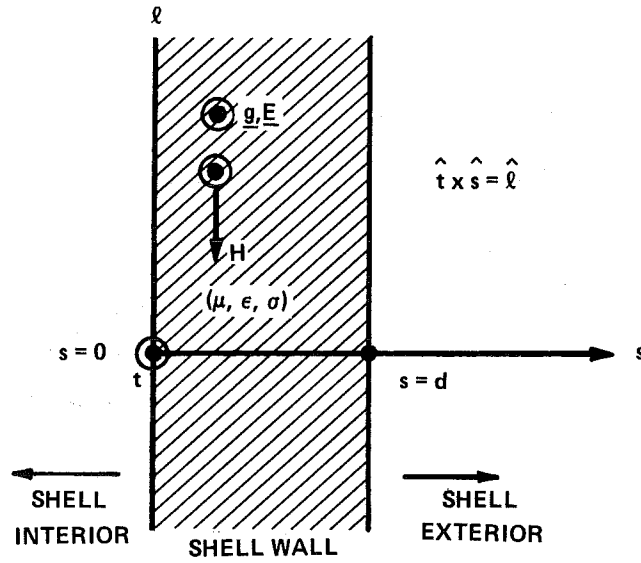


FIGURE 7. INFINITE SLAB MODEL.

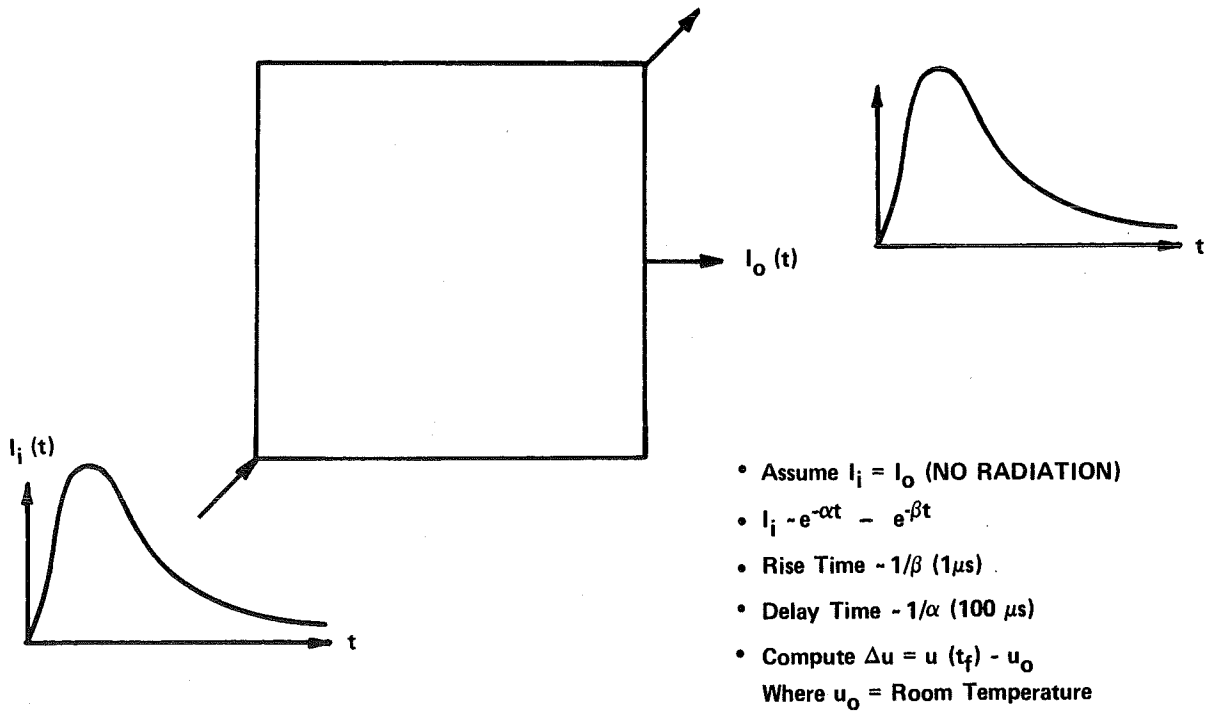


FIGURE 8. TEMPERATURE RISE IN PLATE DUE TO CURRENT INJECTION.

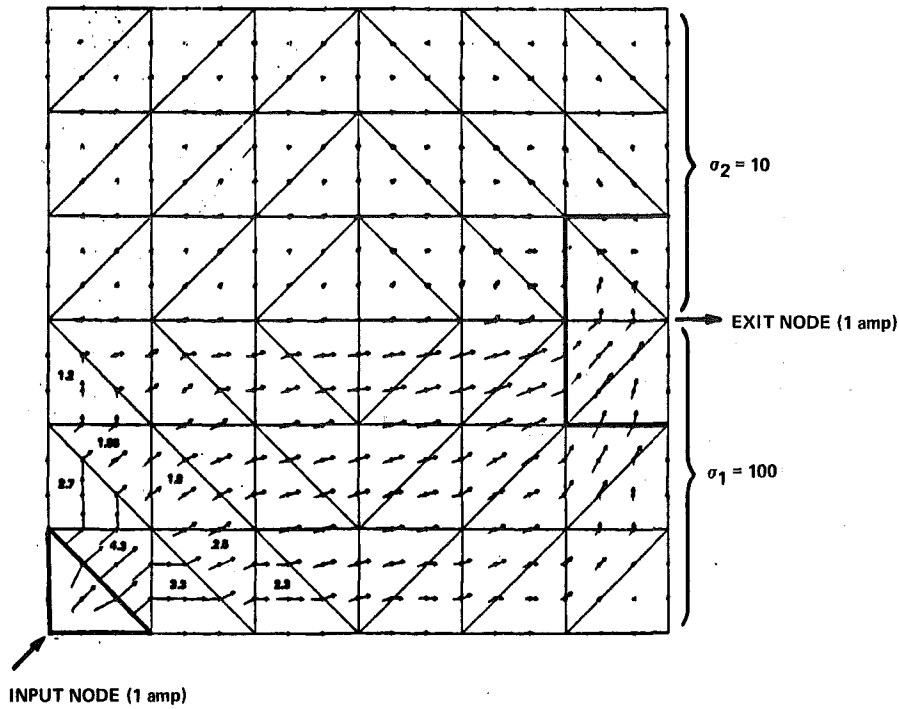


FIGURE 9. CURRENT DENSITY ON 1 m SQUARE PLATE FOR INJECTION CURRENT AT 0.1 MHZ WITH TOP HALF AND BOTTOM HALF HAVING DIFFERENT CONDUCTIVITIES.

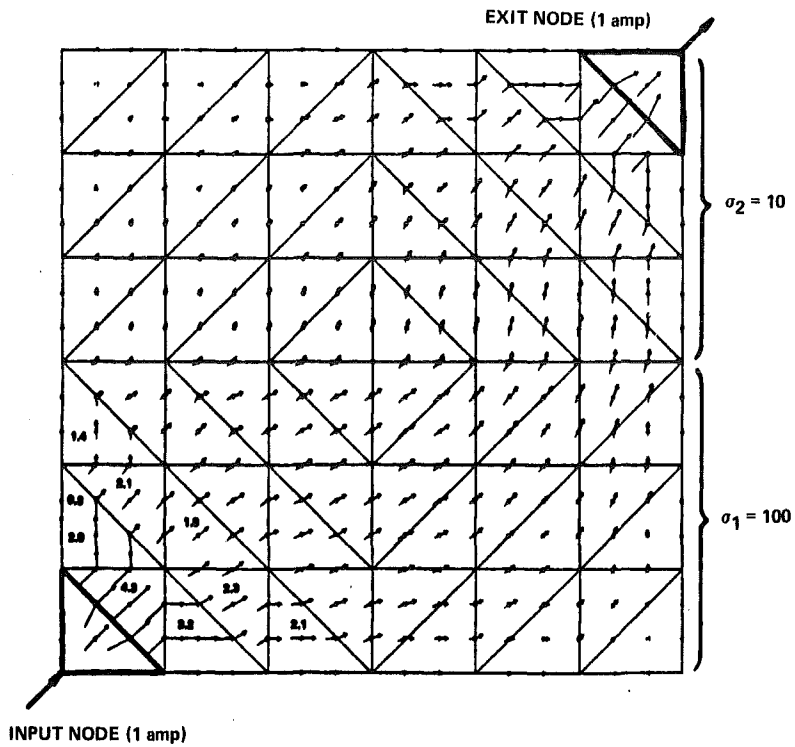


FIGURE 10. CURRENT DENSITY ON 1 m SQUARE PLATE FOR INJECTION CURRENT AT 0.1 MHZ WITH TOP HALF AND BOTTOM HALF HAVING DIFFERENT CONDUCTIVITIES.

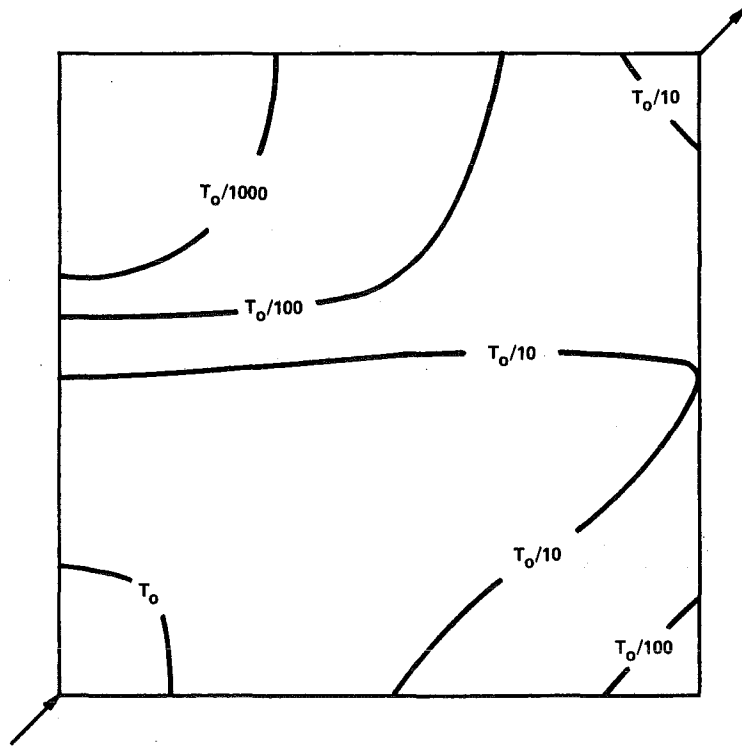


FIGURE 11. CONTOURS OF CONSTANT TEMPERATURE DISTRIBUTION ON SQUARE PLATE OF FIGURE 10.

BLANK

STRUCTURE OF POLARITON MODES

H. Weil and T.B.A. Senior
 Radiation Laboratory
 Department of Electrical and Computer Engineering
 The University of Michigan
 Ann Arbor, Michigan 48109

ABSTRACT

The structure of the bulk and surface polariton modes within a non-spherical particle is examined for a particle which is small compared to the wavelength of the ambient exciting field.

We consider the field generated inside a small homogeneous dielectric particle by an incident electromagnetic wave. When the frequency is in an absorption band of the bulk material, the electromagnetic and the internal vibrational modes of oscillation are strongly coupled; and the resulting combined disturbance, referred to as a polariton mode, is in fact a natural or characteristic mode of oscillation. The geometrical structure of the internal polariton field is influenced by the particle shape, and it is this effect which is studied here.

The analysis is limited to the case when the particle size is small compared to the wavelength of the electromagnetic excitation so that the internal field is well approximated by the corresponding electrostatic field. The frequency then affects only the complex refractive index n or complex dielectric constant ϵ of the bulk material. In the resonant frequency region $\text{Im } \epsilon$ is very large and $\text{Re } \epsilon$ changes from positive to negative as the frequency increases through the resonant value. A simplified expression for ϵ which is adequate for illustrative purposes is

$$\epsilon = 1 + \frac{a^2}{1 - \Omega^2 - i\gamma\Omega} \quad (1)$$

where a and γ are constants and Ω is a frequency normalized so that $\Omega = 1$ at resonance. The real and imaginary parts of ϵ are plotted in Fig. 1.

The theoretical results obtained are based on the following formulation [1,2] of the low frequency or Rayleigh scattering problem. An incident plane wave whose amplitude is $\vec{E}^{\text{inc}} = \hat{a}$ induces in a particle with boundary surface B a dipole moment \vec{p} ,

$$\vec{p} = \epsilon_0 \vec{\bar{P}} \cdot \hat{a} \quad (2)$$

where $\vec{\bar{P}}$ is the electric polarizability tensor. If x_i , $i = 1,2,3$, are Cartesian coordinates, the elements of $\vec{\bar{P}}$ are

$$P_{ij} = (1 - \epsilon) \int_B \hat{n} \cdot \hat{x}_i \phi_j dS \quad (i,j = 1,2,3) \quad (3)$$

where \hat{n} is an outward unit vector normal to B, and ϕ_j are potential functions satisfying the integral equation

$$\phi_j(\vec{r}) = -\frac{2}{1+\epsilon} x_j + \frac{1-\epsilon}{1+\epsilon} \int_B \phi_j(\vec{r}') \frac{\partial}{\partial n'} \left(\frac{1}{R} \right) dS' \quad (4)$$

on B, where $R = |\vec{r} - \vec{r}'|$. In terms of the boundary values, the potential at any point inside B is

$$\phi_j(\vec{r}) = -\frac{1}{\epsilon} x_j + \frac{1-\epsilon}{2\epsilon} \int_B \phi_j(\vec{r}') \frac{\partial}{\partial n'} \left(\frac{1}{R} \right) dS' \quad (5)$$

A program DIELCOM has been written [3] to solve the integral equation and compute the P_{ij} for particles with cylindrical symmetry about the x_3 axis. For these bodies $P_{22} = P_{11}$ and $P_{ij} = 0$ if $j \neq i$, and from a knowledge of the P_{ij} the scattering and absorption can be obtained. In particular, if all orientations of the particle relative to \hat{a} are equally probable, the average total scattering cross section $\langle \sigma_E \rangle$ and average extinction cross section $\langle \sigma_T \rangle$ are given by [4]

$$\begin{aligned} \langle \sigma_T \rangle &= \frac{\omega^2}{18\pi c^4} \{ 2|P_{11}|^2 + |P_{33}|^2 \} \\ \langle \sigma_E \rangle &= \frac{\omega}{3c} \text{Im}(2P_{11} + P_{33}) \end{aligned} \quad (6)$$

where c is the velocity of light in vacuo.

Analytical results are available in the case of a spheroid. If ϵ is the dielectric constant of the bulk material,

$$P_{ii} = V \left(\alpha_i + \frac{1}{\epsilon - 1} \right) \quad (7)$$

where V is the volume, α_i is the shape factor

$$\alpha_i = \begin{cases} q/2 & \text{if } i = 1, 2 \\ 1-q & \text{if } i = 3 \end{cases}$$

and q is the monotonic function of the length-to-width ratio l/w of the spheroid graphed in Fig. 2. With ϵ defined as shown in (1)

$$P_{ii} = \frac{Va^2}{1 + \alpha_i a^2 - \Omega^2 - i\gamma\Omega} \quad (8)$$

If $\gamma = 0$ so that ϵ is real, P_{ii} and, hence, the averaged cross sections become infinite when

$\epsilon = 1 - 1/\alpha_j$. Thus, P_{11} is infinite when $\epsilon = 1 - 2/q$ and P_{33} is infinite when $\epsilon = -q/(1 - q)$. Both of these ϵ values are negative; and though Fig. 1 suggests that each is achieved at two distinct values of the normalized frequency, (8) shows that $P_{ij} = \infty$ only at $\Omega = (1 + \alpha_j a^2)^{1/2}$. If $\gamma \neq 0$ (which is the realistic case), $\text{Re } P_{ij}$ changes sign when $\Omega = (1 + \alpha_j a^2)^{1/2}$ and, for small γ , $\text{Im } P_{ij}$ has a maximum at

$$\Omega = (1 + \alpha_j a^2)^{1/2} - \frac{\gamma^2}{8} (1 + \alpha_j a^2)^{-1/2} + O(\gamma^4) .$$

These formulas are the basis for the spheroid curves reproduced [1,2] in Fig. 3 showing the values of $-\text{Re } \epsilon$ at which the tensor elements P_{11} and P_{33} for a spheroid resonate as a function of the length-to-width ratio. Using (1) the abscissa can be converted to a normalized frequency demonstrating the shift away from the resonant frequency $\Omega = 1$ of the bulk material. For three different spheroids, the real and imaginary parts of P_{11} are plotted as functions of Ω in Fig. 4.

For a spheroid with $\vec{E}^{\text{inc}} = \hat{x}_j$ the potential at any point in the interior is

$$\phi_j = \frac{x_j}{1 - \epsilon} \frac{P_{ij}}{V}$$

and the field is therefore uniform for any ϵ . This is not true for other particles which can support resonant modes quite distinct from those of a spheroid. Indeed, as the particle departs more from a spheroid, a considerable number of these additional modes can be excited with significant strength.

To explore the geometric structure of these resonances, we have examined in some detail the internal resonant fields for a smooth particle which is distinct from, yet similar to, a spheroid. The particle chosen was, for $l/w > 1$, a hemispherically capped cylinder (see Fig. 5) and for $l/w < 1$ a bevelled disk. The transitional shape having $l/w = 1$ is a sphere, which is also a special case of a spheroid.

The resonances were computed from the eigenvalues of the matrix obtained in the solution of the integral equation (4) by the moment method, and the potentials throughout the interior of the particle were determined using (5). For each of P_{11} and P_{33} two resonant modes were found having roughly comparable intensities, and the resonant values of $-\text{Re } \epsilon$ as functions of l/w are included in Fig. 4. The computations showed that the mode which has almost the same locus as the spheroid mode has an internal field which is nearly uniform, whereas the other mode has a structure which is highly non-uniform and shape dependent. The former is referred to as a bulk polariton mode and the latter as a surface polariton mode. In the past the structure of surface polariton modes at low frequencies has been studied [5] only for spheres and infinite cylinders (both solid and shell-like) by expansion in terms of the solutions of Laplace's equation in the appropriate coordinates. For a hemispherically capped cylinder having $l/w = 4$, we now present a series of illustrations which support

our remarks about the field structure. Figures 6 and 7 show the magnitudes of the potential ϕ_3 along the symmetry axis for an axially directed external field as a function of the axial distance z measured from the symmetry plane of the particle. As $\text{Re } \epsilon$ approaches the value -13.2 for the bulk resonance, there is a general scaling up in the magnitude of $|\phi_3|$ but the field remains relatively uniform apart from a slight decrease near the cylinder ends. In particular, no complex field structure develops. On the other hand, as $\text{Re } \epsilon$ approaches the surface resonance at -1.735 (see Figs. 7 and 8) the potential not only increases in magnitude but also displays an oscillatory behavior. This is a consequence of a cellular structure which characterizes a surface mode and is more dramatically displayed in Fig. 8, showing the iso-potential curves and their orthogonal trajectories, the electric field lines, in a meridional plane. As $\text{Re } \epsilon$ increases from -4, a "cell" of perturbed field forms near the end and progresses towards the center, followed by a second cell which forms for $\text{Re } \epsilon \geq -2$ and also drifts inward.

The analogous plots for the potential ϕ_1 corresponding to a transverse external field are shown in Fig. 9. The iso-potential lines are now basically longitudinal, and far from the surface mode resonance the field is almost uniform with only a slight distortion near the ends of the particle. As $\text{Re } \epsilon$ approaches the surface mode resonance at -1.738, the distortion develops into a significant perturbation. The iso-potential lines bend round to form a single cell at resonance which rapidly dissipates as $\text{Re } \epsilon$ increases beyond the resonance. Once again, there is no such structure near the volume resonance at $\text{Re } \epsilon = -1.118$.

References

- [1] H. Weil and T.B.A. Senior, "When are spheroids good models for Rayleigh scatterers?", Proc. 1982 CSL Conference on Obscuration and Aerosol Research (to appear).
- [2] T.B.A. Senior and H. Weil, "On the validity of modelling Rayleigh scatterers by spheroids," Appl. Phys., vol. B29, 117-124 (1982).
- [3] T.B.A. Senior and T. M. Willis III, "Rayleigh scattering by dielectric bodies," IEEE Trans. Antennas Propagat., vol. AP-30, 1271 (1982).
- [4] T.B.A. Senior, "Effect of particle shape on low frequency absorption," Appl. Opt., vol. 19, 2483-2485 (1980).
- [5] R. Englman and R. Ruppin, "Optical lattice vibrations in finite ionic crystals," J. Phys. C (Proc. Phys. Soc.), Ser. 2, vol. 1, 614-629 (1968).

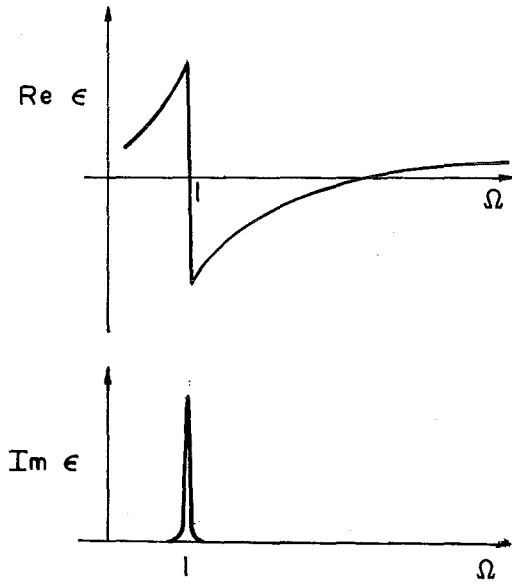


Fig. 1: Typical complex dielectric constant ϵ as a function of the normalized frequency Ω .

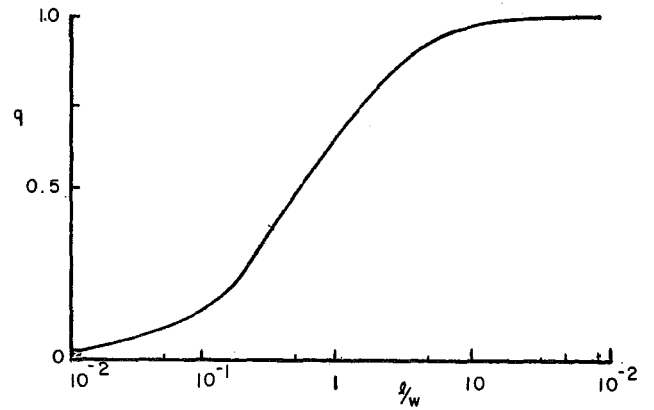


Fig. 2: The monotonic function q for spheroids.

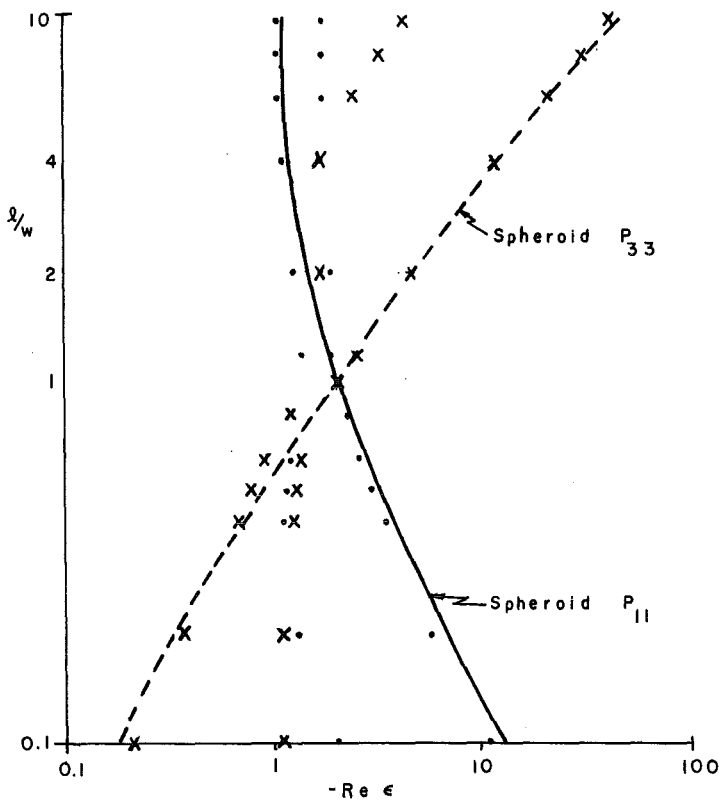


Fig. 3: Resonances of P_{11} (•••) and P_{33} (xxx) for spherically capped cylinders ($l/w > 1$) and bevelled disks ($l/w < 1$). The lines show the spheroid resonances.

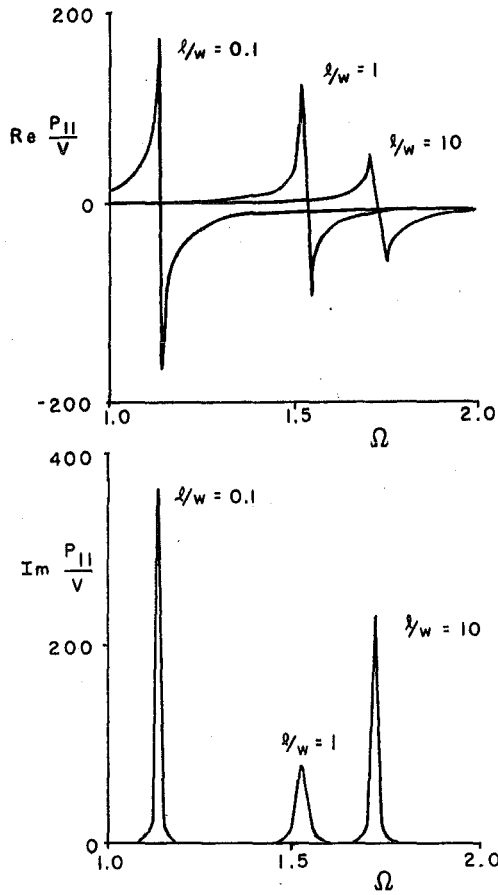


Fig. 4: Real and imaginary parts of P_{11}/V for three different spheroids computed from (8) with $a = 2$ and $\gamma = 0.01$.

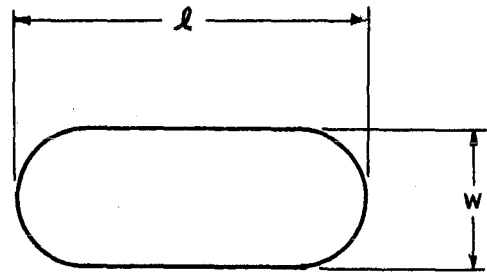


Fig. 5: Hemispherically capped cylinder with length l and width w .

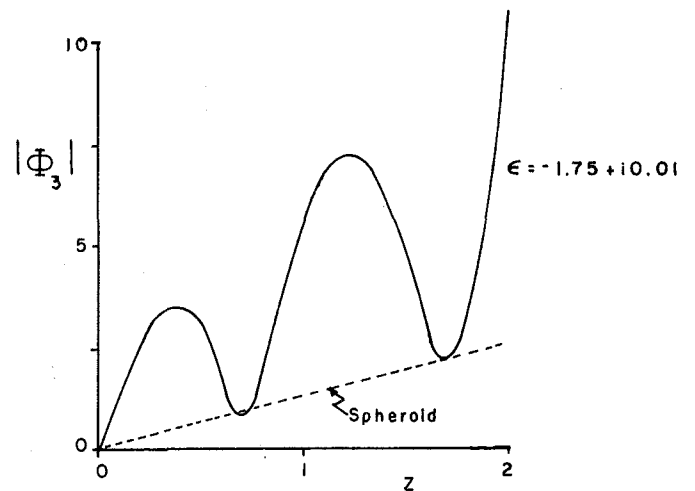
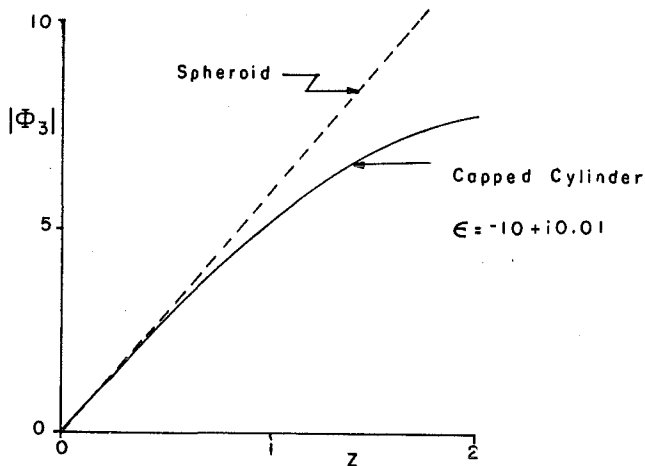
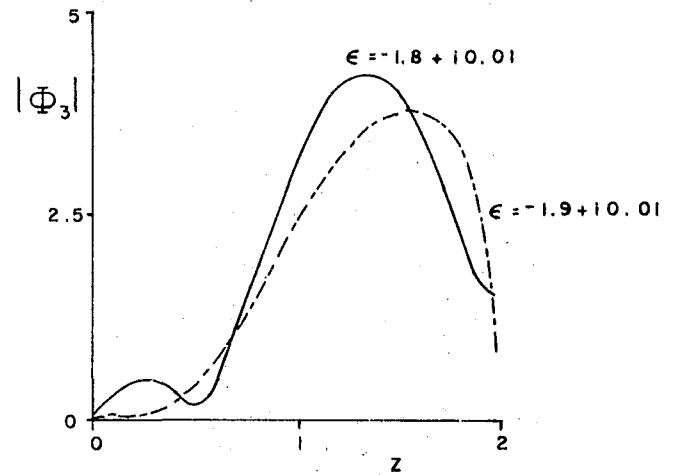
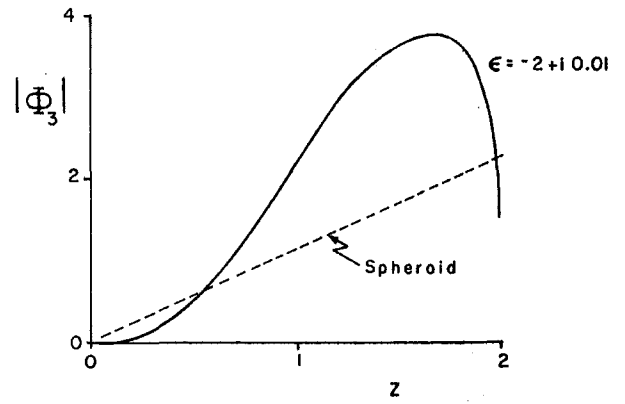
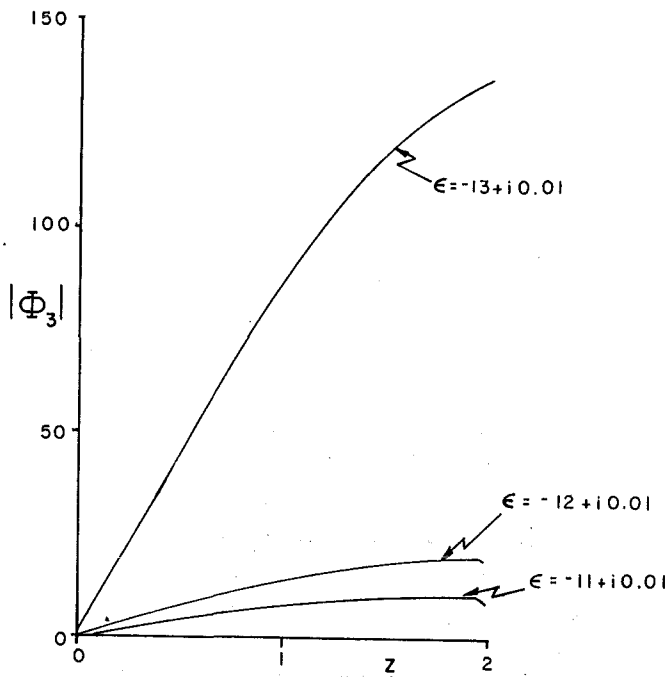


Fig. 6: Axial variation of $|\Phi_3|$ for a hemispherically capped cylinder with $\ell/w = 4$ as the volume resonance at $\text{Re } \epsilon = -13.2$ is approached.

Fig. 7: Axial variation of $|\Phi_3|$ for $\ell/w = 4$ as the surface resonance³ at $\text{Re } \epsilon = -1.735$ is approached.

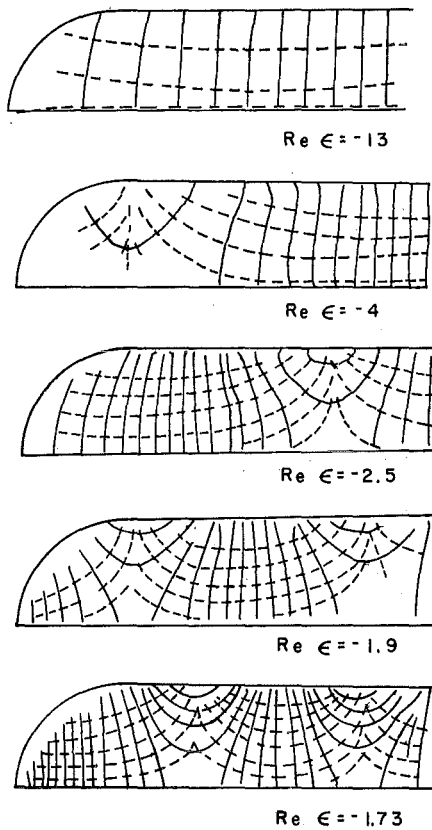


Fig. 8: Equipotentials (—) and electric field lines (---) for axial excitation. The volume resonance occurs at $\text{Re } \epsilon = -13.2$ and the surface resonance at $\text{Re } \epsilon = -1.735$.

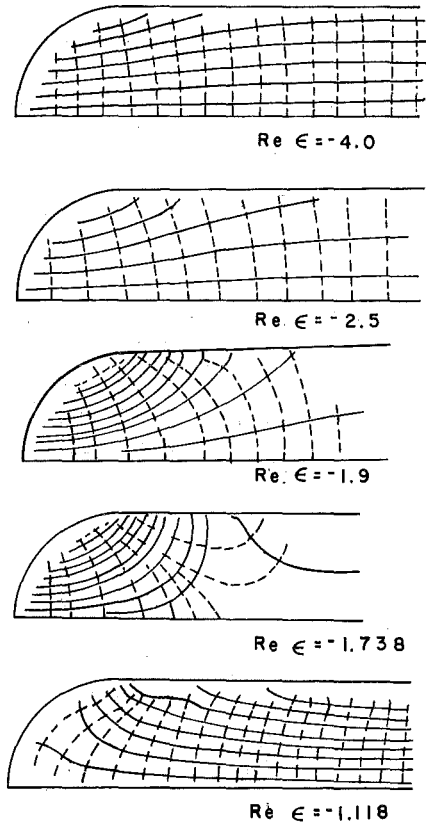


Fig. 9: Equipotentials (—) and electric field lines (---) for transverse excitation. The surface resonance occurs at $\text{Re } \epsilon = -1.738$ and the volume resonance at $\text{Re } \epsilon = 1.118$.

PERTURBATION THEORY FOR SCATTERING FROM DIELECTRIC
SHORT CYLINDERS

by

R.D. Haracz

L.D. Cohen

A. Cohen

Department of Physics and Atmospheric Science

Drexel University

Philadelphia, Pennsylvania 19104

Abstract

The perturbation theory suggested by Shifrin is applied through the second order to the scattering of light from finite cylinders. In the case of short dielectric cylinders, this technique provides an accurate prediction of the scattering pattern in its range of applicability, and this prediction is especially useful as no exact scattering solution exists.

The results for the finite cylinder are refined from our previous work by a careful construction of the internal electrostatic solution. This allows the calculation of intensities for short cylinders.

1. Introduction.

The scattering of radiation by infinite cylinders has been studied for perpendicular incidence from the early history of the application of Maxwell's theory by Lord Rayleigh¹ and Mie² and more recently for oblique incidence by Mentzner³ for perfect conductors and Wait, et al.⁴ for arbitrary materials. The exact solution is presented in detail in Kerker.⁵

We recently presented the theory for finite dielectric cylinders⁶ using a perturbative approach due to Shifrin⁷ and applied to spherical targets by Acquista.⁸ Acquista has also given the necessary modifications for application to other target shapes including cylinders and spheroids.

In Ref. 6, the treatment of the internal field for the finite cylinder was based on comparison with an inscribed spheroid. Here, we make an accurate calculation of the internal field in the electrostatic case. This allows us to present results for short cylinders (Ref. 6 restricted application to cylinders of aspect ratio 20 or greater.).

2. The Generalized Perturbation Theory for Scattering from a Dielectric Target of Arbitrary Shape.

We start with the solution of Maxwell's equations for an isotropic and nonmagnetic medium of index of refraction m :

$$E(\vec{r}) = \vec{E}_0 \exp(ik_0 r) + \nabla \times \nabla \times \int d^3r' \left(\frac{m^2 - 1}{4\pi} \right) \frac{\exp(ik_0 |\vec{r} - \vec{r}'|)}{|\vec{r} - \vec{r}'|} E(\vec{r}') - (m^2 - 1) E(\vec{r}), \quad (1)$$

where the integration is over the target. The electric field inside the target can be expressed in terms of the ambient electric field as

$$E_i(r^1) = A_{ij} E_{0j} \exp(ik r') \quad (2)$$

where A is the polarization matrix. The coordinates implied are shown in Fig. 1 as x_1, y_1, z_1 with z_1 the symmetry axis of the target. However, A is known for only a few special shapes in the electrostatic limit, and consequently Eq. (2) needs to be modified in order to be useful. We therefore represent the internal field as

$$E_i(r') = \bar{A}_{ij} E_{\text{eff},j}(r'), \quad (3)$$

where \bar{A} is the polarization matrix for the electrostatic case. It is known for spheres, spheroids, and infinite cylinders, and it can be constructed, as will be shown, for finite cylinders. For axially-symmetrical targets,

$$\bar{A} = \begin{pmatrix} a_{TE} & 0 & 0 \\ 0 & a_{TM} & 0 \\ 0 & 0 & a_{TM} \end{pmatrix}. \quad (4)$$

Here, TE refers to the electric field being perpendicular to the axis and TM refers to the field being parallel to the axis. Of course, \vec{E}_{eff} in Eq. (3) is still unknown, and it is found term by term using an expansion in $\alpha \equiv (m^2 - 1)/4\pi$:

$$\vec{E}_{\text{eff}}(r) = \vec{E}_0 \exp(ik_0 \cdot \vec{r}) + \sum_{n=1}^{\infty} \alpha^n \vec{E}_{\text{eff}}^{(n)}(\vec{r}). \quad (5)$$

The substitution of the expansion (5) into Eq. (1) leads after simplification to the first two orders of the perturbation theory :

$$E_{\text{eff}}^{(1)}(r) = \frac{k_0^2 \exp(ik_0 r)}{r} u(k_0 \hat{r} - \hat{k}_0) \left[(E_{0x} \hat{i}_1 + E_{0y} \hat{j}_1) a_{TE} + E_{0z} \hat{k}_0 a_{TM} \right]_{TM} \quad (6)$$

$$E_{\text{eff}}^{(2)}(r) = \frac{k_0^2 \exp(ik_0 r)}{2\pi^2 r} \rho \int d^3 p \frac{u(\vec{p} + k_0 \hat{r}) u(-\vec{p} - \hat{k}_0)}{\rho^2 - k_0^2} \left\{ k_0^2 \left[a_{TE}^2 (E_{0x} \hat{i}_1 + E_{0y} \hat{j}_1) + a_{TM}^2 E_{0z} \hat{k}_1 \right] - \left[a_{TE}^2 (\vec{p} \cdot (E_{0x} \hat{i}_1 + E_{0y} \hat{j}_1) + E_{0z} \hat{k}_1) + a_{TM}^2 E_{0z} \vec{p} \cdot \hat{k}_1 \right] \vec{p}_{\perp} + \frac{\rho^2 k_0^2}{m^2 - 1} \left[a_{TE} (1 - a_{TE}) (E_{0x} \hat{i}_1 + E_{0y} \hat{j}_1) + a_{TM} (1 - a_{TM}) E_{0z} \hat{k}_1 \right] \right\} \quad (7)$$

In these equations, the principal part of the integral is to be taken, and

$$u(\vec{x}) = \int d^3 r U(\vec{r}) \exp(i \vec{x} \cdot \vec{r}) \quad (8)$$

The unit vectors $\hat{i}_1, \hat{j}_1, \hat{k}_1$, are target coordinates as shown in Fig. 1, and

$$x_1 \equiv \hat{r} \cdot \hat{x} \cdot \hat{r} - \hat{x} \cdot \hat{x} \quad (9)$$

3. The Finite Dielectric Cylinder.

The perturbation theory described here relies on an accurate determination of the electrostatic polarization matrix. Though known for the infinite cylinder, this matrix is not available for the

finite cylinder. We next present a method for finding \bar{A} by a technique outlined in a book by Van Bladel.⁹

The electrostatic potential $\phi(\vec{r}_0)$ inside the cylinder is related to the surface potential as

$$m^2 \phi(\vec{r}_0) = \phi_0(\vec{r}_0) - \frac{m^2 - 1}{4\pi} \oint dS \phi(\vec{r}') \frac{\partial}{\partial n} \left(\frac{1}{|\vec{r} - \vec{r}'_0|} \right), \quad (10)$$

where ϕ_0 is the ambient potential, the integral is over the cylindrical surface, and $\partial/\partial n$ is the outward normal gradient to the surface. It follows that the electric field inside the cylinder is

$$m^2 \vec{E}(\vec{r}_0) = \vec{E}_0 + \frac{m^2 - 1}{4\pi} \oint dS \nabla_0 \left(\frac{\partial}{\partial n} \left(\frac{1}{|\vec{r} - \vec{r}'_0|} \right) \right). \quad (11)$$

Here, \vec{E}_0 is the ambient electrostatic field. This internal field is related to the electrostatic polarization matrix as in Eq. (2), and we are led to the following equation for the matrix elements:

$$(m^2 a_i - 1) E_{0i} = \frac{m^2 - 1}{4\pi} \oint dS \phi(\vec{r}') \frac{\partial}{\partial n} \left[\frac{(\vec{r} - \vec{r}'_0)_i}{|\vec{r} - \vec{r}'_0|^3} \right], \quad (12)$$

where $a_{TE} = a_1 = a_2$ and $a_{TM} = a_3$.

Therefore, the matrix \bar{A} is known if we know the surface potential ϕ , and it is determined from the equation

$$\phi(\vec{r}_s) = \frac{2}{m^2 - 1} \phi_0(\vec{r}_s) - \frac{m^2 - 1}{m^2 + 1} \frac{1}{2\pi} \oint dS \frac{\partial}{\partial n} \left(\frac{1}{|\vec{r} - \vec{r}'_0|} \right), \quad (13)$$

where \vec{r}_s is on the cylindrical surface. We choose to solve Eq. (13) by an iteration process starting with $\phi = \phi_0$ as the first guess. For the TE elements of \bar{A} , $\vec{E}_0 = E_0 \hat{z}_1$ and $\phi_0 = -r \cos\theta E_0$. For the TM element, $\vec{E}_0 = E_0 \hat{k}_1$ and $\phi_0 = -z_1 E_0$. Convergence occurs rapidly for an index of refraction of 1.33 where only two iterations are necessary. The integrations over the surface are performed using the cylindrical coordinates shown in Fig. 2

The results for the elements a_{TE} and a_{TM} are given in Fig. 3 for the aspect ratios $h/2a = 1/2$, 1, and 5. The values are given along the symmetry axis z_1 , but they are similar along a perpendicular axis.

It is observed that for an aspect ratio of 5, the elements are quite constant in the central region of the cylinder with values near those for an infinite cylinder. The values of the elements decrease near the ends. The same general variation occurs for the other aspect ratios.

4. Results for the Finite Cylinder.

The amplitudes I_1 and I_2 are evaluated using the electrostatic polarization matrix elements of the last section. These results for the finite dielectric cylinder are plotted in the Figures 4 through 7.

In Fig. 4, the result for a cylinder of aspect ratio 1/2 is shown with volume $3.22 \mu\text{m}^3$. In the perturbative calculation, the second-order correction is generally about 26%.

In Fig. 5 the cylinder has a volume $4.19 \mu\text{m}^3$. Here, the second-order correction is generally about 22%.

Figs. 6 and 7 show the respective amplitudes I_1 and I_2 for a cylinder of aspect ratio 5. The volume is $4.81 \mu\text{m}^3$. The second-order correction here is about 25%.

5. Discussion and Conclusions.

We continue our study of the Shifrin perturbation theory for the scattering of radiation of wavelength λ from particles of size a in the range where $2\pi(m-1)/\lambda \approx 1$. This theory has two obvious advantages. First, the analytic first-order contribution is a fair representation of the scattering and provides an easy-to-calculate approximation. Second, this perturbation theory provides an accurate means for calculating the scattering pattern for the short dielectric cylinder where no exact theory exists.

This theory relies on an accurate determination of the electrostatic field within the target. This internal field is used as the first-order kernel term upon which the successive approximations are built. The results are then applicable to the scattering of radiation of wavelength only slightly larger than the target.

In the case of the short dielectric cylinder (aspect ratios < 10), the internal electrostatic field is not known. A technique is presented for constructing this field by a rapidly converging iterative scheme.

Acknowledgement

This work was supported in part by the U.S. Army Chemical Systems Laboratory at Edgewood Arsenal.

References

1. J.W. Strutt (Lord Rayleigh), *Philos. Mag.* 12, 81 (1881).
2. G. Mie, *Ann. Phys. Leipzig* 25, 377 (1908).
3. J.R. Mentzner, Scattering and Diffraction of Radio Waves (Pergamon, Oxford, 1955).
4. J.R. Wait, Electromagnetic Radiation by Small Particles (Wiley, N.Y., 1957).
5. M. Kerker, The Scattering of Light and Other Electromagnetic Radiation (Academic, N.Y., 1969).
6. L.D. Cohen, R.D. Haracz, A. Cohen, *Appl. Opt.* 21, 748 (1983).
7. K.S. Shifrin, Scattering of Light in a Turbid Medium (Moscow, 1951), NASA TTF-477, Washington, D.C., 1968.
8. C. Acquista, *Appl. Opt.* 15, 2932 (1976).
9. J. Van Bladel, Electromagnetic Fields (McGraw Hill, N.Y., 1964), pages 68-77.

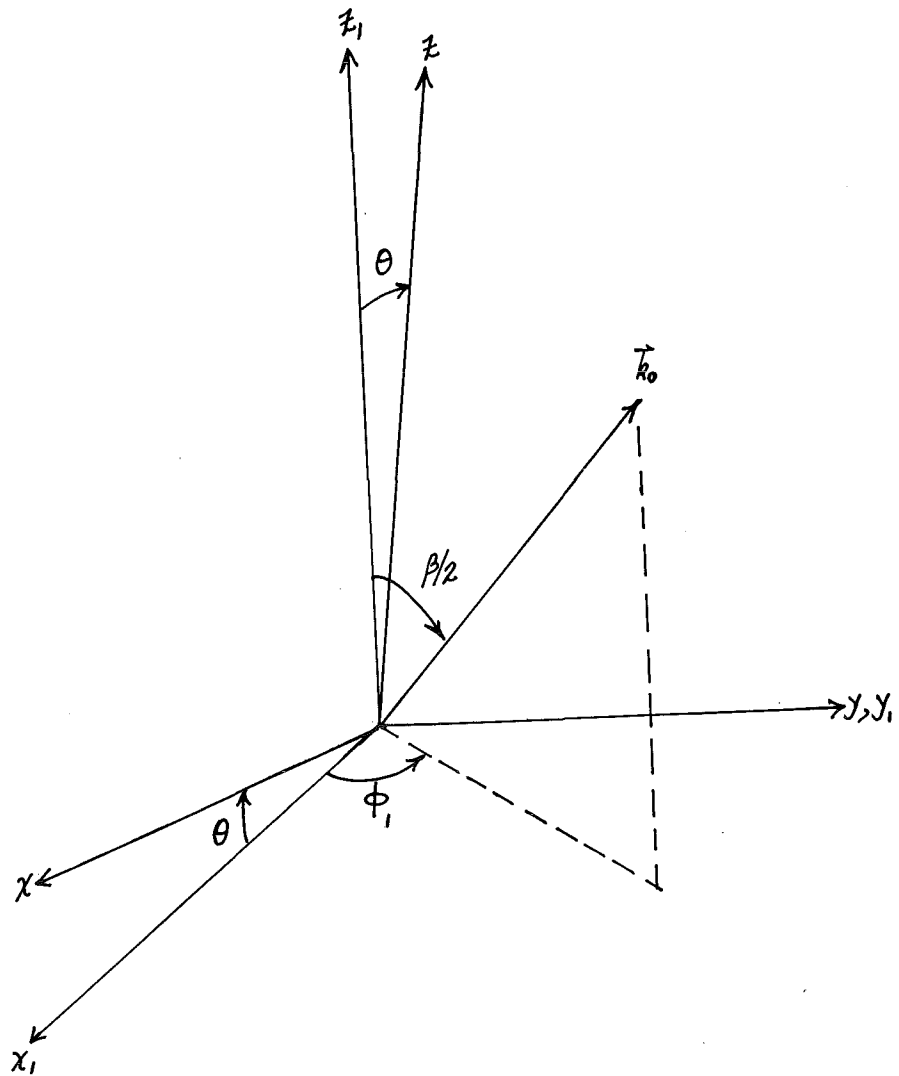


Fig. 1. The geometry of the scattering process. The axes x_1, y_1, z_1 are the target axes with z_1 the axis of symmetry. The axes x, y, z are the detector axes with z the direction toward the detector. The incident wave vector \vec{k}_0 has the spherical coordinates $(k, \beta/2, \phi_1)$ in the target frame.

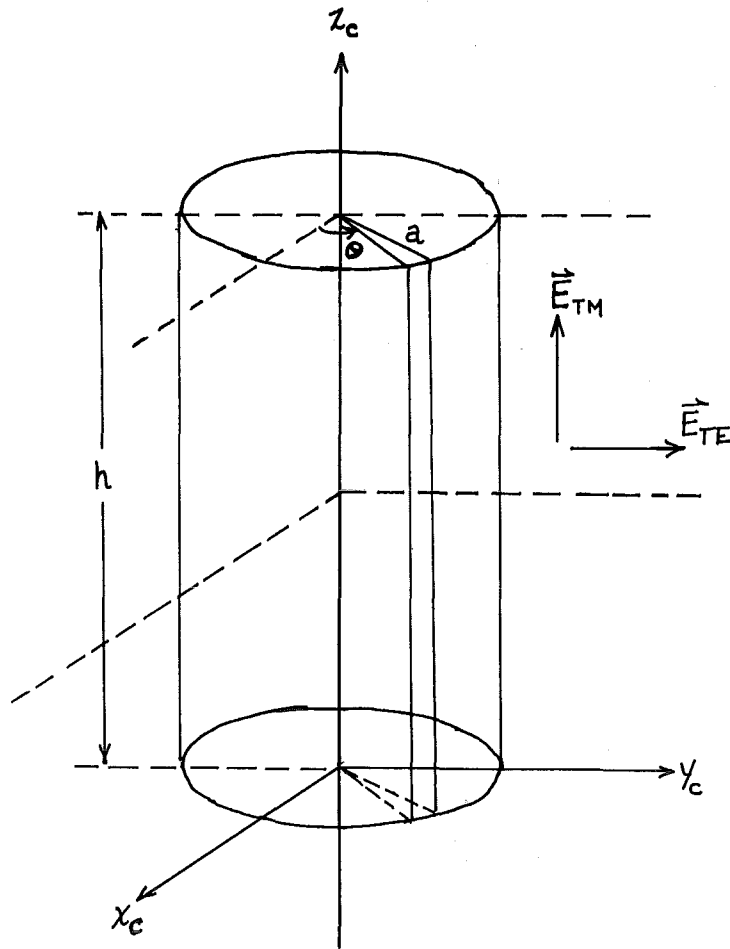


Fig. 2. The geometry of the cylinder used to calculate the internal electrostatic field. Polar coordinates are used in evaluating the surface integrals (see text).

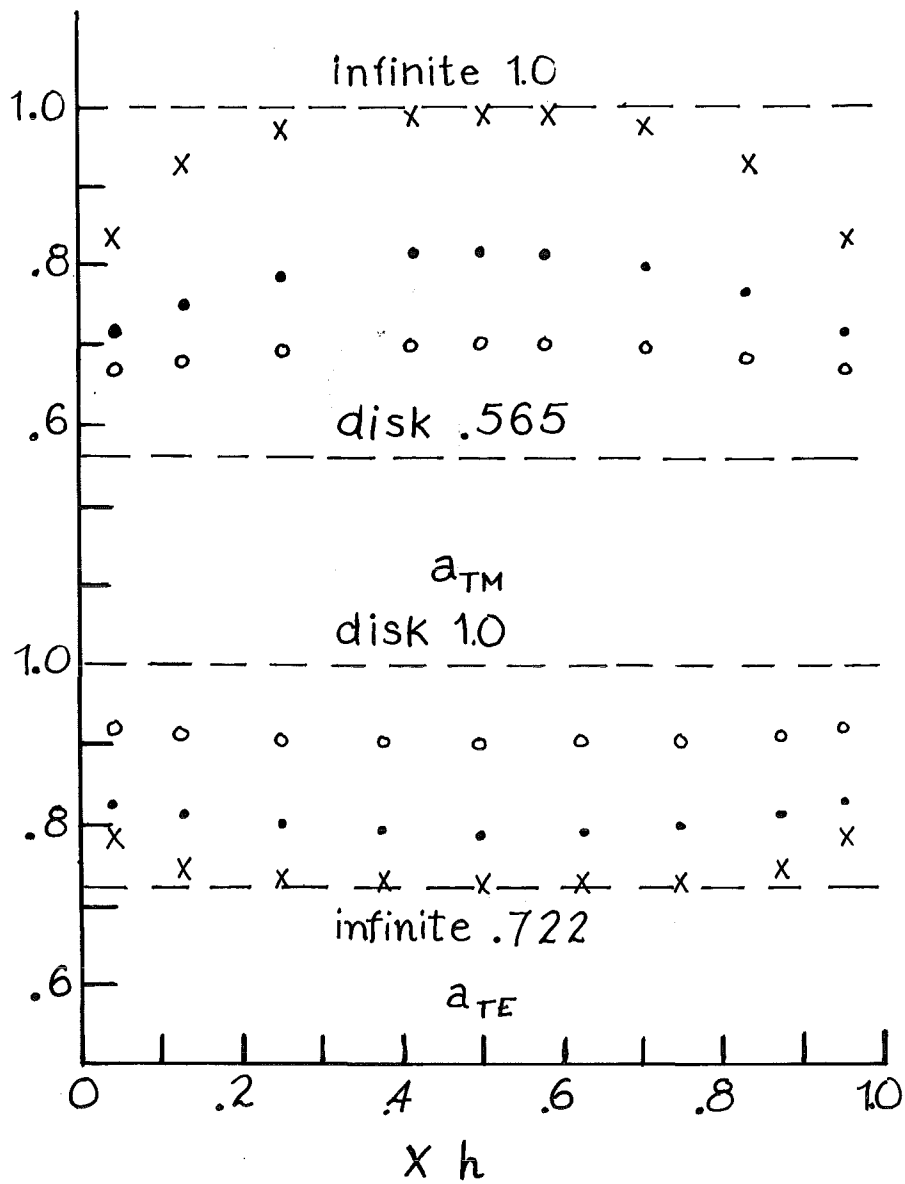


Fig. 3. The polarization matrix elements for the finite dielectric cylinders. The crosses (x) represent an aspect ratio of 5, the solid circles 1, and the open circles 1/2. The results are plotted along the axis of the cylinder. The top portion of the figure is for an ambient electric field directed parallel to the axis (TM), and the bottom portion is for an ambient field perpendicular to the axis (T.E).

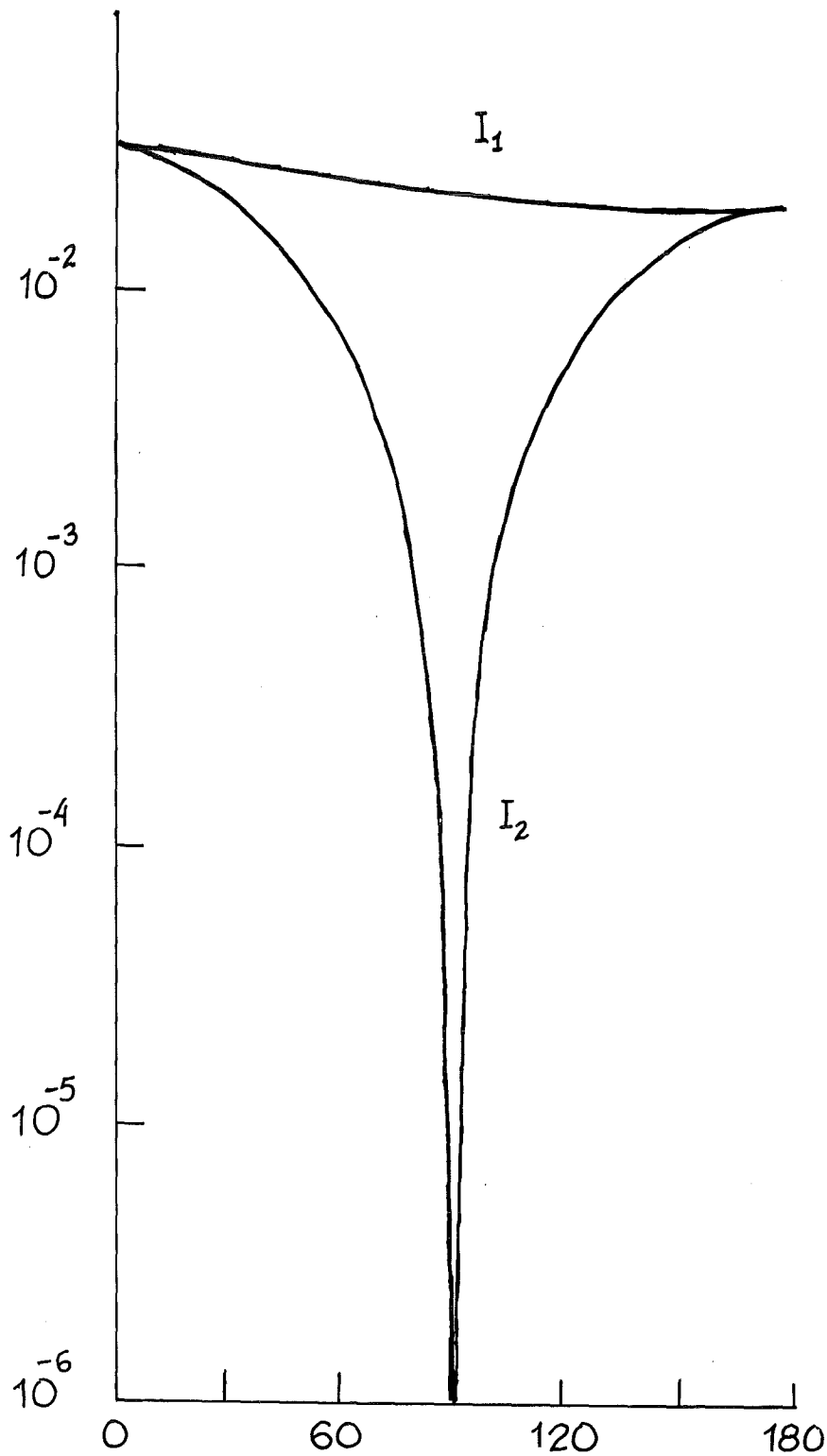


Fig. 4. The scattering amplitudes I_1 and I_2 for light of wavelength $\lambda = 2\pi \mu\text{m}$ incident along the axis of symmetry. Target has an index of refraction $m = 1.33$ and the volume is $3.22 \mu\text{m}^3$.

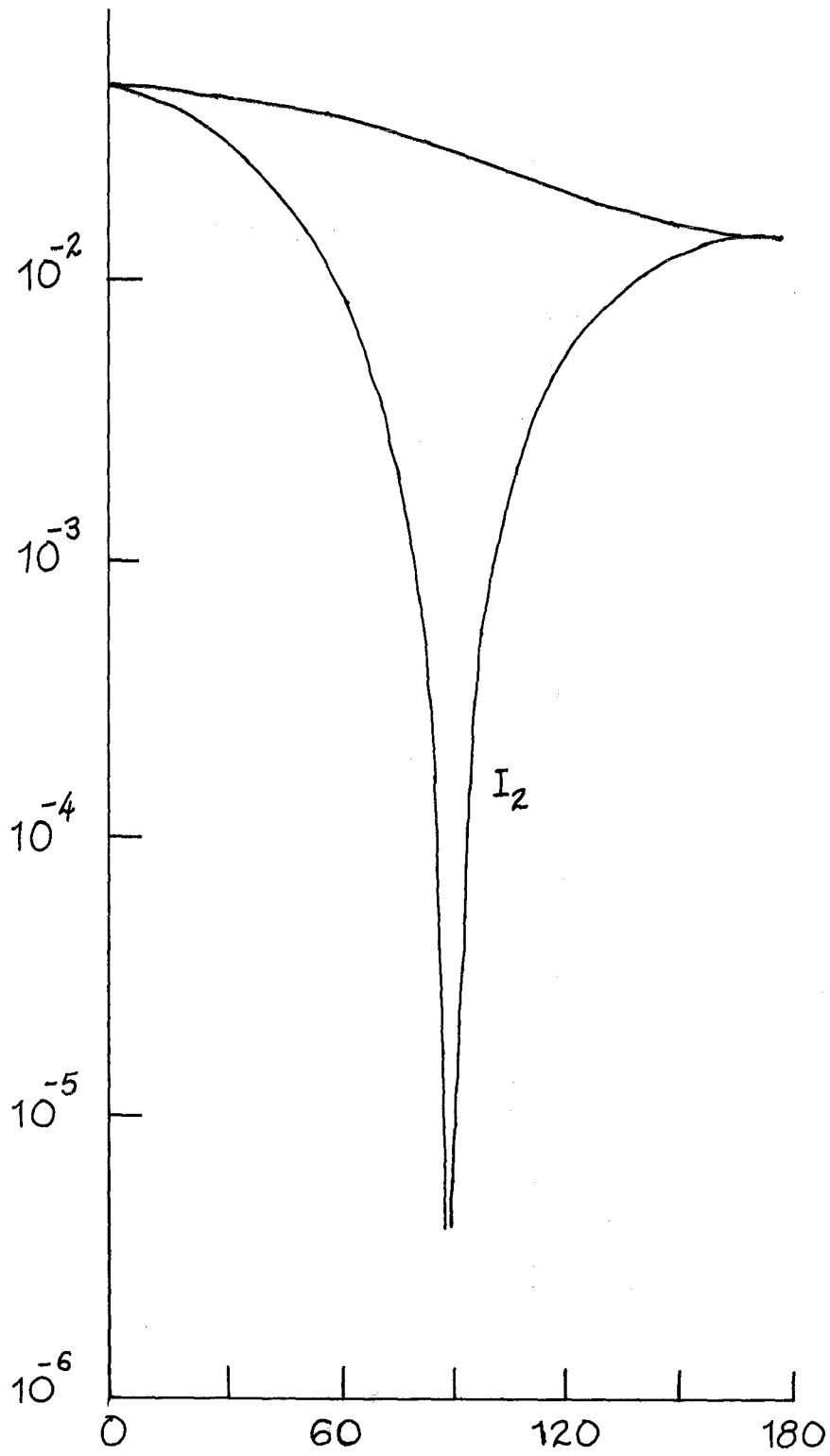


Fig. 5. The amplitudes I_1 and I_2 for light incident along the axis of symmetry. The volume of the target is $4.19 \mu\text{m}^3$ and its aspect ratio is 1.

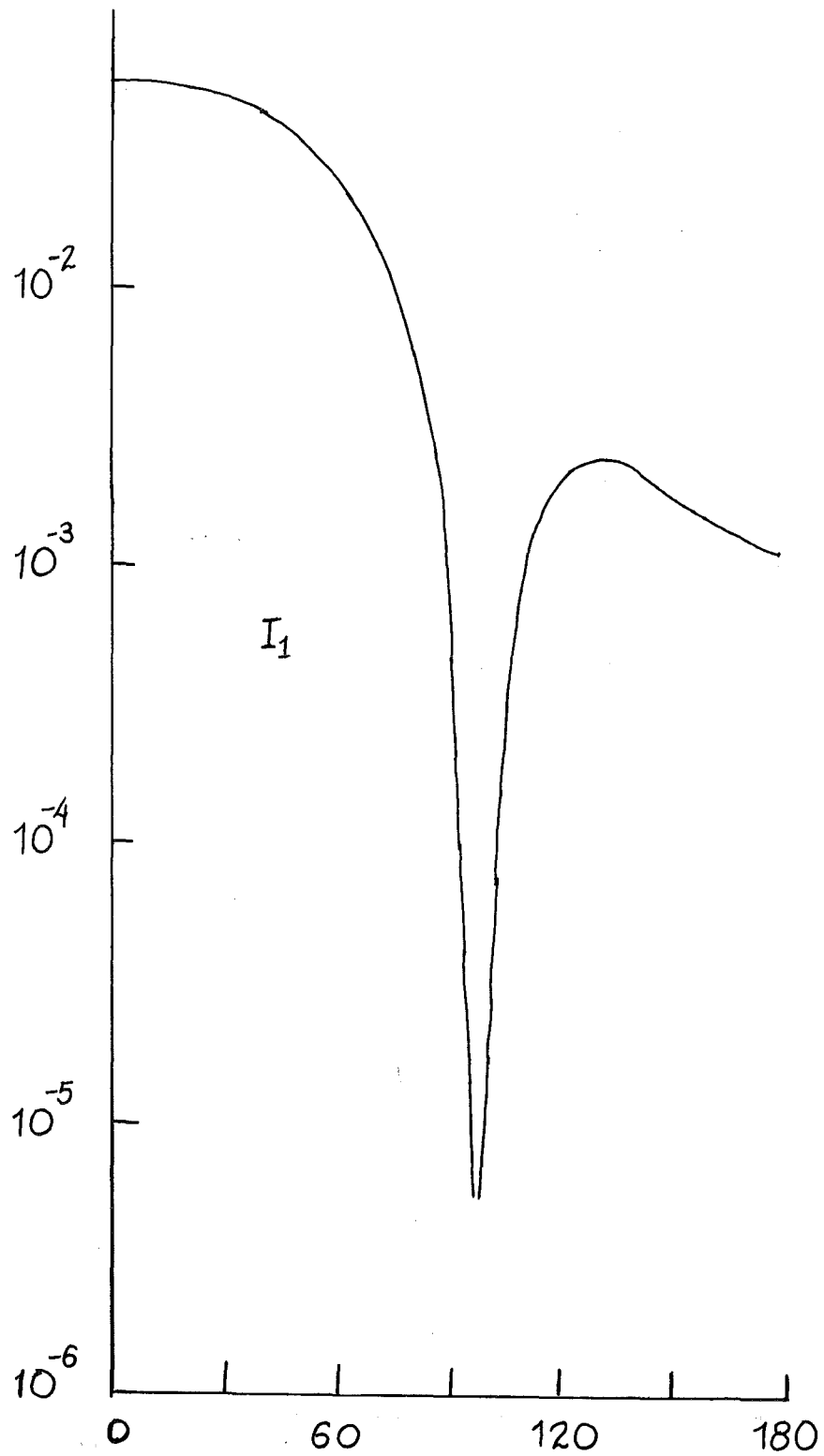


Fig. 6. The amplitude I_1 for light incident along the axis of symmetry. The volume is $4.81 \mu\text{m}^3$ and the aspect ratio 5.

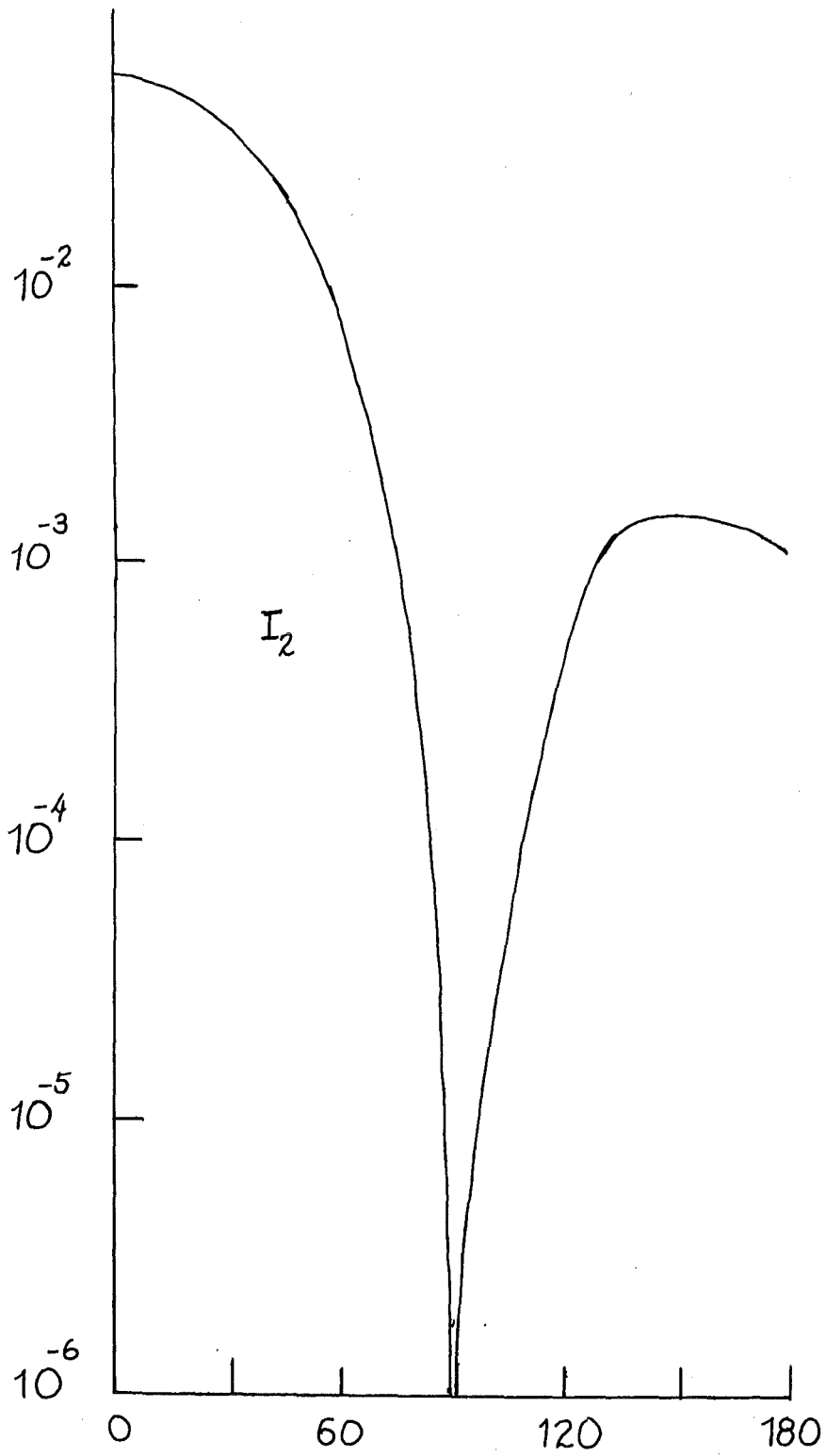


Fig. 7. The amplitude I_2 for the same case as Fig. 4.

BLANK

NEW THEORETICAL APPROACH TO SCATTERING FROM THIN FIBERS

Melvin Lax

Physics Department of the City College* of the City University of New York,
New York, N.Y. 10031

Gaelen Daum†

Ballistic Research Laboratory, Aberdeen Proving Ground,
Aberdeen, Maryland 21005

ABSTRACT

A careful formulation is made of the scattering of electromagnetic waves from dielectric, conducting fibers possessing a symmetry axis z , a finite length $2b$, and a profile $\rho = a(z)$. The problem is simplified for the case of thin fibers: $ka_{\max} \ll 1$ with no limitation on the ratio b/a . Our procedure includes the "metallic" case in which the skin depth is small compared to the radius and the "dielectric case" in which the skin depth is large compared to the radius, but we emphasize here the latter case. The objective of this paper is to reduce the problem to coupled one-dimensional integral equations for the z dependence of the average field or of the on-axis field.

1. INTRODUCTION

Scattering of electromagnetic waves from "metallic" fibers can be found in the literature as the receiving antenna problem. It has received attention from Nobel prize winners,¹ formulated in a variational manner by Tai² and treated in the case of long cylinders $kb \gg 1$ using Weiner-Hopf techniques by Chen and Wu.³ We shall rely on these papers for a review of the extensive literature (including books) on the antenna problem.

In an important sense, the antenna problem is simpler than the dielectric problem, because in the former case, the field is known to be concentrated in the vicinity of the surface. Most of the

*Work at City College supported in part by the Army Research Office

†Now at Global Analytics, 10065 Old Grove Rd., San Diego, CA 92131

¹J. H. Van Vleck, F. Bloch and M. Hamermesh, "Theory of Radar Reflection from Wires or Thin Metallic Strips," *J. Applied Phys.* **18**, 274-294 (1947).

²C. T. Tai, "Electromagnetic Back-Scattering from Cylindrical Wires," *J. Appl. Phys.* **23**, 909-916 (1952).

³Chin-Lin Chen and Tai Tsun Wu "Theory of the Long Dipole Antenna" in *Antenna Theory, Part I* by Robert Collin and Frances J. Zucker, McGraw-Hill, New York (1969)

emphasis in the above reported work is therefore concentrated on solving a single one-dimensional integral equation for the total current (or average field) as a function of z .

A corresponding simplification could be made in the dielectric case, if one could specify the radial distribution of the current density or the field. Uzunoglu, Alexopoulos and Fikioris⁴ specialize to the rotationally symmetric ($m = 0$) part of the solution and assume that the radial distribution is uniform. Even there, they are cautious and apply their procedure only to the case of a field incident at right angles to the cylinder. Although they give no reason for their caution, the work of Wait⁵⁻⁷ suggests that their caution is warranted for two reasons: for small ka , solutions with azimuthal symmetry $\exp(im\phi)$ are important for $m = 1$ as well as $m = 0$, and the $m = 0$ contribution is coupled to the $m = 1$ contribution for non-normal incidence.

When a Fourier representation is used for the field, the assumption of a uniform field is equivalent to neglecting a term of order $(\rho/a)^2$ compared to one of order $\ln(1/ka)$. This is warranted, of course, when ka is extremely small (of order 10^{-10}) but not if we merely have $ka < 10^{-2}$.

In summary, we expect to find not one one-dimensional integral equation, but a pair of coupled integral equations. The problem of the radial dependence of the fields is solved by assuming a uniform field for the $m = 0$ component, and a ρ dependence for the $m = 1$ component, but only inside a variational expression. An alternative procedure, based on a Fourier-Bessel representation is also introduced. Here, equations are obtained for fields on the cylinder axis. Greatly simplified equations are obtained by neglecting all Fourier components of order $1/a$ or higher.

⁴N. K. Uzunoglu, N. G. Alexopoulos and J. G. Fikioris, "Scattering From Thin and Finite Dielectric Fibers," J. Opt. Soc. Amer. **68**, 194-197 (1978).

⁵J. R. Wait, "Scattering of a Plane Wave from a Circular Dielectric Cylinder at Oblique Incidence," Can. J. Phys. **33**, 189-195 (1955).

⁶J. R. Wait, *Electromagnetic Radiation from Cylindrical Structures*, Pergamon Press, Oxford, (1959).

⁷J. R. Wait, "The Long Wavelength Limit in Scattering from a Dielectric Cylinder at Oblique Incidence," Can. J. Phys. **43**, 2212-2215 (1965).

2. FORMULATION

An exact integral formulation for a scatterer described by a complex index of refraction n

$$\mathbf{E}(\mathbf{r}) = \mathbf{E}^{\text{inc}}(\mathbf{r}) + k^2 \mathbf{F} + \nabla(\nabla \cdot \mathbf{F}(\mathbf{r})) \quad (2.1)$$

$$\mathbf{F}(\mathbf{r}) = \int \frac{\exp(ikR)}{4\pi R} [n^2(\mathbf{r}') - 1] \mathbf{E}(\mathbf{r}') d\mathbf{r}' \quad (2.2)$$

where

$$R^2 = |\mathbf{r} - \mathbf{r}'|^2 = (z - z')^2 + \rho^2 + \rho'^2 - 2\rho\rho' \cos(\phi - \phi') \quad (2.3)$$

and $k = \omega/c$.

Symmetry about an axis can be exploited by making the expansions

$$E(z, \rho, \phi) = \sum_{m=-\infty}^{\infty} E_m(z, \rho) \exp(im\phi) \quad (2.4)$$

$$\mathbf{F}(z, \rho, \phi) = \sum_{m=-\infty}^{\infty} \mathbf{F}_m(z, \rho) \exp(im\phi) \quad (2.5)$$

where

$$F_m(z, \rho) = \frac{1}{2} \int G_m(z - z', \rho, \rho') [n^2(z', \rho') - 1] E_m(z', \rho') \rho' d\rho' dz' \quad (2.6)$$

and

$$G_m(z - z', \rho, \rho') = \frac{1}{2\pi} \int_{-\pi}^{\pi} d\phi \frac{\exp(ikR)}{R} e^{im\phi} \quad (2.7)$$

This results in a set of equations for the triplet E_m^z , E_{m+1}^+ and E_{m-1}^- where

$$E^+ = E_x + i E_y \quad ; \quad E^- = E_x - i E_y \quad (2.8)$$

are components of circular polarization:

$$\begin{aligned} E_m^z = E_m^{\text{inc}z} + \left(k^2 + \frac{\partial^2}{\partial z^2} \right) F_m^z + \frac{1}{2} \left[\frac{\partial}{\partial \rho} - \frac{m-1}{\rho} \right] \frac{\partial}{\partial z} F_{m-1}^- \\ + \frac{1}{2} \left[\frac{\partial}{\partial \rho} + \frac{m+1}{\rho} \right] \frac{\partial}{\partial z} F_{m+1}^+ \end{aligned} \quad (2.9)$$

$$E_{m+1}^+ = E_{m+1}^{inc+} + \left\{ k^2 + \frac{1}{2} \left[\nabla_\rho^2 - \frac{(m+1)^2}{\rho^2} \right] \right\} F_{m+1}^+ + \left(\frac{\partial}{\partial \rho} - \frac{m}{\rho} \right) \frac{\partial}{\partial z} F_m^z - \frac{1}{2} \left[\frac{\partial}{\partial \rho} - \frac{m}{\rho} \right] \left[\frac{\partial}{\partial \rho} - \frac{m-1}{\rho} \right] F_{m-1}^- \quad (2.10)$$

$$E_{m-1}^- = E_{m-1}^{inc-} + \left\{ k^2 + \left[\nabla_\rho^2 - \frac{(m-1)^2}{\rho^2} \right] \right\} F_{m-1}^- + \left(\frac{\partial}{\partial \rho} + \frac{m}{\rho} \right) \frac{\partial}{\partial z} F_m^z + \frac{1}{2} \left(\frac{\partial}{\partial \rho} + \frac{m}{\rho} \right) \left(\frac{\partial}{\partial \rho} + \frac{m+1}{\rho} \right) F_{m+1}^+ \quad (2.11)$$

where

$$\nabla_\rho^2 = \frac{1}{\rho} \frac{\partial}{\partial \rho} \left(\rho \frac{\partial}{\partial \rho} \right) \quad (2.12)$$

Equation (2.11) can be omitted in the future, since it can be replaced by the simpler statement

$$E_m^- = \pm E_m^+ \quad (2.13)$$

with the upper sign, the important case for thin scatterers, used below.

3. CROSS-SECTIONS

The absorption cross-section can readily be shown to take the form:

$$\sigma_{\text{abs}} = k \operatorname{Im} \int (n^2 - 1) \frac{|E|^2}{|E^{\text{inc}}|^2} d\tau, \quad (3.1)$$

whereas the total scattering cross-section into polarization e can be written:

$$\sigma_{\text{sc}} = \frac{k^4}{4\pi} \int |\mathbf{e} \cdot \mathbf{g}(\theta, \phi)|^2 \frac{d\Omega}{4\pi} \quad (3.2)$$

where the scattering amplitude g is defined by

$$\mathbf{g}(\theta, \phi) = \int \exp[-ik\mathbf{n} \cdot \mathbf{r}] [n^2(\mathbf{r}) - 1] \mathbf{E}(\mathbf{r}) d\tau \quad (3.3)$$

Complete results can be obtained by inserting the expression Eq. (2.4) for E(r).

4. ORDER OF MAGNITUDE IN THE THIN SCATTERER LIMIT

By examining Wait's expressions for E_m , we can (with some labor) conclude that the dominant term in $E_m(\rho, z)$ is of order

$$E_m(\rho, z) \sim (k\rho)^m \sim (ka)^m . \quad (4.1)$$

Thus the dominant term in the cross-sections, Eqs. (3.1) and (3.2) may be obtained by replacing $E(z, \rho, \phi)$ by $E_0(z, \rho)$. Thus if we neglect terms of order $(ka)^2$ and set the incident field E^{inc} to have unit amplitude, the absorption cross-section and scattering amplitude reduce to

$$\sigma_{\text{abs}} = 2\pi k \text{Im} \int (n^2-1) |E_0(z, \rho)|^2 \rho d\rho dz , \quad (4.2)$$

$$g(\theta, \phi) \approx 2\pi \int \exp(-kz \cos\theta) (n^2-1) E_0(z, \rho) \rho d\rho dz . \quad (4.3)$$

A more detailed examination of Wait's results for the infinite cylinder case (plus several pages of algebra) leads us to conclude that in the thin cylinder case the inside field

$$E_m^+ \approx \frac{E_m^{\text{inc}+}}{\frac{1}{2} + \frac{1}{2}(n^2-1)} , \quad (4.4)$$

is reduced relative to the incident field $E_m^{\text{inc}+}$ by the depolarization factor

$$(1-L_m) + L_m(n^2-1) , \quad (4.5)$$

where the depolarization coefficient

$$L_m = 1/2 \text{ for all } m \neq 1 \quad (4.6)$$

A similar remark applied to all E_m^- with $m \neq -1$. In any case, for $m = 0$, $L = 1/2$.

In this paper, we are not concerned with the trivial case in which both

$$(ka)^2 \ll 1 \text{ and } (n^2-1)(ka)^2 \ll 1 , \quad (4.7)$$

for then the incident field is already a good enough approximation to use in the cross-section equations. If, however,

$$(n^2-1)(ka)^2 \gg 1 \text{ (antenna)} \quad (4.8)$$

or

$$(n^2-1)(ka)^2 < 1 \text{ (lossy dielectric)} , \quad (4.9)$$

[which describe the cases of skin depth small or large compared to the radius, respectively] then we are concerned with the case in which

$$(ka)^2 \ll 1 \text{ and } (n^2-1) \gg 1 . \quad (4.10)$$

Depolarization effects then guarantee that

$$E_0^+ \ll E_0^- \text{ and } E_0^- \ll E_0^+ . \quad (4.11)$$

Thus the differential scattering cross-section simplifies to the form

$$\sigma_{sc}(\theta) = \frac{\pi}{4} |n^2-1|^2 \sin^2\theta \int_{-b}^b [ka(z)]^4 \langle E_0^-(z) \rangle e^{(ik \cos\theta)z} dz , \quad (4.12)$$

where $\langle \rangle$ denotes an average over the radial dependence:

$$\langle E_m(z) \rangle = 2\pi \int_0^{a(z)} E_m(z, \rho) \rho d\rho / [\pi a^2(z)] . \quad (4.13)$$

and the absorption cross-section can be written

$$\sigma_{abs} = \pi k \text{Im} (n^2-1) \int_{-b}^b a^2(z) \langle |E_0^-(z)|^2 \rangle dz , \quad (4.14)$$

where

$$\langle |E_0^-(z)|^2 \rangle = 2\pi \int_0^{a(z)} |E_0^-(z, \rho)|^2 \rho d\rho / [\pi a^2(z)] . \quad (4.15)$$

5. COUPLED LOWEST ORDER EQUATIONS

To obtain $E_0(z, \rho)$ we obtain rigorous equations by setting $m = 0$ in Eqs. (2.11), (2.10) and use Eq. (2.13) to obtain

$$E_0^- = E_0^{\text{inc}^-} + \left[k^2 + \frac{\partial^2}{\partial z^2} \right] F_0^- + \frac{\partial}{\partial \rho} \frac{\partial}{\partial z} F_1^+ , \quad (5.1)$$

$$E_1^+ = E_1^{\text{inc}^+} + \left[k^2 + \left[\nabla_\rho^2 - \frac{1}{\rho^2} \right] \right] F_1^+ + \frac{\partial}{\partial \rho} \frac{\partial}{\partial z} F_0^- , \quad (5.2)$$

where the incident fields are given by

$$E_0^{\text{inc}^-} = S_0 J_0(k\rho S_0) e^{ikz C_0} \approx S_0 e^{ikz C_0} , \quad (5.3)$$

$$E_1^{\text{inc}^+} = -C_0 i J_1(k\rho S_0) e^{ikz C_0} \approx -C_0 e^{ikz C_0} (ik\rho S_0) , \quad (5.4)$$

for a field in the $x-z$ plane at an angle θ_0 from perpendicularity to the cylindrical axis, and polarized in the direction

$$e_E = [-C_0, 0, S_0] \quad (5.5)$$

where

$$C_0 = \cos \theta_0, \quad S_0 = \sin \theta_0, \quad (5.6)$$

Although E_1^{inc} can be seen to be small, of order ka , in Eq. (5.4), E_1^+ is also excited by the last term in Eq. (5.2). Moreover, the effect of E_1^+ on E_0^+ can *not* be neglected, even though E_1^+ is small near the axis $\rho = 0$, because it is the radial derivative of E_1^+ that influences E_0^+ !

Equations (5.1) and (5.2) constitute the maximum simplification that can be achieved merely by neglecting terms of order $(ka)^2$. Moreover, these equations are still applicable to both the "antenna" and "dielectric" cases.

6. VARIATIONAL PROCEDURE

Although we anticipate that the dominant term in the expansion of $E_m(z, \rho)$ near $\rho = 0$ has the form $\rho^m B_m(z)$,

$$E_m(z, \rho) \approx \rho^m B_m(z), \quad (6.1)$$

it is hazardous to insert this assumption directly into the equations of motion. Indeed, if this insertion is made into Eqs. (2.9), (2.10) and (2.11), the solutions do not agree with the known solutions for the infinite cylinder case. Indeed, it took me many months to learn that the correct solutions are obtained only if one retains three terms in the expansion:

$$E_m(z, \rho) = \rho^m B_m^{(0)}(z) + \rho^{m+2} B_m^{(2)}(z) + \rho^{m+4} B_m^{(4)}(z). \quad (6.2)$$

[Unless one does this, the last term in Eq. (2.10) vanishes!] If, however, one inserts a solution of this form, one can expect to get an infinite set of coupled equations involving $B_m^{(2n)}(z)$ of all order $2n$.

The above mentioned difficulty is less severe for the case $m=0$ since we can make the replacement

$$F_0^- = F_1^+ \quad (6.3)$$

A less dangerous procedure than inserting the radial dependence $\rho^m B_m(z)$ into the equations of motion is to make this insertion into a variational procedure. For this purpose, we need a variational procedure for scattering problems applicable to the dissipative case. We have previously developed just such a procedure⁷ as a generalization of the Lippman-Schwinger⁸ variational method. We consider an

⁷M. Lax, "A Variational Method for Non-Conservative Collisions," Phys. Rev. 78, 306-307

equation of the form

$$\Psi_a = \Phi_a + L V \Psi_a , \quad (6.4)$$

where Φ_a is the incident wave, V is non-Hermitian, and L is in general, an integral operator. Because of the dissipative nature of the problem, it is necessary to consider the associated equation:

$$\Psi_b' = \Phi_b + L' V' \Psi_b' , \quad (6.5)$$

Time reversal considerations in general show that

$$\Psi_b' = (\Psi_{-b})^* . \quad (6.6)$$

where Ψ_{-b} is a solution whose incident wave propagates in a direction opposite to that associated with Ψ_b .

The transition ("T") matrix that determines both scattering and absorption is given by

$$T_{ba} = (\Phi_b, V \Psi_a) = (\Psi_b', V \Phi_a) , = (\Psi_b', [V - V L V] \Psi_a) \quad (6.7)$$

The alternative forms of T_{ba} , obtained with the help of the field equations (6.4), (6.5) can be combined to yield the normalization insensitive variational principle

$$T_{ba} = \frac{(\Psi_b', V \Psi_a) (\Phi_b, V \Psi_a)}{(\Psi_b', V \Psi_a) - (\Psi_b', V L V \Psi_a)} \quad (6.8)$$

If the ansatz (6.1) is inserted into the variational principle, and the z dependence is left arbitrary, integration over ρ results in a reduced variational principle for the z dependence. This leads to a pair of coupled integral equations for $\langle E_0^{\pm}(z) \rangle$ and $\langle E_1^{\pm}(z) \rangle$ where the $\langle \rangle$ denotes the radial average, Eq. (4.13). These equations are valid both in the "antenna" and "dielectric" limits. In the "dielectric" limit (when $nka < 1/4$), the average fields are expressed as ratios to the incident fields. The ratios $R(z)$ (for $\langle E_0^{\pm}(z) \rangle$) and $R^+(z)$ (for $\langle E_1^{\pm}(z) \rangle$) are found to obey the equations

$$\begin{aligned} R(z) = & \exp(ik C_0 z) + \frac{1}{2} (n^2 - 1) \int K_{00}(z, z') [a(z')^2/2] dz' R(z') \\ & - (i C_0 k/4) (n^2 - 1) \int K_{01}(z, z') [a(z')^3/3] dz' R^+(z') \end{aligned} \quad (6.9)$$

(1950).

⁸B. A. Lippman and J. Schwinger, "Variational Principles for Scattering Processes. I," Phys. Rev. 79, 469 (1950).

$$R^+(z) = \exp(ik C_0 z) + \frac{4i(n^2-1)}{3k C_0 a(z)} \int K_{10}(z, z') \frac{a(z')^2}{2} dz' R(z') + \frac{2}{3} \frac{(n^2-1)}{a(z)} \int K_{11}(z, z') \frac{a(z')^3}{3} dz' R^+(z') \quad (6.10)$$

where the kernels K_{ij} are given by

$$K_{00} = \int_0^{a(z)} f_0(\rho) d\rho (k^2 + \partial^2/\partial z^2) \int_0^{a(z')} G_0(z-z', \rho, \rho') f_0(\rho') d\rho' \quad (6.11)$$

$$K_{01} = \int_0^{a(z)} f_0(\rho) d\rho \left(\frac{\partial}{\partial \rho} + \frac{1}{\rho} \right) \frac{\partial}{\partial z} \int_0^{a(z')} G_1(z-z', \rho, \rho') f_1(\rho') d\rho' \quad (6.12)$$

$$K_{10} = \int_0^{a(z)} f_1(\rho) d\rho \frac{\partial}{\partial \rho} \frac{\partial}{\partial z} \int_0^{a(z')} G_0(z-z', \rho, \rho') f_0(\rho') d\rho' \quad (6.13)$$

$$K_{11} = \int_0^{a(z)} f_1(\rho) d\rho \left[k^2 + \frac{\partial}{\partial \rho} \left(\frac{\partial}{\partial \rho} + \frac{1}{\rho} \right) \right] \int_0^{a(z')} G_1(z-z', \rho, \rho') f_1(\rho') d\rho' \quad (6.14)$$

where $f_m(\rho) = (m+2)\rho^{m+1}/a^{m+2}$, $\rho \leq a$, and $a = a(z)$. In $f(\rho')$, $a(z)$ is replaced by $a(z')$. Results for the antenna limit are available, but not quoted here.

For the special case of a finite uniform cylinder for which $a(z) = a(z') = a$ for $|z| \leq b$ the most important kernel can be simplified (by performing some non-trivial double radial integrals) to get

$$K_{00} \approx (k^2 + \partial^2/\partial z^2) \frac{\exp(ik|z-z'|)}{a} f\left(\frac{|z-z'|}{a}\right), \quad (6.15)$$

where terms of order $(ka)^2$ have been neglected and

$$f(u) = 2 \left[\sqrt{u^2+4} - |u| \right] + 2\sqrt{u^2+4} \left[1 - (2/\pi) E(\kappa) \right], + \frac{8}{3\pi\kappa} \left\{ E(\kappa) + 2 \left[\frac{1}{\kappa^2} - 1 \right] [E(\kappa) - K(\kappa)] \right\}. \quad (6.16)$$

Here

$$\kappa^2 = [1 + (u/2)^2]^{-1},$$

and $E(\kappa)$ and $K(\kappa)$ are the complete elliptic integrals as defined in Jahnke-Emde⁹ A plot of $f(u)$ and $u f(u)$ is given in Fig. 1. The remaining kernels can be calculated although possibly not in explicit,

⁹E. Jahnke and F. Emde, *Tables of Functions*, Dover (1943).

analytical form.

7. FOURIER-BESSEL REPRESENTATION

An alternative procedure to the variational method of the preceding section consists in the introduction of a Fourier-Bessel representation

$$E_m(z, \rho) = \int \exp(i\xi z) J_m(\rho \sqrt{(nk)^2 - \xi^2}) E_m(\xi) d\xi \quad (7.1)$$

This procedure avoids the Taylor expansion in ρ of Eq. (6.2). If one could get an integral equation for $E_m(\xi)$, it would be the equivalent of reducing the problem to an integral equation just over z since ξ is merely the Fourier transform variable. We have not succeeded in this objective because we are unable to invert Eq. (7.1) to obtain $E_m(\xi)$ in terms of $E_m(z, \rho)$. We can, however, obtain a rigorous expression for $F_m(z, \rho)$ defined by Eq. (2.6):

$$F_m(z, \rho) = \int \frac{d\xi}{2\pi} E_m(\xi) \int d\mu e^{i\mu z} \int dz' e^{i(\xi-\mu)z'} \frac{n^2-1}{\beta^2-\alpha^2} U_m(\rho, z'), \quad (7.2)$$

where U is given exactly by

$$U_m(\rho, z') = J_m(\beta\rho) - [1 - C_m(a')] (\beta/\alpha)^m J_m(\alpha\rho), \quad (7.3)$$

$$\alpha = \sqrt{k^2 - \mu^2}, \quad \beta = \sqrt{(nk)^2 - \xi^2}, \quad a' = a(z') \quad (7.4)$$

and

$$C_m(a) = (\beta^2 - \alpha^2) a^2 \hat{C}_m(a), \quad (7.5)$$

$$a^2 \hat{C}_m(a) = \frac{i\pi}{2} \left(\frac{\alpha}{\beta} \right)^m \int_0^a H_m(\alpha\rho) J_m(\beta\rho) \rho d\rho \quad (7.6)$$

For future reference, we note that for small a

$$\hat{C}_m(a) \approx 1/(4m) \quad m \geq 1 \quad (7.7)$$

$$\hat{C}_0(a) \approx \frac{1}{2} g_0 = \frac{1}{2} \left[\ln \frac{2}{\alpha a} + \frac{1}{2} - \gamma + i \frac{\pi}{2} \right]. \quad (7.8)$$

where $\gamma = 0.5772$ is the Euler-Mascheroni constant.

This is as far as we can proceed without approximation. We now wish to exploit the fact that the scatterer is thin. Let us do this by attempting to evaluate the fields in the immediate vicinity of the $\rho=0$ axis, namely $E_0(z, \rho=0)$ and in general $E_m(z, \rho)/\rho^m$ as $\rho \rightarrow 0$. Although we must again make an expansion of the form Eq. (6.2), the coefficients $B_m^{(0)}$, $B_m^{(2)}$ and $B_m^{(4)}$ are now no longer independent,

since they are all determined by the same $E_m(\xi)$ via Eq. (7.1).

This expansion is now an expansion in powers of $\alpha\rho$ and $\beta\rho$. Although α and β depend on the integration variables ξ and μ , we assume that our solution will be sufficiently smooth that

$$\alpha a_{\max} \ll 1 ; \beta a_{\max} \ll 1 . \quad (7.9)$$

This may not be true near the ends of the cylinder, but it should be true as long as $|x \mp b| \gg a$. Thus for long cylinders, the scattering amplitude will be dominated by the smooth part of the field. In this case, it is valid to use the expansion

$$U_m(\rho) / (\beta^2 - \alpha^2) \approx \frac{(\beta\rho/2)^m}{m!} \left[(a')^m \hat{C}_m(a') - \frac{\rho^2}{4(m+1)} + \frac{\beta^2 + \alpha^2}{32(m+1)(m+2)} \rho^4 + \dots \right]. \quad (7.10)$$

The above expansion produces an enormous simplification in Eq. (2.10). The method of simplification can be illustrated by evaluating explicitly one term:

$$I = \left[k^2 + \frac{1}{2} \left(\nabla_\rho^2 - \frac{m^2}{\rho^2} \right) \right] F_m^+(z, \rho) . \quad (7.11)$$

If we use the lemma

$$\left[\nabla_\rho^2 - \frac{m^2}{\rho^2} \right] \rho^s = (s^2 - m^2) \rho^{s-2} , \quad (7.12)$$

then correct to lowest order in ρ

$$\begin{aligned} I &\approx \frac{1}{2}(n^2 - 1) \int \frac{d\xi}{2\pi} E_m^+(\xi) \int d\mu e^{i\mu z} \int dz' e^{i(s-\mu)z'} \times \frac{(\beta/2)^m}{m!} \left\{ -\frac{1}{4(m+1)} [(m+2)^2 - m^2] \rho^m \right\} \\ &= -\frac{1}{2}(n^2 - 1) \int dz' \int \frac{d\mu}{2\pi} e^{i\mu(z-z')} \int d\xi \frac{(\beta\rho/2)^m}{m!} e^{i\xi z'} E_m^+(\xi) . \end{aligned} \quad (7.13)$$

After restoration of the Bessel function the use of Eq. (7.1) results in the simple form

$$I = -\frac{1}{2} (n^2 - 1) E_m^+(z, \rho) . \quad (7.14)$$

which describes depolarization with a depolarization factor

$$L_m = \frac{1}{2} . \quad (7.15)$$

Similar procedures, with the addition of the replacements

$$\xi = -i \partial / \partial z' , \quad \mu = -i \partial / \partial z , \quad (7.16)$$

permit the remaining terms in Eq. (2.10) to be simplified with the result

$$\begin{aligned} E_m^+(z, \rho) = & -e^{ikC_0 z} C_0 (ikS_0 \rho / 2)^m / m! - \frac{1}{2} (n^2 - 1) E_m^+(z, \rho) - \frac{1}{2} (n^2 - 1) \frac{\rho}{m} \frac{\partial E_{m-1}^+(z, \rho)}{\partial z} \\ & + \frac{(n^2 - 1) \rho^2}{8m(m-1)} \left[2 \frac{\partial^2}{\partial z^2} + (n^2 + 1) k^2 \right] E_{m-2}^+(z, \rho) \end{aligned} \quad (7.17)$$

Equation (2.9) can be simplified in a similar manner to become:

$$\begin{aligned} E_m^z(z, \rho) = & S_0 \frac{(ik\rho S_0 / 2)^m}{m!} e^{ikC_0 z} + \frac{(n^2 - 1)}{4m} \left[k^2 + \frac{\partial^2}{\partial z^2} \right] \left[a^2(z) E_m^z(z, \rho) \right] \\ & - \frac{(n^2 - 1)}{4m} \rho \frac{\partial E_{m-1}^-(z, \rho)}{\partial z} + \frac{(n^2 - 1)}{4\rho} \frac{\partial}{\partial z} \left[a^2(z) E_{m+1}^+(z, \rho) \right] . \end{aligned} \quad (7.18)$$

Our equations are understood to be correct only to the lowest order in ρ . In effect, we have obtained a differential equation for $B_m^{(0)}(z)$ that is uncoupled to $B_m^{(2)}(z)$ and $B_m^{(4)}(z)$ of Eq. (6.2). The information contained in the latter has been correctly incorporated into our problem by the use of the Fourier-Bessel representation. By assuming only a ρ^m dependence for $E_m(z, \rho)$ in Eqs. (7.17), (7.18) we will obtain our desired one-dimensional equation. It is convenient to express our results in terms of ratios $R_m(z)$ to the incident field defined by

$$E_m^+(z, \rho) = E_m^{\text{inc}+}(z=0, \rho) R_m^+(z) \quad (7.19)$$

$$E_m^z(z, \rho) = E_m^{\text{inc}z}(z=0, \rho) R_m^z(z) , \quad (7.20)$$

where only the dominant ρ^m dependence is understood. The resulting equations are

$$\left[1 + \frac{1}{2} (n^2 - 1) \right] R_m^+(z) = e^{ikC_0 z} + \frac{n^2 - 1}{ikC_0} \frac{\partial}{\partial z} R_{m-1}^+(z) - \frac{1}{2} (n^2 - 1) \frac{(n^2 + 1) k^2 + 2 \frac{\partial^2}{\partial z^2}}{k^2 S_0^2} R_{m-2}^+(z) \quad (7.21)$$

$$R_m^z(z) = e^{ikC_0 z} + (n^2 - 1) \left(k^2 + \frac{\partial^2}{\partial z^2} \right) \frac{C_0}{2 S_0^2} a^2(z) R_m^z(z) + \frac{C_0^2}{ikC_0} \frac{(n^2 - 1)}{2 S_0^2} \frac{\partial}{\partial z} R_{m-1}^z(z)$$

$$+ \frac{(k C_0)^2}{8(m+1)} \frac{\partial}{\partial z} [a^2(z) R_{m+1}^+(z)] . \quad (7.22)$$

For $m \geq 1$, the last term is of order $(ka)^2$ and can be omitted.

We are primarily concerned with the coupling between R_{δ}^{\dagger} and R_{\dagger}^{\dagger} . For $m = 1$, the last term in Eq. (7.17) is incorrect since it would involve dividing by zero. However, this arises because the index $m = 2$ has gone negative. For negative indices, we need not evaluate this term at all, because the symmetry relations

$$E_{-m}(z, \rho) = E_m(z, \rho) , \quad F_{-m}(z, \rho) = F_m(z, \rho) , \quad (7.23)$$

permit the last term in Eq. (2.10) to be rewritten for $m = 1$ as

$$\frac{1}{2} \frac{\partial}{\partial \rho} \left(\frac{\partial}{\partial \rho} + \frac{1}{\rho} \right) F_{-1}^-(z, \rho) = \frac{1}{2} \left(\nabla_{\rho}^2 - \frac{1}{\rho^2} \right) F_{\dagger}^+(z, \rho) . \quad (7.24)$$

Thus the last term in Eq. (2.10) can be omitted and the second term doubled. The final result is

$$n^2 R_{\dagger}^+(z) = e^{ik C_0 z} + \frac{n^2 - 1}{ik C_0} \frac{\partial R_{\delta}^{\dagger}(z)}{\partial z} . \quad (7.25)$$

For $m = 0$ in Eq. (2.10), we learn similarly that the third term is identical to the last. We therefore omit the third term and double the last. Thus all negative subscripts have been avoided with the result

$$R_{\delta}^{\dagger}(z) = \exp(ik C_0 z) + (n^2 - 1)(k^2 + \partial^2 / \partial z^2) \hat{C}_0 a^2(z) R_{\delta}^{\dagger}(z) + \frac{(k C_0)^2 (n^2 - 1)}{4 ik C_0} \frac{\partial}{\partial z} [a^2(z) R_{\dagger}^+(z)] \quad (7.26)$$

If we solve Eq. (7.25) for R_{\dagger}^+ , and omit the small first term, the result may be inserted into Eq. (7.26). It is also permissible to replace $(n^2 - 1)^2 / n^2$ by $(n^2 - 1)$ because the difference is of order unity and it multiplies terms of order $a^2 \partial^2 / \partial z^2 \sim (ka)^2$. Thus we arrive at

$$R_{\delta}^{\dagger}(z) = \exp(ik C_0 z) + (n^2 - 1)(k^2 + \partial^2 / \partial z^2) [\hat{C}_0 a^2(z) R_{\delta}^{\dagger}(z)] - 1/4 (n^2 - 1) \partial / \partial z [a^2(z) \partial R_{\delta}^{\dagger}(z) / \partial z] \quad (7.27)$$

A partial test of the accuracy of our algebra was obtained by considering the infinite cylinder case $a(z) = a$ and comparing with the results of Wait⁵⁻⁷ in the small ka limit. This was successful for all R_m^z and R_m^{\dagger} .

There is one difficulty that was concealed in the above derivation. The quantity \hat{C}_m can be replaced by the number $1/(4m)$ for all $m \neq 0$. For $m = 0$, it remains an operator

$$\hat{C}_0(\mu, \xi) \rightarrow \hat{C}_0 \left[-i \frac{\partial}{\partial z} - i \frac{\partial}{\partial z'} \right]. \quad (7.28)$$

However, there is no way to describe simply the action of an operator such as

$$\ln[(k^2 - \mu^2) a^2] = \ln[(k^2 + \frac{\partial^2}{\partial z^2}) a^2], \quad (7.29)$$

which arises in Eq. (7.8) other than by transferring to wave-vector space and back. If this is done, we arrive at the equation

$$\begin{aligned} R_\delta(z) = \exp(ik C_0 z) + \frac{1}{2} (n^2 - 1) (k^2 + \partial^2 / \partial z^2) \int dz' G_0(z - z', \rho = 0) \frac{a(z')^2}{2} R_\delta(z') \\ - \frac{1}{4} (n^2 - 1) \partial / \partial z [a^2(z) \partial R_\delta(z) / \partial z] \end{aligned} \quad (7.30)$$

where

$$\begin{aligned} [a(z')^2 / 2] G_0(z - z', 0) = \int_0^{a'} \frac{\exp[ik \sqrt{(z - z')^2 + \rho'^2}]}{\sqrt{(z - z')^2 + (\rho')^2}} \rho' d\rho' \\ = \frac{2}{ik} \left[\exp(ik \sqrt{(z - z')^2 + a'^2}) - \exp(ik |z - z'|) \right] \end{aligned} \quad (7.31)$$

For comparison with $f(u)$ in the double averaged Green's function of Eqs. (6.15), we can rewrite Eq. (7.31) in the same form as (6.15):

$$(k^2 + \partial^2 / \partial z^2) \frac{\exp(ik |z - z'|)}{a} g \left(\frac{|z - z'|}{a} \right), \quad (7.32)$$

where

$$g(u) = \frac{2}{ika} \left\{ \exp \left[ik \left(\sqrt{(z - z')^2 + a^2} - |z - z'| \right) \right] - 1 \right\} \approx 2 \left[\sqrt{u^2 + 1} - |u| \right]. \quad (7.33)$$

For large u

$$g(u) \rightarrow \frac{1}{u} - \frac{1}{4} \frac{1}{u^3}, \quad (7.34)$$

which is similar but not identical to the double average result

$$f(u) \rightarrow \frac{1}{u} - \frac{1}{2} \frac{1}{u^3}. \quad (7.35)$$

Another difference can be seen at $u=0$ (or $|z - z'|=0$):

$$g(0) = 2 ; f(0) = \frac{16}{3\pi} = 1.70 . \quad (7.36)$$

The functions $f(u)$ and $g(u)$ are plotted in Fig. 1.

The difference between $f(u)$ and $g(u)$ should not be regarded as a discrepancy. Equation (7.30) is for the on axis ($\rho=0$) electric field whereas Eqs. (6.9), (6.10) are equations for the radially averaged field.

8. COMPARISON WITH PREVIOUS WORK

The work that is closest to ours is that of Uzunoglu, Alexopoulos and Fikioris (UAF).⁴ They assumed that by restricting the problem to normal incidence, they could confine the calculations to the $m=0$ terms. This assumption seems natural, since at normal incidence $C_0 \rightarrow 0$. Thus it would appear that the last term in Eq. (7.26) could be discarded, breaking the coupling between R_0^- and R_1^+ . However, R_1^+ contains a term of order $1/C_0$ - see Eq. (7.25). Thus, even at normal incidence, the $m=1$ mode feeds back and modifies the $m=0$ results.

The UAF procedure deals with the average field, rather than the on-axis field, so that their analysis should, more appropriately, be compared with Section 7 of this paper. In effect, they set $K_{01} = 0$ and therefore only need K_{00} . They do not, however, obtain a closed form for K_{00} that can be compared with Eq. (6.15). This is because in obtaining K_{00} they do not succeed in taking advantage of the smallness of ka .

UAF seek a solution in the form of a Fourier series in z . This is a procedure that we shall also exploit. Since they truncate their Fourier series at components μ such that $\mu a < 1$, the approximations made in Section 7 of this paper become valid. Numerical approaches to the solution of our integral equation Eq. (7.30), or the variational set of coupled equations (6.11)-(6.14) will be discussed in a future publication.

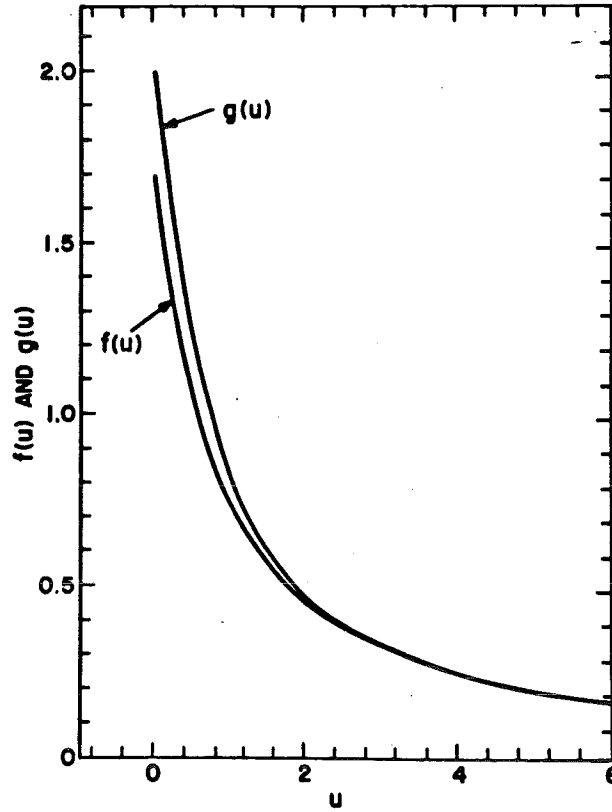


FIG. 1. The double averaged Green's function of Eqs. (6.11), (6.15), (6.16) is

$$\left(\frac{2}{a^2}\right)^2 \int_0^a \int_0^a G_0(z-z', \rho, \rho') \rho d\rho \rho' d\rho' \approx \frac{\exp(ik|z-z'|)}{a} f\left(\frac{|z-z'|}{a}\right)$$

where $f(u)$ is plotted above. The single averaged on-axis Green's function of Eq. (7.33)

$$\frac{2}{a^2} \int_0^a G_0(z-z', \rho=0, \rho') \rho' d\rho' \approx \frac{\exp(ik|z-z'|)}{a} g\left(\frac{|z-z'|}{a}\right)$$

is given by $g(u) = 2\left[\sqrt{u^2+1} - |u|\right]$ and plotted above for comparison with $f(u)$.

EXTINCTION OF ELECTROMAGNETIC
RADIATION BY FINE CONDUCTING FIBERS

D. H. Holze, C. D. Capps and G. M. Hess
The Boeing Aerospace Company
P.O. Box 3999, Seattle, WA. 98124

ABSTRACT

Results of a small IR and D study of IR extinction by small metal fibers are reported. The analysis is easily extended to other electromagnetic bands. Large extinctions (10's to 100's of m^2/gm) are predicted if the rigorous Rayleigh conditions can be met. A separate analysis suggests that good extinctions can be obtained if only the fiber diameter meets the Rayleigh condition.

INTRODUCTION

Rayleigh studied the scattering of light from small ellipsoidal particles.¹ For the theory to hold rigorously, the wavelength both inside and outside the particle must be large compared with any particle dimension. The present study analyzes the extinction produced by prolate spheroidal or fiber-like particles. (The theory also holds for oblate spheroidal or flake-like particles, but these are reserved for a separate analysis. They may offer the advantage of simple dispersal.)

The Rayleigh extinction, γ , for fibers is given by

$$\gamma = \frac{4\pi}{3\lambda\rho} \frac{nk}{(L(n^2 - k^2) + 1 - L)^2 + (2nkL)^2} \quad (1)$$

where n and k are the real and imaginary parts of the complex refractive index $m = n - ik$, and L is the depolarization factor

$$L = \frac{1 - e^2}{e^2} \left(\frac{1}{2e} \ln \left(\frac{1 + e}{1 - e} \right) - 1 \right) \quad (2)$$

where $e^2 = 1 - 1/A^2$ and A is the fiber aspect ratio. If the wavelength, λ , is given in micrometers and the fiber density, ρ , is given in gm/cm^3 then the extinction will be in m^2/gm .

The depolarization factor is quite small even for rather small aspect ratios. For example $L = 0.02$ for $A = 10$. Note that for very small L , Eq. (1) reduces to

$$\gamma = \frac{4\pi nk}{3\lambda\rho} \quad (3)$$

If electrical properties, viz., the dielectric constant ϵ and conductivity, σ , are available instead of n and k (e.g., in the far infrared or radar wavelengths) then the complex refractive index is

$$m = \left(\epsilon - \frac{1}{\omega} \right)^{1/2} \quad (4)$$

from Maxwell's equations. (Gaussian units are used in this paper.) Here ω is the angular frequency of the radiation. Figure 1 compares n and k values for copper from the AIP handbook² with those calculated using Eq. (4). (An electron relaxation time of 8×10^{-15} sec was used for this fit.) Note that n and k are nearly equal at wavelengths of 1 mm and above.

RAYLEIGH EXTINCTION CALCULATIONS

The calculations below show that it is possible to achieve high extinctions in the IR with fibers of rather low aspect ratio. Low aspect ratio is of crucial importance in achieving high chaff cloud extinction. For example in the case of conventional 8-12 GHz half-wavelength chaff with an aspect ratio of about 600, some chaff experts believe the chaff cloud radar cross section is its geometric area. This is far less than the calculated cross section obtained by multiplying the individual fiber cross section and the number of fibers. "Birdnesting" is believed to be a major contributor to this reduced cross section.

Figure 2 gives extinction versus IR wavelength for copper fibers of various aspect ratios. Extremely high extinctions are possible for fibers with reasonable aspect ratios. (Extinctions of 1 to 5 m^2/gm are generally felt to be quite good.) Note that if fiber aspect ratios were uniformly spread from about 10 to 100, high extinction could be achieved across the wavelength band of interest. Also, note that for $A = 1000$ the extinction peak occurs far above the band of interest but the extinction from 1 to 10 μm is still good to excellent. (The infinite fiber case will be discussed below.)

Figure 3 shows the conductivity needed to give peak extinction as a function of wavelength and aspect ratio. (Conductivities in the more familiar units of mhos/meter can be found by dividing the conductivities in Figure 3 by 9×10^9 . For example, the conductivity of copper is $5.3 \times 10^{17}/sec$ or 5.9×10^7 mho/m.) The conductivities of several metals have been superimposed. The extinction spikes in Figure 2 correspond with the intersections of the aspect ratio curves with the copper conductivity trace in Figure 3. (The inexact correspondences result from the imperfect fits in Figure 1.) Two important conclusions can be drawn from Figure 3:

1. Aspect ratios above 100 are not useful in the 1 to 10 μm IR band since conductivities above those of copper or silver are not practical for an operational chaff.
2. Conductivities below about $10^{15}/sec$ are not useful since the minimum achievable aspect ratio is $A = 1$ (for a sphere). Note that metals with low conductivities, such as iron or titanium, allow small aspect ratios to be achieved.

Figure 4 shows extinction versus aspect ratio for several promising elements (strictly from an extinction standpoint) at a midband wavelength. Sodium and potassium are obviously unsuitable for chaff use while some other metals (at Rayleigh sizes) are apt to be pyrophoric. Since Ref. 2 contains refractive indices only on elements, calculations were not carried out on any alloys. It is known, for example, that good extinctions have been obtained using flakes of several types of brass.

Figure 4 strongly suggests that metals could be found which would give high extinctions with reasonable aspect ratios. In fact, it was found after calculations were made at other wavelengths that beryllium fibers with aspect ratios ranging from 10 to 25 give extinctions above 10 across the 1 to 10 μm band.

Now consider the Rayleigh condition. This is discussed for spheres in Section 3.9.1 in Ref. 1. The rough guide discussed on page 87 is that the diameter should be no greater than 0.1λ where λ is measured in the medium. Here this criterion will be applied to the fiber length. Thus the maximum fiber lengths for $\lambda = 1$ and $10 \mu\text{m}$ are 0.1 and $1 \mu\text{m}$.

If the diameter of a fiber is comparable to the electron mean free path (MFP) in the metal, then Dingle³ showed that the conductivity of the metal dropped below that of the bulk metal. Consider the specific case of copper fibers with an aspect ratio of 10. For $\lambda = 1$ and $10 \mu\text{m}$, the maximum diameters are 0.01 and $0.1 \mu\text{m}$. The MFP for copper is $0.016 \mu\text{m}$. (It ranges from about 0.01 to $0.02 \mu\text{m}$ for the metals listed in Figure 4.) The Dingle correction must be made in the shorter wavelength region of the IR band.

Consider the $1 \mu\text{m}$ wavelength case. If the ratio of the fiber diameter to the wavelength is less than 0.5, then the corrected conductivity is just

$$\sigma = \frac{\text{DIAMETER}}{\lambda} \sigma_{\text{BULK}} \quad (5)$$

which gives $\sigma = 5.3 \times 10^{15}/\text{sec}$. From Figure 3 this conductivity is too low to give good Rayleigh extinction.

Since aspect ratios greater than ten are needed, this reduction in conductivity is expected to crop up for any choice of metal. The next section suggests that the stringent Rayleigh conditions might possibly be relaxed.

INFINITE FIBER EXTINCTION

The general problem of scattering from an infinite cylinder is solved in Chapter 6 of Ref. 1. That analysis was applied to the special case of a fiber with Rayleigh diameter. The result was Eq. (3), which is intriguing since the infinite length is obviously not Rayleigh. For copper fibers, this means that one can at least achieve the extinctions given for $A = 1000$ in Figure 2. One hopes that the infinite fiber results can be applied to much shorter fibers so the more favorable extinctions can be obtained.

Consider fibers with the largest allowable Rayleigh diameter of interest, viz., 0.1λ . For the small aspect ratios of most interest these fibers display resonant behavior. For example, for $A = 5$ the fiber length is $\lambda/2$ -- the familiar dipole chaff deployed since the middle of World War II. For $A = 10$, the fibers are full-wave dipoles, etc. A nonrigorous argument was presented in a previous study⁴ to the effect that, if a cloud of such fibers had a range of lengths over the resonant region, then one could hope for good extinction. Clearly resonant region analyses and tests are called for.

RECOMMENDATIONS

1. Extend the calculations to oblate spheroids ("disks"). Other workers have stated that these are effective in the IR. They are undoubtedly simpler to dispense.
2. Obtain and test fibers which meet the Rayleigh condition in diameter but not in length.
3. Perform a literature search to determine whether extinctions can be calculated for such particles even if only in special cases. If so, compare results with test data.
4. Optimize material choice and particle aspect ratios.

REFERENCES

1. Kerker, M., The Scattering of Light, Academic Press, NY, 1969.
2. AIP Handbook, edited by D. E. Gray, McGraw Hill, NY, 1963.
3. Dingle, R. B., "The Electrical Conductivity of Thin Wires," Proc. Roy. Soc. A, 201, 545, 1950.
4. Capps, C. D., Holze, D. H., "Extinction Chaff," Boeing Document D180-27297-1, December, 1982.

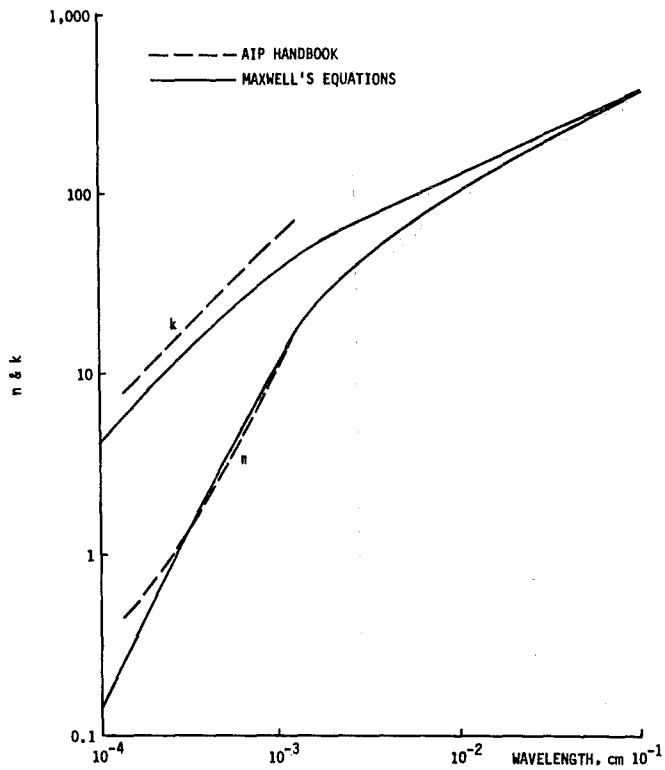


FIGURE 1. REFRACTIVE INDICES FOR COPPER

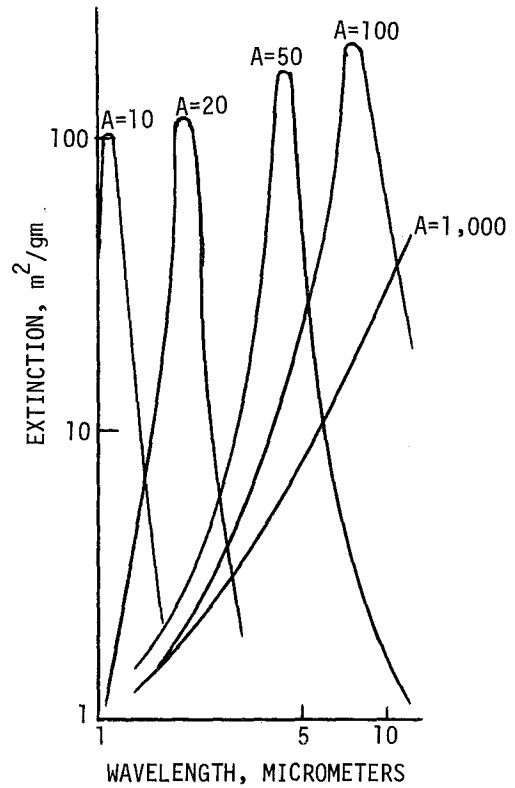


FIGURE 2. PEAK EXTINCTIONS FOR COPPER

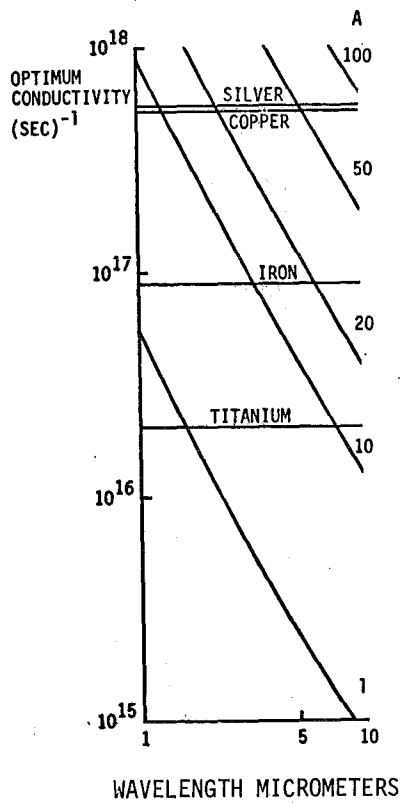


FIGURE 3. CONDUCTIVITIES NEEDED TO GIVE PEAK EXTINCTIONS

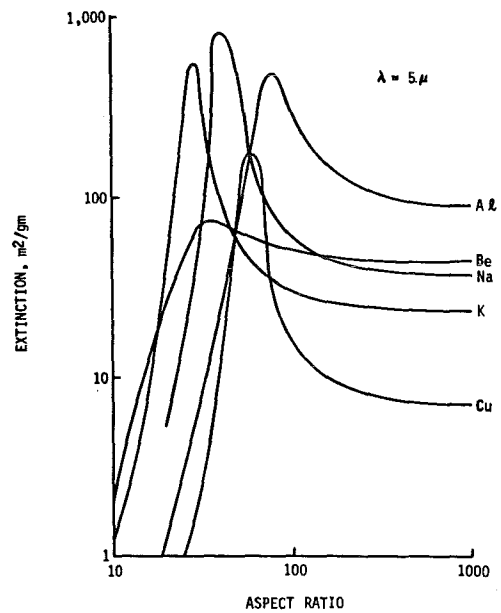


FIGURE 4. PEAK EXTINCTIONS FOR OTHER METALS

BLANK

ELECTROMAGNETIC THEORY OF SCATTERING AND
 ABSORPTION FROM FINITE ELONGATED OBJECTS

Jeanne C. Pedersen
 Norman E. Pedersen
 Peter C. Waterman

Panametrics, Inc.
 221 Crescent Street
 Waltham, MA 02254

The purpose of this paper is to present a summary of work which we have done and which is presently underway with the Chemical Systems Laboratory in the area of electromagnetic cross sections of highly elongated conductive particles.

THEORY

The present theory is based upon a variational procedure first set forth by Tai for perfectly conducting wires ¹ and later extended to the case of finite conductivity by Cassedy and Fainberg who, however, considered only broadside incidence.² In the present theory, scattering, absorption, extinction, and radar cross sections are calculated for arbitrary angles of incidence. The results can then be averaged over all angles of incidence to obtain results for a cloud of randomly oriented particles.

Consider a plane electromagnetic wave incident upon a cylindrical wire of finite conductivity at arbitrary angle of incidence, θ_i , with the axis of the cylinder and arbitrary polarization angle, ψ ,

Assuming the wire is sufficiently thin for the current to be uniform around the axis at any position along the wire, one may consider the current as a current filament $I(z)$ along the axis. As the wire is assumed to be thin, only the component of the electric field parallel to the axis will stimulate a response, and the integral equation for the boundary condition at the cylinder surface may be written

$$E_0 \sin \theta_i \cos \psi e^{jkz} \cos \theta_i = I(z)Z + \frac{1}{2\pi} \int_0^{2\pi} \frac{j\eta k}{4\pi} \int_{-l}^l I(z') \left(1 + \frac{\partial^2}{k^2 \partial z'^2} \right) \frac{e^{-jkR}}{R} dz' d\theta' \quad (1)$$

Here, Z is the skin impedance per unit length of the cylinder and is given by³

$$Z = \frac{g I_0 (ga)}{2\pi a (\sigma + j\omega\epsilon) I_1 (ga)} \quad (2)$$

with

$$g = \omega^2 [(\mu_0\epsilon_0 \cos^2 \theta_i - \mu\epsilon) + \frac{j\mu\sigma}{\omega}]$$

$\eta = \sqrt{\mu_0/\epsilon_0}$ is the characteristic impedance of free space, and

$$R = \sqrt{(z-z')^2 + 4a^2 \sin^2 \left(\frac{\theta - \theta'}{2}\right)}$$

The I_0 and I_1 functions are modified Bessel functions of complex argument.

We have chosen a current function which is a summation of terms which are harmonics of x and qx :

$$I(z) = I_0 \sum_{n=1}^{\infty} [A_n f_{cn}(z) + B_n f_{sn}(z)] \quad (3)$$

$$f_{cn}(z) = \cos nkz \cos nqx - \cos nx \cos nqkz \quad (4)$$

and

$$f_{sn}(z) = \sin nkz \sin nqx - \sin nx \sin nqkz \quad (5)$$

where $q = \cos \theta_i$ and $x = kl$.

Upon substitution of equation (3) into equation (1) and multiplying by $\int_{-l}^l f_{cm}(z) dz$ and $\int_{-l}^l f_{sm}(z) dz$, one arrives at two sets of linear equations for the coefficients A_n and B_n :

$$\left(\frac{E_0 \cos \psi}{I_0}\right) g_{cm} = \frac{jnk}{4\pi} \sum_{n=1}^N A_n (\gamma_{cnm} - \lambda_{cnm}) \quad (6)$$

and

$$\left(\frac{E_0 \cos \psi}{I_0}\right) g_{sm} = \frac{jnk}{4\pi} \sum_{n=1}^N B_n (\gamma_{snm} - \lambda_{snm}) \quad (7)$$

where

$$\gamma_{cnm} = \frac{k}{2\pi} \int_0^{2\pi} d\theta \int_{-l}^l \int_{-l}^l f_{cm}(z) f_{cn}(z') \left(1 + \frac{1}{k^2} \frac{\partial^2}{\partial z'^2}\right) \frac{e^{-jkR}}{R} dz' dz \quad (8)$$

$$\gamma_{snm} = \frac{k}{2\pi} \int_0^{2\pi} d\theta \int_{-l}^l \int_{-l}^l f_{sm}(z) f_{sn}(z') \left(1 + \frac{1}{k^2} \frac{\partial^2}{\partial z'^2}\right) \frac{e^{-jkR}}{R} dz' dz \quad (9)$$

$$B_{cnm} = \frac{4\pi jZ}{\eta} \int_{-l}^l f_{cn}(z) f_{cm}(z) dz \quad (10)$$

$$B_{snm} = \frac{4\pi jZ}{\eta} \int_{-l}^l f_{sn}(z) f_{sm}(z) dz \quad (11)$$

$$g_{cm} = k \sin \theta_i \int_{-l}^l f_{cm}(z) e^{jkz \cos \theta_i} dz \quad (12)$$

$$g_{sm} = k \sin \theta_i \int_{-l}^l f_{sm}(z) e^{jkz \cos \theta_i} dz \quad (13)$$

Since A_n , B_n , g_{cm} , g_{sm} , γ_{cnm} , γ_{snm} , λ_{cnm} and λ_{snm} are complex, equations (6) and (7) each results in $2N$ linear equations which can be solved by matrix inversion for the real and imaginary parts of the A_n 's and B_n 's. At the present, this programming is underway and we are looking for convergence of the coefficients as the number of terms in the series is increased. This convergence should indicate the number of terms necessary to specify the scattering of a cylinder of a given kl .

Because of the large task involved in programming for the coefficients by the matrix inversion described above, a simpler approach was first taken to examine the premise of the theory. A single value for n was chosen as the integer closest to kl . When only one term in $I(z)$ is chosen a variational technique can be used to determine A_n and B_n . In fact, A_n can be defined to be unity and only B_n remains to be determined.

A stationary homogeneous functional expression can be constructed for the current in terms of the backscattered amplitude S giving

$$\frac{1}{S} = \frac{(\gamma_{cn} - \lambda_{cn}) + B_n^2 (\gamma_{sn} - \lambda_{sn})}{(g_{cn} + B_n g_{sn})^2} \quad (14)$$

Here the subscript nm has been collapsed to a single n .

By the variational technique, the constant B_n may now be evaluated by setting

$$\frac{\partial}{\partial B_n} \left(\frac{1}{S} \right) = 0, \quad (15)$$

yielding

$$B_n = \frac{g_{sn} (\gamma_{cn} - \lambda_{cn})}{g_{cn} (\gamma_{sn} - \lambda_{sn})}. \quad (16)$$

From the definition of backscattered amplitude one has

$$4\pi E_0 S \cos \psi = j\eta k^2 \sin \theta_i \int_{-l}^l I(z) e^{jkz \cos \theta_i} dz \quad (17)$$

and it now follows that

$$\frac{I_0}{E_0} = \frac{4\pi \cos \psi}{j\eta k} \left(\frac{g_{cn}}{\gamma_{cn} - \lambda_{cn}} \right). \quad (18)$$

The general far-field scattering amplitude $S(\theta, \theta_i)$ is defined by the equations.

$$\frac{E_{S\theta}(\theta, \theta_i)}{E_0 \cos \psi} = \frac{e^{-jkR}}{kR} S(\theta, \theta_i) \quad (19)$$

$$S(\theta, \theta_i) = \frac{jk^2 \eta \sin \theta}{4\pi E_0 \cos \psi} \int_{-l}^l I(z) e^{jkz \cos \theta} dz \quad (20)$$

where $E_{S\theta}$ is the component of the scattered E field polarized in the θ direction. Upon substitution of the previous results the scattered amplitude becomes, after integration,

$$\begin{aligned} S(\theta, \theta_i) = & 2 \sqrt{1 - p^2} \left\{ \left(\frac{g_{cn}}{\gamma_{cn} - \lambda_{cn}} \right) \left[\frac{\cos nqkl}{(n^2 - p^2)} \right. \right. \\ & \cdot (n \sin nkl \cos pkl - p \cos nkl \sin pkl) - \frac{\cos nkl}{(n^2 q^2 - p^2)} \\ & \left. \left. \cdot (nq \sin nqkl \cos pkl - p \cos nqkl \sin pkl) \right] \right. \\ & + j \left(\frac{g_{sn}}{\gamma_{sn} - \lambda_{sn}} \right) \left[\frac{\sin nqkl}{(n^2 - p^2)} (p \sin nkl \cos pkl - n \cos nkl \sin pkl) \right. \\ & \left. - \frac{\sin nkl}{(n^2 q^2 - p^2)} (p \sin nqkl \cos pkl - nq \cos nqkl \sin pkl) \right] \left. \right\} \quad (21) \end{aligned}$$

where

$$\begin{aligned} q &= \cos \theta_i \\ p &= \cos \theta. \end{aligned}$$

This is the basic equation from which the various cross sections are computed.

By definition, the differential scattering cross section is given as

$$\begin{aligned}\sigma(\theta, \theta_i) &= R_o^2 \left| \frac{E_{S\theta}}{E_o} \right|^2 \\ &= \frac{\cos^2 \psi}{k^2} \left| S(\theta, \theta_i) \right|^2\end{aligned}\quad (22)$$

The total scattering cross section is then

$$\sigma_S = \frac{2\pi \cos^2 \psi}{k^2} \int_0^\pi \left| S(\theta, \theta_i) \right|^2 \sin \theta \, d\theta. \quad (23)$$

The extinction cross section is defined by the well-known forward amplitude theorem as

$$\begin{aligned}\sigma_e &= \frac{4\pi}{k} \cos^2 \psi \operatorname{Im} S(\pi - \theta_i, \theta_i) \\ &= \frac{4\pi}{k^2} \cos^2 \psi \operatorname{Im} \left\{ \frac{g_{cn}^2}{\gamma_{cn} - \lambda_{cn}} - \frac{g_{sn}^2}{\gamma_{sn} - \lambda_{sn}} \right\}.\end{aligned}\quad (24)$$

The absorption cross section is just the rms power absorbed in the scatterer divided by the rms intensity of the incident beam. The rms power absorbed in the wire is given by

$$P_a = \operatorname{Re}(Z) \int_{-l}^l \left| I(z) \right|^2 dz$$

and the rms intensity of the θ component of the incident beam is

$$I_\theta = \frac{E_o^2}{2\eta} \cos^2 \psi$$

so that the absorption cross section, after substitution of the expression for current, becomes,

$$\begin{aligned}\sigma_a &= \frac{4\pi}{k} \frac{\operatorname{Re}(Z)}{|Z|} \cos^2 \psi \left\{ \left| \frac{g_{cn}}{\gamma_{cn} - \lambda_{cn}} \right|^2 \times \left| \lambda_{cn} \right| \right. \\ &\quad \left. + \left| \frac{g_{sn}}{\gamma_{sn} - \lambda_{sn}} \right|^2 \times \left| \lambda_{sn} \right| \right\}\end{aligned}\quad (25)$$

Finally, the radar cross section is defined to be

$$\begin{aligned}
\sigma_{\text{RCS}} &= 4\pi \sigma(\theta_i, \theta_i) \\
&= \frac{4\pi}{k^2} \cos^4 \psi \left| S(\theta_i, \theta_i) \right|^2 \\
&= \frac{4}{k^2} \cos^4 \psi \left| \frac{\epsilon_{cn}^2}{(\gamma_{cn} - \lambda_{cn})} + \frac{\epsilon_{sn}^2}{(\gamma_{sn} - \lambda_{sn})} \right|^2.
\end{aligned} \tag{26}$$

NUMERICAL RESULTS

Figures 1-8 show experimental data made by Webb in the microwave region, for radar cross section in square wavelengths as function of angle of incidence. The experiments were carried out at 9.3 GHz on 1 mil tungsten wire, having a conductivity of 1.81×10^7 mho/m. The points are the experimental values and the solid lines our theoretical results using only the 1st term in the series for the trial current function. The theory shows excellent agreement with the experimental results from $2l/\lambda = 0.437$ to $2l/\lambda = 1.051$. In Fig. 7 the theoretical peaks (not shown) all fall slightly above unity.

Figure 9 plots theoretical results for extinction, scattering and absorption cross sections normalized to particle cylinder volume over a range of wavelengths. A single n was chosen for each point as mentioned previously. The graph also includes the 1965 Rayleigh scattering theory results in the appropriate regions.

Figure 10 shows a theoretical plot of extinction efficiency as a function of wavelength and Figure 11 plots the ratio $\sigma_{\text{abs}}/\sigma_{\text{ext}}$, $\sigma_{\text{sc}}/\sigma_{\text{ext}}$ and the asymmetry as a function of wavelength. In Figures 9-11, the scattering cross sections have been integrated with respect to the scattering angle and the incident angle.

Plots have also been made of differential scattering cross section as a function of the angle of incidence, but we have not been able to find sufficient experimental data for adequate comparison with the theory.

REFERENCES

1. Tai, C.-T., Electromagnetic Backscattering from Cylindrical Wires, J. Appl. Phys., Vol. 23, pp. 909-916 (August 1952).
2. Cassedy, E. S., and Fainberg, J., Electromagnetic Cross Sections of Cylinders of Finite Conductivity, The Johns Hopkins Laboratory Technical Report No. AF-81, August 1960.
3. Ramo, S., and Whinnery, J. R., Fields and Waves in Modern Radio, John Wiley and Sons, Inc., New York, NY 1949.
4. Weber, J. R., Radar Backscatter Measurements for Tungsten and Copper Dipoles, Lockheed-Georgia Company Report No. ER-6948, June 1964.
5. Pedersen, J., and Pedersen, N., Electromagnetic Theory of Scattering and Absorption from Finite Elongated Objects, Proc. of 1979 C S L Scientific Conference on Observation and Aerosol Research, December 1980.

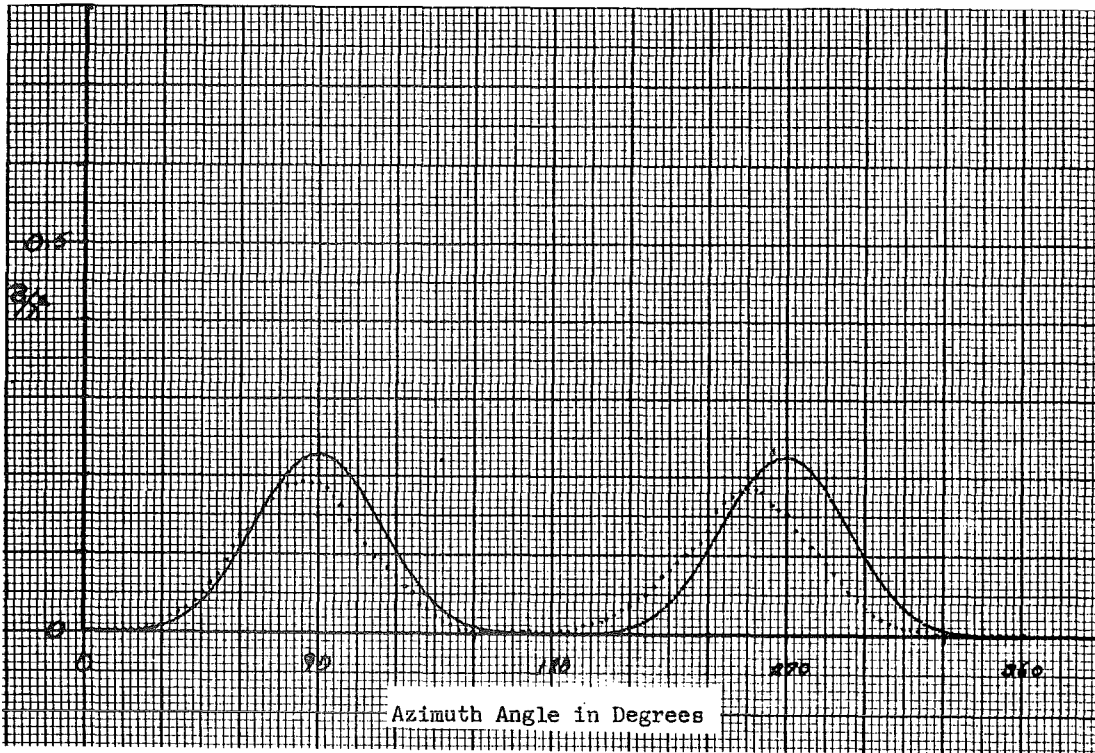


FIGURE 1. RADAR CROSS SECTION. Tungsten wire experimental (points) and theoretical (solid lines); $2l/\lambda = 0.437$, $2l/d = 550$.

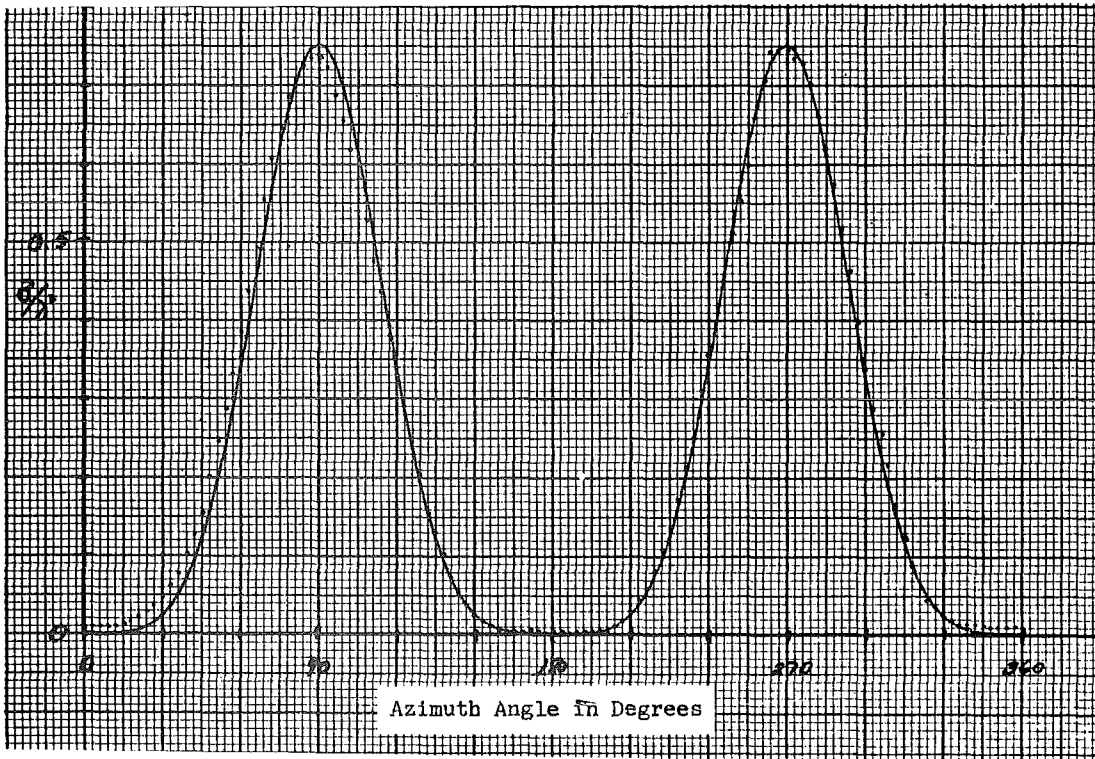


FIGURE 2. RADAR CROSS SECTION. Tungsten wire experimental (points) and theoretical (solid lines); $2l/\lambda = 0.480$, $2l/d = 605$.

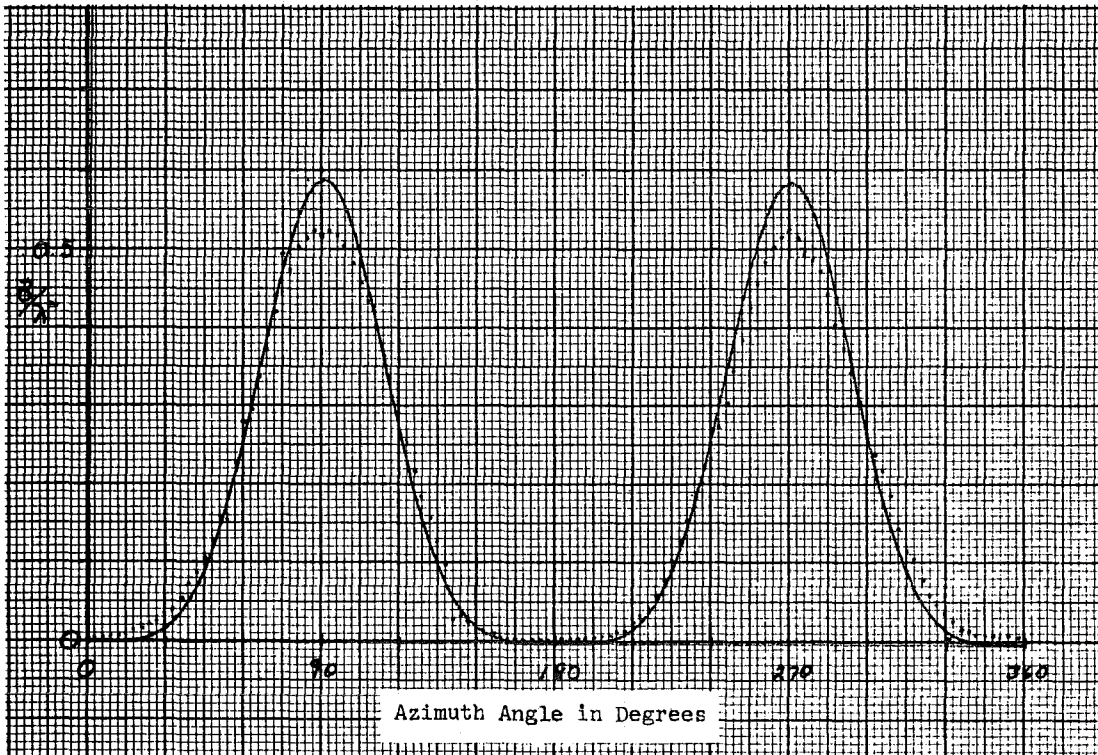


FIGURE 3. RADAR CROSS SECTION. Tungsten wire experimental (points) and theoretical (solid lines); $2l/\lambda = 0.496$, $2l/d = 625$.

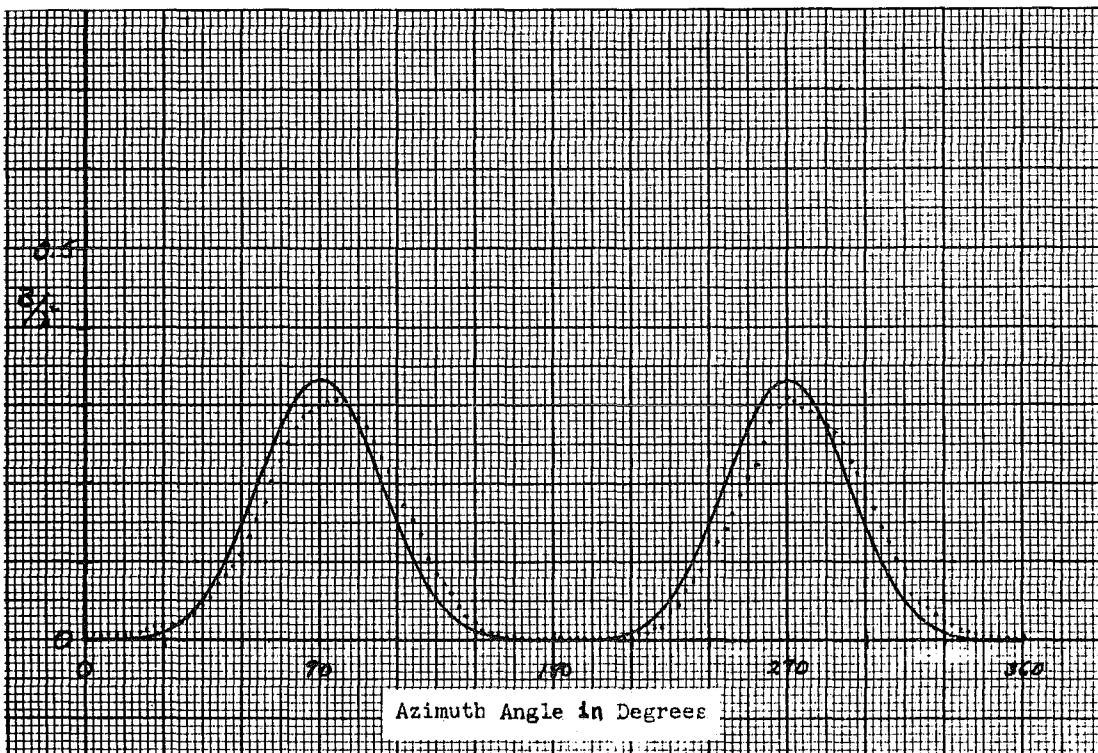


FIGURE 4. RADAR CROSS SECTION. Tungsten wire experimental (points) and theoretical (solid lines); $2l/\lambda = 0.525$, $2l/d = 660$.

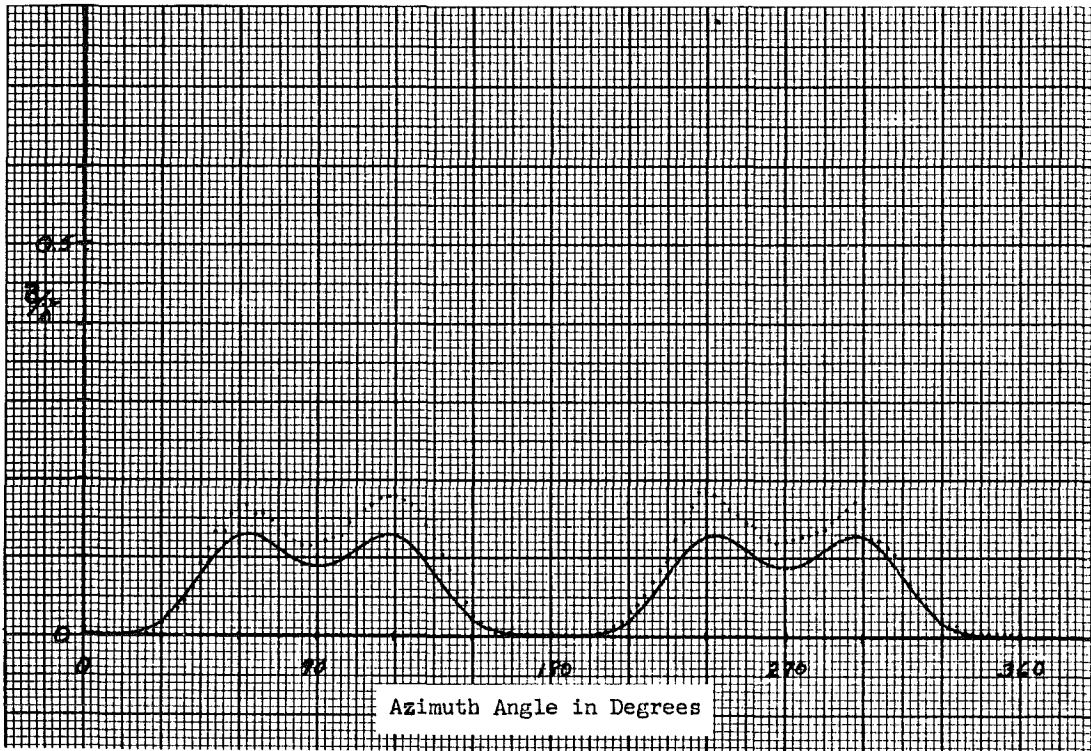


FIGURE 5. RADAR CROSS SECTION. Tungsten wire experimental (points) and theoretical (solid lines); $2l/\lambda = 0.854$, $2l/d = 717$.

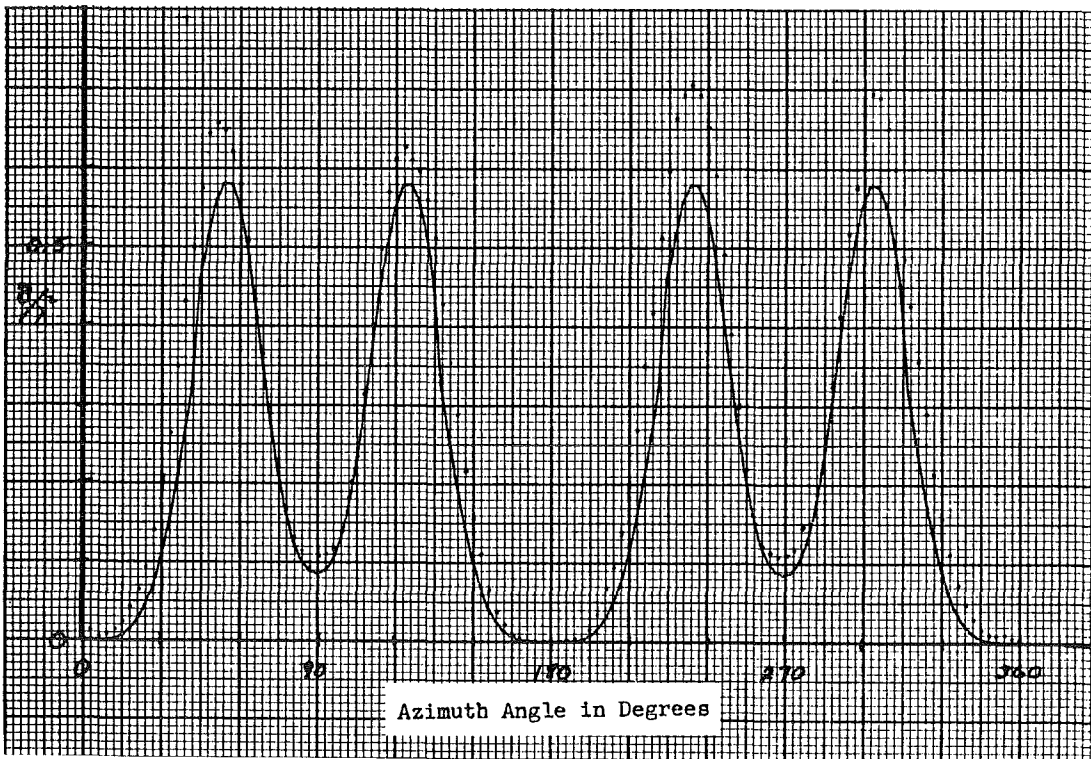


FIGURE 6. RADAR CROSS SECTION. Tungsten wire experimental (points) and theoretical (solid lines); $2l/\lambda = 0.929$, $2l/d = 780$.



FIGURE 7. RADAR CROSS SECTION. Tungsten wire experimental (points) and theoretical (solid lines); $2l/\lambda = 0.992$, $2l/d = 834$.

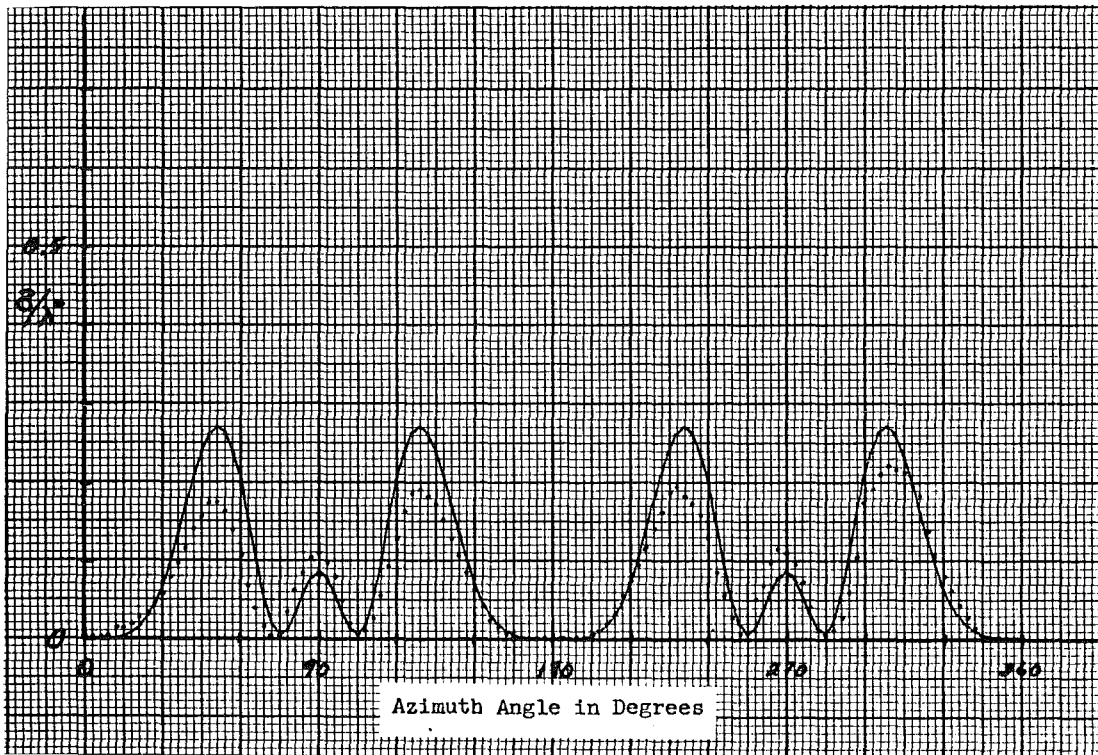


FIGURE 8. RADAR CROSS SECTION. Tungsten wire experimental (points) and theoretical (solid lines); $2l/\lambda = 1.051$, $2l/d = 884$.

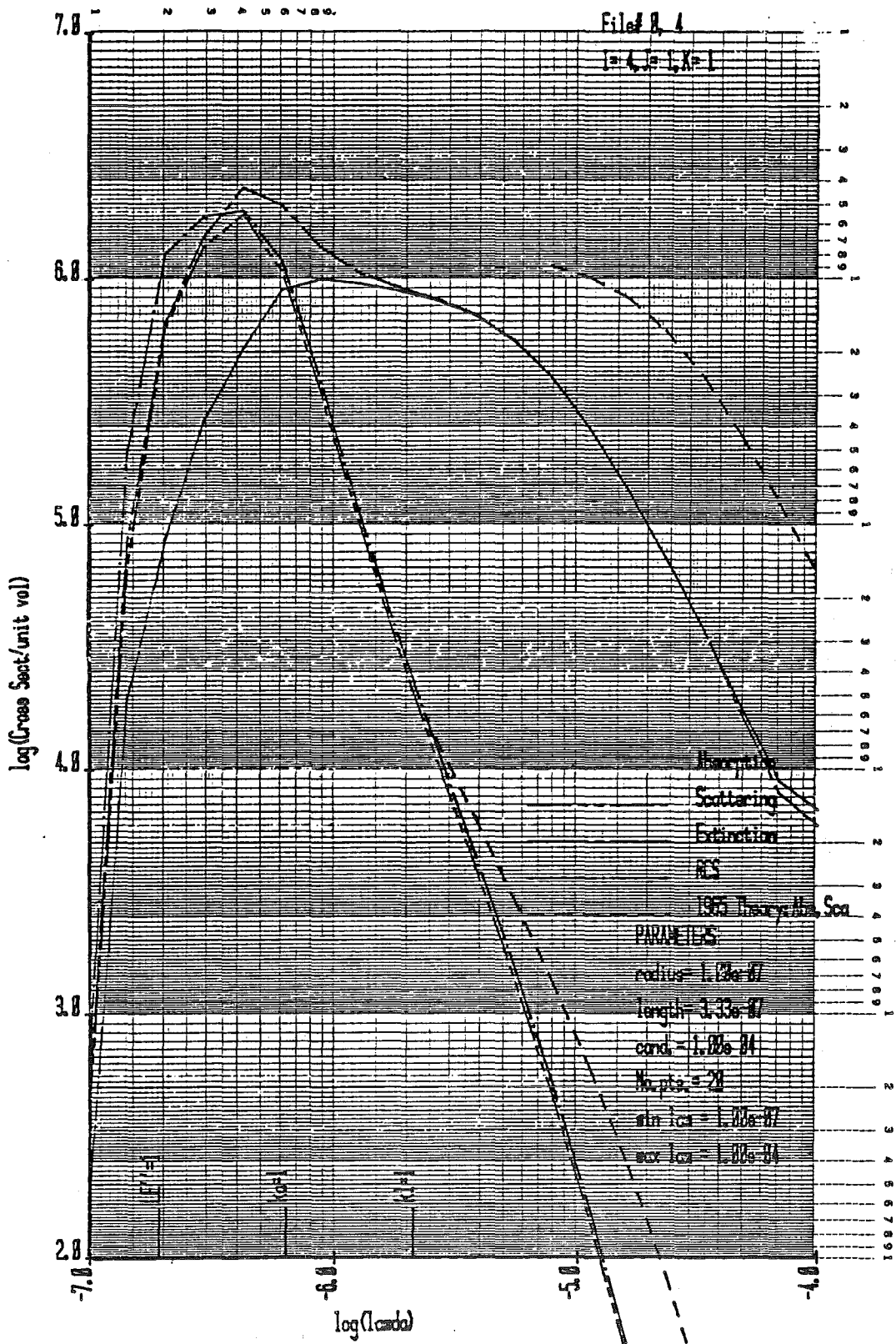


FIGURE 9. ELECTROMAGNETIC CROSS SECTIONS VS. WAVELENGTH. MKS units

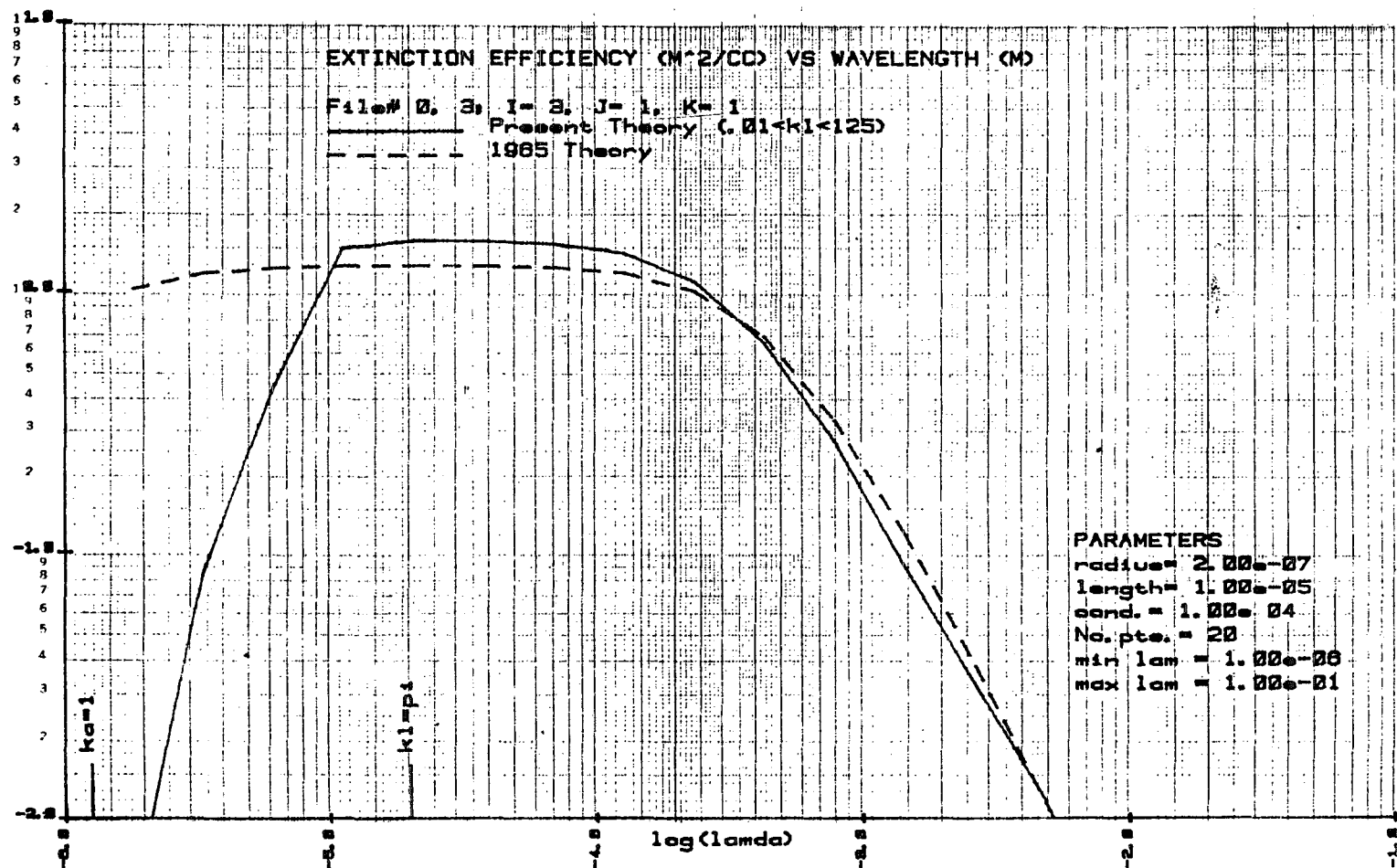


FIGURE 10. EXTINCTION EFFICIENCY (M^2/cc) VS. WAVELENGTH (M).

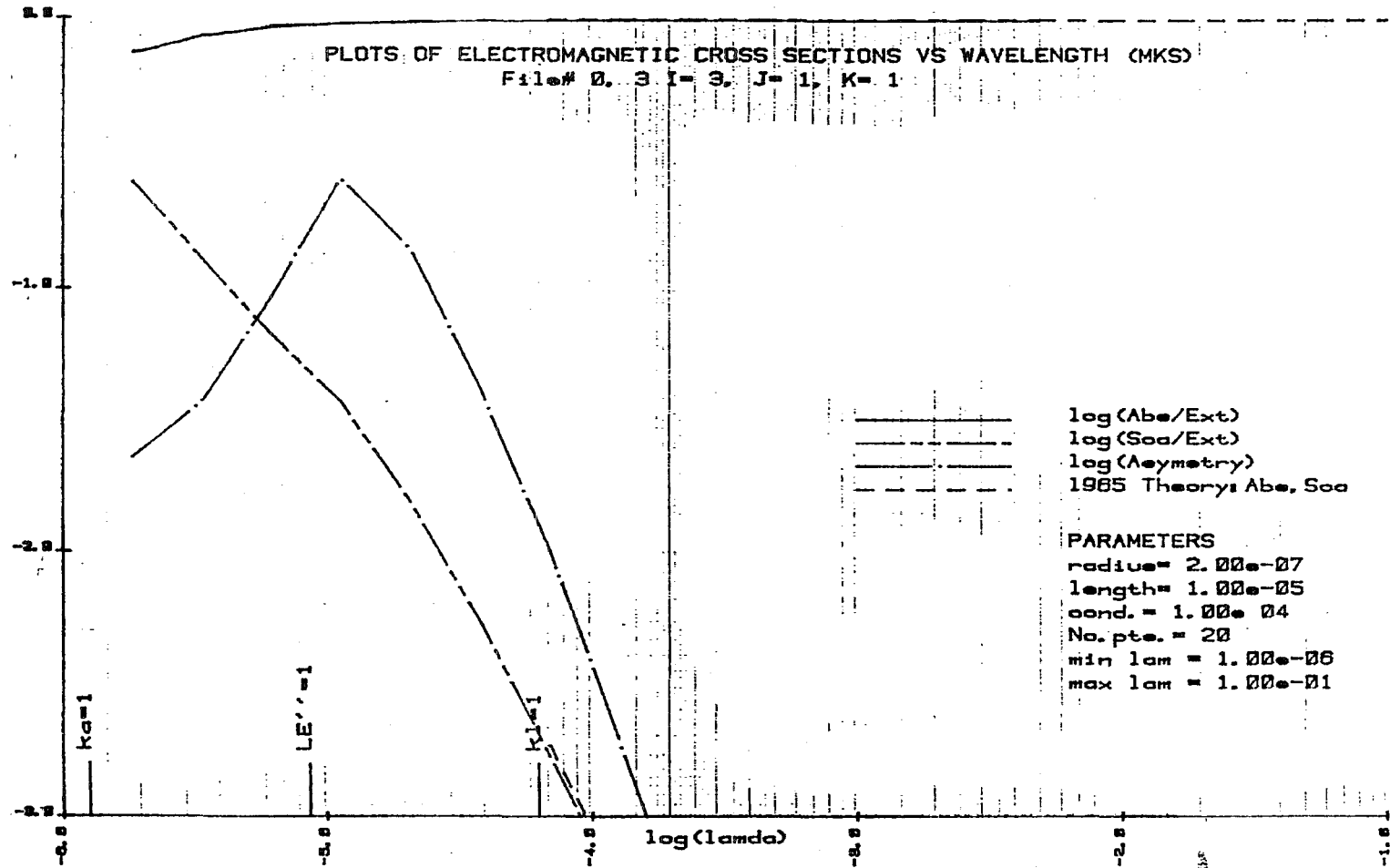


FIGURE 11. CROSS SECTION RATIOS VS. WAVELENGTH (M).

THEORETICAL INVESTIGATION OF FIBERS

D. L. Dye, D. H. Holze and G. M. Hess
The Boeing Aerospace Co.
Seattle, Wa. 98124

and

R. L. Dow
CSL, ARRADCOM
Edgewood, Md. 21010

ABSTRACT

Effective Medium Theory was used to predict dielectric constants of conductive fiber-loaded composites. Measurements made of these parameters in such materials show that they may be promising for quarter-wave plate applications at microwave frequencies.

INTRODUCTION

The purpose of the investigation described here briefly was to determine the potential of fibers as inclusions within dielectric materials suitable for EM wave absorption. The approach taken to this effort involved both theory and experiment. Effective Medium Theory (EMT) was used to predict constitutive properties of potentially useful materials, and measurements were made of these properties. A fuller discussion will be found in the final contract report, scheduled for release late in 1983.

QUARTER-WAVE PLATE

Consider a metal plate overlaid with a dielectric material of thickness t , as indicated in Figure 1. The dielectric has EM constitutive parameters, ϵ and μ , dielectric constant and permeability, respectively, which are complex numbers in general. Let

$$\begin{aligned} \epsilon &= \epsilon' + i\epsilon'' \\ \text{and } \mu &= \mu' + i\mu''. \end{aligned}$$

Consider a ray or beam of EM radiation having free-space wavelength, λ , incident upon this dielectric layer at an angle, θ , to the normal, and reflecting from both the front surface of the dielectric and the metal backing. There may also be multiple reflections within the dielectric. If the values of ϵ , μ and t are suitably related to λ , then the fields reflected from the front surface and the metal plate may be exactly out of phase and cancel. This geometry is sometimes referred to as a quarter-wave plate and is the basis for many radar cross section (RCS) reduction schemes.

The values of ϵ and μ of the dielectric required to provide zero reflectance, i.e., for a quarter-wave plate, have been calculated. For example, see Ref. 1. The centerlines of the bands in Figure 2 show ϵ' and ϵ'' values, if $\mu = 1 + i0$, for this condition for a dielectric plate of thickness t and radiation of wavelength λ . The bands on Figure 1 show ϵ' and ϵ'' values for which reflectance is less than 0.01, or the reflected intensity is 20 dB down from the incident.

EFFECTIVE MEDIUM THEORY

The question addressed by this investigation is the feasibility of tailoring fiber-loaded dielectric materials, having suitable complex ϵ and μ values, for quarter-wave plate applications at radar frequencies. The approach taken was to apply effective medium theory (EMT), specifically in the form of Maxwell Garnet (M-G). This approach allows one to determine the constitutive parameters of a composite material if those of the host and inclusion materials are known. The "effective field" on any dipole (inclusion) in the medium is determined as the average field due to the host and other inclusions (Ref. 2). For application of M-G theory, we assume that the inclusions, in our case fibers, are Rayleigh particles (short compared to a wavelength in the particle) and that they are uniformly and sparsely enough distributed so that they act independently. It is then straightforward to derive the equation relating the permittivities of the composite, the host and the inclusion materials:

$$\frac{\epsilon_c - \epsilon_H}{L\epsilon_c + (1-L)\epsilon_H} = f \frac{\epsilon_I - \epsilon_H}{L\epsilon_I + (1-L)\epsilon_H}$$

where subscript c refers to composite, H to host, I to inclusion; f is the volume fraction of inclusions; and L is the "depolarization factor" that accounts for particle shape. For fibers (assumed to be highly prolate spheroids) of aspect ratio, A (= length/diameter),

$$L = \frac{1 - e^2}{e^2} \left[\frac{1}{2e} \ln \left(\frac{1+e}{1-e} \right) - 1 \right],$$

where $e = 1 - 1/A^2$. A similar equation holds for permeability.

To use these equations for tailoring composites we need values of ϵ' and ϵ'' for host and inclusion materials. Host materials are generally organics with known or directly measureable (in principle) permittivity at frequencies of interest. However, the complex permittivity of conductive inclusion materials is not as well known by direct measurement. In this case, we make use of the fact that ϵ'' , the imaginary part of permittivity, is related to conductivity, σ , by (Ref. 3):

$$\epsilon'' = \frac{2\sigma}{\nu},$$

where ν is the frequency. At radar and millimeter wave frequencies, σ is close to the dc conductivity.

For metal inclusions, such as copper or iron fibers, and even for carbon fibers, at frequencies below 10^{11} Hz (100 GHz), ϵ'' has a very large value. In equation (1) a large ϵ''_I has the effect of making the resulting ϵ_c independent of ϵ'_I over a wide range of reasonable values.

A computer code was developed to solve Eq. (1) for ϵ' and ϵ''_c in terms of the other parameters involved, A, σ , ϵ_H , ϵ_I , and f. Two of the resulting dependencies are plotted in Figures 3 and 4. As

a function of volume fraction, ϵ'_c and ϵ''_c are plotted for 18 GHz; in Figure 3 the conductivity is held constant at $9 \times 10^{16} \text{ sec}^{-1}$ (bulk iron) and aspect ratio of the fibers is varied between 250, 500 and 1000. Note that both ϵ'_c and ϵ''_c increase with A, at a given f, and that ϵ''_c is the more strongly affected by A. In Figure 4, two aspect ratios are considered, 500 and 1000, and the dependencies of ϵ'_c and ϵ''_c examined as conductivity vary between 9×10^{16} and 9×10^{17} (copper). Note that increasing σ affects ϵ''_c more strongly than ϵ'_c .

These theoretical results show that it is possible to design a fiber-loaded composite having various ϵ'_c and ϵ''_c values depending upon fiber conductivity, σ , fiber shape, A, and fiber volume fraction, f. Host permittivity also plays a part, of course, in the design of a tailored dielectric material.

MEASUREMENTS

Experiments were undertaken to characterize some available fibers, and to measure ϵ'_c and ϵ''_c of composite materials made from these fibers and known host materials. The test samples were fabricated by forming a surface layer of fibers of known areal density on host material films then making multilayer sandwiches of these films. In this way f was a controlled variable. The fibers were random in two dimensions.

Samples of the same production lot(s) of fibers were characterized geometrically by use of a high-powered light microscope, with automated measurements of lengths and diameters, to arrive at a distribution of length, diameter and aspect ratios. We report here on the results for two types of fibers: (1) copper-coated iron, where typically the copper coating was $0.1 \mu\text{m}$ thick over a 1 to 2 μm diameter, 200-500 μm long iron fiber; and (2) iron-coated carbon fibers, where typically the iron coating was 1 μm thick over a 4 μm diameter, 1000 μm long carbon fiber. Microphotographs of these fibers show that they are not "textbook" cylinders nor ellipsoids but rather tend to cling together and to bend and twist.

Acetate film sandwiches with a density $2.3 \times 10^{10} \text{ fibers/m}^3$ (copper-coated iron) were fabricated within K_u band waveguide flange blanks for measurements at 12-18 GHz. Epoxy loaded with $1.2 \times 10^{10} \text{ fibers/m}^3$ (iron-coated carbon) was applied to a Kapton film over an area large enough to measure in the Boeing Millimeter Wave Dielectrometer at 45 GHz; then the Kapton samples were cut up into K_u -band waveguide size pieces and sandwiched for 12-18 GHz measurements.

The dielectrometers used for measurement determined both the complex permittivity and the permeability of test samples. The results are shown in Table 1, along with predicted values of ϵ' and ϵ'' assuming $\mu = 1 + i0$, for the measured A and f values and assumed σ values. In every case controls of the same host material(s) without fibers were measured to obtain the values of ϵ_H used in the prediction.

DISCUSSION

The agreement of M-G theory with experimental values for the case of copper-clad iron fibers is considered fortuitous, in view of the assumptions made concerning fiber geometry, and the fact that

the mean of the aspect ratio distribution was used for the calculation. In another paper at this conference it was suggested that a distribution of A would affect ϵ''_c of the composite medium (Ref. 4).

However, the approach shows promise for development of tailored dielectrics for quarter wave plate applications. How this might be is indicated schematically in Figure 5. Shown on the left is a plot of ϵ'_c , ϵ''_c versus f for the frequency of interest, and for various values of A and σ ; on the right Figure 2 is replotted to show the ϵ'_c , ϵ''_c values required for zero (or low) reflection at some thickness and wavelength. It appears feasible to vary f , σ and A to find ϵ'_c and ϵ''_c values, given some suitable host material, such that the zero reflectance conditions are met.

REFERENCES

1. Ruck, G. T., Editor, "Radar Cross Section Handbook, Vol. 2, Plenum Press, 1970.
2. Landauer, Rolf, "Electrical Conductivity in Inhomogeneous Media," in Electrical transport and Optical Properties of Inhomogeneous Media, A.I.P. Conference Proceedings #40, 1978.
3. Jackson, John D., Classical Electrodynamics, John Wiley & Sons, Inc., New York, 1962.
4. Chylek, Peter, and Vandana Srivasta, "Dielectric Constant of a Composite Inhomogeneous Medium," Physical Review B, Vol.27, p. 5098, 15 April 1983.

Table 1. Permittivity* Values

Composite/Frequency	ϵ_c Calculated Using M-G	Dielectrometer Measurement of ϵ_c
Cu-coated Fe Fibers in Acetate		
12-18 GHz		$3.3 \pm 0.3 + i (0.11 \pm 0.03)$
15 GHz	$3.3 + i 0.11$	
Fe-coated C Fibers in Epoxy/Kapton		
12-18 GHz		$5 \pm 1.2 + i (2.2 \pm 0.4)$
15 GHz	$6.6 + i 1.3$	
45 GHz	$5.2 + i 1.8$	$3.6 \pm 0.2 + i (1.4 \pm 0.2)$

*Measured permeability values close to $1 + i0$ in all cases; calculated values assume $\mu = 1 + i0$.

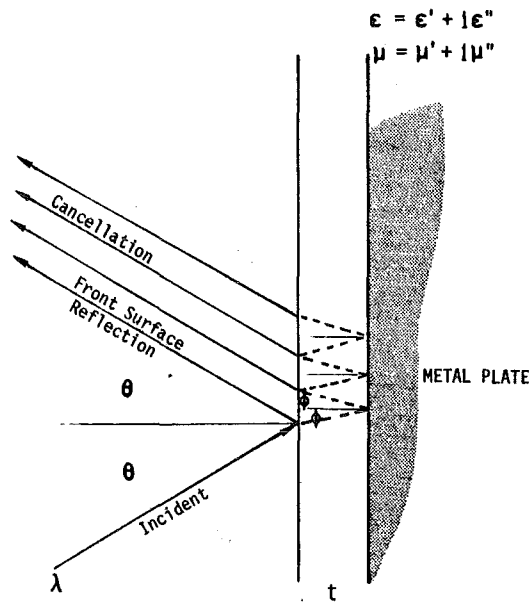


FIGURE 1. REFLECTION CANCELLATION IN QUARTER-WAVE PLATE

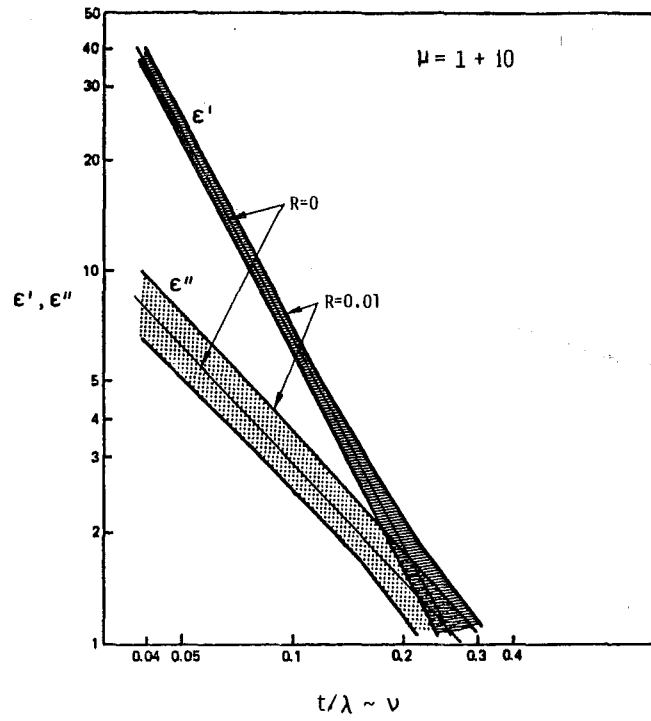


FIGURE 2. PERMITTIVITY REQUIREMENTS FOR QUARTER-WAVE PLATE

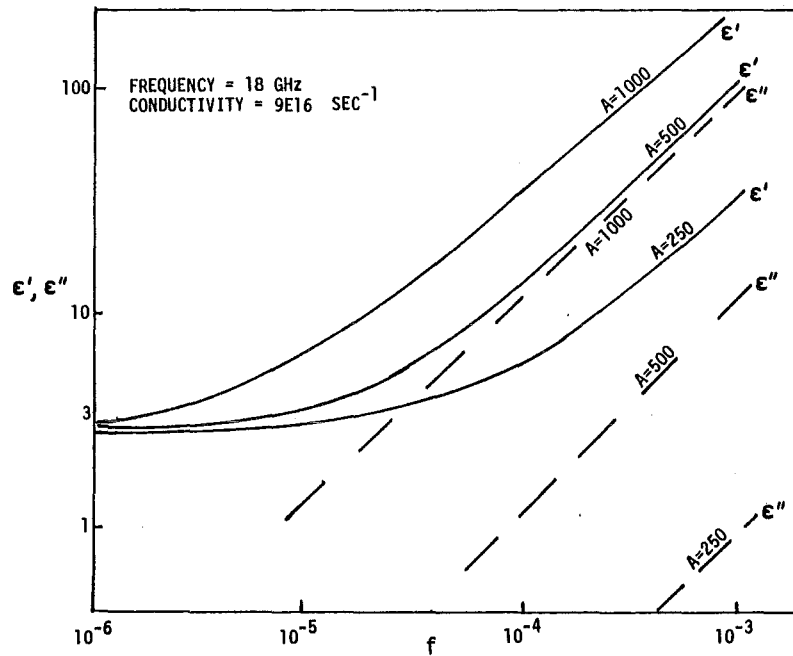


FIGURE 3. ϵ' , ϵ'' DEPENDENCE UPON VOLUME FRACTION AND ASPECT RATIO

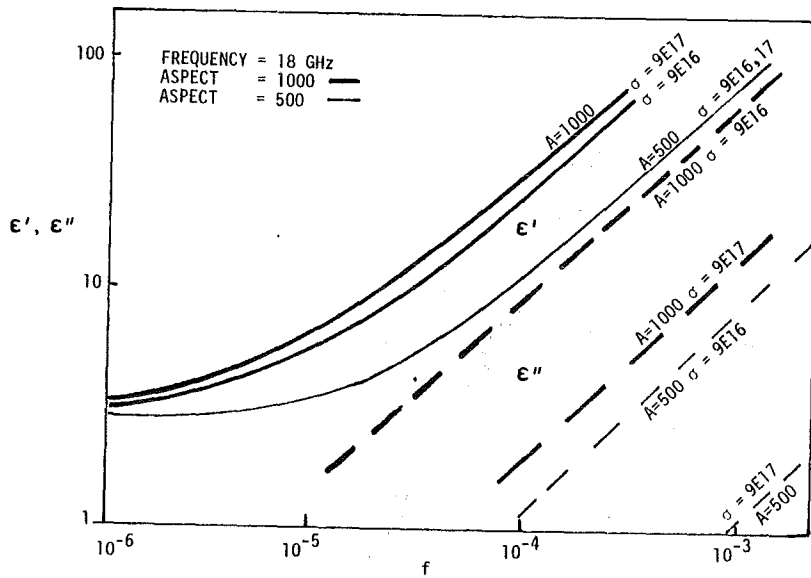


FIGURE 4. ϵ' , ϵ'' DEPENDENCE UPON VOLUME FRACTION AND CONDUCTIVITY

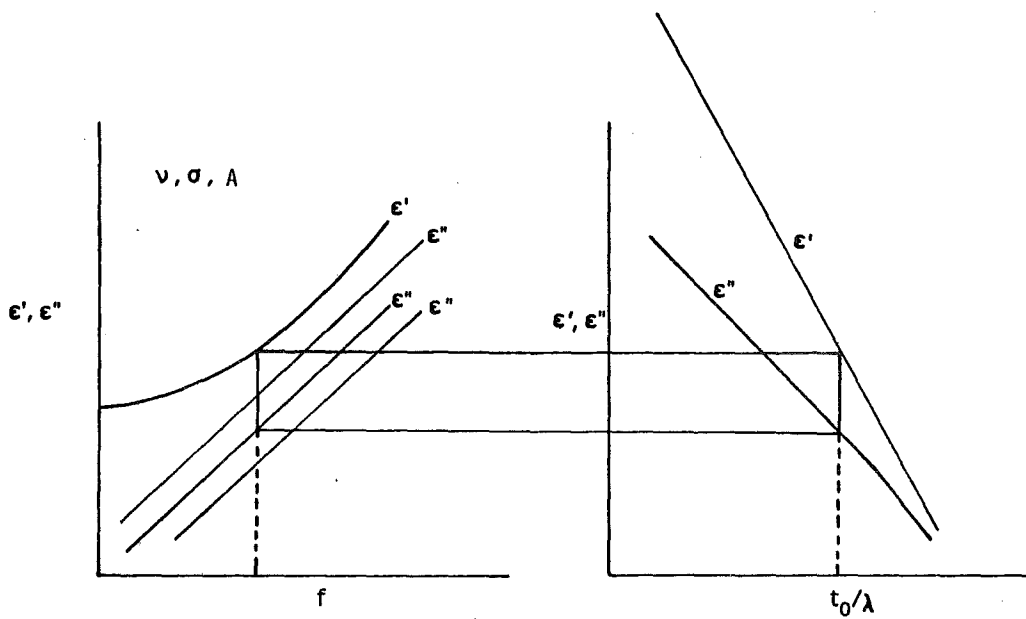


FIGURE 5. APPLICATION OF MAXWELL GARNET THEORY TO QUARTER WAVE PLATE MATERIAL DESIGN

BLANK

Double Scattering by Randomly Oriented
Long Cylinders

by

Ariel Cohen*, Leonard Cohen and Richard Haracz
Department of Physics and Atmospheric Sciences
Drexel University

and

Smadar Egert
Department of Atmospheric Sciences
The Hebrew University of Jerusalem

ABSTRACT

Double scattering lidar events involving long cylindrical particles are discussed. The scatterers are allowed to be randomly oriented and the geometry required in the scattering solution is described in detail. The geometry is general and made to be applicable to any type of particle for which the single scattering matrix is provided, relative to the main axis of the scatterer. Results of the double scattering calculations are presented for the penetration of the lidar light into clouds of different optical depth τ ($\tau < 0.5$). [A. Cohen, L. Cohen, R. Haracz, S. Egert, submitted to J. Appl. Optics (1983).]

INTRODUCTION

The interaction of electromagnetic radiation with thick naturally occurring or artificial aerosol layers is of interest in several applications in remote sensing, radiative transfer and communication. For example, in lidar applications the backscattered light from a thick layer is a result of single and multiple scattering processes.

As long as single scattering is dominant the distance between the lidar and the scattering volume is well determined. But, when multiple scattering events become significant, the lidar spatial resolution is reduced and only average properties can be analyzed from single measurements. Moreover, all inversion methods relating lidar signals to number densities and size distribution must be modified since the multiple scattering affects the direct analysis. The contribution of the multiple scattering effect to the lidar signal is dependent on the optical depth (τ). Therefore, the laser radar analysis based on the assumption that multiple scattering can be neglected is limited to cases characterized by low values of optical depth ($\tau < 0.1$) which do not include scattering from clouds and artificial smoke.

On the other hand, the direct problem of multiple scattering can be calculated and has been previously approached by several authors¹⁻⁴ for spherical scatterers. Here, we study the effect of double scattering on non-spherical scatterers (long cylinders) applicable mainly for relatively low values of optical depths in the cloud layer ($0.1 < \tau < 0.3$).

*A. Cohen is on leave from the Hebrew University, Department of Atmospheric Sciences.

It is important to emphasize that the geometry discussed below deals with long cylinders having arbitrary orientations relative to another scatterer and to the incident polarization plane. The scattering matrix has then to be rotated accordingly by an angle which is a function of the tilting angle, the scattering angle and the incident polarization angle. The determination of the rotation angles of each scattering event is the main difference between the multiple scattering process involving spherical scatterers and multiple scattering of non-spherical particles the main axis of which are known. Such non-spherical particles are not restricted to a particular shape and therefore the angles determined are applicable to shapes other than right circular cylinders as well.

The Geometry of Double Scattering Processes Involving Cylinders

In order to calculate the sum of all possible double scattering events resulting in a simultaneous signal in the receiver, the following statistical approach has been used:

Two randomly chosen positions for the two scatterers were determined by the computer--the first having the constraint of being within the laser field of view and the second within the telescope field of view. In each position it is assumed that all possible orientations can be found; however, each orientation in the first location corresponds to one scattering angle pointing towards the second location. This is due to the fact that the light scattered by a unit length of the cylinder is limited to the surface of a cone⁵ based on the assumption that the scattering function is that of an infinite cylinder.

The second scatterer at B can also be randomly oriented in space. But, as in the case of the first scatterer, each orientation corresponds to one scattering angle θ_2 which would be in the direction of the lidar receiving system. From Fig. 1 it can be seen that when $\phi = \phi_0$ (the scattering and the incident planes are the same), the second cylinder must also be contained within the same plane and the second TILT angle is given by $\phi_{02} = \pi/2 - \phi_0$.

Discussion

The double scattering effect of randomly oriented long cylinders was calculated for number densities varying from 10^2 to 10^3 (Fig. 2) and from 10^3 to 10^4 (Fig. 3). In general the behaviour of the double scattering profile as a function of penetration depth resembles the scattering by dense clouds of spherical particles. As can be seen in Fig. 2 the double scattering effect (relatively low number densities) is to produce a maximum scattering layer which approaches the cloud base with an increased value of number density.

It is important to emphasize that the geometrical approach discussed is applicable for other non-spherical particles the scattering matrixes of which are expressed in respect to their main axis.

ACKNOWLEDGEMENT

This research was partially supported by the Army Chemical Systems Laboratory.

REFERENCES

- 1) A. Cohen, M. Kleiman, J. Cooney: Appl. Opt. 16, 1955 (1978).
- 2) A. Deepak, A. Zardecki, U. Farukmand, M. Box, "Atmospheric Aerosols", A. Deepak (ed), Spectrum Press, Hampton, Virginia (1982).
- 3) H.C. van de Hulst, "Multiple Light Scattering", Academic Press, New York (1980).
- 4) E.W. Eloranta, S.T. Shipley, "Atmospheric Aerosols", A. Deepak (ed), Spectrum Press, Hampton, Virginia (1982).
- 5) M. Kerker, "The Scattering of Light", Academic Press, New York (1969).

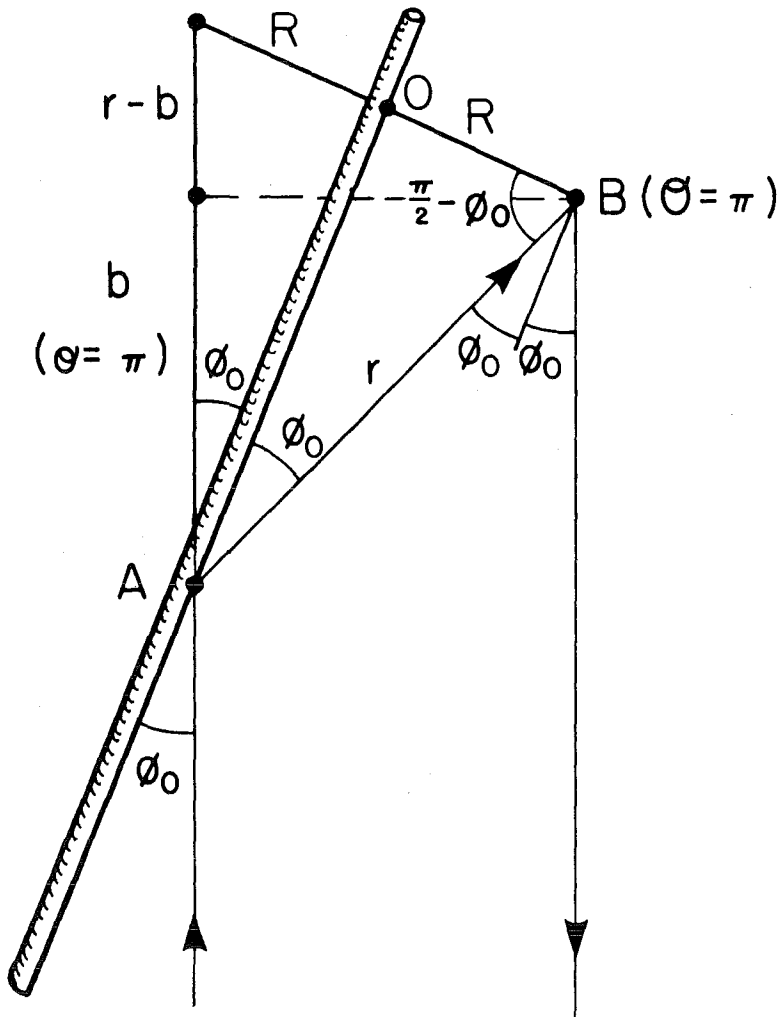


Figure 1. Geometry for the definition of the TILT angle . When the cylinder axis is in the plane defined by the incident and first-scattered directions, the only TILT angle possible for the cylinder is ϕ_0 .

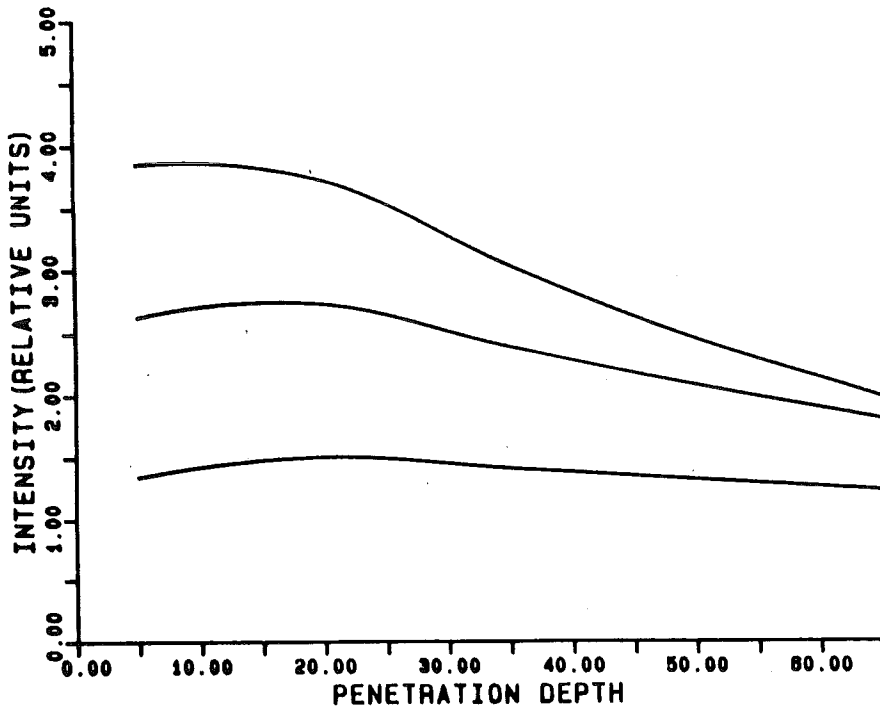


Figure 2. The double scattering intensities as a function of penetration depth in meters for three different number densities (10^2 to 10^3).

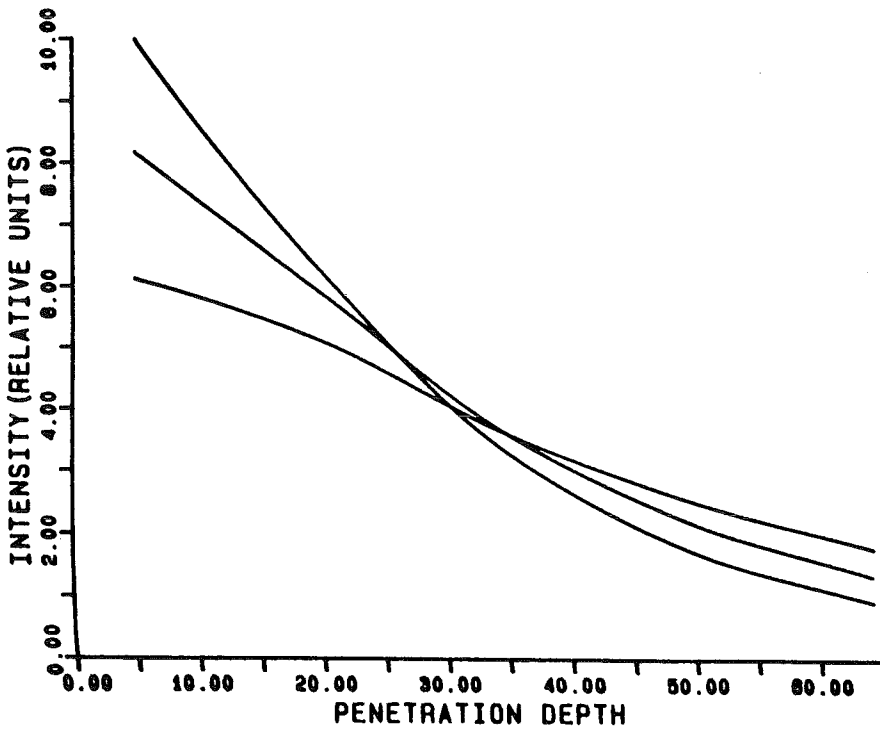


Figure 3. Same as Figure 2 for the number densities from 10^3 to 10^4 .

BLANK

MULTIPLE-SCATTERING-INDUCED FALSE TARGETS

A. Zardecki, S. A. W. Gerstl
Theoretical Division, MS-B279
Los Alamos National Laboratory
Los Alamos, New Mexico 87545
and
J. F. Embury
Chemical Systems Laboratory
Aberdeen Proving Ground, MD 21010

ABSTRACT

The two-dimensional discrete-ordinates finite-element radiation transport code TWOTRAN is applied to describe the resolution problem that arises for a distant observer attempting to distinguish spatially between two thermal radiation sources located behind an obscuring medium (e.g., smoke cloud). For certain optical properties of the obscuring medium the received signal gives the appearance of the targets at other than the true locations. A strong dependence of this false target effect on optical depth and single scattering albedo is found.

INTRODUCTION

Recently, we have applied the discrete-ordinates finite-element radiation transport code TWOTRAN to describe the multiple scattering of a laser beam from a reflecting target¹. The effect of multiple scattering, being dominant for weakly absorbing media with large optical depth ($\tau \gtrsim 1$), needs to be taken into account to predict the amount of radiant energy available from a beam². As shown by Bugnolo³, even for unit optical thickness there is a significant probability of triple scattering in the forward direction. This is the reason why electro-optical and millimeter wave devices incorporated into modern weapon systems are strongly influenced by the multiple scattering effects that will as a rule exist in a battlefield environment. Apart from laser sources, which emit well-collimated Gaussian beams, one encounters in practice, mainly in telephotometer and transmissometer measurements, also natural sources radiating spherical waves^{4,5}. To a good approximation, in battlefield conditions the moving vehicles, tanks, as well as stationary weapon systems can be regarded as isotropically emitting sources of thermal radiation. There is thus a need to perform numerical modeling of multiple scattering effects for isotropic radiation sources.

In this paper, we address the resolution problem that arises for a distant observer attempting to distinguish spatially between two thermal sources radiating into a turbid medium. For a model scenario involving two isotropic sources at the entrance plane of a finite turbid medium, we analyze the received power in a narrow field-of-view detector at the output plane. The detector resolves the details of the

radiance distribution function within a finite spatial interval. Varying the scattering medium's parameters, such as optical depth, single scattering albedo and asymmetry of the scattering phase function, we study parametrically the resolution effect for different source separations.

MODEL SCENARIO

As was shown in Ref. 1, a realistic 3-D scenario can adequately be represented by using a 2-D x-y geometry description. This approach is valid when one neglects the direction of radiation close to the normal to the x-y plane. The symmetry condition of translational invariance with respect to the z-axis allows us to choose the scattering region as a finite area in the x-y plane. Specifically, we take a square ABCD of width 42 m and divide this scattering region into 42 x 42 square mesh cells of 1 m width. This will imply, when the spatial coordinates are thus discretized, that the scattering region has been divided into 1764 square cells and that the details of the radiation field distribution are known within a 1 m resolution.

Imagine now a symmetry axis PQ of our square perpendicular to two of its sides, say AB and CD. Two isotropic sources S_1 and S_2 of radiation, separated by a distance d , are located on the side CD symmetrically with respect to the axis PQ. Our problem is then to determine the radiation field along the side AB when a distant detector scans the segment AB. Since the spatial resolution of the radiation field is assumed to be $\Delta\ell = 1$ m, a narrow-field-of-view detector located at a distance ℓ from AB has the angular resolution $\theta_v = \Delta\ell/\ell$. For example, when $\ell = 1$ km, $\theta_v = 1$ mrad.

Let us first analyze the power received by the detector in a vacuum. In the absence of scatterers, we assume that each source emits the power P_0 radially into space. In 2-D plane geometry, when the medium as well as the source are imagined infinite in $\pm z$ -direction, the geometric factor $4\pi r^2$ is replaced by the factor $2\pi r$ where r is the distance from the source to the observation point. It is evident that the narrow-field-of-view detector will measure the power proportional to the radiance distribution function across the segment AB. This distribution will be zero unless the detector is located on a straight line perpendicular to AB, passing through the source S_i , $i = 1, 2$. The measured power will then be proportional to the radiance P_{vac} given as

$$P_{\text{vac}} = \frac{P_0}{2\pi r} \quad (1)$$

For $r = 42$ m, we obtain at the location of the exit-face of the aerosol cloud

$$P_{\text{vac}} = 3.7894 \times 10^{-3} \text{ W/rad} \cdot \text{m} \quad (2)$$

where we have assumed $P_0 = 1$ W.

SOLUTION ALGORITHM

For calculations reported here, the general-purpose code TWOTRAN-II⁶ has been adapted to radiative transfer calculations in a turbid medium.

In problems with isolated sources in absorbing media, there exists a well-known flux distortion introducing defect of the discrete ordinates approximation to the transport equation. This defect, called descriptively the ray effect, is due to the discretization of the angular variable of the divergence operator in the discrete ordinates approximation. Since the radiation emerging from the first-collision processes is always much less localized than the true source, the radiance distribution originated by a first collision source is also much less subject to ray effects than the radiance from the original source⁷. For these reasons the first-collision source approach is the procedure that we adopt in the following.

Simply stated, the equation of transfer to be solved is

$$\begin{aligned} \vec{\Omega} \cdot \nabla I(\vec{r}, \vec{\Omega}) + \sigma_t(\vec{r}) I(\vec{r}, \vec{\Omega}) \\ = \int \sigma_s(\vec{r}, \mu) I(\vec{r}, \vec{\Omega}') d\Omega' \quad , \end{aligned} \quad (3)$$

where $\sigma_t(\vec{r})$ is the volume extinction coefficient and $I(\vec{r}, \vec{\Omega})$ is the radiance distribution function. The differential scattering cross-section $\sigma_s(\vec{r}, \mu)$, where μ is the cosine of the angle between $\vec{\Omega}'$ and $\vec{\Omega}$, is related to the scattering phase function $P(\vec{r}, \mu)$ by

$$P(\vec{r}, \mu) = \sigma_s(\vec{r}, \mu) / \sigma_s^0(\vec{r}) \quad (4)$$

In Eq. (4), $\sigma_s^0(\vec{r})$ is the volume scattering coefficient. Equation (3) must be solved with boundary conditions specifying the incoming radiation flux.

At this point it is convenient to divide the total radiance into two parts--the reduced radiance I_r and the diffuse radiance I_d . The reduced radiance satisfies the equation

$$\vec{\Omega} \cdot \nabla I_r(\vec{r}, \vec{\Omega}) + \sigma_t(\vec{r}) I_r(\vec{r}, \vec{\Omega}) = 0 \quad . \quad (5)$$

The other part, I_d , which is created within the medium due to scattering, by virtue of Eq. (1) and (5), obeys

$$\begin{aligned} \vec{\Omega} \cdot \nabla I_d(\vec{r}, \vec{\Omega}) + \sigma_t(\vec{r}) I_d(\vec{r}, \vec{\Omega}) \\ = \int \sigma_s(\vec{r}, \mu) I_d(\vec{r}, \vec{\Omega}') d\Omega' + Q(\vec{r}, \vec{\Omega}) \quad . \end{aligned} \quad (6)$$

Here $Q(\vec{r}, \vec{\Omega})$, the first-collision source, is

$$Q(\vec{r}, \vec{\Omega}) = \int \sigma_s(\vec{r}, \mu) I_r(\vec{r}, \vec{\Omega}') d\Omega' \quad . \quad (7)$$

In the case of our scenario, where the incoming radiation is due to two sources S_1 and S_2 , $I_r(\vec{r}, \vec{\Omega})$ can be given analytically by

$$I_r(\vec{r}, \vec{\Omega}) = \frac{P_0}{2\pi\ell_1} e^{-\sigma\ell_1} \delta(\vec{\Omega} - \vec{s}_1) + \frac{P_0}{2\pi\ell_2} e^{-\sigma\ell_2} \delta(\vec{\Omega} - \vec{s}_2) \quad , \quad (8)$$

where we have assumed a constant extinction coefficient σ throughout the smoke cloud. The vectors \vec{s}_1 and \vec{s}_2 are the unit vectors in the directions determined by the lines joining S_1 and S_2 with the observation point \vec{r} ; P_0 is the power emitted by each source; ℓ_1 and ℓ_2 are the distances between \vec{r} and S_1 and S_2 , respectively.

As Eq. (8) gives explicitly the reduced radiance, the first-collision source, given by Eq. (7), can readily be determined. What remains to be done is to represent $Q(\vec{r}, \vec{\Omega})$ in terms of a series expansion in spherical harmonics functions. The details of this derivation will be presented elsewhere.

NUMERICAL RESULTS

It should be clear from our previous considerations referring to the propagation in a vacuum that the false target effect becomes only possible when there is a sufficient amount of the diffuse radiation to dominate the reduced radiator.

The parameters that were varied in our modeling were the total optical depth τ of the smoke cloud, single scattering albedo ω , and asymmetry of the scattering phase function. The asymmetry parameter is defined as the average cosine of the scattering angle.

In Figs. 1-3, we show the average intensity distribution function $\langle I(\vec{r}) \rangle$ in the x-y plane. The average intensity, defined as

$$\langle I(\vec{r}) \rangle = \frac{1}{4\pi} \int I(\vec{r}, \vec{\Omega}) d\Omega \quad , \quad (9)$$

is proportional to the radiant energy at a spatial mesh point \vec{r} . We choose, to begin with, the optical depth $\tau = 4$, single scattering albedo $\omega = 0.9000$ and asymmetry factor $g = 0.1$. The contour plot in Fig. 1 shows the distribution of the total intensity, whereas the 3-D plots of Figs. 2 and 3 show the diffuse part and the total intensity. The source separation of 15 m in Figs. 1 to 3 is now allowed to vary from 5 to 35 m in Fig. 4. Figure 4 shows the radiance distribution function along the boundary of the scattering medium opposite the source location radiating in the direction normal to the boundary.

As we let the asymmetry parameter g take the value 0.9 for strong forward scattering and $\omega = 0.9999$, the scattered (diffuse) contribution of radiation becomes relatively stronger. This is illustrated in Figs. 5 to 7, for $\tau = 8$ and a source separation of 15 m. Figures 8 to 10 illustrate the evolution of false targets as the optical depth increases from 2 to 8.

CONCLUSIONS

In this study, we have applied the TWOTRAN-II transport code to investigate potential false target situations. For a homogeneous medium we have eliminated the ray effect through the first-collision source approach. What we have found in this investigation is a strong dependency of the false target effect on optical depth and the single scattering albedo. When $\tau = 4$, apparent false targets are pro-

duced for source separations of the order of 25 m or larger. For $\tau = 8$, the effect persists independently of the source separation.

REFERENCES

1. A. Zardecki, S. A. W. Gerstl, and J. F. Embury, "Application of the 2-D Discrete-Ordinates Method to Multiple Scattering of Laser Radiation," *Appl. Opt.* 22, 1346 (1983).
2. A. Zardecki, "Multiple Scattering Corrections to the Beam-Lambert Law," SPIE Vol. 410--Laser Beam Propagation in the Atmosphere (SPIE, Bellingham, 1983).
3. P. S. Bugnolo, "In the Question of Multiple Scattering in the Troposphere," *J. Geoph. Res* 65, 879-884 (1980).
4. R. W. L. Thomas, "The Information Content of Telephotometer Data," 1982 CSL Scientific Conference, Chemical Systems Laboratory report ARCSL-SP-83011, June 1983.
5. J. D. Mill and E. P. Shettle, "A Preliminary Lowtran Snow Model," Snow Symposium II, CRREL, Hanover, NH, August 1982.
6. K. D. Lathrop and F. B. Brinkley, "TWOTRAN-II: An Interfaced Exportable Version of the TWOTRAN Code for Two-Dimensional Transport," Los Alamos Scientific Laboratory report LA-4848-MS (July 1973).
7. K. D. Lathrop, "Remedies for Ray Effects," *Nucl. Sci. Eng.* 45 255-268 (1971).

MODEL AEROSOL

OPTICAL DEPTH = 4.00

SEPARATION = 15.00M, ALB = 0.9000, ASYM = 0.1000

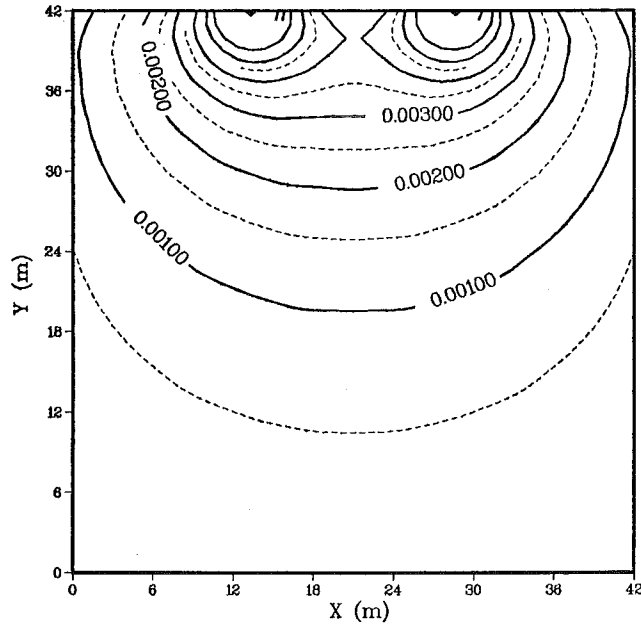


FIGURE 1. CONTOUR PLOT OF TOTAL INTENSITY DISTRIBUTION in the x-y plane. $\tau = 4$, $w = 0.9000$, $g = 0.1$.

MODEL AEROSOL

OPTICAL DEPTH = 4.00

SEPARATION = 15.00M, ALB = 0.9000, ASYM = 0.1000

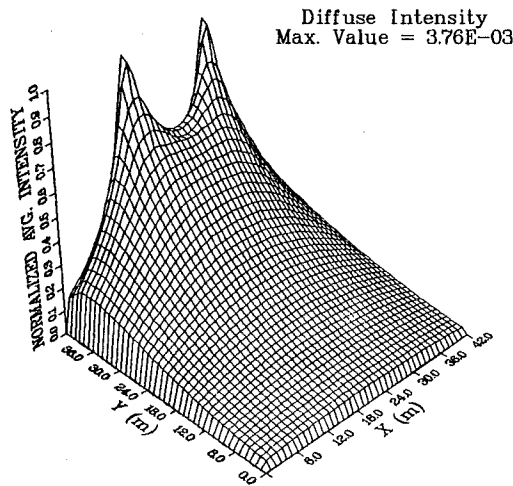


FIGURE 2. DIFFUSE INTENSITY DISTRIBUTION in the x-y plane. $\tau = 4$, $w = 0.9000$, $g = 0.1$.

MODEL AEROSOL OPTICAL DEPTH = 4.00
 SEPARATION = 15.00M, ALB = 0.9000, ASYM = 0.1000

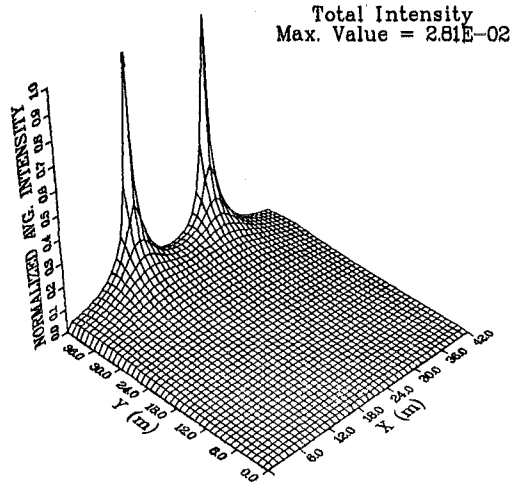


FIGURE 3. TOTAL INTENSITY DISTRIBUTION in the x-y plane. $\tau = 4$, $w = 0.900$, $g = 0.1$.

MODEL AEROSOL OPTICAL DEPTH = 4.00
 ALBEDO = .9000 ASYMMETRY FACTOR = .1000

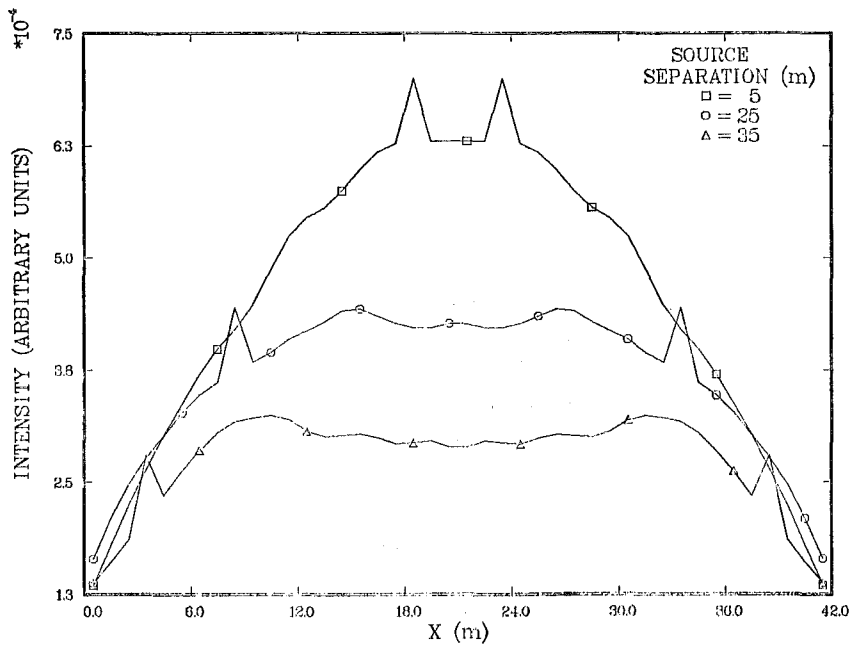


FIGURE 4. ANGULAR INTENSITY NORMAL TO THE X-AXIS AS A FUNCTION OF X for three different source separations. $\tau = 4$, $w = 0.9000$, $g = 0.1$.

MODEL AEROSOL OPTICAL DEPTH = 8.00

SEPARATION = 15.00M, ALB = 0.9999, ASYM = 0.9000

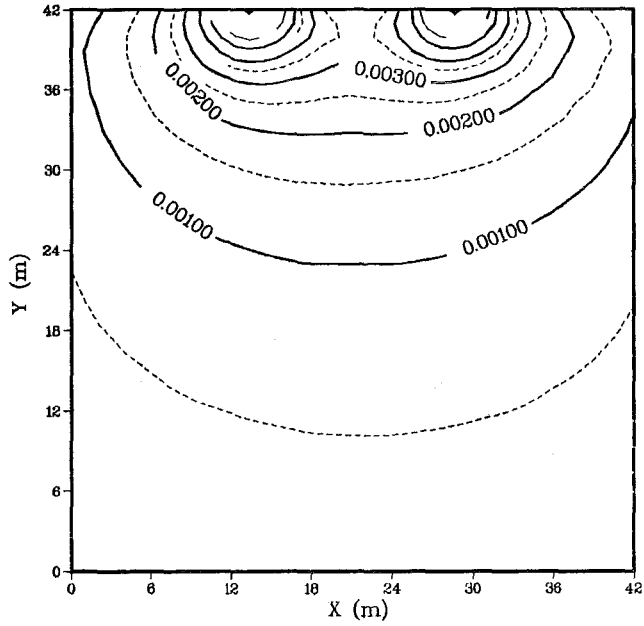


FIGURE 5. CONTOUR PLOT OF TOTAL INTENSITY DISTRIBUTION in the x-y plane. $\tau = 8$, $w = 0.9999$, $g = 0.9$.

MODEL AEROSOL OPTICAL DEPTH = 8.00

SEPARATION = 15.00M, ALB = 0.9999, ASYM = 0.9000

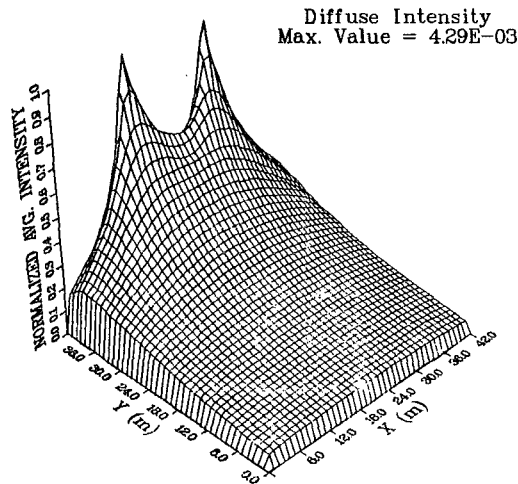


FIGURE 6. DIFFUSE INTENSITY DISTRIBUTION in the x-y plane. $\tau = 8$, $w = 0.9999$, $g = 0.9$.

MODEL AEROSOL

OPTICAL DEPTH = 8.00

SEPARATION = 15.00M, ALB = 0.9999, ASYM = 0.9000

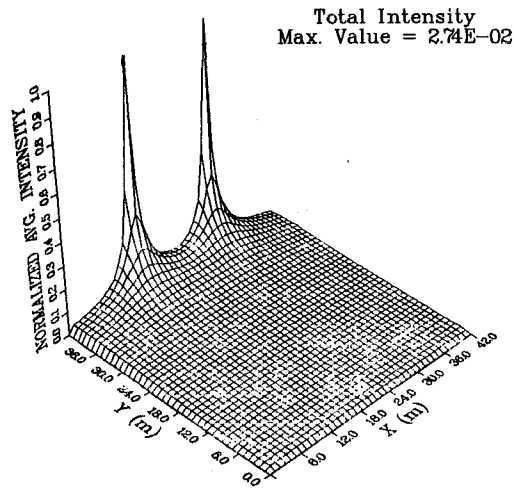


FIGURE 7. TOTAL INTENSITY DISTRIBUTION in the x-y plane. $\tau = 8$, $w = 0.9999$, $g = 0.9$.

MODEL AEROSOL

OPTICAL DEPTH = 2.00

ALBEDO = .9999

ASYMMETRY FACTOR = .9000

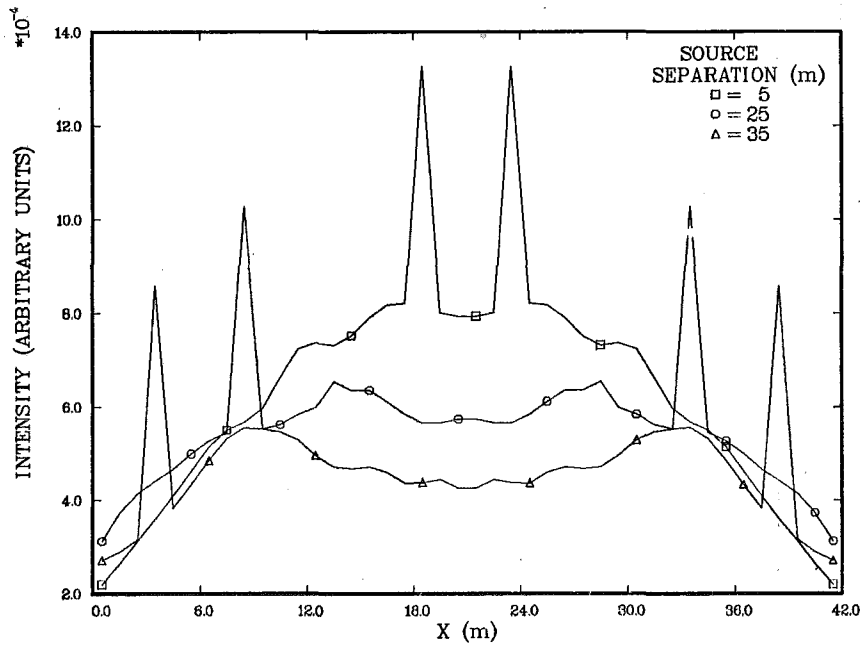


FIGURE 8. ANGULAR INTENSITY NORMAL TO THE X-AXIS AS A FUNCTION OF X for three different source separations. $\tau = 2$, $w = 0.9999$, $g = 0.9$.

MODEL AEROSOL OPTICAL DEPTH = 4.00
ALBEDO = .9999 ASYMMETRY FACTOR = .9000

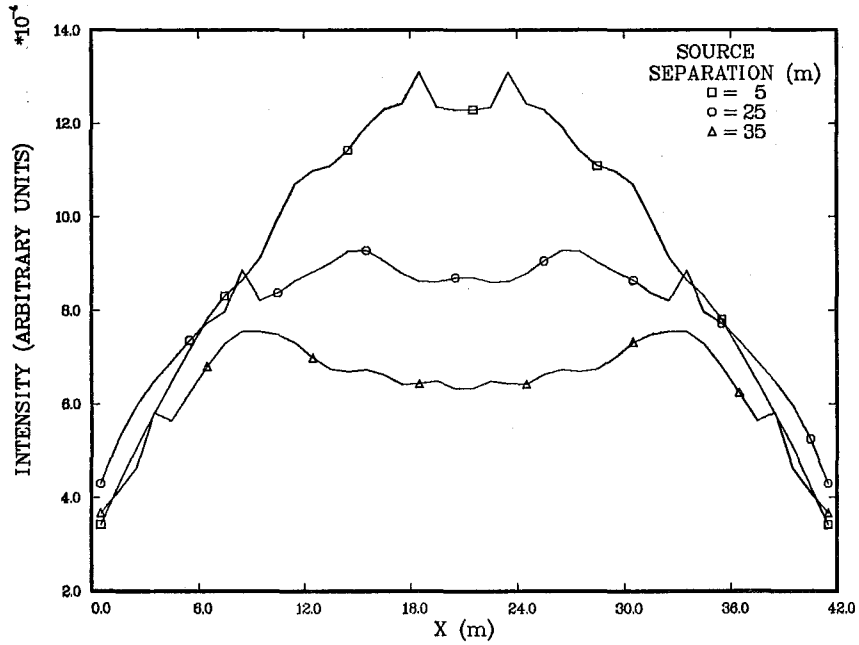


FIGURE 9. ANGULAR INTENSITY NORMAL TO THE X-AXIS AS A FUNCTION OF X. $\tau = 4$, $w = 0.9999$, $g = 0.9$.

MODEL AEROSOL OPTICAL DEPTH = 8.00
ALBEDO = .9999 ASYMMETRY FACTOR = .9000

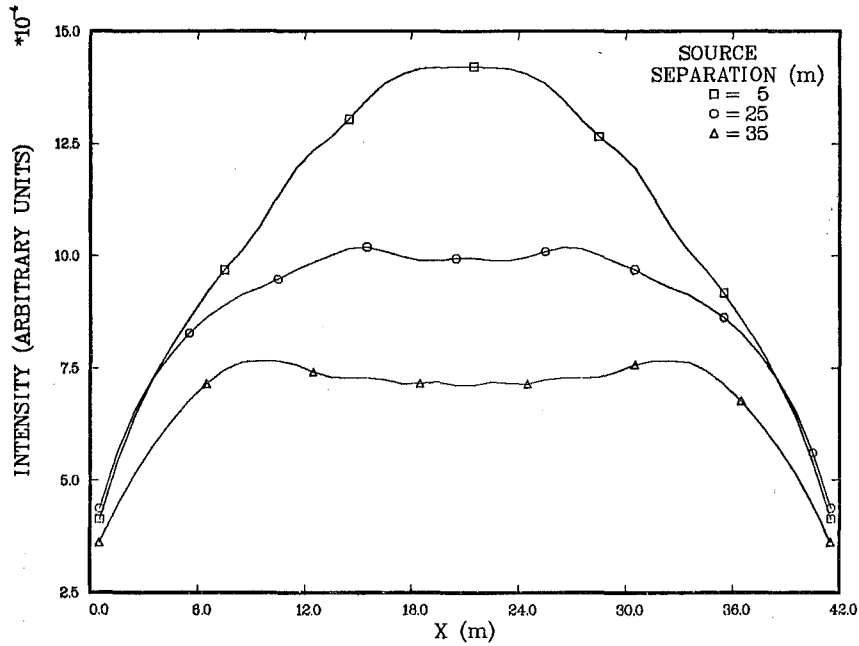


FIGURE 10. ANGULAR INTENSITY NORMAL TO THE X-AXIS AS A FUNCTION OF X. $\tau = 8$, $w = 0.9999$, $g = 0.9$.

BLANK

COMPUTATION OF RADIATIVE TRANSFER

Peter C. Waterman
Jeanne C. Pedersen
Norman E. Pedersen

Panametrics, Inc.
221 Crescent Street
Waltham, MA 02254

A simple and versatile computer program has been developed for evaluating radiative transfer by slab regions containing absorbing/scattering particles. Innovations over existing methods include a new technique for obtaining starting values in the doubling method and complete flexibility in choosing the angular discretization. Methods for treating individual particle scattering inputs are described, and some results are shown.

INTRODUCTION

With the support of the Chemical Systems Laboratory, Panametrics is engaged in a program involving radiative transfer (RT) computations. The purpose of the work is two-fold. First, we are developing a simple, efficient computer program to handle the numerical computation of radiative transfer in slabs for a wide range of scattering/absorbing particle parameters. Second, we are integrating the RT program with a computer program that treats the scattering and absorption specifically by lossy conductive fibers in order to determine the overall electromagnetic behavior of such configurations.

The basic RT theory has been described earlier.^{1,2} Essentially, we are using the van de Hulst doubling method with a Taylor series representation for the starting (thin-layer) values of the transmission and reflection matrices including up to fourth-power terms in the optical depth. This innovative treatment of starting values enables us to avoid the cumulative error build-up incurred when one begins with infinitesimal starting layer thicknesses.

As described below, the details of the interfacing problem have been worked out and programmed allowing us to input the results of the conductive fiber computation (or other quite general single scatterer results) to the RT program. A plotting routine has also been developed which gives the angular radiation patterns reflected and transmitted.

ANALYTICAL CONSIDERATIONS

The basic single-particle inputs needed to the RT program are the albedo

$$a = \frac{\text{scattering cross-section}}{\text{extinction cross-section}}, \quad (1)$$

and the phase function $p_0(\mu, \mu')$, obtained by simply integrating the scattered power $p(\mu, \theta; \mu', \theta')$ over all azimuths θ, θ' . Here $\mu = \cos \theta$ and θ are the angles of incidence and $\mu' = \cos \theta', \theta'$ the angles of observation.

There are two ways of proceeding depending on whether or not analytical expressions are available for the phase function. The two simplest analytical cases are

$$p_0(\mu, \mu') = 1 \quad (\text{Isotropic}) \quad (2)$$

and

$$p_0(\mu, \mu') = \frac{3}{4} \left[1 + \mu^2 \mu'^2 + \frac{1}{2} (1 - \mu^2)(1 - \mu'^2) \right], \quad (\text{Rayleigh}) \quad (3)$$

the latter being appropriate for small conducting particles with unpolarized incident radiation. These cases are useful for verifying the validity and accuracy of the computer program; numerical results are readily available for them in the literature.

In the absence of analytical expressions the phase function must be handled in tabular form. Following Ishimaru,³ this is done as follows. For inputs we employ the single-scatterer intensities $S(\mu_i)$ evaluated at $(3s + 1)$ equally-spaced points in μ . The reflection and transmission matrices R and T will each have dimensions $(3s + 1)/2 \times (3s + 1)/2$. Note that $S(\mu)$ represents the scattered intensity averaged over all scatterer orientations for incidence in the direction $\mu = \mu_1 = 1$ (the forward direction).

The phase function can now be determined from

$$p_0(\mu, \mu') = \sum_{m=0}^M W_m P_m(\mu) P_m(\mu'), \quad (4)$$

in terms of the Legendre polynomials P_m . The latter are determined in standard fashion

using a recursion sub-routine based on the formulas

$$P_0 = 1$$

$$P_1 = \mu ,$$

and

$$P_{m+1}(\mu) = \left(\frac{1}{m+1}\right) [(2m+1)\mu P_m(\mu) - m P_{m-1}(\mu)] . \quad (5)$$

The constants W_m are given by

$$W_m = \left(\frac{2}{2m+1}\right) \int_{-1}^{+1} d\mu P_m(\mu) S(\mu) , \quad (6)$$

and the summation of Eq. (4) is terminated when the W_m become negligible. The integral of Eq. (6) is approximated using Simpson's 3/8 rule:

$$\int_{-1}^{+1} d\mu f(\mu) \doteq (3h/8) [f(\mu_1) + 3f(\mu_2) + 3f(\mu_3) + 2f(\mu_4) + 3f(\mu_5) + \dots + f(\mu_{3s+1})] , \quad (7)$$

with grid spacing $h = 2/3s$.

The doubling method can now be applied to obtain the reflection and transmission matrices for layers of any desired optical length. In order to obtain physical results, matrix elements must then be weighted appropriately to allow for the specific quadrature rule employed. If we define normalizing constants

$$c(n) \equiv (a_n \mu_n)^{1/2} , \quad n = 1, 2, \dots, \frac{1}{2}(3s+1) , \quad (8)$$

where the a_n are the 3/8-rule weighting coefficients, then the net fluxes reflected in the back hemisphere, or transmitted in the forward hemisphere, are given respectively by

$$\bar{R} = \frac{1}{c(1)} \sum_{n=1}^{\frac{1}{2}(3s+1)} R(n,1) c(n) \quad (9)$$

$$\bar{T} = \frac{1}{c(1)} \sum_{n=1}^{\frac{1}{2}(3s+1)} T(n,1) c(n) .$$

These equations are for radiation incident normally on the slab which explains why only the first columns of R and T are needed. For isotropically incident radiation, all elements of R and T would come into play.

For the angular intensity patterns, on the other hand, one has

$$\begin{aligned}\hat{R}(n) &= R(n,1)/2c(1)c(n), \\ \hat{T}(n) &= T(n,1)/2c(1)c(n), \quad n = 1, 2, \dots, \frac{1}{2}(3s+1).\end{aligned}\tag{10}$$

NUMERICAL RESULTS

A plotter routine has been developed for the reflected and transmitted intensity patterns, and some typical results will now be shown for normal incidence on slabs of optical thickness x .

In Fig. 1 angular patterns are shown versus observation direction $\mu = \cos \theta$ for lossless isotropic scatterers. For this case $s = 9$, and R and T are of dimension 14×14 . Note that our quadrature scheme avoids the equatorial plane $\mu = 0$ where analytical difficulties arise (the curves are easily extrapolated if desired, however). In the transmitted patterns the coherent field, that portion of the originally incident beam which has survived, is represented by a discrete version of the delta function (sharply rising curves near $\mu = 1$, truncated at unit intensity for clarity). As was observed earlier² these results, including the discrete delta function contribution, exactly satisfy energy balance constraints.

The same computation is carried out in Fig. 2, but for much coarser grid spacing (matrix dimension 5×5). Aside from the obvious change in the discrete delta function contribution, these curves are seen to be effectively identical with those of Fig. 1. This demonstrates the stability of the computer program with respect to grid spacing at least for this simple case and also confirms the ease with which grid spacing can be adjusted to fit the problem at hand.

In Figs. 3 and 4 (albedo = 0.8, 0.5 respectively) losses are introduced with

corresponding reduction in the intensities. For all of these results, checks with the numerical tables of van de Hulst⁴ give excellent agreement.

Figures 5, 6 and 7 show the intensity distributions obtained using the Rayleigh phase function of Eq. (3) and albedos of 1.0, 0.8, . 0.5. Note that there is not too much difference from the isotropic case. The Rayleigh case differs in that single-particle scattering is now more concentrated in the forward and back directions. In terms of scattering angle γ , the single-particle intensity is given by³

$$\frac{3}{4} (1 + \cos^2 \gamma). \quad (11)$$

The effect of this is evident when one compares the reflection curves, which have become relatively somewhat larger in the back direction ($\mu = -1$), although not much change has occurred in the transmission curves.

DISCUSSION

The RT computer program is now effectively completed. The procedure described above for dealing with the conductive fiber case has been programmed although results are not yet available because the fiber computation itself is presently undergoing further refinements.⁵ A documented version of the RT program will be made available by the end of the present contract year.

REFERENCES

1. P. C. Waterman, Matrix-exponential description of radiative transfer, J. Opt. Soc. Am. 71, 410-422 (1981).
2. Norman E. Pedersen, Peter C. Waterman, and Jeanne C. Pedersen, Final Report on Theoretical Investigation of Absorptive Properties, Panametrics, Inc., December 21, 1982.
3. A. Ishimaru, Wave Propagation and Scattering in Random Media (Academic Press, New York, 1978), Vol. 1, p. 205.
4. H. C. van de Hulst, Multiple Light Scattering (Academic Press, New York, 1980), Vol. 1, Table 12.
5. Jeanne C. Pedersen, Norman E. Pedersen, and Peter C. Waterman, Electromagnetic theory of scattering and absorption from finite elongated objects, these Proceedings.

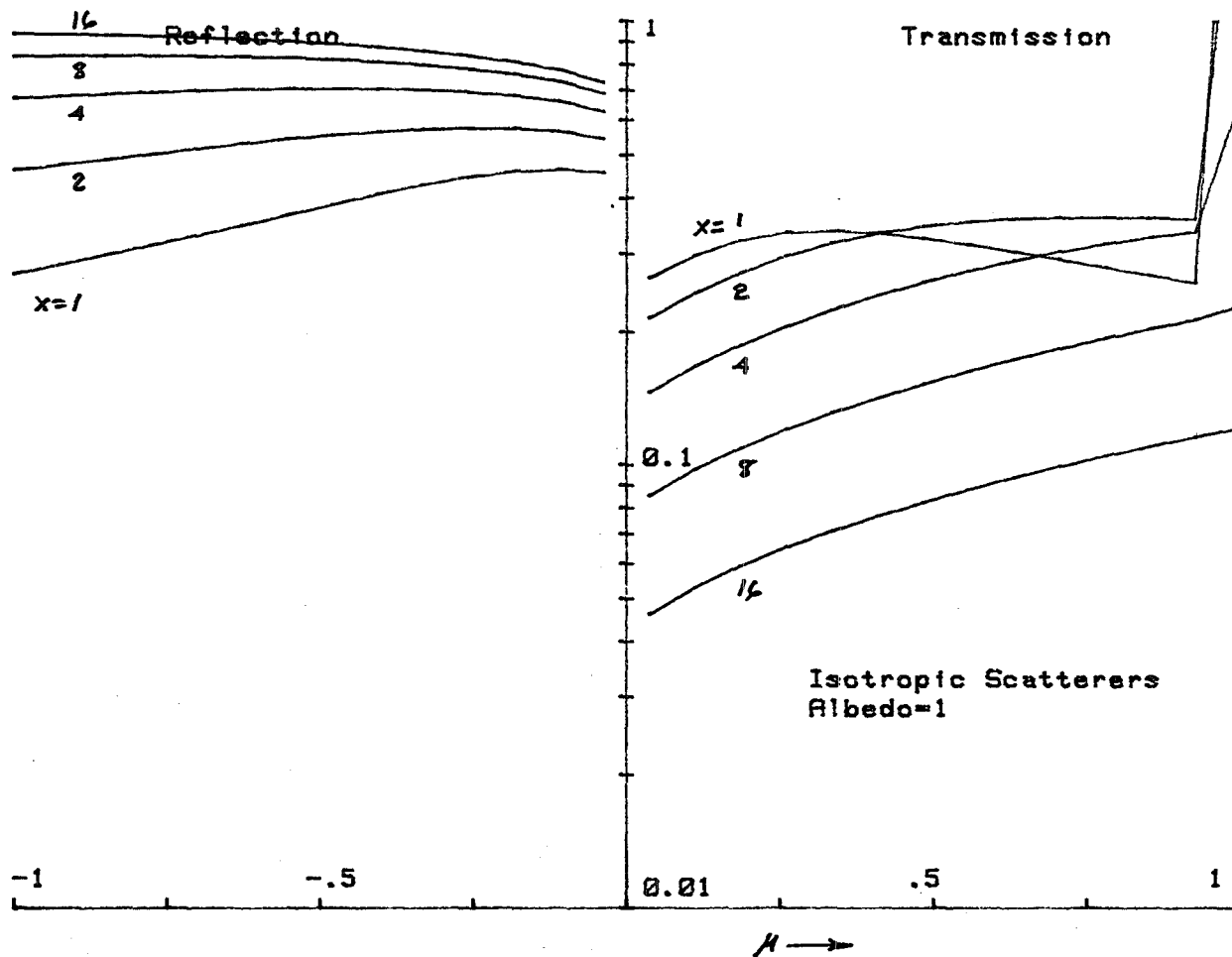


FIGURE 1. REFLECTED AND TRANSMITTED INTENSITIES. Plots versus observation angle $\mu = \cos \theta$ for several optical depths x .

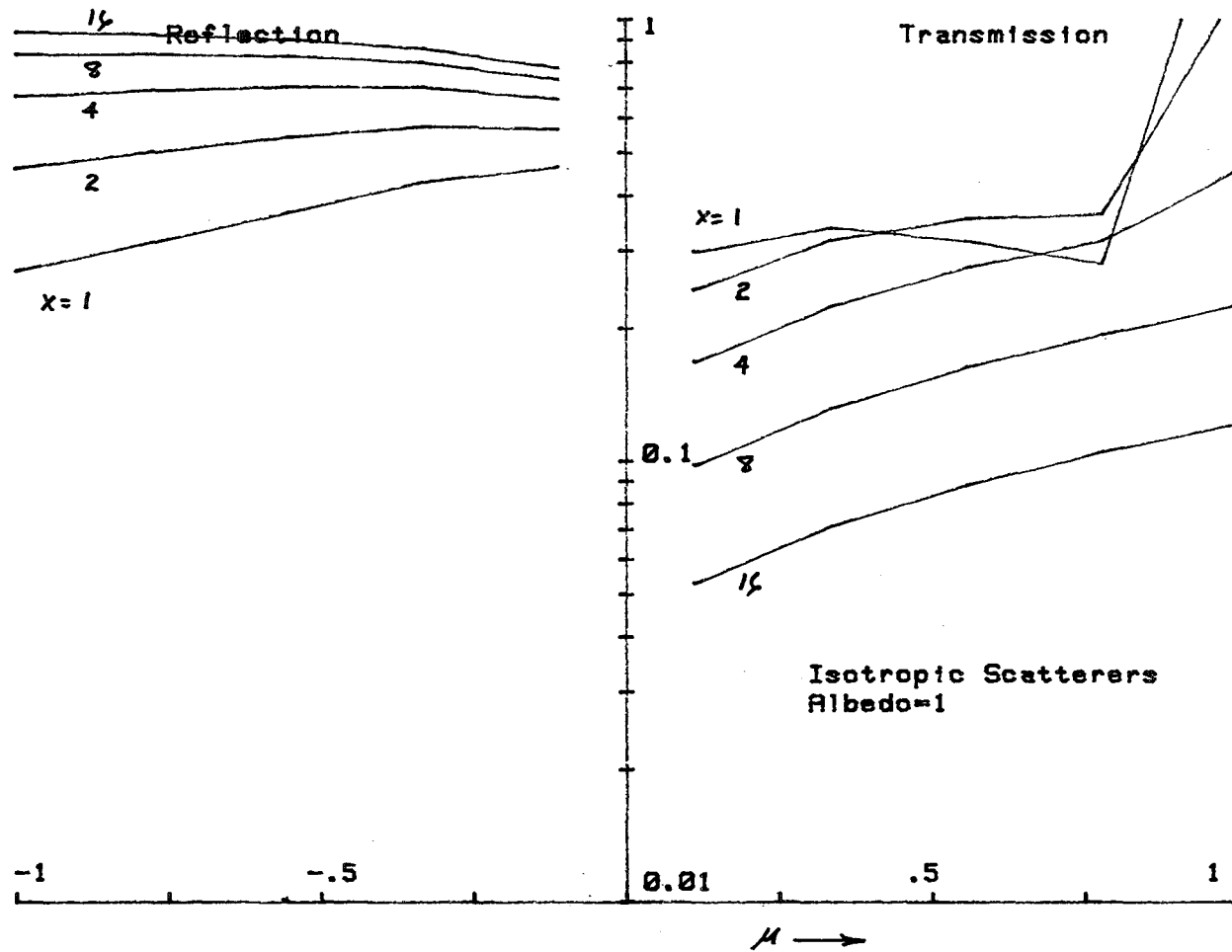


FIGURE 2. REFLECTED AND TRANSMITTED INTENSITIES. Coarse discretization is evident here.

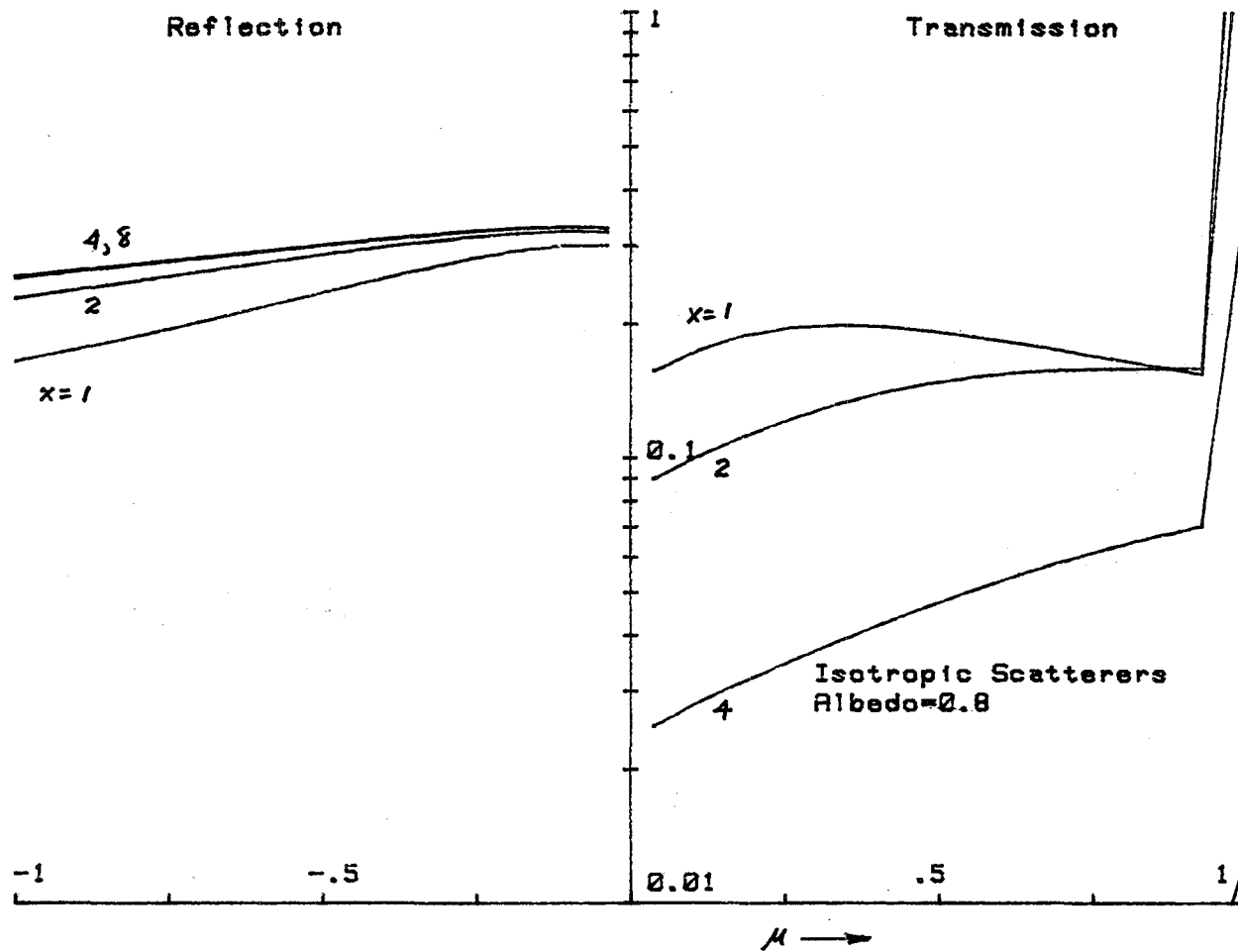


FIGURE 3. REFLECTED AND TRANSMITTED INTENSITIES. Results with moderate losses present.

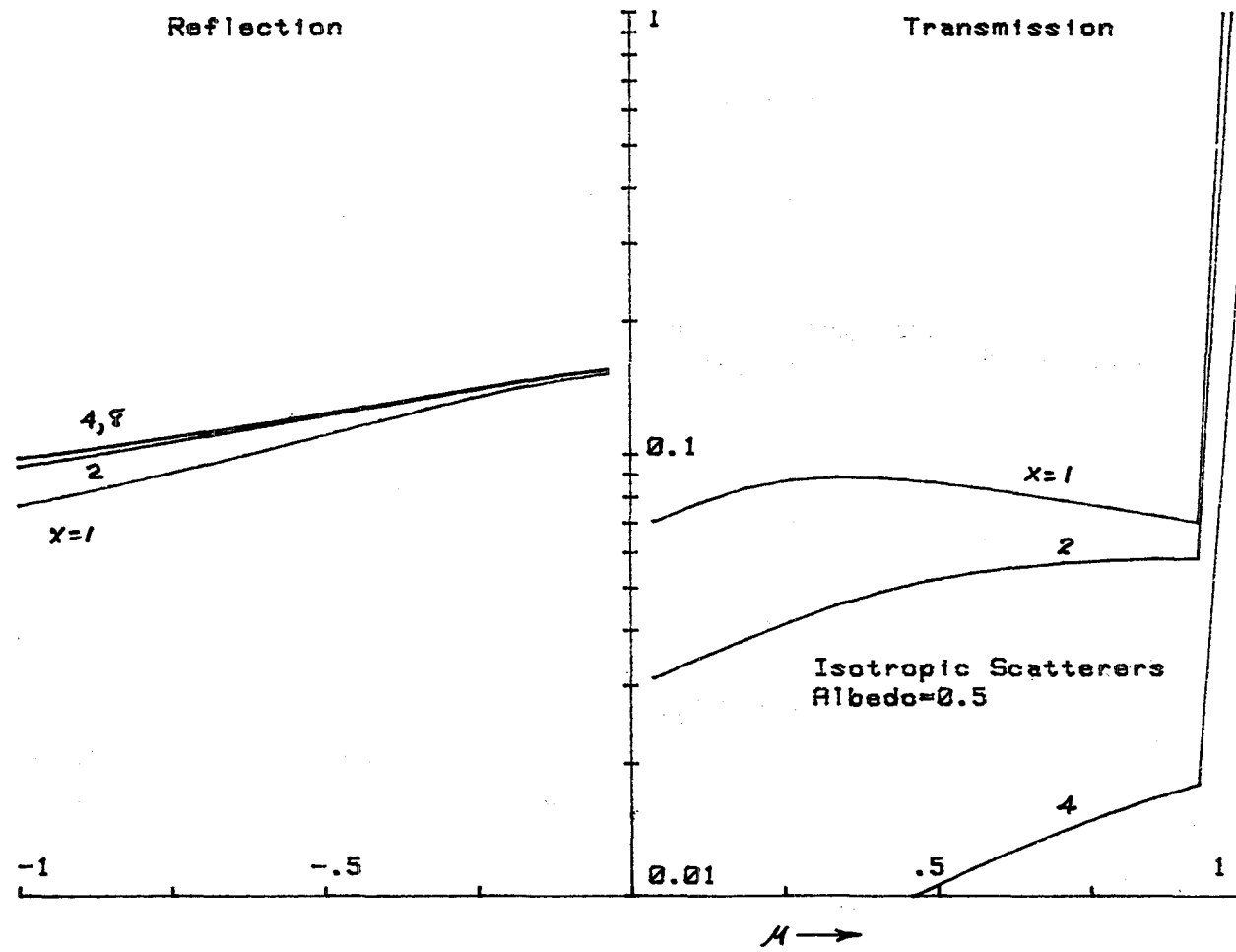


FIGURE 4. REFLECTED AND TRANSMITTED INTENSITIES. For this case the single-particle scattering and absorption cross-sections are equal.

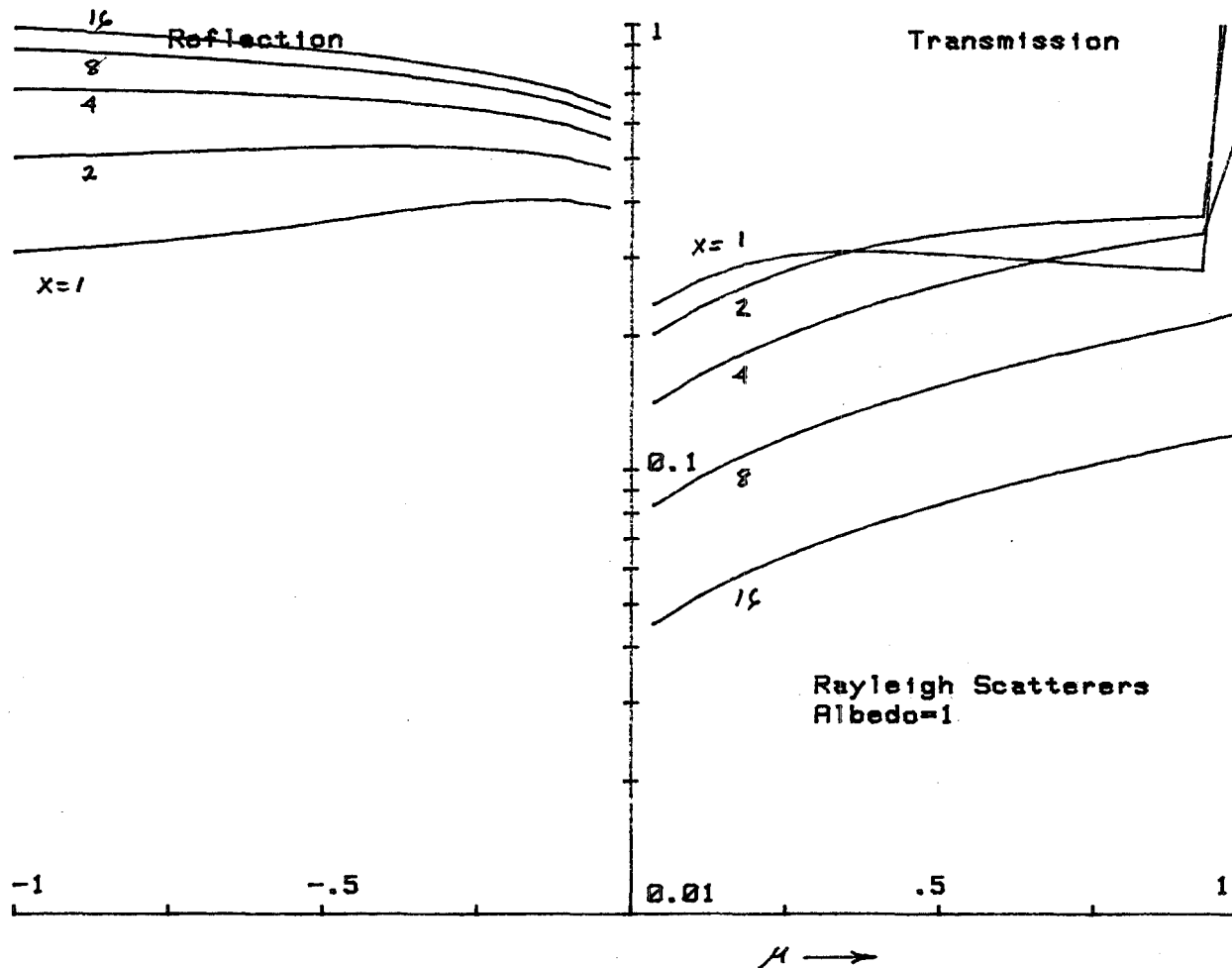


FIGURE 5. REFLECTED AND TRANSMITTED INTENSITIES. Results for lossless Rayleigh scatterers.

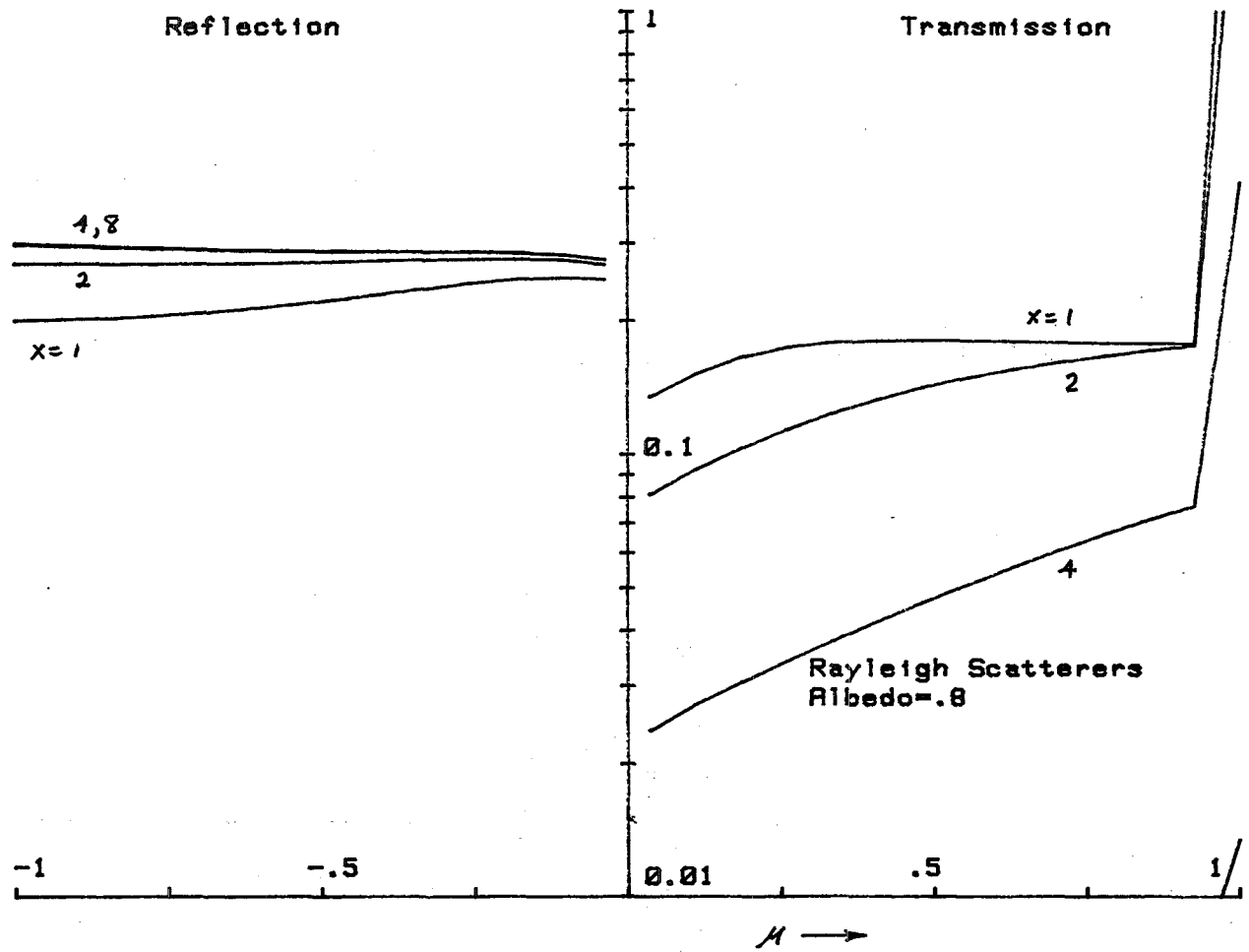


FIGURE 6. REFLECTED AND TRANSMITTED INTENSITIES. Rayleigh scatterers with moderate loss.

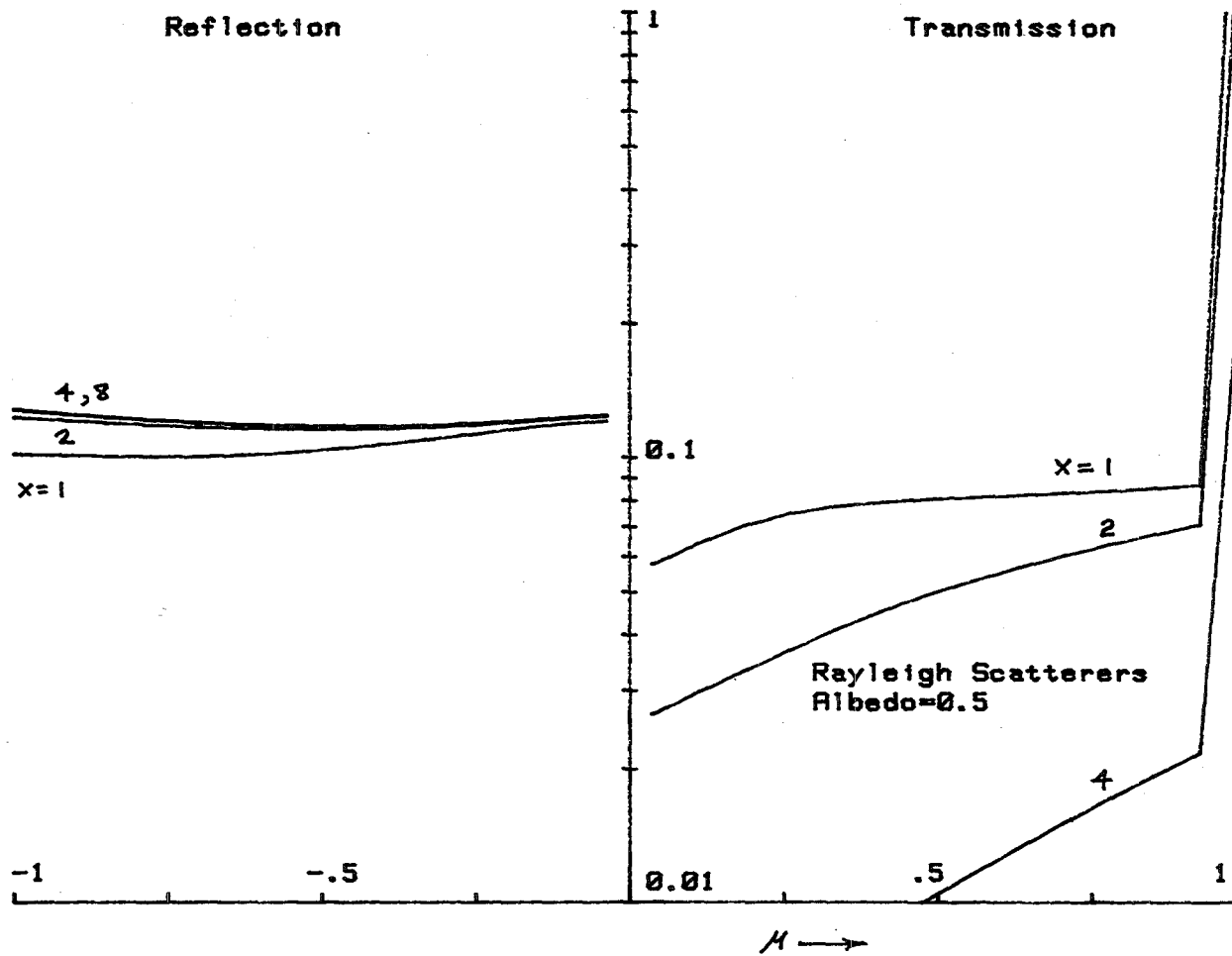


FIGURE 7. REFLECTED AND TRANSMITTED INTENSITIES. Rayleigh scatterers with equal scattering and absorption cross-sections.

MULTIPLE SCATTERING OF OPTICAL PULSES IN SCALE MODEL CLOUDS

Richard A. Elliott
Oregon Graduate Center
Beaverton, Oregon

Experiments to measure pulse stretching, delay and attenuation of optical pulses due to multiple scattering have been performed on systems which are in effect scale model clouds. The plane parallel geometry of the idealized scattering system is illustrated in Fig. 1 and some predicted relationships between the scattered optical pulse parameters and the properties of the scattering medium are listed in Fig. 2.

The scattering media used in these experiments were emulsions of either mineral oil or diiodomethane (DIM) in water stabilized with lauryl sulphate as a surfactant. The latter is of particular interest since the relative index of refraction, $1.74/1.33 = 1.30$, is nearly that of water in air and thus simulates scattering in clouds and fog. The preparation technique involved forming a coarse emulsion passing it through uclepore filters to refine the droplet size distribution and finally exploiting the differential drift velocity under the influence of gravity of droplets of different radii to further reduce the variance of the size distribution. It is practical by this means to produce tens of liters of the scattering medium with well-controlled parameters.

The parameters determining the single scattering characteristics of these emulsions have been determined from direct measurement of the index of refraction of the liquids and the size distribution of the droplets. The diameter of the droplets was obtained by drawing samples from the scattering media taking microphotographs at 400X and measuring the size of the images. Since the volume of the sample viewed under the microscope was known, the number density of the scatterers and the complete size distribution could be constructed (Fig. 3). The mean and standard deviation of the droplet diameters of the systems studied ranged from $d = 1.86 \mu\text{m}$, $\sigma_d = 0.85 \mu\text{m}$ to $d = 13.1 \mu\text{m}$, $\sigma_d = 3.6 \mu\text{m}$. The number density of the scatterers ranged from 1.7×10^{12} to $8.8 \times 10^{13} \text{ m}^{-3}$.

The mean scattering cross section, the mean of the cosine of the scattering angle and the average single scatter albedo were calculated using a computer code for Mie scattering for each of the prepared emulsions. The albedo for all the oil/water systems is unity to six significant figures while for the DIM/water system the lowest calculated albedo was 0.99926. The inverse of the mean scattering cross section times the number density is the optical mean free path, $b = (N\sigma_s)^{-1}$. For the systems studied, b ranged from 0.45 to 3.42 mm. The asymmetry factor $g = 1 - \langle \cos \theta \rangle$ ranged from 0.061 to 0.171. The range of cross sections and number densities available enabled measurements to be made on systems whose optical thickness varied from 0.1 to 160 all in a scattering cell 12 cm long and 40 cm in

diameter (see Fig. 4).

The multiple scattering experiments performed involved the measurement of the time delay, stretching and attenuation of 532 nm laser pulses initially of 25 ps duration with a Hamamatsu C979X streak camera. The pulses were produced by frequency doubling the output of a passively modelocked Nd:YAG laser as illustrated in Fig. 5. Figure 6 shows a typical streak camera record for a pulse transmitted through 1.2 cm of DIM/water emulsion and Fig. 7 shows a similar event but in this case the path is 4.2 cm.

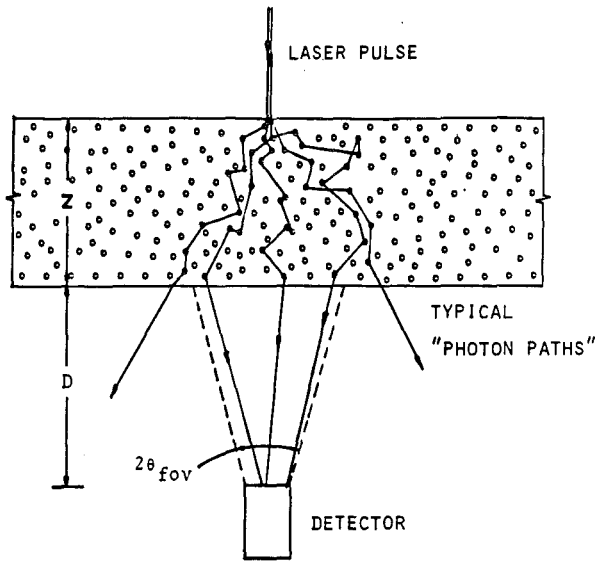
Figures 8 and 9 show least square fits of a two-gamma distribution form, $A\exp(-at)+B\exp(-bt)$, to pulses scattered through optical thicknesses of 167 and 107 respectively.

The measured delay in the mean time of arrival as a function of optical thickness for one oil/water and two diiodomethane/water emulsions is shown in Fig. 10 while the measured pulse stretching for four oil/water emulsions is displayed in Fig. 11. All of the oil/water results gave relatively poor agreement with the theoretical predictions. This is probably due to the extreme degree of forward scattering: $g = 0.08$ compared to $g = 1.5$ for the diiodomethane emulsions.

The relative energy of the scattered pulses for four diiodomethane systems is plotted against optical thickness in Fig. 12. The functional dependence agrees rather well with the theory but the constant of proportionality is off because the geometry of the experiment is not the same as that assumed for the theoretical calculations.

Some measurements of beam spreading were also made using a cw Argon ion laser (514 nm). Figure 13 shows the irradiance profile at the exit window of the scattering cell for several different optical thicknesses of an oil/water emulsion and Fig. 14 displays the measured half-power points measured from these curves plotted against optical thickness.

The results presented here are reported in more detail in an article published under the same title in Applied Optics Vol. 22, pp. 2670-2681 (1983).



Due to multiple scattering:
 mean path length, $\bar{L} > Z + D$,
 variance, $(L - \bar{L})^2 > 0$,
 beam radius, $R_z \gg R_0$,
 received energy, $E_z \ll E_0$

FIGURE 1.

Theoretical Predictions for Optically Thick Media
 (Monte Carlo simulations and/or analytic approximations)

Laser pulse delay,

$$\Delta t = (L - Z - D)/C$$

$$= 0.62 b g^{0.9} \tau^{1.9} c^{-1}.$$

RMS laser pulse width

$$\sigma_t = 0.64 b g^{0.8} \tau^{1.8} c^{-1}$$

Pulse energy

$$E_t = 1.69(g\tau + 1.42)^{-1} E_0$$

Beam radius

$$R_t = 0.78 b g^{-0.07} \tau^{0.93}$$

with $b = (N \sigma_s)^{-1}$ - scattering length

N - number density

σ_s - average scatter cross section

$\tau = z/b$ - optical thickness

Z - geometric thickness

$g = 1 - \overline{\cos\theta}$, $\overline{\cos\theta}$ - average scattering angle

FIGURE 2.

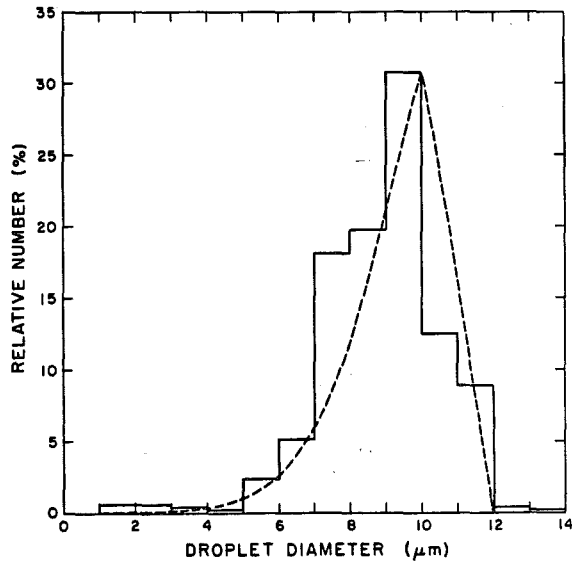
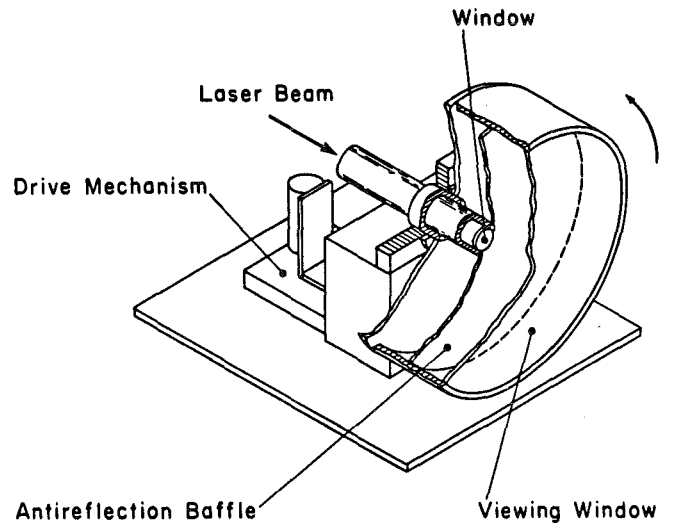


FIGURE 3. SIZE DISTRIBUTION HISTOGRAM. The dashed line is the theoretical distribution. The measured mean diameter and standard deviation are 9.39 and 1.69 μm compared to the predicted values of 9.32 and 1.30 μm , respectively. A total of 802 droplet diameters was measured on 400X micrographs of samples of the emulsion.



Scattering Cell

FIGURE 4. SCATTERING CELL. The cylinder rotates at a constant speed of 1 rpm to prevent the emulsion droplets from collecting at the top or bottom. The distance between the entrance and exit windows is variable between 0.2 and 11.7 cm. All interior surfaces are flat black to reduce reflection of escaping radiation back into the scattering medium.

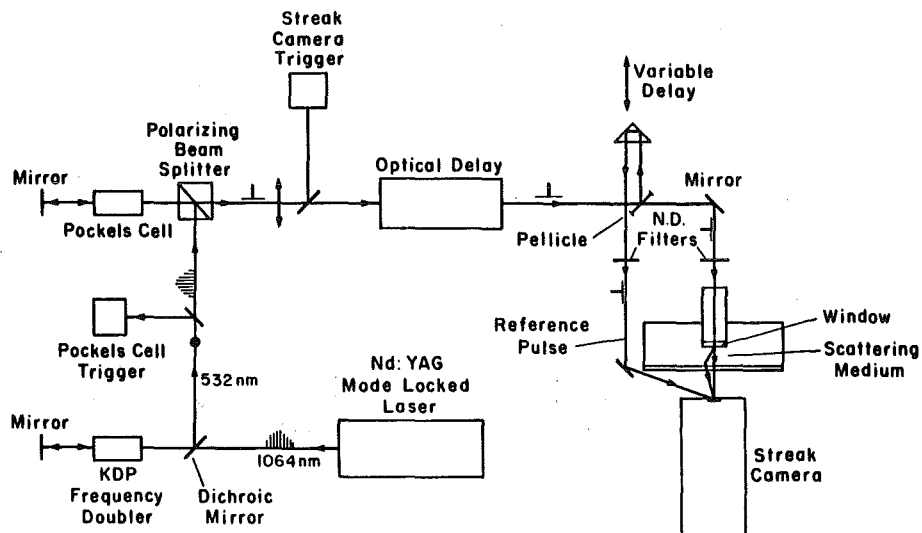


FIGURE 5. Schematic layout of the optical system.

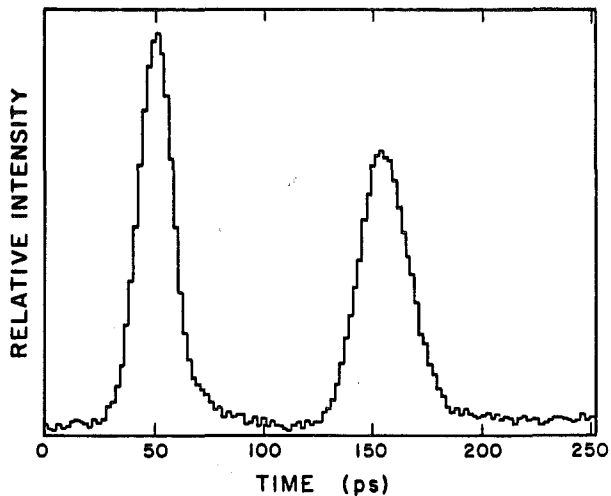


FIGURE 6. Typical intensity vs time streak camera record. The left-hand pulse is the reference, and the right-hand is the pulse which has passed through the scattering medium. Optical thickness $\tau = 18$.

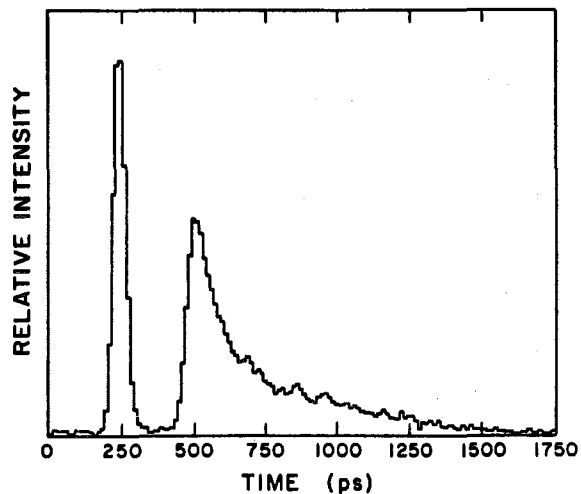


FIGURE 7. Typical intensity vs time streak record. The left-hand pulse is the reference, and the right-hand is the pulse which has passed through the scattering medium. Optical thickness $\tau = 63$.

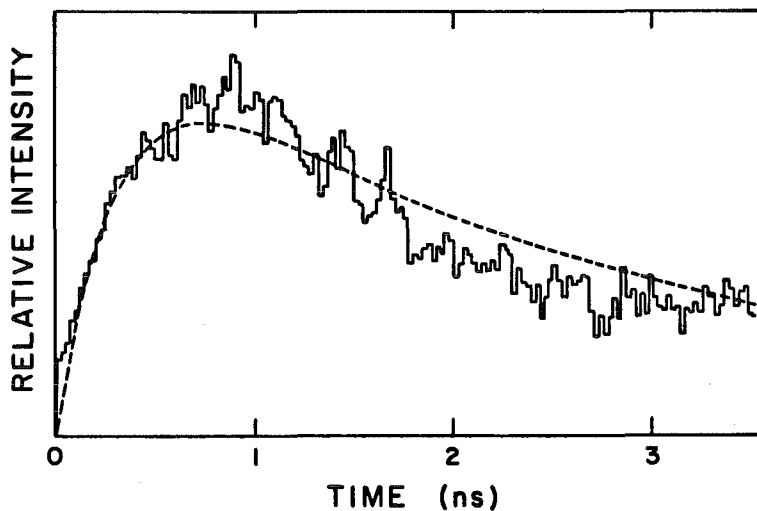


FIGURE 8. Least squares fit of two-gamma distribution function form to pulse scattered by 167 optical thicknesses of diiodomethane emulsion: ---, $0.94t \exp(-1.94t) + 0.27t \exp(-0.60t)$, t in nanoseconds.

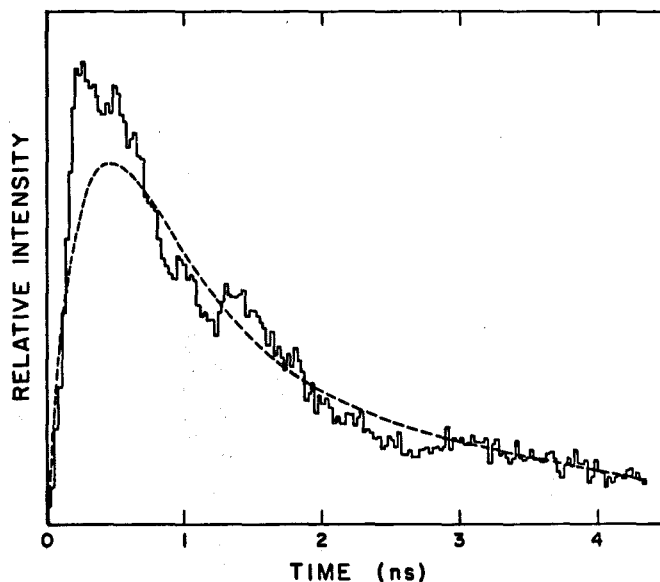


FIGURE 9. Least squares fit of two-gamma distribution function form to pulse scattered by 107 optical thicknesses of paraffin oil emulsion: ---, $3.28t \exp(-2.78t) + 0.34t \exp(-0.77t)$, t in nanoseconds.

- ◇ : oil/water, $b = 1.27$ mm, $g = 0.078$
- △ : diiodomethane/water, $b = 0.454$ mm, $g = 0.142$
- : diiodomethane/water, $b = 0.389$ mm, $g = 0.171$

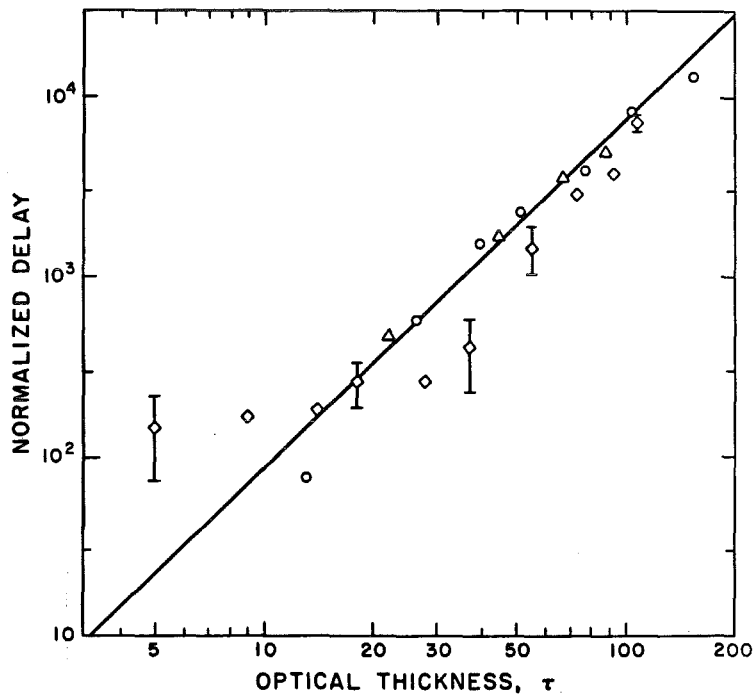


Figure 10. Delay in the mean arrival time due to multiple scattering vs optical thickness. Measured delay times have been normalized by multiplying by $cb^{-1}g^{-0.94}/0.62$. The line is $\tau^{1.94}$.

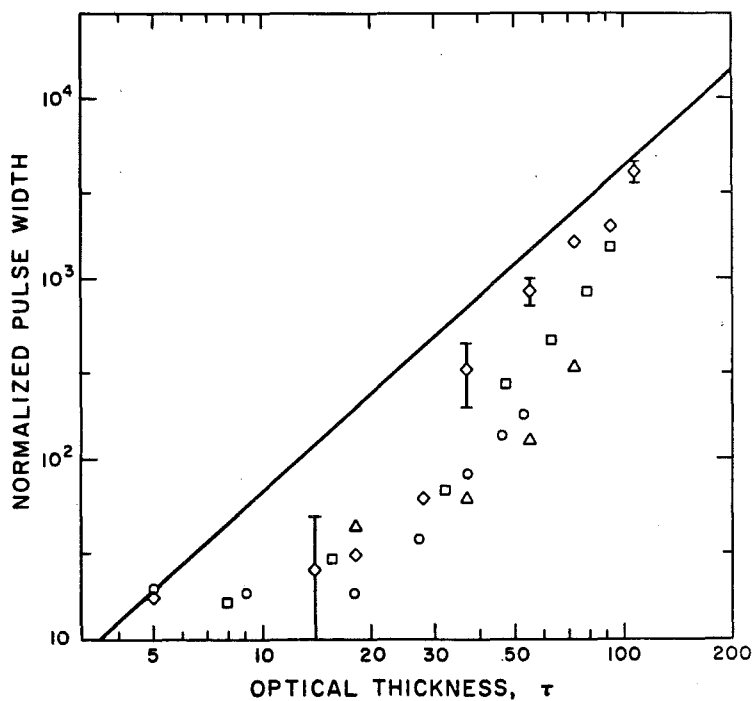


FIGURE 11. Pulse stretching normalized by multiplication by $cb^{-1}g^{-0.81}/1.28$ vs optical thickness for paraffin oil emulsions. The line is $\tau^{1.81}$.

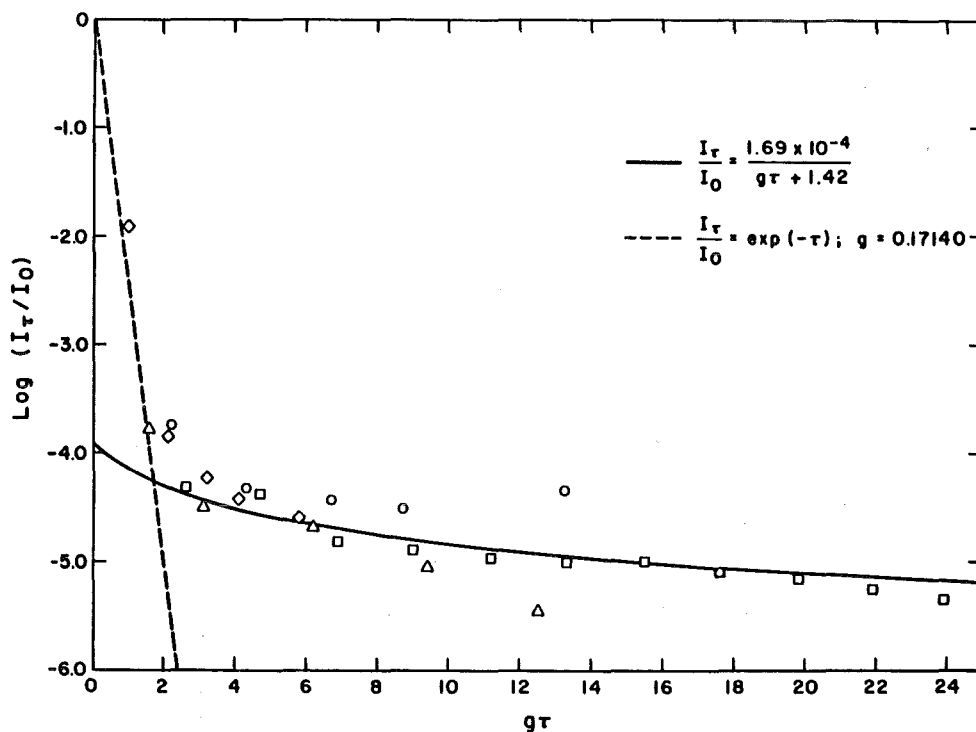


FIGURE 12. Logarithm of the relative integrated intensity of scattered pulses vs optical thickness times the asymmetry factor for diiodomethane emulsions.

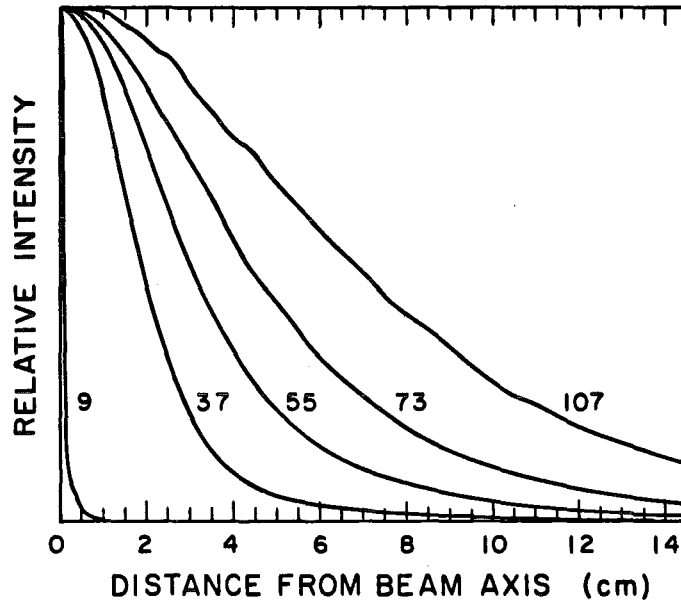


FIGURE 13. Profiles of the irradiance at the exit window of the scattering cell for the optical thicknesses indicated on the curves for a paraffin oil emulsion.

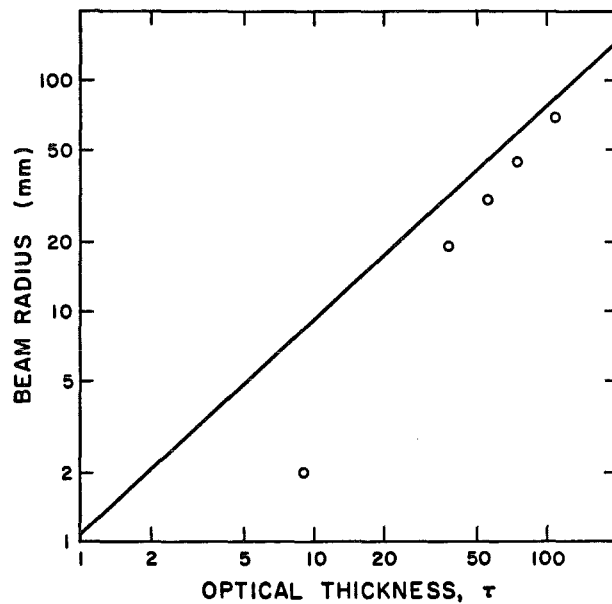


FIGURE 14. Beam radius vs optical thickness as measured from the half-power points on the profiles displayed above. The line $r = 0.78bg^{-0.7}\tau^{0.93}$.

INDEXES FOR PAPERS IN THESE PROCEEDINGS

Index	Page
A	Index of Authors 377
B	Index of Authors' Organizations. 379

BLANK

INDEX A
INDEX OF AUTHORS
OF PAPERS IN THESE PROCEEDINGS

Adams, R. L. 249
Alexander, R. W., Jr. 159, 161
Andreo, R. H. 257
Ase, P. 185
Auckland, D. T. 257

Bahar, Ezekiel 215
Balog, P. P. 187
Bell, R. J. 159, 161
Brazell, R. S. 11
Brock, J. R. 35

Capps, C. D. 139, 249, 309
Castleman, A. W., Jr. 25
Cha, C. C. 257
Chakrabarti, Swapan 215
Chen, H. 71
Cipolla, J. W., Jr. 193
Cohen, Ariel 281, 337
Cohen, Leonard D. 281, 337
Curry, B. P. 125

Daum, Gaelen 293
Dow, R. L. 329
Dye, D. L. 329

Egert, Smadar 337
Elliott, Richard A. 367
Embury, J. F. 343

Gallily, Isaiah 49, 115
Gentry, J. W. 59
Gerstl, S. A. W. 343
Gieseke, J. A. 71
Gustafson, B. A. S. 237

Haracz, R. D. 281, 337
Hess, G. M. 139, 249, 309, 329
Holmberg, R. W. 11
Holze, D. H. 309, 329

Kerker, Milton 207, 209, 211, 213
Kiech, E. L. 125
Klett, James D. 121
Krushkal, E. M. 49

LaMuth, H. L. 187
Latham, J. 41
Lax, Melvin 191, 293
Lee, K. W. 71, 187
Long, L. L. 159, 161

Martin, J. J. 99
Möller, K. D. 141, 171
Moneyhun, J. H. 11
Morse, T. F. 193

Ordal, M. A. 159, 161
Paul, R. E. 161
Pedersen, Jeanne C. 315, 355
Pedersen, Norman E. 315, 355
Podzimek, J. 99

Querry, Marvin R. 147

Remaly, R. 185
Roberts, Daryl L. 83
Rubel, G. O. 59

Senior, B. A. 273
Snelson, A. 23, 185

Tokuda, A. R. 249
Tomaselli, V. P. 141, 171

Wang, R. T. 223, 237
Waterman, Peter C. 315, 355
Weil, H. 273

Zardecki, A. 343

BLANK

INDEX B

INDEX OF AUTHORS' ORGANIZATIONS
AND COUNTRIES (IF NOT U.S.A)
FOR PAPERS IN THESE PROCEEDINGS

- Aberdeen Proving Ground (US Army) 59, 293
AMCCOM (US Army Munitions & Chemical Command)
 Chemical Research and Development
 Center 59, 329, 343
Army, US 59, 121, 293, 329, 343
Arnold Air Force Station (US Air Force) 125
Atmospheric Sciences Laboratory (ASL)
 (US Army) 121
- Ballistic Research Laboratory (US Army) 293
Battelle
 Columbus Laboratories 71, 187
Boeing Aerospace Company 139, 249, 309, 329
Britain 41
Brown University 193
- Calspan Field Services 125
Chemical Research and Development Center (CRDC)
 (US Army) 59, 329, 343
Chemical Systems Laboratory (CSL) See Chemical
 Research and Development Center (new name
 as of July 1, 1983)
- City College of the City University of New York
 Physics Department 191, 293
Clarkson College of Technology 207, 209, 211, 213
- Drexel University
 Department of Physics and Atmospheric
 Science 281, 337
- England 41
ERADCOM (US Army Electronics Research and
 Development Command) 121
- Fairleigh Dickinson University 141, 171
Florida (see University of)
- Graduate Center for Cloud Physics Research
 (University of Missouri-Rolla) 99
- Hebrew University of Jerusalem (Israel)
 Department of Atmospheric Sciences 49, 115, 337
- Illinois Institute of Technology (IIT)
 Research Institute 23, 185
Israel 49, 115, 337
- Los Alamos National Laboratory 343
- Maryland (see University of)
Missouri (see University of)
Michigan (see University of)
- National Research Council 121,
Nebraska (see University of)
Northeastern University 193
- Oak Ridge National Laboratory 11
Oregon Graduate Center 367
- Panametrics 315, 355
Pennsylvania State University
 Department of Chemistry 25
Physics Research Laboratory (Fairleigh
 Dickinson University) 141, 171
- Space Astronomy Laboratory (University of
 Florida) 223, 237
SRI International 83
Syracuse Research Corporation 257
- Texas (see University of)
- University of Florida
 Space Astronomy Laboratory 223, 237
University of Manchester (England)
 Institute of Science and Technology 41
University of Maryland
 Department of Chemical Engineering 59
University of Michigan
 Department of Electrical and Computer
 Engineering 273
University of Missouri
 Kansas City
 Department of Physics 147
Rolla
 Department of Mechanical and Aerospace
 Engineering 99
 Graduate Center for Cloud Physics Research 99
 Physics Department 159, 161
University of Nebraska
 Lincoln
 Electrical Engineering Department 215
University of Texas
 at Austin
 Department of Chemical Engineering 35
- White Sands Missile Range (US Army) 121

BLANK

APPENDIXES

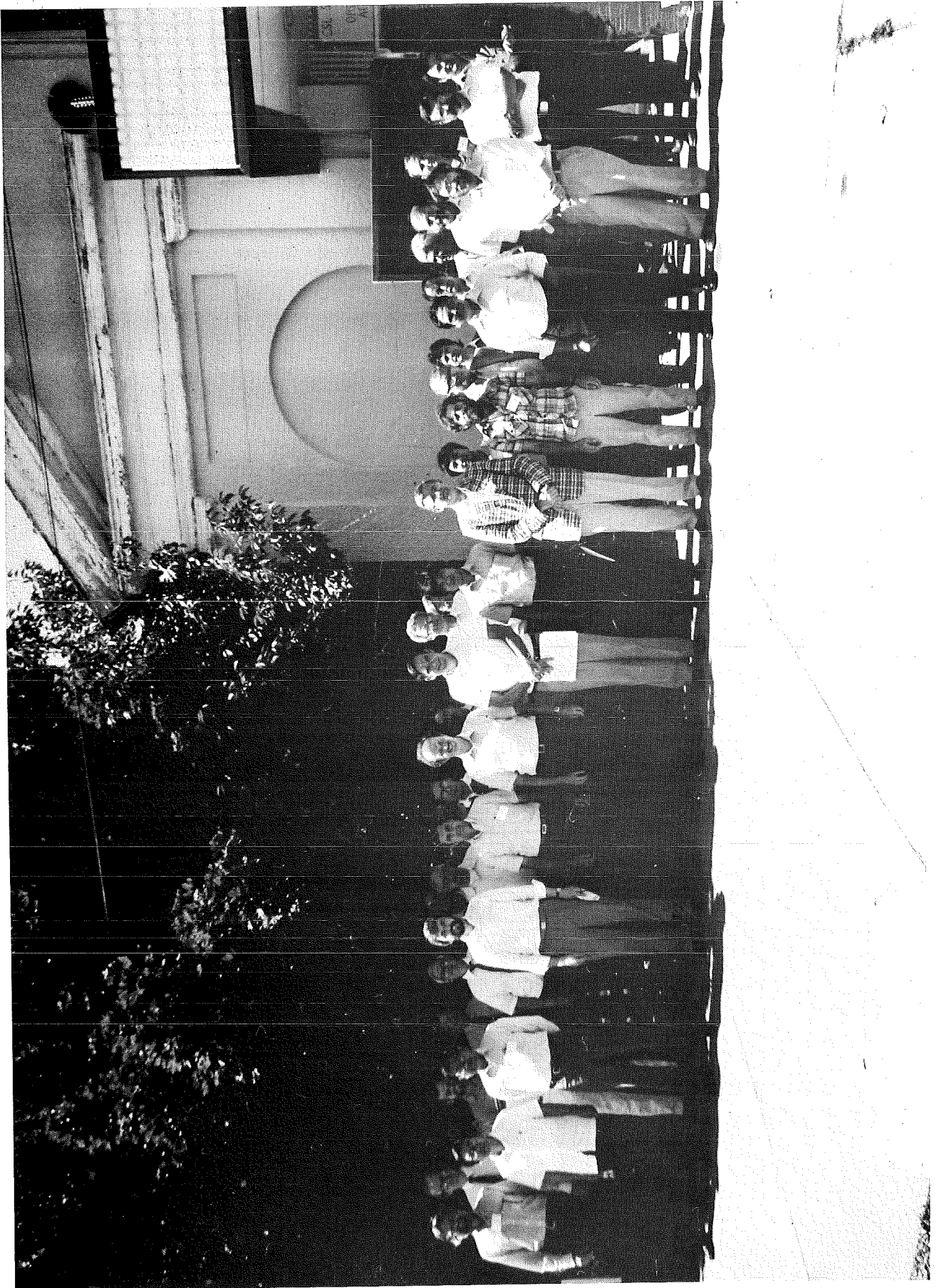
Appendix		Page
A	Photographs of Conference Attendees	383
B	List of Conference Attendees.	389
C	Conference Agenda	399
D	Contents of the Conference Sessions	401

BLANK

APPENDIX A

PHOTOGRAPHS OF CONFERENCE ATTENDEES

1983 CSL SCIENTIFIC CONFERENCE ON OBSCURATION AND AEROSOL RESEARCH



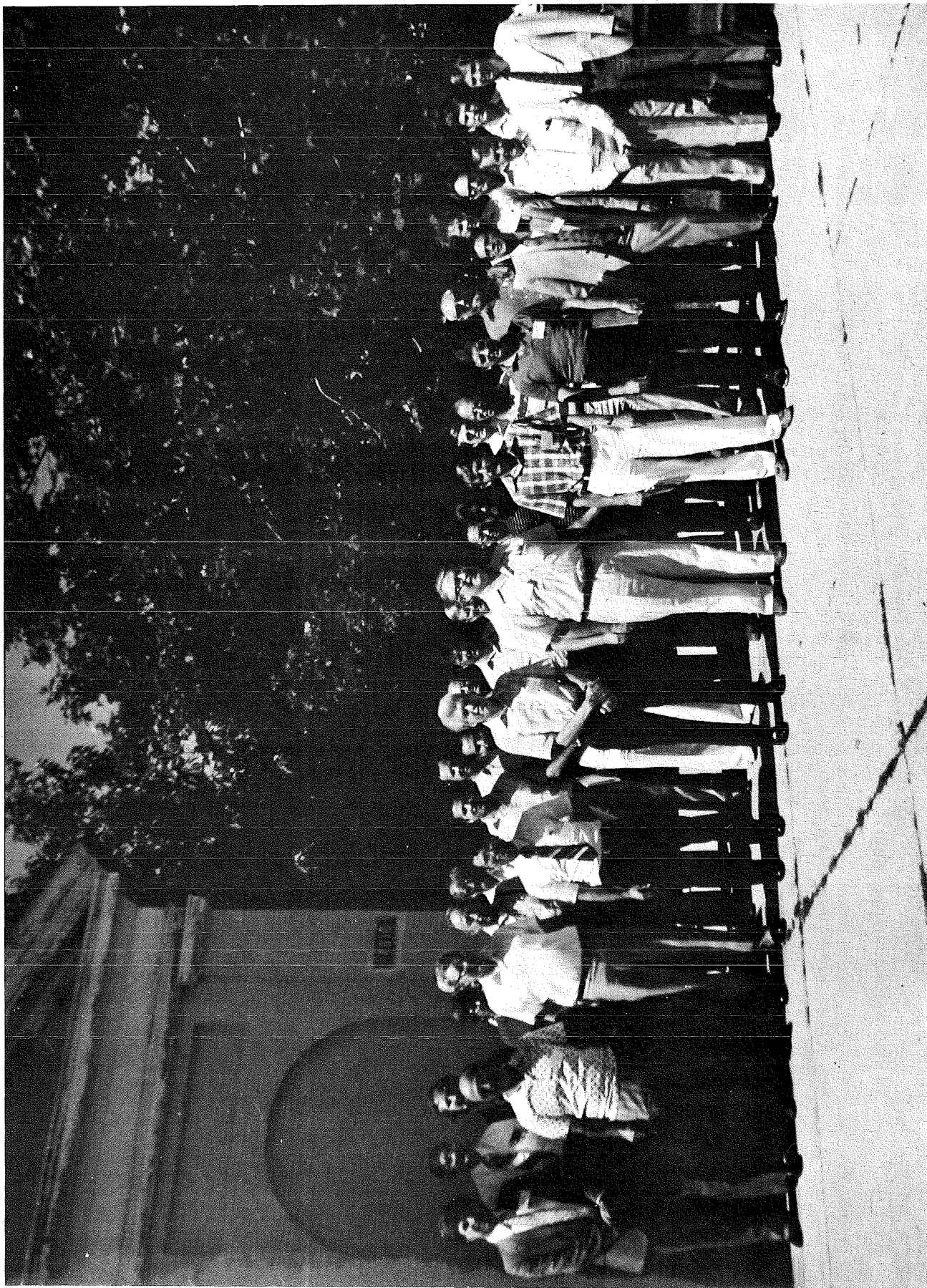
LEFT HALF (left to right)

Third Row: Brent Smith, Dave Ensor, A. Snelson, D. Capps, D. Farouhy, Richard Gleeson, Tony Pluchino, H. Massoudi, Ed Fry, Stephen Arnold

Second Row: Rolf Kluchert, Rich Pitter, Jim Wallace, Robert Frickel, Art Jordan, Al Carswell, Ming Leung, Isaiah Gallily, Ben Herman, Jim Weinman, Len Cohen

First Row: William S. Bickel, Seung Soo Hong, Paul Ase, Dwight L. Jaggard, Vincent Tomaselli, Bob Thomas, Ariel Cohen, Peter Chang, Dick Haracz, Avishay Ben-David, C. V. Mathai, Jerry Bottiger

1983 CSL SCIENTIFIC CONFERENCE ON OBSCURATION AND AEROSOL RESEARCH



RIGHT HALF (left to right)

Third Row: Bill Curry, Pete Waterman, Ed Stuebing, Irwin S. Goldberg, Roger H. Lang, Ru T. Wang, Peter Barber, Willard Wells

Second Row: David L. Dye, Robert H. Andreo, Jeanne Pedersen, Norm Pedersen, Atef Ghuniem, Hamido Saleh, Tim Rogne,
John Cipolla, Ted Morse, Bill Sedlacek, Jim Hanley, Dick Reitz

First Row: A. Coletti, J. Aronson, D. H. Holze, A. R. Tokuda, W. Weil, M. Lax, A. Gauss, R. A. Elliott,
J. C. Uhrmacher, Paul Guthals, Douglas L. Marker

Not Pictured: Ronald Kohl

BLANK

APPENDIX B

COMPLETE
ATTENDEES LIST*

1983 CSL SCIENTIFIC CONFERENCE ON
OBSCURATION AND AEROSOL RESEARCH
20-24 June 1983

ADAMS, DAN
Project Manager, Smoke Obscurants
Attn: DRCPM-SMK-T
Aberdeen Proving Ground, MD 21005
(301) 278-5411

ARONSON, JAMES R. DR.
Arthur D. Little, Inc.
15 Acorn Park
Cambridge, MA 02140
(617) 864-5770, ext. 2369

ALEXANDER, RALPH W., JR. PROF.
Physics Department
University of Missouri-Rolla
Rolla, MO 65401
(314) 341-4031 or 4878

ASE, PAUL K.
IIT Research Institute
10 W. 35th St.
Chicago, IL 60616
(312) 567-4287

ANDERSON, DAVID CSL
DRDAR-CLB-PS
phone: 2324

BAHAR, EZEKIEL DR.
Dept. of Electrical Engineering
University of Nebraska-Lincoln
Lincoln, NE 68588
(402) 488-4074

ANDREO, ROBERT H. DR.
Syracuse Research Corporation
Merrill Lane
Syracuse, NY 13210
(315) 425-5100

BARBER, PETER DR.
Dept. of Electrical Engineering
Clarkson College of Technology
Potsdam, NY 13676
(315) 268-6511

ARMSTRONG, ROBERT L. CSL
(Summer Address)
DRDAR-PLB-CS
phone:
(Permanent Address after Aug. 12)
Department of Physics, 3D
New Mexico State University
Las Cruces, NM 88003

BELL, ROBERT J.
Physics Department
University of Missouri-Rolla
Rolla, MO 65401
(314) 341-4781

ARNOLD, STEPHEN PROF.
Department of Physics
Polytechnical Institute of New York
333 Jay Street
Brooklyn, NY 11201
(212) 643-4371

BEN-DAVID, AVISHAY
3550 E. Cody
Tucson, AZ 85716
(602) 795-3708

*Entries for Chemical Systems Laboratory (CSL) personnel give the missing information indicated by xxx's in the following:

Commander/Director
Chemical Systems Laboratory
ATTN: xxxxxxxxxx
Aberdeen Proving Ground, MD 21010
AV 584-xxxx or (301) 671-xxxx

ATTENDEES LIST (continued)

BICKEL, WILLIAM DR.
 Department of Physics
 University of Arizona
 Tucson, AZ 85721
 (602) 621-2524/2534

BIRD, JOSEPH F.
 Applied Physics Lab.
 Johns Hopkins University
 Laurel, MD 20707
 (301) 953-7100, ext. 2582

BIVENZVIGE, AMNON CSL
 DRDAR-CLB-PO
 phone: 4252

BOTTIGER, JERRY CSL
 DRDAR-CLB-PS
 phone: 2395

BRADLEY, BRAD W.
 Director
 US Army Material Systems Analysis
 Activity
 Attn: DRXSY-CS
 Aberdeen Proving Ground, MD 21005
 (301) 278-6231 or AV 283-6231

BRAZELL, ROSE
 Oak Ridge National Laboratory
 P.O. Box 10
 Oak Ridge, TN 37830
 (615) 574-4870

BROCK, JAMES R. PROF.
 Dept. of Chemical Engineering
 University of Texas
 Austin, TX 78712
 (512) 471-3348

BROWN, JAMES
 Department of Physics
 Colorado School of Mines
 Golden, CO 80401
 (303) 279-0300, ext. 2835

CAPPS, C. DAVID DR.
 Boeing Aerospace Company
 P.O. Box 3999, MS 8C-23
 Seattle, WA 98124
 (206) 773-1425

CARSWELL, ALLAN I. PROF.
 Department of Physics
 York University
 4700 Keele Street
 Downsview, Ontario
 Canada
 (416) 667-3316

CASTLEMAN, A. WELFORD, JR. PROF.
 Department of Chemistry
 152 Davey Laboratory
 Pennsylvania State University
 University Park, PA 16802
 (814) 865-7242

CERMAK, J. E. DR.
 Colorado State University
 Dept. of Civil Engineering
 Ft. Collins, CO 80523
 (303) 491-6696

CHANG, PETER
 SRI International
 333 Ravenswood Ave.
 Menlo Park, CA 94587
 (415) 487-1289

CHYLEK, PETR DR.
 Physics Department
 State University of New York
 Albany, NY 12222
 (518) 457-3300

CIPOLLA, JOHN
 ME Dept. (435 LA)
 Northeastern University
 Boston, MA 02115
 (617) 437-3805

COHEN, ARIEL PROF.
 Dept. of Atmospheric Sciences
 Hebrew University
 Jerusalem, Israel
 (Summer Address)
 Dept. of Physics & Atmospheric Sciences
 Drexel University
 Philadelphia, PA 19104
 (215) 895-2707

ATTENDEES LIST (continued)

COHEN, LEN DR. Dept. of Physics & Atmospheric Sciences Drexel University Philadelphia, PA 19104 (215) 895-2710		FAROUGHY, D. Systems & Applied Sciences Corporation 1100 South Claudina Place Anaheim, CA 92805 (714) 999-1081	
COLETTI, ALESSANDRO Georgia Tech. School of Geophysical Sciences Atlanta, GA 30332 (404) 894-3891		FARRELL, RICHARD DR. Johns Hopkins University Applied Physics Laboratory Johns Hopkins Road Laurel, MD 20707 (301) 792-7800, ext. 571	
CURRY, WILLIAM MR. PWT/ATD Calspan, Inc. MS 650 Arnold Air Force Station, TN 37389 (615) 455-2611, ext. 7200 or AV 340-7200		FERRITER, JOHN M. DRDAR-CLC-B phone: 3358	CSL
DAVIDSON, S. W. Dept. of Chemical Engineering University of Maryland College Park, MD 20742 (301) 454-5098/2341		FLANIGAN, DENNIS MR. DRDAR-CLC-R phone: 3484/3884	CSL
DE KINDER, ROBERT E., JR. Project Manager, Smoke/Obscurants Attn: DRCPM-SMK-T Aberdeen Proving Ground, MD 21005 (301) 278-5411/5605 or AV 283-5411/5605		FLOOD, WALTER A. US Army Research Office P.O. Box 12211 Research Triangle Park, NC 27709 (919) 549-0641	
DIMMICK, RICHARD DRDAR-CLB phone: 2849	CSL	FRASER, ROBERT S. NASA Goddard Space Flight Center Attn: Code 915 Greenbelt, MD 20771 (301) 344-9008	
DYE, DAVID L. The Boeing Company P.O. Box 3999 MS 8C-23 Seattle, WA 98124 (206) 773-0368		FRICKEL, ROBERT DRDAR-CLB-PS phone: 3854	CSL
ELLIOTT, R. A. DR. Oregon Graduate Center 19600 N.W. Walker Road Beaverton, OR 97006 (503) 645-1121		FRITCH, WILLIAM DRDAR-CLW-CR phone: 3505	CSL
EMBURY, JANON DR. DRDAR-CLB-PS phone: 4256/2326	CSL	FROST, WALTER DR. FWG, Inc. R 2, Box 271A Tullahoma, TN 37388 (615) 455-1982	
ENSOR, DAVID S. Research Triangle Institute P.O. Box 12194 Research Triangle Park, NC 27709 (919) 541-6735		FRY, EDWARD S. DR. Department of Physics Texas A&M University College Station, TX 77843 (713) 845-1910	

ATTENDEES LIST (continued)

GALLILY, ISAIAH PROF.
 Dept. of Atmospheric Sciences
 Hebrew University
 Jerusalem 91904, Israel
 02-639003

HANLEY, JAMES T.
 Calspan Corporation
 P.O. Box 400
 Buffalo, NY 14225
 (716) 632-7500

GAUSS, ARTHUR
 BRL
 Attn: DRDAR-BLB
 Aberdeen Proving Ground, MD 21005
 (301) 278-4884

HARACZ, DICK
 Dept. of Physics & Atmospheric Sciences
 Drexel University
 Philadelphia, PA 19104
 (215) 895-2719

GEBHARDT, FREDERICK G. DR.
 Science Applications, Inc.
 3 Preston Court
 Bedford, MA 01730
 (617) 275-2200

HARRIS, B. L. DR.
 The Engineering Research Co.
 of Glen Arm, MD, Inc.
 11323 Glen Arm Road
 Glen Arm, MD 21057
 (301) 668-7352

GHUNIEM, ATEF
 5773 Rayburn Ave., #260
 Alexandria, VA 22311
 (703) 671-4155

HERMAN, BENJAMIN M. PROF.
 Institute of Atmospheric Physics
 University of Arizona
 Tucson, AZ 85721
 (602) 621-6846

GILMAN, JERRY
 DRDAR-CLC-R
 phone: 3884
 CSL

HERMANN, GARY
 DRDAR-CLT-ST
 phone: 4168
 CSL

GLEESON, RICHARD
 Naval Weapons Center
 Code 3542
 China Lake, CA 93555
 (619) 939-6275

HESS, GEORGE DR.
 The Boeing Company
 P.O. Box 3999
 MS 8C-23
 Seattle, WA 98124
 (206) 773-9678

GOLDBERG, IRWIN S.
 Dept. of Engineering & Physics
 St. Mary's University
 San Antonio, TX 78284
 (512) 436-3305

HOLST, GERALD
 DRDAR-CLB-PS
 phone: 2326
 CSL

GOREN, SIMON L.
 Dept. of Chemical Engineering
 University of California
 Berkeley, CA 94720
 (415) 642-4574

HOLT, HOWARD DR.
 Cdr/Dir
 US Army ERADCOM
 Atmospheric Sciences Lab.
 White Sands Missile Range, NM 88002
 (505)

GUTHALS, PAUL
 MS J514
 Los Alamos National Lab.
 Los Alamos, NM 87545
 (505) 667-4039

HOLZE, DICK H.
 The Boeing Company
 P.O. Box 3999, MS 8C-23
 Seattle, WA 98124
 (206) 773-0368

ATTENDEES LIST (continued)

HONG, SEUNG-SOO DR.
Space Astronomy Lab.
University of Florida
1810 NW 6th St.
Gainesville, FL 32601
(904) 392-5450

HUTCHINS, DARRELL K.
University of Arkansas
Graduate Institute of Technology
1201 McAlmont
Little Rock, AR 72203
(501) 373-2734

HWANG, S. Y.
Dept. of Chemical Engineering
University of Maryland
College Park, MD 20742
(301) 454-5098/2341

JAGGARD, DWIGHT
Moore School of Electrical Engineering
University of Pennsylvania
Philadelphia, PA 19096
(215) 898-4411

JAKUBOWSKI, PAUL R. CSL
DRDAR-CLC-BK
phone: 3893

JENNINGS, S. G. DR.
Department of Physics
University College
Galway, Ireland
(091) 24411, ext. 704

JORDAN, ARTHUR DR.
Commander
Naval Research Laboratory
Code 7942
Washington, DC 20375
(202) 767-6609 or AV 297-6609

KAGAN, J. CSL
DRDAR-CLB-PS
phone: 2326

KAHN, MARVIN
SRI International
P.O. Box 5768
Pikesville, MD 21208
(301) 486-2728

KAUFMAN, YORAM J. DR.
NASA Goddard Space Flight Center
Attn: Code 915
Greenbelt, MD 20771
(301) 344-4977

KEEFER, DENNIS
Applied Physics Research Group
University of Tennessee Space Institute
Tullahoma, TN 37388
(615) 455-0631

KERKER, MILTON PROF.
Clarkson College of Technology
Potsdam, NY 13676
(315) 268-2390

KIMBALL, DAVID MR. CSL
DRDAR-CLB-PO
phone: 4194

KLETT, JAMES DR.
NRC Dr. Res. Assoc. at ASL
965 No. Alameda
Las Cruces, NM 88002
(505) 524-7505

KLUCHERT, R. E.
Canadian Defence Liaison Staff
2450 Massachusetts Ave.
Washington, DC 20008
(202) 483-5505 or AV 851-1840

KOHL, RONALD H. DR.
Ronald H. Kohl & Associates
R 2, Box 283B
Tullahoma, TN 37388
(615) 454-9060

LAMUTH, HENRY L.
Battelle Columbus Labs.
505 King Ave.
Columbus, OH 43201
(614) 424-4430

LANG, ROGER H.
Dept. of EECS
George Washington University
Washington, DC 20052
(202) 676-6199

ATTENDEES LIST (continued)

LATHAM, J. PROF.
 Dept. of Pure & Applied Physics
 U.M.I.S.T.
 P.O. Box 88
 Manchester M60 IQD, England
 061-236-3311, ext. 2962

LAWLESS, PHIL A.
 Research Triangle Institute
 Durham, NC 27709
 (919) 541-6782

LAX, MELVIN DR.
 12 High Street
 Summit, NJ 07901
 (201) 582-6527

LAYE, RANDOLPH G. CSL
 DRDAR-CLW-CR
 phone: 3505

LEE, KEN W. DR.
 Battelle Columbus Laboratories
 505 King Ave.
 Columbus, OH 43201
 (614) 424-4891

LESNIEWSKI, ROBERT CSL
 DRDAR-CLC-R
 phone: 734-6947

LEUNG, K. MING
 Department of Physics
 Polytechnic Institute of New York
 333 Jay St.
 Brooklyn, NY 11201
 (212) 643-3247

LOEROP, WILLIAM CSL
 DRDAR-CLC-R
 phone: 3884

MANNING, JOE
 Optimetrics, Inc.
 2000 Hogback Road #3
 Ann Arbor, MI 48104
 (313) 973-1177

MANUEL, HENRY CSL
 DRDAR-CLB-PS
 phone: 4294

MARKER, DOUGLAS L.
 Naval Surface Weapons Center
 Attn: F-11
 Dahlgren, VA 22448
 (703) 663-8781 or AV 249-8781

MASSOUDI, HABIB
 Electrical Engineering Department
 University of Utah
 Salt Lake City, UT 84112
 (801) 581-5827

MATHAI, C. V. DR.
 AeroVironment, Inc.
 145 N. Vista Ave.
 Pasadena, CA 91107
 (213) 449-4392

MATISE, BRIAN
 Optimetrics, Inc.
 2000 Hogback Road #3
 Ann Arbor, MI 48104
 (313) 973-1177

MILHAM, MERRILL CSL
 DRDAR-CLB-PS
 phone: 3854

MOELLER, K. D. PROF.
 Department of Physics
 Fairleigh Dickinson University
 Teaneck, NJ 07666
 (201) 692-2287

MONEYHUN, JACK H.
 Oak Ridge National Laboratory
 P.O. Box X
 Oak Ridge, TN 37830
 (615) 574-4869

MORSE, T. F. PROF.
 Division of Engineering
 Brown University
 Providence, RI 02912
 (401) 863-1444

MCMILLAN, RONNIE C.
 The BDM Corporation
 2227 Drake Ave.
 Huntsville, AL 35807
 (205) 882-4900

ATTENDEES LIST (continued)

PEARCE, WILLIAM A. DR.
EG&G
Washington Analytical Services Center
P.O. Box 398
Riverdale, MD 20737
(301) 779-2800, ext. 247

PEDERSEN, JEANNE DR.
Panametrics
221 Crescent Street
Waltham, MA 02154
(617) 899-2719

PEDERSEN, NORMAN DR.
Panametrics
221 Crescent Street
Waltham, MA 02154
(617) 899-2719

PENDLETON, J. DAVID
NAVELEX
ELEX 621
Washington, DC 20363
(202) 692-6413

PINNICK, RONALD DR.
Commander/Director
Atmospheric Sciences Laboratory
Attn: DELAS-EO-ME
White Sands Missile Range, NM 88002
(505) 678-5634 or AV 258-5634

PITTER, RICHARD L. DR.
Desert Research Institute
Atmospheric Sciences Center
P.O. Box 60220
Reno, NV 89506
(702) 972-1676

PLUCHINO, ANTONINO MR.
The Aerospace Corporation
Bldg. A 6-1647
P.O. Box 92957
Los Angeles, CA 90009
(213) 648-5000

PODZIMEK, JOSEF PROF.
Graduate Center for Cloud
Physics Research
109 Norwood Hall
University of Missouri-Rolla
Rolla, MO 65401
(314) 341-4338

POZIOMEK, ED CSL
DRDAR-CLB
phone: 3250

QUERRY, MARVIN PROF.
Department of Physics
University of Missouri
Kansas City, MO 64110
(816) 276-1604

RANADE, MADHAV DR.
Research Triangle Institute
P.O. Box 12194
Research Triangle Park, NC 27709
(919) 541-6925

RAUSA, MICHAEL D. CSL
DRDAR-CLB-TE
phone: 2107/2131

REAGAN, JOHN A. PROF.
Dept. of Electrical and Computer
Engineering
Engineering Bldg. #20
University of Arizona
Tucson, AZ 85721
(602) 621-6203

REITZ, RICHARD G.
Project Manager, Smoke/Obscurants
Bldg. 24
Aberdeen Proving Ground, MD 21005
(301) 278-4716/5355 or AV 283-4716/5355

RILEY, ERICA CSL
DRDAR-CLB-PS
phone: 4294

RILEY, MICHAEL A. CSL
DRDAR-CLB-PS
phone:

RIN, CHUN-HSUN DR. CSL
DRDAR-CLC-R
phone:

ROBERTS, DARYL L. DR.
SRI International
333 Ravenswood Ave.
Menlo Park, CA 94025
(415) 859-6224

ATTENDEES LIST (continued)

ROGNE, TIM
Optimetrics, Inc.
2000 Hogback Road #3
Ann Arbor, MI 48104
(313) 973-1177

ROSENWASSER, H. DR.
Naval Air Systems Command
AIR-320R
Washington, DC 20361
(202) 692-2521

RUBEL, GLENN O. MR. CSL
DRDAR-CLB-PS
phone: 2760

RUHNKE, LOTHAR H. DR.
Naval Research Laboratory
Code 4110
Washington, DC 20375
(202) 767-2951 or AV 297-2951

SALEH, HAMIDO A.
3200 S. 28th St., #202
Alexandria, VA 22302
(703) 845-0271

SALISBURY, DAVID CSL
DRDAR-CLB-PS
phone: 4294

SCHLEIN, MARK CSL
DRDAR-CLC-R
phone: 3884

SEDLACEK, WILLIAM A.
Los Alamos National Lab.
MS J514
P.O. Box 1663
Los Alamos, NM 87545
(505) 667-5442/4498

SHAW, DAVID DR.
Dept. of Electrical Engineering
SUNY-Buffalo
4232 Ridge Lea Road
Buffalo, NY 14226
(716) 831-3059

SMALLEY, HOWARD M.
Project Manager, Smoke/Obscurants
DRCPPM-SMK-T
Aberdeen Proving Ground, MD 21005
(301) 278-5411 or AV 283-5411

SMITH, R. B.
Optech, Inc.
701 Petrolia Road
Downsview, Ontario
Canada M3J 2N6
(416) 661-5904

SNELSON, ALAN DR.
Illinois Institute of Technology
Research Institute
10 W. 35th Street
Chicago, IL 60616
(312) 567-4260

STUEBING, EDWARD W. DR. CSL
DRDAR-CLB-PS
phone: 3089

SWAHN, FREDERICK, JR.
3322 Ady Road
Street, MD 21154
(301) 452-8577

THOMAS, ROBERT W. L. DR.
EG&G
Washington Analytical Services Center
6801 Kenilworth Ave.
Riverdale, MD 20737
(301) 779-2800, ext. 202

TILLERY, MARVIN
Los Alamos National Lab.
Los Alamos, NM 87545
(505) 667-

TOKUDA, ALAN
The Boeing Company
P.O. Box 3999
MS 8C-23
Seattle, WA 98124
(206) 773-2638

TOMASELLI, VINCENT PROF.
Physics Research Laboratory
Fairleigh Dickinson University
30 Van Orden Place
Hackensack, NJ 07601
(201) 692-2286

TURETSKY, ABE CSL
DRDAR-CLB-PS
phone: 2395

ATTENDEES LIST (continued)

UHRMACHER, J. CARL
Carltech Associates
P.O. Box 1158
Columbia, MD 21044
(301) 997-5155

WALLACE, JAMES DR.
Far Field, Inc.
6 Thoreau Way
Sudbury, MA 01776
(617) 443-9214

WANG, RU T. DR.
Space Astronomy Laboratory
University of Florida
1810 NW 6th Street
Gainesville, FL 32601
(904) 392-5450

WASEL, W. DAVID
DRDAR-CLB-PO
phone: 2796

CSL

WATERMAN, PETER DR.
Panametrics
8 Baron Park Lane
Burlington, MA 01803
(617) 272-4494

WEIL, HERSCHEL PROF.
Dept. of Electrical and Computer
Engineering
University of Michigan
Ann Arbor, MI 48109
(313) 764-0500

WEINMAN, JIM PROF.
Dept. of Meteorology
University of Wisconsin
1225 West Dayton St.
Madison, WI 53706
(608) 262-1905

WELLS, WILLARD H.
Tetrattech, Inc.
630 N. Rosemead Blvd.
Pasadena, CA 91107
(213) 449-6400

YEH, CAVOUR PROF.
EMtec Engineering, Inc.
Suite 2032
1100 Glendon Ave.
Los Angeles, CA 90024
(213) 825-2970

YEH, HSU-CHI
LoveIace - ITRI
P.O. Box 5890
Albuquerque, NM 87185
(505) 844-2151

YU, P.
Dept. of Chemical Engineering
University of Maryland
College Park, MD 20742
(301) 454-5098/2341

ZARDECKI, ANDREW
Los Alamos National Laboratory
MS B279
Attn: T-DOT
Los Alamos, NM 87545
(505) 667-7646

BLANK

APPENDIX C

AGENDA

1983 CSL SCIENTIFIC CONFERENCE ON OBSCURATION AND AEROSOL RESEARCH

20-24 June, Bldg. E4810 (Post Theater)

DETAILS OF EACH SESSION ARE GIVEN ON THE ENCLOSED LIST OF SESSION CONTENTS*

MONDAY 20 June

- 9:30 Registration Opens
10:00 Opening of Conference
Welcome - Dr. B. Richardson, Deputy Director, CSL
Administrative Remarks - R. Kohl
10:15 Smoke Research and Development Programs - G. Holst and E. Stuebing
11:45 Lunch
1:00 Session I.A. Physical and Chemical Properties of Aerosols:
Particle Formation, Evolution and Composition
2:25 Session I.B. Physical and Chemical Properties of Aerosols:
Plume Mechanics
3:55 Session I.C. Physical and Chemical Properties of Aerosols:
Particle Dynamics: Orientation Effects, Concentration
Sampling and Size/Shape Analysis (Talks 1-4)
5:35 Adjournment
Cocktails and dinner at The Red Fox, Bel Air, MD

TUESDAY 21 June

- 8:15 Session I.C. Physical and Chemical Properties of Aerosols:
Particle Dynamics: Orientation Effects,
Concentration Sampling and Size/Shape
Analysis (concludes with Talks 5-10)
10:45 Session I.D. Physical and Chemical Properties of Aerosols:
Aerosol Elimination
11:10 Session II.A. Aerosol Characterization Methods (Other than
Aerodynamic Methods - See Session I.C.):
Particle Shape Descriptions and the Value of
Effective Size Parameters
12:10 Lunch
1:25 Session II.B. Aerosol Characterization Methods:
Optical Inversion Methods for Size Distribution
(Including Optical Particle Size Analyzers)
4:15 Session II.C. Aerosol Characterization Methods:
Optical Constants of Liquids and Powders (Talks 1-3)
5:20 Adjournment
Cocktails and dinner at Hausner's Restaurant, Baltimore, MD
or
Cocktails and dinner at Giovanni's, Edgewood, MD

*Half hour breaks are scheduled beginning near 10:00 a.m. (± 15 minutes)
and near 3:15 p.m. (± 15 minutes).

WEDNESDAY 22 June

- 8:15 Session II.C. Aerosol Characterization Methods:
Optical Constants of Liquids and Powders
(concludes with Talks 4-6)
- 9:15 Session III.A. Optical Properties of Aerosols:
Infrared Emission from Aerosols
- 10:40 Session III.C. Optical Properties of Aerosols:
Interaction of Radiation and Spherical (Including
Layered) Particles (Talks 1-5)
- 12:20 Lunch
- 1:35 Session III.C. Optical Properties of Aerosols:
Interaction of Radiation and Spherical Particles
(concludes with Talks 6 & 7)
- 2:15 Session III.B. Optical Properties of Aerosols:
Nonlinear Phenomena at High Energy
- 5:25 Adjournment to
Happy Hour at Officers Club followed by
Beef and Burgundy Dinner at the Officers Club
(casual dress, service from 6:00 to 8:00)

THURSDAY 23 June

- 8:15 Session III.D. Optical Properties of Aerosols:
Interaction of Radiation and Nonspherical Particles
(Including Aggregates) with or without Cooperative
Effects (Talks 1-11)
- 12:15 Lunch
- 1:30 Session III.D. Optical Properties of Aerosols:
Interaction of Radiation and Nonspherical Particles
with or without Cooperative Effects (concludes
with Talks 12-17)
- 4:20 Session III.E. Optical Properties of Aerosols:
Propagation/Multiple Scattering in Aerosol Media
and Radiative Transfer (Talks 1-4)
- 5:40 Adjournment
- 6:30 Crab Feast at Gabler's Shore Restaurant on the
Bush River (hamburger & chicken available)

FRIDAY 24 June

- 8:15 Session III.E. Optical Properties of Aerosols:
Propagation/Multiple Scattering in Aerosol Media
and Radiation Transfer (concludes with Talks 5-10)
- 10:45 Session IV. Discussion: Directions for Future Research in
the Army Smoke Program
- 12:00 Adjournment

APPENDIX D

SESSION CONTENTS

1983 CSL SCIENTIFIC CONFERENCE ON OBSCURATION AND AEROSOL RESEARCH

20-24 June

I. Physical and Chemical Properties of Aerosols

A. Particle Formation, Evolution and Composition (Mon. p.m.)

1. Rose S. Brazell, Jack H. Moneyhun and R. W. Holmberg (Oak Ridge National Laboratory), Chemical Composition of Phosphorus Smoke
2. Alan Snelson (IIT Research Institute), Cryogenic Sampling and IR Analysis of Phosphorus Acid Aerosols
3. A. W. Castleman, Jr. (Pennsylvania State University), The Photoionization of Clusters and the Onset of Metallic Conductivity
4. J. R. Brock (University of Texas), Ferromagnetic Chain Aerosol Growth Processes

B. Plume Mechanics (Mon. p.m.)

1. John Latham (U.M.I.S.T.), Turbulent Mixing Processes
2. J. R. Brock (University of Texas), Aerosol Plume Dispersion
3. Jack Cermak (Colorado State University), Effects of Atmospheric Stability on Dispersion

C. Particle Dynamics: Orientation Effects, Concentration Sampling, and Size/Shape Analysis (Mon. p.m. & Tues. a.m.)

1. Walter Frost (FWG Associates, Inc.), Review of Analytical Modeling Techniques for Two-Phase Flow Applicable to Explosive Dissemination of Aerosol Particles
2. M. B. Ranade (Research Triangle Institute), Deagglomeration of Powders
3. David Shaw (State University of New York), The Generation, Dispersion, and Measurement of Fiber-Like and Flake-Like Particles: A General Review and Recent Results
4. Isaiah Gallily (Hebrew University), The Orientation Distribution of Nonspherical Aerosol Particles in the Atmosphere: New Developments

SESSION CONTENTS (continued)

I.C. (continued)

5. P. Yu and James Gentry (University of Maryland), A Critical Comparison of Inversion Algorithms for Size and Mobility Distributions
6. H. C. Yeh, G. J. Newton and Y. S. Cheng (Lovelace-ITRI), Aerosol Size Measurements for Inhalation Toxicity Studies
7. S. W. Davidson and James Gentry (University of Maryland), A Review of Models for Diffusion Charging of Free Molecule Transition Regime Aerosol Particles
8. Glenn O. Rubel and James Gentry (University of Maryland), Measurement of the Kinetics of Solution Droplets in Continuously Mixed Chambers
9. Ken W. Lee (Battelle Columbus Laboratories), Time Evolution of the Particle Size Distribution During Aerosol Coagulation
10. Daryl L. Roberts (SRI International), Coagulation of Charged, Nonspherical Particles

D. Aerosol Elimination (Tues a.m.)

1. Josef Podzimek and J. J. Martin (University of Missouri), Progress in the Clearing or Modifying of Aerosol Clouds by Scavenging Techniques

II. Aerosol Characterization Methods (Other than Aerodynamic Methods - See Session I-C)

A. Particle Shape Descriptions and the Value of Effective Size Parameters (Tues a.m.)

1. Isaiah Gallily (Hebrew University), What is the Physical Meaning of a "Size" of a Nonspherical Aerosol Particle? Fallacies and Possible Solution
2. David Shaw (State University of New York), Irregular Particle Effective Size and Shape Factors: A Review of Their Importance and Implications to Obscuration and Aerosol Research
3. Peter Barber (Clarkson College), presented by Ed Stuebing (CSL), Analogs to the Size Parameter Observed in Optical Calculations

SESSION CONTENTS (continued)

B. Optical Inversion Methods for Size Distribution (Including Optical Particle Size Analyzers) (Tues p.m.)

1. James Klett (ASL), A New Method of Multi-Spectral Inversion Based on the Anomalous Diffraction Model
2. A. K. Jordan (Naval Research Laboratory) and Dwight Jaggard (University of Pennsylvania), Inverse Methods for Polydisperse Distributions
3. B. P. Curry and E. L. Kiech (Calspan), A Constrained Eigenfunction Expansion Method and a Nonlinear Regression Procedure for the Inversion of Mie Scattering Data
4. David Capps and G. M. Hess (Boeing Aerospace Company), Quantitative Determination of the Effects of Constraints on Solutions to Inversion Problems
5. R. L. Adams, David Capps and G. M. Hess (Boeing Aerospace Company), Inversion of Simulated Experimental Data to Obtain Size Distributions (not presented)
6. William Pearce (EG&G), Comments on the Inference of Aerosol Size Distributions
7. Benjamin Herman (University of Arizona), Inversion Studies to Recover Non-Smoothed Size Distributions

C. Optical Constants of Liquids and Powders (Tues p.m. & Weds a.m.)

1. Petr Chylek (New Mexico State University), Refractive Index of Composite Aerosol Particles
2. Marvin Querry (University of Missouri), Optical Properties of Solids and Powders
3. Ralph Alexander, R. J. Bell, M. A. Ordal and L. L. Long (University of Missouri), Optical Constants of Natural Minerals in the Far Infrared
4. Ray Paul, Mark A. Ordal, L. L. Long, R. W. Alexander and R. J. Bell (University of Missouri), Electromagnetic Properties of Some Metals in the mm Wavelength Region
5. Karl Möller (Fairleigh Dickinson University), Wavefront Dividing Beam Splitter for Michelson Interferometers
6. Vincent Tomaselli (Fairleigh Dickinson University), ATR Method for Determining Optical Constants of Powders

SESSION CONTENTS (continued)

III. Optical Properties of Aerosols

A. Infrared Emission from Aerosols (Weds a.m.)

1. R. Mackay and M. Suresh (Drexel University), Infrared Emission from Gas-Aerosol Reaction (not presented)
2. P. Ase (IIT Research Institute), IR Emissive Clouds Based on Aluminum Alkyls
3. W. H. Wurster and T. M. Albrechtinski (Calspan ATC) and G. Hermann (CSL), Facility for Ranking Emissive Smoke Performance; Early Results (not presented)

B. Nonlinear Phenomena at High Energy (Weds p.m. after III.C)

Reviews

1. James Wallace (Far Field, Inc.), Modeling High Energy Laser Propagation through Smokes: A Review
2. David Smith (United Technology Research Center), Aerosol-Induced Gas Breakdown and Thermal Blooming: A Review

Current and Future Work and Needs

3. Fred Gebhardt (SAI), Nonlinear Aerosol Propagation Effects Modeling
4. Janon Embury (CSL), Extinction Mechanics at High Energies in Aerosols
5. Henry LaMuth (Battelle Columbus Laboratories), Interaction of a 5 kW Laser Beam with Particulate Aerosols
6. Melvin Lax (City College of New York), Interaction of HEL Radiation with Matter

Discussion: Directions for Future Research in High Energy Laser Propagation in Aerosols

C. Interaction of Radiation and Spherical (Including Layered) Particles (Weds a.m. & p.m.)

1. Ted Morse (Brown University), Laser-Induced Thermophoresis in Aerosol Particles
2. Stephen Arnold (Polytechnical Institute of New York), Experimental Basis for the Theory of Photophoresis: Critical Tests

SESSION CONTENTS (continued)

III.C. (continued)

3. A. B. Pluchino (The Aerospace Corporation), Diffraction and the Radiometric Levitation of Spherical Carbon Particles
 4. Milton Kerker (Clarkson College), Surface Enhanced Raman Scattering (Theory)
 5. Milton Kerker (Clarkson College), Surface Enhanced Raman Scattering (Experiments)
 6. K. Ming Leung (Polytechnical Institute of New York), Quantum Size Effects in the Scattering of Light from Small Metal Particles
 7. Ezekiel Bahar (University of Nebraska), Scattering Cross Sections for Large Finitely Conducting Spheres with Rough Surfaces--Full Wave Solutions
- D. Interaction of Radiation and Nonspherical Particles (Including Aggregates) with or without Cooperative Effects (Thurs a.m. & p.m.)
1. A. Coletti (Georgia Tech), Light Scattering by Non-Homogeneous Particles: Measurements and Interpretation
 2. R. T. Wang (University of Florida), Extinction by Randomly Oriented Nonspherical Particles
 3. R. T. Wang (University of Florida), Angular Scattering and Polarization by Randomly Oriented Dumbbells and Chains of Spheres
 4. David Capps, A. R. Tokuda and G. M. Hess (Boeing Aerospace Company), Fourier Analysis of Light Scattered from Nonspherical Particles
 5. William S. Bickel (University of Arizona), Information Content in the Matrix Elements of Complex Scattering Systems: Its Masking and Its Sensitivity to Structural Changes in the Scatterer
 6. T. B. A. Senior and H. Weil (University of Michigan), Structure of Polariton Modes
 7. R. G. Pinnick (ASL), Infrared Scattering Characteristics of Spheroidal Dust Particles
 8. D. T. Auckland and R. H. Andreo (Syracuse Research Corporation), A Method-of-Moments, Triangular-Surface-Patch Technique for the Extinction by Arbitrarily-Shaped Particles

SESSION CONTENTS (continued)

III.D. (continued)

9. Habib Massoudi (University of Utah), An Improved Method for Calculation of Electromagnetic Scattering Cross-Section: Particles with Arbitrary Shape
 10. Peter Barber (Clarkson College) and Richard Chang (Yale University), Scattering and Absorption by Conductive Particles
 11. Dick Holze, David Dye and G. M. Hess (Boeing Aerospace Company), Extinction of Electromagnetic Radiation by Fine Conducting Fibers
 12. David Dye, Dick Holze, G. M. Hess (Boeing Aerospace Company) and Robert L. Dow (CSL), Theoretical Investigation of Fibers
 13. Melvin Lax (City College of New York), New Theoretical Approach to Scattering from Thin Fibers
 14. Len Cohen, Ariel Cohen and Dick Haracz (Drexel University), Light Scattering from Finite Cylinders
 15. Dick Haracz, Len Cohen and Ariel Cohen (Drexel University), Scattering from Finite Cylinders: The Internal Field
 16. Jeanne Pedersen and Norman Pedersen (Panametrics), Absorption and Scattering by Conductive Fibers
- E. Propagation/Multiple Scattering in Aerosol Media and Radiative Transfer
(Thurs p.m. & Fri a.m.)
1. Peter Waterman, Jeanne Pedersen and Norman Pedersen (Panametrics), Radiation Transfer by Conductive Fibers
 2. Ariel Cohen, Len Cohen and Dick Haracz (Drexel University), Multiple Scattering and Long Cylinders
 3. S. G. Jennings (University College, Ireland), R. G. Pinnick (ASL), and W. T. Grandy, Jr. (University of Wyoming), Measurements of Backscatter and Extinction in Water Clouds
 4. R. B. Smith, A. I. Carswell and J. D. Houston (Optech), Backscattering of 1.06 μm Radiation from Dense Clouds
 5. Robert W. L. Thomas (EG&G), Radiative Transfer Modeling and Characterization in Arrays of Finite Clouds
 6. R. A. Elliott (Oregon Graduate Center), Multiple Scattering of Optical Pulses in Scale Model Clouds
 7. A. Zardecki and S. Gerstl (Los Alamos National Laboratory) and J. F. Embury (CSL), Multiple Scattering Induced False Targets

SESSION CONTENTS (continued)

III.E. (continued)

8. Cavour Yeh (EMtec), Scattering by an Ensemble of Nonspherical Particles
 9. V. K. Varadan and V. V. Varadan (Pennsylvania State University), Polarization-Dependent Wave Propagation in Random Distributions of Nonspherical Dielectric Scatterers (not presented)
 10. R. H. Andreo (Syracuse Research Corporation), Dispersion Relations from the Method of Smoothing for Coherent Wave Propagation in Discrete Random Media
 11. Willard Wells (Tetrattech, Inc.) Radiation Transfer with Strong Forward Scattering
- IV. Discussion: Directions for Future Research in the Army Smoke Program (Fri a.m.)

☆U.S. GOVERNMENT PRINTING OFFICE: 1984 461 025 20085